Ultimate Limit State Design of Steel-Plated Structures

Jeom Kee Paik

Department of Naval Architecture and Ocean Engineering
Pusan National University, Korea

Anil Kumar Thayamballi

Chevron Shipping Company
San Ramon, USA

JOHN WILEY & SONS, LTD

John Wiley & Sons Ltd, The Atrium, Southern Gate, Chichester,
West Sussex PO19 8SQ, England

Telephone (+44) 1243 779777

Email (for orders and customer service enquiries): cs-books@wiley.co.uk
Visit our Home Page on www.wileyeurope.com or www.wiley.com

Other Wiley Editorial Offices

John Wiley & Sons Inc., 111 River Street, Hoboken, NJ 07030, USA

Jossey-Bass, 989 Market Street, San Francisco, CA 94103-1741, USA

Wiley-VCH Verlag GmbH, Boschstr. 12, D-69469 Weinheim, Germany

John Wiley & Sons Australia Ltd, 33 Park Road, Milton, Queensland 4064, Australia

John Wiley & Sons (Asia) Pte Ltd, 2 Clementi Loop #02-01, Jin Xing Distripark, Singapore 129809

John Wiley & Sons Canada Ltd, 22 Worcester Road, Etobicoke, Ontario, Canada M9W 1L1

Wiley also publishes its books in a variety of electronic formats. Some content that appears in print may not be available in electronic books.

Library of Congress Cataloging-in-Publication Data

Paik, Jeom Kee.
Ultimate limit state design of steel plated structures / Jeom Kee Paik, Anil Kumar Thayamballi.
p. cm.
Includes bibliographical references and index.
ISBN 0-471-48632-9 (alk. paper)
1. Building, Iron and steel. 2. Plates, Iron and steel. I. Thayamballi, Anil Kumar, II. Title.
TA684.P24 2003
624.1′821–dc21 2002029648

British Library Cataloguing in Publication Data

A catalogue record for this book is available from the British Library

ISBN 0-471-48632-9

Typeset in 10/12pt Times by Laserwords Private Limited, Chennai, India
Printed and bound in Great Britain by Biddles Ltd, Guildford, Surrey
This book is printed on acid-free paper responsibly manufactured from sustainable forestry in which at least two trees are planted for each one used for paper production.

Contents

Preface

Steel-plated structures are important in a variety of marine and land-based applications, including ships, offshore platforms, box girder bridges, power/chemical plants, bins, bunkers and box girder cranes. The basic strength members in steel-plated structures include support members (such as stiffeners, plate girders), plates, stiffened panels/grillages, and box girders. During their lifetime, the structures constructed using these members are subjected to various types of loading which is for the most part operational, but may in some cases be extreme or even accidental.

In the past, criteria and procedures for the design of steel-plated structures were primarily based on allowable stresses and simplified buckling checks for structural components. However, it is now well recognized that the limit state approach is a better basis for design since it is difficult to determine the real safety margin of any structure using linear elastic methods alone. It also readily follows that it is of crucial importance to determine the true limit state if one is to obtain consistent measures of safety which can then form a fairer basis for comparisons of structures of different sizes, types and characteristics. An ability to better assess the true margin of safety would also inevitably lead to improvements in related regulations and design requirements as well.

The design of marine structures such as FPSOs (floating, production, storage and offloading systems), mobile offshore drilling units, the deck structures of jacket platforms and even relatively novel concepts such as tension leg platforms by and large now tends to be perhaps less limit state oriented than land-based structures such as bridges, where the preference is now clearly for limit state design.

To obtain a safe and economic structure, the limit-state-based capacity as well as structural behavior under known loads must be assessed accurately. The structural designer can perform such a relatively refined structural safety assessment even at the preliminary design stage if there are simple expressions available for predicting the limit state behavior accurately. A designer may even desire to do this not only for the intact structure, but also for structures with premised damage, in order to assess their damage tolerance and survivability.

Most structural engineers in the industry are very skilled and well experienced in the practical structural design aspects based on the traditional criteria, but may need a better background in the concept of limit state design and related engineering tools and data. Hence there is a need for a relevant engineering book on the subject, which has an exposition of basic knowledge and concepts. Many structural specialists in research institutes continue to develop more advanced methodologies for the limit state design of steel-plated structures, but may sometimes lack the useful engineering data to validate them. Students in universities want to learn more about the fundamentals and practical

procedures regarding the limit state design, and thus need a book that provides useful insights into the related disciplines.

This book reviews and describes both fundamentals and practical design procedures for the ultimate limit state design of ductile steel-plated structures. Serviceability limit state based on buckling and accidental limit state based on collision and grounding accidents are also described. Existing mechanical model test results as well as nonlinear finite element solutions are included where relevant. The book is basically designed as a textbook so that the derivation of the basic mathematical expressions is presented together with a thorough discussion of the assumptions and the validity of the underlying expressions and solution methods.

It is the intention of the authors that the reader should be able to obtain an insight into a wider spectrum of limit state design considerations in both an academic and a practical sense. The present book is also to be seen in part as an easily accessed design tool box that hopefully facilitates learning by applying the concepts of the limit state for practice. Selected computer software which automates design methodologies or expressions presented in the book will hence be made available on an as-is basis through an internet web site. The user's manuals for the software, including illustrative example data sheets, will also be provided at the web site as noted in the appendices to this book.

The present book is primarily based on the two authors' own insights and developments obtained over more than a total of 40 years of professional experience, as well as existing information and findings by numerous other researchers and limit state practitioners. Wherever possible, we have tried our best to acknowledge the invaluable efforts of other investigators and practitioners, and if we have failed anywhere in this regard, it was solely inadvertent. Any additional information brought to our notice in this regard will of course be included in the future editions of this book.

The initiation of this book originated from a desire to summarize existing knowledge and also bring more advanced developments and insights obtained through various research projects undertaken by the Pusan National University, the American Bureau of Shipping (ABS), and of course many others in the past several years. In this regard, sincere thanks are given to many ABS staff members including Dr. Donald Liu, Dr. John Spencer, Dr. Yung Sup Shin and Dr. Ge Wang. Dr. Anil K. Thayamballi formerly worked for ABS for a number of years.

We are very pleased to acknowledge all those individuals who helped make this book possible. Dr. Ge Wang (American Bureau of Shipping, USA) and Prof. Manolis Samuelides (National Technical University of Athens, Greece) were involved in writing major sections of Chapter 9, while Prof. Weicheng Cui (Shanghai Jiaotong University, China) was involved in writing major sections of Chapter 10.

A number of experts kindly reviewed the draft manuscript and provided quite valuable and comprehensive comments to improve it at an earlier stage. Prof. Rene Maquoi (University of Liege, Belgium) reviewed Chapter 7. Prof. Norman Jones (University of Liverpool, UK) reviewed Chapter 9. Prof. Susumu Machida (Chiba University, Japan) reviewed Chapter 10. Mr. Hwa Soo Kim (Hyundai Heavy Industries, Korea) reviewed major parts of the entire draft manuscript. Prof. Toshiyuki Kitada (Osaka City University, Japan) and Prof. Norman Jones (University of Liverpool, UK) provided a number of useful references for Chapters 7 and 9, respectively. Dr. Ge Wang (American Bureau of Shipping, USA) provided some illustrations for Chapter 8, while Dr. Shengming Zhang (Lloyd's Register of Shipping, UK) and Prof. Preben T. Pedersen (Technical University of Denmark, Denmark) provided some illustrations for Chapter 9.

In the initial stage of organizing the table of contents for this book, a number of experts, colleagues and friends provided valuable comments and interests. These individuals, in alphabetical order of their names include: Prof. Bilal M. Ayyub (University of Maryland, USA), Dr. Yong Bai (Doris Inc., USA), Prof. Wolfgang Fricke (University of Hamburg, Germany), Dr. Paul A. Frieze (PAFA Consulting Engineers, UK), Prof. Owen F. Hughes (Virginia Polytechnic Institute and State University, USA), Prof. Toshiyuki Kitada (Osaka City University, Japan), Prof. Jae Wook Lee (Inha University, Korea), Prof. Alaa E. Mansour (University of California at Berkeley, USA), Prof. Robert E. Melchers (The University of Newcastle, Australia), Prof. Preben T. Pedersen (Technical University of Denmark, Denmark), Dr. Sherif M. H. Rashed (MSC Software Japan Ltd., Japan), Dr. Philippe Rigo (University of Liege, Belgium), Prof. Yutaka Toi (Tokyo University, Japan), Prof. Yasumitsu Tomita (Osaka University, Japan), Prof. Yukio Ueda (Kinki University, Japan), Prof. Tomasz Wierzbicki (Massachusetts Institute of Technology, USA) and Prof. Tetsuya Yao (Osaka University, Japan).

We gratefully acknowledge permission from Elsevier Science to reprint the following:

Chapter 11 and Figures 11.1–11.16 from *Thin Walled Structures*, Vol. 39, Paik, J.K., Thayamballi, A.K., Lee, S.K. & Kang, S.J. A semi-analytical method for the elastic–plastic large deflection analysis of welded steel or aluminum plating under combined in-plane and lateral pressure loads, 125–152, 2001. Figures 6.10(a)–(c) from *Thin Walled Structures*, Vol. 40, Paik, J.K. & Kim, B.J. Ultimate strength formulations for stiffened panels under combined axial load, in-plane bending and lateral pressure: a benchmark study, 45–83, 2002. Figures 9.31(a) and (b) and 9.34(a) and (b) from *Ocean Engineering*, Vol. 27, Pedersen, P.T. & Zhang, S. Effect of ship structure and size on grounding and collision damage distributions, 1161–1179, 2000.

We also acknowledge the extensive efforts of graduate students at the Ship Structural Mechanics Laboratory of the Pusan National University, without whose interest and dedication to learning this book would not have been possible. In particular, special thanks are given to Young Il Park, Bong Ju Kim and Man Ju Ko, who carried out various numerical computations for this book, and also developed many of the illustrations in this book.

Finally, we take this opportunity to thank our wives and families for their unfailing patience and support while this book was being written.

Jeom Kee Paik
Anil Kumar Thayamballi
February 2002

About the Authors

Jeom Kee Paik is Professor of Ship Structural Mechanics at the Pusan National University, Korea. He received his Bachelor of Science degree from the Pusan National University in 1981 and both the Master of Engineering (1984) and Doctor of Engineering (1987) degrees from Osaka University, Japan, from the faculties of naval architecture and ocean engineering. He has 20 years experience in teaching and research in the areas of limit state design, ultimate strength, impact mechanics (e.g. collision and grounding), fracture mechanics, age related degradation models and reliability of steel and aluminum alloy structures. Currently he is a standing committee member of the Royal Institution of Naval Architects in London. He has taken part in the activities of the International Ship and Offshore Structures Congress (ISSC). He has been a member of the ISSC Technical Committee on Ultimate Strength, and he currently chairs the ISSC Specialist Committee on Collision and Grounding. Prof. Paik is the author or co-author of over 300 publications in journals, conference proceedings and research reports. He is also the author of several textbooks and book chapters including *Computational Analysis of Complex Structures* published by the American Society of Civil Engineers (ASCE). He has received outstanding paper awards from the Royal Institution of Naval Architects (1995), the Society of the Naval Architects of Korea (1996), the Association of the Korea Science and Engineering Societies (1996) and the (US) Society of Naval Architects and Marine Engineers (2000). He is listed in the *Marquis Who's Who in Science and Engineering*, and *Who's Who in the World*. He was recently elected by the *Barons Who's Who* as one of the 500 new-century leaders for technology in the world as well as in Asia. Prof. Paik's e-mail address is `jeompaik@pusan.ac.kr`.

Anil K. Thayamballi is a senior staff consultant with the Marine Services Group of the Chevron Shipping Company, San Ramon, California, specializing in marine structural design and life cycle care. He obtained his Bachelor of Technology degree, with honors, from the Indian Institute of Technology at Kharagpur, and his Masters and Ph.D. degrees from the University of California at Berkeley, from the departments of naval architecture and offshore engineering. During and subsequent to his graduate studies, he worked for Mansour Engineering Consultants in Berkeley, California, and Imodco Offshore in Calabasas, California, in addition to a long stint at the marine classification society, American Bureau of Shipping, in New York. He was also Visiting Lecturer in Naval Architecture and Offshore Engineering at the University of California at Berkeley for two years. Dr. Thayamballi's professional experience spans 20 years. He has served on the ASCE Committee for Fatigue and Fracture Reliability, the American Petroleum Institute Resource Group RG-4 on Structural Element Behavior, and on the International Ship and Offshore

Structures Congress Technical Committee on Design Procedures and Philosophy, including as its Chairman. He currently serves on the Marine Technology Committee of the Society of Naval Architects and Marine Engineers (SNAME) in New York. Dr. Thayamballi is the author or co-author of over 60 refereed technical publications in the areas of limit state design, ultimate strength, fracture mechanics, fatigue technology, and reliability of steel structures. He received an outstanding paper award from SNAME in 2000 for a joint paper with Prof. Paik. He currently lives in Lafayette, California, in the San Francisco Bay area. Dr. Thayamballi's e-mail address is `athayamballi@compuserve.com`.

How to Use This Book

The intention behind writing this book is to develop a textbook and handy source to the principles of limit state design of steel-plated structures. This book has been designed to be well suited to university students who would be approaching the limit state design technology of steel-plated structures perhaps for the first time. In terms of more advanced and sophisticated design methodologies being presented, the book should also meet the needs of structural designers or researchers who are involved in the field of naval architecture, offshore, civil, architectural and mechanical engineering.

Hence, apart from its value as a ready reference and an aid to continuing education for the established practitioners, this book can be used as a textbook in teaching courses on limit state design of steel structures at the university level. The book in fact perhaps covers a wide enough range of topics which may be considered for more than one semester course! A teaching course of 45 hours for undergraduate students in structural mechanics or thin-walled structures may cover Chapter 1, Principles of Limit State Design, Chapter 2, Buckling and Ultimate Strength Behavior of Plate–Stiffener Combinations: Beams, Columns and Beam–columns, Chapter 3, Elastic and Inelastic Buckling of Plates, Chapter 5, Elastic and Inelastic Buckling of Stiffened Panels and Grillages, and Chapter 7, Ultimate Strength of Plate Assemblies: Plate Girders, Box Columns/Girders and Corrugated Panels. During that course, it is suggested that the student should carry out practice problems related to the design of steel-plated structures using the computer programs introduced in this book and available from the web site given in the appendices.

For graduate students who pass the teaching course for the undergraduate students noted above, a more advanced course of 45 hours may cover Chapter 1, Principles of Limit State Design (repeated), Chapter 4, Post-buckling and Ultimate Strength Behavior of Plates, Chapter 6, Post-buckling and Ultimate Strength Behavior of Stiffened Panels and Grillages, Chapter 8, Ultimate Strength of Ship Hulls (for students on a naval architecture course), Chapter 9, Impact Mechanics and Structural Design for Accidents, Chapter 10, Fracture Mechanics and Ultimate Strength of Cracked Structures, and together with hands-on practice of ultimate limit state design using in part the related computer programs.

Chapters 11, 12 and 13 as well as the rest of the chapters may be utilized by practitioners in industry or research institutes both for their work and for continuing education where desired. The computer programs together with more sophisticated design methodologies presented in this book will certainly be very useful for those researchers who want to study, facilitate and develop more advanced design concepts. The authors, in any event, have attempted to serve these many lofty aims in developing this book. They sincerely hope that their effort has been successful, however modestly!

1 Principles of Limit State Design

1.1 Design Philosophies for Steel Structures

Steel-plated structures are likely to be subjected to various types of loads and deformations arising from service requirements that may range from the routine to the extreme or accidental. The mission of the structural designer is to design a structure that can withstand such demands throughout its expected lifetime.

In design, the structure is hence required to have an adequate margin of safety against such demands, the safety factor being necessary to account for various uncertainties due to natural variability, inaccuracy in procedures used for the evaluation and control of loads or load effects (e.g., stress, deformation), similar uncertainties in structural resistance (capacity) and its determination, and also variations in building procedures.

A 'demand' is analogous to load, and a 'capacity' is analogous to strength necessary to resist that load, both measured consistently (e.g., as stress, deformation, resistive or applied load or moment, or energy either lost or absorbed, and so on). The partial safety-factor-based design criterion for a structure under multiple types of loads applied at the same time is expressible as follows:

$$D_\mathrm{d} < C_\mathrm{d} \quad \text{or} \quad \text{safety measure} = C_\mathrm{d}/D_\mathrm{d} > 1 \tag{1.1}$$

where $D_\mathrm{d} = \gamma_0 \sum_i D_{\mathrm{k}i}(F_{\mathrm{k}i}, \gamma_{\mathrm{f}i})$ = design 'demand', $C_\mathrm{d} = C_\mathrm{k}/\gamma_\mathrm{M}$ = design 'capacity', $D_{\mathrm{k}i}(F_{\mathrm{k}i}, \gamma_{\mathrm{f}i})$ = characteristic measure of demand for load type i, calculated from the characteristic measures of loads, F_k, and magnified by the partial safety factor, γ_f, taking account of the uncertainties related to loads, γ_0 = partial safety factor taking into account the degree of seriousness of the particular limit state in regard to safety and serviceability accounting of economical and social consequences as well as any special circumstance (e.g., the mission of the ship, type of cargo, interaction of the limit state considered with the others, etc.), C_k = characteristic measure of capacity, $\gamma_\mathrm{M} = \gamma_\mathrm{m}\gamma_\mathrm{c}$ = capacity-related safety factor, γ_m = partial safety factor taking account of the uncertainties due to material properties, γ_c = partial safety factor taking account of the uncertainties on the capacity of the structure, such as quality of the construction, corrosion, method considered for determination of the capacity. More discussion about the design format may be found in Section 1.10.

A nominal or characteristic measure of demand or capacity is defined to correspond to a specified percentage of the area below the probability curve for the corresponding random variable. For instance, one may base characteristic strength or capacity on a lower bound or 95% exceedence value, while a characteristic load or demands may be based on an upper bound or a 5% exceedence value. The partial safety factors applied may be based on past experience, but are in principle meant to provide an acceptable level of safety or performance. To achieve a successful design, criteria similar to Equation (1.1) must be satisfied for each limit state for which structural performance must be assured.

Limit state design is different from the traditional allowable stress design. In the allowable stress design, the focus is on keeping the stresses resulting from the design loads under a certain working stress level that is usually based on successful similar past experience. In the marine context, regulatory bodies or classification societies usually specify the value of the allowable stress as some fraction of the mechanical properties of materials (e.g., uniaxial yield or ultimate tensile strength).

In contrast to the allowable stress design, the limit state design is based on the explicit consideration of the various conditions under which the structure may cease to fulfill its intended function. For these conditions, the applicable capacity or strength is estimated and used in design as a limit for such behavior.

The load-carrying capacity of a structure is for this purpose normally evaluated using simplified design formulations or by using more refined computations such as nonlinear elastic–plastic large-deformation finite element analyses with appropriate modeling related to geometric/material properties, initial imperfections, boundary condition, load application, and finite element mesh sizes, as appropriate.

During the last two decades, the emphasis in structural design has been moving from the allowable stress design to the limit state design since the latter approach makes possible a rigorously designed, yet economical, structure considering the various relevant modes of failure directly.

A limit state is formally defined by the description of a condition for which a particular structural member or an entire structure fails to perform the function that is expected of it. From the viewpoint of a structural designer, four types of limit states are considered for steel structures, namely:

- serviceability limit state (SLS);
- ultimate limit state (ULS);
- fatigue limit state (FLS); and
- accidental limit state (ALS).

SLS conventionally represents failure states for normal operations due to deterioration of routine functionality. SLS considerations in design may address:

- local damage which reduces the durability of the structure or affects the efficiency of structural elements;
- unacceptable deformations which affect the efficient use of structural elements or the functioning of equipment relying on them;
- excessive vibration or noise which can cause discomfort to people or affect the proper functioning of equipment; and
- deformations and deflections which may spoil the aesthetic appearance of the structure.

ULS (also called ultimate strength) typically represents the collapse of the structure due to loss of structural stiffness and strength. Such loss of capacity may be related to:

- loss of equilibrium in part or of entire structure, often considered as a rigid body (e.g., overturning or capsizing);
- attainment of the maximum resistance of structural regions, members or connections by gross yielding, rupture or fracture; and
- instability in part or of the entire structure resulting from buckling and plastic collapse of plating, stiffened panels and support members.

FLS represents fatigue crack occurrence of structural details due to stress concentration and damage accumulation (crack growth) under the action of repeated loading.

ALS represents excessive structural damage as a consequence of accidents, e.g., collisions, grounding, explosion and fire, which affect the safety of the structure, environment and personnel.

It is important to emphasize that in limit state design, these various types of limit states may be designed against different safety levels, the actual safety level to be attained for a particular type of limit state being a function of its perceived consequences and ease of recovery from that state to be incorporated in design. Within the context of Equation (1.1), for useful guidelines in determining the partial safety factors related to limit state design of steel structure, ISO 2394 (1998), NTS (1998) and ENV 1993-1-1 (1992) of Eurocode 3 may be referred to.

1.2 Considerations in Limit State Design

1.2.1 Serviceability Limit State Design

The structural design criteria used for the SLS design of steel-plated structures are normally based on the limits of deflections or vibration for normal use. In reality, excessive deformation of a structure may also be indicative of excessive vibration or noise, and so, certain interrelationships may exist among the design criteria being defined and used separately for convenience.

The SLS criteria are normally defined by the operator of a structure, or by established practice, the primary aim being efficient and economical in-service performance without excessive routine maintenance or down-time. The acceptable limits necessarily depend on the type, mission and arrangement of structures. Further, in defining such limits, other disciplines such as machinery designers must also be consulted. As an example, the limiting values of vertical deflections for beams in steel structures are indicated in Table 1.1.

Table 1.1 Serviceability limit values for vertical deflections of beams, see Figure 1.1 (ENV 1993-1-1 1992).

Condition	Limit for δ_{max}	Limit for δ_2
Deck beams	$L/200$	$L/300$
Deck beams supporting plaster or other brittle finish or non-flexible partitions	$L/250$	$L/350$

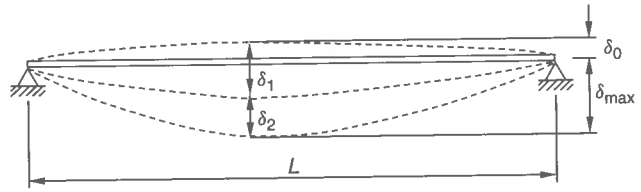

Figure 1.1 Nomenclature: lateral deflections of a beam

In Table 1.1, L is the span of the beam between supports. For cantilever beams, L may be taken as twice the projecting length of the cantilever. δ_{max} is the maximum deflection which is given by $\delta_{max} = \delta_1 + \delta_2 - \delta_0$, where δ_0 is the pre-camber, δ_1 is the variation of the deflection of the beam due to permanent loads immediately after loading, and δ_2 is the variation of the deflection of the beam due to variable loading plus any subsequent variant deflections due to permanent loads.

For steel-plate elements, criteria based on elastic buckling control are often employed for SLS design, in some cases to prevent such an occurrence, and in other cases to allow elastic buckling to a known and controlled degree. Elastic plate buckling, and the related effects such as relatively large lateral deflections, must be prevented if such effects are likely to be detrimental. On the other hand, since a plate may have some reserve strength beyond elastic buckling until its ultimate strength is reached, to allow elastic buckling in a controlled manner can in some cases lead to a more efficient structure. Later in Chapters 3 and 5 of this book, the use of such elastic buckling strength SLS design methodologies for steel-plated structural members will be presented and discussed further.

1.2.2 Ultimate Limit State Design

The structural design criteria to prevent the ULS are based on plastic collapse or ultimate strength. The simplified ULS design of many types of structures including merchant ship structures has in the past tended to rely on estimates of the buckling strength of components, usually from their elastic buckling strength adjusted by a simple plasticity correction. This is represented by point A in Figure 1.2. In such a design scheme based on strength at point A, the structural designer does not use detailed information on the post-buckling behavior of component members and their interactions. The true ultimate strength represented by point B in Figure 1.2 may be higher although one can never be sure of this since the actual ultimate strength is not being directly evaluated.

In any event, as long as the strength level associated with point B remains unknown (as it is with traditional allowable stress design or linear elastic design methods), it is difficult to determine the real safety margin. Hence, more recently, the design of structures such as those of navy ships as well as offshore platforms and land-based structures such as steel bridges has tended to be based on the ultimate strength.

The safety margin of structures can be evaluated by a comparison of ultimate strength with the extreme applied loads (load effects) as depicted in Figure 1.2. To obtain a safe and economic structure, the ultimate load-carrying capacity as well as the design load must be assessed accurately. The structural designer may even desire to estimate the ultimate strength not only for the intact structure, but also for structures with existing or premised damage, in order to assess their damage tolerance and survivability.

The ULS design criterion can also be expressed by Equation (1.1). The characteristic measure of design capacity, C_d, in Equation (1.1) is in this case the ultimate strength while

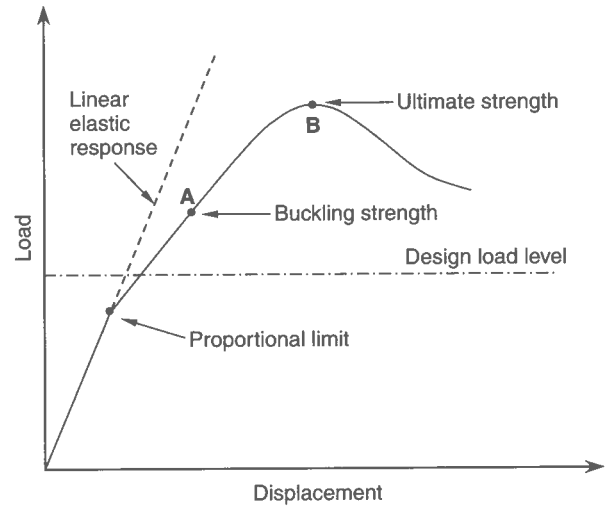

Figure 1.2 Structural design considerations based on the ultimate limit state

D_d is the related load or demand measure. For the ULS design, the resulting capacity factor, γ_M, related to variability of design capacity, C_d, is sometimes taken as $\gamma_M = 1.15$ for marine structures (NTS 1998).

It is of importance to note that any failure in a structure must ideally occur in a ductile rather than brittle manner. This is because avoiding brittle failure will lead to a structure that does not collapse suddenly, since ductility allows the structure to redistribute internal stresses and thus absorb greater amounts of energy prior to global failure. Adequate ductility in the design of a structure is facilitated by:

- meeting requisite material toughness requirements;
- avoiding failure initiation situations of combined high stress concentration and undetected weld defects in the structural details;
- designing structural details and connections so as to allow a certain amount of plastic deformation, i.e., avoiding 'hard spots'; and
- arranging the members such that a sudden decrease of structural capacity would not take place due to abrupt transitions or member failure.

This book is primarily concerned with ULS design methodologies for structural members and systems constituted of such ductile members.

1.2.3 Fatigue Limit State Design

The FLS design is carried out to ensure that the structure has an adequate fatigue life. Also the predicted fatigue life can be a basis for planning efficient inspection programs during operation of the structure. Although this book is concerned with the ULS design of steel structures, we discuss fatigue design here for the sake of completeness since no other part of the book will include the topic of fatigue design. The treatment here is not meant to be comprehensive but rather, introductory.

The design fatigue life for structural components is normally based on the structure service life required by the operator or other responsible body such as a class society.

For marine structures, the fatigue life is often taken as 20 years or longer. The shorter the design fatigue life, or the higher the required reliability, the smaller the inspection intervals need to be if an operation free from crack problems is to be assured.

The FLS design and analysis should in principle be undertaken for every suspect source of fatigue cracking which includes welded joints and local areas of stress concentrations. The structural design criteria for the FLS are usually based on the cumulative fatigue damage of a structure under repeated fluctuation of loading, as measured by the Palmgren–Miner cumulative damage accumulation rule. A particular value of the Miner sum (e.g., unity) is taken to be synonymous with the formation or initiation of a crack. The structure is designed so that when analyzed for fatigue, a reduced target Miner sum results, implying that cracks will not form with a given degree of certainty.

The fatigue damage at a crack initiation site is affected by many factors such as the stress ranges experienced during the load cycles, local stress concentration characteristics, and the number of stress range cycles. A comprehensive literature review on the fatigue damage analysis methods has been made by many investigators (e.g., Fricke *et al.* 2000, among others).

Two types of the FLS design approach are typically considered for steel structures, namely:

- $S-N$ curve approach (S = fluctuating stress, N = associated number of cycles)
- fracture mechanics approach.

In the $S-N$ curve approach, the Palmgren–Miner cumulative damage rule is applied together with the relevant $S-N$ curve. This application normally follows three steps, namely (1) define the histogram of cyclic stress ranges, (2) select the relevant $S-N$ curve, and (3) calculate the cumulative fatigue damage.

One of the most important factors in fatigue design is the characteristic stress to be employed in both defining the $S-N$ curve (the capacity) and also in the stress analysis (the fluctuating local fatigue stresses being the demand on the structure). Four types of methods have been suggested on this basis, namely:

- the nominal stress method;
- the hot spot stress method;
- the notch stress method; and
- the notch strain method.

The nominal stress method uses the nominal stresses in the field far from the stress concentration area together with $S-N$ curves that must include the effects of both structural geometry and the weld implicitly. In the nominal stress method, therefore, the $S-N$ curve should be selected for structural details depending on the detail type and weld geometry involved. A large number of $S-N$ curves for various types of weld as well as geometry are generally needed, and, indeed, are available. When a limited number of standard $S-N$ curves are used, any structural detail being considered must be categorized as belonging to one of those categories; this requires a certain amount of judgment.

The hot spot stress method uses a well-defined hot spot stress in the stress concentration area to take into account the effect of structural geometry alone, while the weld effect is incorporated into the $S-N$ curve. This is a very popular approach today, but certain practical difficulties must be conceded. The most basic of these pertains to the hot spot stress concept itself, which is more appropriate for surface cracks than imbedded cracks.

Difficulties can also arise in the consistent definition of hot spot stresses across a range of weld and structural geometries, and the estimation of the hot spot structural stress needed for the application of the technology in regions of stress concentration. For instance, attention should be paid to the extrapolation of the stress to the weld toe for calculating the stress concentration factor, while the need for the appropriate selection of a relevant $S-N$ curve among those for different weld types is still significant.

The notch stress method uses the stresses at the notch calculated by taking into account the effects of both structural geometry and weld, while the $S-N$ curve is developed representing the fatigue properties of either the base material, the material in the heat-affected zone, or the weld material, as appropriate. A significant advantage of the notch stress method is that it can address specific weld toe geometry in the calculation of fatigue damage. A related difficulty is that the relevant parameters (e.g., the weld toe angle) in the case of the actual structure must be known with some confidence.

The notch strain method uses the strains at the notch when low-cycle fatigue is predominant, because the working stresses in this case sometimes likely approach the material yield stress and the stress-based approaches are hence less appropriate.

The fracture mechanics approach considers that one or more premised cracks of a small dimension exist in the structure, and predicts the fatigue damage during the process of their crack propagation including any coalescence and break through the thickness, and subsequent fracture. In this approach to design, a major task is to pre-establish the relevant crack growth equations or 'laws'. The crack growth rate is often expressed as a function of only the stress intensity factor range at the crack tip, on the assumption that the yielded area around the crack tip is relatively small. In reality, the crack propagation behavior is affected by many other parameters (e.g., mean stresses, load sequence, crack retardation, crack closure, crack growth threshold, stress intensity range) in addition to stress intensity factor range.

While the fracture mechanics will be dealt with later in Chapter 10, the $S-N$ curve approach using nominal stresses is now briefly described under the assumption of the linear cumulative damage rule, i.e., the Palmgren–Miner rule.

In the fatigue damage assessment of welded structural details, of primary concern is the ranges of cyclic maximum and minimum stresses rather than mean stresses, as shown in Figure 1.3, because of the usual presence of residual mean stresses near yield magnitude. This tends to make the entire stress range damaging. The situation in non-welded cases is of course different, and in such cases mean stresses can be important.

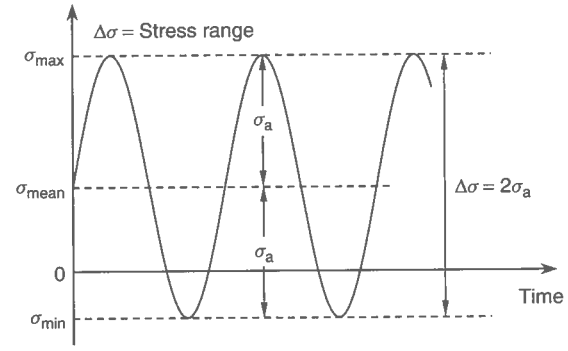

Figure 1.3 Cyclic stress range versus time

For practical FLS design using the nominal stress-based approach, the relevant $S-N$ curves must be developed for various types of weld joints. To do this, fatigue tests are carried out for various types of specimen which are subjected to cyclic stress ranges of uniform amplitude. As indicated in Figure 1.3, the maximum and minimum stresses are denoted by σ_{max} and σ_{min}, respectively. In such tests, the effect of mean stress, $\sigma_{mean} = (\sigma_{max} + \sigma_{min})/2$, on fatigue damage can be quantified, which is necessary in non-welded cases. For convenience, the fatigue tests for specimens incorporating non-welded geometries are usually carried out at either $\sigma_{min} = 0$ or $\sigma_{max} = -\sigma_{min}$ with constant stress range, i.e., $\Delta\sigma = \sigma_{max} - \sigma_{min} = 2\sigma_a$, where σ_a is the stress amplitude.

Based on the fatigue test results, the number of stress cycles, N_I or N_F, the former being the crack initiation life, i.e., until a crack initiates, and the latter being the fracture life, e.g., until a small-scale test specimen is separated into two pieces, are obtained. Through a series of such tests for a variety of stress ranges, $\Delta\sigma$, the $S-N$ curves for the particular structural details may typically be plotted as shown in Figure 1.4. The curves for design are usually expressible by curve fitting the test results plotted on a log–log scale, namely

$$\log N = \log a - 2s - m \log \Delta\sigma \tag{1.2a}$$

$$N(\Delta\sigma)^m = A \tag{1.2b}$$

where $\Delta\sigma$ = stress range, N = number of stress cycles with constant stress range, $\Delta\sigma$, until failure, m = negative inverse slope of the $S-N$ curve, $\log A = \log a - 2s$, a = life intercept of the mean $S-N$ curve, s = standard deviation of $\log N$.

For the FLS design criterion based on the $S-N$ curve approach, Equation (1.1) may be rewritten in the non-dimensional form when the distribution of a long-term stress range is given by a relevant stress histogram in terms of a number of constant amplitude stress range blocks, $\Delta\sigma_i$, each with a number of stress fluctuations, n_i, as follows:

$$D = \sum_{i=1}^{B} \frac{n_i}{N_i} = \frac{1}{A} \sum_{i=1}^{B} n_i (\Delta\sigma_i)^m \le D_{cr} \tag{1.3}$$

where D = accumulated fatigue damage, B = number of stress blocks, n_i = number of stress cycles in stress block i, N_i = number of cycles until failure at the ith constant amplitude stress range block, $\Delta\sigma_i$, D_{cr} = target cumulative fatigue damage for design.

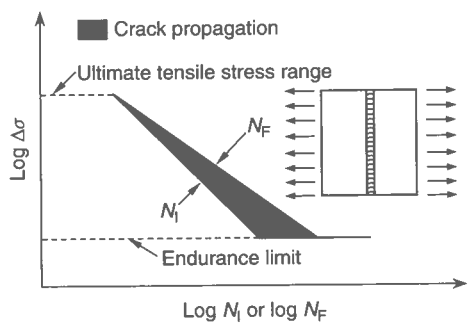

Figure 1.4 Typical $S-N$ curves from constant amplitude tests

To achieve greater fatigue durability in a structure, it is of importance to minimize stress concentrations, potential flaws (e.g., misalignment, poor materials) and structural degradation including corrosion and fatigue effects. Interrelated to fatigue design is the maintenance regime to be used. In some cases, it may be more economical in design to allow a certain level of possibility of fatigue damage, as long as the structure can perform its function until repairs are made after the fatigue symptoms are detected. In other cases, fatigue damage may not be allowed to occur, if it is inconvenient to inspect the structure or interrupt production. The former approach may thus be applied as long as regular inspections and related maintenances are possible, while the latter concept is obviously more relevant if there are likely to be difficulties associated with inspections and thus the high likelihood of undetected fatigue damage.

1.2.4 Accidental Limit State Design

The primary aim of the ALS design for steel structures may be characterized by the following three broad objectives, namely:

- to avoid loss of life in the structure or the surrounding area;
- to avoid pollution of the environment; and
- to minimize loss of property or financial exposure.

In ALS design, it is necessary to achieve a design such that the main safety functions of the structure must not be impaired during any accidental event or within a certain time period after the accident. The structural design criteria for the ALS are based on limiting accidental consequences such as structural damage and environmental pollution.

Since the structural damage characteristics and the behavior of damaged structures depend on the types of accidents, it is not straightforward to establish universally applicable structural design criteria for the ALS. Typically, for a given type of structure, design accidental scenarios and associated performance criteria must be decided upon the basis of risk assessment.

In the case of merchant ships or warships, possible accidental events that may need to be considered for ALS include collisions, grounding, significant hydrodynamic impact (slamming) leading to deck buckling or bottom damage, excessive loads from human error, berthing or dry docking, internal gas explosions in oil tanks or machinery spaces, and underwater or atmospheric explosions. In land-based structures, the accidental scenarios may include fire, explosion, foundation movements or related structural damage from earthquakes.

In selecting the design target ALS performance levels for such events, the approach is normally to tolerate a certain level of damage consistent with a greater aim such as survivability or minimized consequences; not to do so would result in an uneconomical structure.

The main safety functions of the structure that should not be compromised during any accident event or within a certain time period after the accident include:

- usability of escape ways;
- integrity of shelter areas; and control spaces;
- global load-bearing capacity;
- integrity of the environment.

Therefore, the ALS-based design criteria should be formulated so that the main safety functions mentioned above will work successfully, and the following are considered to adequate levels:

- energy dissipation related to structural crashworthiness;
- capacity of local strength members or structures;
- capacity of the global structure;
- allowable tensile strains to avoid tearing or rupture; and
- endurance of fire protection.

For the ALS design, the integrity of the structure will be typically checked in two steps. In the first step, the structural performance against design accident events will be assessed, while post-accident effects such as damage to the environment are evaluated in the second step.

In the case of accidents to ships, for instance, the primary concern of the ALS design is to keep the watertightness of ship compartments, the containment of dangerous or pollutant cargoes (e.g., chemicals, bulk oil, liquefied gas), and the integrity of reactor compartments of nuclear-powered ships. To continue normal operations for the structure's mission, it is also of importance to keep the integrity and residual strength of damaged structures at a certain level, immediately after the accidents occur.

The different types of accident events normally require different methodologies to analyze the resistance of the structure. For ALS design criteria under predominantly impact-oriented loading, Equation (1.1) may typically be rewritten using energy-dissipation-related criteria adopted with the view that the safety of the structure or the environment is not lost, as follows:

$$E_k \gamma_k \leq \frac{E_r}{\gamma_r} \tag{1.4}$$

where E_k = kinetic energy lost during the accident, E_r = available energy absorption capability until critical damage occurs, γ_k, γ_r = partial safety factors related to kinetic energy loss and energy absorption capability.

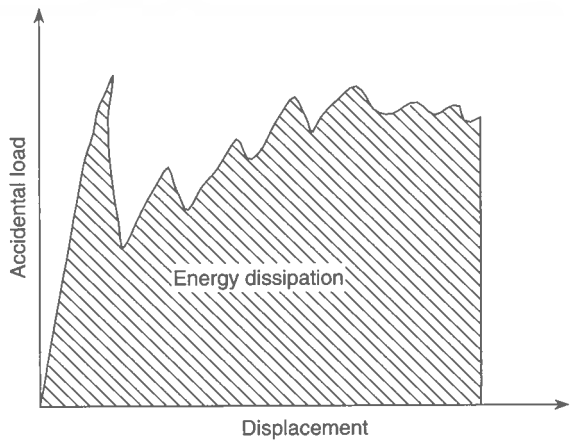

Figure 1.5 Energy absorption of the structure under accidental loading

The dissipated energy of the structure during the accident may usually be calculated by integrating the area below the load–displacement curve of the structure under accidental loading as shown in Figure 1.5. In Chapter 9, a more elaborate description for the ALS design of marine structures is presented.

1.3 Material Behavior of Structural Steels

In structural design, it is of obvious importance to select suitable materials. In this regard, in addition to strength, attention should be paid to ductility or toughness, weldability and corrosion resistance requirements for the steel concerned.

Steels used for structural applications are typically classified into four groups with progressively increasing strengths, namely carbon steels, high-strength low-alloy (HSLA) steels, heat-treated carbon and HSLA steels and heat-treated alloy steels.

The structural designer must have a better understanding of the mechanical properties of a structural steel, which depend on many factors such as its composition, heat treatment and thickness (the grain size of thinner rolled steel plating tends to be smaller, for instance), and also the effects of temperature and strain rate on mechanical properties.

In the following, the characteristics of mechanical properties for structural steels are briefly noted. For more elaborate descriptions, Brockenbrough for example (1983, 1991) may be referred to.

1.3.1 Monotonic Tensile Stress–Strain Curve

Figure 1.6(a) shows typical stress–strain curves for structural steels which are obtained by using monotonic tensile coupon tests, the stress versus strain curves representing

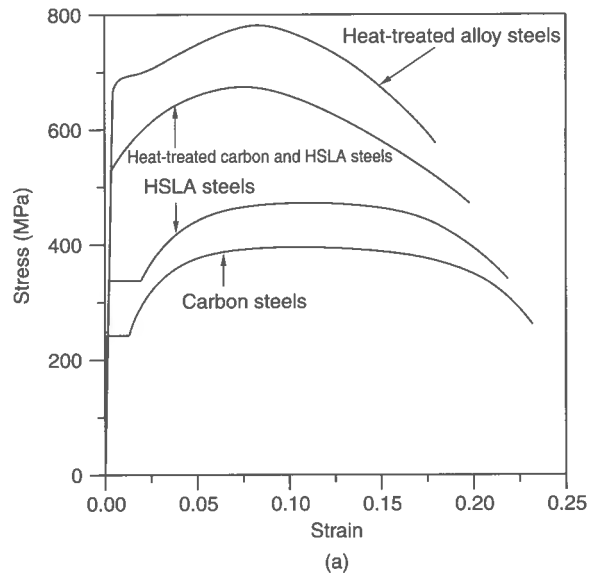

Figure 1.6 (a) Typical stress–strain curves for structural steels (Brockenbrough & Johnston 1981); (b) Idealized monotonic stress–strain relationship for structural steels; (c) A schematic of stress–strain curve and offset yield stress for heat-treated higher tensile steels

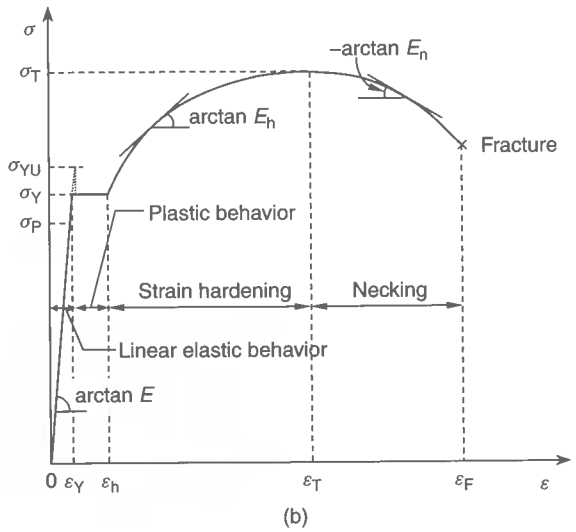

(b)

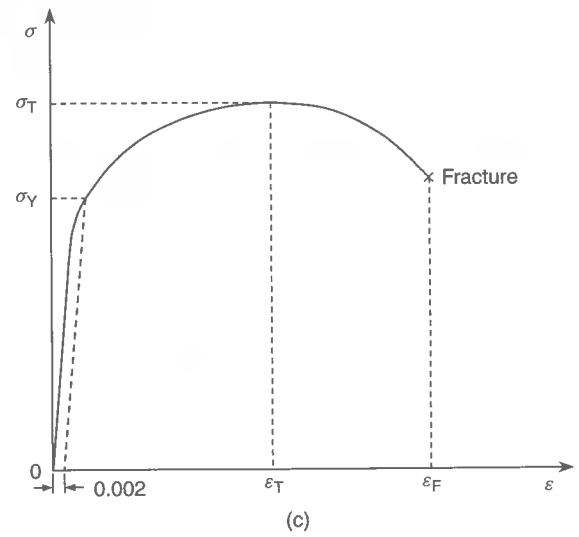

(c)

Figure 1.6 (*continued*)

repeated cyclic behavior being usually different. Figure 1.6(b) represents typical schematic relationships between nominal stress, σ, and strain, ε, for structural steels.

Mechanical Property Characterization

For the ULS design, the relevant mechanical properties of structural steels can be characterized by the following parameters, namely:

- Young's modulus (or modulus of elasticity), E
- proportional limit, σ_P
- upper yield point, σ_{YU}

- lower yield point, σ_{YL} ($\approx\sigma_Y$)
- yield strength, σ_Y
- yield strain, ε_Y
- strain-hardening strain, ε_h
- strain-hardening tangent modulus, E_h
- ultimate tensile strength, σ_T
- ultimate tensile strain, ε_T
- necking tangent modulus, E_n
- fracture strain, ε_F
- Poisson's ratio, ν

Young's Modulus, E

The initial relationship between stress and strain is linear elastic wherein the steel recovers perfectly upon unloading. The slope of the linear portion of the stress–strain relationship in the elastic regime is defined as the modulus of elasticity, E (also called Young's modulus). Table 1.2 indicates typical values of Young's moduli for selected metals and metal alloys at room temperature.

Poisson's Ratio, ν

Poisson's ratio, ν, is the ratio of the transverse strain to longitudinal strain of the coupon under axial load in the elastic regime. For structural steels, the value of ν is in the range 0.25–0.33, and is typically taken as 0.3 for ULS analysis of steel-plated structures, as indicated in Table 1.2.

Elastic Shear Modulus, G

The mechanical properties of steels under shear are usually defined using principles of structural mechanics rather than by tests. The elastic shear modulus, G, is expressed by a function of Young's modulus, E, and Poisson's ratio, ν, as follows:

$$G = \frac{E}{2(1+\nu)} \tag{1.5}$$

Proportional Limit, σ_P

The maximum stress in the elastic regime, i.e., immediately before initial yielding, is termed proportional limit, σ_P.

Table 1.2 Typical values of Young's moduli and Poisson's ratios for metals and metal alloys at room temperature (Callister 1997).

Material	E (GPa)	ν
Aluminum and aluminum alloys	69	0.33
Copper	110	0.34
Steels (plain carbon)	207	0.30
Titanium and titanium alloys	104–116	0.34

Yield Point, Yield Strength, σ_Y, Yield Strain, ε_Y

Most lower yield strength steels have upper and lower yield points. The latter typically has an extended plateau in the stress–strain curve, being approximated by yield strength, σ_Y, and the corresponding yield strain, $\varepsilon_Y = \sigma_Y/E$.

Mechanical properties of steel vary with the amount of work and heat treatment applied during the rolling process. Typically plates which receive more work have higher yield strength than plates that do not. The yield strength of a steel is also increased by the heat treatments (e.g., quenching, tempering) or cold forming.

For heat-treated (i.e., quenched or tempered) or cold-formed higher tensile steels, the stress versus strain curve monotonically increases until it reaches a maximum value and neither upper nor lower yield points may appear, as shown in Figure 1.6(c). Thus the yield strength may not be determined based on the definition indicated above. In this case, the yield strength is commonly defined as the stress at the intersection of the stress–strain curve and a straight line passing through an offset point strain, i.e., $(\sigma, \varepsilon) = (0, 0.002)$, which is parallel to the linear portion of the stress–strain curve in the elastic regime.

For structural design purposes, regulatory bodies or classification societies identify a 'minimum' yield strength required of a particular steel, and its chemical composition and heat treatment. The specified yield stresses are normally in the range of 205–290 MPa for carbon steels, 290–450 MPa for HSLA steels, 315–515 MPa for heat-treated and HSLA steels and 620–690 MPa for heat-treated alloy steels (Brockenbrough 1983).

Strain-hardening Tangent Modulus, E_h

Beyond the yield stress or strain, the steel flows plastically without appreciable changes in stress until the strain-hardening strain, ε_h, is reached. The slope of the stress–strain curve in the strain-hardening regime is defined as the strain-hardening tangent modulus, E_h, which may not be constant, but is typically 5 to 15% of the Young's modulus for structural steels.

The stress beyond the yield strength of the elastic–plastic material with strain hardening, σ_Y^h, is often expressed at a certain level of plastic strain as follows:

$$\sigma_Y^h = \sigma_Y + \frac{E E_h}{E - E_h}\varepsilon_p \tag{1.6}$$

where ε_p = effective plastic strain.

Figure 1.7 shows the illustrative effect of strain hardening on the elastic–plastic large-deflection behavior (i.e. average stress–strain curve) of a steel rectangular plate under uniaxial compressive loads in the longitudinal direction, as predicted by nonlinear finite element analysis. The plate is simply supported at all edges, keeping them straight. It is evident that because of the strain-hardening effect the steel plate ultimate strength can be larger than that obtained by neglecting it. For pessimistic strength assessment of steel-plated structures, however, an elastic and perfectly plastic material model, i.e., without strain hardening, may be considered sufficient.

Ultimate Tensile Strength, σ_T

When strain exceeds the strain-hardening strain, ε_h, the stress increases above the yield stress, σ_Y, because of strain-hardening, and this behavior can continue until the ultimate

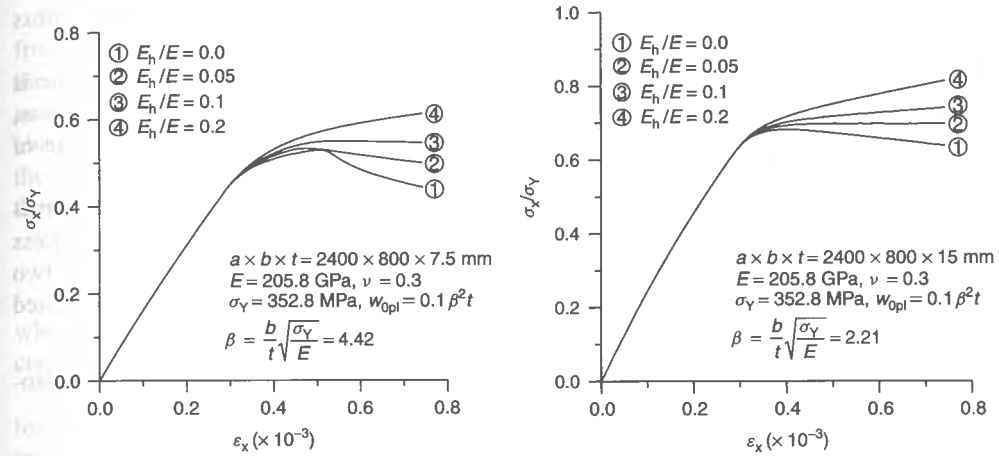

Figure 1.7 The effect of strain hardening on the ultimate strength of a steel plate under axial compression (w_{0pl} = buckling mode initial deflection of the plate)

tensile strength (also simply termed tensile strength), σ_T, is reached. The value of σ_T is obtained by the maximum axial tensile load divided by the original cross-sectional area of the coupon.

The specified tensile strengths are normally in the range of 380–620 MPa for carbon steels, 415–550 MPa for HSLA steels, 450–790 MPa for heat-treated and HSLA steels and 760–895 MPa for heat-treated alloy steels (Brockenbrough 1983). The ultimate tensile strength, σ_T, of structural steels must normally be greater than 1.2 times the minimum yield strength, σ_Y, for a sufficient ductility or rupture margin. The ultimate tensile strain, ε_T, of low-strength structural steels is usually at least 20 times the yield strain, ε_Y.

Necking Tangent Modulus, E_n

With further increase in the strain, the large local reduction of cross-section which is termed necking occurs. The internal stress decreases in the necking regime. The slope of the stress–strain curve in the necking regime is sometimes defined as necking tangent modulus, E_n.

Fracture Strain, ε_F

The steel ruptures when the strain reaches the fracture strain, ε_F, perhaps 20% for bare steel, but considerably less for the material of the heat-affected zone, and even less (e.g., 8%) for the weldment material. When any defect such as notches or premised cracks exists, the fracture strain can significantly decrease further. The fracture strain, ε_F, of structural steels on a gauge length of $5.65\sqrt{A_0}$ (A_0 = original cross-sectional area) must not be less than 15% (ENV 1993-1-1 1992).

1.3.2 Yield Condition under Multiple Stress Components

For a one-dimensional strength member under uniaxial tensile or compressive loading, the yield strength determined from a uniaxial tension test can be used to check the state

of yielding, the essential question to be answered being simply whether the axial stress reaches the yield strength.

A plate element which is the principal strength member of steel-plated structures is likely to be subjected to a combination of biaxial tension/compression and shear stress, which can be usually considered to be in a plane stress state (as contrasted to a state of plane strain).

For an isotropic two-dimensional steel member for which the dimension in one direction is much smaller than those in the other two directions, and with three in-plane stress components (i.e., two normal stresses, σ_x, σ_y, and shear stress, τ_{xy}) or equivalently, two principal stress components (i.e., σ_1, σ_2), three types of yield criteria are usually adopted as follows:

(1) Maximum principal-stress-based criterion: The material yields if the maximum absolute value of the two principal stresses reaches a critical value, namely

$$\max(|\sigma_1|, |\sigma_2|) = \sigma_Y \tag{1.7a}$$

(2) Maximum shear-stress-based criterion (also called the Tresca criterion): The material yields if the maximum shear stress, τ_{max}, reaches a critical value, namely

$$\tau_{max} = \left|\frac{\sigma_1 - \sigma_2}{2}\right| = \frac{\sigma_Y}{2} \tag{1.7b}$$

(3) Strain-energy-based criterion (also called the Mises–Hencky or Huber–Hencky–Mises criterion): The material yields if the strain energy due to geometric changes reaches a critical value, which corresponds to that where the equivalent stress, σ_{eq}, reaches the yield strength, σ_Y, determined from the uniaxial tension test as follows:

$$\sigma_{eq} = \sqrt{\sigma_x^2 - \sigma_x\sigma_y + \sigma_y^2 + 3\tau_{xy}^2} = \sigma_Y \tag{1.7c}$$

It is recognized that the yield condition Equation (1.7a) is relevant for a brittle material, and that the last two conditions, Equations (1.7b) and (1.7c) are more appropriate for a ductile material. The shear yield strength, τ_Y, under pure shear, can be determined by solving Equation (1.7c) with regard to τ_{xy} when $\sigma_x = \sigma_y = 0$, the result being as follows:

$$\tau_Y = \frac{\sigma_Y}{\sqrt{3}} \tag{1.7d}$$

1.3.3 Effect of Temperature

During fabrication and operation, steel structures can be exposed to different levels of temperatures, and thus the designer needs to account for the influence of temperature on the behavior of structural steels. Mechanical properties of a structural steel vary with temperature. In material behavior, changes in temperature can cause the following effects, namely:

- elastic constants (e.g., E, ν) of the material can change;
- strain can develop without mechanical loading;
- material yield strength decreases with increase in temperature; and
- the material can lose ductility with decrease in temperature.

For many structural materials, a change in temperature of a few tens of degrees Celsius from room temperature may not result in much change in the elastic constants. Therefore, the effect of temperature on the elastic constants is often neglected in the structural design as long as changes in temperature are not significant. The strain caused by a temperature change is termed thermal strain. When change in temperature is relatively small, the thermal strain is nearly a linear function of the temperature change. If the temperature of the material is changed from T_0 to T, then the thermal strain, ε^T, is approximated by

$$\varepsilon^T = \alpha(T - T_0) \tag{1.8a}$$

where α is the linear coefficient of thermal expansion. Table 1.3 indicates the linear coefficients of thermal expansion for selected metals and metal alloys at room temperature.

The total strain in a structure is generally the sum of the strains due to mechanical loading and temperature change. For instance, the total strain, ε, of a bar under axial tensile stress, σ, and with a change in temperature is given in the material elastic regime as follows:

$$\varepsilon = \frac{\sigma}{E} + \alpha(T - T_0) \tag{1.8b}$$

The important properties in determining the performance of steel at a specified temperature are its strength, deformation, thermal expansion, specific heat and thermal conductivity characteristics. At high enough temperatures, the stiffness and strength of structural steels may be reduced even if the ductility increases. At low temperature, the yield strength tends to increase while brittle fracture can more easily initiate and propagate since the ductility is reduced. However, it is noted that temperature is not usually the sole reason of brittle fracture, which can occur by a sufficiently adverse combination of tensile strength, temperature, strain rate and geometrical discontinuity (notch) and so on.

For fire safety of steel structures, the capacity of structural members should be adequate to resist the applied loads in a fire. While the behavior of steel in fire is affected by the heating rate, steel begins to lose strength at temperatures above 300 °C and reduces in strength at an approximately steady rate until around 800 °C, as shown in Figure 1.8 (Lawson 1992). The strength reduction factor in Figure 1.8 represents the yield strength of steel at a particular temperature relative to that at room temperature. To avoid excessive deformations due to fire, regulations recommend strain limits: ECCS (1982) uses a 0.5% limit for temperatures exceeding 400 °C, BS 5950 (1985) uses a 1.5% limit for beams and 0.5% limit for columns, and ENV 1993-1-2 (1992) of Eurocode 3 uses a 2% limit. These

Table 1.3 Linear coefficients of thermal expansion for selected metals and metal alloys at room temperature (Callister 1997).

Material	Thermal expansion coefficient, 10^{-6}/°C
Aluminum	23.6
Aluminum alloys (cast)	18.0–24.5
Aluminum alloys (wrought)	19.5–24.2
Copper	17.0
Steels (low alloy)	11.1–12.8
Steels (plain carbon)	11.0–12.0
Titanium and titanium alloys	7.6–9.8

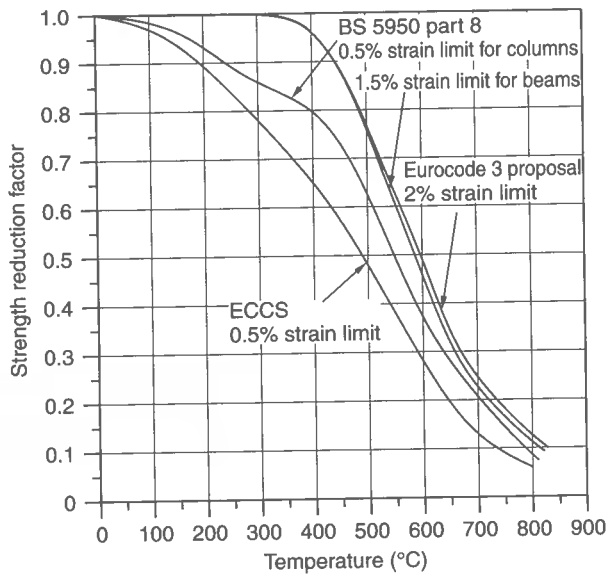

Figure 1.8 Strength reduction factor for structural steel at elevated temperatures (Lawson 1992)

strain limits can be useful to define the ALS criteria against fire accidents; ALS-related design was previously noted in Section 1.2.4.

1.3.4 The Bauschinger Effect – Cyclic Loading

During operation, structural members are likely to be subjected to load cyclic effects, as shown in Figure 1.9. If a steel that has been plastically strained in tension is unloaded and subsequently strained in compression, the stress–strain curve for the compression loading deviates from a linear relationship at stresses well below the yielding point of the virgin material, but it returns to the point of maximum stress and strain for the first tension loading cycle. The same effect is observed for the opposite loading cycle, i.e., compression first and tension next. In this case, the modulus of elasticity is reduced, as shown by the shape of the stress–strain curve of Figure 1.9. This phenomenon is typically termed the Bauschinger effect. When stiffness is of primary concern, e.g., in evaluating buckling or deflection, the Bauschinger effect may be of interest.

Within an acceptable level of accuracy, however, the mechanical properties of a particular steel as determined by uniaxial tension testing are also approximately accepted as being valid for the same steel under uniaxial compression.

1.3.5 Limits of Cold Forming

Excessive strain during cold forming can exhaust ductility and cause cracking. Hence the strain in cold forming structural shapes must be limited not only to prevent cracking but also to prevent buckling collapse of structural elements subject to compressive loads. The cold-forming-induced strain is usually controlled by requiring the ratio of bending radius to the plate thickness to be large, e.g., 5 to 10.

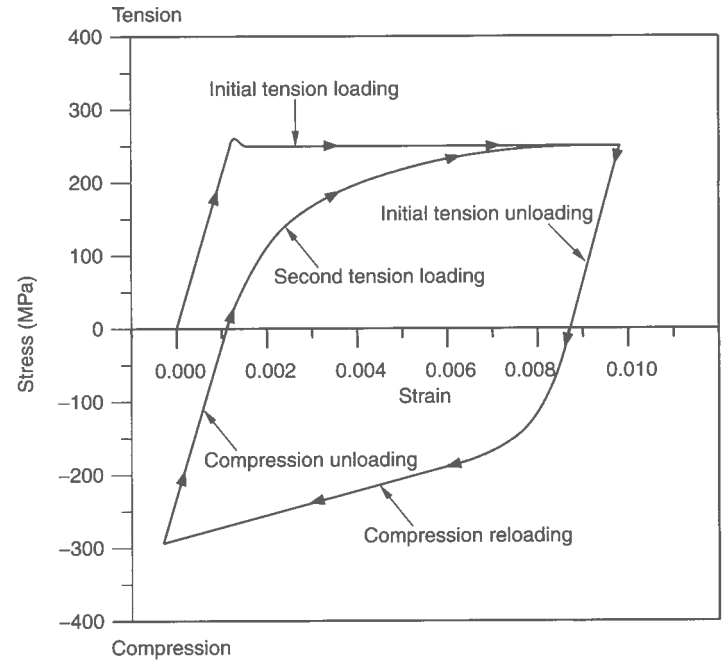

Figure 1.9 The Bauschinger effect in carbon steels (Brockenbrough & Johnston 1981)

1.3.6 Lamellar Tearing

In most cases of steel-plated structures, of primary concern related to load effects are the behavior in the length and breadth direction of plates. The steel behavior in the wall thickness direction is normally not of interest. In heavy welded steel constructions, particularly in joints with thick plates and heavy structural shapes, however, crack-type separation or delamination can take place in the wall thickness direction underneath the surface of steel plates or at weld toes. This failure is typically caused by large through-thickness strain, sometimes associated with weld metal shrinkage in highly restrained joints. This phenomenon is termed lamellar tearing. Careful selection of weld details, filler metal and welding procedure, and the use of steels with controlled through-thickness properties (the so-called Z grade steels), can be effective to control this failure mode.

1.3.7 Variability in Mechanical Properties

The mechanical properties of structural steels as obtained by the tensile coupon tests in any specific case may vary from specified minimum values for several reasons. One reason is due to locations of the test specimen taken. According to a comparative study on the yield point at various selected sample locations of coupon test specimens, the mean difference was found to be −5 MPa (AISI 1974), for example. However, this is usually offset by the fact that the official test value is usually greater than the specified minimum value, since the mean yield stress and COV (coefficients of variation) are normally in the range of 1.05–1.10 and 0.10–0.11, respectively (Brokenbrough 1991). This implies that for ULS design purposes the specified minimum values of structural steels may be safely used.

1.4 Strength Member Types for Steel-Plated Structures

The geometrical configuration of a steel-plated structure is determined primarily depending on the function of the particular structure. Figure 1.10 shows a basic part of a typical steel-plated structure. A major difference between plated and framed structures is that principal strength members of the former type of structure are plate panels together with support members, while the latter typically consists of truss or beam members for which the dimension in the axial direction is usually much greater than those in the other two directions. Typical examples of steel-plated structures are ships, deck structures of offshore platforms and box girder bridges.

Basic types of structural members usually making up steel-plated structures are as follows:

- plate panels: plating, stiffened panel, corrugated plate;
- small support members: stiffener, beam, column, beam–column; and
- strong main support members: plate girder, box girder.

To improve the stiffness and strength of plate panels, increasing the stiffener dimensions is usually more efficient than simply increasing the plate thickness, and thus the plate panel is usually reinforced by beam members (stiffeners) in the longitudinal or transverse direction. Figure 1.11 shows typical beam members used for the stiffening of plating. A

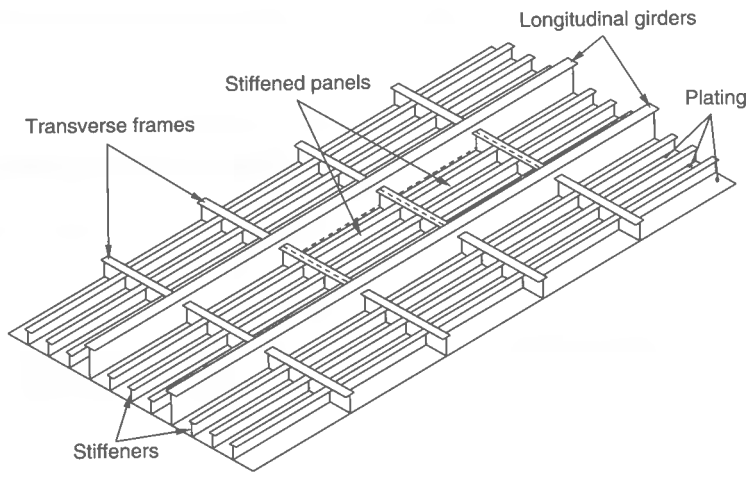

Figure 1.10 Typical steel-plated structure

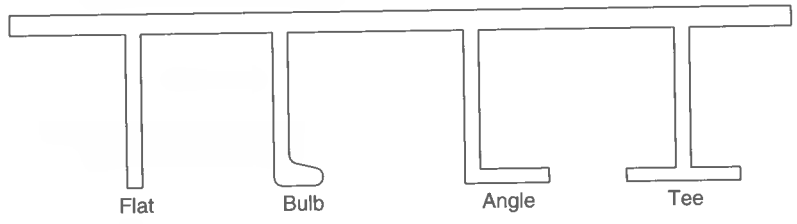

Figure 1.11 Various types of beam members (stiffeners)

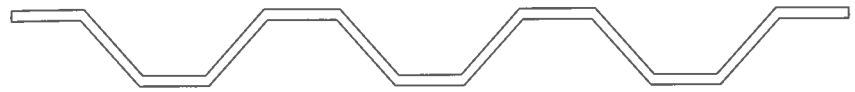

Figure 1.12 A self-stiffened plate – corrugated panel

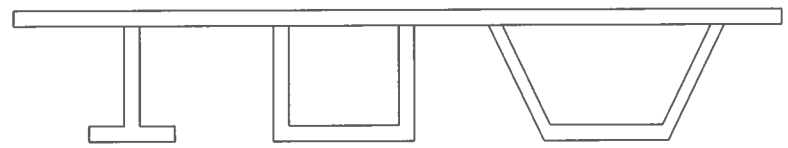

Figure 1.13 Various types of strong main support members

self-stiffened plate, e.g., corrugated plate as shown in Figure 1.12, may also be used in some cases.

When the stiffened panels are likely to be subjected to lateral loads or out-of-plane bending, or just for lateral support, they are supported by stronger beam members. Figure 1.13 shows typical strong main support members used for building steel-plated structures. For marine structures, plate girders which are composed of deep webs and wide flanges are typically employed for main support members. The deep web of a plate girder is often stiffened vertically and/or horizontally. Box-type support members which consist of plate panels are used for construction of land-based steel bridges. Diaphragms or transverse floors are arranged at a relevant spacing in the box girder.

While plating primarily sustains in-plane loads, support members resist out-of-plane (lateral) loads and bending. A plate panel between stiffeners is called 'plating' and the plating with stiffeners is termed 'stiffened panel'. A large stiffened panel supported by heavy support members is sometimes idealized by a grillage, which in concept is essentially a set of intersecting beam members. When a one-dimensional strength member is predominantly subjected to axial compression, it is called a 'column', while it is termed a 'beam' under the action of lateral loads or bending. A one-dimensional strength member under combined axial compression and bending is called a 'beam–column'.

Strong main support members are normally called 'girders' when they are located in the primary loading direction (i.e., longitudinal direction in a box girder or a ship hull), while they are sometimes called 'frames' or main support members when they are located in the direction orthogonal to the primary load direction (i.e., in the transverse direction in a box girder or a ship hull).

For strength analysis of steel-plated structures, stiffeners or some support members together with their associated plating are often modeled as beams, columns or beam–columns.

1.5 Types of Loads

The terminology related to the classification of applied loads for marine structures is similar to that for land-based structures. The types of loads to which steel-plated structures or strength members are likely to be subjected may be categorized into the following four groups, namely:

- dead loads;
- live loads;
- environmental loads; and
- accidental loads.

Dead loads (also called permanent loads) are time-independent, gravity-dominated service loads. Examples of dead loads are the weight of structures or permanent items that remain in place throughout the life of the structure. Dead loads are typically static loads and they can usually be determined accurately even if the weight of some items may in some cases be unknown until the structural design has been completed.

Live loads are gravity loads that vary in magnitude and location during normal operation of the structure. Examples of live loads are weight of persons, furniture, movable equipment, wheel loads from vehicles and stored consumable goods. In the design of land-based bridges, highway vehicle loading is usually separately classified under highway live loads. While some live loads (e.g., persons and furniture) are practically permanent and static, others (e.g., cranes and various types of machinery) are highly time dependent and dynamic. Since the magnitude, location and density of live load items are generally unknown in a particular case, the determination of live loads for design purposes is not straightforward. For this reason, regulatory bodies sometimes prescribe the design live loads which are based on experience and proven practice.

Environmental loads are loads related to wind, current, waves, snow and earthquake. Most environmental loads are time dependent and repeated in some fashion, i.e., cyclic. The determination of design environmental loads in the marine field is often specified by classification society rules, typically using the concept of a mean return period. The design loads of snow or wind, for instance, may be specified based on a return period of 50 years, indicating that extreme snowfall or wind velocity that is expected to occur once in 50 years is used for design.

Accidental loads are loads arising from accidents such as collision, grounding, fire, explosion and dropped objects. Accidental loads typically have a dynamic or impact effect on structural behavior. Guidelines for predicting and accounting for accidental loads are more meager because of the unknown nature of accidents. But it is important to treat such loads in design, particularly where novel types of structures are involved, about which past experience may be lacking. This often happens in the offshore field, where several new types of structures have been introduced in the last two decades.

The maxima of the various types of loads mentioned above are not always applied simultaneously, but more than one load type normally coexist and interact. Therefore, the structural design needs to account for the effects of phasing for defining the combined loads. Usually, this involves the consideration of multiple load combinations for design, each representing a load at its extreme value together with the accompanying values of other loads. Guidelines for relevant combinations of loads to be considered in design are usually specified by regulatory bodies or classification societies for particular types of structures.

1.6 Basic Types of Structural Failure

This book is concerned with the fundamentals and practical procedures for limit state design of steel-plated structures. One primary task in limit state design is to determine the level of imposed loads which causes structural failure of individual members and

overall structure. Therefore, it is of crucial importance to better understand what types of structural failure can primarily occur.

Failure of ductile steel structures is normally related to either one or both of the following nonlinear types of behavior, namely:

- geometric nonlinearity associated with buckling or large deflection;
- material nonlinearity due to yielding or plastic deformation.

For steel members, many basic types of structural failure are considered, the more important of which being as follows:

- large local plasticity;
- instability (also called buckling);
- fatigue cracking related to cyclic loading;
- ductile or brittle fracture, given fatigue cracking or pre-existing defects; and
- excessive deformations.

All of the basic failure types mentioned above do not always occur simultaneously, but more than one phenomenon may in principle be involved until the structure reaches the ULS. For convenience, the basic types of structural failure noted above are often described and treated separately.

As the external loads increase, the most highly stressed region inside a structural member will yield first resulting in local plastic deformation, and this decreases the member stiffness. With further increase in the loads, local plastic deformation will grow larger and/or occur at several different regions. The stiffness of the member with large local plastic regions becomes quite small and the displacements increase rapidly, eventually becoming so large that the member is considered to have failed.

Instability or buckling can occur in any structural member which is predominantly subjected to load sets that result in compressive effects in the structure. In buckling-related design, two types of buckling are considered, namely bifurcation and non-bifurcation buckling. The former type is seen for an ideal perfect member without initial imperfections, while the latter typically occurs in an actual member with some initial imperfections. For instance, a straight elastic column has an alternative equilibrium position at a critical axial compressive load which causes a bent shape to suddenly occur at a certain value of the applied load. This threshold load which separates into two different equilibrium conditions is called buckling or bifurcation load for the member.

An initially deflected column or a beam–column induces bending from the beginning of the loading contrary to the straight column, and lateral deflection increases progressively. The member stiffness is reduced by a large deflection and local yielding, and eventually it becomes zero at a peak load. The deflection of the member with very small or zero stiffness becomes so large that the member is considered to have collapsed. In this case, an obvious sudden buckling point does not appear until the member collapses, and this type of failure is called non-bifurcation instability or limit-load buckling (Galambos 1988).

Due to repeated fluctuation of loading, fatigue cracking can initiate and propagate in the stress concentration areas of the structure. Fracture is a type of structural failure caused by the rapid extension of cracks. Three types of fracture are considered, namely brittle fracture, rupture and ductile fracture. Brittle fracture normally takes place in low-toughness materials or below a certain temperature when the ultimate tensile strength of

steel diminishes sharply. For very high-toughness materials, rupture occurs by necking of the member typically at room or higher temperature. Ductile fracture is an intermediate fracture mode between the two extreme failure modes, namely brittle fracture and rupture. In steels, the tendency to fracture is related not only to the temperature, but also to the rate at which loading is applied. The higher the loading rate, the greater the tendency toward brittle fracture.

1.7 Fabrication-related Initial Imperfections

Steel structures are typically fabricated by flame cutting and welding, and thus initial imperfections in the form of initial distortions and residual stresses may develop and will reduce the structural capacity. Therefore, these initial imperfections should be included in structural design as parameters of influence.

When local heating is input to structural steels, the heated part will expand, but because of adjacent cold parts it will be subjected to compressive stress and distortion. When the heated part is cooled down, it will be locally shrunk rather than revert to its initial shape and thus now be subjected to tensile stress.

While some efforts have been made to predict the initial imperfections theoretically or numerically, e.g., Masubuchi (1980) or Ueda (1999), approximate methods based on the insights from measurements are usually adopted for design purposes, both because of the complexity of the phenomena involved and because the related effects in flat-plated structures are normally of a secondary rather than primary interest.

Both the residual stresses and welding distortions should be minimized by application of proper welding procedures and fabrication methods. While in practice heat treatments for stress relief may usually not be undertaken to reduce the welding residual stresses, the control of welding procedures will help, including (1) proper positioning of the components of joints before welding, (2) selection of welding sequences determined by experience and expertise, (3) deposition of a minimum volume of weld metal with a minimum number of passes for the design condition, and (4) preheating. Weld procedures are validated by shop testing (AISC 1993).

1.7.1 Weld Distortions

Figure 1.14 shows various types of welding-induced distortions. In practice, both angular change and longitudinal bending distortion are of greater concern, while the shrinkages in the longitudinal or transverse direction may often be neglected.

Figure 1.15 shows some typical initial deflection shapes of welded one-dimensional members and their possible idealizations. For practical design purposes, the initial deflection shape of a welded one-dimensional member may be idealized as the dotted line in Figure 1.15 which can be approximately expressed in mathematical form as follows:

$$w_0 = \delta_0 \sin \frac{\pi x}{L} \tag{1.9}$$

where w_0 = initial deflection function, δ_0 = initial deflection amplitude, which is often taken as $0.0015\,L$ for a practical strength calculation at an 'average' level of imperfections, L = member length between supports.

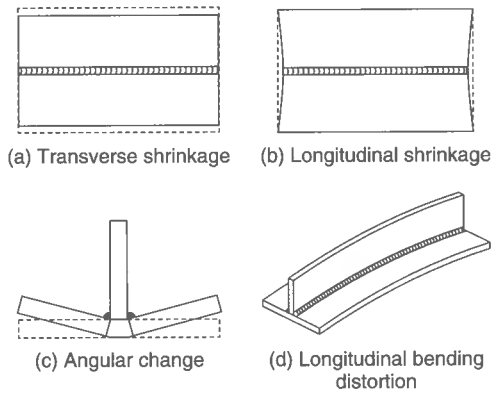

Figure 1.14 Various shapes of welding-induced distortions

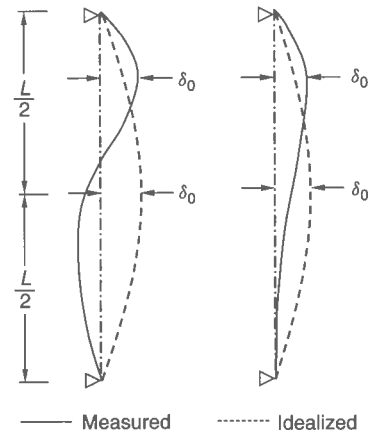

Figure 1.15 Idealization of initial deflection shapes for welded one-dimensional members

Figure 1.16 represents a schematic of fabrication-related initial deflections in steel-stiffened plate structures. According to measured data for welding-induced initial deflections of plates in merchant steel ship structures (e.g., Carlsen & Czujko 1978, Antoniou 1980, Kmiecik *et al.* 1995), the geometric configuration of such initial deflections is quite complex. The insights developed by such measurements lead to the following expression for the post-weld initial deflection of steel plating between stiffeners, namely

$$\frac{w_0}{w_{0\text{pl}}} = \sum_{i=1}^{M} \sum_{j=1}^{N} B_{0ij} \sin \frac{i\pi x}{a} \sin \frac{j\pi y}{b} \tag{1.10a}$$

where a = plate length, b = plate breadth. B_{0ij} indicates the welding-induced initial deflection amplitude normalized by the maximum initial deflection, $w_{0\text{pl}}$, which can be determined based on the initial deflection measurements. The subscripts i and j denote the corresponding half-wave numbers in the x and y directions.

If measured data for the initial deflection for plating are available, the initial deflection amplitudes of Equation (1.10a) can be determined by expanding Equation (1.10a)

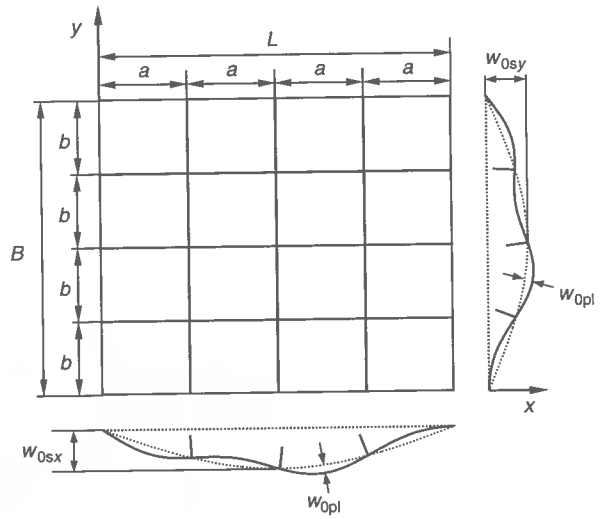

Figure 1.16 Fabrication-related initial deflections in steel-stiffened panels

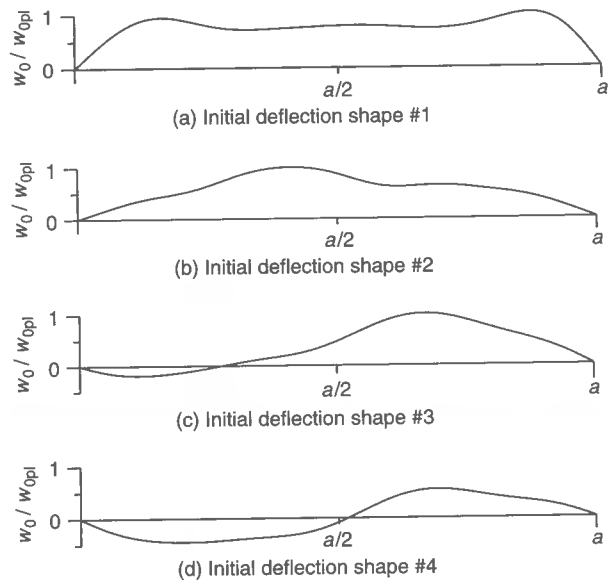

Figure 1.17 Some typical initial deflection patterns in steel plating between stiffeners in the long (plate length) direction

appropriately using a selected number of terms, M and N, depending on the complexity of the initial deflection shape.

For practical design purposes, further idealization may sometimes be necessary. The measurements of initial deflection for plate elements in steel-plated structures show that a multi-wave shape is predominant in the long direction, as shown in Figure 1.17, while one half wave is found in the short direction, as shown in Figure 1.18.

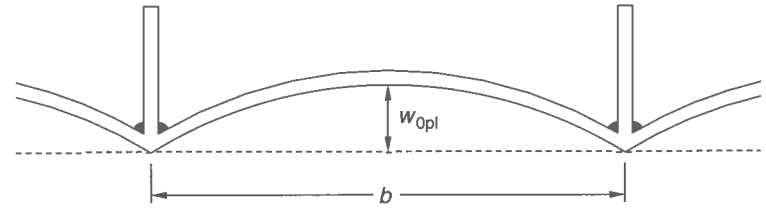

Figure 1.18 A typical initial deflection pattern in steel plating between stiffeners in the short (plate breadth) direction

For a nearly square plate element, therefore, Equation (1.10a) may simplify by taking $M = N = 1$. For a long plate element with a multi-wave shape in the x direction and one half wave in the y direction, Equation (1.10a) becomes

$$\frac{w_0}{w_{0pl}} = \sum_{i=1}^{M} B_{0i} \sin \frac{i\pi x}{a} \sin \frac{\pi y}{b} \tag{1.10b}$$

In practice, M in Equation (1.10b) may be taken as an integer which corresponds to about three or more times the a/b ratio greater than 1 (Paik & Pedersen 1996). On this basis, B_{0i} of Equation (1.10b) can be determined for the assumed M if the initial deflection measurements are available. The values of coefficients, B_{0i}, for the initial deflection shapes shown in Figure 1.17 are given in Table 1.4, by taking $M = 11$.

When relevant initial deflection measurements are not available, the initial deflection amplitudes may be approximately defined by assuming an appropriate initial deflection configuration as previously noted. For this purpose, some empirical formulations of the maximum plate initial deflection are relevant for steel plates between stiffeners, namely:

- Faulkner (1975):

$$\frac{w_{0pl}}{t} = \begin{cases} k\beta^2(t_w/t) & \text{for } t_w < t \\ k\beta^2 & \text{for } t_w \geq t \end{cases} \tag{1.11a}$$

where $\beta = (b/t)\sqrt{(\sigma_Y/E)}$, b = plate breadth (between stiffeners), t = plate thickness, E = Young's modulus, σ_Y = material yield strength, t_w = thickness of stiffener web, k = coefficient which may be in the range 0.05–0.15 for marine structures and less than 0.1 for land-based structures. Faulkner (1975) adopted for his sample calculations

Table 1.4 Initial deflection amplitudes for various initial deflection shapes indicated in Figure 1.17.

Initial deflection shape	B_{01}	B_{02}	B_{03}	B_{04}	B_{05}	B_{06}	B_{07}	B_{08}	B_{09}	B_{010}	B_{011}
#1	1.0	−0.0235	0.3837	−0.0259	0.2127	−0.0371	0.0478	−0.0201	0.0010	−0.0090	0.0005
#2	0.8807	0.0643	0.0344	−0.1056	0.0183	0.0480	0.0150	−0.0101	0.0082	0.0001	−0.0103
#3	0.5500	−0.4966	0.0021	0.0213	−0.0600	−0.0403	0.0228	−0.0089	−0.0010	−0.0057	−0.0007
#4	0.0	−0.4966	0.0021	0.0213	−0.0600	−0.0403	0.0228	−0.0089	−0.0010	−0.0057	−0.0007

$k = 0.12$ for $\beta \leq 3$ and $k = 0.15$ for $\beta > 3$, while Antoniou (1980) suggested $k = 0.091$ for $t_w < t$ and $k = 0.0628$ for $t_w \geq t$.

- Carlsen & Czujko (1978):

$$\frac{w_{0pl}}{t} = 0.016\frac{b}{t} - 0.36 \quad \text{for } \frac{b}{t} > 40 \tag{1.11b}$$

- Antoniou (1980) (modified Carlsen & Czujko's formula):

$$\frac{w_{0pl}}{t} = \begin{cases} 0.018b/t - 0.55 & \text{for } t \leq 14\,\text{mm} \\ 0.014b/t - 0.32 & \text{for } t > 14\,\text{mm} \end{cases} \tag{1.11c}$$

- Smith *et al.* (1988):

$$\frac{w_{0pl}}{t} = \begin{cases} 0.025\beta^2 & \text{for slight level} \\ 0.1\beta^2 & \text{for average level} \\ 0.3\beta^2 & \text{for severe level} \end{cases} \tag{1.11d}$$

- Masaoka (1996):

$$\frac{w_{0pl}}{t} = k\left(\frac{b}{t}\right)^2 \tag{1.11e}$$

where k = coefficient which may be taken as $k = 8 \times 10^{-5}$ for merchant ship structures.

Classification societies or other regulatory bodies specify construction tolerances of strength members as related to the maximum initial deflection with the intention that the initial distortions in the fabricated structure must be less than the corresponding specified values. Some examples of the limit for the maximum plate initial deflection are as follows:

- Det Norske Veritas:

$$\frac{w_{0pl}}{b} \leq 0.01$$

where b is as defined in Equation (1.11a).

- Shipbuilding quality standards of Japan and Germany:

$$w_{0pl} \leq 7\,\text{mm for bottom plate}$$

$$w_{0pl} \leq 6\,\text{mm for deck plate}$$

- Steel box girder bridge quality standards of the UK:

$$w_{0pl} \leq \min\left(\frac{t}{6} + 2, \frac{t}{3}\right), \quad t \text{ in mm}$$

Related to this, it is of interest to note that quite often, specifications of quality to be achieved are developed (and used) without specific reference to the loads and response at a particular location. In that case, the corresponding specifications suggest what can be generally achieved in an economical way, rather than what should be achieved in the context of a particular situation.

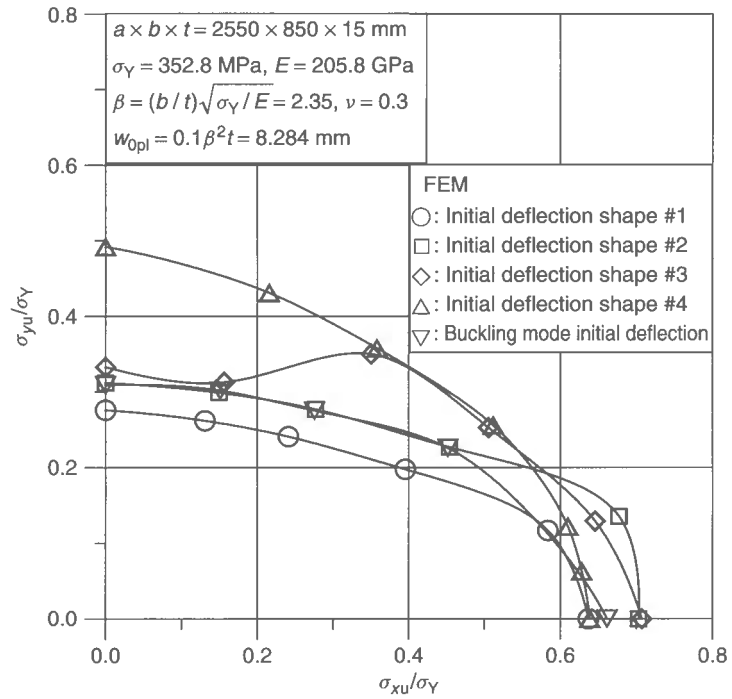

Figure 1.19 Effect of initial deflection shape on the ultimate strength of a simply supported steel plate under biaxial compression (assuming that buckling mode initial deflection = W_{0pl})

It has been recognized that the initial deflection shape may affect the ultimate strength behavior of steel plating as well. Figure 1.19 shows the effect of initial deflection shape on the ultimate strength of a simply supported plate under biaxial compression. The solutions by the nonlinear finite element method (FEM) were obtained by using the shapes of initial deflection indicated in Figure 1.17 or Table 1.4.

1.7.2 Welding-induced Residual Stresses

Figure 1.20 shows typical residual stress distributions in welded steel members, representing the tensile residual stresses that develop in heat-affected zones and the compressive residual stresses that then must also exist to achieve a self-equilibrium condition in the plane of the member.

For practical design purposes, the welding residual stress distributions of a plate element between support members for which welding has been carried out along its four edges may be idealized to be composed of tensile and compressive stress blocks, such as those shown in Figure 1.21. Among them, Figure 1.21(c) is a typical idealization of the welding residual stress distribution in a plate element.

Along the welding line, tensile residual stresses are usually developed with magnitude σ_{rtx} in the x direction and σ_{rty} in the y direction, the welding being normally performed in both x and y directions, see Figure 1.22. To obtain equilibrium, corresponding compressive residual stresses with magnitude σ_{rcx} in the x direction and σ_{rcy} in the y direction

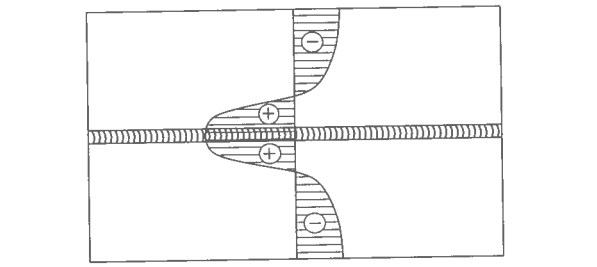

(a) Butt-welded plate

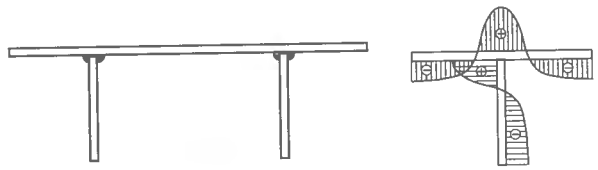

(b) Welded stiffened panel

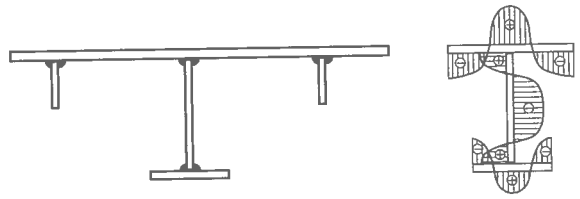

(c) Welded plate girder

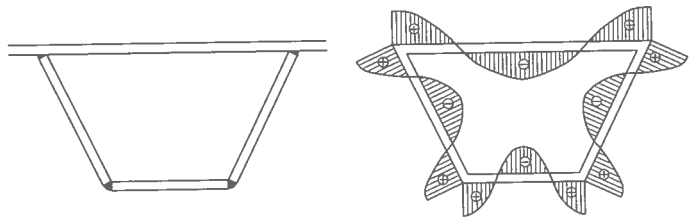

(d) Welded box section

Figure 1.20 Schematic illustration of residual stress distributions in welded steel members (+: tension, −: compression)

are developed in the middle part of the plate element. From equilibrium considerations, the breadth or length of the related tensile residual stress blocks in the x and y directions can be shown to be as follows:

$$2b_t = \frac{\sigma_{rcx}}{\sigma_{rcx} - \sigma_{rtx}} b, \; 2a_t = \frac{\sigma_{rcy}}{\sigma_{rcy} - \sigma_{rty}} a \tag{1.12}$$

The above-noted idealizations are largely consistent with the measurements of welding-induced residual stresses in steel plate between two longitudinal stiffeners (Kmiecik 1970, Cheng *et al.* 1996), see Figures 1.23(a) and 1.23(b). These figures indicate that the maximum tensile residual stress in such cases may well reach the yield stress. In evaluating

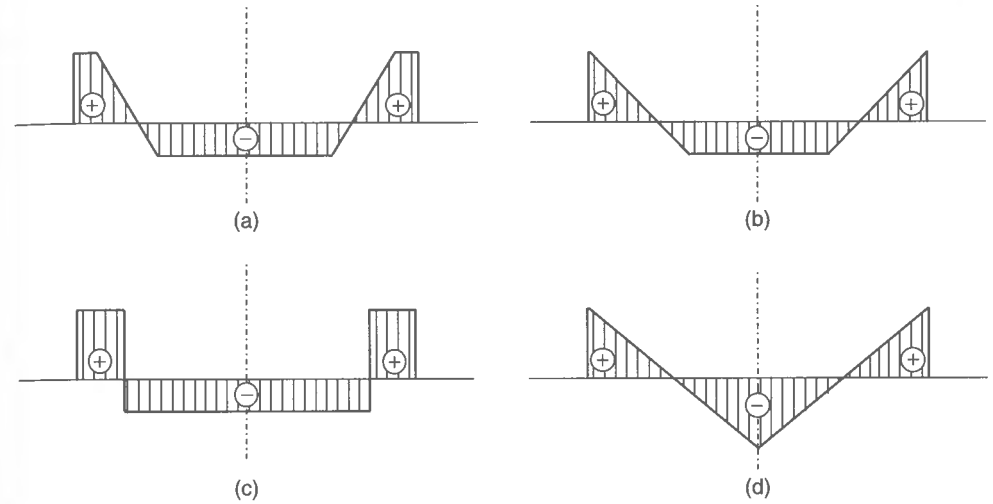

Figure 1.21 Various idealizations of residual stress distribution in a plate element (+: tension, −: compression)

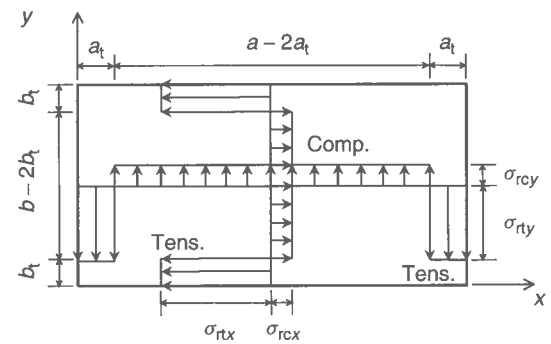

Figure 1.22 A typical idealized welding-induced residual stress distribution inside the steel-plate element in the x and y directions

the effect of residual stresses on the compressive buckling strength, a somewhat reduced tensile residual stress (e.g., 80% of the yield stress) may be used for idealization of the welding residual stress distribution as indicated by the dotted line in Figure 1.23(b) if potential shake-down effects are thought to be present.

Once the magnitudes of the compressive and tensile residual stresses are defined, the breadths of the tensile residual stress blocks can be determined from Equation (1.12). One can then define the residual stress distributions in the x and y directions, as expressed by

$$\sigma_{rx} = \begin{cases} \sigma_{rtx} & \text{for } 0 \le y < b_t \\ \sigma_{rcx} & \text{for } b_t \le y < b - b_t \\ \sigma_{rtx} & \text{for } b - b_t \le y \le b \end{cases} \quad \sigma_{ry} = \begin{cases} \sigma_{rty} & \text{for } 0 \le x < a_t \\ \sigma_{rcy} & \text{for } a_t \le x < a - a_t \\ \sigma_{rty} & \text{for } a - a_t \le x \le a \end{cases} \tag{1.13}$$

The magnitude of post-weld residual stresses in the longer direction will normally be larger because the weld length is longer. The residual stresses of plates in either

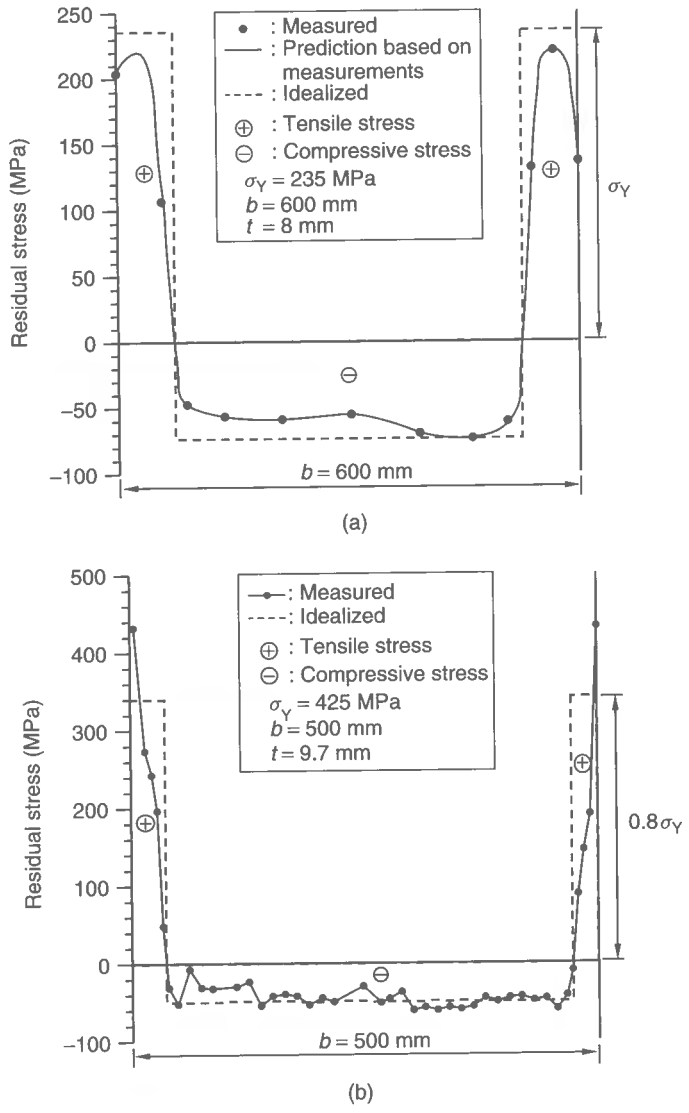

Figure 1.23 (a) Example of residual stress distribution in mild steel plating between stiffeners, based on the measurements of Kmiecik (1970); (b) Sample of residual stress distribution in a high tensile steel plating between stiffeners, based on the measurements of Cheng *et al.* (1996)

the unloaded or the shorter direction are often neglected. However, where needed, the transverse (plate breadth direction) residual stresses may be approximated pessimistically as follows:

$$\sigma_{rcy} = c\frac{b}{a}\sigma_{rcx} \tag{1.14}$$

where c = correction factor which typically takes a value less than 1.0 in steel plates. When the applied stress is predominant in the x direction, $c = 0$ is often assumed.

Based on the measurements for steel plates of naval ship structures, Smith *et al.* (1988) suggest the following representative values for the overall strength offsetting effect of welding-induced compressive residual stress of steel plates in the longitudinal (x) direction (taking compressive stress as negative), namely

$$\frac{\sigma_{rcx}}{\sigma_Y} = \begin{cases} -0.05 & \text{for slight level} \\ -0.15 & \text{for average level} \\ -0.3 & \text{for severe level} \end{cases} \tag{1.15}$$

These values of welding compressive residual stresses may be considered together with the corresponding characteristic values of initial deformation levels as noted in Equation (1.11).

1.8 Age-related Structural Degradation

In aging steel structures, of significance are defects related to corrosion and fatigue cracks, sometimes in a marine environment. In a number of damage cases for aging marine and land-based steel structures that have been reported, it is possible that corrosion damage and fatigue cracks may have existed in primary and other strength members. In any event, fatigue and corrosion are the two most important factors affecting structural performance over time.

It is therefore of importance that the structural designer and operator should have a better understanding of the location and extent of structural damage formed during operation of the structure and how it can affect the structural capacity. One reason that this is necessary is to facilitate repair decisions. Another possible broad reason may be to support a structural life extension decision later in life.

1.8.1 Corrosion Damage

Due to corrosion damage, the structural capacity can be decreased, and/or leakages can take place in oil/watertight boundaries, the latter possibly leading to undesirable pollution, cargo mixing, or gas accumulation in enclosed spaces. The corrosion process is time variant and the amount of corrosion damage is normally defined by a corrosion rate with units of, say, mm/year, representing the depth of corrosion diminution per year. The corrosion rate itself can be a function of time in some cases, due for example to effects such as increased structural flexibility as the corrosion process proceeds.

Figure 1.24 shows some of the more typical types of corrosion-related damage which affect the strength of steel structures. The 'general' corrosion (also called 'uniform' corrosion) uniformly reduces the thickness of structural members as shown in Figure 1.24(a),

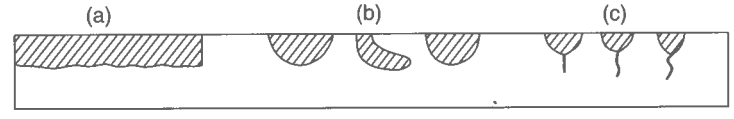

Figure 1.24 Typical types of corrosion damage: (a) general corrosion; (b) localized corrosion; (c) fatigue cracks arising from localized corrosion

while localized corrosion (e.g., pitting or grooving) causes degradation in local regions as shown in Figure 1.24(b). Sometimes fatigue cracks may arise from localized corrosion, as shown in Figure 1.24(c).

The corrosion damage of steel structures is influenced by many factors including the corrosion protection system and various operational parameters (Afanasieff 1975, Schumacher 1979, Melchers & Ahammed 1994). In general, the corrosion protection systems employed for ships or offshore platforms are coatings (paint) and anodes. The operational parameters include maintenance, repair, percentage of time in ballast, frequency of tank cleaning, temperature profiles, use of heating coils, humidity conditions, water and sludge accumulation, microbial contamination, composition of inert gas, etc. To date, basic work to understand the effect of many of these factors and their interactions is lacking in the case of marine structures.

To predict likely corrosion damage tolerance, it is necessary to be able to make estimates of the corrosion rates for various structural members grouped by type, location and other parameters. To generalize this further, there are four aspects related to corrosion that one ideally needs to define for structural members, as follows:

- Where is corrosion likely to occur?
- When does it start?
- What is its extent?
- What are the likely corrosion rates as a function of time?

The first question would normally be answered using historical data of some form, e.g., results of previous surveys. As to when corrosion starts, this again is information that should come from prior surveys for the particular structure. Lacking specific data, assumptions as to time of start of corrosion can of course be made, depending on the use of the protection system, characteristics of coatings and anode residence time.

For the residual strength and similar performance assessment of corroded steel structures, one needs to clarify how corrosion develops and proceeds in structural members, the spatial extents of member degradation, and the likely effects of such corrosion on structural performance measures such as strength and leakage characteristics. These considerations are complicated by the sheer number of factors potentially affecting corrosion, including type of protection employed, type of cargo, temperature, humidity, etc. Also, to take into account the various uncertainties associated with corrosion, a probabilistic treatment is essential.

The extent of corrosion presumably increases with time, but our ability to predict the spatial progress of corrosion remains meager. The only real alternative is then to pessimistically assume more of a corrosion extent than is really likely, such as what one would do in the case of nominal design corrosion values. To put this in another way, one can assess the structural performance based on premised extents of corrosion where specific information on extent of corrosion is lacking or unavailable.

Where coatings are present, the progress of corrosion would normally very much depend on the degradation of such coatings. Related to this, most classification societies usually recommend carrying out maintenance for the corrosion protection system over time, and most owners do carry out such maintenance, so the particular maintenance philosophy used also has a significant effect on the structural reliability considering corrosion effects in the long term.

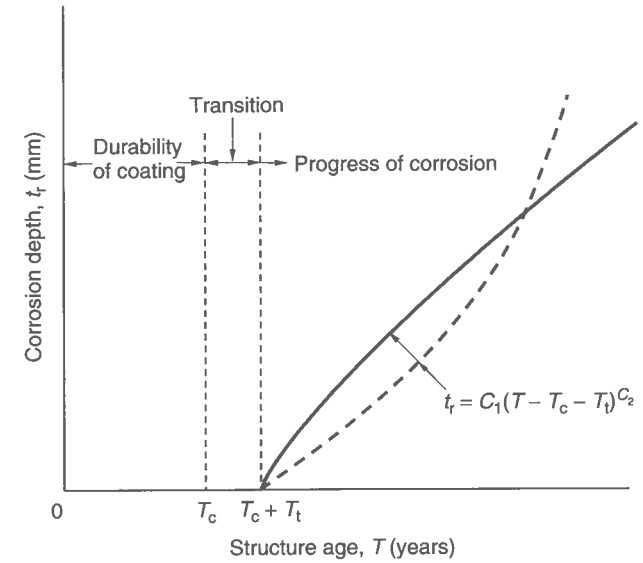

Figure 1.25 A schematic of the corrosion process for steel structures

Figure 1.25 represents a plausible schematic of the corrosion process for a coated area in a steel structure. It is assumed in Figure 1.25 that there is no corrosion as long as the coating is effective and also during a short transition time after breakdown of the coating. Therefore, the corrosion model accounts for three factors, namely (1) durability of coating, (2) transition and (3) progress of corrosion.

The curve showing corrosion progression indicated by the solid line in Figure 1.25 is a little convex, but it may in some cases be a concave curve in dynamically loaded structures as indicated by the dotted line where flexing continually exposes additional fresh surface to the corrosion effects. However, one may take a linear approximation between them for practical assessment.

The life (or durability) of a coating essentially corresponds to the time when the corrosion starts after the contribution of a structure, or the application of a coating in a previously bare case, or repair of a coating area to a good, intact standard. The life of a coating typically depends on the type of coating systems used and relevant maintenance, among other factors. The coating life to a predefined state of breakdown is often assumed to follow the log-normal distribution, given by

$$f(T_c) = \frac{1}{\sqrt{2\pi}\sigma_c} \exp\left[-\frac{(\ln T_c - \mu_c)^2}{2\sigma_c^2}\right] \tag{1.16}$$

where μ_c = mean value of $\ln T_c$ in years, σ_c = standard deviation of $\ln T_c$, T_c = coating life in years.

The coating systems are sometimes classified by their target life. For example, IMO (1995) uses three groups for marine structures, namely coating systems I, II and III, where the corresponding target durability of coating is 5, 10 and 15 years, respectively. But this particular classification is by no means universal. TSCF (2000) defines the requirements for 10, 15 and 25 year coating systems for ballast tanks in oil tankers. Generally, however,

a 5 year coating life may be considered to represent an undesirable situation, while 10 years or longer would be representative of a relatively more desirable state of affairs. The selection of a target life to be achieved is primarily economical. For any given mean or median coating life, the uncertainty of coating life is high and the coefficient of variation (COV) of coating life is sometimes taken as $\sigma_c/\mu_c = 0.4$ for $\ln T_c$ (NK 1995).

After the effectiveness of a coating is lost, some transition time, i.e., duration between the time of coating effectiveness loss and the time of corrosion initiation, is considered to exist before the corrosion 'initiates' over a large enough and easily measured area. The transition time is sometimes considered to be an exponentially distributed random variable following other past work. As an example, the mean value of the transition time for transverse bulkhead structures of bulk carriers is shown to be 3 years for deep-tank bulkheads, 2 years for watertight bulkheads and 1.5 years for stool regions (Yamamoto & Ikegami 1998). When the transition time is assumed to be zero (i.e., $T_t = 0$), it is implied that the corrosion will start immediately after the coating effectiveness is lost.

As shown in Figure 1.25, the wear of plate thickness due to corrosion may be generally expressed as a function of the time (year) after the corrosion starts, namely

$$t_r = C_1 T_e^{C_2} \tag{1.17}$$

where t_r = corrosion depth (or wear of plate thickness due to corrosion) in mm, T_e = exposure time in years after breakdown of the coating, which is taken as $T_e = T - T_c - T_t$, T = age of structure in years, T_c = life of coating in years, T_t = duration of transition in years which may be pessimistically taken as $T_t = 0$. C_1 and C_2 are coefficients.

The coefficient C_2 in Equation (1.17) determines the trend of corrosion progress, while the coefficient C_1 is in part indicative of the annualized corrosion rate which can be obtained by differentiating Equation (1.17) with respect to time. As may be surmised from Equation (1.17), the two coefficients closely interact, and they can simultaneously be determined based on the carefully collected statistical corrosion data of existing structures. However, this approach is in most cases not straightforward to apply, mainly because of differences in data collection sites typically visited over the life of the structure. That is, it is normally difficult to track corrosion at a particular site based on the typically available gauging data. This is part of the reason for the relatively large scatter of corrosion data in many studies. An easier alternative is to determine the coefficient C_1 at a constant value of the coefficient C_2. This is mathematically a simpler model, but it does not negate any of the shortcomings due to the usual methods of data collection in surveys. It does, however, make possible the postulation of different modes of corrosion behavior over time depending on the value adopted for C_2 in an easy-to-understand way.

For corrosion of marine structures, past studies indicate that the coefficient C_2 can sometimes be in the range of 0.3–1.5 (Yamamoto & Ikegami 1998, Melchers 1999). This implies a behavior wherein the corrosion rates are not constant while they apparently decrease or stabilize over time. While for statically loaded structures, such behavior is plausible, for dynamically loaded structures in which corrosion scale is continually being lost and new material is being exposed to corrosion because of structural flexing, such values of C_2 may not always be appropriate or safe.

Figure 1.26 plots Equation (1.17) which shows curve fits to a total of 1279 points of corrosion data gathered from the thickness measurements of outer bottom plates for 109 existing bulk carriers, varying the coefficient, C_2. In Figure 1.26, it is assumed that the

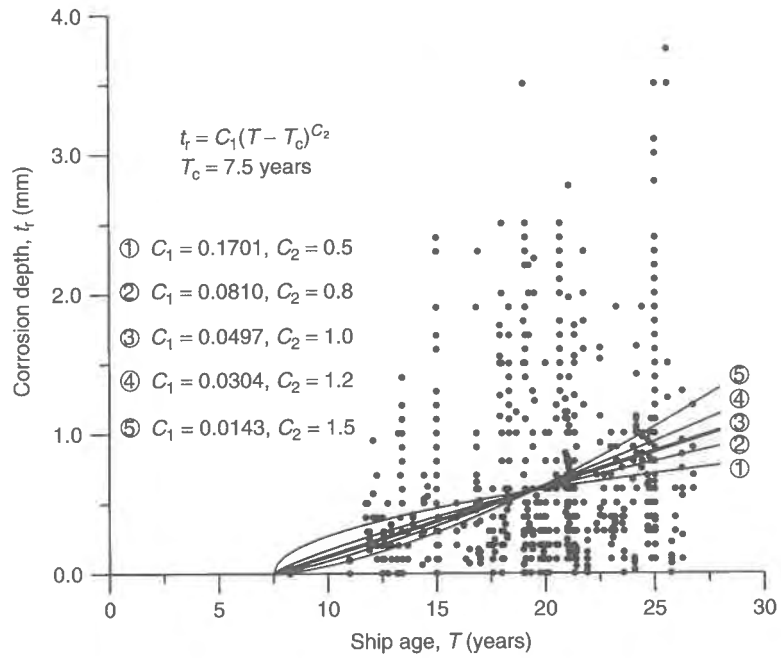

Figure 1.26 Sample formulations for the corrosion depth measured for outer bottom plates of existing bulk carrier structures as a function of ship age

coating life is 7.5 years and the corrosion initiates without a transition time after the effectiveness of coating is lost. It is seen from Figure 1.26 that the trend of the corrosion progress slightly varies with the coefficient C_2, as would be expected, but its effect may be ignored as the ship gets older. For practical design purposes, therefore, $C_2 = 1$ may be taken. For more refined treatments, C_2 may of course be taken as a random variable so that the corrosion model can represent the variation of annualized corrosion rate over time.

Once the coefficient C_2 is set to be a constant value, the next step is to determine the coefficient C_1, which corresponds to the annualized corrosion rate, and its statistics (mean, variance and type of probability density). It is evident that the characteristics of the coefficient C_1 must be evaluated in such a probabilistic form because of the uncertainties involved.

From Equation (1.17), the coefficient C_1 can be readily given for a sampling point when the transition time is taken as $T_t = 0$ as follows:

$$C_1 = \frac{t_r}{(T - T_c)^{C_2}} \tag{1.18}$$

Thus, given a set of available statistical corrosion data, the coefficient C_1 may be calculated from Equation (1.18), and the relative frequency of the coefficient C_1 can then be evaluated. It is apparent from Equation (1.18) that the coating life may significantly affect the coefficient C_1, and hence the annualized corrosion rate which is extremely uncertain in nature.

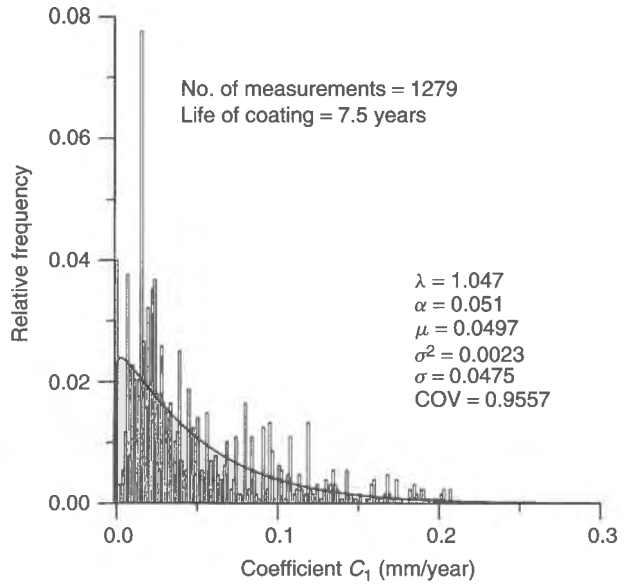

Figure 1.27 The Weibull-type probability density distribution for the coefficient C_1, with $C_2 = 1.0$ and $T_c = 7.5$ years, corrosion data for the outer bottom plates of existing bulk carriers

Figure 1.27 shows the best fit of a Weibull-type probability density distribution of the coefficient C_1, with $C_2 = 1.0$ and $T_c = 7.5$ years, corrosion data for the outer bottom plates of bulk carriers. It is recognized that the probability density function of the coefficient C_1 in marine immersion corrosion typically follows the Weibull distribution as follows (Paik *et al.* 1998):

$$f(x)_{C_1} = \frac{\lambda}{\alpha}\left(\frac{x}{\alpha}\right)^{\lambda-1} \exp\left[-\left(\frac{x}{\alpha}\right)^{\lambda}\right] \tag{1.19}$$

where α and λ are scale and shape parameters, respectively, which will be determined through a probability density distribution fit using the method of moments, the maximum likelihood method or other appropriate method. The choice of a Weibull density distribution offers us some flexibility as it is capable of representing a range of types of exponential behavior.

Hence, the cumulative distribution function of the coefficient C_1 may be given by

$$F(x)_{C_1} = 1 - \exp\left[-\left(\frac{x}{\alpha}\right)^{\lambda}\right] \tag{1.20}$$

It is now necessary to determine the mean and standard deviation of the coefficient C_1 for evaluating the probabilistic characteristics of corrosion. Their calculation using Equation (1.19) or (1.20) may be possible in several ways, and an approximate procedure may be used. For instance, Equation (1.20) is rewritten in terms of

$$Y = \lambda X - \lambda \ln \alpha \tag{1.21}$$

where $X = \ln x$, $Y = \ln\{-\ln[1 - F_{C_1}(x)]\}$.

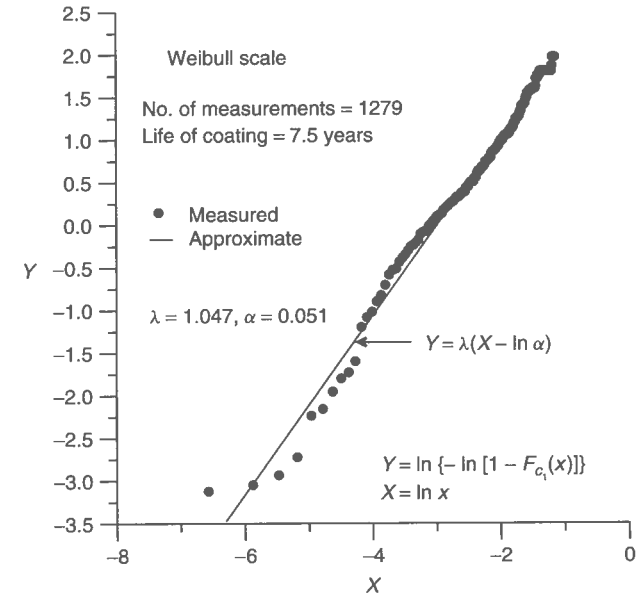

Figure 1.28 The best fit of Equation (1.21) for the outer bottom plates of existing bulk carriers having a coating life of 7.5 years

By using the least squares method, the unknown parameters, α and λ, are determined for each primary member type for which corrosion data have been collected over time. Figure 1.28 shows a typical example of determining parameters α and λ so obtained for the bulk carrier bottom corrosion data. This figure indicates that a Weibull density function can be an adequate fit in this case. However, whether it is the best fit is of course open to question lacking a goodness of fit study using other types of probability distributions.

Once the scale and shape parameters (i.e., α and λ) are determined the mean value and standard deviation of the coefficient C_1 can be calculated in terms of the gamma function as follows:

$$\mu_{C_1} = \int_0^{\infty} x f_{C_1}(x)\,dx = \alpha\Gamma\left(1 + \frac{1}{\lambda}\right) \tag{1.22a}$$

$$\sigma_{C_1}^2 = \int_0^{\infty} (x - \mu)^2 f_{C_1}(x)\,dx = \alpha^2\left\{\Gamma\left(1 + \frac{2}{\lambda}\right) - \left[\Gamma\left(1 + \frac{1}{\lambda}\right)\right]^2\right\} \tag{1.22b}$$

where μ_{C_1} and σ_{C_1} = mean and standard deviation of the coefficient C_1.

The mean and standard deviation (or the coefficient of variation) for the coefficient C_1 can thus characterize the annualized corrosion rate. Based on the available statistical corrosion data, these values can then be determined for every necessary member location/category of a structure.

It is important to realize that the annualized corrosion rate for structural members can differ between types of structures or even member locations within the same structure. In evaluating the probabilistic characteristics of corrosion diminution, the prescribed corrosion diminution interval must be small enough to reduce the level of the coefficient

of variation. Figure 1.29 shows the effect of the interval, Δ, of coefficient C_1 on the resulting mean value and COV of the annualized corrosion rate for the outer bottom plates of bulk carriers. It is apparent that the interval (bin width) may in this case need to be taken as 0.0014 mm/year or smaller.

Figure 1.30 shows the mean value and COV of the annualized corrosion rate for the 23 longitudinal strength member locations/categories of bulk carrier structures, obtained

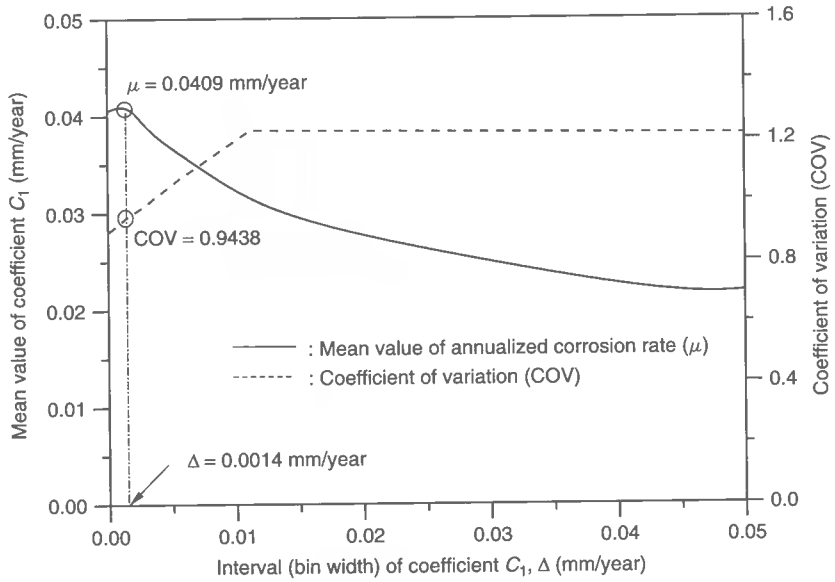

Figure 1.29 Effect of the interval (bin width), Δ, of coefficient C_1 on the annualized corrosion rate characteristics for the outer bottom plates of existing bulk carriers

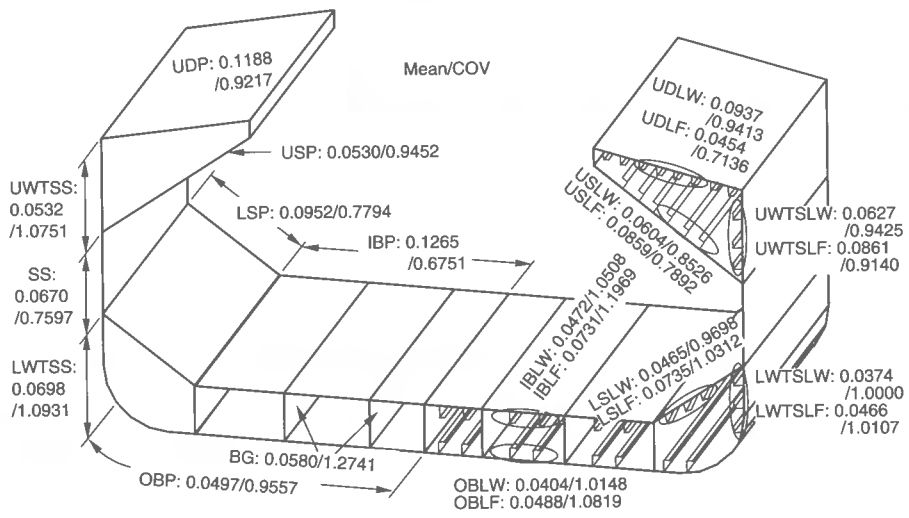

Figure 1.30 Mean and COV of the annualized corrosion rate for the 23 member location/category groups of a bulk carrier structure

based on the method noted above. In this case, the interval of coefficient C_1 was taken as $\Delta = 0.0014$ mm/year. The reference coating life of IBP (inner bottom plates) and LSP (lower sloping plates) was supposed to be 5 years, while that of the rest of the member locations was considered to be 7.5 years. Different, possibly equally useful, corrosion rate models have also been suggested by other investigators for bulk carrier structures (e.g., Ivanov 1986, Yamamoto & Ikegami 1998) and also for oil tanker structures (e.g., Hart *et al.* 1985, Løseth *et al.* 1994, Paik & Park 1998), amongst others.

The effects of corrosion damage will be addressed in Chapter 4 on the ultimate strength of steel plates and in Chapter 8 on the ultimate strength of ship hulls.

1.8.2 Fatigue Cracks

Under the action of repeated loading, fatigue cracks may be initiated in the stress concentration areas of the structure. Initial defects or cracks may also be formed in the structure by the fabrication procedures applied. In addition to their fatigue propagation under repeated cyclic loading, cracks, as they grow, may also propagate under monotonically increasing extreme loads, a circumstance which eventually can lead to catastrophic failure of the structure when given the possibility of rapid and uncontrolled crack extension without arrest, or if the crack attains such a length resulting in significant degradation in structural capacity.

For residual strength assessment of aging steel structures under extreme loads as well as under fluctuating loads, it is thus often necessary to take into account an existing crack as a parameter of influence. The ultimate strength of steel-plated structures with existing crack damage will be presented in Chapter 10.

1.9 Accident-induced Damage

Potential accidents such as collision, grounding, impact due to dropped objects or mishandled cargo loading/unloading, fire, explosions, etc., can result in structural damage which reduces structural resistance or leads to even total loss of the structure.

Collision and grounding accidents typically result in crushing (folding), yielding and tearing. Hydrodynamic impact can raise plastic deformation damage. Dropped objects can cause local dents and/or global permanent deformation. Because of fire or explosions the steel can be exposed to high temperatures, the latter being also accompanied by impact. Exposure to a fire at very high temperatures can cause not only structural damage but also metallurgical changes. For fire safety and the resistance of steel structures, Lawson (1992) and Nethercot (2001) may be referred to.

In this book, ship collision and grounding mechanics as well as the dynamic/impact response of structural members are described in Chapter 9. The effect of collision and grounding damage on the ultimate strength of ship hulls is presented in Chapter 8.

1.10 Ultimate Limit State Design Format

For the ULS design of steel-plated structures, the basic variables which characterize load effects, material properties and geometric parameters should be identified first. Methodologies or simplified models for computing the load effects and the load-carrying capacities

must be established. Once the two models, i.e., for calculating both load effects and ultimate strength, are obtained, the ULS function, G, can be given from Equation (1.1) as a function of the basic variables $x_1, x_2, \ldots, x_n$, as follows:

$$G(x_1, x_2, \ldots, x_n) = 0 \tag{1.23}$$

When $G \geq 0$, the structure is considered to be the desired state. The models always have uncertainties due to many reasons. The computation model is in fact a function of random variables, namely

$$Y_m = Y(x_1, x_2, \ldots, x_n) \tag{1.24}$$

where Y_m = value computed by the model, Y = function of the model, x_i = random variables.

As long as the random variables are uncertain, the modeling function is not exact so that Y_m may always have some errors. This is typically due to lack of knowledge or simplification in developing the model. The exact solution, Y_0, of the problem may be expressed by

$$Y_0 = Y^*(x_1, x_2, \ldots, x_n, \delta_1, \delta_2, \ldots, \delta_m) \tag{1.25}$$

where δ_i = random variables related to the model uncertainties, Y^* = exact function.

In Equation (1.25), the statistical properties of δ_i may normally be determined from experiments or observations. For the ultimate strength model, the mean of δ_i can be determined as the average value which correctly predicts the test results.

It is necessary to ensure that the structure has an adequate degree of reliability against the ULS. Two types of design format are normally used, namely (ISO 2394 1998)

- the direct probabilistic design format
- the partial safety factor format.

While the latter format is typically used for normal design purposes, the former is sometimes more relevant for specific design problems or for calibration of the partial safety factors. The design condition of a structure in the partial safety factor format is expressed as follows:

$$C_d - D_d = \frac{C_k}{\gamma_m \gamma_c} - \gamma_0 \sum D_{ki}(F_{ki}, \gamma_{fi}) \geq 0 \tag{1.26}$$

The actions are normally dynamic and varying in nature and may have the following representative values (ISO 2394 1998):

- characteristic value;
- load combination value;
- frequent value; and
- quasi-permanent value.

The characteristic value of load effects is determined so that it may have a specified probability being exceeded toward unfavorable values during the reference period. The combination value is determined so that the probability that the load effects arising from the load combination will be exceeded is approximately the same as that for a single

action. The frequent value is determined so that the total time which it will be exceeded during the reference period is limited to a specified short period or the frequency of its exceedance is limited to a specified small value. The quasi-permanent value is determined so that the total time which it will be exceeded during the reference period is of the magnitude of perhaps half the reference period.

The partial factors may depend on the design situation and the types of the limit states. In most cases, while D_k is defined as the characteristic value noted above, γ_f is defined taking into account the possibility of unfavorable deviations of the action values from the representative values and the uncertainties in the model of load effects.

Similarly, while the characteristic value of C_k against the limit state is calculated using more sophisticated models as presented in this book, γ_m is defined taking into account the possibility of unfavorable deviations of material properties from the characteristic (specified) values and the uncertainties in the conversion factors. γ_c may be determined taking into account the possibility of unfavorable deviations of geometric parameters from the characteristic (specified) values including the severity (importance) of variations, the tolerance specifications and the control of the deviations, and the cumulative effect of a simultaneous occurrence of several geometric deviations, the possibility of unfavorable consequences of progressive collapse, and the uncertainties of the models as quantified by deviations from measurements or benchmark calculations.

References

Afanasieff, L. (1975). Corrosion mechanisms, corrosion defense and wastage. Chapter 16 in *Ship Structural Design Concepts*. Cornell Maritime Press, Cambridge, MA.

AISC (1993). *Manual of steel construction: load and resistance factor design specification for structural steel buildings*. American Institute of Steel Construction, Chicago.

AISI (1974). *The variation of product analysis and tensile properties – carbon steel plates and wide flange shapes*. American Iron and Steel Institute, New York.

Antoniou, A.C. (1980). On the maximum deflection of plating in newly built ships. *Journal of Ship Research*, 24(1): 31–39.

Brockenbrough, R.L. (1983). Structural steel design and construction. Chapter 9 in *Standard Handbook for Civil Engineers*. McGraw-Hill, New York.

Brockenbrough, R.L. (1991). Material properties. Chapter 1.2 in *Constructional Steel Design, An International Guide*. Elsevier Applied Science, London and New York.

Brockenbrough, R.L. & Johnston, B.G. (1981). *USS steel design manual*. USC Corp., Pittsburgh, PA.

BS 5950 (1985). *The structural use of steelwork in building. Part 8*. British Standards Institution, London.

Callister, W.D. (1997). *Materials science and engineering*, Fourth Edition. John Wiley & Sons, New York.

Carlsen, C.A. & Czujko, J. (1978). The specification of post-welding distortion tolerance for stiffened plates in compression. *The Structural Engineer*, 56A(5): 133–141.

Cheng, J.J.R., Elwi, A.E., Grodin, G.Y. & Kulak, G.L. (1996). Material testing and residual stress measurements in a stiffened steel plate. In *Strength and Stability of Stiffened Plate Components*. Ship Structure Committee, SSC-399, Washington, DC.

ECCS (1982). *European recommendations for the fire safety of steel structures*. ECCS Technical Committee 3, European Convention for Constructional Steelwork.

ENV 1993-1-1 (1992). *Eurocode 3: design of steel structures, part 1.1 general rules and rules for buildings*. British Standards Institution, London.

ENV 1993-1-2 (1992). *Eurocode 3: design of steel structures, part 1.2 fire resistance*. British Standards Institution, London.

Faulkner, D. (1975). A review of effective plating for use in the analysis of stiffened plating in bending and compression. *Journal of Ship Research*, 19(1): 1–17.

Fricke, W., Berge, S., Brennan, F., Cui, W., Josefson, L., Kierkegaard, H., Kihl, D., Koval, M., Mikkola, T.P., Parmentier, G., Toyosada, M. & Yoon, J.H. (2000). *Fatigue and fracture. Report of Technical Committee III.2, Proceedings of the 14th International Ship and Offshore Structures Congress, Nagasaki, Japan*. Elsevier, Amsterdam, I: 323–392.

Galambos, T.V. (1988). *Guide to stability design criteria for metal structures*. John Wiley & Sons, New York.

Hart, D.K., Rutherford, S.E. & Wickham, A.H.S. (1985). Structural reliability analysis of stiffened panels. *RINA Transactions*, 128: 293–310.

IMO (1995). *Guidelines for the selection, application and maintenance of corrosion prevention systems of dedicated seawater ballast tanks*. Resolution A.798(19), International Maritime Organization, London.

ISO 2394 (1998). *General principles on reliability for structures*, Second Edition. International Organization for Standardization, Geneva.

Ivanov, L.D. (1986). Statistical evaluation of the ship's hull cross-section geometrical characteristics as a function of her age. *International Shipbuilding Progress*, 387: 198–203.

Kmiecik, M. (1970). The load carrying capacity of axially loaded longitudinally stiffened plates having initial deformation. Ship Research Institute, Technical Report No. R80, Trondheim.

Kmiecik, M., Jastrzebski, T. & Kuzniar, J. (1995). Statistics of ship plating distortions. *Marine Structures*, 8: 119–132.

Lawson, R.M. (1992). Fire resistance and protection of structural steelwork. Chapter 7.3 in *Constructional Steel Design, An International Guide*. Elsevier Applied Science, London.

Løseth, R., Sekkeseter, G. & Valsgård, S. (1994). Economics of high tensile steel in ship hulls. *Marine Structures*, 7(1): 31–50.

Masaoka, K. (1996). Development and application of an efficient ultimate strength analysis method for ship structures. Dr. Eng. Dissertation, Osaka University, Osaka, (in Japanese).

Masubuchi, K. (1980). *Analysis of welded structures*. Pergamon Press, Oxford.

Melchers, R.E. (1999). Corrosion uncertainty modeling for steel structures. *Journal of Constructional Steel Research*, 52: 3–19.

Melchers, R.E. & Ahammed, M. (1994). Nonlinear modeling of corrosion of steel in marine environments. Research Report No. 106.09.1994, Department of Civil, Surveying and Environmental Engineering, The University of Newcastle, Australia.

Nethercot, D.A. (2001). *Limit states design of structural steelwork*, Third Edition based on Revised BS 5950: Part 1, 2000 Amendment. Spon Press, London.

NK (1995). *Guidance for corrosion protection system of hull structures for water ballast tanks and cargo oil tanks*, 2nd Revision. Nippon Kaiji Kyokai, Tokyo.

NTS (1998). *Design of steel structures, N-004*. Norwegian Technology Standards Institution, Oslo.

Paik, J.K. & Park, Y.I. (1998). A probabilistic corrosion rate estimation model for longitudinal strength members of tanker structures. *Journal of the Society of Naval Architects of Korea*, 35(2): 83–93 (in Korean).

Paik, J.K. & Pedersen, P.T. (1996). A simplified method for predicting the ultimate compressive strength of ship panels. *International Shipbuilding Progress*, 43: 139–157.

Paik, J.K., Kim, S.K. & Lee, S.K. (1998). Probabilistic corrosion rate estimation model for longitudinal strength members of bulk carriers. *Ocean Engineering*, 25(10): 837–860.

Schumacher, M. (ed.) (1979). *Seawater corrosion handbook*. Noyes Data Corporation, Park Ridge, New Jersey.

Smith, C.S., Davidson, P.C., Chapman, J.C. & Dowling, P.J. (1988). Strength and stiffness of ships' plating under in-plane compression and tension. *RINA Transactions*, 130: 277–296.

TSCF (2000). Guidelines for ballast tank coating systems and edge preparation. Tanker Structure Cooperative Forum, Presented at the TSCF Shipbuilders Meeting in Tokyo, Japan, October.

Ueda, Y. (1999). *Computational welding mechanics (a volume of selected papers in the commemoration of the retirement from Osaka University)*. Joining and Welding Research Institute, Osaka University, Osaka, Japan, March.

Yamamoto, N. & Ikegami, K. (1998). A study on the degradation of coating and corrosion of ship's hull based on the probabilistic approach. *Journal of Offshore Mechanics and Arctic Engineering*, 120: 121–128.

2 Buckling and Ultimate Strength Behavior of Plate–Stiffener Combinations: Beams, Columns and Beam–Columns

2.1 Structural Idealizations of Plate–Stiffener Assemblies

A steel-plated structure is typically composed of plate panels and rolled or built-up support members usually termed stiffeners, as shown in Figure 2.1. The overall failure of the structure is certainly affected and can be governed by the buckling and plastic collapse of these individual members. In the ultimate limit state (ULS) design, therefore, a primary task is to accurately calculate the buckling and plastic collapse strength of such structural members.

Structural elements making up steel-plated structures do not work separately, resulting in a high degree of redundancy and complexity, in contrast to those of steel-framed structures. To enable the behavior of such structures to be analyzed, simplifications or idealizations must essentially be made considering the accuracy needed and the degree of complexity of the analysis to be used. Generally the more complex the analysis the greater is the accuracy that may be obtained. However, the amount of structural simplifications normally depends on the particular situation surrounding the problem. For instance, the ability to provide a reasonable answer quickly, with considerably less information, is often of greater importance than extreme accuracy for an initial estimate while a final check solution should of course be as accurate as the circumstances allow.

A steel-plated structure may be idealized into an assembly of many simpler 'mechanical structural element models' or 'idealized elements', each type of which behaves similarly

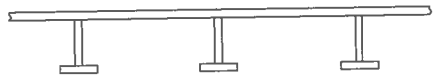

Figure 2.1 A continuous stiffened plate structure

under given load application, and the assembly of which behaves in the (nearly) same way as the actual structure.

Typical examples of structural idealization to model a continuous stiffened panel shown in Figure 2.1 are as follows:

- plate–stiffener (beam) combination model (also called beam–column model);
- plate–stiffener (beam) separation model; and
- orthotropic plate model.

One of the most typical approaches is the plate–stiffener combination idealization which models a continuous stiffened panel as an assembly of possibly unsymmetric I-beams together with attached plating (i.e., flanges) assuming that the flanges support bending moments while stiffener webs resist shear loads, see Figure 2.2(a). The torsional rigidity of the stiffened panel, the Poisson ratio effect and the effect of the intersecting beams are all neglected in this modeling. The degree of accuracy for this approach may therefore become critical when the flexural rigidity of the stiffeners is small compared to the plate stiffness, but the plate–stiffener combination model may be relevant when support members (i.e., stiffeners) are of a medium or larger structural dimension so that they would behave as a beam–column together with the associated plating. The plate–beam combination approach may also be applied to model a cross-stiffened panel as a system of discrete intersecting beams (or called grillage), each beam being composed of stiffener and associated effective plating. In this chapter, the primary concern is to examine the behavior of the plate–stiffener combinations.

Alternatively a mechanical idealization may be feasible by separating support members from plate panels at plate/web junctions, see Figure 2.2(b). The so-called 'plate–beam separation model' will be more appropriate when structural dimensions of the support members are relatively large so that the stiffener web as well as the plating between

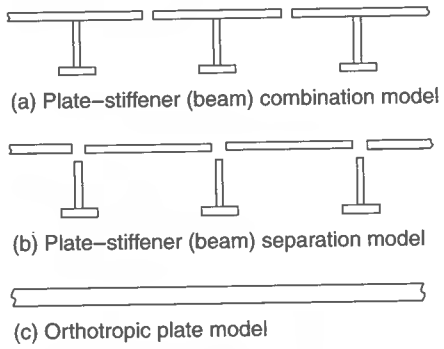

Figure 2.2 Three types of structural idealizations possible for a steel-plated structure

stiffeners may be regarded as a plate panel in itself. In this case, local buckling of the stiffener web as well as the attached plating will be a primary failure mode since support members are strong enough to remain straight well after plate failure. Buckling and collapse of plating between stiffeners are described later in Chapters 3 and 4, respectively.

On the other hand, if support members are relatively weak, they will deflect together with plate panels so that the behavior of the stiffened panel may in this case be idealized as that of an 'orthotropic plate' by smearing the stiffeners into the plating, as shown in Figure 2.2(c). The orthotropic plate approach will be useful for computation of the panel ultimate strength based on the overall grillage collapse mode. In this approach, the orthotropic plate theory is used. This implies that stiffeners are relatively numerous and small (i.e., they deflect together with the plating) and that they remain stable through the ranges of orthotropic plate behavior. The validity of representing the stiffened panel by an equivalent orthotropic plate normally depends on the number of stiffeners in each direction, their spacing, and how identical they are as far as their stiffness characteristics are concerned. It has been said that the application of the orthotropic plate theory to cross-stiffened panels must be restricted to stiffened panels with more than three stiffeners in each direction (Smith 1966, Troitsky 1976, Mansour 1977). In addition, stiffeners in each direction must be similar. The orthotropic plate approach will be described later in Chapters 5 and 6.

It is therefore important to realize that different mechanical modeling for the same type of structure may be required to analyze actual behavior under different structural dimensions or load applications. Clearly it may be necessary to idealize a structure by combining the modeling methods mentioned above in some cases. For instance, a longitudinally stiffened panel between strong transverse frames may be modeled by either an assembly of the plate–beam combinations or an orthotropic plate, while heavy transverse frames or plate girders may be idealized by using the plate–beam separation modeling where their webs are modeled as plate panels.

In any event, the idealized structure should of course be similar or nearly the same in behavior to the actual structure. The real ultimate strength of the structure will then be determined at the limit state which provides the lowest load-carrying capacity among those obtained for the various failure modes.

In the ULS design of plate–stiffener combinations using Equation (1.1) of Chapter 1, the design load effects (e.g., stress, bending) are calculated by classical theory of structural mechanics, while the structural capacity may be determined by relevant ultimate strength formulations. This chapter describes the ultimate strength formulations of plate–stiffener combinations under a variety of loading and end conditions. It also presents the axial stress–strain relationships of plate–stiffener combination elements until and after the ULS is reached.

2.2 Geometric and Material Properties

In a continuous stiffened plate structure, a stiffener (support member) with attached plating is idealized by the plate–beam combination model whose span extends between two

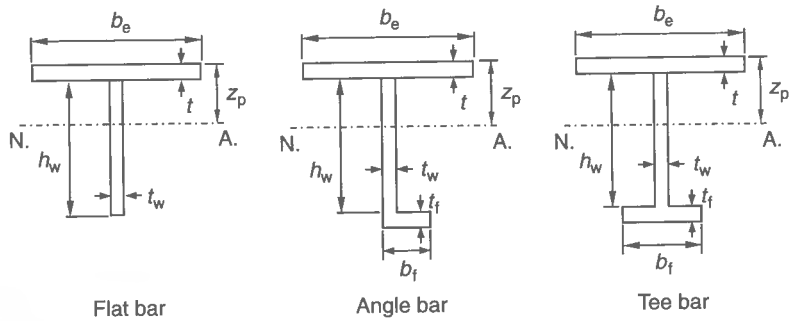

Figure 2.3 Typical types of plate–beam combination models made up of a stiffener and its attached effective plating (N.A. = neutral axis)

Table 2.1 Properties of a plate–stiffener combination section with full or effective plating.

Property	Expression
Cross-sectional area	$A = A_p + A_w + A_f$, $A_e = A_{pe} + A_w + A_f$ where $A_p = bt$, $A_{pe} = b_e t$, $A_w = h_w t_w$, $A_f = b_f t_f$
Equivalent yield strength over the cross-section	$\sigma_{Yeq} = \dfrac{A_p\sigma_{Yp} + A_w\sigma_{Yw} + A_f\sigma_{Yf}}{A}$
Distance from outer surface of attached plating to elastic horizontal neutral axis	$z_0 = \dfrac{0.5bt^2 + A_w(t + 0.5h_w) + A_f(t + h_w + 0.5t_f)}{A}$
	$z_p = \dfrac{0.5b_e t^2 + A_w(t + 0.5h_w) + A_f(t + h_w + 0.5t_f)}{A_e}$
Moment of inertia	$I = \dfrac{bt^3}{12} + A_p\left(z_0 - \dfrac{t}{2}\right)^2 + \dfrac{h_w^3 t_w}{12} + A_w\left(z_0 - t - \dfrac{h_w}{2}\right)^2 + \dfrac{b_f t_f^3}{12} + A_f\left(t + h_w + \dfrac{t_f}{2} - z_0\right)^2$
	$I_e = \dfrac{b_e t^3}{12} + A_{pe}\left(z_p - \dfrac{t}{2}\right)^2 + \dfrac{h_w^3 t_w}{12} + A_w\left(z_p - t - \dfrac{h_w}{2}\right)^2 + \dfrac{b_f t_f^3}{12} + A_f\left(t + h_w + \dfrac{t_f}{2} - z_p\right)^2$
Radius of gyration	$r = \sqrt{\dfrac{I}{A}}$, $r_e = \sqrt{\dfrac{I_e}{A}}$
Column slenderness ratio	$\lambda = \dfrac{L}{\pi r}\sqrt{\dfrac{\sigma_{Yeq}}{E}}$, $\lambda_e = \dfrac{L}{\pi r_e}\sqrt{\dfrac{\sigma_{Yeq}}{E}}$
Plate slenderness ratio	$\beta = \dfrac{b}{t}\sqrt{\dfrac{\sigma_{Yp}}{E}}$

Note: The subscript 'e' represents the effective cross-section.

adjacent major support members in the other direction. The attached plating takes the 'effective width' instead of full width as will be described in Section 2.5.

Figure 2.3 shows geometrical configurations of typical plate–beam combination sections together with the attached effective plating. For convenience, the x axis is taken in the longitudinal direction of the member and its length (span) between supports is denoted by L. The full and effective widths of the attached plating are denoted by b and b_e, respectively.

While the material of the web and flange of the stiffener is usually the same, it is sometimes different from that of attached plating, e.g., higher tensile steel for web and flange and mild steel for plating. For general purposes, the yield strengths of the stiffener web, flange and attached plating are herein defined separately by σ_{Yw}, σ_{Yf} and σ_{Yp}, respectively. The modulus of elasticity is E and Poisson's ratio is ν. The shear modulus is

$$G = \frac{E}{2(1+\nu)}.$$

Some important properties of the plate–stiffener combination sections with the attached full or effective plating are given in Table 2.1.

It is noted that the expressions of Table 2.1 are of course valid for flat bars with $b_f = t_f = 0$ and also symmetric I-sections. The equivalent yield strength over the cross-section and the slenderness ratio of the attached plating between stiffeners are calculated for the full section, i.e., with full width of the attached plating.

2.3 Modeling of End Conditions

The end conditions (also called boundary conditions) of support members in steel-plated structures are affected by the joining methods and rigidities of support members in the other direction. In welded steel-plated structures, the ends of support members typically have a certain degree of restraint to rotation and/or translation which is sometimes not straightforward to model mathematically. For practical design purposes, however, the end condition of the plate–beam combination model is typically idealized by one or more of the five types shown in Figure 2.4.

At a free end, no restraints are present. The simply supported end represents a condition wherein rotation freely takes place with zero bending moment while lateral deflection (translation) is fixed. At the fixed or clamped end, both rotation and lateral deflection are not allowed. Depending on the possibility of axial movements, two different situations may be relevant, namely Figure 2.4(b) or (c) for the simply supported end and Figure 2.4(d) or (e) for the fixed end. With axial restraints, membrane axial tension may develop as

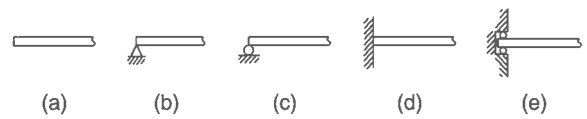

Figure 2.4 Typical idealized end conditions for plate–beam combination models: (a) free; (b) simply supported or pinned but translationally restrained; (c) simply supported or pinned; (d) fixed; (e) clamped

the member deflects, while a free axial movement can occur when axial restraints are not provided.

The same end condition may sometimes be applied at each end, but the possibility of different conditions must in general be considered in accordance with the dimensions and joining methods of support members. However, at least one end should accommodate the condition that the translation is restrained in order to remove rigid-body motion.

While both the upper and lower flanges of I-beams in typical steel-framed structures away from the I beam's ends are normally free to move, it is important to realize that the edges of flanges (the attached plating) of the plate–beam combination models in continuous steel-plated structures may be restricted from deforming sideways as may be surmised from Figure 2.2(a), since the symmetric condition is attained along the edges of the plate–beam combination, i.e., the center line between two adjacent support members (stiffeners), even if the stiffener flanges are free to deflect vertically and rotate sideways. This will essentially cause a different failure mode behavior for plate–beam combination models of steel-plated structures when contrasted to those for simple I-beams of steel-framed structures.

2.4 Loads and Load Effects

The plate–beam combination model for steel-plated structures is likely to be subjected to various types of loads such as axial compression/tension, concentrated or distributed lateral load and end moment, as shown in Figure 2.5.

Lateral loads distributed over the attached plating may typically be idealized as a lateral line load of $q = pb$ (i.e., multiplied by uniform lateral pressure p and the full breadth of attached plating between support members), assuming that the stiffener web resists all shear forces caused by the distributed lateral loads.

A one-dimensional structural member such as the plate–beam combination model is called a column under axial compression, while it is called a beam under lateral load or end moment subsequent to occurrence of bending from the beginning of loading. The member is called a beam–column under combined axial compression and bending. While axial tension normally stabilizes the behavior of beams, the beam under combined bending and axial tension is sometimes termed a tension-beam.

The load effects (e.g., stress, bending) of the plate–beam combination as an element of a complex structure are normally computed by a global analysis using the linear elastic finite element method. They can also be analyzed by the classical theory of structural mechanics as described in many textbooks (e.g., Timoshenko & Goodier 1970, Chen & Atsuta 1976, 1977).

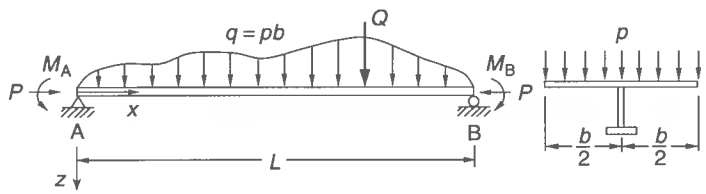

Figure 2.5 Typical load applications on a plate–beam combination

2.5 Effective Breadth/Width of Attached Plating

The attached plating of the plate–beam combination model does not work separately from the adjacent members and it is restricted from deforming sideways while the stiffener flange may be free to deflect vertically and sideways. When a stiffened plate structure is idealized as an assembly of plate–beam combination elements, therefore, one of the primary questions is to what degree and extent the attached plating reinforces the associated strut web.

Related to this problem, two concepts, namely effective width and shear lag, are relevant to characterize the ineffectiveness of the attached plating arising from the non-uniform stress distribution.

The former concept is used to model the effectiveness of plate elements that have buckled under predominantly axial compression or have inherently initial deflections subsequent to occurrence of the non-uniform stress distribution in the regime of post-buckling or large deflection.

On the other hand, the latter (i.e., shear lag) is primarily due to the action of lateral loads or out-of-plane bending. In a wide flanged beam (i.e., plate–beam combination model) under out-of-plane bending, classical beam theory provides a uniform distribution of longitudinal stress across the flange section. In reality, however, the non-uniform stress distribution can occur, because the longitudinal stress caused by bending is transmitted to the flange non-uniformly through shear at the junction between the flange and the web.

As a result, the distribution of the stress across the flange is not uniform but larger at the edges (i.e., intersections between the plating and stiffener web) than at the middle, showing a lag with increasing distance from the web, as shown in Figure 2.6. The departure of the non-uniform stress from the uniform stress assumed by the classical beam theory is termed 'shear lag', which essentially arises from the fact that the shear modulus of the material takes a finite value.

The problem of the effective width, i.e., for steel plating under in-plane compression, was initially raised by John (1877), a naval architect, who investigated the strength of a ship which had broken into two pieces during heavy weather, presumably as a result of high stress induced by sagging moment. He pointed out that the light plating of the deck and topsides could not be considered as fully effective under compression. To account for this effect in the calculation of section modulus of the ship, he reduced the thickness

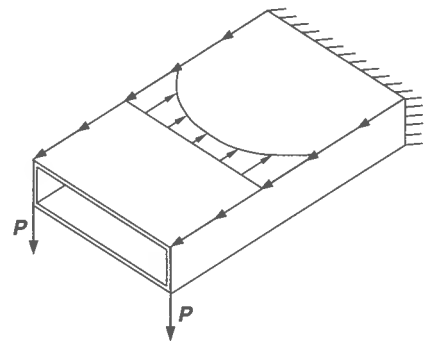

Figure 2.6 Shear-lag-induced non-uniform stress distribution

of the plating, keeping the stress (which could be calculated without considering buckling) unchanged.

A pioneer of using an analytical approach for the plate effective width is Bortsch (1921) who employed an approximate analytical effective width formula for the practical problems related to bridge engineering. The modern era in the effective width concept was started by von Karman (1924) who developed a general method to solve the problem theoretically, and introduced for the first time the term 'effective width'. He calculated the stress distribution of two-dimensional problems using the stress function approach to evaluate the effective width. A remarkable advancement of the Karman method was achieved by Metzer (1929) who studied the effective flange width of simple beams and continuous beams.

In the 1930s, a large series of compression tests on steel plates were undertaken by Schuman & Back (1930). Based on the test results, they noted that the buckled steel plate may behave as if only part of its width is effective in carrying loads. By applying the effective width concept, this phenomenon was investigated theoretically by von Karman *et al.* (1932) who obtained the first effective width expression of plating, which was later shown to be equivalent to $b_e/b = \sqrt{(\sigma_{cr}/\sigma_Y)}$, where b = full plate width, b_e = effective plate width, σ_{cr} = plate buckling stress, σ_Y = material yield stress.

To make a distinction between the two concepts mentioned above, the reduced effectiveness of the flange breadth due to shear lag is sometimes called the 'effective breadth' or 'effective flange width', while the compressive-buckling-induced reduction of the plate effectiveness is termed the 'effective width', although in some situations the plate flange itself may be blissfully unaware of whether its distress is because of effective breadth or effective width effects.

Figure 2.7 shows a typical non-uniform stress distribution of plating between stiffeners. The maximum membrane stress occurs at the intersection between the plate and stiffener web while the stresses inside the plate are comparatively smaller. This implies that the effectiveness of the plate in carrying load through a uniform stress may be idealized as confined to only a part near the plate/web junctions (plate edges). It is thus quite usual in such a situation that the total load is carried by two strips of combined width, b_e, situated near the plate edges, carrying the maximum stress uniformly as a representative, instead of actual stress distribution.

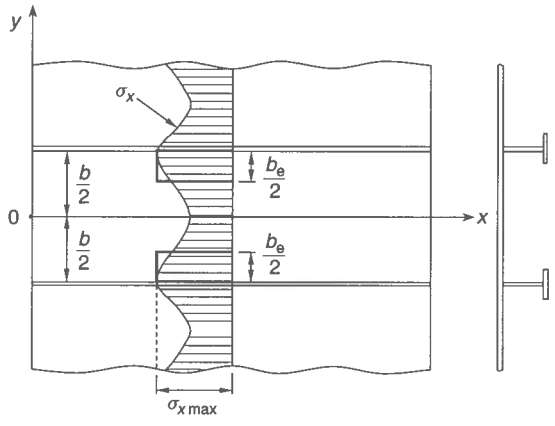

Figure 2.7 Effective width of the attached plating in a stiffened panel

No matter what the reason of the non-uniform stress distribution is, the plate effectiveness may typically be characterized by a parameter b_e, which is a width (breadth) over which the maximum membrane stress at the intersection of the flange and web is idealized to occur uniformly, the total force thus carried being the same as that supplied by the (actual) non-uniform stress distribution across the flange (attached plating).

Following the coordinate system as that shown in Figure 2.7, the effective width (breadth), b_e, can be evaluated by

$$b_e = \frac{\int_{-b/2}^{b/2} \sigma_x \, dy}{\sigma_{x\,max}} = b\frac{\sigma_{xav}}{\sigma_{x\,max}} \tag{2.1}$$

where σ_x = non-uniform membrane stress, σ_{xav} = average stress, $\sigma_{x\,max}$ = maximum membrane stress at plate/web junctions.

2.5.1 Shear-lag-induced Ineffectiveness

An analytical formulation of the effective breadth for a plate–beam combination under predominantly shear lag or bending on wide flange is now derived. For a review of various methods to derive analytical formulations of the shear-lag-oriented effective breadth for wide flanged beams (plate–beam combination), the interested reader may refer to Troitsky (1976).

It is evident from Equation (2.1) that the non-uniform membrane stress distribution must be known to calculate the effective breadth. To compute the stress distribution, the classical theory of elasticity (Timoshenko & Gere 1961) can be applied. For two-dimensional problems, the relationship between strains and displacements is given by

$$\varepsilon_x = \frac{\partial u}{\partial x}, \quad \varepsilon_y = \frac{\partial v}{\partial y}, \quad \gamma_{xy} = \frac{\partial u}{\partial y} + \frac{\partial v}{\partial x} \tag{2.2}$$

where $\varepsilon_x, \varepsilon_y$ = normal strains in the x or y direction, γ_{xy} = shear strain, u, v = displacements in the x or y direction.

The relationship between stresses and strains for two-dimensional problems is given by

$$\varepsilon_x = \frac{1}{E}(\sigma_x - \nu\sigma_y), \quad \varepsilon_y = \frac{1}{E}(\sigma_y - \nu\sigma_x), \quad \gamma_{xy} = \frac{2(1+\nu)}{E}\tau_{xy} \tag{2.3}$$

where σ_x, σ_y = normal stresses in the x or y direction, τ_{xy} = shear stress, ν = Poisson's ratio.

The stress distribution for two-dimensional problems can be obtained by solving the following compatibility equation:

$$\frac{\partial^4 F}{\partial x^4} + 2\frac{\partial^4 F}{\partial x^2 \partial y^2} + \frac{\partial^4 F}{\partial y^4} = 0 \tag{2.4}$$

where F is Airy's stress function which satisfies the following condition:

$$\sigma_x = \frac{\partial^2 F}{\partial y^2}, \quad \sigma_y = \frac{\partial^2 F}{\partial x^2}, \quad \tau_{xy} = -\frac{\partial^2 F}{\partial x \partial y} \tag{2.5}$$

To calculate the non-uniform longitudinal stress distribution in the attached plating, it is assumed that the plate lateral deflection is proportional to $\sin(2\pi x/\omega)$ where ω is the deflection wave length depending on the rigidities of the stiffener and the type of load application. For stiff transverse frames, one may approximately take $\omega = L$.

In this case, the longitudinal axial displacement, u, along the plate/web intersection, i.e., at $y = \pm b/2$, may be calculated as follows (Yamamoto *et al.* 1986):

$$u = -u_0 \cos\frac{2\pi x}{\omega} \tag{2.6}$$

where u_0 = amplitude of the axial displacement function.

The axial strain, ε_x, at $y = \pm b/2$ can then be calculated by substituting Equation (2.6) into Equation (2.2) as follows:

$$\varepsilon_x|_{y=\pm b/2} = \left.\frac{\partial u}{\partial x}\right|_{y=\pm b/2} = \varepsilon_0 \sin\frac{2\pi x}{\omega} \tag{2.7}$$

where $\varepsilon_0 = u_0(2\pi/\omega)$.

To satisfy Equation (2.4), the stress function, F, may be expressed as follows:

$$F = f(y)\sin\frac{2\pi x}{\omega} \tag{2.8}$$

where

$$f(y) = C_1\frac{2\pi y}{\omega}\sinh\frac{2\pi y}{\omega} + C_2\cosh\frac{2\pi y}{\omega}$$

with C_1, C_2 = constants to be determined by the boundary conditions.

To determine the two unknowns, C_1 and C_2, of Equation (2.8), two boundary conditions are applied. While Equation (2.7) can be one boundary condition, the other one is provided so that the symmetric condition must be attained along the center line of the attached plating between two adjacent stiffeners, which is given by

$$\left.\frac{\partial v}{\partial x}\right|_{y=0} = 0 \tag{2.9}$$

By substituting Equation (2.5) into Equation (2.3), the axial strain, ε_x, can be expressed in terms of the Airy stress function as follows:

$$\varepsilon_x = \frac{1}{E}\left(\frac{\partial^2 F}{\partial y^2} - \nu\frac{\partial^2 F}{\partial x^2}\right) \tag{2.10}$$

By substituting Equation (2.8) into Equation (2.10) and considering Equation (2.7), the first boundary condition can be written as

$$\frac{\mathrm{d}^2 f(y)}{\mathrm{d}y^2} + \nu\omega^2 f(y) = E\varepsilon_0 \text{ at } y = \pm\frac{b}{2} \tag{2.11}$$

The second boundary condition, Equation (2.9), can be rewritten using Equation (2.2) as follows:

$$\frac{\partial \gamma_{xy}}{\partial x} = \frac{\partial^2 u}{\partial x\partial y} + \frac{\partial^2 v}{\partial x^2} = \frac{\partial^2 u}{\partial x\partial y} = \frac{\partial \varepsilon_x}{\partial y} \text{ at } y = 0 \tag{2.12}$$

Substituting Equations (2.2), (2.3), (2.5) and (2.8) into Equation (2.12), the second boundary condition becomes the following third-order differential equation:

$$\frac{\mathrm{d}^3 f(y)}{\mathrm{d}y^3} - (2+\nu)\omega^2\frac{\mathrm{d}f(y)}{\mathrm{d}y} = 0 \text{ at } y = 0 \tag{2.13}$$

By substituting $f(y)$, Equation (2.8), into Equations (2.11) and (2.13) and solving the set of resulting two simultaneous equations with regard to C_1 and C_2, we get

$$\begin{aligned} C_1 &= C_3\sinh\frac{\pi b}{\omega}, \quad C_2 = C_3\left[\left(\frac{1-\nu}{1+\nu}\right)\sinh\frac{\pi b}{\omega} - \frac{\pi b}{\omega}\cosh\frac{\pi b}{\omega}\right] \\ C_3 &= E\varepsilon_0\left(\frac{\omega}{2\pi}\right)^2\left[\left(\frac{3-\nu}{2}\right)\sinh\frac{2\pi b}{\omega} - (1+\nu)\frac{\pi b}{\omega}\right]^{-1} \end{aligned} \tag{2.14}$$

The membrane stress, σ_x, can now be obtained by substituting Equations (2.8) and (2.14) into Equation (2.5) as follows:

$$\sigma_x = \left(\frac{2\pi}{\omega}\right)^2\left[C_1\frac{2\pi y}{\omega}\sinh\frac{2\pi y}{\omega} + (2C_1 + C_2)\cosh\frac{2\pi y}{\omega}\right]\sin\frac{2\pi x}{\omega} \tag{2.15}$$

By substituting Equations (2.14) and (2.15) into Equation (2.1), the effective breadth, b_e, can be calculated as follows:

$$b_e = \frac{4\omega\sinh^2(\pi b/\omega)}{\pi(1+\nu)[(3-\nu)\sinh(2\pi b/\omega) - 2(1+\nu)(\pi b/\omega)]} \tag{2.16}$$

The effective breadth normally varies along the span of plate–beam combination, but for practical design purposes it may be taken to have the smallest value which occurs at the location where the maximum longitudinal stress develops. Since b_e must be smaller than b, Equation (2.16) may be approximated to be

$$\frac{b_e}{b} = \begin{cases} 1.0 & \text{for } b/\omega \le 0.18 \\ 0.18\ L/b & \text{for } b/\omega > 0.18 \end{cases} \tag{2.17}$$

As previously noted, the wave length, ω, Equation (2.16) or (2.17), may approximately be taken as $\omega = L$ for the attached plating between two stiff transverse frames. Figure 2.8 shows the variation of the effective breadth from Equations (2.16) and (2.17) versus the ratio of stiffener spacing to the beam span when $\omega = L$. It is seen from Figure 2.8 that the normalized effective breadth significantly decreases as the breadth of the attached plating becomes wider or the span length becomes longer.

Equation (2.16) or (2.17) can then be used to evaluate the effective breadth for the attached plating of a plate–beam combination model under predominantly out-of-plane bending.

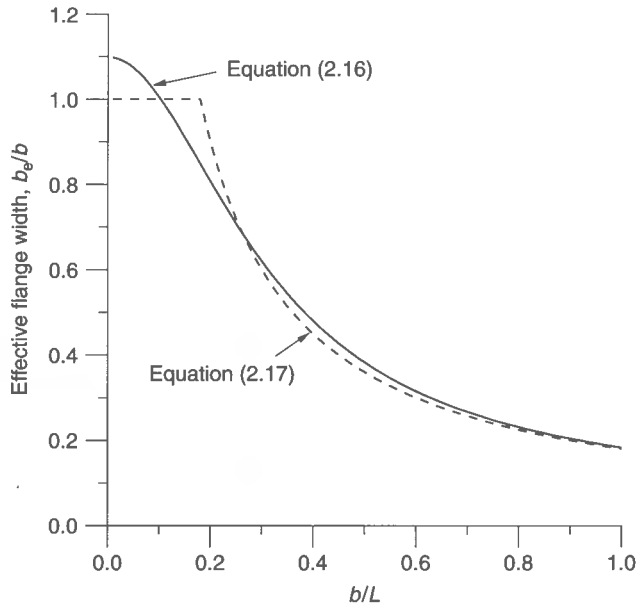

Figure 2.8 Variation of the effective breadth versus the ratio of stiffener spacing to the beam span when $\omega = L$

2.5.2 Buckling-induced Ineffectiveness

Strictly speaking, three different aspects of the term 'effective width' have in fact been applied in the analysis of plate post-buckling behavior, namely the effective width for strength, the effective width for stiffness and the reduced tangent modulus width.

Immediately after buckling of a perfect plate under axial compression, the maximum stress becomes larger than the average stress. It may be apparent in this case that the ratio of effective width to full width is the same as the ratio of the average stress to the maximum stress as defined in Equation (2.1). It has been shown that the maximum load-carrying capacity of a plate is close to that load at which the maximum membrane stress reaches the material yield stress. Since the effective width in terms of the maximum membrane stress is useful in predicting the ultimate strength of a plate, it is termed the effective width for strength.

The tendency of increasing the average strain with the average stress is of course greater after buckling than that before buckling. As long as the plate/web junction remains straight, the average value of the maximum membrane stress along the plate edges may be obtained for a uniaxially compressed plate as follows:

$$\sigma_{x\,\max} = E\varepsilon_{x\mathrm{av}} = E\frac{u}{L} \tag{2.18}$$

where $\varepsilon_{x\mathrm{av}}$ is the average axial strain of the attached plating which may approximately be taken as the average value of axial strain along the plate/web junctions, i.e., $\varepsilon_{x\mathrm{av}} = \varepsilon_x$ at $y = \pm b/2$, and u is the end displacement.

In this case, the effective width can also be evaluated from Equation (2.1) but replacing $\sigma_{x\,\max}$ by the axial strain of Equation (2.18). An effective width for stiffness, i.e., based

on the average axial strain, may be used to characterize the overall stiffness of a buckled plate under predominantly axial compression.

The plate stiffness against axial compression is reduced immediately after buckling. While this behavior may be characterized by the effective width for stiffness, it is sometimes of interest to know the magnitude of the tangent stiffness or the slope of the average stress–strain curve after buckling, which can mathematically be computed by $\partial\sigma_{x\mathrm{av}}/\partial\varepsilon_{x\mathrm{av}}$ in the post-buckling regime. The tangent stiffness after buckling is termed the 'tangent effective width' or the 'effective Young's modulus', E^*. Using this formulation the ratio of the compressive stiffness after buckling to that before buckling is given by E^*/E. For a perfect plate simply supported at four edges, it is known that $E^*/E \approx 0.5$ after buckling. As long as unloaded edges remain straight so that some transverse stresses are developed along unloaded edges, it is recognized that E^*/E corresponds to $\partial\sigma_{x\mathrm{av}}/\partial\sigma_{x\,\max}$, while the former is always greater than the latter when unloaded edges are free to move in plane subsequent to no stresses along them (Rhodes 1982).

Extensive reviews of the derivation of the effective width formulas for plates, undertaken in studies made until the mid 1970s and early 1980s, have been made by Faulkner (1975) and Rhodes (1982). Since then, Ueda *et al.* (1986) derived the effective width formula for a plate under combined biaxial compression and edge shear taking into account the effects of initial deflections and welding-induced residual stresses. Usami (1993) studied the effective width of plates buckled in compression and in-plane bending.

While the concept of effective width is aimed at the evaluation of in-plane stiffness of plate elements buckled in compression, Paik (1995) suggested a new concept for the effective shear modulus to evaluate the effectiveness of plate elements buckled in edge shear. The effective shear modulus concept is useful for computation of the post-buckling behavior of plate girders under predominant shear forces.

One of the most typical effective width expressions for compressive strength of long plates which are often employed by merchant ship classification societies is given in the following form:

$$\frac{b_e}{b} = \begin{cases} 1.0 & \text{for } \beta < 1 \\ C_1/\beta - C_2/\beta^2 & \text{for } \beta \geq 1 \end{cases} \tag{2.19a}$$

where C_1 and C_2 are constants depending on the plate boundary conditions. β is the non-dimensional plate slenderness ratio for the full section, as defined in Table 2.1. Based on the analysis of available experimental data for steel plates with initial deflections at a moderate level but without residual stresses, Faulkner (1975) proposes $C_1 = 2.0$ and $C_2 = 1.0$ for plates simply supported at all (four) edges, or $C_1 = 2.25$ and $C_2 = 1.25$ for plates clamped at all edges.

While the original von Karman effective width expression of plates, i.e., $b_e/b = \sqrt{(\sigma_{cr}/\sigma_Y)}$, is considered reasonably accurate for relatively thin plates, it is found to be optimistic for relatively thick plates with initial imperfections. In this regard, Winter (1947) modified the von Karman equation as follows:

$$\frac{b_e}{b} = \sqrt{\frac{\sigma_{cr}}{\sigma_{max}}}\left(1 - 0.25\sqrt{\frac{\sigma_{cr}}{\sigma_{max}}}\right) \tag{2.19b}$$

where σ_{max} is the applied maximum (edge) stress which may be taken as $\sigma_{max} = \sigma_Y$.

Equation (2.19b) has been widely used to evaluate post-buckling strength for cold-formed steel plates (AISI 1996, ENV 1993-1-1 1993). In some design codes, the term 0.25 in Equation (2.19b) is changed to 0.218 or 0.22.

Equations (2.19) may be used for evaluating the effective width for the attached plating of a plate–beam combination model under predominantly axial compressive loads. The plate effective width expressions will be further described later in Chapter 4.

2.5.3 Combined Shear-lag- and Buckling-induced Ineffectiveness

In reality, it is important to realize that the plating in steel-plated structures is likely to be subjected to combined in-plane and lateral loads, resulting in both shear lag and buckling. In this case, the effectiveness of plating must of course be evaluated taking into account both effects.

In this case, $\sigma_{x\,\max}$ of Equation (2.1) must be the maximum compressive stress which is expressed as a function of combined in-plane and lateral loads and initial imperfections, as will be presented in detail later in Chapter 4.

2.6 Plastic Cross-sectional Capacities

In the conventional allowable stress design method, 'first yield' is typically employed for a design criterion. This is despite the fact that most steel structures can experience local yielding and still may be able to withstand some further increase of loading since internal stresses are redistributed because of the ductility of steel.

In contrast, the structural design criteria for the ULS design are based on maximum load-carrying capacity or ultimate strength based on plastic theory. When the ultimate strength of a plate–beam combination is being so considered, plastic cross-sectional capacities are sometimes of interest when the effects of local buckling and strain hardening are not of primary concern.

In the subsequent sections, the cross-sectional capacities of plate–beam combination models at either first or full (complete) yield are presented under axial load, sectional shear, bending or their combinations.

2.6.1 Axial Capacity

The plastic capacity, P_P, for axial load is calculated by

$$P_P = \pm(A_p\sigma_{Yp} + A_w\sigma_{Yw} + A_f\sigma_{Yf}) \tag{2.20}$$

where Equation (2.20) is valid for axial tension as well as axial compression when local buckling does not take place, and a relevant sign convention is used (e.g., positive sign for tension or negative sign for compression).

2.6.2 Shear Capacity

It is practically considered that only the cross-section part parallel to the direction of shearing force contributes to the shear structural resistance. When the vertical sectional

shear force (with positive sign for positive shear and negative sign for negative shear) is considered, for instance, only the stiffener web cross-sectional area of a plate–beam combination model is included in the calculation of shear capacity, F_P, as follows:

$$F_P = \pm(A_w\tau_{Yw}) \tag{2.21}$$

where $\tau_{Yw} = \sigma_{Yw}/\sqrt{3}$ = shear yield stress of web.

2.6.3 Bending Capacity

In a beam with uniform material properties, the first yield occurs at the outer fiber of the cross-section where the highest bending develops in the span. With further loading, the cross-section will become entirely plastic. The plastic bending capacity of beams typically depends on the cross-sectional geometry as well as material properties. The capacity formulas take positive sign for positive bending and negative sign for negative bending.

Rectangular Cross-Section

Before the plastic bending capacity of the plate–beam combination is calculated, a simpler case with rectangular cross-section is considered. The neutral axis (N.A.) is in this case located at a half height of the web due to the symmetry, as shown in Figure 2.9.

The first yield bending capacity, M_Y, can then be obtained by the first moment of axial stresses with regard to the neutral axis when either the upper or lower outer fiber just yields as follows:

$$M_Y = \pm\int_{-h_w/2}^{h_w/2} \sigma_x t_w z\,dz = \pm Z_Y\sigma_{Yw} \tag{2.22}$$

where $Z_Y = t_w h_w^2/6$ = first yield section modulus.

The bending capacity at first yield can also be predicted by applying simple beam theory, leading to the following linear relationship between bending moment and bending stress:

$$M = \pm\frac{\sigma_x}{z}I \tag{2.23}$$

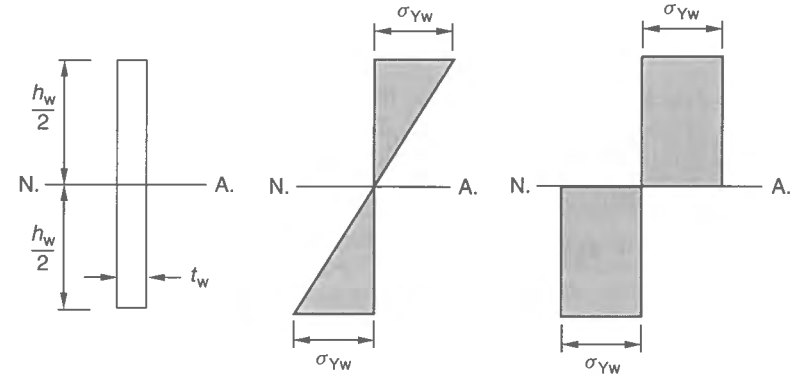

Figure 2.9 Stress distribution of a rectangular cross-section beam at first and full yielding

where M = bending moment, σ_x = bending stress, I = moment of inertia, z = distance from the neutral axis.

In the case of the rectangular cross-section beam, since $I = t_w h_w^3/12$, and $\sigma_x = \sigma_{Yw}$ at the outer fiber, i.e., $z = \pm h_w/2$, the first yield bending capacity obtained from Equation (2.23) corresponds to Equation (2.22). The position of the plastic neutral axis is determined so that the areas on two parts, i.e., in the tension or compression side, are equal. For a symmetric rectangular cross-section beam, the plastic neutral axis is located at a half height of the web.

The full plastic bending capacity, M_P, is calculated by the first moment of axial stresses with regard to the plastic neutral axis when the cross-section entirely yields as shown in Figure 2.9, namely

$$M_P = \pm \int_{-h_w/2}^{h_w/2} \sigma_x t_w z \, dz = \pm Z_P \sigma_{Yw} \tag{2.24}$$

where $Z_P = t_w h_w^2/4$ = plastic section modulus.

Plate–beam Combination Section

Since the elastic neutral axis and moment of inertia for the effective section of a plate–beam combination are given by Table 2.1, the first yield bending capacity, M_Y, can be calculated by applying classical simple beam theory as follows:

$$M_Y = \begin{cases} \pm Z_{Yp}\sigma_{Yp} & \text{for first yield at attached plating} \\ \pm Z_{Yf}\sigma_{Yf} & \text{for first yield at stiffener flange} \end{cases} \tag{2.25}$$

where $Z_{Yp} = I_e/z_p$ = first yield section modulus at outer fiber of attached plating side, $Z_{Yf} = I_e/(h_w + t + t_f - z_p)$ = first yield section modulus at outer fiber of stiffener flange side, z_p, I_e = as defined in Table 2.1.

The full plastic bending capacity, M_P, is now calculated. In this case, three types of calculations are basically necessary in accordance with the location of the plastic neutral axis, i.e., on (1) the attached plating, (2) the stiffener web or (3) the stiffener flange. In reality, case (3) may not be considered as long as the stiffener flange is relatively small compared to the attached plating, and hence the bending capacity formula is herein derived for cases (1) and (2). Figures 2.10(a) and (b) represent stress distributions of plate–beam combination sections at full yield for cases (1) and (2), respectively.

(1) $A_{pe}\sigma_{Yp} \geq A_w\sigma_{Yw} + A_f\sigma_{Yf}$: In this case, the plastic neutral axis of the plate–beam combination where the plate itself is very thick can be located in the attached plating. Since the location of the plastic neutral axis is determined so that the total cross-sectional area is equally divided into two, we then have

$$b_e e \sigma_{Yp} = \frac{A_{pe}\sigma_{Yp} + A_w\sigma_{Yw} + A_f\sigma_{Yf}}{2} \quad \text{or} \quad e = \frac{A_{pe}\sigma_{Yp} + A_w\sigma_{Yw} + A_f\sigma_{Yf}}{2b_e\sigma_{Yp}} \tag{2.26}$$

The plastic bending capacity is calculated as the first moment of axial stresses with regard to the plastic neutral axis over the entire cross-sectional area. In the interest of simplicity, the yield strength of the entire cross-section material may be represented by

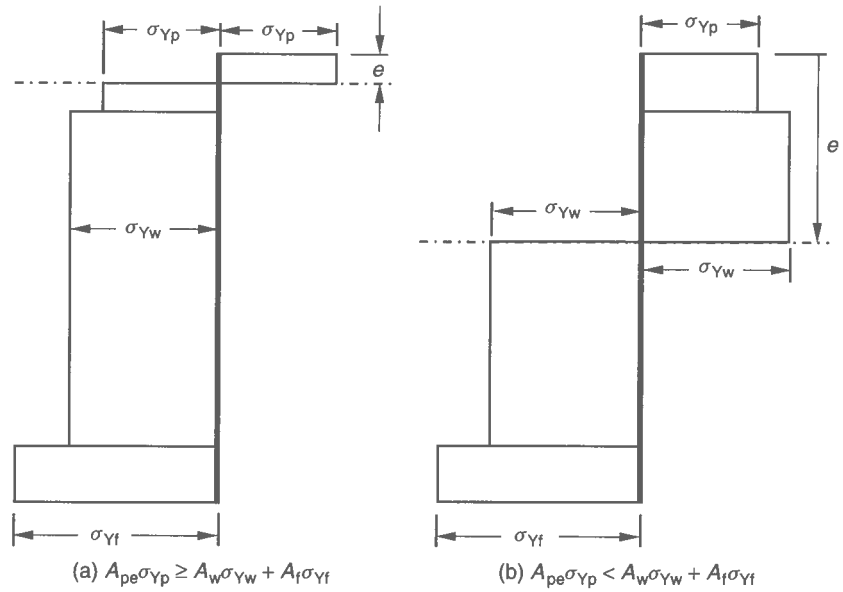

Figure 2.10 Stress distribution of the plate–beam combination section at full yield

the equivalent yield stress, σ_{Yeq}. In this case, since $e = 0.5A_e/b_e$, the plastic bending capacity formula simplifies to

$$M_P = \pm Z_P \sigma_{Yeq} \tag{2.27}$$

where $Z_P = C_1 + (C_2/b_e) + C_3$ = plastic section modulus, $C_1 = \frac{1}{2}(b_e t^2 + t_w h_w^2 + b_f t_f^2)$, $C_2 = -\frac{1}{4}(b_e t - t_w h_w - b_f t_f)^2$, $C_3 = h_w b_f t_f$.

(2) $A_{pe}\sigma_{Yp} < A_w\sigma_{Yw} + A_f\sigma_{Yf}$: In this case, the plastic neutral axis will be located on the stiffener web, which is determined by

$$b_e t \sigma_{Yp} + t_w(e - t)\sigma_{Yw} = \frac{A_{pe}\sigma_{Yp} + A_w\sigma_{Yw} + A_f\sigma_{Yf}}{2} \quad \text{or}$$

$$e = \frac{-A_{pe}\sigma_{Yp} + A_w\sigma_{Yw} + A_f\sigma_{Yf}}{2t_w\sigma_{Yw}} + t \tag{2.28}$$

In this case, if the yield strength of the entire cross-section is represented by the equivalent yield strength, σ_{Yeq}, the plastic bending capacity formula can also be given by Equation (2.27), but replacing the plastic section modulus, Z_P, by the following equation since $e = [(-A_{pe} + A_w + A_f)/2t_w] + t$, namely

$$Z_P = C_1 + \frac{C_2}{t_w} + C_3 \tag{2.29}$$

where C_1, C_2, C_3 = as defined in Equation (2.27).

2.6.4 Capacity under Combined Bending and Axial Load

When combined bending and axial loading is applied, the stress distribution at full yield of the cross-section can be presumably considered as that shown in Figure 2.11. The axial load, P, and bending moment, M, can then be calculated by integration of the stress distribution over the cross-section as follows:

$$P = \int_A \sigma_x \, dA, \quad M = \int_A \sigma_x z \, dA \tag{2.30}$$

where $\int_A (\,) \, dA$ represents the integration over the cross-sectional area.

In Equation (2.30), P and M will be expressed as a function of an unknown parameter, e, which is the distance from the outer fiber of the attached plating to the plastic neutral axis. Combining these two equations with regard to the unknown parameter, an interaction relationship between P and M can be obtained. It is to be recognized that the plastic capacity of the sections under combined bending and axial load will be less than that for bending alone.

Rectangular Cross-section

Before the plastic capacity of the plate–beam combination under combined M and P is calculated, a simpler case with rectangular cross-section is considered. The stress distribution over a rectangular cross-section at full yield may be presumed as that shown in Figure 2.12. In this case, the stress distribution can be divided into two parts, namely one for pure bending stress and the other for pure axial stress.

Based on the presumed stress distribution, the reduced bending moment capacity, M, and the associated axial load, P, can be calculated by

$$P = t_w(h_w - 2e)\sigma_{Yw} \tag{2.31a}$$

$$M = M_P - M_{Pe} = M_P - Z_{Pe}\sigma_{Yw} = \frac{t_w h_w^2}{4}\sigma_{Yw} - \frac{t_w(h_w - 2e)^2}{4}\sigma_{Yw} \tag{2.31b}$$

where $P_P = t_w h_w \sigma_{Yw}$, $M_P = (t_w h_w^2/4)\sigma_{Yeq}$, $M_{Pe} = Z_{Pe}\sigma_{Yw}$ = plastic bending capacity for the cross-section of e, $Z_{Pe} = [t_w(h_w - 2e)^2]/4$ = plastic section modulus for the cross-section of e.

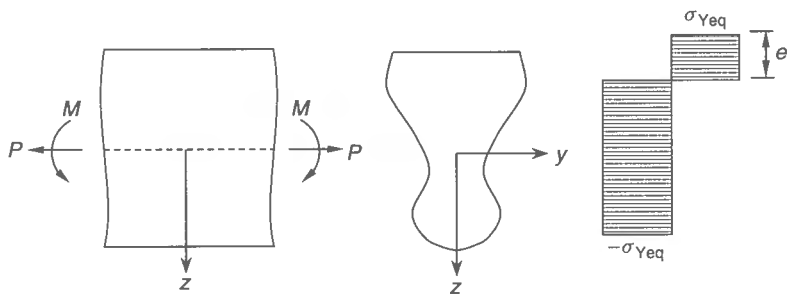

Figure 2.11 Stress distribution over an arbitrary cross-section under combined bending and axial load

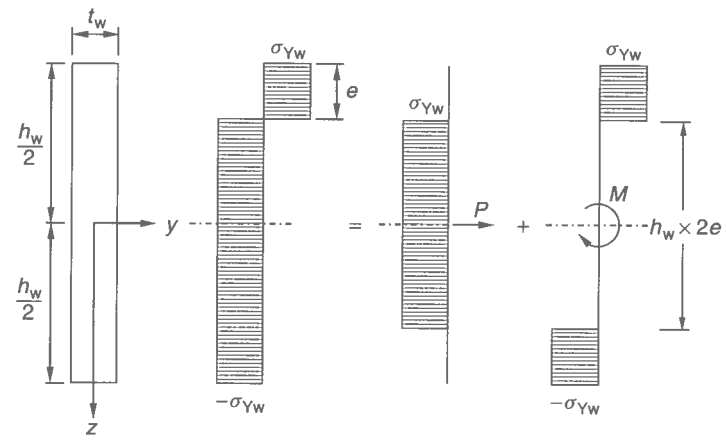

Figure 2.12 Stress distribution of a rectangular cross-section under combined bending and axial load

Combining Equations (2.31a) and (2.31b), the plastic capacity interaction equation of the plate–beam combination under M and P is given by

$$\left|\frac{M}{M_P}\right| + \left(\frac{P}{P_P}\right)^2 = 1 \tag{2.32}$$

Figure 2.13 shows the above interaction curve for rectangular cross-sections under combined (positive) bending and (positive) axial load. As evident from Figure 2.13, the plastic bending capacity significantly decreases with increase in the axial load.

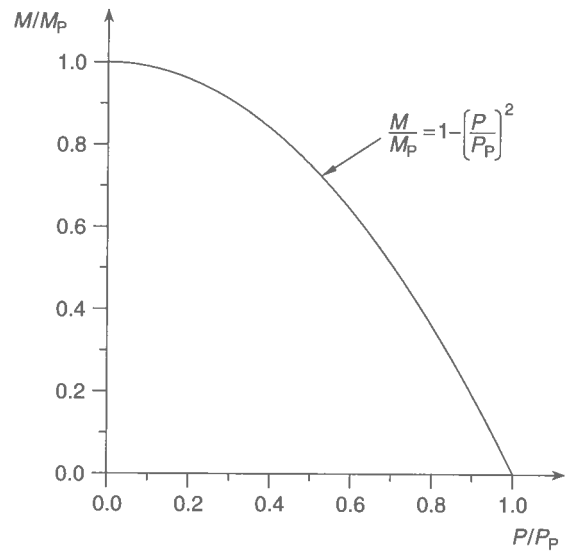

Figure 2.13 The interaction curve for a rectangular cross-section under combined bending and axial load

Plate–beam Combination Section

The plastic stress distribution of a plate–beam combination whose cross-section is subject to combined bending and axial load may be described in terms of the position of the plastic neutral axis, e, which is the distance from the outer fiber of the attached plating to the plastic neutral axis, as those shown in Figure 2.14 (Ueda & Rashed 1984).

In contrast to the symmetric rectangular cross-section, the expressions of the plastic capacity interaction relationships of plate–beam combinations under M and P may be different in accordance with the direction of load application.

Based on the presumed stress distribution for each state of load combination, the reduced bending moment, M, and the associated axial load, P, can be expressed as a function of the unknown, e. By omitting e between the two expressions, an interaction relationship for the plastic capacity is then derived. For an elaborate description of the plastic capacity interaction relationships, the interested reader may refer to Ueda & Rashed (1984).

In the interest of simplicity, Equation (2.32) may often be employed for the plastic capacity interaction formula of the plate–beam combinations under M and P, but using P_P and M_P for the plate–beam combination, the latter being defined in Equation (2.27) depending on the section dimensions, i.e., either $A_{pe}\sigma_{Yp} \geq A_w\sigma_{Yw} + A_f\sigma_{Yf}$ or $A_{pe}\sigma_{Yp} < A_w\sigma_{Yw} + A_f\sigma_{Yf}$.

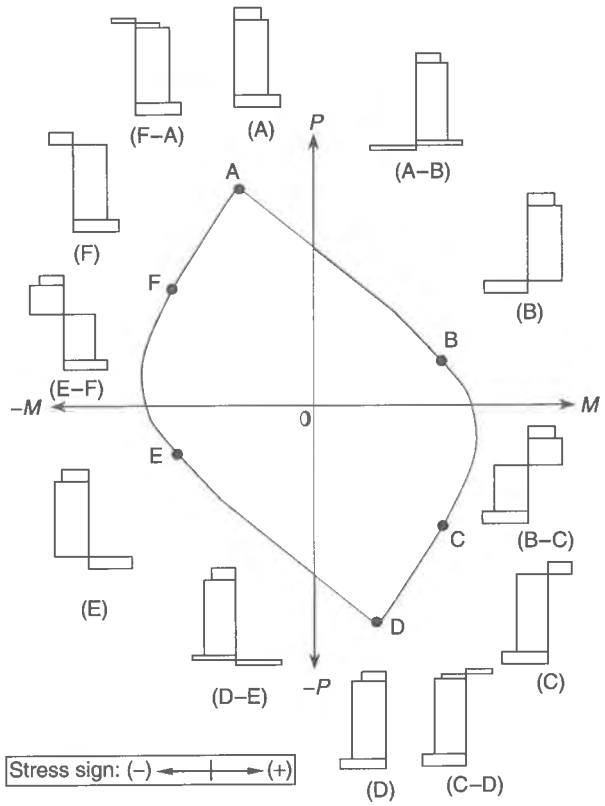

Figure 2.14 Presumed stress distributions over the plate–beam combination model cross-section for varying states of combined bending and axial load

2.6.5 Capacity under Combined Bending, Axial Load and Shearing Force

When combined bending, M, axial load, P, and shearing force, F, are applied, stress distributions similar to that for combined bending and axial load may be adopted, assuming that the shearing forces will be sustained by the stiffener web alone. In this regard, a reduced yield strength, σ_{Yv}, for the stiffener web may be introduced by the Tresca yield criterion as follows (ENV 1993-1-1 3 1992):

$$\sigma_{Yv} = 2\left[\left(\frac{\sigma_{Yw}}{2}\right)^2 - \left(\frac{F}{A_w}\right)^2\right]^{0.5} \tag{2.33}$$

where F = applied shearing force.

For combined bending, axial load and shearing forces, therefore, the reduced plastic bending capacity of the plate–beam combination section can approximately be obtained from Equation (2.32) with P_P and M_P for the plate–beam combination, but replacing the stiffener web yield stress σ_{Yw} by σ_{Yv} of Equation (2.33).

2.7 Ultimate Strength of Beams

Any steel structure can collapse when it develops sufficient plastic hinges to form a plastic mechanism. The plastic collapse strength formulas of beams with many types of loading and end conditions can typically be derived applying rigid plastic theory (Hodge 1959, Neal 1977).

Belenkiy & Raskin (2001) showed that the ultimate strength of beams determined by rigid plastic theory corresponds quite well to a 'threshold' (ultimate) load obtained by nonlinear finite element analysis. This threshold load is defined so as to separate the linear elastic regime from the plastic regime. Figure 2.15 illustrates the threshold ultimate load concept for beams. In this figure, the load–deflection curve indicated by the solid

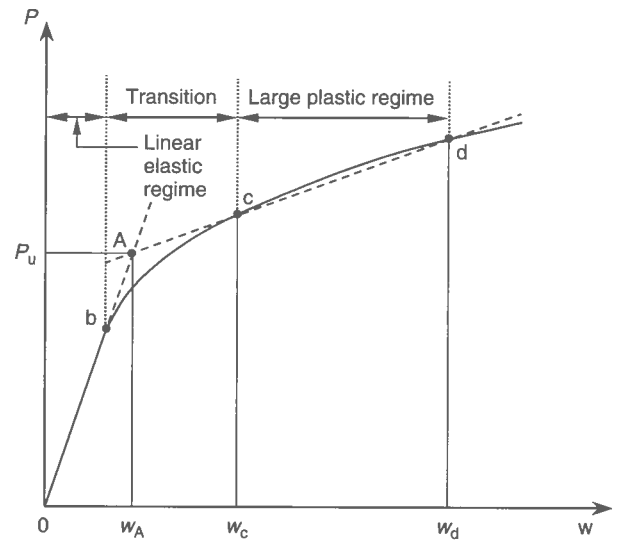

Figure 2.15 A schematic representation of the threshold (ultimate) load of beams

line may be divided into three regimes, namely the linear elastic regime (0b), transitional regime (bc) where plastic deflection starts to grow, and large deflection regime (cd).

The true load–deflection curve was shown to be approximated by a bilinear relation, i.e., 0Ad, where the deflections w_c and w_d could be taken as $w_c = 0.005L$ and $w_d = 0.01L$. The threshold ultimate load is then defined as the load, P_u, at point A. Based on the comparisons of ultimate loads of beams with various types of end conditions and load applications as determined by rigid plastic theory with the threshold loads obtained by the nonlinear finite element analyses, Belenkiy & Raskin (2001) also developed some important insights: (1) the plastic deflection, w_A, corresponding to the threshold loads is normally in the range of $0.001L$–$0.004L$; and (2) the effects of strain hardening and membrane stress on the threshold loads are usually small.

For the use of rigid plastic theory to derive ultimate strength formulations of beams, the basic assumptions noted below are typically assumed to be adequate:

- strain-hardening effects can be ignored;
- the Tresca yield criterion is applicable;
- small deformations are involved, and hence the membrane effects may be neglected;
- local buckling does not take place;
- the localized plastic region does not expand into the longitudinal (axial) direction of beams and hence the plastic hinge is considered to remain fixed at a particular cross-section; and
- the cross-section of the beam remains plane, i.e., it does not distort in the axial direction.

In the following sections, the plastic strength formulas of beams neglecting the effect of local buckling are derived for various loading and end conditions. In this case, the plastic strength formulas are expressed as functions of the full plastic bending moment, M_P, of the beam. The ultimate strength of beams taking into account the effect of local buckling may then be approximately estimated from those plastic strength formulas but replacing M_P by the ultimate bending moment, M_u, which is determined by considering the local buckling effect at the cross-section, as will be described in Chapter 7.

2.7.1 Cantilever Beams

The plastic collapse strength formulas for cantilever beams under various types of load applications as shown in Figure 2.16 are first derived.

When a beam is subjected to point load Q at the free end as shown in Figure 2.16(a), the bending moment along the beam span is given by

$$M = Q(L - x) \tag{2.34}$$

As the point load increases, the plastic region around the fixed end will initiate and expand through the thickness. The beam will collapse by formation of the plastic hinge mechanism if the cross-section at the fixed end entirely yields; that is, when the bending moment at the fixed end reaches the plastic bending moment, M_P.

Therefore, the plastic collapse load, Q_c, is in this case established as follows:

$$Q_c = \frac{M_P}{L} \tag{2.35}$$

where $M_P =$ as defined in Section 2.6.3.

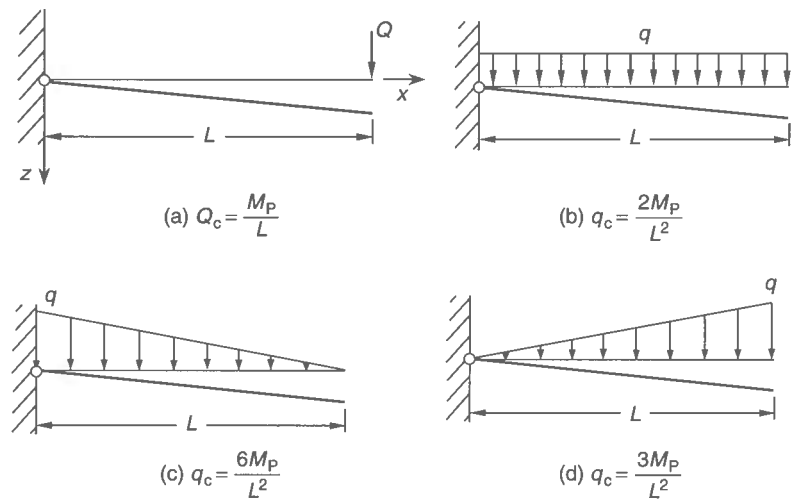

Figure 2.16 Plastic collapse loads of a cantilever beam under various types of load applications

Using the same method as described above, the plastic collapse loads of the cantilever beam under different load applications are determined as shown in Figures 2.16(b), (c) and (d).

2.7.2 Beams Simply Supported at Both Ends

The plastic collapse strength formulas for beams simply supported at both ends, and subject to various types of load applications such as those shown in Figure 2.17, are now derived.

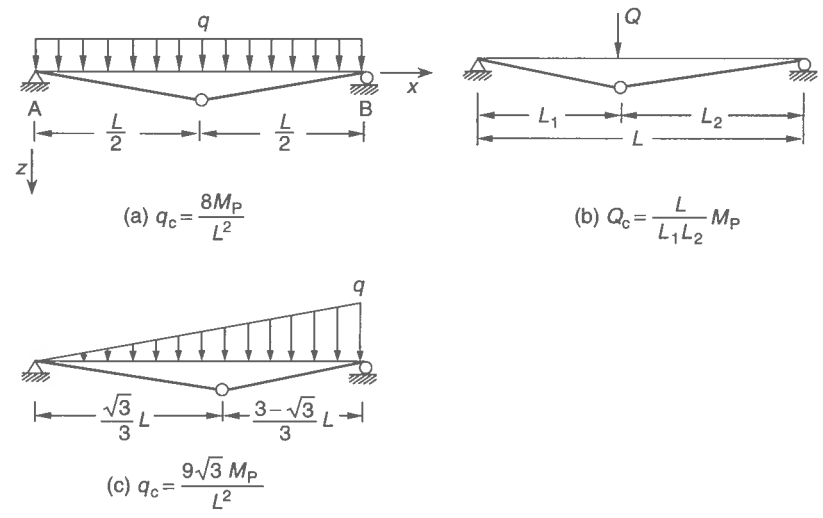

Figure 2.17 Plastic collapse loads of a beam under various types of load applications, simply supported at both ends

When a beam is subjected to uniformly distributed line loads, as shown in Figure 2.17(a), it will collapse if the cross-section yields at any one location inside the span since both ends are already pinned. Because of the symmetric load application, i.e., as that shown in Figure 2.17(a), the maximum bending occurs at mid-span at which the cross-section will yield first.

The reaction forces at both ends and the bending moment distribution are in this case given by

$$R_A = R_B = \frac{qL}{2}, M = R_A x - \frac{1}{2}qx^2 = \frac{1}{2}qx(L-x) \tag{2.36}$$

Thus the maximum bending moment at mid-span, i.e., $x = L/2$, is obtained as follows:

$$M_{max} = \frac{qL^2}{8} \tag{2.37}$$

By equating Equation (2.37) with the plastic bending capacity, M_P, the plastic collapse strength, q_c, is obtained by replacing q in Equation (2.37) with q_c as follows:

$$q_c = \frac{8M_P}{L^2} \tag{2.38}$$

The same procedure noted above can also be applied to calculate the plastic collapse strengths of simply supported beams under different load applications, with results as shown in Figure 2.17(b) or (c). The collapse strength formula of a beam simply supported at both ends and under linearly varying lateral pressure but with non-zero pressure load at ends is derived later in Section 2.7.5.

2.7.3 Beams Simply Supported at One End and Fixed at the Other End

The plastic collapse strength formulas for statically indeterminate beams, simply supported at one end and fixed at the other end, under various types of load applications such as those shown in Figures 2.18 and 2.19 are now considered.

When a beam is subjected to uniformly distributed line loads as shown in Figure 2.18, the equilibrium condition gives the following equations for the reaction forces and end moment:

$$R_A = \frac{qL}{2} + \frac{M_A}{L}, \quad R_B = \frac{qL}{2} - \frac{M_A}{L} \tag{2.39}$$

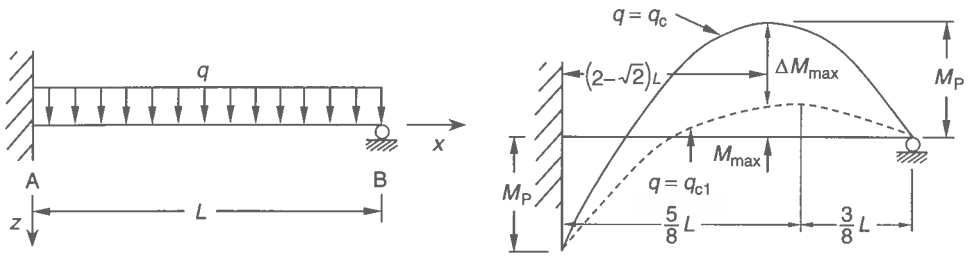

Figure 2.18 Moment distribution of a beam under uniform line load, simply supported at one end and fixed at the other end

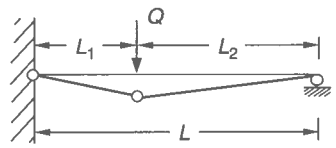

(a) $Q_{c1} = \frac{2L^3}{L_1^3 L_2 (3L - L_1)} M_P$, $Q_c = \frac{2L - L_1}{L_1 L_2} M_P$ for $L_1 \geq (2-\sqrt{2})L$

$Q_{c1} = \frac{2L^2}{L_1 L_2 (2L - L_1)} M_P$, $Q_c = \frac{2L - L_1}{L_1 L_2} M_P$ for $L_1 < (2-\sqrt{2})L$

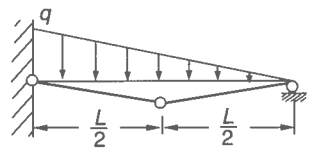

(b) $q_{c1} = \frac{15M_P}{L^2}$, $q_c = \frac{24M_P}{L^2}$

Figure 2.19 Plastic collapse loads of a beam under other types of load applications, simply supported at one end and fixed at the other end (Note: Q_{c1} or q_{c1} indicates the critical load when the plastic hinge is just formed at the fixed end)

where R_A, R_B = reaction forces at points A and B, M_A = redundant reaction (bending moment) at end A.

The bending moment along the span can be expressed in terms of the redundant reaction, M_A, as follows:

$$M = -M_A + R_A x - \frac{q}{2}x^2 = -M_A\left(1 - \frac{x}{L}\right) + \frac{qL}{2}x - \frac{q}{2}x^2 \tag{2.40}$$

The bending strain energy, U, of a beam with the effective cross-section properties is given by

$$U = \int_0^L \frac{M^2}{2EI_e}\,dx \tag{2.41}$$

Applying the so-called Castigliano principle, the rotation at the fixed end which may be calculated by differentiating the strain energy with regard to the associated bending moment must be zero because of the fixed end condition, namely

$$\theta_A = \frac{\partial U}{\partial M_A} = \int_0^L \frac{M}{EI_e}\frac{\partial M}{\partial M_A}\,dx = 0 \tag{2.42}$$

where θ_A = rotation at end A.

By substituting Equation (2.40) into Equation (2.42), the redundant reaction, M_A, is determined by

$$M_A = \frac{qL^2}{8} \tag{2.43}$$

As the load increases, the maximum bending moment occurs at the fixed end, i.e., $x = 0$. When the maximum bending moment at end A reaches the plastic bending capacity $|M_P|$, the fixed end will become a plastic hinge. The critical lateral load in this state is defined by replacing q with q_{c1} as follows:

$$q_{c1} = \frac{8M_P}{L^2} \tag{2.44}$$

Even after the cross-section at the fixed end has yielded, the beam may be able to sustain further loading because a plastic hinge mechanism is not formed yet. Until $q = q_{c1}$, the maximum bending moment inside the span, $M_{max\,1}$, occurs at $x = \frac{5}{8}L$. Since end A is now considered to be pinned, keeping the bending moment constant at $-M_P$, the additional bending moment, ΔM, due to the additional lateral load, i.e., $q - q_{c1}$, is given as for a beam simply supported at both ends, namely

$$\Delta M = \tfrac{1}{2}(q - q_{c1})(Lx - x^2) \tag{2.45}$$

The beam will collapse if the total (accumulated) maximum bending moment inside the span reaches the plastic bending moment since a plastic hinge mechanism is then formed as follows:

$$M_{max} = M^*_{max\,1} + \Delta M_{max} \tag{2.46}$$

where M_{max} occurs at $x = (2 - \sqrt{2})L$ which does not correspond to the location of $M_{max\,1} \cdot M^*_{max\,1}$ is calculated by $M_{max\,1} = M$ using Equations (2.40) and (2.43) at $q = q_{c1}$ and $x = (2 - \sqrt{2})L$, and ΔM_{max} is obtained by $\Delta M_{max} = \Delta M$ using Equation (2.45) at $x = (2 - \sqrt{2})L$.

The beam eventually collapses if the accumulated maximum bending moment inside the span reaches the plastic bending moment, i.e., $M_{max} = M_P$. In this state, the plastic collapse strength of the beam subject to evenly distributed line loads is given by

$$q_c = \frac{2(3 + 2\sqrt{2})M_P}{L^2} \tag{2.47}$$

For the other types of load applications as shown in Figures 2.19(a) and (b), the first critical and plastic collapse loads may be calculated using the same approach noted above. The collapse strength formula of a beam simply supported at one end and fixed at the other end, and under linearly varying lateral pressure but non-zero load at the ends, is derived later in Section 2.7.5.

2.7.4 Beams Fixed at Both Ends

The plastic collapse load formulas for statically indeterminate beams fixed at both ends under various types of load applications as shown in Figures 2.20 and 2.21 are now considered. In this case, the beams will collapse if the cross-sections at both ends as well as any one location inside the span yield.

For a beam subjected to uniformly distributed line loads as shown in Figure 2.20, the plastic hinges will simultaneously be formed at both ends where the maximum bending moments take place because of the symmetric loading and end conditions. Even after the occurrence of the plastic hinges at both ends, the beam will be able to withstand further loading until the cross-section at mid-span yields, leading to the plastic hinge mechanism.

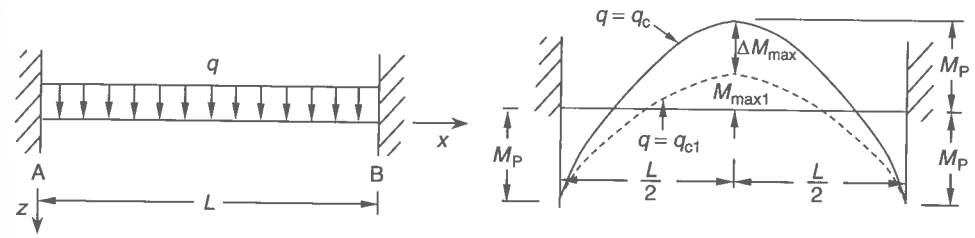

Figure 2.20 Moment distribution of a beam under uniform line load, fixed at both ends

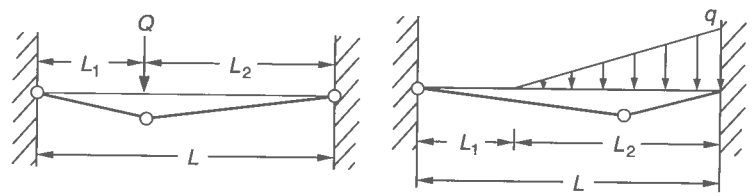

(a) $Q_{c1} = \frac{L^2}{L_1 L_2^2} M_P$, $Q_c = \frac{2L}{L_1 L_2} M_P$ (b) $q_{c1} = \frac{30L^2}{L_2(10L_1 L + 3L_2^2)} M_P$

Figure 2.21 Plastic collapse loads of a beam under other types of load applications, fixed at both ends. (For Q_{c1} or q_{c1}, refer to Figure 2.19)

In Figure 2.20, the bending moment along the span may be given by considering the symmetric load condition with regard to mid-span as follows:

$$M = -M_A + \frac{qL}{2}x - \frac{q}{2}x^2 \tag{2.48}$$

where $M_A = M_B$ = bending moment at beam ends.

Since the bending strain energy, U, of the beam with the effective cross-section is calculated from Equation (2.41) and the rotation at fixed end A must be zero, Equation (2.42) is satisfied. By solving Equation (2.42) together with Equation (2.48), M_A is determined by

$$M_A = \frac{qL^2}{12} \tag{2.49}$$

Now we get a critical load, q_{c1}, when both ends just yield; that is, the end moment at $x = 0$ or L reaches the plastic bending moment, $-M_P$, namely

$$q_{c1} = \frac{12M_P}{L^2} \tag{2.50}$$

The maximum bending moment, $M_{max\,1}$, which occurs at mid-span, i.e., $x = L/2$ until both ends just yield, is calculated from Equation (2.48) with Equation (2.49) since $q = q_{c1}$

as follows:

$$M_{\max 1} = \frac{q_{c1} L^2}{24} \tag{2.51}$$

Even after both ends have yielded, the beam may sustain further loading until the cross-section at mid-span yields. While the end moment is kept constant at $-M_P$, the bending moment inside the span will increase. Since the beam can now be considered to be simply supported at both ends, the additional bending moment, ΔM, inside the span due to further loading is given by neglecting the membrane stress effects, namely

$$\Delta M = \frac{q - q_{c1}}{2}\left(Lx - x^2\right) \tag{2.52}$$

Since the maximum additional bending moment, $\Delta M_{\max}$, occurs at mid-span, the total (accumulated) maximum bending moment, $M_{\max}$, at mid-span is obtained as follows:

$$M_{\max} = M_{\max 1} + \Delta M_{\max} = \frac{q_{c1} L^2}{24} + \frac{(q - q_{c1})L^2}{8} = \frac{qL^2}{8} - 2M_P \tag{2.53}$$

where $\Delta M_{\max} = [(q - q_{c1})/8]L^2$.

Since a plastic hinge mechanism is formed when the cross-section at mid-span yields, with $M_{\max} = M_P$, the plastic collapse load, q_c, of the beam is finally determined by

$$q_c = \frac{16 M_P}{L^2} \tag{2.54}$$

Using a method similar to that used above, the first critical or plastic collapse loads of the beams under other load applications, such as those shown in Figures 2.21(a) and (b), can be calculated.

2.7.5 Beams Elastically Restrained at Both Ends

When the beam is connected to adjoining structures, angular rotation at the ends can be restrained to some degree. A beam elastically restrained at both ends is considered. The beam is subjected to a lateral pressure distribution with a trapezoidal pattern which varies linearly between two ends as shown in Figure 2.22(a), which is given by

$$q = -\frac{q_B - q_D}{L}x + q_B \tag{2.55}$$

where q_B, p_D = lateral pressures at ends B or D.

The end moments arise from the constraints against angular rotation of the beam at the junctures of the beam and the adjoining structure, as indicated in Figure 2.22(a). They thus depend on the torsional rigidity of the adjoining structures.

From the bending moment equilibrium condition, the constraints at the ends of the beam can be defined as follows:

at the end B: $$\left(\frac{d^2 w}{dx^2}\right)_{x=0} = \frac{C_B}{L}\left(\frac{dw}{dx}\right)_{x=0} \tag{2.56a}$$

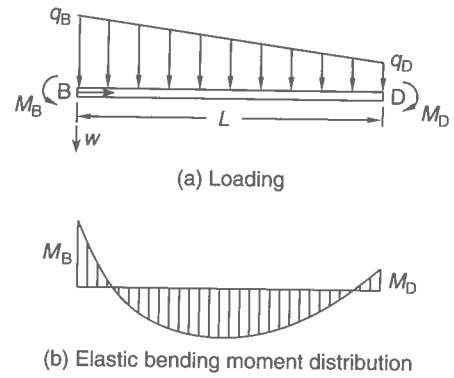

Figure 2.22 A beam elastically restrained at both ends and under lateral pressure

at the end D: $$\left(\frac{d^2 w}{dx^2}\right)_{x=L} = \frac{C_D}{L}\left(\frac{dw}{dx}\right)_{x=L} \tag{2.56b}$$

where w is the lateral deflection of the beam, and C_B and C_D are constraint constants at the two ends of the beam, respectively. For simply supported or clamped ends, these two constants will become either zero or infinity, respectively.

The elastic bending moment distribution of the beam is expressed by applying the simple beam theory as follows:

$$M = EI_e \frac{d^2 w}{dx^2} = M_B - \frac{x}{L}(M_B - M_D) + \frac{q_B}{2}(x^2 - Lx) + \frac{q_B - q_D}{6}\left(Lx - \frac{x^3}{L}\right) \tag{2.57}$$

where I_e = moment of inertia of the beam with effective section.

Figure 2.22(b) represents the elastic bending moment distribution of the corrugation beam. It is seen from the figure that three extreme values of the bending moments are developed, i.e., at end B, end D and inside the span. By performing the double integration of Equation (2.57) and considering the end conditions, the lateral deflection, w, may be expressed by

$$w = \frac{q_B + q_D}{24EI_e}\left(\frac{x^4}{2} - Lx^3 + \frac{L^3 x}{2}\right) + \frac{q_B - q_D}{24EI_e}\left(-\frac{x^5}{5L} + \frac{x^4}{2} - \frac{Lx^3}{3} + \frac{L^3 x}{30}\right) + \frac{M_B}{EI_e}\left(-\frac{x^3}{6L} + \frac{x^2}{2} - \frac{Lx}{3}\right) + \frac{M_D}{EI_e}\left(\frac{x^3}{6L} - \frac{Lx}{6}\right) \tag{2.58}$$

The end moments at ends B and D can be calculated as a function of the constraint coefficients by substituting Equation (2.58) into the equilibrium condition, Equation (2.56), as follows:

$$M_B = \frac{C_B L^2}{120}\left[\frac{(q_B - q_D)(2 - C_D) + (q_B + q_D)(30 - 5C_D)}{12 + 4C_B - 4C_D - C_B C_D}\right] \tag{2.59a}$$

$$M_D = \frac{C_D L^2}{120}\left[\frac{(q_B - q_D)(2 + C_B) - (q_B + q_D)(30 + 5C_B)}{12 + 4C_B - 4C_D - C_B C_D}\right] \tag{2.59b}$$

The extreme value of the bending moment inside the span will occur at the location where the condition of $dM/dx = 0$ is satisfied. When both ends and any one point inside the span yield, a collapse hinge mechanism is formed. Depending on the end condition, the loading and other details related to the formation of the collapse mechanism will vary.

For the ideal end conditions previously described in Section 2.7.2 or 2.7.3, the beam will collapse if the following criteria are fulfilled.

(1) A beam simply supported at both ends:

$$\frac{q_B}{2}(x_p^2 - Lx_p) + \frac{q_B - q_D}{6}\left(Lx_p - \frac{x_p^3}{L}\right) = M_P \tag{2.60}$$

where

$$x_p = \frac{L}{2} \quad \text{for } q_D = q_B$$

$$x_p = \frac{L}{q_B - q_D}\left(q_B - \sqrt{\frac{q_B^2 + q_D^2 + q_D q_B}{3}}\right) \quad \text{for } q_B > q_D$$

(2) A beam fixed at end B and simply supported at end D:

$$\frac{x_p[(L^2 - x_p^2)q_D + (2L^2 - 3Lx_p + x_p^2)q_B]}{6(2L - x_p)} = M_P \tag{2.61}$$

where x_p is the distance from end B to the plastic hinge inside the span, which is taken so that q_B or q_D should be a minimum.

2.7.6 Tripping under Lateral Load

A beam under lateral load which is bent about its major axis can buckle sideways if its compression flange does not have sufficient stiffness in the lateral direction. At a critical load, the plate–beam combination can become unstable since the compression flange may twist sideways.

This phenomenon is sometimes termed tripping (also called lateral–torsional buckling) which is normally supposed to be one of the many behaviors that may lead to the ULS of the plate–beam combination. Hence it is of importance to calculate the tripping strength of beams under lateral loading. For this problem, Section 2.9.2 is referred to.

2.8 Ultimate Strength of Columns

Unlike plate panels as will be described in Chapter 4, columns cannot be expected to have residual strength after the inception of buckling and thus buckling strength typically is considered to be synonymous with the ultimate strength for column members.

In this section, ultimate strength formulations for plate–beam combinations subject to predominantly axial compressive loads are described.

2.8.1 Large-deflection Behavior of Straight Columns

From classical large-deflection column theory, the length, dL', of an infinitesimal element AB of a bent column, as shown in Figure 2.23, which initially was of length dx, can be calculated by (Shames & Dym 1993)

$$(dL')^2 = (dx)^2(1 + 2\varepsilon_x) \tag{2.62}$$

where $\varepsilon_x = du/dx + \frac{1}{2}(du/dx)^2 + \frac{1}{2}(dw/dx)^2$ = axial strain of the straight column taking into account the large deformation effects, u = axial displacement, w = lateral deflection.

If the column neutral axis is supposed to be incompressible during its bending from the straight-line configuration, then $dL' = dx$. Therefore, Equation (2.62) becomes

$$\left(1 + \frac{du}{dx}\right)^2 + \left(\frac{dw}{dx}\right)^2 = 1 \tag{2.63}$$

From geometric consideration of Figure 2.23, the rotation of the segment AB can be calculated by

$$\sin\theta = \frac{(dw/dx)dx}{\overline{AB}} = \frac{(dw/dx)dx}{\sqrt{(1 + du/dx)^2 + (dw/dx)^2}(dx)} = \frac{dw}{dx} \tag{2.64}$$

since Equation (2.63) is satisfied as long as the column is incompressible.

After deformation, the curvature, $1/R$, of the column is given by considering $dL' = dx$, namely

$$\frac{1}{R} \equiv \frac{d\theta}{dL'} = \frac{d\theta}{dx} = \frac{d^2w/dx^2}{\cos\theta} = \frac{d^2w/dx^2}{\sqrt{1 - (dw/dx)^2}} \tag{2.65}$$

since $\cos\theta(d\theta/dx) = d^2w/dx^2$ from Equation (2.64) and $\cos\theta = \sqrt{(1 - \sin^2\theta)} = \sqrt{[1 - (dw/dx)^2]}$.

When the column deflection is supposed to be small enough, Equation (2.65) often simplifies to

$$\frac{1}{R} \cong \frac{d^2w}{dx^2} \tag{2.66}$$

since $dw/dx \ll 1$ and hence $(dw/dx)^2 \approx 0$ in this case.

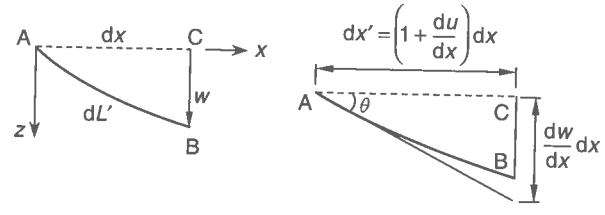

Figure 2.23 Large deflection of a bent column

The total shortening of the entire column can be calculated by considering Equation (2.63) as follows:

$$u = \int_0^L \frac{\mathrm{d}u}{\mathrm{d}x}\,\mathrm{d}x = \int_0^L \left[\sqrt{1-\left(\frac{\mathrm{d}w}{\mathrm{d}x}\right)^2} - 1\right]\mathrm{d}x \cong -\frac{1}{2}\int_0^L \left(\frac{\mathrm{d}w}{\mathrm{d}x}\right)^2 \mathrm{d}x \tag{2.67}$$

where it is important to realize that the shortening expression above accommodates only the effect of bending deflection while the column neutral axis is incompressible.

We now calculate the strain energy of the column due to bending. Using the Euler–Bernoulli hypothesis for the bending of beams, the strain energy, U, can be obtained by

$$U = \frac{1}{2}\int_{\mathrm{Vol}} \sigma_x \varepsilon_x \,\mathrm{dVol} = \frac{E}{2}\int_{\mathrm{Vol}} \varepsilon_x^2 \,\mathrm{dVol} = \frac{E}{2}\int_{\mathrm{Vol}} \left(\frac{z}{R}\right)^2 \mathrm{dVol} = \frac{EI_{\mathrm{e}}}{2}\int_0^L \left(\frac{1}{R}\right)^2 \mathrm{d}x \tag{2.68}$$

since $\varepsilon_x = z/R$, $I_{\mathrm{e}} = \iint z^2\,\mathrm{d}A_{\mathrm{e}}$, and $\sigma_x =$ axial stress. The subscript e represents the effective section.

Substituting Equation (2.66) into Equation (2.68), the strain energy, U, may approximately be calculated by

$$U \cong \frac{EI_{\mathrm{e}}}{2}\int_0^L \left(\frac{\mathrm{d}^2 w}{\mathrm{d}x^2}\right)^2 \mathrm{d}x \tag{2.69}$$

On the other hand, the external potential energy, W, can be obtained using Equation (2.67) as follows:

$$W = Pu = P\int_0^L \frac{\mathrm{d}u}{\mathrm{d}x}\,\mathrm{d}x \cong -\frac{P}{2}\int_0^L \left(\frac{\mathrm{d}w}{\mathrm{d}x}\right)^2 \mathrm{d}x \tag{2.70}$$

The total potential energy, Π, can be given by a sum of the strain energy, U, and the external potential energy, W, as follows:

$$\Pi = U + W \tag{2.71}$$

which results in

$$\Pi = \frac{EI_{\mathrm{e}}}{2}\int_0^L \left(\frac{1}{R}\right)^2 \mathrm{d}x - P\int_0^L \frac{\mathrm{d}u}{\mathrm{d}x}\,\mathrm{d}x \cong \frac{EI_{\mathrm{e}}}{2}\int_0^L \left(\frac{\mathrm{d}^2 w}{\mathrm{d}x^2}\right)^2 \mathrm{d}x - \frac{P}{2}\int_0^L \left(\frac{\mathrm{d}w}{\mathrm{d}x}\right)^2 \mathrm{d}x$$

for the straight column.

The large-deflection behavior of columns can then be analyzed by applying the principle of minimum potential energy to Equation (2.71). For instance, when the lateral deflection, w, is supposed to be a Fourier series function which satisfies the boundary condition of the column and includes several unknown constants, C_i, the function of w is substituted into Equation (2.71). The constants C_i are then determined by the principle of minimum potential energy since $\partial\Pi/\partial C_i = 0$; refer also to Equation (2.90).

2.8.2 Elastic Buckling of Straight Columns

To study the ultimate strength of columns, of primary interest is elastic buckling. To illustrate the column buckling phenomenon, a simply supported straight column is considered, as shown in Figure 2.24.

When the column deflection is considered to be small enough, the following values for the column with effective section are obtained:

$$\text{internal bending moment:} \quad M = -EI_{\mathrm{e}}\frac{1}{R} = -EI_{\mathrm{e}}\frac{\mathrm{d}^2 w}{\mathrm{d}x^2} \tag{2.72a}$$

$$\text{external bending moment:} \quad M = Pw \tag{2.72b}$$

since the curvature is given by Equation (2.66).

Considering the equilibrium condition for the bending moment, the following governing differential equation emerges:

$$-EI_e\frac{\mathrm{d}^2 w}{\mathrm{d}x^2} = Pw \quad \text{or} \quad \frac{\mathrm{d}^2 w}{\mathrm{d}x^2} + k^2 w = 0 \tag{2.73}$$

where $k = \sqrt{(P/EI_{\mathrm{e}})}$.

The general solution of Equation (2.73) reads

$$w = C_1 \sin kx + C_2 \cos kx \tag{2.74}$$

where C_1 and C_2 are constants to be determined in accordance with the end conditions.

Since both ends are simply supported, $w = 0$ at $x = 0$ and $x = L$. Substituting this end condition into Equation (2.74), the following two conditions emerge:

$$C_2 = 0,\ C_1 \sin kL = 0 \tag{2.75}$$

Considering the first condition of Equation (2.75), the form of the solution becomes $w = C_1 \sin kx$. This means that the coefficient C_1 should not be zero, otherwise no deflection exists. Thus, the second condition of Equation (2.75) provides a non-trivial solution as follows:

$$\sin kL = 0 \quad \text{or} \quad kL = \pi, 2\pi, 3\pi, \ldots, n\pi, \ldots \tag{2.76}$$

The smallest value of the applied load, P, is given when $kL = \pi$. Thus, the so-called Euler buckling load, P_{E}, is calculated by

$$P_{\mathrm{E}} = \frac{\pi^2 EI_{\mathrm{e}}}{L^2} \tag{2.77}$$

After buckling, the deflection pattern of the column simply supported at both ends is therefore expressed by $w = \sin(\pi x/L)$.

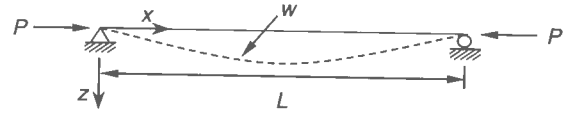

Figure 2.24 A straight column simply supported at both ends

2.8.3 Effect of End Conditions

The Euler buckling load for columns was obtained above under the condition that both ends are simply supported. In reality, the ends are usually welded to other members and thus are restrained against rotation. The amount of this restraint typically varies with the properties of the different structural members involved.

For an infinitesimal part of the column with a certain type of end condition(s) as shown in Figure 2.25, the force equilibrium considerations lead to the basic fourth-order differential equation for flexural buckling of columns, when $dw/dx \approx 0$, as follows:

$$\frac{d^2}{dx^2}\left(EI_e\frac{d^2w}{dx^2}\right) + P\frac{d^2w}{dx^2} = 0 \tag{2.78}$$

When the cross-section is uniform along the span, Equation (2.78) can be rewritten as follows:

$$EI_e\frac{d^4w}{dx^4} + P\frac{d^2w}{dx^2} = 0 \tag{2.79}$$

The general solution of Equation (2.79) is given by

$$w = C_1\cos kx + C_2\sin kx + C_3x + C_4 \tag{2.80}$$

where $k =$ as defined in Equation (2.73).

Considering lateral deflection w, slope dw/dx, bending moment $EI_e\, d^2w/dx^2$, and shear force $EI_e\, d^3w/dx^3 + P\, dw/dx$, in the z direction, the end conditions of the column may be mathematically expressed by

at simply supported end: $w = 0, \quad \dfrac{d^2w}{dx^2} = 0$

at fixed end: $w = 0, \quad \dfrac{dw}{dx} = 0$

at free end: $\dfrac{d^2w}{dx} = 0, \quad \dfrac{d^3w}{dx^3} + k^2\dfrac{dw}{dx} = 0$

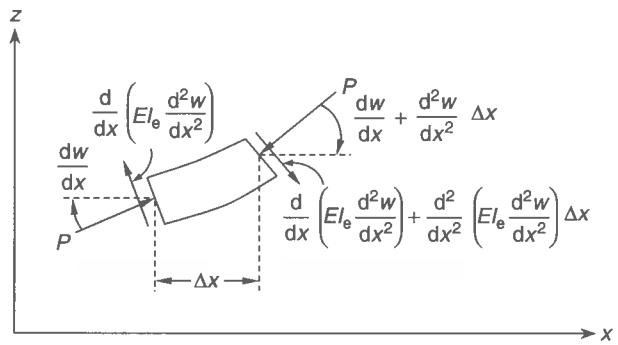

Figure 2.25 Force components acting on a column free-body element

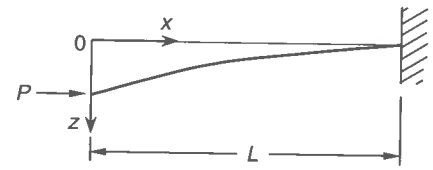

Figure 2.26 A cantilever column

Since two boundary conditions at each end exist, a total of the four unknown constants in Equation (2.80) must be determined in a given case. The lateral deflection, w, will then have solutions different from zero only if the determinant for a set of linear homogeneous equations with regard to C_1–C_4 vanishes. The buckling load can be calculated as the minimum value which satisfies the condition that the determinant becomes zero.

For instance, buckling of a column is now considered when one end is fixed and the other end is free, such as that shown in Figure 2.26. The end conditions are in this case given by

at $x = 0$ (free end): $\dfrac{d^2w}{dx} = 0, \quad \dfrac{d^3w}{dx^3} + k^2\dfrac{dw}{dx} = 0$

at $x = L$ (fixed end): $w = 0, \quad \dfrac{dw}{dx} = 0$

By substituting these boundary conditions into Equation (2.80), we get

$$C_1 = C_3 = 0,\ C_2\sin kL + C_4 = 0,\ C_2k\cos kL = 0 \tag{2.81}$$

The second and third conditions of Equation (2.81) become

$$C_4 = -C_2\sin kL = C_2(-1)^n,\ C_2 \neq 0, k \neq 0$$
$$\cos kL = 0 \rightarrow kL = (2n-1)\frac{\pi}{2},\ n = 1, 2, 3\ldots \tag{2.82}$$

The buckling load is then obtained from the last equation of Equation (2.82) when the smallest load is obtained with $n = 1$, as follows:

$$kL = \frac{\pi}{2} \rightarrow P_E = \frac{\pi^2EI_e}{4L^2} = \frac{\pi^2EI_e}{(2L)^2} \tag{2.83}$$

After buckling, the lateral deflection pattern of the cantilever column is given by $w = 1 - \sin(\pi x/2L)$.

As rotational restraints of the adjacent members increase, the column ends may approach fixed conditions. In this case, the buckling wave length between points of inflection becomes shorter. For instance, the buckling wave length of the cantilever column may become 200% of the original length as evident from Equation (2.83), see Figure 2.27(b). For the column fixed at both ends, the buckling wave length is 50% of the original length, see Figure 2.27(c). When one end is fixed and the other is pinned, the buckling wave length becomes 70% of the original length, see Figure 2.27(d).

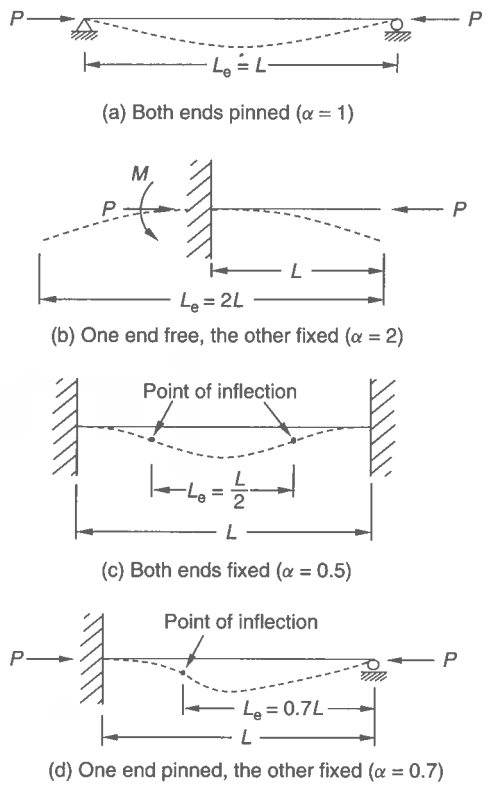

Figure 2.27 Effective length of columns varying the end conditions

It is apparent that the buckling wave length decreases as the rotational restraints at the column ends increase. Also, the shorter the buckling wave length the larger the buckling load. For convenience, the term 'effective length' (also called 'buckling length') is typically employed to account for the effect of the column end conditions so that the elastic buckling loads of columns with various types of end conditions can be determined by the Euler formula, but replacing the original (or system) length, L, by the effective length, L_e, as follows:

$$P_E = \frac{\pi^2 E I_e}{L_e^2} = \frac{\pi^2 E I_e}{(\alpha L)^2} \quad \text{or} \quad \sigma_E = \frac{P_E}{A} = \frac{\pi^2 E}{(\alpha L/r_e)^2} \tag{2.84}$$

where α = constant accounting for the effect of column end condition.

For various end conditions, the applicable theoretical values of the effective length, L_e, or constant α, are given as those of Figure 2.27.

2.8.4 Effect of Initial Imperfections

As previously noted in Section 1.7, the actual columns in welded steel-plated structures will have initial imperfections in the form of initial deflections (out-of-straightness) and residual stresses which affect the structural behavior and load-carrying capacity.

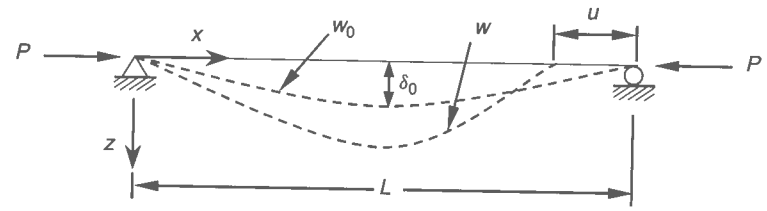

Figure 2.28 An initially deflected column simply supported at both ends

An initially deflected pin-ended column as shown in Figure 2.28 is now considered. The geometric configuration of the initial deflection, w_0, may approximately be defined by Equation (1.9) in Chapter 1, i.e., $w_0 = \delta_0 \sin(\pi x/L)$, which takes the half sinusoidal wave pattern. The total (initial plus added) deflection, w, after buckling, may also take a similar shape to the initial deflection as follows:

$$w = \delta \sin \frac{\pi x}{L} \tag{2.85}$$

where δ = amplitude of the total deflection.

The bending moment equilibrium is in this case given by

$$E I_e \frac{d^2(w - w_0)}{dx^2} + P w = 0 \tag{2.86}$$

where the first term on the left hand side represents internal bending moments due to added deflection alone since the initial deflection does not contribute to internal bending, while the second term is the external bending moment imposed by the total deflection.

The axial strain of the column with initial deflection may be given as being similar to that of a straight column defined in Equation (2.62), by taking into account the large-deflection effects, but by neglecting the large axial displacement effects as follows:

$$\varepsilon_x = \frac{\partial u}{\partial x} + \frac{1}{2}\left(\frac{\partial^2 w}{\partial x^2}\right)^2 - \frac{1}{2}\left(\frac{\partial^2 w_0}{\partial x^2}\right)^2 \tag{2.87}$$

where the first term on the right hand side of Equation (2.87) represents the small strain component, while the second and third terms portray the large-deflection effects.

To determine the amplitude of total deflection in Equation (2.85), the strain-energy-based approach is employed. The elastic strain energy, U, of the initially deflected column may be read from Equation (2.69) as follows:

$$U = \frac{E I_e}{2} \int_0^L \left(\frac{\partial^2 w}{\partial x^2} - \frac{\partial^2 w_0}{\partial x^2}\right)^2 dx = \frac{\pi^4 E I_e}{4L^3}(\delta - \delta_0)^2 \tag{2.88}$$

since

$$\int_0^L \sin^2 \frac{\pi x}{L}\, dx = \int_0^L \frac{1}{2}\left(1 - \cos \frac{2\pi x}{L}\right) dx = \frac{L}{2}$$

The external potential energy, W, of the compressive load, P, related to lateral deflection is calculated from Equation (2.70), by neglecting the small strain component, as follows:

$$W = Pu = -\frac{P}{2}\int_0^L \left[\left(\frac{\partial^2 w}{\partial x^2}\right)^2 - \left(\frac{\partial^2 w_0}{\partial x^2}\right)^2\right] \mathrm{d}x = -\frac{P\pi^2}{4L}(\delta^2 - \delta_0^2) \tag{2.89}$$

The total potential energy, Π, of the initially deflected column is obtained from Equation (2.71), but using the strain energy, U, of Equation (2.88) and the external potential energy, W, of Equation (2.89).

Applying the principle of minimum potential energy, the amplitude of the total deflection can be found as follows:

$$\frac{\partial \Pi}{\partial \delta} = 0 = \frac{\pi^4 E I_e}{2L^3}(\delta - \delta_0) - \frac{P\pi^2}{2L}\delta \quad \text{or} \quad \delta = \frac{\delta_0}{1 - P/P_E} = \phi\delta_0 \tag{2.90}$$

where P_E = Euler buckling load as defined in Equation (2.77), $\phi = 1/(1 - P/P_E)$ = magnification factor.

Substituting Equation (2.90) into Equation (2.85), the total deflection is given by

$$w = \frac{\delta_0}{1 - P/P_E}\sin\frac{\pi x}{L} = \phi\delta_0 \sin\frac{\pi x}{L} \tag{2.91}$$

Figure 2.29 plots Equation (2.91) representing the applied compressive load versus the total deflection of the column, varying the magnitude of initial deflection. As evident from Figure 2.29, the deflection increases progressively from the very beginning of compressive loading when initial deflection exists and a bifurcation buckling point does not exist in this case. Also, the load-carrying capacity decreases as the magnitude of initial deflection increases.

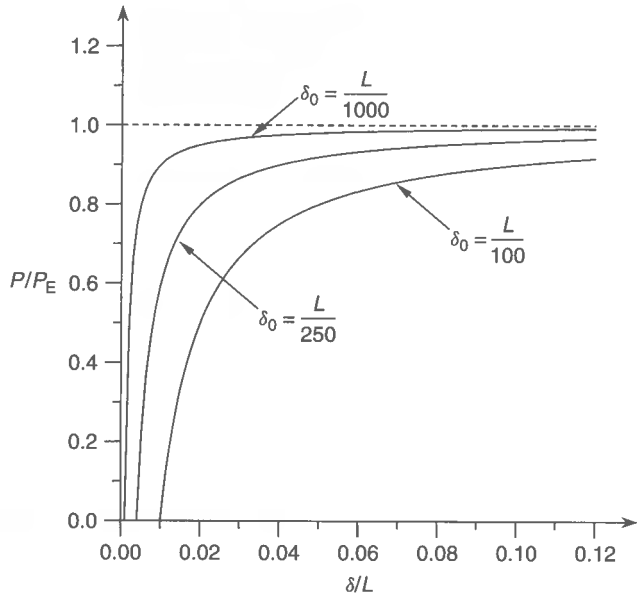

Figure 2.29 The behavior of a column with initial deflection

On the other hand, the existence of any compressive residual stresses will further reduce the buckling strength of columns. For practical design purposes, the effect of compressive residual stress on the column buckling strength is sometimes included by reducing the compressive residual stress from the computed buckling strength.

2.8.5 Collapse Strength of Columns

The elastic buckling strength formulas derived so far are valid as long as the material remains in the elastic regime. This may be true for slender perfect columns without initial imperfections. Since the Euler buckling stress must be less than the proportional limit of material, σ_P, a limit of the column slenderness ratio for use of the Euler formula may be given from Equation (2.84) as follows:

$$\frac{L}{r_e} \geq \frac{\pi}{\alpha}\left(\frac{E}{\sigma_P}\right)^{1/2} \tag{2.92}$$

since $\sigma_E \leq \sigma_p$.

For instance, if the proportional limit of material is taken as $\sigma_P = 200$ MPa, $E = 2.1 \times 10^5$ MPa and $\alpha = 1.0$, the column slenderness ratio must satisfy $L/r_e \geq \pi(210\,000/200)^{1/2} = 101.7$ so that the Euler formula result is valid to use.

For stocky or imperfect columns, however, the elastic proportional limit is often exceeded and a certain degree of plasticity takes place before the inception of buckling. As a result, the real buckling load will in this case be less than the Euler buckling load.

Therefore, the Euler buckling formula will not be directly available for stocky or imperfect columns, which are more common in actual structures. However, since the Euler formula provides very useful insight into column buckling behavior, many researchers have attempted to utilize it to the extent possible even for elastic–plastic buckling of columns, with corrections applied to some of the parameters involved. For instance, some classical theories such as double modulus theory or tangent modulus theory resembling the original Euler formulation have been suggested to deal with elastic–plastic effects on column buckling (Bleich 1952).

In reality, a stocky column that has a high value of computed elastic buckling strength will not buckle in the elastic regime, but will actually reach the ULS with a certain degree of plasticity. To account for this behavior, some approximate formulas based on the insights developed from experiments, such as the so-called Gordon–Rankine formula, the Tetmajer formula and the Johnson–Ostenfeld formula, are often used.

For modern practical design purposes, the various available ultimate strength formulations for plate–beam combinations under predominantly axial compression are typically based on one of the three common approaches, namely

- the Johnson–Ostenfeld (or Bleich–Ostenfeld) formulation
- the Perry–Robertson formulation
- a purely empirical formulation.

Among these, most classification societies in marine industry employ the Johnson–Ostenfeld formulation to take into account the effect of plasticity in the elastic buckling strength. The resulting 'elastic–plastic' buckling strength is often termed the 'critical' buckling strength.

The Perry–Robertson formulation considers that the plate–beam combination will collapse when the maximum compressive stress at the extreme fiber reaches the yield strength of the material. Two possible collapse modes for the Perry–Robertson formulation of a plate–beam combination model are usually treated depending on the compressed side, namely plate- or stiffener-induced failure, the former being initiated by compression at the attached plating side and the latter being initiated by compression at the stiffener flange side.

In empirical approaches, the ultimate strength formulations are developed by curve fitting based on mechanical collapse test results or numerical solutions. These types of empirical formulas can often be cast as simple closed-form expressions which have certain advantages in getting first-cut estimates, while their use may be restricted to a specified range of dimensions or be subject to other limitations.

Johnson–Ostenfeld Formula

The critical buckling strength based on the Johnson–Ostenfeld formula is given as follows:

$$\sigma_{cr} = \begin{cases} \sigma_E & \text{for } \sigma_E \le 0.5\sigma_F \\ \sigma_F[1 - \sigma_F/(4\sigma_E)] & \text{for } \sigma_E > 0.5\sigma_F \end{cases} \tag{2.93}$$

where σ_E = elastic buckling stress, σ_{cr} = critical (elastic–plastic) buckling stress, σ_F = reference yield stress; $\sigma_F = \sigma_Y$ for compressive stress and $\sigma_F = \tau_Y = \sigma_Y/\sqrt{3}$ for shear stress, σ_Y = material yield stress. For the plate–stiffener combinations, σ_Y may be taken as the equivalent yield stress, i.e., $\sigma_Y = \sigma_{Yeq}$. In using Equation (2.93), the sign of the compressive stress is taken as positive.

In ship rules from different sources, Equation (2.93) may appear with somewhat different constants depending on the structural proportional limit value assumed; the above form assumes a structural proportional limit of 50% of the applicable yield value. Equation (2.93) is also used for steel plates as well as columns.

Perry–Robertson Formula

In the Perry–Robertson formulation, it is assumed that the column will collapse if the maximum compressive stress at the extreme fiber of the column cross-section reaches the yield stress. For an initially deflected column simply supported at both ends, see Figure 2.28, the maximum bending moment, M_{max}, can be calculated, if local buckling effects can be neglected, using the total deflection, δ, at mid-span as given by Equation (2.90) as follows:

$$M_{max} = P\delta = \frac{P\delta_0}{1 - P/P_E} \tag{2.94}$$

where Equation (2.94) cannot be valid further if local buckling or tripping occurs in the plate–beam combination. For this case, Section 2.8.6 or 2.8.7 may be referred to.

The maximum compressive stress at the outer fiber of the cross-section can therefore be obtained by the sum of axial stress and bending stress as follows:

$$\sigma_{max} = \frac{P}{A} + \frac{M_{max}}{I_e} z_c = \frac{P}{A} + \frac{z_c}{I_e}\frac{P\delta_0}{1 - P/P_E} = \sigma + \frac{A\delta_0 z_c}{I_e}\frac{\sigma}{1 - \sigma/\sigma_E} \tag{2.95}$$

where $\sigma = P/A$, z_c = distance from elastic neutral axis to outer fiber of the compressed side.

Following the Perry–Robertson approach, the ultimate strength of the column is then obtained from Equation (2.95) by replacing σ with σ_u when σ_{max} reaches the equivalent yield stress, σ_{Yeq}, namely

$$\sigma_{max} = \sigma_{Yeq} = \sigma_u\left(1 + \frac{\eta}{1 - \sigma_u/\sigma_E}\right) \tag{2.96}$$

where $\eta = A\delta_0 z_c/I_e = \delta_0 z_c/r_e^2$.

The real ultimate strength, σ_u, is taken as the minimum value of the two solutions obtained by solving Equation (2.96) with regard to σ_u as follows:

$$\frac{\sigma_u}{\sigma_{Yeq}} = \frac{1}{2}\left(1 + \frac{1+\eta}{\lambda_e^2}\right) - \left[\frac{1}{4}\left(1 + \frac{1+\eta}{\lambda_e^2}\right)^2 - \frac{1}{\lambda_e^2}\right]^{0.5} \tag{2.97}$$

where $\lambda_e = (L/\pi r_e)\sqrt{(\sigma_{Yeq}/E)} = \sqrt{(\sigma_{Yeq}/\sigma_E)}$, $\eta =$ as defined in Equation (2.96).

For a straight column, i.e., without initial deflection, the constant η becomes $\eta = 0$. Therefore, it is evident that Equation (2.97) is reduced to the Euler formula when $\lambda_e \ge 1$, namely

$$\frac{\sigma_u}{\sigma_{Yeq}} = \frac{1}{\lambda_e^2} \tag{2.98}$$

The direction of column deflection may be primarily governed by that of initial deflection, lateral loading not being present. Since the nature of initial deflection is somewhat uncertain, the failure mode of a plate–beam combination model may be one of the two, namely plate-induced failure (PIF) or stiffener-induced failure (SIF). It is for this reason that the ultimate strength for the Perry–Robertson formula may be determined as the minimum value of the two strengths.

In a continuous stiffened plate structure, SIF is a trigger to the collapse of the entire panel. The original idea of the Perry–Robertson formula assumes that SIF occurs if the tip of the stiffener yields. This assumption may in some cases be too pessimistic in terms of the collapse strength predictions. Rather, plasticity may grow into the stiffener web as long as lateral–torsional buckling or stiffener web buckling does not take place, so that the stiffener may resist the further loading even after the first yielding occurs at the extreme fiber of the stiffener. As will be described later in Section 2.11.4 or Chapter 6, therefore, only the PIF-based Perry–Robertson formula, i.e., excluding the SIF, is often adopted for prediction of the ultimate strength of the plate–stiffener combination as representative of a continuous stiffened panel.

Empirical Formula

While a vast number of empirical formulations (sometimes called column curves) for the ultimate strength of simple I-beams in steel-framed structures have been developed (e.g., Chen & Atsuta 1976, 1977, ECCS 1978, among others), relevant empirical formulas for plate–beam combination models in steel-plated structures are also available.

As an example, Paik & Thayamballi (1997) developed an empirical formula for predicting the ultimate strength of a plate–stiffener combination under axial compression in terms of both column and plate slenderness ratios, based on existing mechanical collapse test data for the ultimate strength of stiffened panels under axial compression and with initial imperfections (initial deflections and residual stresses) at an 'average' level, as described in Equation (1.11d) or (1.15) of Chapter 1.

Since the ultimate strength of columns must be less than the elastic column buckling strength, the Paik–Thayamballi empirical formula is given by

$$\frac{\sigma_u}{\sigma_{Yeq}} = \frac{1}{\sqrt{0.995 + 0.936\lambda^2 + 0.170\beta^2 + 0.188\lambda^2\beta^2 - 0.067\lambda^4}} \leq \frac{1}{\lambda^2} \tag{2.99}$$

where λ, β = column and plate slenderness ratios for the full section, as defined in Table 2.1.

Equation (2.99) implicitly includes the possible effects of local buckling or tripping as well as initial imperfections (initial deflection and welding residual stress) at an 'average' level. Also, both column and plate slenderness ratios used in Equation (2.99) are calculated for the full section, i.e., without evaluating the effective width of the attached plating. This may sometimes be of benefit when evaluation of the plate effective width is difficult.

Figure 2.30 compares the Johnson–Ostenfeld formula, the Perry–Robertson formula and the Paik–Thayamballi empirical formula for the column ultimate strength for a plate–beam combination model varying the column slenderness ratios, for selected initial

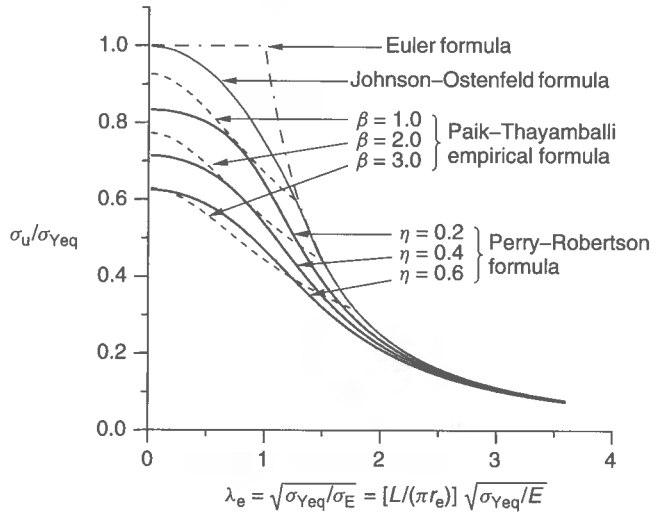

Figure 2.30 A comparison of the ultimate strength formulations for plate–stiffener combinations under axial compression

eccentricity and plate slenderness ratios. For convenience in the present comparisons, it was assumed that $\lambda_e = \lambda$.

2.8.6 Local Web or Flange Buckling under Axial Compression

The local buckling can in some cases take place in the web or flange of a stiffener in a stiffened panel. Once such stiffener web or flange buckling occurs, the stiffened panel may easily fall into the overall collapse mode since the stiffeners may not work further as support members. The local buckling strength of stiffener web or flange is presented later in Chapter 5.

2.8.7 Lateral–Torsional Buckling under Axial Compression

In a plate–stiffener combination under axial compression, the web can twist sideways if the stiffener flange is not strong enough to remain straight. This phenomenon is called lateral–torsional buckling, which occurs suddenly and results in subsequent unloading of the support member.

Hence in those cases it may be regarded as a collapse mode of the stiffened plate structure because once the stiffeners twist sideways the plating is left with essentially no stiffening and as a result a global buckling mode may follow immediately.

For this problem, the reader may refer to Section 2.9.2 of this chapter and Chapter 5, which present the lateral–torsional buckling strength for plate–stiffener combinations under combined axial compression and lateral load.

2.9 Ultimate Strength of Beam–Columns

In this section, the ultimate strength formulations for plate–beam combinations under combined axial compression and lateral load are derived by taking into account the effect of initial imperfections.

2.9.1 Modified Perry–Robertson Formula

Originally, the Perry–Robertson formula was developed to calculate the collapse strength of the plate–beam combination under predominantly axial compressive loads, when local buckling does not take place. The original Perry–Robertson approach considers that the column will collapse if the maximum compressive stress at the outer fiber of the cross-section reaches the yield stress.

For plate–beam combinations under combined axial compression and lateral load, the Perry–Robertson approach may also be applied to calculate the ultimate strength, but the maximum compressive stress at the outer fiber of the plate–beam combination section is now a function of lateral load as well as axial compression.

For a beam–column under combined axial compression, P, and lateral line load, q, the internal bending moment along the span can be obtained by

$$M = M_q + Pw \tag{2.100}$$

where M_q = bending moment due to lateral line load q, w = lateral deflection.

Using Equation (2.100), the bending equilibrium of the beam–column reads

$$EI_e\frac{d^2w}{dx^2} = -M = -M_q - Pw \quad \text{or} \quad \frac{d^2w}{dx^2} + k^2w = -\frac{M_q}{EI_e} \tag{2.101}$$

where $k =$ as defined in Equation (2.73).

The lateral deflection and bending moment distribution of a beam–column can be obtained by solving Equation (2.101) under prescribed boundary and loading conditions. For instance, the lateral deflection and bending moment of a beam–column pinned at both ends under combined axial compressive load, P, and lateral line load, q, are given by

$$w = \frac{q}{Pk^2}\left\{1 - \frac{\cos[k(L/2-x)]}{\cos(kL/2)}\right\} + \frac{q}{2P}x(L-x), \quad M = \frac{q}{k^2}\left\{1 - \frac{\cos[k(L/2-x)]}{\cos(kL/2)}\right\} \tag{2.102}$$

Since the maximum lateral deflection, w_{max}, or the maximum bending moment, M_{max}, occurs at mid-span, i.e., $x = L/2$,

$$w_{max} = C_1 w_{q\,max},\ M_{max} = C_2 M_{q\,max} \tag{2.103}$$

where

$$C_1 = \frac{384}{5k^4L^4}\left[\sec\left(\frac{kL}{2}\right) - 1 - \frac{k^2L^2}{8}\right],$$

$$C_2 = \frac{8}{k^2L^2}\left[1 - \sec(kL/2)\right], \quad w_{q\,max} = \frac{5qL^4}{384EI_e}, \quad M_{q\,max} = \frac{qL^2}{8}$$

$w_{q\,max}$ and $M_{q\,max}$ are the maximum lateral deflection and the maximum bending moment caused by lateral line load q alone, respectively. The coefficients C_1 and C_2 portray the magnification factors for lateral deflection and bending moment, respectively. As is apparent, the magnification factors may be different depending on load applications or end conditions.

Applying the Perry–Robertson approach, it is considered that the plate–beam combination collapses when the maximum compressive stress at the outer fiber of the cross-section reaches the yield stress. Depending on the direction of lateral loading, the compressed side of the cross-section will be automatically determined.

For practical design purposes, specifically when the direction of lateral loading is unknown beforehand, however, the maximum stress at the cross-section may be taken as the larger value of the stresses at the two extreme fibers, namely

$$\sigma_{max} = \frac{P}{A} + \frac{M_{max}}{I_e}z_{max} = \sigma_{Yeq} \tag{2.104}$$

where $z_{max} =$ larger value of z_p or $h_w + t + t_f - z_p$, $z_p =$ as defined in Table 2.1.

The ultimate axial compressive stress, σ_u, is obtained as the solution of Equation (2.104) with regard to $\sigma = P/A$. An iterative process may be needed to solve Equation (2.104) with regard to the axial load because M_{max} is a nonlinear function of P.

To obtain a closed-form expression of the ultimate compressive strength for a beam–column, a simplification can herein be made. It is assumed that the maximum bending moment of a beam–column is the sum of the bending moment due to lateral loads plus that due to geometric eccentricity which may include lateral deflection caused by external load as well as initial deflection, namely

$$M_{max} = M_{q\,max} + P\phi(w_{q\,max} + \delta_0) \tag{2.105}$$

where $M_{q\,max} =$ maximum bending moment due to lateral load alone, $w_{q\,max} =$ maximum deflection (amplitude) due to lateral load alone, $\delta_0 =$ initial deflection, $\phi =$ magnification factor as defined in Equation (2.90).

To check the accuracy of Equation (2.105), an example is considered when a beam–column is subjected to uniform lateral line load, q, and axial compression $P = 0.5P_E$. We assume that initial deflection does not exist, i.e., $\delta_0 = 0$ so that the exact solution of Equation (2.103) which is $M_{max} = 2.030M_{q\,max}$ can be compared directly to Equation (2.105). Since $w_{q\,max} = 5qL^4/(384EI_e)$ and $\phi = 1/(1 - P/P_E) = 2$, the maximum bending moment by Equation (2.105) results in

$$M_{max} = M_{q\,max} + \frac{5qL^4}{384EI_e}\frac{\pi^2EI_e}{L^2} = M_{q\,max}\left(1 + \frac{5\pi^2}{48}\right) = 2.028M_{q\,max}$$

It is evident that Equation (2.105) is accurate enough in this case since the difference between Equations (2.103) and (2.105) is less than 0.1% for this example. Since the ultimate strength is reached when the maximum stress equals the yield stress, an equation similar to Equation (2.104) appears, namely

$$\sigma_{max} = \frac{P}{A} + \frac{M_{q\,max}}{I_e}z_{max} + \frac{P}{1 - P/P_E}(w_{q\,max} + \delta_0)\frac{z_{max}}{I_e} = \sigma_{Yeq} \tag{2.106}$$

By introducing the following non-dimensional parameters,

$$R = \frac{\sigma_u}{\sigma_{Yeq}},\ \lambda_e = \sqrt{\frac{\sigma_{Yeq}}{\sigma_E}} = \frac{L}{\pi r_e}\sqrt{\frac{\sigma_{Yeq}}{E}},\ \eta = \frac{Az_{max}}{I_e}(w_{q\,max} + \delta_0),\ \mu = \frac{M_{q\,max}}{\sigma_{Yeq}}\frac{z_{max}}{I_e}$$

Equation (2.106) may be expressed as a quadratic function of the axial compressive stress and lateral load, namely

$$\eta R - (1 - R - \mu)(1 - \lambda_e^2 R) = 0 \tag{2.107}$$

Regarding the lateral load as a constant dead load, the ultimate compressive strength of the plate–beam combination under combined axial compression and lateral load is obtained as the minimum value of the two solutions of Equation (2.107) with regard to R, namely

$$R = \frac{1}{2}\left(1 - \mu + \frac{1+\eta}{\lambda_e^2}\right) - \left[\frac{1}{4}\left(1 - \mu + \frac{1+\eta}{\lambda_e^2}\right)^2 - \frac{1-\mu}{\lambda_e^2}\right]^{0.5} \tag{2.108a}$$

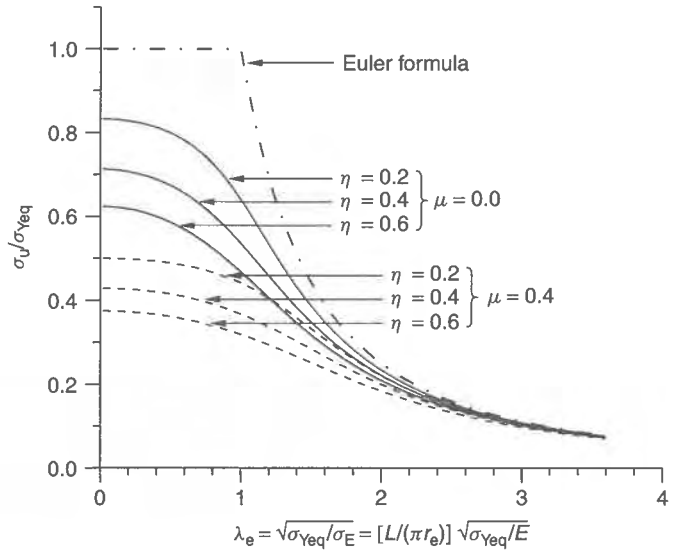

Figure 2.31 Variation of the ultimate compressive strength from the Perry–Robertson formula versus the column slenderness ratio for plate–stiffener combinations under combined axial compression and lateral load

Figure 2.31 shows the variation of R so obtained, versus the column slenderness ratio, for selected values of η and μ. To approximately account for the effect of welding residual stresses, Equation (2.108a) may be modified by multiplying a knock-down factor, K_r, as follows:

$$R = K_r \left\{ \frac{1}{2}\left(1 - \mu + \frac{1+\eta}{\lambda_e^2}\right) - \left[\frac{1}{4}\left(1 - \mu + \frac{1+\eta}{\lambda_e^2}\right)^2 - \frac{1-\mu}{\lambda_e^2}\right]^{0.5} \right\} \tag{2.108b}$$

where the knock-down factor K_r due to compressive residual stress, σ_{rsx}, may sometimes be taken as $K_r = 1.03 - 0.08|\sigma_{rsx}/\sigma_{Yeq}| \leq 1.0$ for built-up sections.

As previously described in Section 2.8.5, the Perry–Robertson-type SIF (i.e., at first yielding of the stiffener tip) may not always represent the actual ULS of the entire panel.

2.9.2 Lateral–Torsional Buckling under Combined Axial Compression and Lateral Load

The lateral–torsional buckling (also called tripping) strength, σ^T, for a plate–stiffener combination under combined axial compression and lateral loads can be calculated as will be described in Chapter 5.

To illustrate the length effect of a plate–stiffener combination under either axial compression alone or combined axial compression and lateral loads, Figure 2.32 shows the variations of the elastic tripping strengths together with the inelastic tripping strengths predicted by using the Johnson–Ostenfeld formula, Equation (2.93). For a comparison, the ordinary flexural Euler column buckling strengths together with the plasticity effect are also plotted.

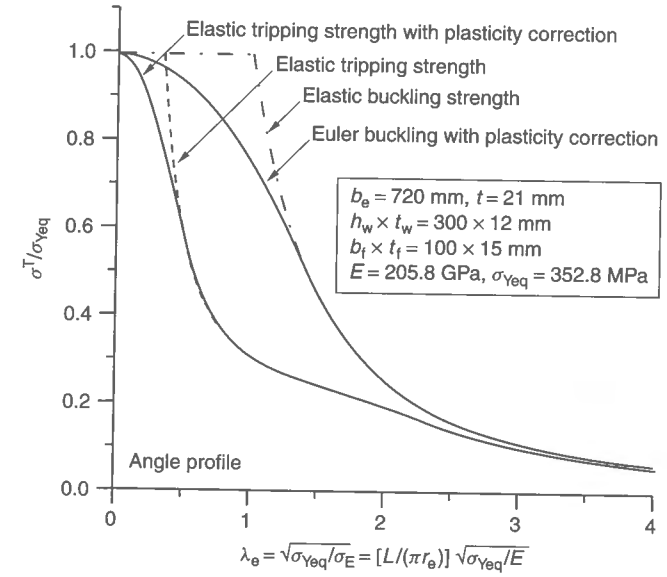

(a) Angle section stiffener with attached effective plating

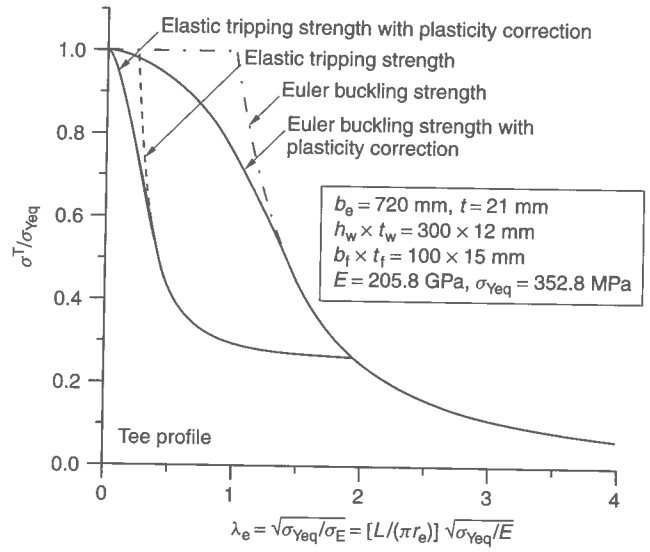

(b) Tee section stiffener with attached effective plating

Figure 2.32 Variation of the tripping strength versus the column slenderness ratio for a plate–beam combination under axial compression alone

As is evident from Figure 2.32, the effects of lateral–torsional deformations are of significance in relatively stocky columns. The tripping strength of stocky columns is then much lower than the Euler column buckling strength which does not accommodate lateral–torsional deformations of the stiffener. For slender columns, however, the tripping effect is negligible at least as far as these examples (with an identical stiffener flange breadth) are concerned.

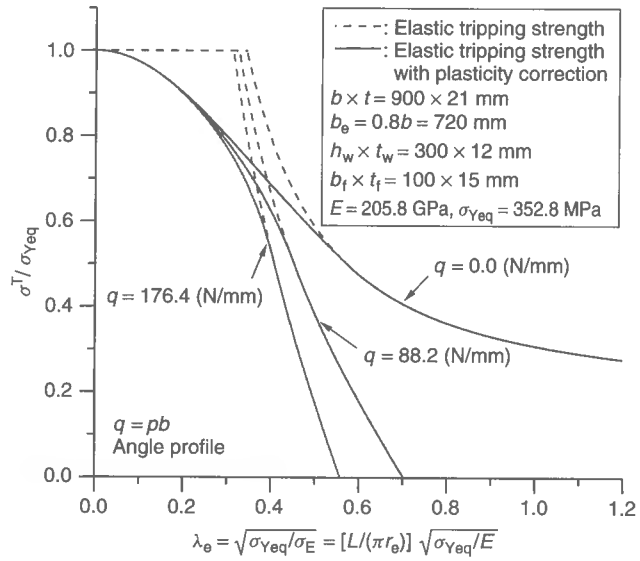

(a) Angle section stiffener

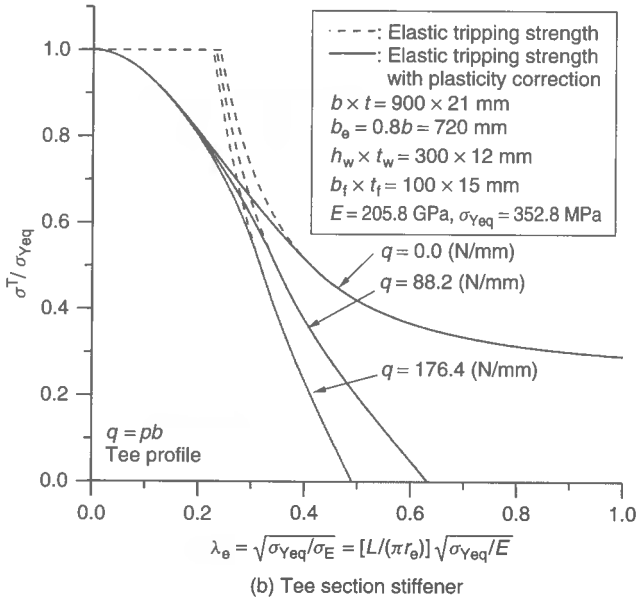

(b) Tee section stiffener

Figure 2.33 Variation of the tripping strength versus the column slenderness ratio for a plate–beam combination under combined axial compression and lateral loads

It may also be surmised that a one-sided (unsymmetric) stiffener flange (e.g., angle section stiffener) can have more desirable performance than a symmetric stiffener flange (e.g., Tee section stiffener) when the column slenderness ratio is small. On the contrary, the symmetric stiffener flange can provide more desirable performance than the unsymmetric stiffener flange when the column slenderness ratio is large. As shown in Figure 2.32(b), the

flexural buckling may be the more dominant failure mode than tripping for the symmetric section stiffener when the column slenderness ratio of the plate–stiffener combination is large.

Figure 2.33 shows the effect of lateral load on the tripping strength of plate–stiffener combinations. It is seen from Figure 2.33 that the lateral loads can significantly reduce the tripping strength of plate–beam combinations under axial compression.

2.10 Ultimate Strength of Plate–Stiffener Combinations and Their Design Considerations

The behavior of structural members typically depends on a variety of factors, namely geometric/material properties, loading characteristics, initial imperfections, boundary conditions and so on. Hence in the ULS design of support members, one or more different mechanical models may be required to deal with the different factors mentioned above. Even within a specific mechanical model, various types of failure modes may potentially take place. As described in the previous sections, three types of failure modes, namely column or beam–column types of collapse, lateral–torsional buckling and web buckling, are relevant for the plate–stiffener combination model.

Calculation of the ultimate strength of a structure taking into account all of the possible failure modes is not straightforward, because of the interplay of the various factors. As an approximation, it may be considered that the collapse of the structure occurs at the lowest value among the various ultimate loads calculated for potential failure patterns. This will lead to an easier alternative approach to ultimate strength, wherein one calculates the individual 'ultimate' strengths for all possible collapse modes separately and then compares them to find the minimum value which is taken to correspond to the real ultimate strength of the structure.

The ULS design is then undertaken so that the ultimate strength must be greater than the design load effects with a relevant margin of safety, as indicated in Equation (1.1) of Chapter 1.

2.11 Axial Stress–Strain Relationships of Beam–Columns

When the progressive collapse behavior of a large plated structure which is idealized as an assembly of the plate–beam combinations and other structural models is considered as will be described in Chapter 13, it is necessary to know the stress–strain relationship of individual plate–beam combination models until and after the ultimate strength is reached. The average stress–strain relationship (or axial load–end shortening formula) can then be utilized to examine the entire history of the structural member behavior, which can be divided into three regimes, namely the pre-ultimate strength regime, ultimate strength regime and post-ultimate strength regime. In the following sections, the load–end shortening formulas of beam–columns simply supported at both ends are derived.

2.11.1 Pre-ultimate Strength Regime

Under combined axial compressive load, P, and lateral line load, q, the total axial displacement (shortening), u, of a plate–beam combination model with initial deflection δ_0

can approximately be obtained using the axial strain defined in Equation (2.87) as follows:

$$u = \int_0^L \varepsilon_x \, dx = \frac{PL}{EA} + \frac{\pi^2}{4L}[\delta^2 - (\delta_0 + w_{q\,\max})^2] \tag{2.109}$$

where $w_{q\,\max}$ is the deflection due to lateral load as defined in Equation (2.103), which is treated as an additional initial deflection.

From Equation (2.90), we obtain $\delta = (\delta_0 + w_{q\,\max})/(1 - P/P_E)$ regarding the lateral-load-induced deflection as an initial deflection. Substituting this into Equation (2.109) and differentiating with respect to P and u, the incremental form of the compressive load versus end shortening of columns until the ULS is reached may approximately be obtained, by neglecting the effect of localized plastification, as follows:

$$\Delta P = k_E \Delta u \tag{2.110}$$

where

$$k_E = \left[\frac{L}{EA} + \frac{\pi^2(\delta_0 + w_{q\,\max})^2}{2L P_E (1 - P/P_E)^3}\right]^{-1}$$

The prefix, Δ, represents an increment of the variable. For axial tension, $k_E = L/EA$ is used with full sectional area of the member since it is in this case assumed that $\delta_0 = w_{q\,\max} = 0$.

The axial stress–strain relationship of the beam–column in the pre-collapse regime can then be given from Equation (2.110) in the incremental form as follows:

$$\Delta\sigma_x = \frac{L}{A} k_E \Delta\varepsilon_x \tag{2.111}$$

As will be described later in Section 13.4 of Chapter 13, the stiffness matrix of a beam–column element needs to be formulated for nonlinear finite element analyses. When the beam–column element has two nodal points, as shown in Figure 13.4, the stiffness equation is given by

$$\begin{Bmatrix} \Delta R_{x1} \\ \Delta R_{x2} \end{Bmatrix} = [K]^E \begin{Bmatrix} \Delta u_1 \\ \Delta u_2 \end{Bmatrix} \tag{2.112}$$

where

$$[K]^E = k_E \begin{bmatrix} 1 & -1 \\ -1 & 1 \end{bmatrix}$$

ΔR_{x1}, ΔR_{x2} = nodal force increments at nodes 1 and 2, Δu_1, Δu_2 = nodal displacement increments at nodes 1 and 2.

2.11.2 Ultimate Limit State

The column or beam–column will collapse if the load reaches the ultimate load. As described in Section 2.10, the real ultimate strength of a plate–stiffener combination will be determined as the lowest value among the various ultimate loads calculated

for potential failure patterns, namely column or beam–column types of collapse, lateral–torsional buckling and stiffener web buckling. For predominantly axial tension, the ultimate strength will be reached by gross yielding, e.g., at $P = P_P$, where P_P = as defined in Equation (2.20).

2.11.3 Post-ultimate Strength Regime

The collapsed member undergoes much larger deformations and the load–displacement behavior beyond the ULS is also of great interest, as long as the entire structure can still sustain further loading. The axial load–end shortening formula for plate–beam combinations is then herein derived using a similar approach to that of Murray (1983).

From Figure 2.34, the axial shortening, u, of the beam–column can approximately be expressed as a function of its geometry and lateral deflection, W, when $W \ll L$, as follows:

$$\begin{aligned} u &= 2\left[\frac{L}{2} - \left(\frac{L^2}{4} - W^2\right)^{1/2}\right] \\ &= 2\frac{L}{2}\left\{1 - \left[1 - \frac{1}{2}\left(\frac{2W}{L}\right)^2 - \frac{1}{8}\left(\frac{2W}{L}\right)^4 - \frac{1}{16}\left(\frac{2W}{L}\right)^2 + \cdots\right]\right\} \\ &= \frac{L}{2}\left(\frac{2W}{L}\right)^2\left[1 + \frac{1}{4}\left(\frac{2W}{L}\right)^2 + \frac{1}{8}\left(\frac{2W}{L}\right)^4 + \cdots\right] \\ &\approx \frac{2W^2}{L} \end{aligned} \tag{2.113}$$

Under combined loads, the reduced plastic bending capacity, M_r, can be predicted from Section 2.6.4 as a function of axial load, P, and/or shearing force, F. For a beam–column simply supported at both ends, the following equilibrium equation must be satisfied at the central plastic hinge after the collapse mechanism is formed, namely

$$PW = M_r \tag{2.114}$$

where M_r = reduced plastic bending moment accounting for the combined load effects.

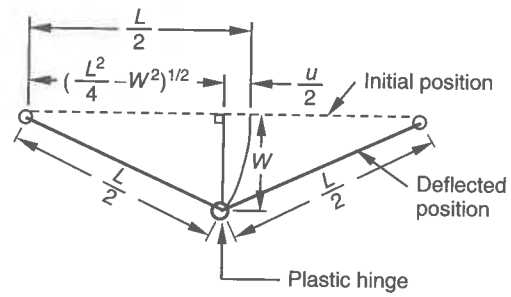

Figure 2.34 Axial shortening, u, caused by lateral deflection, W, at the center of the beam–column

By substituting Equation (2.113) into Equation (2.114), we get the axial load–end shortening relation in the post-ultimate regime as follows:

$$P\left(\frac{L}{2}u\right)^{1/2} = M_r \quad \text{or} \quad u = \frac{2}{L}\left(\frac{M_r}{P}\right)^2 \tag{2.115}$$

The incremental relation between u and P which portrays the tangential axial stiffness can be obtained by differentiating Equation (2.115) as follows:

$$\Delta u = \frac{2}{L}\frac{2M_r(\partial M_r/\partial P)P^2 - 2M_r^2 P}{P^4}\Delta P \quad \text{or} \quad \Delta P = k_u \Delta u \tag{2.116}$$

where

$$k_u = \left\{\frac{4M_r}{LP^3}\left[\left(\frac{\partial M_r}{\partial P}\right)P - M_r\right]\right\}^{-1}$$

The axial stress–strain relationship in the incremental form is given from Equation (2.116) as follows:

$$\Delta\sigma_x = \frac{L}{A}k_u \Delta\varepsilon_x \tag{2.117}$$

For the beam–column element shown in Figure 13.4 of Chapter 13, the stiffness equation in the post-ultimate strength regime is given by

$$\begin{Bmatrix}\Delta R_{x1}\\ \Delta R_{x2}\end{Bmatrix} = [K]^U \begin{Bmatrix}\Delta u_1\\ \Delta u_2\end{Bmatrix} \tag{2.118}$$

where

$$[K]^U = k_u\begin{bmatrix}1 & -1\\ -1 & 1\end{bmatrix}$$

$\Delta R_{x1}, \Delta R_{x2}, \Delta u_1, \Delta u_2 =$ as defined in Equation (2.112).

In calculating Equation (2.118), M_r depends on the geometry of the cross-section. For rectangular cross-sections, we get

$$M_r = M_P\left[1 - \left(\frac{P}{P_P}\right)^2\right], \quad \frac{\partial M_r}{\partial P} = -\frac{2PM_P}{P_P^2} \quad \text{and} \quad k_u = -\left\{\frac{4M_P^2}{LP^3}\left[1 - \left(\frac{P}{P_P}\right)^4\right]\right\}^{-1} \tag{2.119}$$

It is noted that P in Equation (2.119) must be decreased as the end shortening increases. For approximation, Equation (2.119) for rectangular cross-sections may be utilized for a plate–stiffener combination, but using P_P and M_P for the corresponding plate–beam combination model.

2.11.4 Verification Examples

The axial stress–strain formulations of the plate–stiffener combination model noted in Sections 2.11.1 to 2.11.3 are incorporated into the ALPS/ISUM program based on the

idealized structural unit method (ISUM) as will be presented in Chapter 13. The progressive collapse behavior of a continuous stiffened plate structure under uniaxial compressive load, as shown in Figure 2.35, is now analyzed to verify the formulations. This structure has been selected from the bottom panels of large merchant ship structures. The panel with three Tee-type stiffeners is supported by heavy longitudinal girders and transverse frames.

The geometric properties of the structure are: $L = 7920$ mm, $a = 2640$ mm, $B = 3600$ mm, $b = 900$ mm, $t = 21$ mm, $t_w = 12$ mm, $b_f = 100$ mm, $t_f = 15$ mm. Two kinds of stiffener web height, i.e., $h_w = 150$ mm and 210 mm, are considered in the analysis. The material yield stress for both plating and stiffeners is 352.8 MPa, Young's modulus is 205.8 GPa and Poisson's ratio is 0.3. It is assumed that plating between stiffeners has the buckling mode initial deflection of 3.3 mm which corresponds to $0.05\beta^2 t$ where $\beta = (b/t)\sqrt{(\sigma_{Y_p}/E)}$. The column-type or sideways initial deflection of the stiffeners between transverse frames is considered to be $0.0025a$ or $0.0015a$, respectively. Welding residual stresses do not exist.

To solve this problem, the theoretical method presented in this chapter and the nonlinear finite element method are used and their results are compared. For the theoretical calculations, a plate–stiffener combination is taken as representative of the stiffened panel between two transverse frames, as shown in Figure 2.36. Both ends of the plate–stiffener combination model are modeled to be simply supported. The effective width, b_e, of attached plating is assumed to be 100% of the original width, i.e., $b_e = b$. In the theoretical

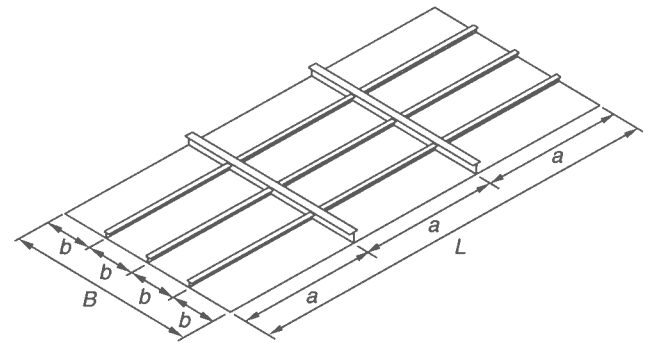

Figure 2.35 A continuous stiffened plate structure under axial compression

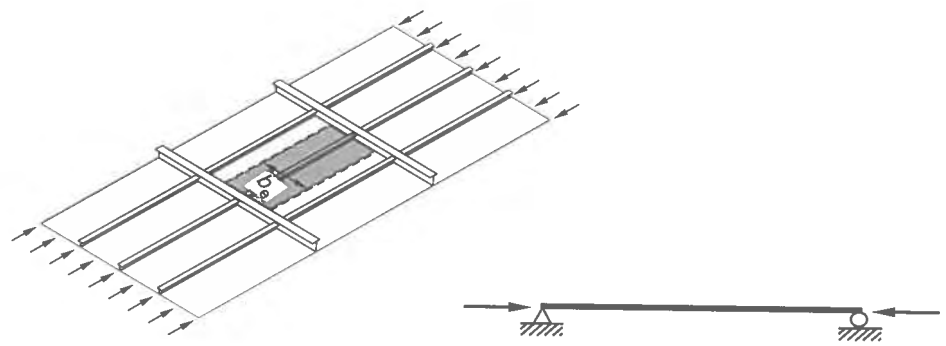

Figure 2.36 Theoretical model – one-bay PSC (plate–stiffener combination) with $b_e = b$

ultimate strength calculations for the column or beam–column types of collapse pattern, the Perry–Robertson formula is applied, but because of too pessimistic aspect of the original Perry–Robertson concept the present calculation does not adopt the criterion that the stiffener tip yields while the plate-induced failure is included.

For FEA (finite element analysis), three types of structural modeling are adopted in terms of the extent of the analysis, as shown in Figures 2.37 to 2.39. Along the transverse

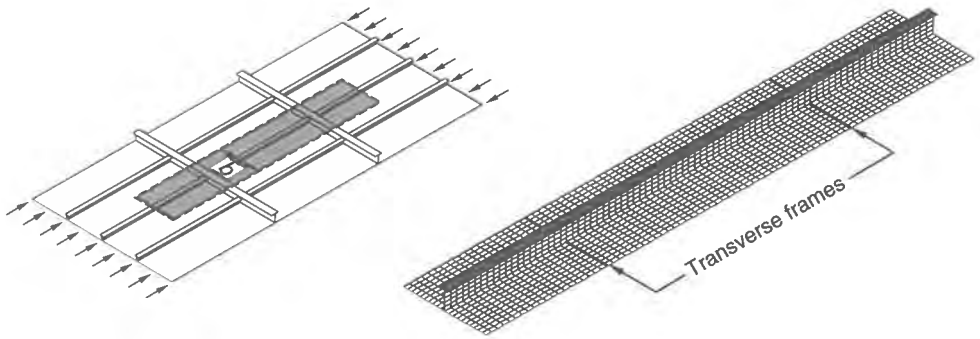

Figure 2.37 FEA model – two-bay PSC (plate–stiffener combination)

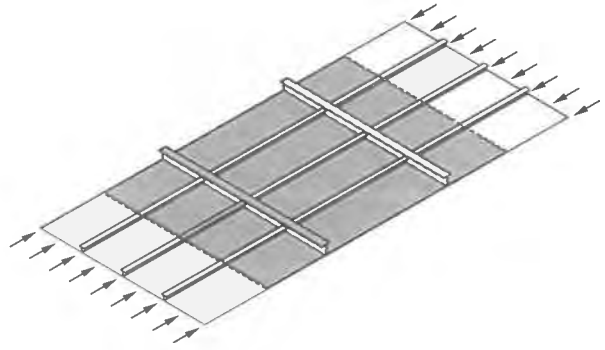

Figure 2.38 FEA model – two-bay SPM (stiffened panel model)

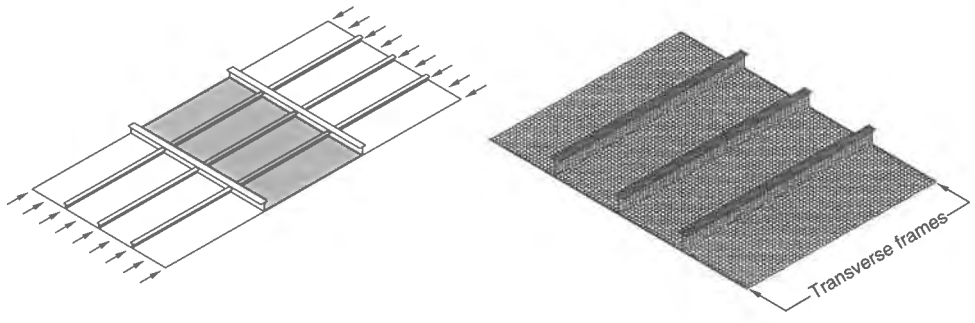

Figure 2.39 FEA model – one-bay SPM (stiffened panel model)

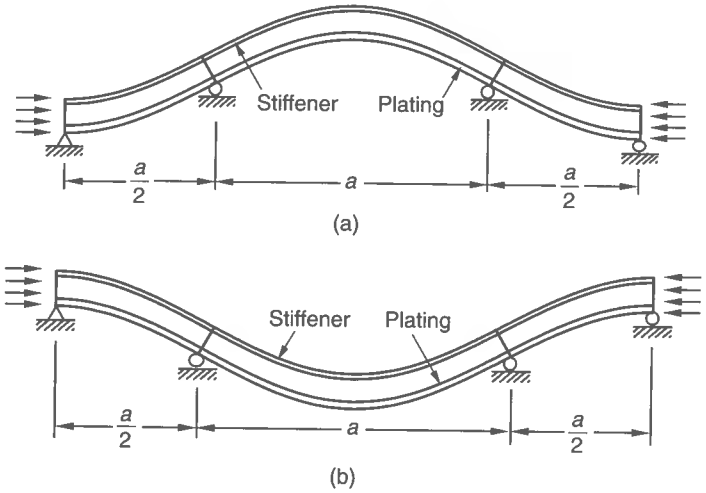

Figure 2.40 A schematic representation of (a) plate-induced failure (PIF) and (b) stiffener-induced failure (SIF) patterns in the two-bay model

frames as well as at unloaded panel edges, the simply supported condition is assumed. Uniform axial compressive displacements are applied. The two-bay modeling technique is beneficial to automatically take into account the longitudinal rotation effect of the longitudinal stiffeners at the transverse frames, since one panel deflects down while the adjacent panels buckle up in the continuous plate structure supported by heavy transverse frames. In contrast, the one-bay SPM (stiffened panel model) is a simpler modeling but the rotation of the longitudinal stiffeners is restrained since the stiffener cross-section remains upright at the transverse frames. The two-bay SPM is of course more refined and appropriate than either the two-bay PSC (plate–stiffener combination) or one-bay SPM in terms of accuracy.

The ultimate strength behavior of a stiffened panel may significantly depend on the deflection pattern. In this regard, two types of panel deflection patterns are considered by handling the direction of initial deflection, as shown in Figure 2.40. That is, one is that lateral deflection develops so that the stiffener flanges are compressed and the other is that the attached plating is compressed. The former type is termed the stiffener-induced failure (SIF) mode and the latter is termed the plate-induced failure (PIF) mode.

Figure 2.41 compares the theoretical solutions with the finite element results. The strain-hardening effect is not included in both the theoretical and numerical analyses. It was observed that the structure with $h_w = 150\,\text{mm}$ reached the ULS by the column-type collapse of stiffeners, while the lateral–torsional buckling of stiffeners caused the entire panel collapse for the case of $h_w = 210\,\text{mm}$. It is seen from Figure 2.41 that the two-bay SPM finite element solutions are similar for both SIF and PIF cases. The two-bay PSC finite element model based on the SIF predicts the ultimate strength pessimistically.

The formulations for a plate–stiffener combination model theoretically derived in this chapter correlate well with more refined nonlinear finite element solutions, while the ultimate strength predictions are somewhat pessimistic.

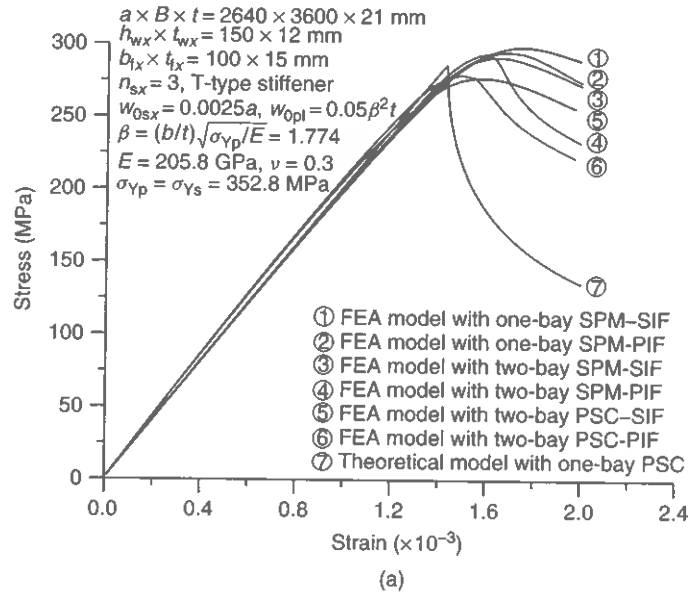

Figure 2.41 The axial stress–strain curves of the stiffened plate structure under axial compression: (a) $h_w = 150$ mm (beam–column-type collapse); (b) $h_w = 210$ mm (tripping failure)

References

AISI (1996). *Specification for the design of cold formed steel structural members*. American Iron and Steel Institute, New York.

Belenkiy, L. & Raskin, Y. (2001). Estimate of the ultimate load on structural members subjected to lateral loads. *Marine Technology*, 38(3): 169–176.

Bleich, F. (1952). *Buckling strength of metal structures*. McGraw-Hill, New York.

Bortsch, R. (1921). Die mitwirkende Plattenbreite. *Der Bauingenieur*, 23: 662–667 (in German).

Chen, W.F. & Atsuta, T. (1976). *Theory of beam–columns, Vol. 1, In-plane behavior and design*. McGraw-Hill, New York.

Chen, W.F. & Atsuta, T. (1977). *Theory of beam–columns, Vol. 2 Space behavior and design*. McGraw-Hill, New York.

ECCS (1978). *European recommendations for steel construction*. European Convention for Constructional Steelwork, March.

ENV 1993-1-1 (1992). *Eurocode 3: design of steel structures, part 1.1 general rules and rules for buildings*. British Standards Institution, London.

Faulkner, D. (1975). A review of effective plating for use in the analysis of stiffened plating in bending and compression. *Journal of Ship Research*, 19(1): 1–17.

Hodge, P.G. (1959). *Plastic analysis of structures*. McGraw-Hill, New York.

John, W. (1877). On the strains of iron ships. *RINA Transactions*, 18: 98–117.

Mansour, A.E. (1977). Gross panel strength under combined loading. *Ship Structure Committee*, SSC-270, Washington, DC.

Metzer, W. (1929). Die mittragende Breite. Dissertation, der Technischen Hochschule zu Aache (in German).

Murray, N.W. (1983). The static approach to plastic collapse and energy dissipation in some thin-walled steel structures. Chapter 2 in *Structural Crashworthiness*. Butterworths, London, 44–65.

Neal, B.C. (1977). *The plastic methods of structural analysis*. Third Edition. Chapman & Hall, London.

Paik, J.K. (1995). A new concept of the effective shear modulus for a plate buckled in shear. *Journal of Ship Research*, 39(1): 70–75.

Paik, J.K. & Thayamballi, A.K. (1997). An empirical formulation for predicting the ultimate compressive strength of stiffened panels. *Proceedings of International Offshore and Polar Engineering Conference, Honolulu*, IV: 328–338.

Rhodes, J. (1982). Effective widths in plate buckling. Chapter 4 in *Developments in Thin-Walled Structures*. Applied Science Publishers, London, 119–158.

Schuman, L. & Back, G. (1930). Strength of rectangular flat plates under edge compression. NACA Technical Report No. 356, National Advisory Committee for Aeronautics, Washington, DC.

Shames, I.H. & Dym, C.L. (1993). *Energy and finite element methods in structural mechanics*. McGraw-Hill, New York.

Smith, C.S. (1966). Elastic analysis of stiffened plating under lateral loading. *RINA Transactions*, 108(2): 113–131.

Timoshenko, S.P. & Gere, J.M. (1961). *Theory of elastic stability*, Second Edition, McGraw-Hill, New York.

Timoshenko, S.P. & Goodier, J.N. (1970). *Theory of elasticity*, Third Edition, McGraw-Hill, New York.

Troitsky, M.S. (1976). *Stiffened plates: bending, stability and vibrations*. Elsevier, Amsterdam.

Ueda, Y. & Rashed, S.M.H. (1984). The idealized structural unit method and its application to deep girder structures. *Computers & Structures*, 18(2): 277–293.

Ueda, Y., Rashed, S.M.H. & Paik, J.K. (1986). Effective width of rectangular plates subjected to combined loads. *Journal of the Society of Naval Architects of Japan*, 159: 269–281 (in Japanese).

Usami, T. (1993). Effective width of locally buckled plates in compression and bending. *ASCE Journal of Structural Engineering*, 119(5): 1358–1373.

von Karman, T. (1924). *Die mittragende Breite. Beitrage zur Technischen Mechanik und Technischen Physik, August Foppl Festschrift*. Julius Springer, Berlin, 114–127 (in German).

von Karman, T., Sechler, E.E. & Donnell, L.H. (1932). Strength of thin plates in compression. *ASME Transactions*, 54(5): 53–57.

Winter, G. (1947). Strength of thin steel compression flanges. Reprint No. 32, Engineering Experimental Station, Cornell University, Ithaca, NY.

Yamamoto, Y., Ohtsubo, H., Sumi, Y. & Fujino, M. (1986). *Ship structural mechanics*. Seisantou Publishing Company, Tokyo (in Japanese).

3 Elastic and Inelastic Buckling of Plates under Complex Circumstances

3.1 Fundamentals of Plate Buckling

The response of a steel-plated structure can be classified into three levels, namely the bare plate element level, the stiffened panel level and the entire plated structure level. This chapter is concerned with buckling for the first level, i.e., the plating between longitudinals and transverses.

As the predominantly compressive stress reaches a critical value, the plate buckles, resulting in a rapid increase of lateral deflection subsequent to a significant decrease of in-plane stiffness.

The phenomenon of buckling is normally categorized (by plasticity) into three classes, namely elastic buckling, elastic–plastic buckling and plastic buckling, the last two being called inelastic buckling. Elastic buckling occurs solely in the elastic regime. Elastic–plastic buckling occurs after a local region inside the plate deforms plastically. Plastic buckling indicates that buckling occurs in the regime of gross yielding, i.e., after the plate has yielded over large areas. Thin plates normally show elastic buckling, while thick plates usually exhibit inelastic buckling.

Buckling of plates between stiffeners, which is a basic failure mode in stiffened panels, is a good indication for the serviceability limit state (SLS) design. To understand the ultimate limit state (ULS)-based design procedure, it is essential to have a basic knowledge on the buckling of steel plates. The buckling behavior of steel plates normally depends on a variety of influential factors, namely geometric/material properties, loading characteristics, boundary conditions, initial imperfections, local damage (e.g., perforations) and so on.

In the SLS design of steel plates using Equation (1.1) in Chapter 1, the characteristic measure of the capacity may be determined on the basis of buckling strength, while the demand represents the extreme value of applied stresses.

This chapter presents classical and more advanced formulations of buckling strength for steel plates under simple and more complex circumstances. Generally in this chapter, new or less well-known results are emphasized. Multiple load components are treated to the most possible extent. The effects of boundary restraints other than idealized simply supported or fixed conditions, the effect of lateral pressure, perforations and residual stresses are also treated. The coverage in this chapter is extensive, but as may be surmised, plate elements constitute the major portion of structural weight in complex steel-plated structures. By extension, it also follows that there are significant benefits to be gained by designing them in an optimal and appropriate manner.

3.2 Geometric and Material Properties

For convenience of plate buckling analysis, the coordinate system for the plate uses x in the long direction and y in the short direction as shown in Figure 3.1. The dimensions of the plate are a in length (i.e., in the x or longer direction), b in breadth (i.e., in the y direction) and t in thickness. The aspect ratio, a/b, is then always greater than 1. Young's modulus is E and Poisson's ratio is ν. The elastic shear modulus is $G = E/[2(1+\nu)]$. The yield stress of the material is σ_Y; $\tau_Y = \sigma_Y/\sqrt{3}$. The plate bending rigidity is $D = Et^3/[12(1-\nu^2)]$.

3.3 Loads and Load Effects

Plate elements in a continuous plated structure are likely to be subjected to combined in-plane and lateral pressure loads. For plate elements in a complex structure, the load effects (stresses) are calculated by linear elastic finite element analysis or the classical

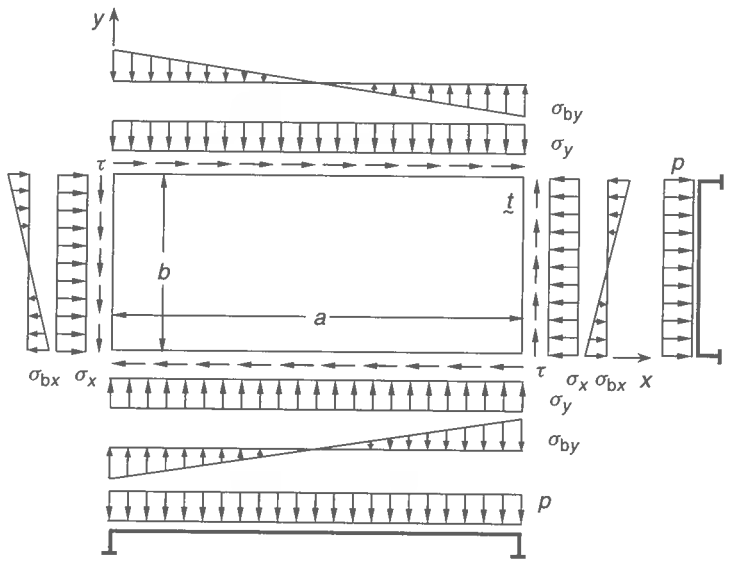

Figure 3.1 A rectangular plate under combined in-plane and lateral pressure loads

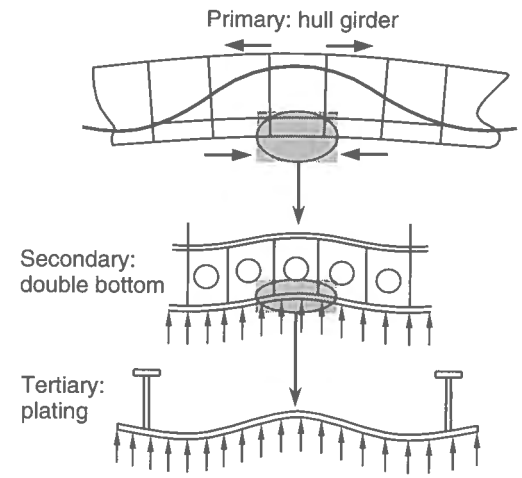

Figure 3.2 Three structural response levels: primary, secondary and tertiary

theory of structural mechanics. The individual load components have both local and overall structural effects.

In calculating the load effects, the structure and the associated load effects are often divided into three levels, i.e., primary, secondary and tertiary levels. Figure 3.2 illustrates a typical example of these three levels in ship structures (Paulling 1988). In this case, the primary level is related to the response of the entire ship's hull as a beam under bending or twisting moments. The secondary level is associated with the load effects of a stiffened panel, e.g., at the outer bottom shell of the double bottom structure between two adjacent transverse bulkheads. The boundaries of the secondary structure (i.e., stiffened panel) are usually formed by other secondary structures (e.g., side shell or bulkheads). The tertiary level represents the load effects of individual plating between stiffeners. The boundaries of the tertiary structure (i.e., plating) are formed by the stiffeners of the secondary structure (i.e., stiffened panel) of which it is a part. It is important to realize that the load effect analysis must account for the three responses noted above.

These load components are not always applied simultaneously, but more than one normally exist and interact. Therefore, the buckling strength formulations need to account for such combined load effects. In the buckling strength design, the plate element is considered to be subjected to average in-plane stresses, $\sigma_x = \sigma_{xav}$, $\sigma_y = \sigma_{yav}$, σ_{bx}, σ_{by}, $\tau = \tau_{av}$, and lateral pressure, p, or their combinations, as shown in Figure 3.1.

For perforated plates under in-plane loads, the membrane stress distribution may be non-uniform even before buckling, and thus average values of the applied stresses of a perforated plate may be smaller than those of a perfect plate, i.e., without perforations. For the practical design of perforated plates in the marine industry, the average stresses of the plates excluding perforations are often used as the characteristic measure of the applied stresses, while smaller, partial safety factors related to the load effects are usually adopted in this case.

For convenience in this chapter, axial compressive stress is taken as positive in sign, while axial tension is taken as negative in sign, unless otherwise specified.

3.4 Boundary Conditions

Plate elements in steel-plated structures are supported by various types of members along the edges, which have finite values of torsional rigidity. This is in contrast to the idealized simply supported boundary conditions often assumed for design purposes.

Depending on the torsional rigidity of support members, the rotation along the plate edges will to some extent be restrained. When the rotational restraints are zero, the edge condition corresponds to a simply supported case, while the edge condition becomes clamped when the rotational restraints are infinite.

Most current practical design guidelines for the buckling and ultimate strength of steel plates are based on boundary conditions in which all (four) edges are idealized edge conditions such as being simply supported or clamped. In real plates of steel-plated structures, such idealized edge conditions rarely if ever occur because of finite rotational restraints.

For more advanced design of steel plates against buckling, it is therefore important to better understand the buckling strength characteristics of plates as a function of the torsional rigidity of support members along the edges.

This chapter deals with the buckling strength of steel plates with various edge conditions which are simply supported, clamped or elastically restrained. The first two types of edge conditions are ideal, but often adequate for practical design purposes.

3.5 Linear Elastic Behavior

The behavior of a plate either before buckling or under predominantly axial tensile loading may be linear elastic until buckling occurs or gross yielding is formed. The linear elastic behavior of either perfect plates before buckling or imperfect plates under predominantly axial tensile loading can typically be represented by the relationship between average stresses and strains in a plane stress state as follows:

$$\begin{Bmatrix} \sigma_{xav} \\ \sigma_{yav} \\ \tau_{av} \end{Bmatrix} = [D_p]^E \begin{Bmatrix} \varepsilon_{xav} \\ \varepsilon_{yav} \\ \gamma_{av} \end{Bmatrix} \tag{3.1}$$

where ε_{xav}, ε_{yav}, γ_{av} = average strain components corresponding to σ_{xav}, σ_{yav}, τ_{av}, respectively,

$$[D_p]^E = \frac{E}{1-\nu^2}\begin{bmatrix} 1 & \nu & 0 \\ \nu & 1 & 0 \\ 0 & 0 & (1-\nu)/2 \end{bmatrix}$$

3.6 Elastic Buckling of Simply Supported Plates under Single Types of Loads

The elastic buckling stress solutions for a plate under single in-plane loading and common idealized edge conditions are widely available from classical works on the theory of elasticity (e.g., Bleich 1952, Timoshenko & Gere 1982). The elastic buckling strength of a plate with $a/b \geq 1$ is typically given in the following formula:

$$\sigma_E = k\frac{\pi^2 E}{12(1-\nu^2)}\left(\frac{t}{b}\right)^2 \tag{3.2}$$

where σ_E = plate buckling strength under a single type of load, k = buckling coefficient for the corresponding load. σ_E and k for various single types of loads are given in Table 3.1.

Table 3.1 Buckling coefficients for a simply supported plate under single types of loads for $a/b \geq 1$.

Load type	σ_E	k
σ_x	$\sigma_{xE,1}$	$k_x = [a/(m_o b) + m_o b/a]^2$ where m_o is the buckling half-wave number for the plate in the x direction which is the minimum integer satisfying $a/b \leq \sqrt{[m_o(m_o+1)]}$. For practical use, the half-wave number m may be taken as $m_o = 1$ for $1 \leq a/b \leq \sqrt{2}$, $m_o = 2$ for $\sqrt{2} < a/b \leq \sqrt{6}$ and $m_o = 3$ for $\sqrt{6} < a/b \leq 3$. If $a/b > 3$, the buckling coefficient can be approximated to $k_x = 4$
σ_y	$\sigma_{yE,1}$	$k_y = \left[1 + (b/a)^2\right]^2$
τ	$\tau_{E,1}$	$k_\tau \approx 4\,(b/a)^2 + 5.34$ for $a/b \geq 1$ ($k_\tau \approx 5.34(b/a)^2 + 4.0$ for $a/b < 1$)
σ_{bx}	$\sigma_{bxE,1}$	$k_{bx} \approx 23.9$
σ_{by}	$\sigma_{byE,1}$	$k_{by} \approx \begin{cases} 23.9 & \text{for } 1 \leq a/b \leq 1.5 \\ 15.87 + 1.87(a/b)^2 + 8.6(b/a)^2 & \text{for } a/b > 1.5 \end{cases}$

Note: The subscript '1' represents buckling under a single type of load.

3.7 Elastic Buckling of Simply Supported Plates under Two Load Components

3.7.1 Biaxial Compression/Tension

An analytical solution for the elastic buckling of a simply supported plate subject to biaxial loads may be given by (Hughes 1988, Paik 1991)

$$\frac{m^2}{a^2}\sigma_x + \frac{n^2}{b^2}\sigma_y - \frac{\pi^2 D}{t}\left(\frac{m^2}{a^2} + \frac{n^2}{b^2}\right)^2 = 0 \tag{3.3}$$

where m and n are the buckling half-wave numbers in the x and y directions, respectively.

One half-wave number is normally taken in either the short edge or the direction in which the axial tensile loads are predominant. For a long plate considered in this chapter, i.e., with $a/b \geq 1$, $n = 1$ can typically be taken. By holding the applied loading ratio

$c = \sigma_y/\sigma_x$ constant, therefore, Equation (3.3) can be rewritten as follows:

$$\sigma_x \left(\frac{m^2}{a^2} + \frac{c}{b^2}\right) - \frac{\pi^2 D}{t}\left(\frac{m^2}{a^2} + \frac{1}{b^2}\right)^2 = 0 \tag{3.4}$$

Since buckling occurs when Equation (3.4) is satisfied, the bifurcation (buckling) stress is obtained by replacing σ_x with $\sigma_{x\mathrm{E}}$ as follows:

$$\sigma_{x\mathrm{E}} = \frac{\pi^2 D}{b^2 t}\frac{\left(1 + m^2 b^2/a^2\right)^2}{c + m^2 b^2/a^2} = \frac{\pi^2 D}{t}\frac{\left(m^2/a^2 + 1/b^2\right)^2}{m^2/a^2 + c/b^2} \tag{3.5}$$

where $\sigma_{x\mathrm{E}}$ indicates the longitudinal axial buckling stress component of a long plate under combined biaxial loading.

Since the buckling strength value should be the same at the transition of the buckling mode, the buckling half-wave number, m, in the x direction of the plate under biaxial loads can be predicted from Equation (3.5) as a minimum integer satisfying the following condition:

$$\frac{(m^2/a^2 + 1/b^2)^2}{m^2/a^2 + c/b^2} \leq \frac{[(m+1)^2/a^2 + 1/b^2]^2}{(m+1)^2/a^2 + c/b^2} \tag{3.6a}$$

where it is evident that the buckling half-wave number is affected by the applied loading ratio as well as the plate aspect ratio.

When $c = \sigma_y/\sigma_x = 0$, Equation (3.6a) is simplified to the well-known criterion as follows:

$$\frac{a}{b} \leq \sqrt{m(m+1)} \tag{3.6b}$$

Since we hold the applied loading ratio, $c = \sigma_y/\sigma_x$, constant, the elastic buckling axial stress in the y direction is obtained by

$$\sigma_{y\mathrm{E}} = c\sigma_{x\mathrm{E}} \tag{3.7}$$

where $\sigma_{y\mathrm{E}}$ is the component of the elastic transverse axial buckling stress of the plate under combined biaxial loading.

By substituting the buckling half-wave number, m, to be calculated from Equation (3.6) and $n = 1$ (for the long plate) into Equations (3.5) and (3.7), the elastic buckling interaction relationship for a simply supported long plate subject to biaxial loads is obtained.

The benefit of Equation (3.5) is that it is applicable to the plates under any combination of biaxial loading, e.g., axial compressive loading in one direction and axial tensile loading in the other direction as well as axial compressive loading in both directions, while an opposite sign convention must be considered for axial tension. It is evident from Equation (3.5) that as long as $c = \sigma_y/\sigma_x$ is greater than $-m^2b^2/a^2$, the buckling phenomenon can occur even if axial tensile loads are applied in one direction.

For a long plate, i.e., with $a/b \geq 1$, Equation (3.3) may be rewritten as a function of stress components normalized by the buckling stresses under the corresponding single

load component as follows:

$$\frac{(m^2b^2/a^2)\,(m_o b/a + a/m_o b)^2}{\left(m^2b^2/a^2 + 1\right)^2}\frac{\sigma_x}{\sigma_{x\mathrm{E},1}} + \frac{\left(b^2/a^2 + 1\right)^2}{\left(m^2b^2/a^2 + 1\right)^2}\frac{\sigma_y}{\sigma_{y\mathrm{E},1}} = 1 \tag{3.8}$$

where $\sigma_{x\mathrm{E},1}$, $\sigma_{y\mathrm{E},1}$ are as defined in Equation (3.2) together with Table 3.1, m is as defined in Equation (3.6), m_o = buckling half-wave number when $c = 0$, as defined in Table 3.1.

Figure 3.3 shows the elastic buckling strength interaction curves of a simply supported rectangular plate under biaxial loads for $a/b = 3$ and 5. It is seen from Figure 3.3 that

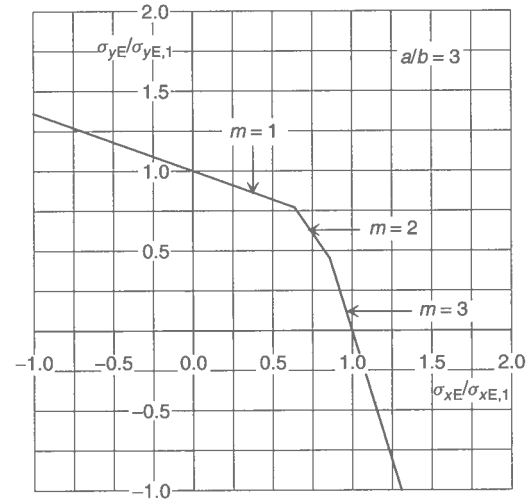

(a)

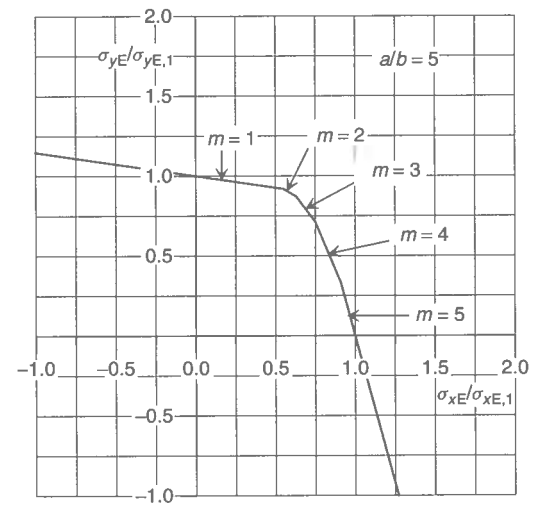

(b)

Figure 3.3 Elastic buckling interaction relationship for a plate under biaxial loads, simply supported at all edges: (a) $a/b = 3$ and $n = 1$; (b) $a/b = 5$ and $n = 1$

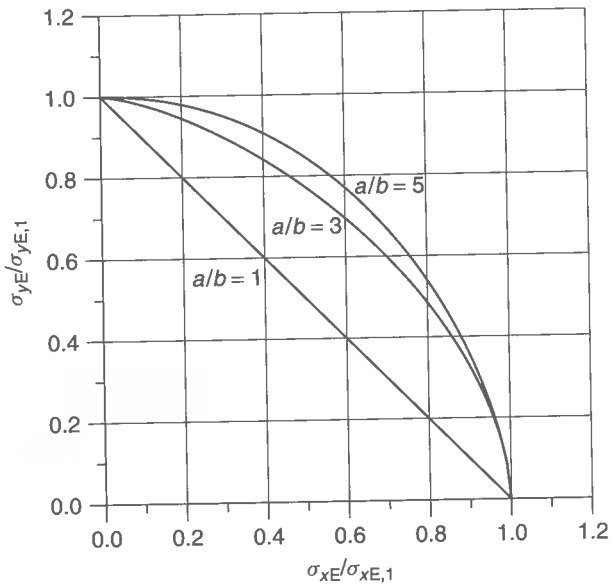

Figure 3.4 Approximate elastic buckling interaction relationships for a plate under biaxial compression with varying aspect ratio, simply supported at all edges, as obtained by Equations (3.9)

the buckling half-wave number in the long direction varies with the loading ratio as well as the plate aspect ratio.

In practice, a numerical iteration process may be necessary to compute the half-wave number, m, by Equation (3.6). It is desirable for structural designers to have an approximate closed-form expression for the resulting plate buckling interaction relationship. Based on a series of computations for a variety of aspect ratios and loading ratios as indicated in Figure 3.3, an empirical buckling interaction equation for the plate subjected to biaxial compressive loading may be derived by curve fitting as follows:

$$\left(\frac{\sigma_{xE}}{\sigma_{xE,1}}\right)^{\alpha_1} + \left(\frac{\sigma_{yE}}{\sigma_{yE,1}}\right)^{\alpha_2} = 1 \tag{3.9a}$$

where α_1 and α_2 are constants that are a function of the plate aspect ratio. Based on the computed results, the constants may be determined empirically as follows:

$$\alpha_1 = \alpha_2 = 1 \quad \text{for } 1 \le a/b \le \sqrt{2} \tag{3.9b}$$

$$\left.\begin{aligned}\alpha_1 &= 0.0293(a/b)^3 - 0.3364(a/b)^2 + 1.5854(a/b) - 1.0596\\ \alpha_2 &= 0.0049(a/b)^3 - 0.1183(a/b)^2 + 0.6153(a/b) + 0.8522\end{aligned}\right\} \quad \text{for } a/b > \sqrt{2} \tag{3.9c}$$

Figure 3.4 shows the elastic buckling strength interaction curves for the plate under biaxial compression with varying aspect ratio, as obtained by Equations (3.9).

3.7.2 Longitudinal Axial Compression and Longitudinal In-plane Bending

The elastic buckling strength interaction relationship of a simply supported plate under combined longitudinal axial compression and longitudinal in-plane bending is typically given by

$$\frac{\sigma_{xE}}{\sigma_{xE,1}} + \left(\frac{\sigma_{bxE}}{\sigma_{bxE,1}}\right)^{c} = 1 \tag{3.10}$$

where the constant, c, is often taken as $c = 2$ (JWS 1971) or $c = 1.75$ (Hughes 1988).

3.7.3 Transverse Axial Compression and Longitudinal In-plane Bending

The elastic buckling strength interaction relationship of a simply supported plate under combined transverse axial compression and longitudinal in-plane bending is typically given by

$$\left(\frac{\sigma_{yE}}{\sigma_{yE,1}}\right)^{\alpha_3} + \left(\frac{\sigma_{bxE}}{\sigma_{bxE,1}}\right)^{\alpha_4} = 1 \tag{3.11a}$$

where the constants, α_3 and α_4, may be estimated as follows (JWS 1971):

$$\alpha_3 = \alpha_4 = 1.50(a/b) - 0.30 \quad \text{for } 1 \le a/b \le 1.6 \tag{3.11b}$$

$$\left.\begin{aligned}\alpha_3 &= -0.625(a/b) + 3.10\\ \alpha_4 &= 6.25(a/b) - 7.90\end{aligned}\right\} \quad \text{for } 1.6 < a/b \le 3.2 \tag{3.11c}$$

$$\left.\begin{aligned}\alpha_3 &= 1.10\\ \alpha_4 &= 12.10\end{aligned}\right\} \quad \text{for } 3.2 < a/b \tag{3.11d}$$

3.7.4 Longitudinal Axial Compression and Transverse In-plane Bending

The elastic buckling strength interaction relationship of a simply supported plate under combined longitudinal axial compression and transverse in-plane bending is typically given by

$$\left(\frac{\sigma_{xE}}{\sigma_{xE,1}}\right)^{\alpha_5} + \left(\frac{\sigma_{byE}}{\sigma_{byE,1}}\right)^{\alpha_6} = 1 \tag{3.12a}$$

where the constants, α_5 and α_6, may be estimated by (Ueda *et al.* 1987)

$$\left.\begin{aligned}\alpha_5 &= 0.930(a/b)^2 - 2.890(a/b) + 3.160\\ \alpha_6 &= 1.20\end{aligned}\right\} \quad \text{for } 1 \le a/b \le 2 \tag{3.12b}$$

$$\left.\begin{aligned}\alpha_5 &= 0.066(a/b)^2 - 0.246(a/b) + 1.328\\ \alpha_6 &= 1.20\end{aligned}\right\} \quad \text{for } 2 < a/b \le 5 \tag{3.12c}$$

$$\left.\begin{aligned}\alpha_5 &= 1.117(a/b) - 3.837\\ \alpha_6 &= -0.167(a/b) + 2.035\end{aligned}\right\} \quad \text{for } 5 < a/b \le 8 \tag{3.12d}$$

$$\left.\begin{aligned}\alpha_5 &= 5.10\\ \alpha_6 &= 0.70\end{aligned}\right\} \quad \text{for } 8 < a/b \tag{3.12e}$$

3.7.5 Transverse Axial Compression and Transverse In-plane Bending

The elastic buckling strength interaction relationship of a simply supported plate under combined transverse axial compression and transverse in-plane bending is typically given by

$$\left(\frac{\sigma_{yE}}{\sigma_{yE,1}}\right)^{\alpha_7} + \left(\frac{\sigma_{byE}}{\sigma_{byE,1}}\right)^{\alpha_8} = 1 \tag{3.13a}$$

where the constants, α_7 and α_8, may be estimated by (Klöppel & Sheer 1960)

$$\left.\begin{aligned}\alpha_7 &= 1.0\\ \alpha_8 &= (14.0 - a/b)/6.5\end{aligned}\right\} \quad \text{for } 1 \le a/b \le 7.5 \tag{3.13b}$$

$$\alpha_7 = \alpha_8 = 1.0 \quad \text{for } 7.5 < a/b \tag{3.13c}$$

3.7.6 Biaxial In-plane Bending

The elastic buckling strength interaction relationship of a simply supported plate under combined biaxial in-plane bending is typically given by

$$\left(\frac{\sigma_{bxE}}{\sigma_{bxE,1}}\right)^{\alpha_9} + \left(\frac{\sigma_{byE}}{\sigma_{byE,1}}\right)^{\alpha_{10}} = 1 \tag{3.14a}$$

where the constants, α_9 and α_{10}, may be estimated by (Ueda *et al.* 1987)

$$\left.\begin{aligned}\alpha_9 &= 0.050(a/b) + 1.080\\ \alpha_{10} &= 0.268(a/b) - 1.248(b/a) + 2.112\end{aligned}\right\} \quad \text{for } 1 \le a/b \le 3 \tag{3.14b}$$

$$\left.\begin{aligned}\alpha_9 &= 0.146(a/b)^2 - 0.533(a/b) + 1.515\\ \alpha_{10} &= 0.268(a/b) - 1.248(b/a) + 2.112\end{aligned}\right\} \quad \text{for } 3 < a/b \le 5 \tag{3.14c}$$

$$\left.\begin{aligned}\alpha_9 &= 3.20(a/b) - 13.50\\ \alpha_{10} &= -0.70(a/b) + 6.70\end{aligned}\right\} \quad \text{for } 5 < a/b \le 8 \tag{3.14d}$$

$$\left.\begin{aligned}\alpha_9 &= 12.10\\ \alpha_{10} &= 1.10\end{aligned}\right\} \quad \text{for } 8 < a/b \tag{3.14e}$$

3.7.7 Longitudinal Axial Compression and Edge Shear

When a plate buckles under edge shear, the deflection pattern is quite complex compared to that under axial compressive loading and thus a number of terms are normally needed to more properly represent the plate deflection by a Fourier series function. Bleich (1952) studied the buckling of a simply supported rectangular plate subject to longitudinal axial compression and edge shear using the energy method and developed a design chart for the plate buckling. Ueda *et al.* (1987) derived an empirical buckling strength interaction equation for the plate under combined longitudinal axial compression and edge shear by curve fitting based on the results of Bleich, as follows:

$$\frac{\sigma_{xE}}{\sigma_{xE,1}} + \left(\frac{\tau_E}{\tau_{E,1}}\right)^{\alpha_{11}} = 1 \tag{3.15a}$$

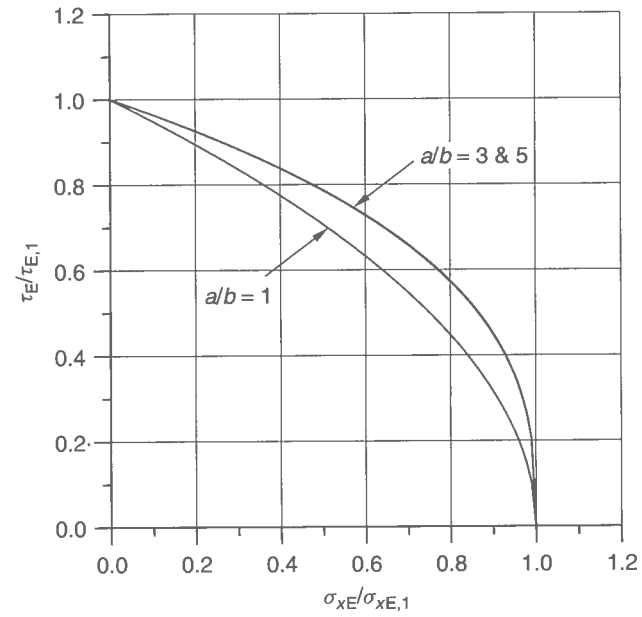

Figure 3.5 Approximate elastic buckling interactions of a plate under longitudinal axial compression and edge shear with varying aspect ratio, simply supported at all edges, as obtained by Equations (3.15)

where the constant, α_{11}, may be given by

$$\alpha_{11} = \begin{cases} -0.160(a/b)^2 + 1.080(a/b) + 1.082 & \text{for } 1 \le a/b \le 3.2\\ 2.90 & \text{for } a/b > 3.2\end{cases} \tag{3.15b}$$

Figure 3.5 shows the elastic buckling strength interaction curves of a simply supported plate under combined longitudinal axial compression and edge shear with varying aspect ratio, as obtained by Equations (3.15).

3.7.8 Transverse Axial Compression and Edge Shear

Based on the theoretical results of the buckling strength for rectangular plates subject to combined transverse axial compression and edge shear as obtained by Bleich (1952) and Timoshenko & Gere (1982), Ueda *et al.* (1987) derived the following buckling interaction equation by curve fitting:

$$\frac{\sigma_{yE}}{\sigma_{yE,1}} + \left(\frac{\tau_E}{\tau_{E,1}}\right)^{\alpha_{12}} = 1 \tag{3.16a}$$

where the constant, α_{12}, may be given by

$$\alpha_{12} = \begin{cases} 0.10(a/b) + 1.90 & \text{for } 1 \le a/b \le 2\\ 0.70(a/b) + 0.70 & \text{for } 2 < a/b \le 6\\ 4.90 & \text{for } 6 < a/b\end{cases} \tag{3.16b}$$

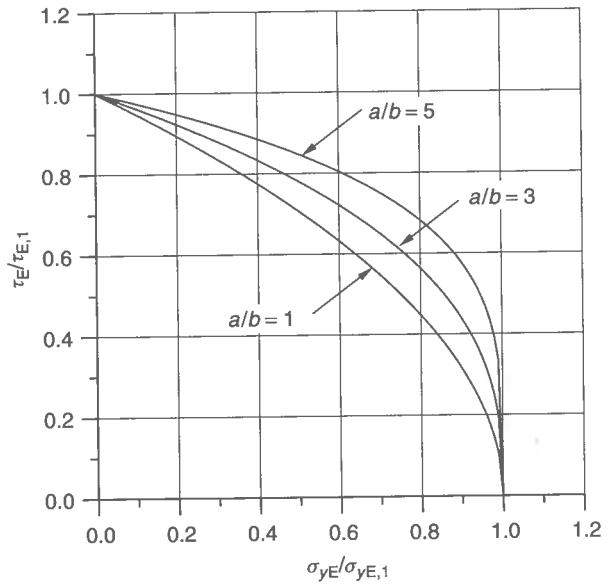

Figure 3.6 Approximate elastic buckling interactions of a plate under transverse axial compression and edge shear with varying aspect ratio, simply supported at all edges, as obtained by Equations (3.16)

Figure 3.6 shows the elastic buckling interaction curves of a simply supported plate under combined transverse axial compression and edge shear with varying aspect ratio, as obtained by Equations (3.16).

3.7.9 Longitudinal In-plane Bending and Edge Shear

The elastic buckling interaction relationship of a simply supported plate under combined longitudinal in-plane bending and edge shear is typically given by

$$\left(\frac{\sigma_{bxE}}{\sigma_{bxE,1}}\right)^c + \left(\frac{\tau_E}{\tau_{E,1}}\right)^c = 1 \tag{3.17}$$

where the constant, c, is sometimes taken as $c = 2$ (JWS 1971).

3.7.10 Transverse In-plane Bending and Edge Shear

The elastic buckling interaction relationship of a simply supported plate under combined transverse in-plane bending and edge shear is typically given by

$$\left(\frac{\sigma_{byE}}{\sigma_{byE,1}}\right)^c + \left(\frac{\tau_E}{\tau_{E,1}}\right)^c = 1 \tag{3.18}$$

where the constant, c, is sometimes taken as $c = 2$ (JWS 1971).

3.8 Elastic Buckling of Simply Supported Plates under More than Three Load Components

The elastic buckling interaction relationship of a plate under a combination of three load components, e.g., longitudinal axial compression, transverse axial compression and edge shear, is now derived based on three sets of interaction relationships between two load components, e.g., the longitudinal axial compression versus transverse axial compression relationship, the longitudinal axial compression versus edge shear relationship and the transverse axial compression versus edge shear relationship.

Figure 3.7 shows a schematic for developing the buckling interaction equation between the three load components. Two sets of interaction relationships between two load components are chosen so that one of the load components will be common to both relationships. These relations are in turn combined to obtain a new relationship between three load components.

Consider that the plate buckles under three load components which are denoted by $\sigma^*_{xE}, \sigma^*_{yE}$ and τ^*_E. When no transverse axial compression is applied, the interaction between $\sigma^*_{xE}, \sigma^*_{yE}$ and τ^*_E corresponds to that of the $\sigma_{xE} - \tau_E$ relation as indicated in Equations (3.15). In this case, the critical value, σ^*_{xE}, of the longitudinal axial compression, σ_x, which causes the buckling together with τ^*_E is obtained from Equations (3.15) as follows:

$$\sigma^*_{xE} = \sigma_{xE,1}\left[1 - \left(\frac{\tau^*_E}{\tau_{E,1}}\right)^{\alpha_{11}}\right] \tag{3.19}$$

Similarly, when no longitudinal axial compression is applied, the critical value, σ^*_{yE}, of transverse axial compression, σ_y, which causes the buckling will be obtained from

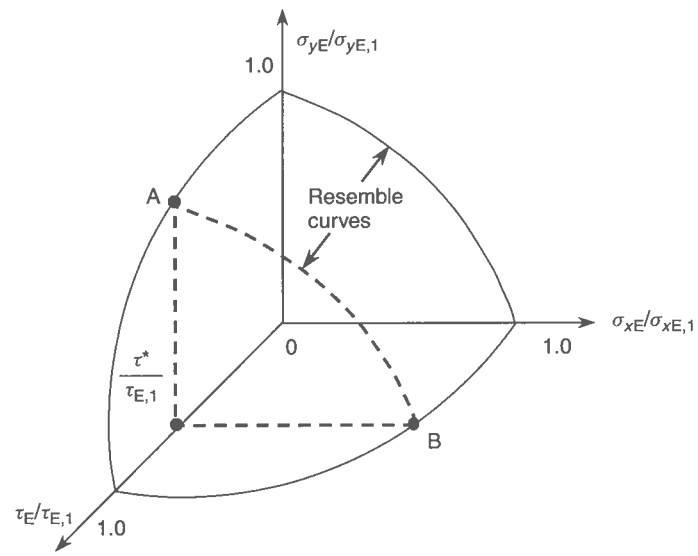

Figure 3.7 A schematic representation for derivation of the buckling interaction relationship between three load components

Equations (3.16):

$$\sigma^*_{yE} = \sigma_{yE,1}\left[1 - \left(\frac{\tau^*_E}{\tau_{E,1}}\right)^{\alpha_{12}}\right] \tag{3.20}$$

It is assumed that a relationship similar to that of Equations (3.9), i.e., for the case under biaxial compression, exists between σ^*_{xE} and σ^*_{yE} in any plane of $\tau^*/\tau_{E,1} = \text{constant}$, i.e., together with any value of edge shear. When we replace $\sigma_{xE,1}$ and $\sigma_{yE,1}$ in Equations (3.9) with σ^*_{xE} and σ^*_{yE} from Equations (3.19) and (3.20), respectively, the following buckling interaction relationship between σ_{xE}, σ_{yE} and τ is obtained when $\tau_E = \tau^*_E$:

$$\left\{\frac{\sigma_{xE}}{\sigma_{xE,1}\left[1 - (\tau_E/\tau_{E,1})^{\alpha_{11}}\right]}\right\}^{\alpha_1} + \left\{\frac{\sigma_{yE}}{\sigma_{yE,1}\left[1 - (\tau_E/\tau_{E,1})^{\alpha_{12}}\right]}\right\}^{\alpha_2} = 1 \tag{3.21}$$

where it is important to realize that the plate can of course buckle in edge shear alone, i.e., if the values of [] in the denominator reach zero or become negative.

The buckling strength interaction equations under other sets of the three load components can also be derived in a similar way to that between σ_x, σ_y and τ. Also, all five potential in-plane load components, namely longitudinal axial compression, transverse axial compression, edge shear, longitudinal in-plane bending and transverse in-plane bending, may be obtained using a similar approach as follows (Ueda *et al.* 1987):

$$\left\{\frac{\sigma_{xE}}{C_1 C_4 \sigma_{xE,1}\left[1 - (\tau_E/(C_3 C_6 \tau_{E,1}))^{\alpha_{11}}\right]}\right\}^{\alpha_1} + \left\{\frac{\sigma_{yE}}{C_2 C_5 \sigma_{yE,1}\left[1 - (\tau_E/(C_3 C_6 \tau_{E,1}))^{\alpha_{12}}\right]}\right\}^{\alpha_2} = 1 \tag{3.22}$$

where

$$C_1 = 1 - \left(\frac{\sigma_{bxE}}{C_7 \sigma_{bxE,1}}\right)^2, \quad C_2 = \left[1 - \left(\frac{\sigma_{bxE}}{C_7 \sigma_{bxE,1}}\right)^{\alpha_4}\right]^{1/\alpha_3}, \quad C_3 = \left[1 - \left(\frac{\sigma_{bxE}}{C_7 \sigma_{bxE,1}}\right)^2\right]^{0.5}$$

$$C_4 = \left[1 - \left(\frac{\sigma_{byE}}{\sigma_{byE,1}}\right)^{\alpha_6}\right]^{1/\alpha_5}, \quad C_5 = \left[1 - \left(\frac{\sigma_{byE}}{\sigma_{byE,1}}\right)^{\alpha_8}\right]^{1/\alpha_7}, \quad C_6 = \left[1 - \left(\frac{\sigma_{byE}}{\sigma_{byE,1}}\right)^2\right]^{0.5}$$

$$C_7 = \left[1 - \left(\frac{\sigma_{byE}}{\sigma_{byE,1}}\right)^{\alpha_{10}}\right]^{1/\alpha_9}$$

In Equation (3.22), $c = 2$ has been used for Equations (3.10), (3.17) and (3.18). As may be surmised from Equation (3.22), the plate can of course buckle in edge shear alone, i.e., when the denominator becomes zero or a negative value.

3.9 Elastic Buckling of Clamped Plates

3.9.1 *Single Types of Loads*

The elastic bifurcation buckling stress of plates with clamped edge conditions and under single types of loads may also be calculated from Equation (3.2), but using different buckling coefficients. Table 3.2 indicates the buckling coefficients of clamped plates with $a/b \geq 1$ where long edges are taken in the x direction and short edges are taken in the y direction.

Table 3.2 Elastic buckling coefficients of clamped plates under single types of loads for $a/b \geq 1$.

Load type	σ_E	BC	k	
σ_x	$\sigma_{xE,1}$	SSLC	$k_x = \begin{cases} 7.39(a/b)^2 - 19.6(a/b) + 20 \\ 6.98 \end{cases}$	for $1.0 \leq a/b \leq 1.33$ for $1.33 < a/b$
		SCLS	$k_x = \begin{cases} -0.95(a/b)^3 + 6.4(a/b)^2 - 14.86(a/b) + 16.34 \\ 0.2(a/b)^2 - 1.4(a/b) + 6.64 \\ -0.05(a/b) + 4.4 \\ 4.0 \end{cases}$	for $1.0 \leq a/b < 2.0$ for $2.0 \leq a/b < 3.0$ for $3.0 \leq a/b < 8.0$ for $8.0 \leq a/b$
		AC	$k_x = \begin{cases} -1.23(a/b)^3 + 7.9(a/b)^2 - 17.65(a/b) + 21.35 \\ 0.2(a/b)^2 - 1.62(a/b) + 10.35 \\ -0.062(a/b) + 7.476 \\ 6.98 \end{cases}$	for $1.0 \leq a/b < 2.0$ for $2.0 \leq a/b < 3.0$ for $3.0 \leq a/b < 8.0$ for $8.0 \leq a/b$
σ_y	$\sigma_{yE,1}$	SSLC	$k_y = [1.0 + (b/a)^2]^2 + 3.01$	for $0.0 < b/a \leq 1.0$
		SCLS	$k_y = \begin{cases} [1.0 + (b/a)^2]^2 + 0.12 \\ [0.95 + 1.89(b/a)^2]^2 \\ 13.98(b/a) - 6.20 \end{cases}$	for $0.0 < b/a < 0.34$ for $0.34 \leq b/a \leq 0.96$ for $0.96 < b/a \leq 1.0$
		AC	$k_y = \begin{cases} [1.0 + (b/a)^2]^2 + 4.8 \\ [1.92 + 1.305(b/a)^2]^2 \end{cases}$	for $0.0 < b/a < 0.8$ for $0.8 \leq b/a \leq 1.0$
τ	$\tau_{E,1}$	SSLC	$k_\tau = 2.4(b/a)^2 + 1.08(b/a) + 9.0$	for $0.0 < b/a \leq 1.0$
		SCLS	$k_\tau = \begin{cases} 2.25(b/a)^2 + 1.95(b/a) + 5.35 \\ 22.92(b/a)^3 - 33.0(b/a)^2 + 20.43(b/a) + 2.13 \end{cases}$	for $0.0 < b/a \leq 0.4$ for $0.4 < b/a \leq 1.0$
		AC	$k_\tau = 5.4(b/a)^2 + 0.6(b/a) + 9.0$	for $0.0 < b/a \leq 1.0$

Notes: SSLC = short (y) edges simply supported and long (x) edges clamped; SCLS = short (y) edges clamped and long (x) edges simply supported; AC = all edges clamped; BC = boundary condition

3.9.2 Combined Loads

For practical purposes, it is often assumed that the elastic buckling interaction relationship between combined loads for a plate with the boundary condition clamped at some or all edges is the same as that for the plate simply supported at all edges, but using the corresponding buckling strength components under single types of loads.

Figures 3.8 and 3.9 show the elastic buckling interaction relationships of rectangular plates clamped at all edges between biaxial compression and between uniaxial

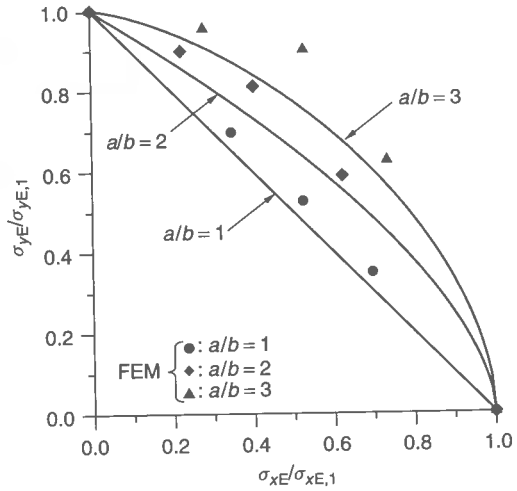

Figure 3.8 Elastic buckling interaction relationships of plates between biaxial compressive loads (line: Equations (3.9) for plates simply supported at all edges; symbols: eigenvalue finite element solutions for plates clamped at all edges)

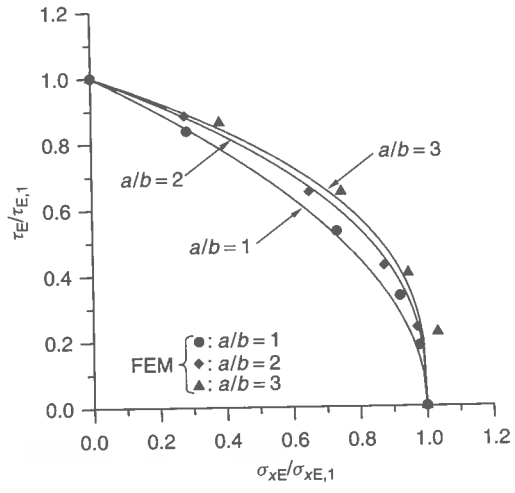

Figure 3.9 Elastic buckling interaction relationships of plates between axial compression and edge shear (line: Equations (3.15) for plates simply supported at all edges; symbols: eigenvalue finite element solutions for plates clamped at all edges)

compression and edge shear, respectively, with varying aspect ratio, as those obtained by the eigenvalue finite element analysis. The corresponding buckling interaction equations for plates simply supported at four edges, i.e., Equations (3.9) and (3.15), are also shown in the figures.

It is seen from Figures 3.8 and 3.9 that due to rotational restraints at the edges the buckling interaction of clamped plates becomes more convex than that of simply supported plates, but the buckling interaction for simply supported plates seems to represent the results fairly well, though slightly on the pessimistic side.

3.10 Elastic Buckling of Elastically Restrained Plates

In a continuous stiffened plate structure, the rotation of the plating at the edges is to some extent restrained depending on the torsional rigidity of support members (stiffeners). This section presents closed-form elastic plate buckling strength formulations taking into account the effect of rotational restraints at the plate edges, originally developed by Paik & Thayamballi (2000). Some similar expressions have of course been suggested, e.g., by Fujikubo & Yao (1999), among others.

3.10.1 Rotational Restraint Parameters

Support members of plate elements have finite values of torsional rigidity and thus the rotation along the plate edges is to some extent restrained. Essentially the buckling strength of plate elements is affected by these rotational restraints.

When the dimensions of support members (stiffeners) are defined as shown in Figure 2.3 of Chapter 2, the rotational restraint parameters of the longitudinal (x) and transverse (y) support members in a continuous plate structure may be given by

$$\zeta_L = C_L \frac{GJ_L}{bD}, \zeta_S = \frac{GJ_S}{aD} \tag{3.23}$$

where ζ_L, ζ_S = rotational restraint parameters for the longitudinal or transverse support member, $J_L = h_{wx}t_{wx}^3 + b_{fx}t_{fx}^3/6$, $J_S = h_{wy}t_{wy}^3 + b_{fy}t_{fy}^3/6$. The support members may in some cases distort sideways due to axial compression before plate buckling so that they will not fully contribute to the rotational restraints along the plate edges. C_L and C_S are constants to take this effect into account and are taken as the values less than 1.0. For simplicity, the constants are assumed to be proportional to the relative torsional rigidity of the support member to the plate part as follows:

$$C_L = \frac{J_L}{J_{PL}} \leq 1.0, C_S = \frac{J_S}{J_{PS}} \leq 1.0 \tag{3.24}$$

where

$$J_{PL} = \frac{bt^3}{3}, J_{PS} = \frac{at^3}{3}.$$

3.10.2 Longitudinal Axial Compression

The elastic bifurcation buckling stress of a plate with elastically restrained edge conditions and under longitudinal axial compression may also be calculated from Equation (3.2), but

using the different buckling coefficient, k_x. In the following, empirical formulas for the buckling coefficient, k_x, which are expressed in terms of the aspect ratio and the torsional rigidity of support members, are presented.

Elastically Restrained at Long Edges and Simply Supported at Short Edges

$$k_x = \begin{cases} 0.396\zeta_L^3 - 1.974\zeta_L^2 + 3.565\zeta_L + 4.0 & \text{for } 0 \le \zeta_L < 2 \\ 6.951 - 0.881/(\zeta_L - 0.4) & \text{for } 2 \le \zeta_L < 20 \\ 7.025 & \text{for } 20 \le \zeta_L \end{cases} \tag{3.25a}$$

The accuracy of Equation (3.25a) is verified in Figure 3.10 by comparison to the exact theoretical solutions as obtained by directly solving the characteristic equation (Paik & Thayamballi 2000).

Elastically Restrained at Short Edges and Simply Supported at Long Edges

$$k_x = d_1\zeta_S^4 + d_2\zeta_S^3 + d_3\zeta_S^2 + d_4\zeta_S + d_5 \tag{3.25b}$$

where

$$d_1 = \begin{cases} -1.010(a/b)^4 + 12.827(a/b)^3 - 52.553(a/b)^2 + 67.072(a/b) - 27.585 & \text{for } 0 \le \zeta_S < 0.4 \\ 0.047(a/b)^4 - 0.586(a/b)^3 + 2.576(a/b)^2 - 4.410(a/b) + 1.748 & \text{for } 0.4 \le \zeta_S < 0.8 \\ -0.017(a/b)^2 + 0.099(a/b) - 0.150 & \text{for } 0.8 \le \zeta_S < 2 \\ 0.0 & \text{for } 2 \le \zeta_S \end{cases}$$

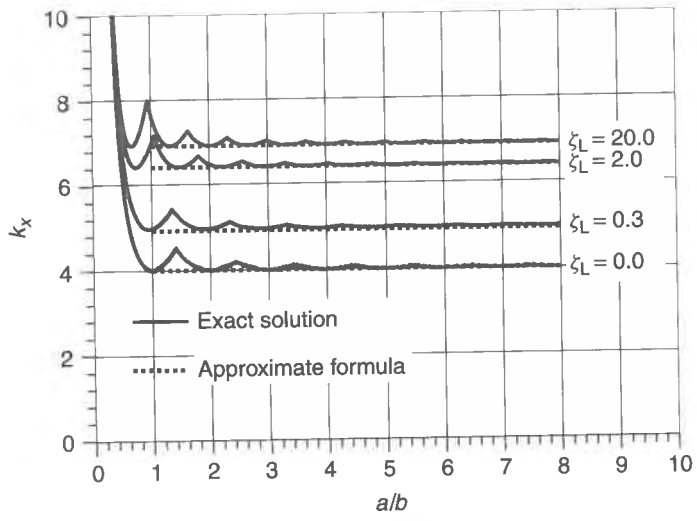

Figure 3.10 Accuracy of Equation (3.25a) for a plate under longitudinal axial compression, elastically restrained at the long edges and simply supported at the short edges

$$d_2 = \begin{cases} 0.881(a/b)^4 - 10.851(a/b)^3 + 41.688(a/b)^2 - 43.150(a/b) + 14.615 & \text{for } 0 \le \zeta_S < 0.4 \\ -0.123(a/b)^4 + 1.549(a/b)^3 - 6.788(a/b)^2 + 11.299(a/b) - 3.662 & \text{for } 0.4 \le \zeta_S < 0.8 \\ 0.138(a/b)^2 - 0.793(a/b) + 1.171 & \text{for } 0.8 \le \zeta_S < 2 \\ 0.0 & \text{for } 2 \le \zeta_S \end{cases}$$

$$d_3 = \begin{cases} -0.190(a/b)^4 + 2.093(a/b)^3 - 5.891(a/b)^2 - 2.096(a/b) + 1.792 & \text{for } 0 \le \zeta_S < 0.4 \\ 0.114(a/b)^4 - 1.412(a/b)^3 + 5.933(a/b)^2 - 8.638(a/b) + 0.224 & \text{for } 0.4 \le \zeta_S < 0.8 \\ -0.457(a/b)^2 + 2.571(a/b) - 3.712 & \text{for } 0.8 \le \zeta_S < 2 \\ 0.0 & \text{for } 2 \le \zeta_S \end{cases}$$

$$d_4 = \begin{cases} 0.004(a/b)^4 - 0.007(a/b)^3 - 0.243(a/b)^2 + 0.630(a/b) + 3.617 & \text{for } 0 \le \zeta_S < 0.4 \\ -0.021(a/b)^4 + 0.184(a/b)^3 - 0.126(a/b)^2 - 2.625(a/b) + 6.457 & \text{for } 0.4 \le \zeta_S < 0.8 \\ 0.822(a/b)^2 - 4.516(a/b) + 6.304 & \text{for } 0.8 \le \zeta_S < 2 \\ -0.106(a/b) + 0.176 & \text{for } 2 \le \zeta_S < 20 \\ 0.0 & \text{for } 20 \le \zeta_S \end{cases}$$

$$d_5 = \begin{cases} 4.0 & \text{for } 0 \le \zeta_S < 0.4 \\ -0.001(a/b)^4 + 0.033(a/b)^3 - 0.241(a/b)^2 + 0.684(a/b) + 3.539 & \text{for } 0.4 \le \zeta_S < 0.8 \\ -0.148(a/b)^2 + 0.596(a/b) + 3.847 & \text{for } 0.8 \ge \zeta_S < 2 \\ -1.822(a/b) + 7.850 & \text{for } 2 \le \zeta_S < 20 \\ 0.041(a/b)^4 - 0.602(a/b)^3 + 3.303(a/b)^2 - 8.176(a/b) + 12.144 & \text{for } 20 \le \zeta_S \end{cases}$$

In calculating k_x of Equation (3.25b), the following conditions must be satisfied in order for the approximations to hold: (1) if $4.0 < a/b \le 4.5$ and $\zeta_S \ge 0.2$ then $\zeta_S = 0.2$, (2) if $a/b > 4.5$ and $\zeta_S \ge 0.1$ then $\zeta_S = 0.1$, (3) if $a/b \ge 2.2$ and $\zeta_S \ge 0.4$ then $\zeta_S = 0.4$, (4) if $a/b \ge 1.5$ and $\zeta_S \ge 1.4$ then $\zeta_S = 1.4$, (5) if $8 \le a/b \le 20$ then $\zeta_S = 8$, and (6) if $a/b \ge 5$ then $a/b = 50$.

Figures 3.11(a) and (b) show the variation of the buckling coefficient, k_x, as a function of the plate aspect ratio and the torsional rigidity of support members at short edges. The accuracy of Equation (3.25b) is verified in Figure 3.11(b) by comparison to the exact theoretical solutions as obtained by directly solving the characteristic equation (Paik & Thayamballi 2000).

Elastically Restrained at Both Long and Short Edges

For design purposes, the elastically restrained boundary conditions at both the long and short edges may be expressed by a relevant combination of the previous two edge conditions as well as the simply supported edge condition. Specifically one can assume

$$k_x = k_{x1} + k_{x2} - k_{x0} \tag{3.25c}$$

where k_x = buckling coefficient of the plate elastically restrained at both the long and short edges, k_{x1} = buckling coefficient of the plate elastically restrained at the long edges and simply supported at the short edges as defined in Equation (3.25a), k_{x2} = buckling coefficient of the plate elastically restrained at the short edges and simply supported at the long edges as defined in Equation (3.25b), and k_{x0} = buckling coefficient of the plate simply supported at all edges as defined in Table 3.1.

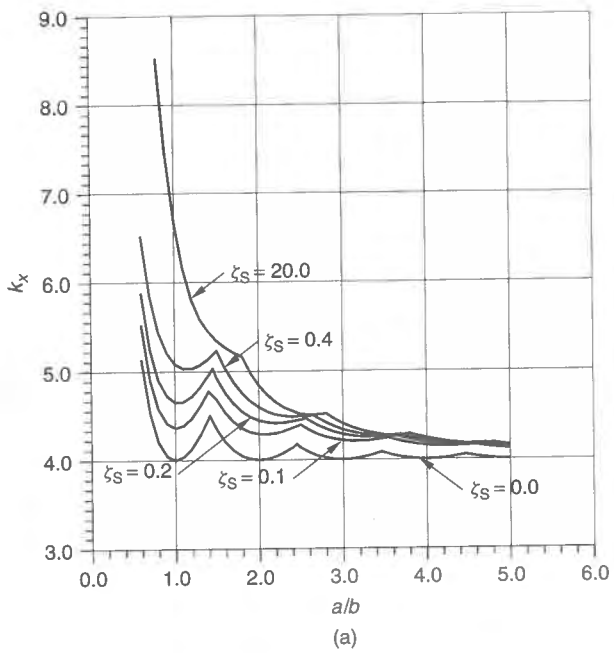

Figure 3.11 (a) Variation of the buckling coefficient, k_x, for a plate under longitudinal axial compression, elastically restrained at the short edges and simply supported at the long edges; (b) accuracy of Equation (3.25b) for a plate under longitudinal axial compression, elastically restrained at the short edges and simply supported at the long edges

3.10.3 Transverse Axial Compression

The elastic bifurcation buckling stress of a plate with elastically restrained edge conditions and under transverse axial compression can also be calculated from Equation (3.2), but using the different buckling coefficient, k_y. In the following, empirical formulas of the buckling coefficient, k_y, which are expressed in terms of the aspect ratio and the torsional rigidity of support members, are presented.

Elastically Restrained at Long Edges and Simply Supported at Short Edges

$$k_y = e_1\zeta_L^2 + e_2\zeta_L + e_3 \tag{3.26a}$$

where

$$e_1 = \begin{cases} 1.322(b/a)^4 - 1.919(b/a)^3 + 0.021(b/a)^2 + 0.032(b/a) & \text{for } 0 \le \zeta_L < 2 \\ -0.463(b/a)^4 + 1.023(b/a)^3 - 0.649(b/a)^2 - 0.073(b/a) & \text{for } 2 \le \zeta_L < 8 \\ 0.0 & \text{for } 8 \le \zeta_L \end{cases}$$

$$e_2 = \begin{cases} -0.179(b/a)^4 - 3.098(b/a)^3 + 5.648(b/a)^2 - 0.199(b/a) & \text{for } 0 \le \zeta_L < 2 \\ 5.432(b/a)^4 - 11.324(b/a)^3 + 6.189(b/a)^2 - 0.068(b/a) & \text{for } 2 \le \zeta_L < 8 \\ -1.047(b/a)^4 + 2.624(b/a)^3 - 2.215(b/a)^2 + 0.646(b/a) & \text{for } 8 \le \zeta_L < 20 \\ 0.0 & \text{for } 20 \le \zeta_L \end{cases}$$

$$e_3 = \begin{cases} 0.994(b/a)^4 + 0.011(b/a)^3 + 1.991(b/a)^2 + 0.003(b/a) + 1.0 & \text{for } 0 \le \zeta_L < 2 \\ -3.131(b/a)^4 + 4.753(b/a)^3 + 3.587(b/a)^2 - 0.433(b/a) + 1.0 & \text{for } 2 \le \zeta_L < 8 \\ 20.111(b/a)^4 - 43.697(b/a)^3 + 30.941(b/a)^2 - 1.836(b/a) + 1.0 & \text{for } 8 \le \zeta_L < 20 \\ 0.751(b/a)^4 - 0.047(b/a)^3 + 2.053(b/a)^2 - 0.015(b/a) + 4.0 & \text{for } 20 \le \zeta_L \end{cases}$$

Figures 3.12(a) and (b) show the variation of the buckling coefficient, k_y, for a plate under transverse axial compression, elastically restrained at the long edges and simply supported at the short edges, as a function of the plate aspect ratio and the torsional rigidity of support members at the long edges. The accuracy of Equation (3.26a) is verified in Figure 3.12(b) by comparison to the exact theoretical solutions as obtained by directly solving the characteristic equation (Paik & Thayamballi 2000).

Elastically Restrained at Short Edges and Simply Supported at Long Edges

$$k_y = f_1\zeta_S^2 + f_2\zeta_S + f_3 \tag{3.26b}$$

where

$$f_1 = \begin{cases} 0.543(b/a)^4 - 1.297(b/a)^3 + 0.192(b/a)^2 - 0.016(b/a) & \text{for } 0 \le \zeta_S < 2 \\ -0.347(b/a)^4 + 0.403(b/a)^3 - 0.147(b/a)^2 + 0.016(b/a) & \text{for } 2 \le \zeta_S < 6 \\ 0.0 & \text{for } 6 \le \zeta_S \end{cases}$$

$$f_2 = \begin{cases} -1.094(b/a)^4 + 4.401(b/a)^3 - 0.751(b/a)^2 + 0.068(b/a) & \text{for } 0 \le \zeta_S < 2 \\ 2.139(b/a)^4 - 1.761(b/a)^3 + 0.419(b/a)^2 - 0.030(b/a) & \text{for } 2 \le \zeta_S < 6 \\ -0.199(b/a)^4 + 0.308(b/a)^3 - 0.118(b/a)^2 + 0.013(b/a) & \text{for } 6 \le \zeta_S < 20 \\ 0.0 & \text{for } 20 \le \zeta_S \end{cases}$$

$$f_3 = \begin{cases} 0.994(b/a)^4 + 0.011(b/a)^3 + 1.991(b/a)^2 + 0.003(b/a) + 1.0 & \text{for } 0 \le \zeta_S < 2 \\ -2.031(b/a)^4 + 5.765(b/a)^3 + 0.870(b/a)^2 + 0.102(b/a) + 1.0 & \text{for } 2 \le \zeta_S < 6 \\ -0.289(b/a)^4 + 7.507(b/a)^3 - 1.029(b/a)^2 + 0.398(b/a) + 1.0 & \text{for } 6 \le \zeta_S < 20 \\ -6.278(b/a)^4 + 17.135(b/a)^3 - 5.026(b/a)^2 + 0.860(b/a) + 1.0 & \text{for } 20 \le \zeta_S \end{cases}$$

Figures 3.13(a) and (b) show the variation of the buckling coefficient, k_y, for a plate under transverse axial compression, elastically restrained at the short edges and simply supported at the long edges, as a function of the plate aspect ratio and the torsional rigidity of support members at the short edges. The accuracy of Equation (3.26b) is verified in

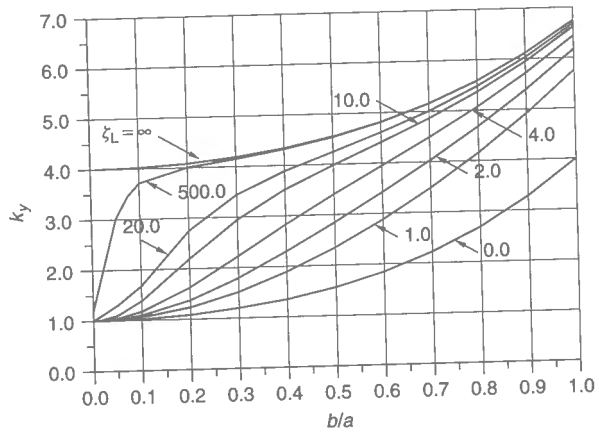

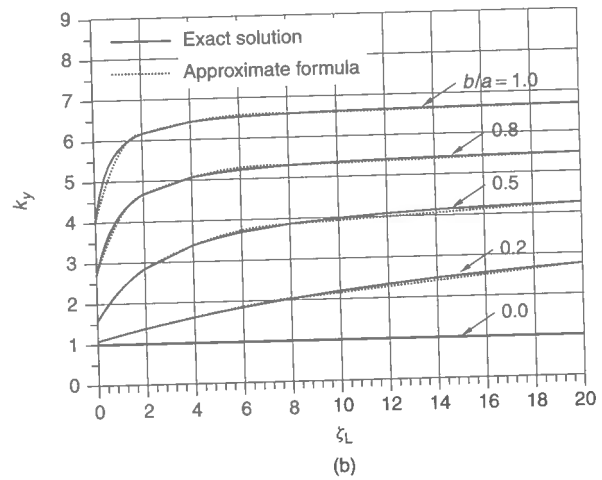

Figure 3.12 (a) Variation of the buckling coefficient, k_y, for a plate under transverse axial compression, elastically restrained at the long edges and simply supported at the short edges; (b) Accuracy of Equation (3.26a) for a plate under transverse axial compression, elastically restrained at the long edges and simply supported at the short edges

Figure 3.13(b) by comparison to the exact theoretical solutions as obtained by directly solving the characteristic equation (Paik & Thayamballi 2000).

Elastically Restrained at Both Long and Short Edges

For a plate elastically restrained at both long and short edges under transverse axial compression, the buckling coefficient, k_y, can be expressed by a relevant combination of the previous two edge conditions in addition to the all-edges simply supported condition as follows:

$$k_y = k_{y1} + k_{y2} - k_{y0} \tag{3.26c}$$

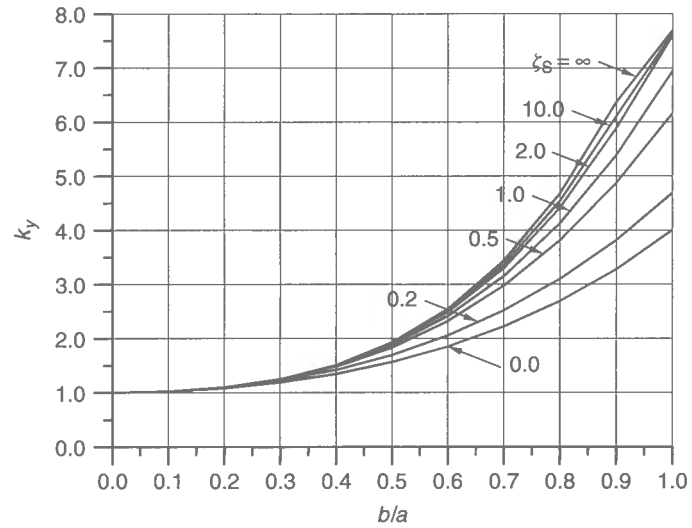

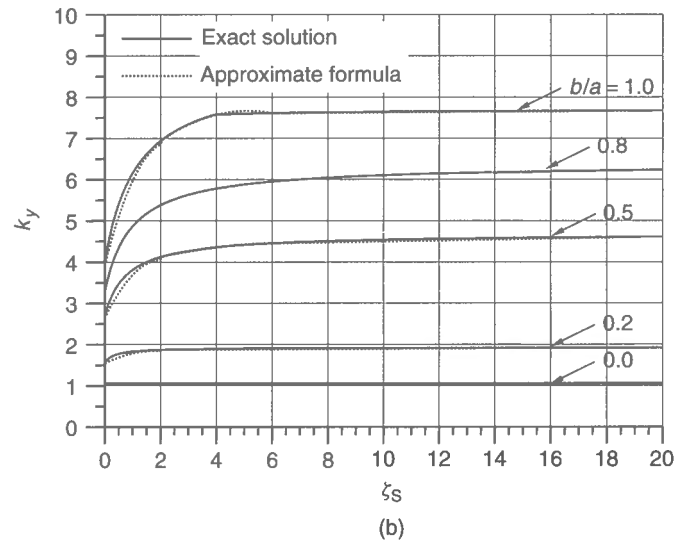

Figure 3.13 (a) Variation of the buckling coefficient, k_y, for a plate under transverse axial compression, elastically restrained at the short edges and simply supported at the long edges; (b) Accuracy of Equation (3.26b) for a plate under transverse axial compression, elastically restrained at the short edges and simply supported at the long edges

where k_y = buckling coefficient of the plate elastically restrained at both long and short edges, k_{y1} = buckling coefficient of the plate elastically restrained at the long edges and simply supported at the short edges as defined in Equation (3.26a), k_{y2} = buckling coefficient of the plate elastically restrained at the short edges and simply supported at the long edges as defined in Equation (3.26b), and k_{y0} = buckling coefficient of the plate simply supported at all edges as defined in Table 3.1.

3.10.4 Combined Loads

It is often assumed with reasonable certainty that the elastic buckling interaction relationship between combined loads for plates elastically restrained at the edges is similar to that for plates simply supported at all edges. Therefore, the same buckling interaction relationships of simply supported plates under combined loads may be employed for the plates elastically restrained at the edges, but replacing the buckling strengths under single types of load components by those for the corresponding edge conditions.

3.11 Effect of Welding-induced Residual Stresses

The welding-induced residual stresses will affect (reduce) the plate buckling strength. For a plate element between stiffeners, the elastic buckling stress may be given by considering that an effective compressive residual stress reduces the buckling strength, as will be presented later in Chapter 4.

Therefore, the elastic buckling stress of a plate under axial compression in the x direction may be approximately calculated from Equation (3.2) considering the effect of welding residual stress, as follows (for the symbols related to residual stresses, Section 1.7.2 in Chapter 1 is referred to):

$$\sigma_{xE,1} = k_x \frac{\pi^2 E}{12(1-\nu^2)} \left(\frac{t}{b}\right)^2 - \sigma_{rex} \tag{3.27a}$$

where

$$\sigma_{rex} = \sigma_{rcx} + \frac{2}{b}(\sigma_{rtx} - \sigma_{rcx}) \left(b_t - \frac{b}{2\pi} \sin \frac{2\pi b_t}{b}\right)$$

is as defined in Equation (4.11) of Chapter 4.

In a similar way, the elastic buckling stress of a plate under axial compression in the y direction may also be calculated from Equation (3.2) after including the effect of welding residual stress, as follows:

$$\sigma_{yE,1} = k_y \frac{\pi^2 E}{12(1-\nu^2)} \left(\frac{t}{b}\right)^2 - \sigma_{rey} \tag{3.27b}$$

where

$$\sigma_{rey} = \sigma_{rcy} + \frac{2}{a}(\sigma_{rty} - \sigma_{rcy}) \left(a_t - \frac{a}{2\pi} \sin \frac{2\pi a_t}{a}\right)$$

is as defined in Equation (4.11) of Chapter 4.

Figure 3.14 shows the influence of welding-induced residual stress on the compressive buckling stress for the simply supported plates with a yield stress of $\sigma_Y = 352\,\text{MPa}$. In the calculations indicated in Figure 3.14, the level of residual stresses and the plate slenderness ratio (i.e., b/t ratio) are varied. It is assumed in the analysis that the magnitude of the tensile residual stresses is 80% of the yield stress, i.e., $\sigma_{rtx} = \sigma_{rty} = 0.8\sigma_Y$. It is evident from Figure 3.14 that the welding residual stresses can significantly reduce the compressive buckling stress of plates in some cases. The reduction tendency of the buckling stress for thin plates is more significant than that for thick plates, as expected.

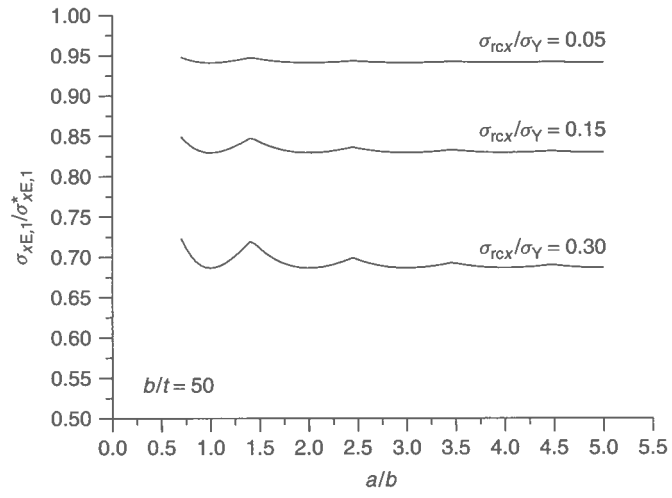

Figure 3.14 Variation of the elastic compressive buckling stress (normalized by the elastic buckling compressive stress without residual stresses) varying the magnitude of welding-induced residual stress for (a) a relatively thick plate and (b) a relatively thin plate

3.12 Effect of Lateral Pressure

When a plate in a continuous stiffened panel is subjected to lateral pressure, the plate edges approach the condition being clamped depending on the thickness of the plate and the pressures involved. Also, the lateral pressure loading may beneficially disturb the occurrence of the inherent plate buckling pattern. As a result, the buckling strength of long plate elements making up a continuous stiffened panel under lateral pressure is normally greater than that without lateral pressure loading.

For practical design purposes, a correction factor may often be employed to take into account the effect of lateral pressure on the plate buckling strength, the factor being applied by multiplication to the buckling strength calculated for the plate without lateral pressure loads.

In this regard, Fujikubo *et al.* (1998) propose plate compressive buckling strength correction factors to account for the effect of lateral pressure, by curve fitting based on the finite element solutions for long plate elements in a continuous stiffened panel, as follows:

$$C_{px} = 1 + \frac{1}{576}\left(\frac{pb^4}{Et^4}\right)^{1.6} \quad \text{for } \frac{a}{b} \geq 2 \tag{3.28a}$$

$$C_{py} = 1 + \frac{1}{160}\left(\frac{b}{a}\right)^{0.95}\left(\frac{pb^4}{Et^4}\right)^{1.75} \quad \text{for } \frac{a}{b} \geq 2 \tag{3.28b}$$

where C_{px} and C_{py} are correction factors of the elastic compressive buckling strength in the x and y direction, respectively, to account for the effect of lateral pressure. p is the magnitude of net lateral pressure loads.

For nearly square plates, i.e., with $a/b \approx 1$, under combined axial compression and lateral pressure, one half-wave deflection occurs from the beginning and thus the bifurcation buckling phenomenon may not appear as axial compressive loads increase. In this case, it is beneficial to define an equivalent buckling strength for practical design purposes. It is considered that the increase of buckling strength due to the rotational restraints and the decrease of buckling strength due to one half-wave deflection caused by lateral pressure may be offset. For square plates, therefore, $C_{px} = C_{py} = 1.0$ may approximately be adopted.

The elastic compressive buckling stress of a plate taking into account the effects of lateral pressure and welding-induced residual stresses can then be calculated from Equations (3.27), but using the multiplicative correction factors of Equations (3.28) as follows:

$$\sigma_{xE,1} = C_{px}\left[k_x \frac{\pi^2 E}{12(1-\nu^2)}\left(\frac{t}{b}\right)^2 - \sigma_{rex}\right] \tag{3.29a}$$

$$\sigma_{yE,1} = C_{py}\left[k_y \frac{\pi^2 E}{12(1-\nu^2)}\left(\frac{t}{b}\right)^2 - \sigma_{rey}\right] \tag{3.29b}$$

Figure 3.15 plots Equations (3.29) for a specific steel plate with $a \times b = 2400 \times 800$ mm and $E = 2.1 \times 10^5$ MPa as a function of the plate thickness and water head when no welding residual stresses exist. It is seen from Figure 3.15 that the increasing tendency of buckling strength due to lateral pressure for thin plates is larger than that for thick plates.

It may be noted that lateral pressure may not affect the buckling strength of perforated plates. This is because the perforated plate may not be subjected to lateral pressure.

3.13 Effect of Openings

In plate elements of steel-plated structures, openings are often located to make a way of access or to lighten the structure. These perforations will reduce the buckling strength of

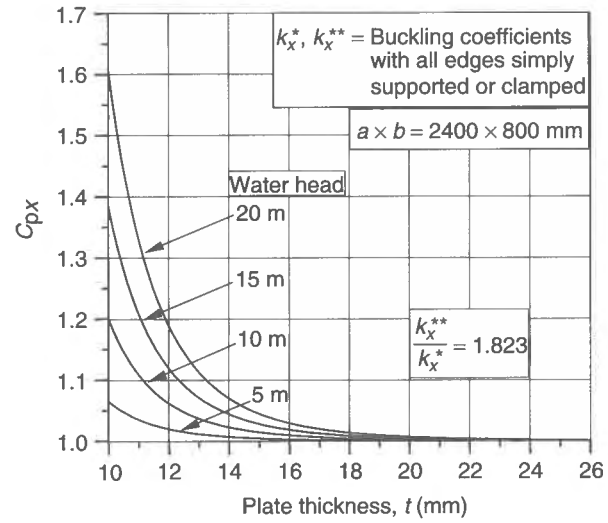

(a) C_{px} versus plate thickness

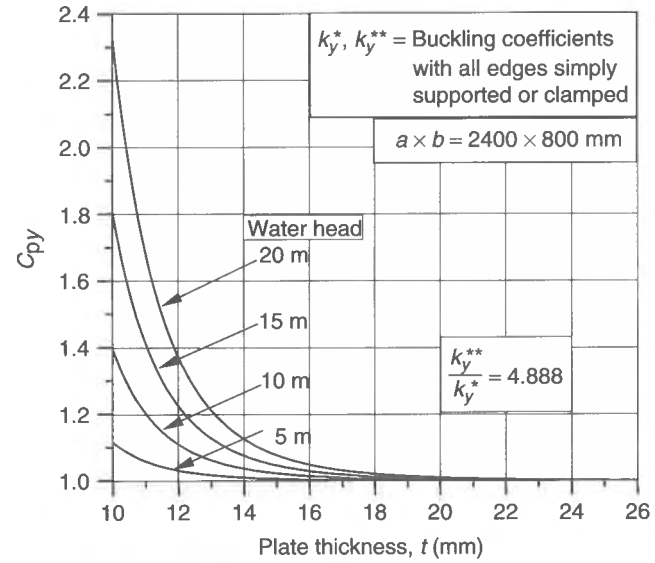

(b) C_{py} versus plate thickness

Figure 3.15 Effect of lateral pressure on the plate compressive buckling strength

plates. The openings may thus need to be included in the buckling strength formulations as a parameter of influence where significant.

In this section, buckling strength formulations of steel plates with a centrally located circular opening and under combined in-plane loads as shown in Figure 3.16 are presented. As previously noted in Section 3.3, the magnitudes of applied stresses are normally defined for the perfect plates, i.e., without perforations, while the partial safety factors may in this

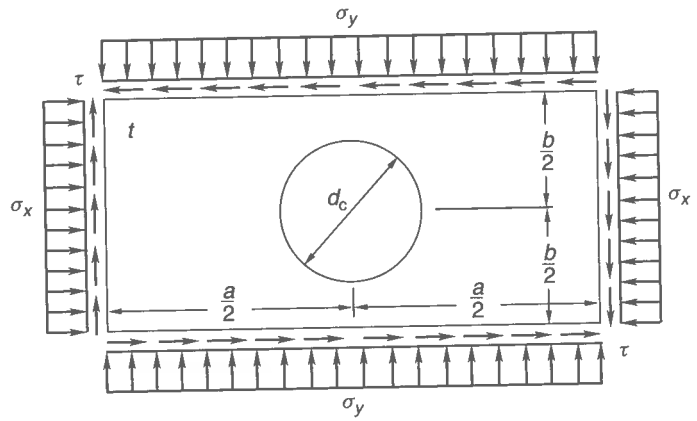

Figure 3.16 A rectangular plate with a centrally located circular hole and under combined in-plane loads

case be adjusted to take into account the effect of openings in applying Equation (1.1) of Chapter 1.

It is considered that all (four) plate edges are simply supported, keeping them straight. To take into account the effect of the opening on the plate buckling strength, a relevant buckling strength reduction factor which is defined as the ratio of the buckling coefficient of perforated plates to that of plates without holes can be employed. In this case, empirical formulations may be derived for the plate buckling strength reduction factors due to openings by curve fitting based on the results of eigenvalue finite element analyses. For openings by curve fitting based on the results of eigenvalue finite element analyses. For buckling of plates with rectangular types of openings, Brown *et al.* (1987), among others, may be referred to. Narayanan & der Avanessian (1984) deal with elastic shear buckling of simply supported and clamped plates with circular and rectangular holes.

3.13.1 Longitudinal Axial Compression

Figure 3.17 shows the variation of the buckling reduction factor, R_{xE}, of the plate under σ_x varying the size of the opening and the plate aspect ratio. In this case, R_{xE} may be defined by a cubic equation in terms of the size of the opening and the plate aspect ratio as follows:

$$R_{xE} = \alpha_{E1}\left(\frac{d_c}{b}\right)^3 + \alpha_{E2}\left(\frac{d_c}{b}\right)^2 + \alpha_{E3}\frac{d_c}{b} + 1 \tag{3.30a}$$

where

$$\alpha_{E1} = \begin{cases} 0.002(a/b)^{8.238} & \text{for } 1 \le a/b < 2 \\ -1.542(a/b)^2 + 7.232a/b - 7.666 & \text{for } 2 \le a/b < 3 \\ -0.052(a/b)^2 + 0.526a/b - 0.964 & \text{for } 3 \le a/b \le 6 \end{cases}$$

$$\alpha_{E2} = \begin{cases} 0.655 + 1/[4.123(a/b) - 8.922] & \text{for } 1 \le a/b < 2 \\ 1.767(a/b)^2 - 7.937a/b + 7.982 & \text{for } 2 \le a/b < 3 \\ 0.071(a/b)^2 - 0.732a/b + 1.631 & \text{for } 3 \le a/b \le 6 \end{cases}$$

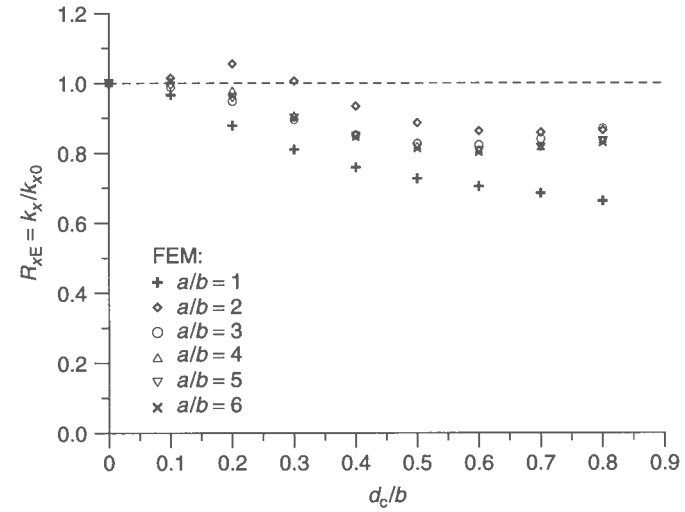

Figure 3.17 Variation of the buckling strength reduction factor of the plate under longitudinal axial compression varying the size of the opening and the plate aspect ratio as obtained by eigenvalue finite element analysis (k_x, k_{x0} = longitudinal compressive buckling coefficients for the plate with and without an opening)

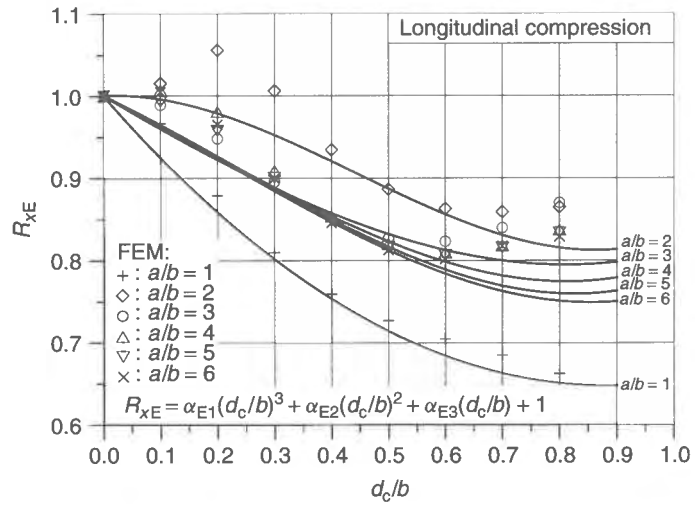

Figure 3.18 Accuracy of Equation (3.30a) for longitudinal axial compressive loading (symbols: finite element analysis)

$$\alpha_{E3} = \begin{cases} -0.945 + 1/[-5.661(a/b) + 12.342] & \text{for } 1 \le a/b < 2 \\ -0.248(a/b)^2 + 0.796a/b - 0.565 & \text{for } 2 \le a/b < 3 \\ -0.020(a/b)^2 + 0.199a/b - 0.826 & \text{for } 3 \le a/b \le 6 \end{cases}$$

Figure 3.18 shows the accuracy of Equation (3.30a) by comparison to the eigenvalue finite element buckling solutions. The corresponding elastic plate buckling stress of plates

with a centrally located circular hole can then possibly be calculated as follows:

$$\sigma_{xE,1} = R_{xE} k_{x0} \frac{\pi^2 E}{12(1-\nu^2)} \left(\frac{t}{b}\right)^2 \tag{3.30b}$$

where k_{x0} = longitudinal compressive buckling coefficient of the plate without an opening.

3.13.2 Transverse Axial Compression

Figure 3.19 shows the variation of the buckling reduction factor, R_{yE}, of the plate under σ_y varying the size of the opening and the plate aspect ratio. In this case, R_{yE} may be defined by a cubic equation in terms of the size of the opening and the plate aspect ratio as follows:

$$R_{yE} = \alpha_{E4} \left(\frac{d_c}{b}\right)^2 + \alpha_{E5} \frac{d_c}{b} + 1 \tag{3.31a}$$

where

$$\alpha_{E4} = \begin{cases} 0.034(a/b)^2 - 0.327a/b + 0.768 & \text{for } 1 \le a/b < 4 \\ 0.004 & \text{for } 4 \le a/b \le 6 \end{cases}$$

$$\alpha_{E5} = -0.008 - 1/[0.967(a/b) + 0.302] \quad \text{for } 1 \le a/b \le 6$$

Figure 3.20 shows the accuracy of Equation (3.31a) by comparison to the finite element buckling eigenvalue solutions. The corresponding elastic plate buckling stress of the

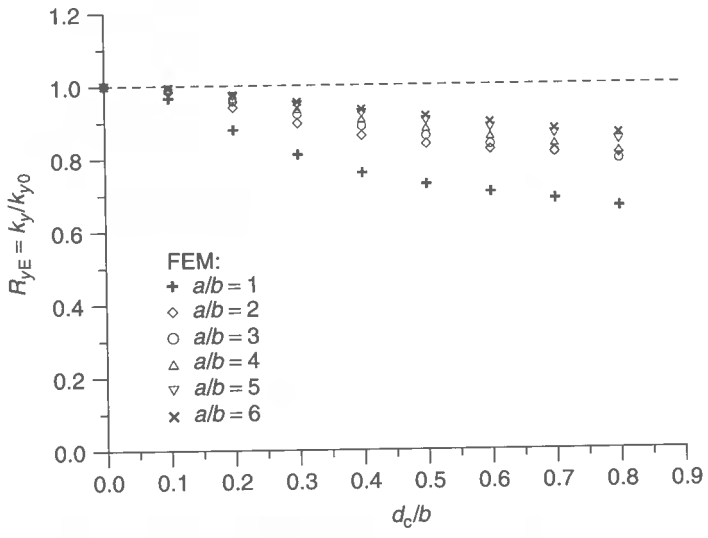

Figure 3.19 Variation of the buckling strength reduction factor of the plate under transverse axial compression varying the size of the opening and the plate aspect ratio as obtained by eigenvalue finite element analysis (k_y, k_{y0} = transverse compressive buckling coefficients for the plate with and without an opening)

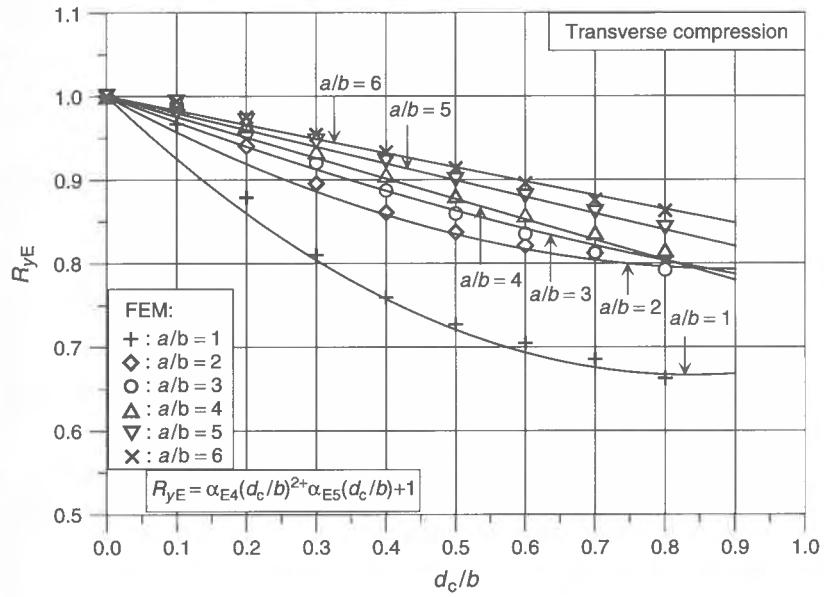

Figure 3.20 The accuracy of Equation (3.31a) for transverse axial compressive loading (symbols: finite element analysis)

perforated plate is then calculated as follows:

$$\sigma_{yE,1} = R_{yE} k_{y0} \frac{\pi^2 E}{12(1-\nu^2)} \left(\frac{t}{b}\right)^2 \tag{3.31b}$$

3.13.3 Edge Shear

Figure 3.21 shows the variation of the buckling reduction factor, $R_{\tau E}$, of the plate under τ varying the size of the opening and the plate aspect ratio. In this case, $R_{\tau E}$ may be defined by a cubic equation in terms of the opening size and the plate aspect ratio as follows:

$$R_{\tau E} = \alpha_{E6} \left(\frac{d_c}{b}\right)^3 + \alpha_{E7} \left(\frac{d_c}{b}\right)^2 + \alpha_{E8} \frac{d_c}{b} + 1 \tag{3.32a}$$

where

$$\alpha_{E6} = \begin{cases} 0.094(a/b)^2 + 0.035a/b + 1.551 & \text{for } 1 \le a/b < 3 \\ 2.502 & \text{for } 3 \le a/b \le 6 \end{cases}$$

$$\alpha_{E7} = \begin{cases} -0.039(a/b)^2 - 0.807a/b - 0.405 & \text{for } 1 \le a/b < 3 \\ -3.177 & \text{for } 3 \le a/b \le 6 \end{cases}$$

$$\alpha_{E8} = \begin{cases} -0.053(a/b)^2 + 0.785a/b - 1.875 & \text{for } 1 \le a/b < 3 \\ 0.003 & \text{for } 3 \le a/b \le 6 \end{cases}$$

Figure 3.22 shows the accuracy of Equation (3.32a) by comparison to the eigenvalue finite element buckling solutions. The corresponding elastic plate buckling stress of the

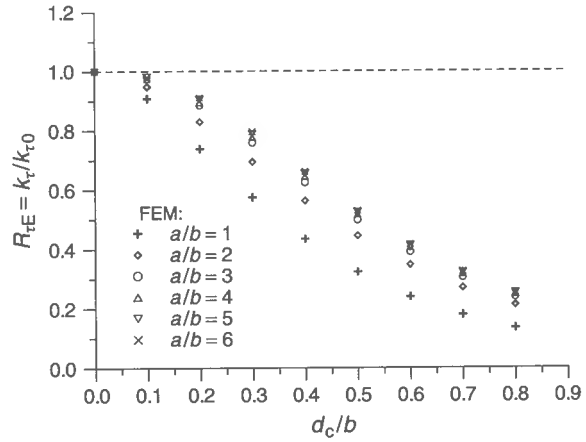

Figure 3.21 Variation of the buckling strength reduction factor of the plate under edge shear varying the size of the opening and the plate aspect ratio as obtained by eigenvalue finite element analysis (k_τ, $k_{\tau 0}$ = shear buckling coefficients for the plate with and without an opening)

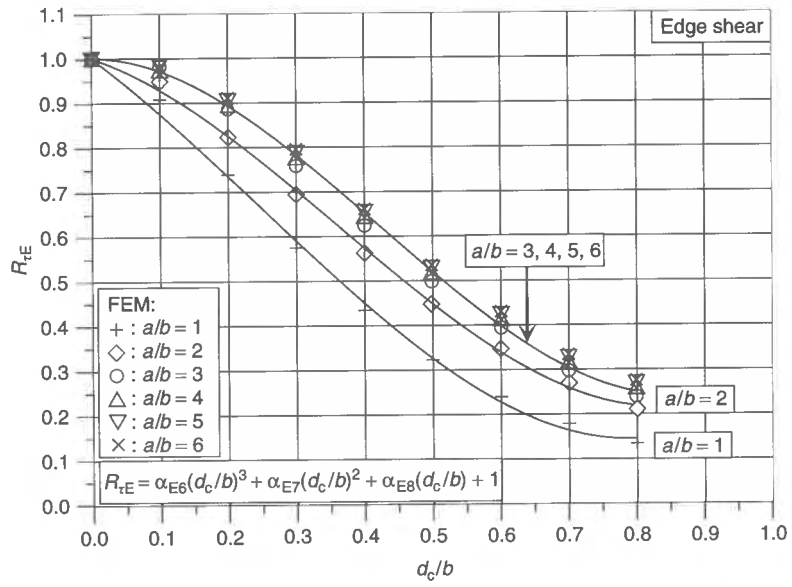

Figure 3.22 The accuracy of Equation (3.32a) for edge shear (symbols: finite element analysis)

perforated plate is then calculated as follows:

$$\tau_{E,1} = R_{\tau E} k_{\tau 0} \frac{\pi^2 E}{12(1-\nu^2)} \left(\frac{t}{b}\right)^2 \tag{3.32b}$$

where $k_{\tau 0}$ = shear buckling coefficient of the plate without an opening.

3.13.4 Combined Loads

For practical design purposes, it may be assumed that the elastic buckling interaction relationship between combined loads for a perforated plate is the same as that for the plate without an opening, but using the corresponding buckling strength components under single types of loads.

Figure 3.23 shows some selected elastic buckling strength interaction curves of steel plates with a centrally located circular hole and under combined loads. The finite element eigenvalue solutions are also compared. It is apparent that the assumption of the buckling interaction relationship made above is relevant.

3.14 Elastic–Plastic Buckling

3.14.1 Single Types of Loads

A stocky plate that has a high elastic buckling strength will not buckle in the elastic regime and will reach the ULS with a certain degree of plasticity. In most design guidelines, the Johnson–Ostenfeld formulation, Equation (2.93), is used to account for this behavior. Under single types of loads, the elastic–plastic buckling stress is then approximately calculated by substituting the computed elastic buckling stress into Equation (2.93). In usage of Equation (2.93), the compressive stress is converted to positive. The elastic–plastic buckling strength as obtained by plasticity correction of the corresponding elastic buckling stress using the Johnson–Ostenfeld formula is often termed the 'critical' buckling strength.

Plates without Openings

Figures 3.24(a)–(c) show the resulting relationship between the critical buckling strength and the elastic buckling strength for steel plates (without perforations) with varying edge conditions. The ultimate strength obtained by the elastic–plastic large-deflection finite element analysis (FEA) neglecting the strain-hardening effect is also shown for comparison. As is evident, regardless of the edge conditions, the Johnson–Ostenfeld formula predicts fairly well the elastic–plastic or plastic buckling strength of relatively thick steel plates (without openings) as a function of the elastic buckling strength, albeit on the pessimistic side.

Perforated Plates

Figures 3.25(a)–(f) compare the critical buckling strength with the ultimate strength for plates with a centrally located circular hole. It is emphasized from these figures that the critical buckling strength for the perforated plates may not always provide pessimistic predictions of the ultimate strength and it may be greater than the real plate ultimate strength when the hole size is relatively large in thick plates. This implies that the ultimate strength is a better and more consistent basis for design than the elastic buckling strength approach together with simple plasticity correction.

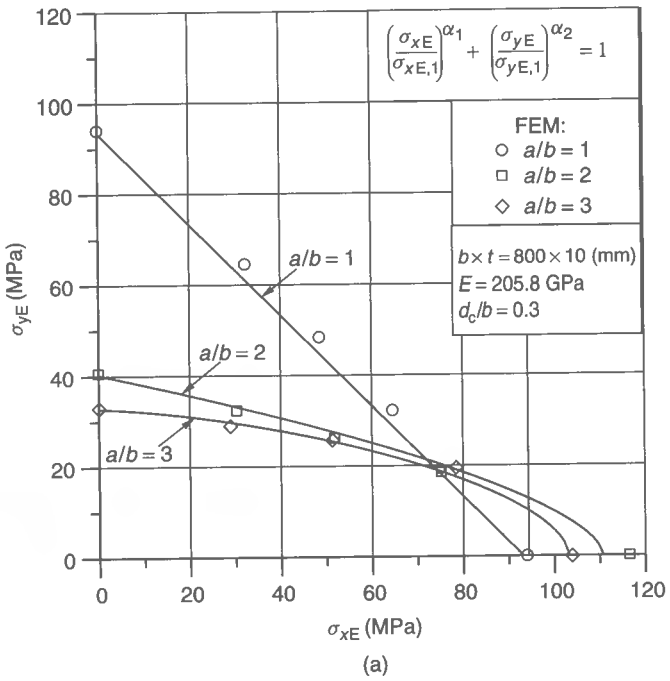

Figure 3.23 Elastic buckling strength interaction of a plate with a centrally located circular hole: (a) under combined longitudinal and transverse axial compression (α_1, α_2 = as defined in Equations (3.9)); (b) under combined longitudinal axial compression and edge shear (α_{11} = as defined in Equations (3.15)); (c) under combined transverse axial compression and edge shear (α_{12} = as defined in Equations (3.16))

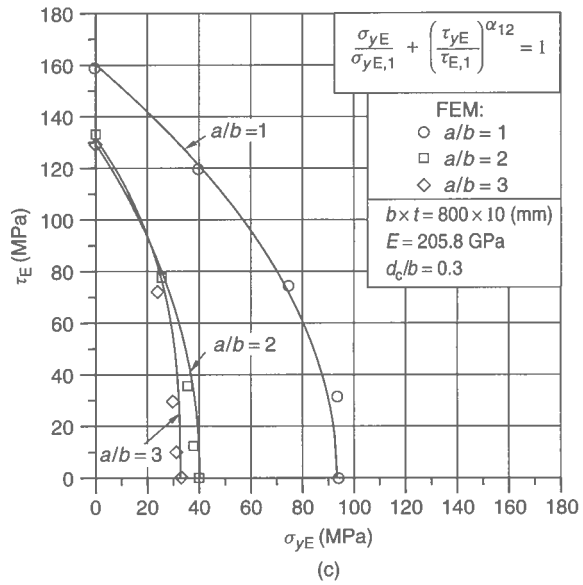

Figure 3.23 (*continued*)

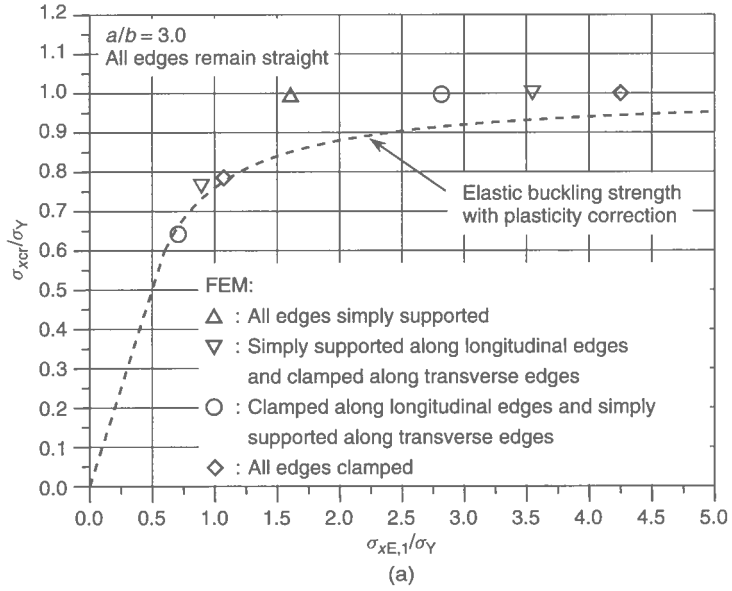

Figure 3.24 (a) The critical buckling stress, σ_{xcr}, versus the elastic bifurcation buckling stress, $\sigma_{xE,1}$, of plates without holes under longitudinal compression alone, $a/b = 3$ (symbols: ultimate strength by FEA); (b) The critical buckling stress, σ_{ycr}, versus the elastic bifurcation buckling stress, $\sigma_{yE,1}$, of plates without holes under transverse compression alone, $a/b = 3$ (symbols: ultimate strength by FEA); (c) The critical buckling stress, τ_{cr}, versus the elastic bifurcation buckling stress, $\tau_{E,1}$, of plates without holes under edge shear alone, $a/b = 3$ (symbols: ultimate strength by FEA)

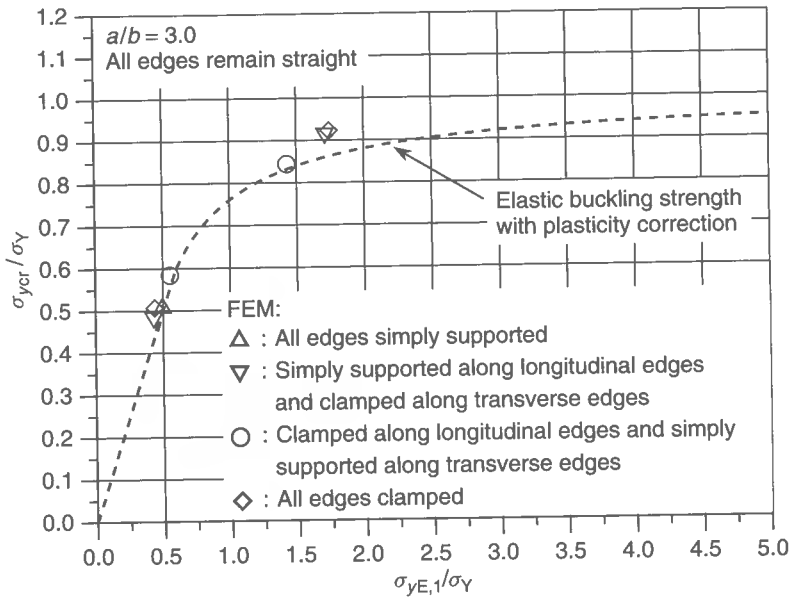

(b)

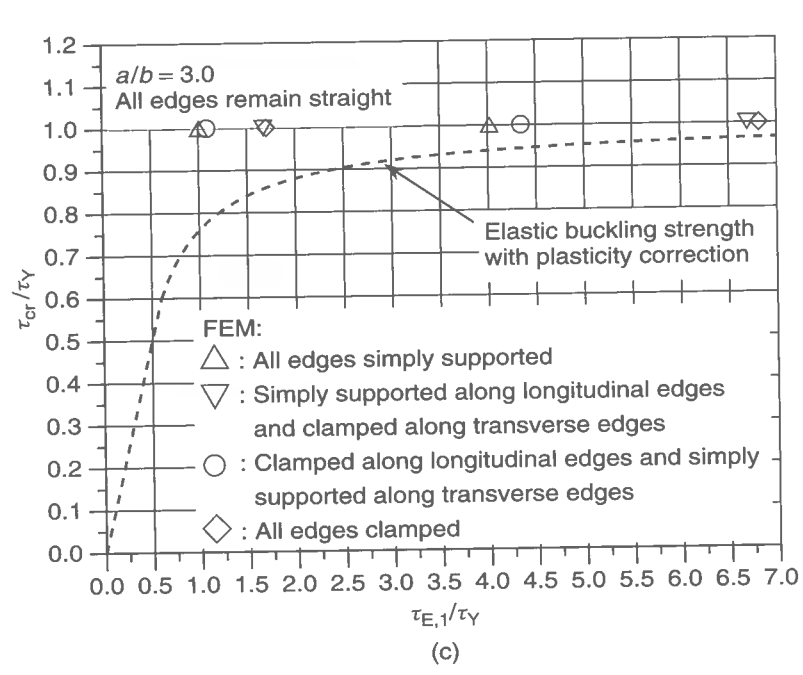

(c)

Figure 3.24 (*continued*)

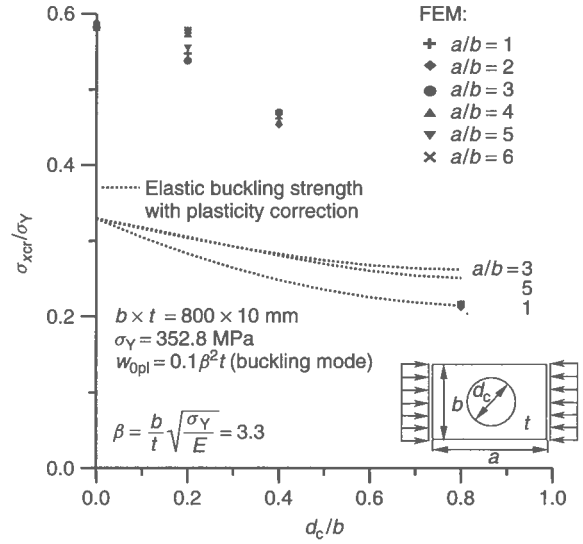

(a)

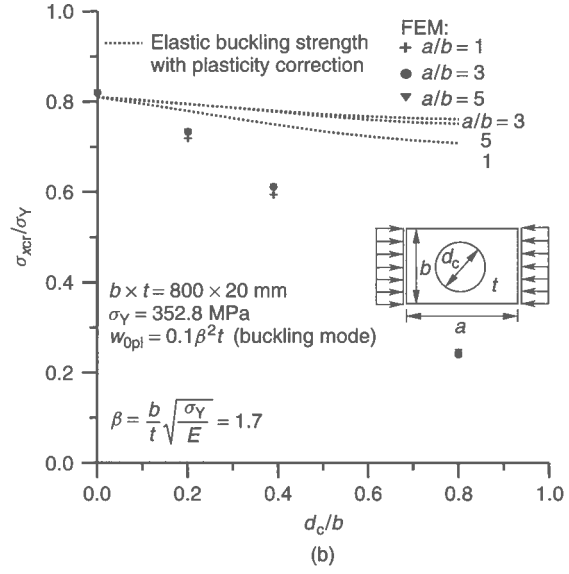

(b)

Figure 3.25 (a) A comparison of the critical buckling strength, σ_{xcr}, with the ultimate strength for plates with a centrally located circular hole and under longitudinal axial compression, $\beta = 3.3$; (b) A comparison of the critical buckling strength, σ_{xcr}, with the ultimate strength for plates with a centrally located circular hole and under longitudinal axial compression, $\beta = 1.7$; (c) A comparison of the critical buckling strength, σ_{ycr}, with the ultimate strength for plates with a centrally located circular hole and under transverse axial compression, $\beta = 3.3$; (d) A comparison of the critical buckling strength, σ_{ycr}, with the ultimate strength for plates with a centrally located circular hole and under transverse axial compression, $\beta = 1.7$; (e) A comparison of the critical buckling strength, τ_{cr}, with the ultimate strength for plates with a centrally located circular hole and under edge shear, $\beta = 3.3$; (f) A comparison of the critical buckling strength, τ_{cr}, with the ultimate strength for plates with a centrally located circular hole and under edge shear, $\beta = 1.7$. (Note for (a)–(f) symbols: ultimate strength by FEA, w_{opl} = plate initial deflection)

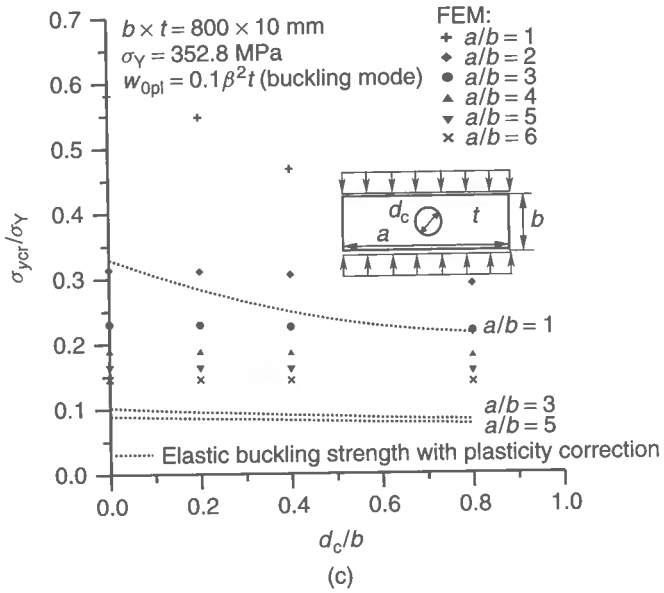

(c)

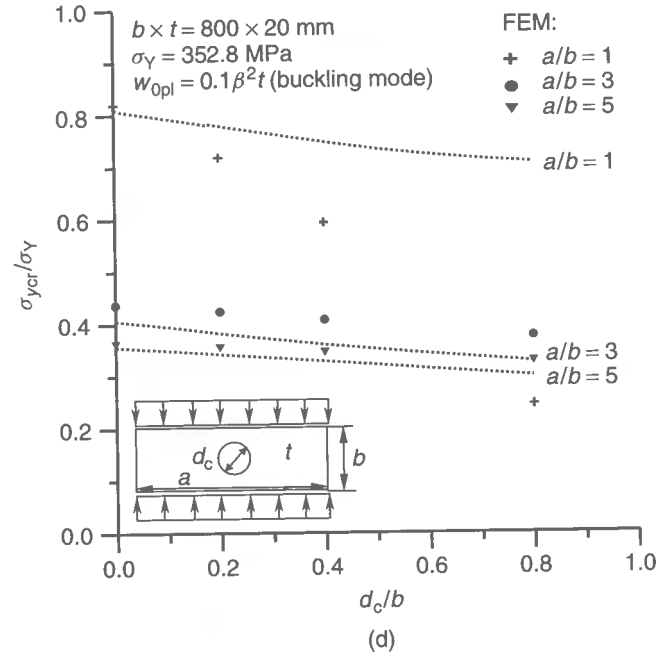

(d)

Figure 3.25 (*continued*)

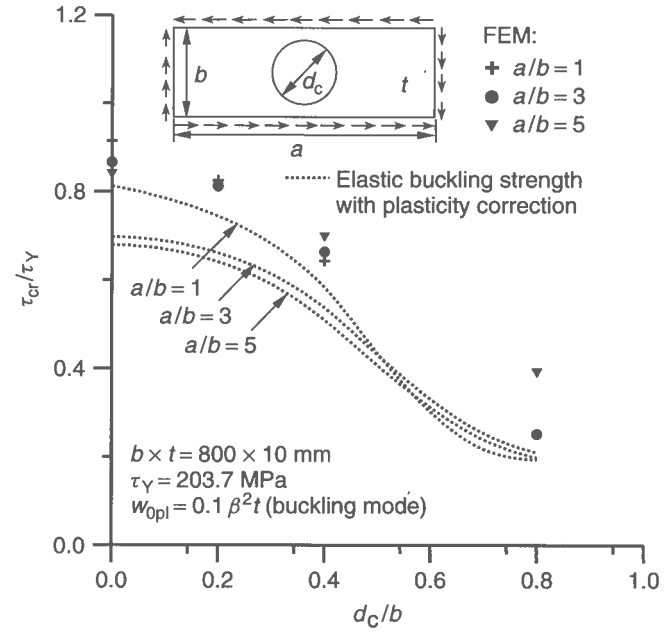

(e)

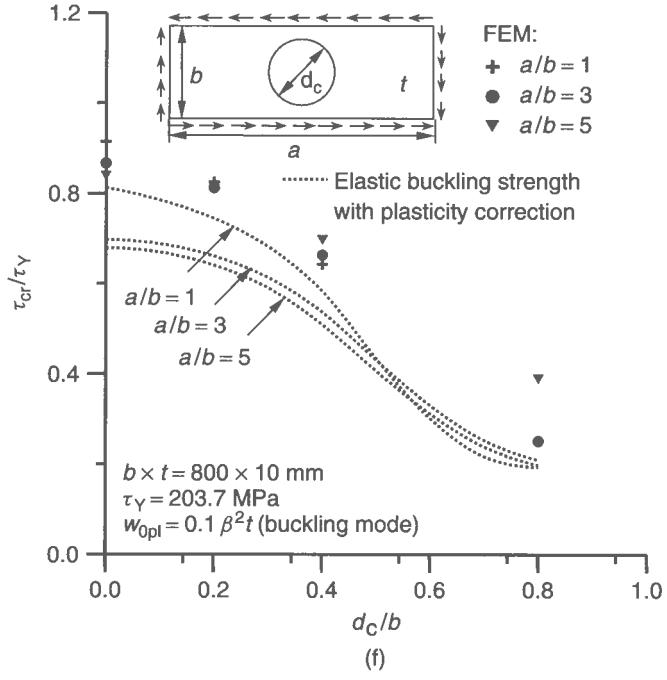

(f)

Figure 3.25 (*continued*)

3.14.2 Combined Loads

For buckling strength design of steel plates under combined longitudinal compression/tension, σ_x, transverse compression/tension, σ_y, and edge shear, τ, the critical buckling strength interaction function, Γ_B, is often expressed as follows:

$$\Gamma_B = \left(\frac{\sigma_x}{\sigma_{xcr}}\right)^2 - \alpha\left(\frac{\sigma_x}{\sigma_{xcr}}\right)\left(\frac{\sigma_y}{\sigma_{ycr}}\right) + \left(\frac{\sigma_y}{\sigma_{ycr}}\right)^2 + \left(\frac{\tau}{\tau_{cr}}\right)^2 - 1 \tag{3.33}$$

where σ_x, σ_y, τ = applied stress components. σ_{xcr}, σ_{ycr} and τ_{cr} represent the critical buckling strength components obtained by the plasticity corrections of $\sigma_{xE,1}$, $\sigma_{yE,1}$ and $\tau_{E,1}$ using the Johnson–Ostenfeld formula, Equation (2.93), respectively. $\alpha = 0$ when both σ_x and σ_y are compressive while $\alpha = 1$ when either σ_x, σ_y or both are tensile. In the usage of Equation (3.33) a compressive stress takes the negative sign while a tensile stress takes the positive sign. Before buckling, the value of Γ_B is smaller than zero, while buckling takes place if Γ_B just reaches zero; buckling has occurred if $\Gamma_B > 0$.

For the buckling design of offshore structures, DNV (1995) proposes the following buckling function:

$$\Gamma_B = \sigma_{eq} - \sigma_{eqcr} \tag{3.34}$$

where $\sigma_{eq} = \sqrt{(\sigma_x^2 + \sigma_y^2 - \sigma_x\sigma_y + 3\tau^2)}$, $\sigma_{eqcr} = \sigma_Y\sqrt{(1 + \lambda_{eq}^4)}$, with

$$\lambda_{eq}^2 = \frac{\sigma_Y}{\sigma_{eq}}\left[\left(\frac{\sigma_x}{\sigma_{xE,1}}\right)^c + \left(\frac{\sigma_y}{\sigma_{yE,1}}\right)^c + \left(\frac{\tau}{\tau_{E,1}}\right)^c\right]^{1/c}$$

and where $c = 2 - b/a$ when $a/b \geq 1$.

Buckling will then occur if $\Gamma_B \geq 0$. It should be noted that Equation (3.34) is valid when axial stress is compressive and assuming that any tensile axial stress is zero. It is important to realize that Equations (3.33) and (3.34) do not usually represent the ULS of relatively thin plates; they can, however, be approximately applied to predict the ultimate strength of relatively thick plates. Also, these equations may not be valid for the design of perforated plates as noted in Section 3.14.1.

3.15 Computer Software ALPS/BUSAP

The buckling strength formulations of plates with or without perforations presented in this chapter are automated within the computer software ALPS/BUSAP, which stands for nonlinear analysis of large plated structures/buckling strength analysis of panels. The program computes the elastic buckling strength of plate panels between support members under combined loads as well as single types of loads. The effect of torsional rigidity at the plate edges is accounted for. The 'critical' buckling strength is computed by plasticity correction of the elastic buckling strength using the Johnson–Ostenfeld formula, Equation (2.93). The program together with the user's manual can be downloaded from the web site noted in the appendices to this book.

References

Bleich, F. (1952). *Buckling strength of metal structures*. McGraw-Hill, New York.

Brown, C.J., Yettram, A.L. & Burnett, M. (1987). Stability of plates with rectangular holes. *ASCE Journal of Structural Engineering*, 113(5): 1111–1116.

DNV (1995). Buckling strength analysis. Classification Notes No. 30.1, Det Norske Veritas, Oslo, July.

Fujikubo, M. & Yao, T. (1999). Elastic local buckling strength of stiffened plate considering plate/stiffener interaction and welding residual stress. *Marine Structures*, 12: 543–564.

Fujikubo, M., Yao, T., Varghese, B., Zha, Y. & Yamamura, K. (1998). Elastic local buckling strength of stiffened plates considering plate/stiffener interaction and lateral pressure. *Proceedings of the International Offshore and Polar Engineering Conference, Montreal*, IV: 292–299.

Hughes, O.F. (1988). *Ship structural design: a rationally-based, computer-aided optimization approach*. The Society of Naval Architects and Marine Engineers, Jersey City, NJ.

JWS (1971). *Handbook of buckling strength of unstiffened and stiffened plates*. The Plastic Design Committee, The Japan Welding Society, Tokyo (in Japanese).

Klöppel, K. & Sheer, J. (1960). *Beulwerte Ausgesteifter Rechteck-platten*. Verlag von Wilhelm Ernst & Sohn, Berlin (in German).

Narayanan, R. & der Avanessian, N.G.V. (1984). Elastic buckling of perforated plates under shear. *Thin-Walled Structures*, 2: 51–73.

Paik, J.K. (1991). An analytical solution of nonlinear behavior of simply supported rectangular plates subjected to biaxial compression. *Journal of the Society of Naval Architects of Korea*, 28(1): 169–181 (in Korean).

Paik, J.K. & Thayamballi, A.K. (2000). Buckling strength of steel plating with elastically restrained edges. *Thin-Walled Structures*, 37: 27–55.

Paulling, J.R. (1988). Strength of ships. Chapter 4 in *Principles of Naval Architecture, Vol. I, Stability and Strength*. The Society of Naval Architects and Marine Engineers, Jersey City, NJ.

Timoshenko, S.P. & Gere, J.M. (1982). *Theory of elastic stability*, Second Edition, McGraw-Hill, London.

Ueda, Y., Rashed, S.M.H. & Paik, J.K. (1987). New interaction equation for plate buckling. *JWRI Transactions*, Joining and Welding Research Institute, Osaka University, Osaka, 14(2): 159–173.

4 Post-Buckling and Ultimate Strength Behavior of Plates

4.1 Fundamentals of Plate Collapse Behavior

While steel plates under predominantly axial tensile loads would fail by gross yielding, the behavior of steel plates under predominantly compressive loads may be classified into five regimes, namely pre-buckling, buckling, post-buckling, collapse (ultimate strength) and post-collapse. Figure 4.1 shows a schematic of the plate collapse behavior under predominantly axial compressive loads.

In the pre-buckling regime, the structural response between loads and displacements is usually linear and the structural component will be stable. As the predominantly compressive stress reaches a critical value, buckling occurs, as previously described in Chapter 3.

Unlike columns, plates buckled in the elastic regime may still be stable in the sense that further loading can be sustained until the ultimate strength is reached, even if the in-plane stiffness significantly decreases after the inception of buckling. In this regard, elastic buckling of plates between stiffeners may in some design cases be allowed to reduce the structural weight. Since the residual strength of a plate is not expected after buckling occurs in the inelastic regime, however, inelastic buckling is sometimes considered to be the ultimate limit state (ULS) of the plate.

As the applied loads increase, the plate eventually reaches the ULS due to expansion of the yielded region. The in-plane stiffness of the collapsed plate takes a 'negative' value in the post-ultimate regime, meaning a high degree of instability. A plate with initial imperfections starts to deflect from the very beginning as the compressive loads increase and so a bifurcation buckling phenomenon does not appear. The ultimate strength of imperfect structures is smaller than that of perfect structures.

The ultimate strength behavior of steel plates normally depends on a variety of influential factors such as geometric/material properties, loading characteristics, initial imperfections (i.e., initial deflections and residual stresses), boundary conditions and existing local damage related to corrosion, fatigue crack and denting.

In the ULS design of steel plates using Equation (1.1) in Chapter 1, the demand indicates the extreme value of applied stresses, while the capacity represents the ultimate

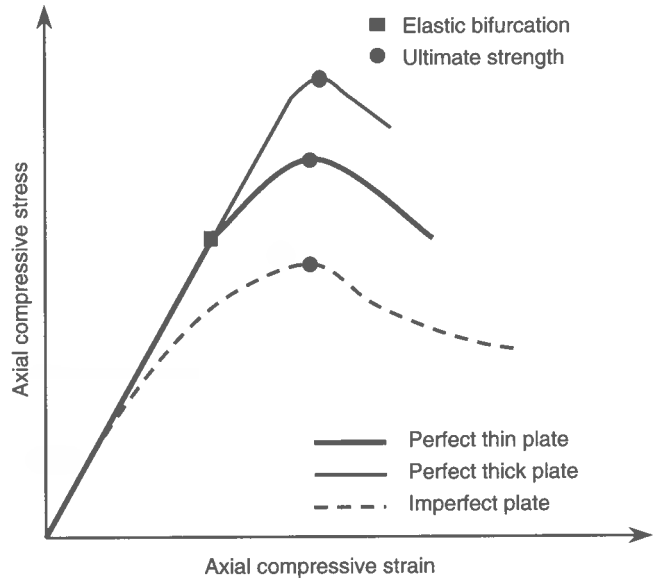

Figure 4.1 A schematic of the collapse behavior of steel plates under predominantly compressive loads

strength. This chapter presents the ultimate strength formulations of steel plates under combined in-plane and lateral pressure loads taking into account the effects of initial imperfections in the form of initial deflection and welding residual stresses. The effects of openings, corrosion wear and fatigue cracking damage on the plate ultimate strength are described. The average stress–strain relationships of steel plates are also presented until and after the ultimate strength is reached.

4.2 Geometric and Material Properties

Figure 4.2 shows a typical steel plate between stiffeners in a stiffened plate structure. The x axis of the plate is taken in any one reference direction and the y axis is taken in the direction normal to the x direction. Therefore, one may not always have to take the plate length to be located along the long edges. One benefit of this type of coordinate system is that computerization of strength calculations is much easier for a large plated structure which is composed of a number of individual plate elements in which some plate elements are 'wide' and others are 'long'. The plate length and breadth are denoted by a and b, respectively. The plate thickness is t.

The material of plates in steel-plated structures is normally either mild steel or high tensile steel, with the yield strength, σ_Y, being typically in the range of 230 to 450 MPa. Young's modulus and Poisson's ratio are E and ν, respectively. The elastic shear modulus is $G = E/[2(1+\nu)]$. The plate bending rigidity is denoted by $D = Et^3/[12(1-\nu^2)]$. The plate reduced slenderness ratio is defined as $\beta = (b/t)\sqrt{(\sigma_Y/E)}$.

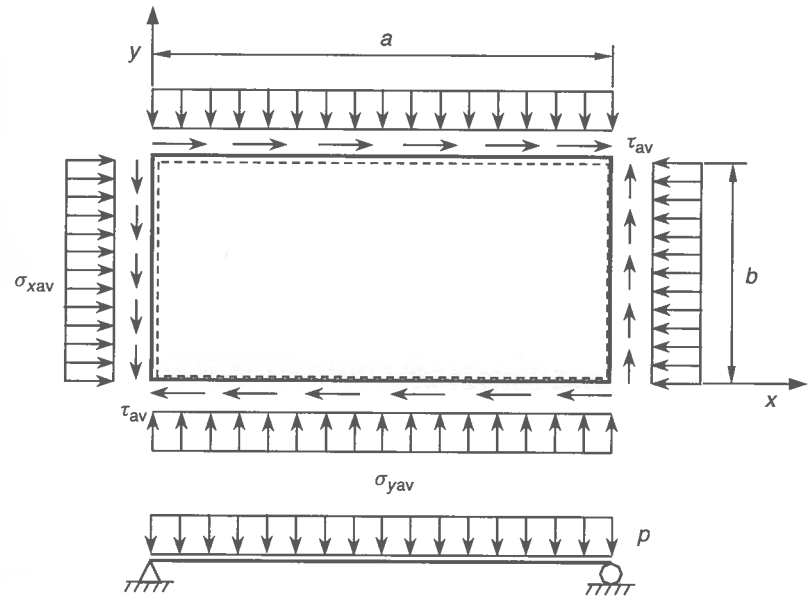

Figure 4.2 A simply supported rectangular plate under biaxial loads, edge shear and lateral pressure

4.3 Loads and Load Effects

When a continuous plated structure is subjected to external loads, the load effects (e.g., stress, deformation) of the plates can be computed by a linear elastic finite element analysis (FEA) or the classical theory of structural mechanics.

The potential number of load components acting on plates is generally of four types (or six load components), namely biaxial loads (i.e., compression or tension), edge shear, biaxial in-plane bending and lateral pressure, as described in Chapter 3. When the plate size is relatively small compared to the entire plated structure, the influence of in-plane bending effects on the plate ultimate strength may be negligible. In contrast, the effect of in-plane bending on the plate buckling strength may need to be accounted for, as previously noted in Chapter 3. In this regard, this chapter deals with three types of loads (or four load components), namely longitudinal compression/tension, σ_{xav}, transverse compression/tension, σ_{yav}, edge shear, $\tau = \tau_{av}$, and lateral pressure loads, p, as shown in Figure 4.2.

In marine structures such as ships, lateral pressure loading arises from water pressure and/or cargo weight. The still-water magnitude of water pressure depends on the ship draft, and the still-water value of cargo pressure is determined by the amount and density of cargo loaded. These still-water pressure values will be normally augmented by wave action and vessel motion. Typically the larger in-plane loads are caused by longitudinal ship hull girder bending, both in still-water and in waves at sea.

In this chapter, it is assumed that the compressive stress is negative and the tensile stress is positive, unless otherwise specified. That is, the longitudinal axial load has a negative value when the corresponding load is compressive, and vice versa.

4.4 Fabrication-related Initial Imperfections

To fabricate steel-plated structures, welding is normally used and thus the post-weld initial imperfections develop in the structure, which may in some cases significantly affect (reduce) the structural capacity. In advanced structural design, therefore, strength calculations of steel plates should accommodate welding-induced initial deflections and residual stresses as parameters of influence. The characteristics of the post-weld initial imperfections are uncertain, and an idealized model is used to represent them, as previously described in Section 1.7 of Chapter 1. The maximum amplitude of the plate initial deflection is w_{opl}, see Figure 1.18 in Chapter 1. The compressive residual stresses in the x and y directions are σ_{rcx} and σ_{rcy}, respectively, while the tensile residual stresses in the x and y directions are σ_{rtx} and σ_{rty}, respectively, see Figure 1.22 in Chapter 1.

4.5 Boundary Conditions

In a continuous plated structure, the edges of the plate elements are usually supported by beam members (e.g., stiffeners). The bending rigidities of the boundary support members are normally quite large compared to that of the plate itself. This implies that the relative lateral deflections of the support members to the plate itself are very small even up to plate collapse. Therefore, it is assumed that the support members at the four plate edges remain in the same plane. The rotational restraints along the plate edges depend on the torsional rigidities of the support members, and these are neither zero nor infinite as previously described in Section 3.10 of Chapter 3.

When predominantly in-plane compressive loads are applied on a continuous plated structure supported by beam members, the buckling pattern of the plates is expected to be asymmetrical, i.e., one plate element will tend to buckle up and the adjacent plate element will tend to deflect down. In this case, i.e., after buckling, rotational restraints along the plate edges can be considered to be small.

When the plated structure is subjected to combined axial compression and lateral pressure loads, however, the buckling pattern of the structure can tend to be symmetrical, at least for large enough pressures, i.e., each adjacent plate element may deflect in the direction of lateral pressure loading. In this case, the edge rotational restraints can become large such that they may be considered to correspond a clamped condition at the beginning of loading. However, if plasticity occurs earlier along the edges where the larger bending moments are developed, the rotational restraints at the yielded edges will then be lessened as the applied loads increase.

In fact, slender stiffeners prone to torsional buckling may even destabilize the plate in the sense that the overall buckling of the stiffened panel, i.e., together with stiffeners, can then occur at a stress level that is smaller than that of a simply supported plate. However, our treatment in this chapter is based on the normal presumption that stiffeners and other support members have been properly designed so that their local instability will not occur prior to failure of the plating. When the stiffeners are very weak, they can buckle together with the plate as part of what is called overall buckling. The design and analysis procedure for the overall buckling of stiffened panels will be treated separately, as will be described later in Chapters 5 and 6.

In some cases, specifically under large lateral pressure loading, the plate edges may not remain straight. This is a special case that must be treated separately. However, as long

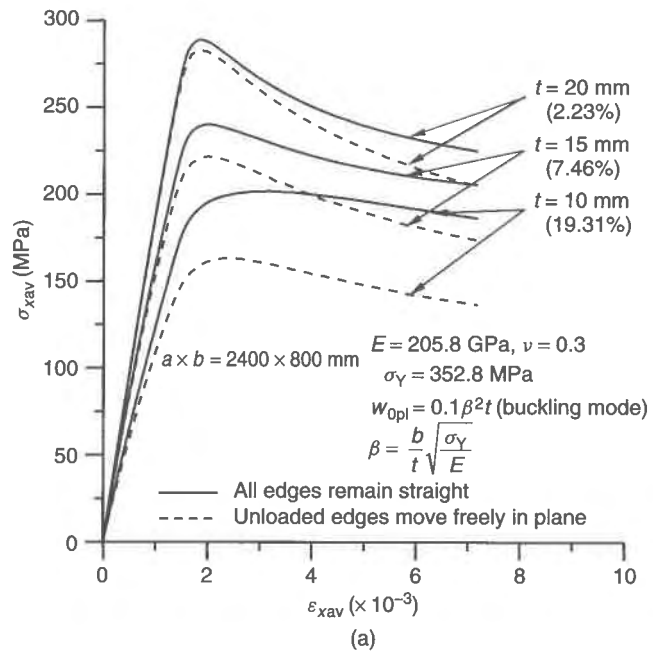

Figure 4.3 Effect of the straight edge condition on the collapse behavior of a simply supported steel plate (a) under longitudinal compression, and (b) under edge shear, as obtained by elastic-plastic large deflection FEA

as the stiffeners are strong enough so that they do not fail prior to buckling of the plate, which is the case that this chapter is concerned with, the plate will fail locally.

In a continuous plated structure when such a hypothesis can be accepted, the edges of individual plate elements will remain almost straight due to the relative structural response to the adjacent plate elements until the ULS is reached.

In this chapter, therefore, it is assumed that the plate edges are simply supported, with zero deflection and zero rotational restraints along four edges, and with all edges kept straight. This is in contrast to our more sophisticated treatment of buckling of plates in Chapter 3, wherein the effects of rotational restraints of support members are accommodated. Part of the reason is mathematical convenience.

Figure 4.3 shows the effect of the straight edge condition on the collapse behavior of a simply supported plate under axial compression or edge shear, as obtained by the nonlinear finite element method. As would be expected, the ultimate strength of a plate with the unloaded edges kept straight is larger than that with the condition that the unloaded edges move freely in plane. For relatively thick plates with $t = 20\,\text{mm}$, the difference of ultimate strength is very small. However, the difference becomes about 20% for relatively thin plates with $t = 10\,\text{mm}$.

Another illustrative example to investigate the effect of the plate boundary condition on the collapse behavior is for a plate under combined axial compression and lateral pressure. Two types of structural idealizations using nonlinear FEA may be relevant: one is a single plate with the condition that all edges are simply supported as shown in Figure 4.4(a) and the other is that a three-bay plate model is taken as the extent of the analysis as shown in Figure 4.4(b). All plate edges are supposed to be simply supported, keeping them straight. In the FEA, the simply supported condition is applied along the transverse frames, while some rotational restraints will be automatically developed due to the action of lateral pressure.

Figure 4.5 shows the progressive collapse behavior on varying the magnitude of lateral pressure, as obtained by nonlinear FEA. It is seen from Figure 4.5 that the ultimate strength of the three-bay plate model is larger than that of the single-bay plate model and the strength increase tends to become larger as the magnitude of lateral pressure increases. This is because the plate edges along the transverse frames become clamped due to the action of lateral pressure and the three-bay plate model automatically takes this effect into account. However, the effect of rotational restraints due to lateral pressure is small and

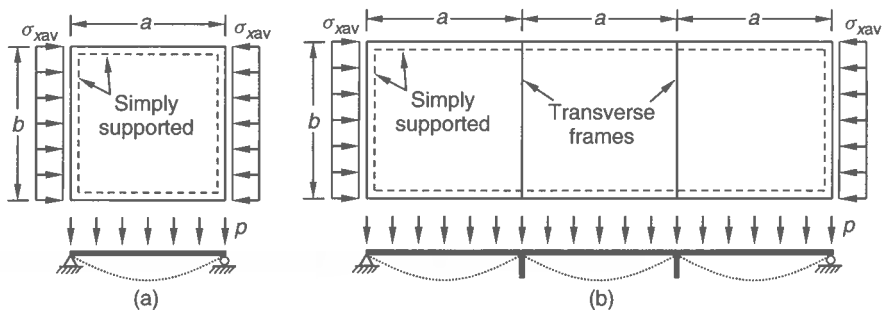

Figure 4.4 A single-bay plate model and (b) a three-bay plate model under combined axial compression and lateral pressure

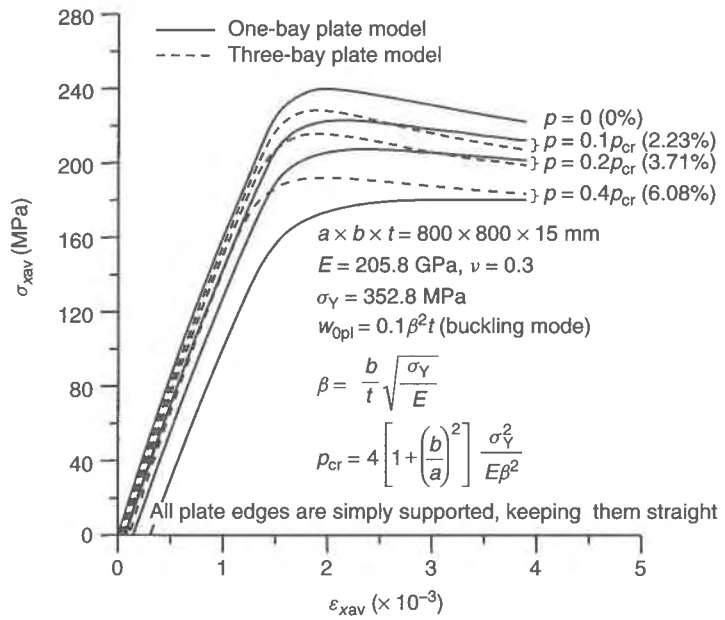

Figure 4.5 Progressive collapse behavior of a plate under combined axial compression and lateral pressure, as obtained by elastic-plastic large deflection FEA

thus the simply supported plate edge condition may be relevant regardless of the lateral pressure load applied.

4.6 Ultimate Strength by Gross Yielding

For plates under predominantly axial tensile loading and/or with very stocky properties, the ULS is reached by gross yielding. In this case, the ULS criterion is typically given by the Mises–Hencky yield condition as follows:

$$\left(\frac{\sigma_{xav}}{\sigma_Y}\right)^2 - \left(\frac{\sigma_{xav}}{\sigma_Y}\right)\left(\frac{\sigma_{yav}}{\sigma_Y}\right) + \left(\frac{\sigma_{yav}}{\sigma_Y}\right)^2 + \left(\frac{\tau_{av}}{\tau_Y}\right)^2 = 1 \tag{4.1}$$

where $\tau_Y = \sigma_Y/\sqrt{3}$.

For any combined load application, it is also usually considered that the plate must satisfy the following design criterion based on gross yielding which is likely to provide an upper limit of the ULS, namely

$$\left(\frac{\sigma_{xav}}{\sigma_Y}\right)^2 - \left(\frac{\sigma_{xav}}{\sigma_Y}\right)\left(\frac{\sigma_{yav}}{\sigma_Y}\right) + \left(\frac{\sigma_{yav}}{\sigma_Y}\right)^2 + \left(\frac{\tau_{av}}{\tau_Y}\right)^2 \le \eta_u \tag{4.2}$$

where η_u = usage factor for the ULS which may be taken as the inverse of the conventional factor of safety.

4.7 Nonlinear Governing Differential Equations of Plates

The post-buckling or large-deflection behavior of plates can be analyzed by solving the two nonlinear governing differential equations of large-deflection plate theory, namely the equilibrium equation and the compatibility equation (Marguerre 1938):

$$D\left(\frac{\partial^4 w}{\partial x^4}+2\frac{\partial^4 w}{\partial x^2\partial y^2}+\frac{\partial^4 w}{\partial y^4}\right) - t\left[\frac{\partial^2 F}{\partial y^2}\frac{\partial^2(w+w_0)}{\partial x^2}-2\frac{\partial^2 F}{\partial x\partial y}\frac{\partial^2(w+w_0)}{\partial x\partial y}+\frac{\partial^2 F}{\partial x^2}\frac{\partial^2(w+w_0)}{\partial y^2}+\frac{p}{t}\right]=0 \quad (4.3a)$$

$$\frac{\partial^4 F}{\partial x^4}+2\frac{\partial^4 F}{\partial x^2\partial y^2}+\frac{\partial^4 F}{\partial y^4} - E\left[\left(\frac{\partial^2 w}{\partial x\partial y}\right)^2-\frac{\partial^2 w}{\partial x^2}\frac{\partial^2 w}{\partial y^2}+2\frac{\partial^2 w_0}{\partial x\partial y}\frac{\partial^2 w}{\partial x\partial y}-\frac{\partial^2 w_0}{\partial x^2}\frac{\partial^2 w}{\partial y^2}-\frac{\partial^2 w}{\partial x^2}\frac{\partial^2 w_0}{\partial y^2}\right]=0 \quad (4.3b)$$

where w, w_0 = added and initial deflections, F = Airy's stress function. When Airy's stress function, F, and the added deflection, w, are known, the stresses inside the plate can be calculated as follows:

$$\sigma_x=\frac{\partial^2 F}{\partial y^2}-\frac{Ez}{1-\nu^2}\left(\frac{\partial^2 w}{\partial x^2}+\nu\frac{\partial^2 w}{\partial y^2}\right) \quad (4.4a)$$

$$\sigma_y=\frac{\partial^2 F}{\partial x^2}-\frac{Ez}{1-\nu^2}\left(\frac{\partial^2 w}{\partial y^2}+\nu\frac{\partial^2 w}{\partial x^2}\right) \quad (4.4b)$$

$$\tau=-\frac{\partial^2 F}{\partial x\partial y}-\frac{Ez}{2(1+\nu)}\frac{\partial^2 w}{\partial x\partial y} \quad (4.4c)$$

where z is the coordinate in the plate thickness direction with $z = 0$ at mid-thickness.

Equations (4.3) are often called the Marguerre equations. By solving the governing differential equations subject to the given boundary conditions, load application and initial imperfections, the membrane stress distribution inside the plate can be calculated and thus it is possible to examine the elastic large-deflection behavior of the plate.

4.8 Elastic Large-deflection Behavior

The in-plane stiffness of perfect plates significantly decreases after buckling, while that of imperfect plates decreases from the very beginning of axial compressive loading. In this section, the effectiveness of plates either with initial imperfections or after buckling is examined, and relevant formulations for representing the plate effective width or length and the average stress–strain relationships are presented.

4.8.1 Combined Longitudinal Axial Load and Lateral Pressure

Non-uniform Membrane Stresses

The elastic large-deflection behavior of a plate under longitudinal axial stress, σ_{xav}, and lateral pressure, p, taking into account the effect of initial imperfections, can be theoretically examined by solving the nonlinear governing differential equations, Equations (4.3), of the plate.

To analytically solve the nonlinear governing differential equations using the energy-principle-based approach, it is necessary to assume relevantly simplified initial and added deflection functions. It is known that for plates under predominantly longitudinal axial compressive loads the deflection term associated with the lowest bifurcation mode plays a dominant role in the elastic large-deflection response, see, for example, Paik & Pedersen (1996), among others. For those purposes where the plate deflection itself is not of primary interest, therefore, the initial deflection function is simplified by including only the buckling mode initial deflection as follows:

$$w_0=A_{0m}\sin\frac{m\pi x}{a}\sin\frac{\pi y}{b} \quad (4.5a)$$

where m is the buckling mode half-wave number in the x direction that primarily depends on the plate aspect ratio. A_{0m} is the amplitude of the buckling mode initial deflection for axial compressive loading, which may be taken as $A_{0m} = B_{0m}w_{opl}$. B_{0m} is defined in Equation (1.10b), while $B_{0m} = 1.0$ is often assumed for practical design purposes. For axial tensile loading, $m = 1$ and $A_{0m} = 0$ are normally adopted.

The added deflection function for analyzing the membrane stress distribution of the plate under predominantly longitudinal axial loads is also assumed including only the buckling mode initial deflection as follows:

$$w=A_m\sin\frac{m\pi x}{a}\sin\frac{\pi y}{b} \quad (4.5b)$$

where A_m = unknown amplitude of the added deflection function, and m is defined in Equation (4.5a).

The deflection functions, Equations (4.5), are used only for the purpose of the membrane stress distribution analysis, while an adequate number of deflection terms should in principle be included for calculating the shape of plate deflection itself.

Considering the idealized initial imperfections, boundary conditions and load application, the membrane stress distribution inside the plate can be analyzed by solving the governing differential equations. To do this, one should start by determining the unknown amplitude of the added deflection, Equation (4.5b), under the applied loading. In the following, the calculation of the membrane stress distribution inside the plate is described in detail. Substitution of Equations (4.5) into Equation (4.3b) results in

$$\frac{\partial^4 F}{\partial x^4}+2\frac{\partial^4 F}{\partial x^2\partial y^2}+\frac{\partial^4 F}{\partial y^4}=-\frac{m^2\pi^4 EA_m(A_m+2A_{0m})}{2a^2b^2}\left(\cos\frac{2m\pi x}{a}+\cos\frac{2\pi y}{b}\right) \quad (4.6)$$

The particular solution, F_P, of the stress function, F, is obtained by solving Equation (4.6) as follows:

$$F_P = \frac{EA_m(A_m + 2A_{0m})}{32}\left(\frac{a^2}{m^2b^2}\cos\frac{2m\pi x}{a} + \frac{m^2b^2}{a^2}\cos\frac{2\pi y}{b}\right) \tag{4.7}$$

The homogeneous solution, F_H, of the stress function, F, which satisfies the loading condition is given by treating the welding-induced residual stress as an initial stress parameter, namely

$$F_H = (\sigma_{xav} + \sigma_{rx})\frac{y^2}{2} + \sigma_{ry}\frac{x^2}{2} \tag{4.8}$$

where σ_{rx}, σ_{ry} = welding-induced residual stresses as defined in Equation (1.13) of Chapter 1.

The applicable stress function, F, may then be expressed as the sum of the particular solution and the homogeneous solution as follows:

$$F = (\sigma_{xav} + \sigma_{rx})\frac{y^2}{2} + \sigma_{ry}\frac{x^2}{2} + \frac{EA_m(A_m + 2A_{0m})}{32}\left(\frac{a^2}{m^2b^2}\cos\frac{2m\pi x}{a} + \frac{m^2b^2}{a^2}\cos\frac{2\pi y}{b}\right) \tag{4.9}$$

By substituting Equations (1.13), (4.5) and (4.9) into Equation (4.3a) and applying the Galerkin method (Fletcher 1984), the following equation is obtained:

$$\int_0^a\int_0^b \left\{D\left(\frac{\partial^4 w}{\partial x^4} + 2\frac{\partial^4 w}{\partial x^2\partial y^2} + \frac{\partial^4 w}{\partial y^4}\right) - t\left[\frac{\partial^2 F}{\partial y^2}\frac{\partial^2(w+w_0)}{\partial x^2} - 2\frac{\partial^2 F}{\partial x\partial y}\frac{\partial^2(w+w_0)}{\partial x\partial y} + \frac{\partial^2 F}{\partial x^2}\frac{\partial^2(w+w_0)}{\partial y^2} + \frac{p}{t}\right]\right\} \times \sin\frac{m\pi x}{a}\sin\frac{\pi y}{b}\,dx\,dy = 0 \tag{4.10}$$

By performing the integration of Equation (4.10) over the entire plate, a third-order equation with respect to the unknown variable, A_m, is obtained. For the integration of Equation (4.10), it may be approximated that the contribution of lateral pressure to nonlinear membrane stresses arises only from the deflection component of $m = 1$ and it is linearly superposed to those by in-plane loads. This results in

$$C_1A_m^3 + C_2A_m^2 + C_3A_m + C_4 = 0 \tag{4.11}$$

where

$$C_1 = \frac{\pi^2 E}{16}\left(\frac{m^4b}{a^3} + \frac{a}{b^3}\right)$$

$$C_2 = \frac{3\pi^2 EA_{0m}}{16}\left(\frac{m^4b}{a^3} + \frac{a}{b^3}\right)$$

$$C_3 = \frac{\pi^2 EA_{0m}^2}{8}\left(\frac{m^4b}{a^3} + \frac{a}{b^3}\right) + \frac{m^2b}{a}(\sigma_{xav} + \sigma_{rex}) + \frac{a}{b}\sigma_{rey} + \frac{\pi^2 D}{t}\frac{m^2}{ab}\left(\frac{mb}{a} + \frac{a}{mb}\right)^2$$

$$C_4 = A_{0m}\left[\frac{m^2b}{a}(\sigma_{xav} + \sigma_{rex}) + \frac{a}{b}\sigma_{rey}\right] - \frac{16ab}{\pi^4 t}p$$

$$\sigma_{rex} = \sigma_{rcx} + \frac{2}{b}(\sigma_{rtx} - \sigma_{rcx})\left(b_t - \frac{b}{2\pi}\sin\frac{2\pi b_t}{b}\right)$$

$$\sigma_{rey} = \sigma_{rcy} + \frac{2}{a}(\sigma_{rty} - \sigma_{rcy})\left(a_t - \frac{a}{2m\pi}\sin\frac{2m\pi a_t}{a}\right)$$

with σ_{rcx}, σ_{rcy}, σ_{rtx}, σ_{rty}, a_t, b_t as defined in Figure 1.22 of Chapter 1.

The solution of Equation (4.11) can be obtained by the so-called Cardano method as follows (or refer to the FORTRAN computer subroutine CARDANO given in the appendices to this book):

$$A_m = -\frac{C_2}{3C_1} + k_1 + k_2 \tag{4.12}$$

where

$$k_1 = \left(-\frac{Y}{2} + \sqrt{\frac{Y^2}{4} + \frac{X^3}{27}}\right)^{1/3}, \quad k_2 = \left(-\frac{Y}{2} - \sqrt{\frac{Y^2}{4} + \frac{X^3}{27}}\right)^{1/3}, \quad X = \frac{C_3}{C_1} - \frac{C_2^2}{3C_1^2},$$

$$Y = \frac{2C_2^3}{27C_1^3} - \frac{C_2C_3}{3C_1^2} + \frac{C_4}{C_1}$$

If the axial compressive stress reaches the buckling stress, the perfect plate, i.e., without initial deflection, buckles, while no bifurcation phenomenon occurs in plates with initial deflection. It is of interest to calculate the compressive buckling (bifurcation) strength of plates taking into account the effect of the welding-induced residual stresses.

Using Equation (4.11) or (4.12), the buckling (bifurcation) strength equation of perfect plates, i.e., without initial deflection but with welding-induced residual stresses, under longitudinal compressive loads alone, i.e., without lateral pressure loading, can be derived. When the initial deflection does not exist, i.e., $A_{0m} = 0$, Equation (4.12) will be given since $C_2 = C_4 = 0$ as follows:

$$A_m = \sqrt{-\frac{C_3}{C_1}} \tag{4.13a}$$

where

$$C_1 = \frac{\pi^2 E}{16}\left(\frac{m^4b}{a^3} + \frac{a}{b^3}\right), C_3 = \frac{\pi^2 D}{t}\frac{m^2}{ab}\left(\frac{mb}{a} + \frac{a}{mb}\right)^2 + \frac{m^2b}{a}(\sigma_{xav} + \sigma_{rex}) + \frac{a}{b}\sigma_{rey}$$

Interestingly, Equation (4.13a) can be further simplified without residual stresses, i.e., when both initial imperfections and lateral pressure are not involved, as follows:

$$A_m = \left\{-\frac{16}{\pi^2 E(m^4/a^4 + 1/b^4)}\left[\frac{m^2}{a^2}\sigma_{xav} + \frac{\pi^2 D}{t}\left(\frac{m^2}{a^2} + \frac{1}{b^2}\right)^2\right]\right\}^{1/2} \tag{4.13b}$$

Since the lateral deflection immediately before the plate buckles must in this case be zero, i.e., $A_m = 0$, the following equation is obtained from Equation (4.13a):

$$\frac{m^2 b}{a}(\sigma_{xav} + \sigma_{rex}) + \frac{a}{b}\sigma_{rey} + \frac{\pi^2 D}{t}\frac{m^2}{ab}\left(\frac{mb}{a} + \frac{a}{mb}\right)^2 = 0 \tag{4.14a}$$

or from Equation (4.13b) when the welding residual stress does not exist,

$$\frac{m^2}{a^2}\sigma_{xav} + \frac{\pi^2 D}{t}\left(\frac{m^2}{a^2} + \frac{1}{b^2}\right)^2 = 0 \tag{4.14b}$$

Equation (4.14a) represents the elastic buckling equation for the plate under longitudinal axial compression taking into account the effect of the welding-induced residual stresses. Hence the elastic buckling strength of a plate under axial compressive loads in the x direction is given from Equations (4.14a) by replacing σ_{xav} with σ_{xE} as follows:

$$\sigma_{xE} = -\frac{\pi^2 D}{b^2 t}\left(\frac{mb}{a} + \frac{a}{mb}\right)^2 - \sigma_{rex} - \frac{a^2}{m^2 b^2}\sigma_{rey} \tag{4.15}$$

where the second and third terms on the right hand side of Equation (4.15) reflect the effect of welding-induced residual stresses on the plate buckling strength.

The buckling half-wave number, m, herein depends on the welding-induced residual stress as well as the plate dimensions. m is then determined from Equation (4.15) as a minimum integer satisfying the following condition since the buckling load must be identical at the transition of buckling half waves, namely

$$\frac{\pi^2 D}{b^2 t}\left(\frac{mb}{a} + \frac{a}{mb}\right)^2 + \frac{a^2}{m^2 b^2}\sigma_{rey} \le \frac{\pi^2 D}{b^2 t}\left[\frac{(m+1)b}{a} + \frac{a}{(m+1)b}\right]^2 + \frac{a^2}{(m+1)^2 b^2}\sigma_{rey} \tag{4.16a}$$

Without the post-weld residual stresses in the y axis normal to the loading direction, i.e., when $\sigma_{rey} = 0$, Equation (4.16a) simplifies to the well-known condition (Timoshenko & Woinowsky-Krieger 1981)

$$\frac{a}{b} \le \sqrt{m(m+1)} \tag{4.16b}$$

For interests of simplicity, the buckling half-wave number in the x direction may often be determined from Equation (4.16b), i.e., by neglecting the effect of residual stress.

Once the added deflection amplitude, A_m, and Airy's stress function, F, are determined, the membrane stresses inside the plate under longitudinal axial and lateral pressure loading can then be given from Equations (4.4). Figure 4.6 shows a typical example of the axial membrane stress distribution inside a plate under predominantly longitudinal compressive loading before and after buckling occurs.

It is important to realize that the membrane stress distribution in the loading (x) direction can become non-uniform as the plate deflects, due to many causes including buckling, initial deflection or lateral pressure loading. The membrane stress distribution in the y direction also becomes non-uniform as long as the unloaded plate edges remain straight,

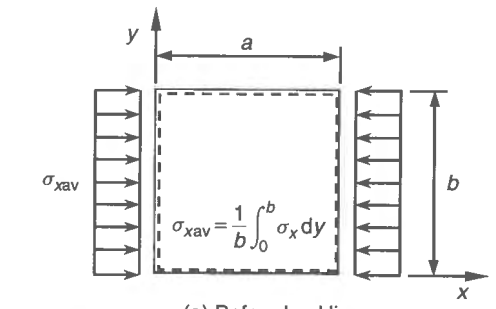

(a) Before buckling

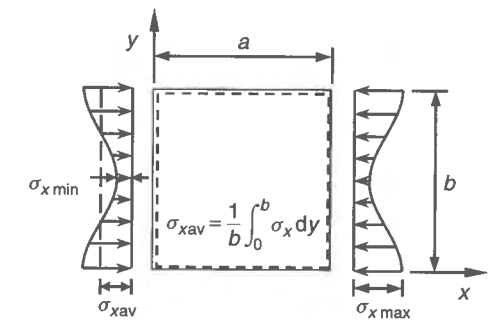

(b) After buckling, unloaded edges move freely in plane

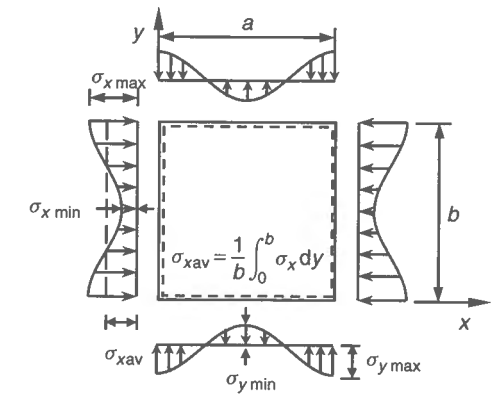

(c) After buckling, unloaded edges remain straight

Figure 4.6 Membrane stress distribution inside the plate under predominantly longitudinal compressive loads

while no membrane stresses will develop in the y direction if the unloaded plate edges move freely in plane.

As is apparent from Figure 4.6, the maximum compressive membrane stresses are developed around the plate edges that remain straight, while the minimum membrane stresses occur in the middle of the plate where a membrane tension field is formed by the plate deflection since the plate edges remain straight. The location of the maximum compressive stresses depends on the residual stresses. If there are no residual stresses the

maximum compressive stresses will develop along the edges. On the other hand, when the residual stresses do exist, the maximum compressive stresses are found inside the plate at the limits of the tensile residual stress block breadths from the plate edges as shown in Figure 4.7.

The maximum or minimum membrane stresses of the plate under combined σ_{xav} and p in the x and y directions are determined from Equations (4.4) as follows (for the symbols related to the residual stresses, Figure 1.22 in Chapter 1 is referred to):

$$\sigma_{x\,\max} = \sigma_x|_{y=b_t,\,b-b_t} \tag{4.17a}$$

$$\sigma_{x\,\min} = \sigma_x|_{y=b/2} \tag{4.17b}$$

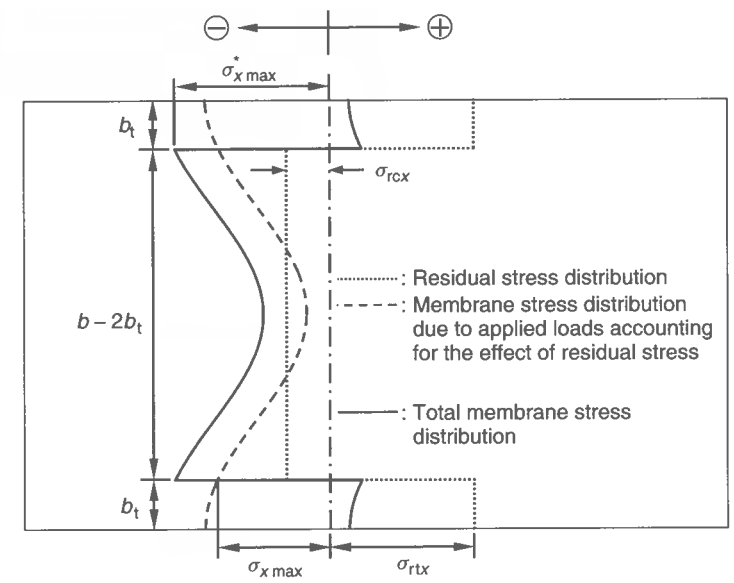

(a) x direction

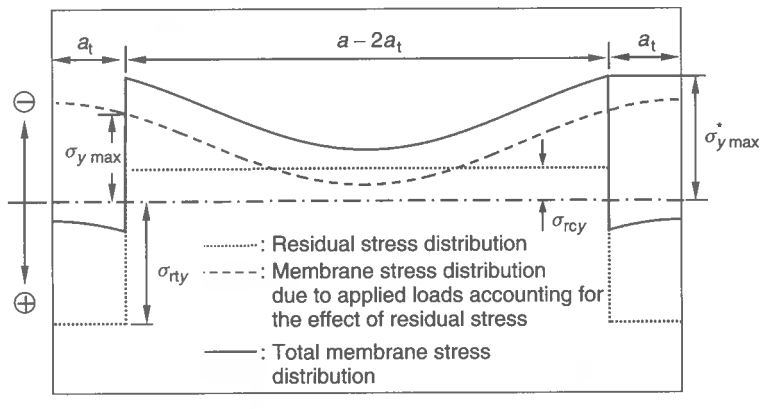

(b) y direction

Figure 4.7 A schematic of the total membrane stress distribution inside the plate

$$\sigma_{y\,\max} = \sigma_y|_{x=a_t,\,a-a_t} \tag{4.17c}$$

$$\sigma_{y\,\min} = \sigma_y|_{x=a/2} \tag{4.17d}$$

where the subscript 'max' or 'min' indicates the maximum or minimum membrane stresses. Equations (4.17) are given in detail as follows:

$$\sigma_{x\,\max} = \sigma_{xav} - \rho_x \frac{m^2\pi^2 EA_m(A_m + 2A_{0m})}{8a^2}\cos\frac{2\pi b_t}{b} \tag{4.18a}$$

$$\sigma_{x\,\min} = \sigma_{xav} + \rho_x \frac{m^2\pi^2 EA_m(A_m + 2A_{0m})}{8a^2} \tag{4.18b}$$

$$\sigma_{y\,\max} = -\rho_x \frac{\pi^2 EA_m(A_m + 2A_{0m})}{8b^2}\cos\frac{2m\pi a_t}{a} \tag{4.18c}$$

$$\sigma_{y\,\min} = \rho_x \frac{\pi^2 EA_m(A_m + 2A_{0m})}{8b^2} \tag{4.18d}$$

where Equations (4.18) implicitly include the lateral pressure, p, as a secondary load parameter.

In Equations (4.18), ρ_x is a correction factor. For a square or long plate, the plate deflection is normally quite similar to a sinusoidal pattern as given by Equations (4.5). For a wide plate under predominantly longitudinal compressive loading, however, the plate deflection may be somewhat different from the sinusoidal pattern as it normally takes the so-called 'bath tub' (or bulb) shape around the plate edges, while the deflected shape in the middle part of the plate is nearly flat, see Figure 4.8(a). Due to the bath-tub-type deflection, the rotation and deflection around the plate edges are normally larger than those of the sinusoidal pattern, resulting in larger values of the membrane stresses.

This implies that the presumed deflection functions, Equations (4.5), with one buckling mode term may not be valid further for a wide plate under compression in the x direction, and a more refined deflection function, i.e., with deflection terms of at least more than 2, may be needed. However, it is in this case not straightforward to analytically solve the nonlinear governing differential equations.

As an easier alternative, while keeping the deflection functions of Equations (4.5), the maximum and minimum membrane stresses along the edges of the wide plate under predominantly longitudinal axial compressive loading are approximately corrected by introducing a factor, ρ_x, to account for the bath tub shape deflection effects.

The correction factor, ρ_x, of Equations (4.18) may be empirically determined by curve fitting based on nonlinear finite element computations obtained for plates by varying the aspect ratio and the load application. For instance, ρ_x may be given in terms of the aspect ratio as follows:

$$\rho_x = \begin{cases} 0.2(b/a - \sqrt{2}) + 2.0 & \text{for } a/b \le 1/\sqrt{2} \\ 1.0 & \text{for } a/b > 1/\sqrt{2} \end{cases} \tag{4.19}$$

where the large-deflection-related terms of membrane stresses are simply amplified to account for the effect of the bath-tub-type deflection pattern. Figure 4.8(b) plots Equation (4.19). ρ_x jumps at $a/b = 1/\sqrt{2}$ where the bifurcation buckling mode is changed.

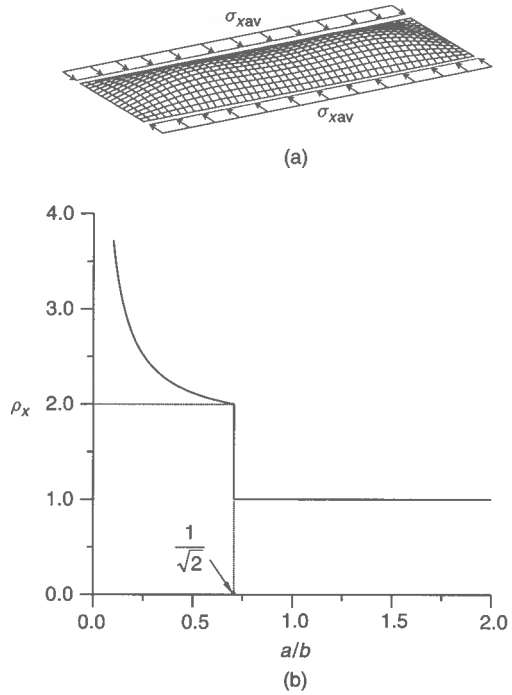

Figure 4.8 The 'bath tub' shape deflection of a wide plate under axial compression; The correction factor, ρ_x, as a function of the plate aspect ratio

The maximum and minimum membrane stress formulations may be simplified when neither initial imperfections nor lateral pressure loads are involved, as follows:

$$\sigma_{x\,\max} = a_1\sigma_{xav} + a_2,\ \sigma_{x\,\min} = b_1\sigma_{xav} + b_2,\ \sigma_{y\,\max} = c_1\sigma_{xav} + c_2,\ \sigma_{y\,\min} = d_1\sigma_{xav} + d_2 \tag{4.20}$$

where

$$a_1 = 1 + \rho_x \frac{2m^4}{a^4(m^4/a^4 + 1/b^4)},\quad a_2 = \rho_x \frac{2m^2}{a^2(m^4/a^4 + 1/b^4)} \frac{\pi^2 D}{t}\left(\frac{m^2}{a^2} + \frac{1}{b^2}\right)^2$$

$$b_1 = 1 - \rho_x \frac{2m^4}{a^4(m^4/a^4 + 1/b^4)},\quad b_2 = -\rho_x \frac{2m^2}{a^2(m^4/a^4 + 1/b^4)} \frac{\pi^2 D}{t}\left(\frac{m^2}{a^2} + \frac{1}{b^2}\right)^2$$

$$c_1 = \rho_x \frac{2m^2}{a^2b^2(m^4/a^4 + 1/b^4)},\quad c_2 = \rho_x \frac{2}{b^2(m^4/a^4 + 1/b^4)} \frac{\pi^2 D}{t}\left(\frac{m^2}{a^2} + \frac{1}{b^2}\right)^2$$

$$d_1 = -\rho_x \frac{2m^2}{a^2b^2(m^4/a^4 + 1/b^4)},\quad d_2 = -\rho_x \frac{2}{b^2(m^4/a^4 + 1/b^4)} \frac{\pi^2 D}{t}\left(\frac{m^2}{a^2} + \frac{1}{b^2}\right)^2$$

Effective Width Formula

Equations (2.19) in Chapter 2 are widely used to evaluate the post-buckling strength of plates under uniaxial compression. As previously noted in Section 2.5.3 of Chapter 2, however, the plate effective width for strength purposes should in general be evaluated by taking into account the effects of both buckling and shear lag, the former arising

from axial compression and the latter being due to lateral pressure loads when both are concurrently involved.

The effective width of plates with initial imperfections under combined in-plane and lateral pressure loads is typically defined as the ratio of the average stress to the maximum stress as follows:

$$\frac{b_e}{b} = \frac{\sigma_{xav}}{\sigma_{x\,\max}} \tag{4.21a}$$

where $\sigma_{x\,\max}$ is the maximum compressive stress which is expressed as a function of combined in-plane and lateral pressure loads as well as initial imperfections, as defined in Equation (4.18a). b_e may also be possibly called the 'effective breadth' if lateral pressure, p, exists, because the shear lag effect in that case also develops.

It is of interest to calculate the ultimate effective width, b_{eu}, at the ULS of the plate which can be obtained from Equation (4.21a) when $\sigma_{xav} = \sigma_{xu}$ as follows:

$$\frac{b_{eu}}{b} = \frac{\sigma_{xu}}{\sigma^u_{x\,\max}} \tag{4.21b}$$

where $\sigma^u_{x\,\max} = \sigma_{x\,\max}$ at $\sigma_{xav} = \sigma_{xu}$, σ_{xu} = plate ultimate strength as will be defined later in Section 4.9.2.

Equation (4.21b) explicitly takes into account the influence of initial imperfections and lateral pressure as parameters of influence. In contrast, the more typical approach in this regard is exemplified by Faulkner (1975) who suggests an empirical effective width formula for simply supported steel plates under longitudinal compression alone, i.e., without lateral pressure, at the ULS as follows:

$$\frac{b_{eu}}{b} = \begin{cases} 1.0 & \text{for } \beta \le 1 \\ 2/\beta - 1/\beta^2 & \text{for } \beta > 1 \end{cases} \tag{4.21c}$$

where Equation (4.21c) implicitly involves the influence of initial imperfections at an 'average' level. In some design codes, the terms 2 and 1 for $\beta > 1$ are changed to 1.8 and 0.9, respectively.

Figure 4.9 plots Equation (4.21a) with increasing σ_{xav}, varying plate slenderness ratio, initial deflections, residual stresses and lateral pressure. The Faulkner formula, Equation (4.21c), is also shown for comparison. The plate ultimate strength, σ_{xu}, as obtained from Section 4.9.2, is also plotted. The Faulkner formula corresponds well to the effective width only for relatively thick plates with an 'average' level of initial imperfections. As is apparent from Figure 4.9, the plate effective width varies with the different levels of initial imperfections as well as applied loads, and Equation (4.21a) or (4.21b) thus embodies the nature of the plate effective width better. It is evident from Figure 4.9(c) that the lateral pressure is a significant factor influencing (reducing) the plate effective 'breadth' as would be expected.

It is often useful to derive a closed-form expression of the reduced (tangent) effective width representing the in-plane effectiveness of the buckled plate, namely

$$\frac{b^*_e}{b} = \left(\frac{\partial\sigma_{x\,\max}}{\partial\sigma_{xav}}\right)^{-1} \tag{4.22}$$

where b^*_e = reduced (tangent) effective width.

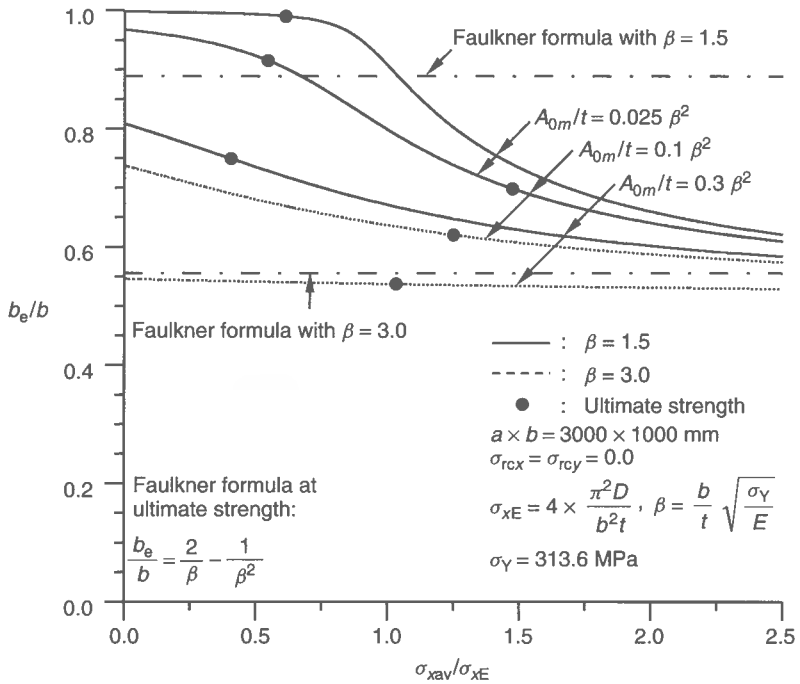

(a) Effect of initial deflection, no welding-induced residual stresses

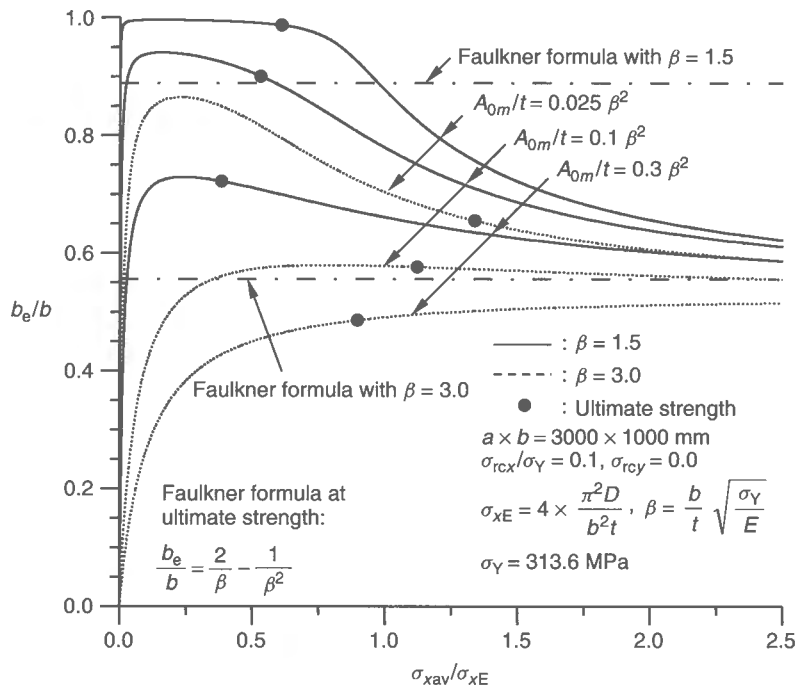

(b) Effect of initial deflection and welding-induced residual stresses

Figure 4.9 Variation of the effective width of a simply supported plate under uniaxial compression (σ_{xE} = elastic compressive buckling stress)

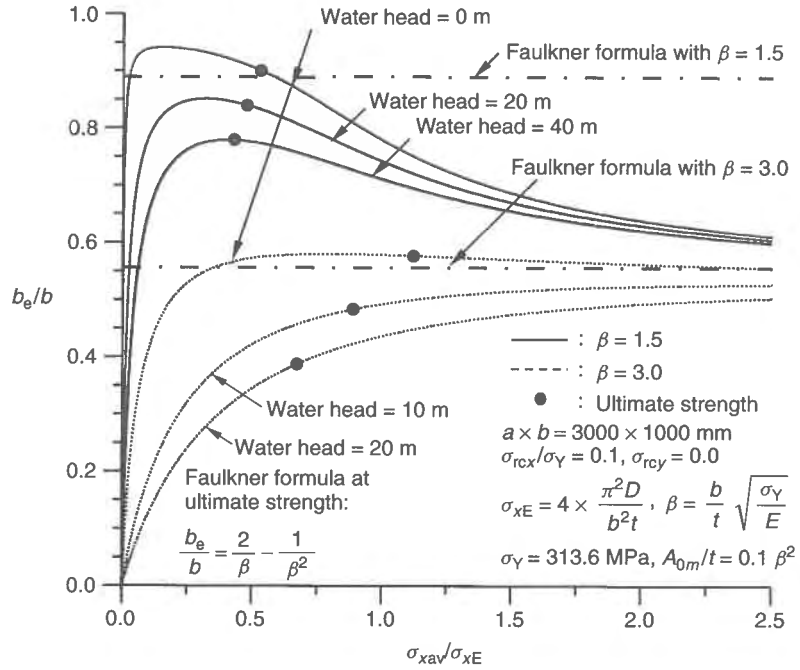

(c) Effect of lateral pressure

Figure 4.9 (*continued*)

When both initial imperfections and lateral pressure are not involved, the plate effective width formula can be expressed from Equation (4.21a) as a function of the average stress as follows (since $\sigma_{x\max} = a_1\sigma_{xav} + a_2$ from Equation (4.20)):

$$\frac{b_e}{b} = \frac{\sigma_{xav}}{a_1\sigma_{xav} + a_2} \tag{4.23a}$$

or as a function of the average strain since $\sigma_{x\max} = a_1\sigma_{xav} + a_2 = E\varepsilon_{xav}$,

$$\frac{b_e}{b} = \frac{1}{a_1}\left(1 - \frac{a_2}{E}\frac{1}{\varepsilon_{xav}}\right) \tag{4.23b}$$

The reduced effective width is obtained from Equation (4.22) when both initial imperfections and lateral pressure are not involved, as follows:

$$\frac{b_e^*}{b} = \frac{1}{a_1} \tag{4.24}$$

Average Stress–Strain Relationship

For imperfect plates under longitudinal axial compression and lateral pressure, the average stress–strain relationship can be given as long as the unloaded edges remain straight, as follows:

$$\varepsilon_{xav} = \frac{1}{E}\sigma_{x\max} = \frac{1}{E}\frac{b}{b_e}\sigma_{xav} \quad \text{or} \quad \sigma_{xav} = \frac{b_e}{b}E\varepsilon_{xav} \tag{4.25a}$$

The incremental form of Equation (4.25a) is given by

$$\Delta\varepsilon_{xav} = \frac{1}{E}\left(\frac{\partial\sigma_{x\,max}}{\partial\sigma_{xav}}\right)\Delta\sigma_{xav} \quad \text{or} \quad \Delta\sigma_{xav} = \left(\frac{\partial\sigma_{x\,max}}{\partial\sigma_{xav}}\right)^{-1} E\,\Delta\varepsilon_{xav} \tag{4.25b}$$

where the prefix, Δ, represents the increment of the variable (throughout this chapter). The numerical approach is often more pertinent for the computation of $\partial\sigma_{x\,max}/\partial\sigma_{xav}$ with infinitesimal stress variations around σ_{xav}.

When both initial imperfections and lateral pressure are not involved, substitution of Equation (4.23b) into Equation (4.25a) results in

$$\sigma_{xav} = \frac{1}{a_1}(E\varepsilon_{xav} - a_2) \tag{4.26a}$$

The incremental form of Equation (4.26a) is then given by

$$\Delta\sigma_{xav} = \frac{E}{a_1}\Delta\varepsilon_{xav} = E^*\Delta\varepsilon_{xav} \tag{4.26b}$$

where

$$E^* = \frac{E}{a_1} = E/\left(1 + \rho_x\frac{2m^4}{m^4 + a^4/b^4}\right)$$

is the effective Young's modulus (tangent modulus) after buckling.

As may be surmised from Equation (4.26b), the tangent modulus of the buckled plate does not change with the applied loads, while it is a function of the plate aspect ratio. Figure 4.10 shows the variation of the tangent modulus of the buckled plate as a function of the plate aspect ratio. It is seen that the effective tangent modulus varies in a cyclic pattern with regard to a mean equal to $E^*/E = 0.5$, and for shorter plates the effect of the aspect ratio is more significant.

4.8.2 Combined Transverse Axial Load and Lateral Pressure

Non-uniform Membrane Stresses

When the plate is subjected to combined transverse axial stress, σ_{yav}, and lateral pressure, p, the dominant term of the initial and added deflection functions can be assumed to take the buckling mode as follows:

$$w_0 = A_{0n}\sin\frac{\pi x}{a}\sin\frac{n\pi y}{b} \tag{4.27a}$$

$$w = A_n\sin\frac{\pi x}{a}\sin\frac{n\pi y}{b} \tag{4.27b}$$

where n = buckling half-wave number in the y direction, A_{0n} = initial deflection amplitude, A_n = unknown amplitude of the added deflection function, and $n = 1$ and $A_{0n} = 0$ are normally used for axial tensile loading.

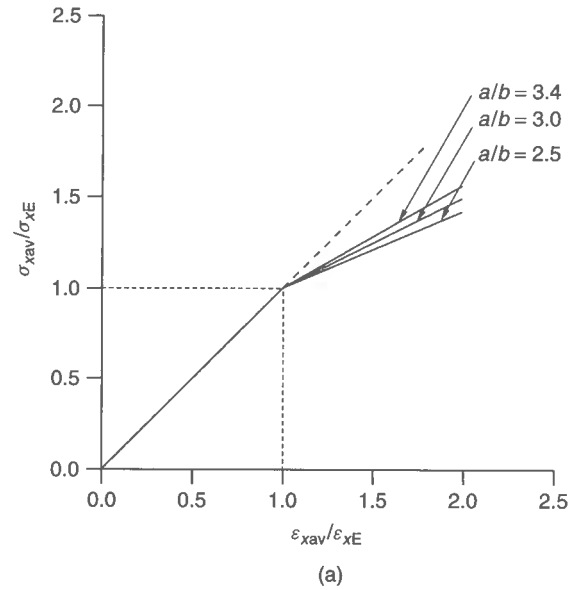

Figure 4.10 The average stress–strain curves of a perfect plate under uniaxial compression in the elastic regime (ε_{xE} = average axial compressive strain at $\sigma_{xav} = \sigma_{xE}$); Variation of the reduced tangent modulus after buckling as a function of the plate aspect ratio

By solving the governing differential equations, Equations (4.3), together with Equations (4.27), the unknown amplitude, A_n, of the added deflection function of Equation (4.27b) can be obtained by the solution of the following equation, in a similar manner to Section 4.8.1:

$$C_1A_n^3 + C_2A_n^2 + C_3A_n + C_4 = 0 \tag{4.28}$$

where

$$C_1 = \frac{\pi^2 E}{16}\left(\frac{b}{a^3} + \frac{n^4 a}{b^3}\right)$$

$$C_2 = \frac{3\pi^2 E A_{0n}}{16}\left(\frac{b}{a^3} + \frac{n^4 a}{b^3}\right)$$

$$C_3 = \frac{\pi^2 E A_{0n}^2}{8}\left(\frac{b}{a^3} + \frac{n^4 a}{b^3}\right) + \frac{b}{a}\sigma_{rex} + \frac{n^2 a}{b}(\sigma_{yav} + \sigma_{rey}) + \frac{\pi^2 D}{t}\frac{n^2}{ab}\left(\frac{b}{na} + \frac{na}{b}\right)^2$$

$$C_4 = A_{0n}\left[\frac{b}{a}\sigma_{rex} + \frac{n^2 a}{b}(\sigma_{yav} + \sigma_{rey})\right] - \frac{16ab}{\pi^4 t}p$$

$$\sigma_{rex} = \sigma_{rcx} + \frac{2}{b}(\sigma_{rtx} - \sigma_{rcx})\left(b_t - \frac{b}{2n\pi}\sin\frac{2n\pi b_t}{b}\right)$$

$$\sigma_{rey} = \sigma_{rcy} + \frac{2}{a}(\sigma_{rty} - \sigma_{rcy})\left(a_t - \frac{a}{2\pi}\sin\frac{2\pi a_t}{a}\right)$$

Again, it is approximated that the contribution of lateral pressure to nonlinear membrane stresses arises only from the lateral deflection component of $n = 1$. Equation (4.28) can be solved with regard to the unknown amplitude, A_n, of the added deflection function by applying Equation (4.12) or the computer subroutine CARDANO given in the appendices to this book. For a perfect plate, i.e., without initial deflections but with welding-induced residual stresses, the elastic buckling stress under transverse compressive loads will be determined with $A_{0n} = 0$ immediately before buckling takes place. We thus have

$$\sigma_{yE} = -\frac{\pi^2 D}{a^2 t}\left(\frac{b}{na} + \frac{na}{b}\right)^2 - \frac{b^2}{n^2 a^2}\sigma_{rex} - \sigma_{rey} \tag{4.29}$$

where the second and third terms on the right hand side reflect the effect of welding-induced residual stresses.

The buckling half-wave number, n, can be determined as the minimum integer satisfying the following condition since buckling load must be identical at the transition of buckling half waves, namely

$$\frac{\pi^2 D}{a^2 t}\left(\frac{b}{na} + \frac{na}{b}\right)^2 + \frac{b^2}{n^2 a^2}\sigma_{rex} \le \frac{\pi^2 D}{a^2 t}\left[\frac{b}{(n+1)a} + \frac{(n+1)a}{b}\right]^2 + \frac{b^2}{(n+1)^2 a^2}\sigma_{rex} \tag{4.30a}$$

Without the welding-induced residual stresses, i.e., when $\sigma_{rex} = \sigma_{rey} = 0$, Equation (4.30a) simplifies to the well-known condition

$$\frac{b}{a} \le \sqrt{n(n+1)} \tag{4.30b}$$

For interests of simplicity, the buckling half-wave number in the y direction may often be determined from Equation (4.30b), i.e., by neglecting the effect of residual stresses.

Applying an approach similar to that used for the longitudinal axial loading case, we can calculate the maximum and minimum membrane stresses, which are given by

$$\sigma_{x\,max} = -\rho_y \frac{\pi^2 E A_n (A_n + 2A_{0n})}{8a^2}\cos\frac{2n\pi b_t}{b} \tag{4.31a}$$

$$\sigma_{x\,min} = \rho_y \frac{\pi^2 E A_n (A_n + 2A_{0n})}{8a^2} \tag{4.31b}$$

$$\sigma_{y\,max} = \sigma_{yav} - \rho_y \frac{n^2\pi^2 E A_n (A_n + 2A_{0n})}{8b^2}\cos\frac{2\pi a_t}{a} \tag{4.31c}$$

$$\sigma_{y\,min} = \sigma_{yav} + \rho_y \frac{n^2\pi^2 E A_n (A_n + 2A_{0n})}{8b^2} \tag{4.31d}$$

where A_n is obtained by the solution of Equation (4.28). ρ_y is a correction factor.

The correction factor, ρ_y, in Equations (4.31) accounting for the effect of the bath tub shape deflection may be empirically determined based on nonlinear finite element calculations for steel plates by varying the aspect ratio and the load application. For instance, ρ_y may be given by an empirical expression as follows:

$$\rho_y = \begin{cases} 0.2(a/b - \sqrt{2}) + 2.0 & \text{for } b/a \le 1/\sqrt{2} \\ 1.0 & \text{for } b/a > 1/\sqrt{2} \end{cases} \tag{4.32}$$

When both initial imperfections and lateral pressure are not involved, the maximum and minimum membrane stresses can be simplified to

$$\sigma_{x\,max} = e_1\sigma_{yav} + e_2,\ \sigma_{x\,min} = f_1\sigma_{yav} + f_2,\ \sigma_{y\,max} = g_1\sigma_{yav} + g_2,\ \sigma_{y\,min} = h_1\sigma_{yav} + h_2 \tag{4.33}$$

where

$$e_1 = \rho_y \frac{2n^2}{a^2 b^2 (1/a^4 + n^4/b^4)},\quad e_2 = \rho_y \frac{2}{a^2(1/a^4 + n^4/b^4)}\frac{\pi^2 D}{t}\left(\frac{1}{a^2} + \frac{n^2}{b^2}\right)^2$$

$$f_1 = -\rho_y \frac{2n^2}{a^2 b^2 (1/a^4 + n^4/b^4)},\quad f_2 = -\rho_y \frac{2}{a^2(1/a^4 + n^4/b^4)}\frac{\pi^2 D}{t}\left(\frac{1}{a^2} + \frac{n^2}{b^2}\right)^2$$

$$g_1 = 1 + \rho_y \frac{2n^4}{b^4 (1/a^4 + n^4/b^4)},\quad g_2 = \rho_y \frac{2n^2}{b^2(1/a_4 + n^4/b^4)}\frac{\pi^2 D}{t}\left(\frac{1}{a^2} + \frac{n^2}{b^2}\right)^2$$

$$h_1 = 1 - \rho_y \frac{2n^4}{b^4 (1/a^4 + n^4/b^4)},\quad h_2 = -\rho_y \frac{2n^2}{b^2(1/a^4 + n^4/b^4)}\frac{\pi^2 D}{t}\left(\frac{1}{a^2} + \frac{n^2}{b^2}\right)^2$$

Effective Length Formula

The plate effective 'length' (effective width for loading along the plate's long direction) is in this case defined as follows:

$$\frac{a_e}{a} = \frac{\sigma_{yav}}{\sigma_{y\,max}} \tag{4.34a}$$

where $\sigma_{y\,max}$ = maximum compressive stress which is expressed as a function of combined in-plane and lateral pressure loads as well as initial imperfections, as defined in Equation (4.31c).

It is again of interest to calculate the ultimate effective length, a_{eu}, at the ULS of the plate which can be obtained from Equation (4.34a) when $\sigma_{yav} = \sigma_{yu}$ as follows:

$$\frac{a_{eu}}{a} = \frac{\sigma_{yu}}{\sigma^{u}_{y\,max}} \tag{4.34b}$$

where $\sigma^{u}_{y\,max} = \sigma_{y\,max}$ at $\sigma_{yav} = \sigma_{yu}$, σ_{yu} = plate ultimate strength as defined in Section 4.9.3.

While Equation (4.34b) explicitly takes into account the influence of initial imperfections and lateral pressure as parameters of influence, the more typical approach is that exemplified by Faulkner *et al.* (1973) who suggest an empirical effective length formula for simply supported steel plates under transverse compression alone, i.e., without lateral pressure, at the ULS as follows:

$$\frac{a_{eu}}{a} = \frac{0.9}{\beta^2} + \frac{b}{a}\frac{1.9}{\beta}\left(1 - \frac{0.9}{\beta^2}\right) \quad \text{for } \frac{a}{b} \geq 1 \tag{4.34c}$$

where Equation (4.34c) implicitly involves the influence of initial imperfections at an 'average' level.

The reduced tangent effective length representing the in-plane effectiveness of the buckled plate is given by

$$\frac{a^*_e}{a} = \left(\frac{\partial \sigma_{y\,max}}{\partial \sigma_{yav}}\right)^{-1} \tag{4.35}$$

where a^*_e = reduced (tangent) effective length.

When both the initial imperfections and lateral pressure are not involved, Equation (4.34a) can be simplified to (since $\sigma_{y\,max} = g_1\sigma_{yav} + g_2$ from Equation (4.33))

$$\frac{a_e}{a} = \frac{\sigma_{yav}}{g_1\sigma_{yav} + g_2} \tag{4.36a}$$

We can recast Equation (4.36a) as a function of the membrane strain since $\sigma_{y\,max} = g_1\sigma_{yav} + g_2 = E\varepsilon_{yav}$ as follows:

$$\frac{a_e}{a} = \frac{1}{g_1}\left(1 - \frac{g_2}{E}\frac{1}{\varepsilon_{yav}}\right) \tag{4.36b}$$

The reduced effective length representing the in-plane effectiveness of the buckled plate is given from Equation (4.35) when both the initial imperfections and lateral pressure are not involved, as follows:

$$\frac{a^*_e}{a} = \frac{1}{g_1} \tag{4.37}$$

Average Stress–Strain Relationship

For imperfect plates under transverse axial compression and lateral pressure, the average stress–strain relationship can be given as long as the unloaded edges remain straight,

as follows:

$$\varepsilon_{yav} = \frac{1}{E}\sigma_{y\,max} = \frac{1}{E}\frac{a}{a_e}\sigma_{yav} \tag{4.38a}$$

The incremental form of Equation (4.38a) is given by

$$\Delta\varepsilon_{yav} = \frac{1}{E}\left(\frac{\partial \sigma_{y\,max}}{\partial \sigma_{yav}}\right)\Delta\sigma_{yav} \quad \text{or} \quad \Delta\sigma_{yav} = \left(\frac{\partial \sigma_{y\,max}}{\partial \sigma_{yav}}\right)^{-1} E\Delta\varepsilon_{yav} \tag{4.38b}$$

where the numerical approach is often more pertinent for the computation of $\partial\sigma_{y\,max}/\partial\sigma_{yav}$ with infinitesimal stress variations around σ_{yav}.

When both the initial imperfections and lateral pressure are not involved, Equation (4.38a) is simplified to

$$\varepsilon_{yav} = \frac{1}{E}(g_1\sigma_{yav} + g_2) \quad \text{or} \quad \sigma_{yav} = \frac{1}{g_1}(E\varepsilon_{yav} - g_2) \tag{4.39a}$$

The incremental form of Equation (4.39a) is given by

$$\Delta\sigma_{yav} = \frac{E}{g_1}\Delta\varepsilon_{yav} \tag{4.39b}$$

4.8.3 The Concept of the Effective Shear Modulus for a Plate Buckled in Edge Shear

While the effective width is recognized as an efficient approach to evaluate the elastic large-deflection behavior of a plate under predominantly axial compressive loads, the concept of the 'effective shear modulus' suggested by Paik (1995) may be useful for representing the behavior of a plate buckled in edge shear.

The basic concept of the effective shear modulus for plates buckled in edge shear is now described. In plane stress problems, the relationship between membrane shear stress, τ, and shear strain, γ, is given by

$$\tau = G\gamma \tag{4.40}$$

where $G = E/[2(1 + \nu)]$ = shear modulus.

While the shear strain distribution would be uniform inside the plate before buckling, it is no longer uniform after shear buckling occurs. The shear strain at any point inside the buckled plate may be calculated by taking into account the large-deflection effects as follows:

$$\gamma = \left(\frac{\partial u}{\partial y} + \frac{\partial v}{\partial x}\right) + \left(\frac{\partial w}{\partial x}\frac{\partial w}{\partial y} + \frac{\partial w}{\partial x}\frac{\partial w_0}{\partial y} + \frac{\partial w_0}{\partial x}\frac{\partial w}{\partial y}\right) \tag{4.41}$$

where u and v are axial displacements in the x and y directions, respectively. The first bracketed term on the right hand side of the above equation represents the membrane shear strain component and the second term indicates the additional shear strain component due to large-deflection effects.

The basic idea of either the effective width or the effective shear modulus concepts is to regard the deflected (buckled) plate as an equivalent 'flat' (undeflected) one, but with

a reduced (effective) in-plane stiffness. Therefore, the membrane shear strain component, γ_m, of the buckled plate must in this case be evaluated as follows:

$$\gamma_m = \frac{\partial u}{\partial y} + \frac{\partial v}{\partial x} = \frac{\tau}{G} - \left(\frac{\partial w}{\partial x}\frac{\partial w}{\partial y} + \frac{\partial w}{\partial x}\frac{\partial w_0}{\partial y} + \frac{\partial w_0}{\partial x}\frac{\partial w}{\partial y}\right) \tag{4.42}$$

The membrane shear strain at any point inside the plate can in a real case be computed using numerical methods such as the finite element method. The mean membrane shear strain, γ_{av}, may be defined as an average of shear strains thus computed over the entire plate as follows:

$$\gamma_{av} = \frac{1}{ab}\int_0^a \int_0^b \gamma_m \, dx \, dy \tag{4.43}$$

Since the shear stress at the plate edges may equal the average shear stress, i.e., $\tau = \tau_{av}$, the effective shear modulus, G_e, representing the effectiveness of the plate buckled in edge shear can be defined by

$$G_e = \frac{\tau_{av}}{\gamma_{av}} \tag{4.44}$$

An empirical expression for the effective shear modulus can be developed by curve fitting based on numerical computations and varying influential factors such as the plate aspect ratio and initial imperfections. For instance, the effective shear modulus formula of simply supported rectangular plates with initial deflections may be empirically derived based on the results of the semi-analytical method as will be presented in Chapter 11, as follows (Paik 1995):

$$\frac{G_e}{G} = \begin{cases} c_1 V^3 + c_2 V^2 + c_3 V + c_4 & \text{for } V \le 1.0 \\ d_1 V^2 + d_2 V + d_3 & \text{for } V > 1.0 \end{cases} \tag{4.45a}$$

where

$$c_1 = -0.309W_0^3 + 0.590W_0^2 - 0.286W_0$$
$$c_2 = 0.353W_0^3 - 0.644W_0^2 + 0.270W_0$$
$$c_3 = -0.072W_0^3 + 0.134W_0^2 - 0.059W_0$$
$$c_4 = 0.005W_0^3 - 0.033W_0^2 + 0.001W_0 + 1.0$$
$$d_1 = -0.007W_0^3 + 0.015W_0^2 - 0.018W_0 + 0.015$$
$$d_2 = -0.022W_0^3 + 0.006W_0^2 + 0.075W_0 - 0.118$$
$$d_3 = 0.008W_0^3 + 0.025W_0^2 - 0.130W_0 + 1.103$$

with $V = \tau_{av}/\tau_E$, $W_0 = w_{opl}/t$, τ_E = elastic shear buckling stress of the plate, as defined in Chapter 3.

When the initial deflection is not involved, Equation (4.45a) is simplified to

$$\frac{G_e}{G} = \begin{cases} 1.0 & \text{for } \tau_{av}/\tau_E \le 1 \\ 0.015(\tau_{av}/\tau_E)^2 - 0.118\tau_{av}/\tau_E + 1.103 & \text{for } \tau_{av}/\tau_E > 1 \end{cases} \tag{4.45b}$$

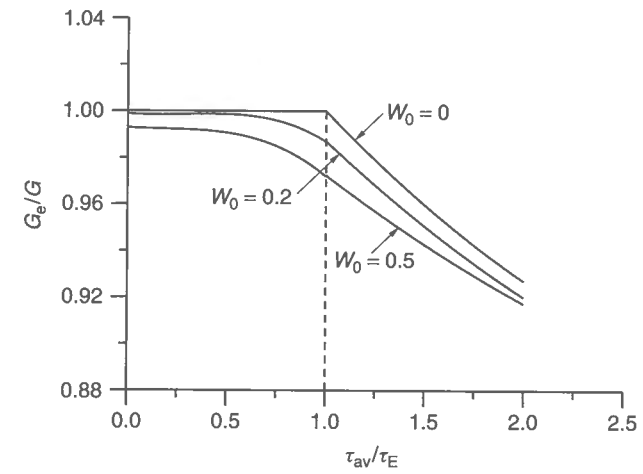

Figure 4.11 Variation of the effective shear modulus of a plate with increase in edge shear

Figure 4.11 plots Equations (4.45). As is apparent from the figure, the effective shear modulus of a plate decreases after buckling as the edge shear increases. Also, the initial deflection reduces the effective shear modulus as would be expected.

4.8.4 Average Stress–Strain Relationship under Combined Loads

The membrane strain components of deflected or buckled plate elements under combined biaxial loads, edge shear and lateral pressure can be given by

$$\varepsilon_{xav} = \frac{1}{E}(\sigma_{x\,max} - \nu\sigma_{yav}) \tag{4.46a}$$

$$\varepsilon_{yav} = \frac{1}{E}(-\nu\sigma_{xav} + \sigma_{y\,max}) \tag{4.46b}$$

$$\gamma_{av} = \frac{\tau_{av}}{G_e} \tag{4.46c}$$

where $\sigma_{x\,max}$, $\sigma_{y\,max}$ = maximum membrane stresses in the x or y direction, G_e = effective shear modulus as defined in Equations (4.45).

Since $\sigma_{x\,max}$, $\sigma_{y\,max}$ and G_e are nonlinear functions with regard to the corresponding average stress components, Equations (4.46) indicate a set of nonlinear relationships between membrane stresses and strains. The incremental form of the membrane stress–strain relationship is relevant by differentiating Equations (4.46) with regard to the corresponding average stress components as follows:

$$\Delta\varepsilon_{xav} = \frac{1}{E}\left[\frac{\partial\sigma_{x\,max}}{\partial\sigma_{xav}}\Delta\sigma_{xav} + \left(\frac{\partial\sigma_{x\,max}}{\partial\sigma_{yav}} - \nu\right)\Delta\sigma_{yav}\right] \tag{4.47a}$$

$$\Delta\varepsilon_{yav} = \frac{1}{E}\left[\left(\frac{\partial\sigma_{y\,max}}{\partial\sigma_{xav}} - \nu\right)\Delta\sigma_{xav} + \frac{\partial\sigma_{y\,max}}{\partial\sigma_{yav}}\Delta\sigma_{yav}\right] \tag{4.47b}$$

$$\Delta\gamma_{av} = \frac{1}{G_e}\left(1 - \frac{\tau_{av}}{G_e}\frac{\partial G_e}{\partial \tau_{av}}\right)\Delta\tau_{av} \tag{4.47c}$$

The differentiation of maximum membrane stresses may often be carried out numerically with infinitesimal stress variations around the corresponding average stress. Equations (4.47) can then be rewritten in matrix form as follows

$$\begin{Bmatrix} \Delta\sigma_{xav} \\ \Delta\sigma_{yav} \\ \Delta\tau_{av} \end{Bmatrix} = [D_p]^B \begin{Bmatrix} \Delta\varepsilon_{xav} \\ \Delta\varepsilon_{yav} \\ \Delta\gamma_{av} \end{Bmatrix} \tag{4.48}$$

where

$$[D_p]^B = \frac{1}{A_1B_2 - A_2B_1}\begin{bmatrix} B_2 & -A_2 & 0 \\ -B_1 & A_1 & 0 \\ 0 & 0 & 1/C_1 \end{bmatrix}$$

is the stress–strain matrix of the plate in the post-buckling regime, with

$$A_1 = \frac{1}{E}\frac{\partial\sigma_{x\max}}{\partial\sigma_{xav}}, \quad A_2 = \frac{1}{E}\left(\frac{\partial\sigma_{x\max}}{\partial\sigma_{yav}} - \nu\right)$$

$$B_1 = \frac{1}{E}\left(\frac{\partial\sigma_{y\max}}{\partial\sigma_{xav}} - \nu\right), \quad B_2 = \frac{1}{E}\frac{\partial\sigma_{y\max}}{\partial\sigma_{yav}}$$

$$C_1 = \frac{1}{G_e}\left(1 - \frac{\tau_{av}}{G_e}\frac{\partial G_e}{\partial\tau_{av}}\right)$$

When the interaction effect between combined in-plane loads on the maximum membrane stresses is neglected, $\sigma_{x\max}$ and $\sigma_{y\max}$ can be approximately calculated from Equation (4.18a) or Equation (4.31c), respectively. In this case,

$$\frac{\partial\sigma_{x\max}}{\partial\sigma_{yav}} = \frac{\partial\sigma_{y\max}}{\partial\sigma_{xav}} = 0$$

Under biaxial tensile loading, the differentiations in Equation (4.48) may be simplified to

$$\frac{\partial\sigma_{x\max}}{\partial\sigma_{xav}} = \frac{\partial\sigma_{y\max}}{\partial\sigma_{yav}} = 1 \quad \text{and} \quad \frac{\partial\sigma_{x\max}}{\partial\sigma_{yav}} = \frac{\partial\sigma_{y\max}}{\partial\sigma_{xav}} = \frac{\partial G_e}{\partial\tau_{av}} = 0$$

In this case, the stress–strain relationship results in that in the linear elastic regime, as defined in Equation (3.1) of Chapter 3.

4.9 Ultimate Strength

This section presents the ultimate strength formulations for steel plates under combined biaxial loads, edge shear and lateral pressure, which take into account the effect of initial imperfections.

4.9.1 Basic Concepts to Derive the Ultimate Strength Formulations

Existing analytical methods to calculate the ultimate strength of steel plates may be categorized into two approaches:

- the membrane stress method; and
- the rigid–plastic theory method.

In the former approach, the membrane stresses inside the plate are computed typically by solving the nonlinear governing differential equations of large-deflection plate theory and it is considered that the plate will collapse if the membrane stress reaches a critical value (e.g., the yield stress) or if any relevant criterion in terms of membrane stresses is satisfied.

In the latter approach, the kinematically admissible collapse mechanisms of the plate at the ULS are presumed and the ultimate strength is then determined by applying the classical energy principle so that the internal strain energy is in equilibrium with the external potential energy (Murray 1986). To account for the large-deflection effect, the rigid–plastic approach is typically combined with the elastic large-deflection theory of plates.

This section uses the former approach, while application examples of the latter method to the collapse strength of plates may be found for lateral pressure (Wood 1961, Jones 1989), for axial compression (Paik & Pedersen 1996) and for combined axial compression and lateral pressure (Fujita *et al.* 1979), among others.

With an increase in the plate deflection, the upper and/or lower fibers inside the middle of the plate will initially yield by the action of bending. However, as long as it is possible to redistribute the applied loads to the straight plate boundaries by membrane action, the plate will not collapse. Collapse will then occur when the most stressed boundary locations yield, since the plate can no longer keep the boundaries straight, resulting in a rapid increase of lateral plate deflection.

Because of the nature of combined membrane axial stresses in the x and y directions, three possible locations at edges, namely plate corners, longitudinal edges and transverse edges, which could initially yield are generally considered as shown in Figure 4.12. The stress status for the two edge locations, i.e., at each longitudinal or transverse edge, can be expected to be the same as long as the longitudinal or transverse axial stresses are uniformly applied, i.e., without in-plane bending. Depending on the predominant half-wave mode in the long direction, the location of the possible plasticity can vary at the long edges, because the location of the minimum membrane stresses can be different, while it is always the mid-edges in the short direction.

The occurrence of yielding can be assessed by using the Mises–Hencky yield criterion. The three resulting ultimate strength criteria for the most probable yield locations will be found as follows:

(1) Yielding at corners:

$$\left(\frac{\sigma_{x\max}}{\sigma_Y}\right)^2 - \left(\frac{\sigma_{x\max}}{\sigma_Y}\right)\left(\frac{\sigma_{y\max}}{\sigma_Y}\right) + \left(\frac{\sigma_{y\max}}{\sigma_Y}\right)^2 + \left(\frac{\tau_{av}}{\tau_Y}\right)^2 = 1 \tag{4.49a}$$

(2) Yielding at longitudinal edges:

$$\left(\frac{\sigma_{x\max}}{\sigma_Y}\right)^2 - \left(\frac{\sigma_{x\max}}{\sigma_Y}\right)\left(\frac{\sigma_{y\min}}{\sigma_Y}\right) + \left(\frac{\sigma_{y\min}}{\sigma_Y}\right)^2 + \left(\frac{\tau_{av}}{\tau_Y}\right)^2 = 1 \tag{4.49b}$$

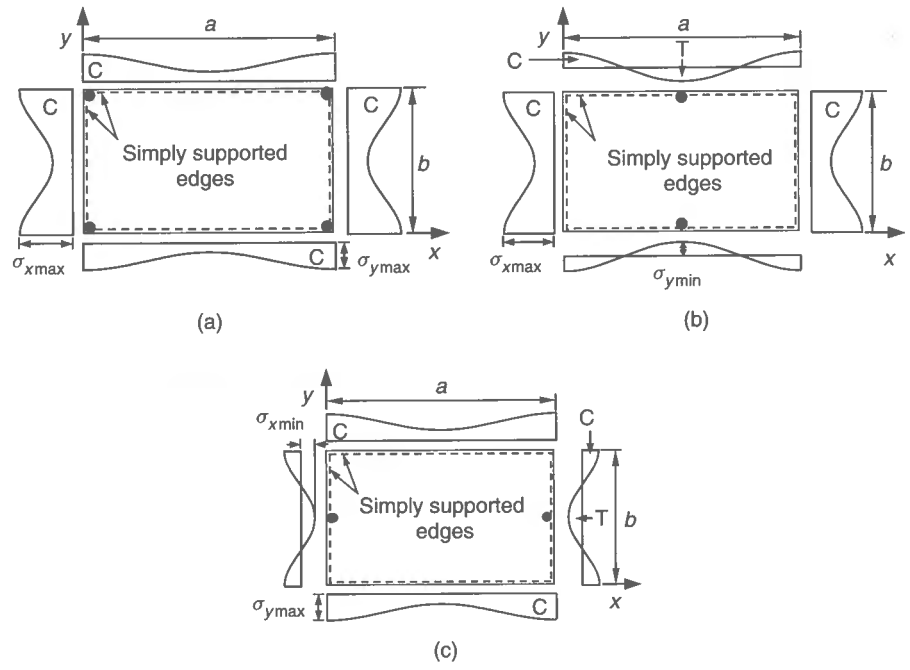

Figure 4.12 Three possible locations for the initial plastic yield at the plate edges under combined loads: (a) plasticity at corners; (b) plasticity at longitudinal edges; (c) plasticity at transverse edges (•, expected yielding locations; T, tension; C, compression)

(3) Yielding at transverse edges:

$$\left(\frac{\sigma_{x\,\min}}{\sigma_Y}\right)^2 - \left(\frac{\sigma_{x\,\min}}{\sigma_Y}\right)\left(\frac{\sigma_{y\,\max}}{\sigma_Y}\right) + \left(\frac{\sigma_{y\,\max}}{\sigma_Y}\right)^2 + \left(\frac{\tau_{av}}{\tau_Y}\right)^2 = 1 \tag{4.49c}$$

While the maximum or minimum membrane stresses of deflected plates under simple types of load applications such as uniaxial compression or combined uniaxial compression and lateral pressure loads may be calculated relatively easily as described in Section 4.8, it is not straightforward to calculate the maximum and minimum membrane stresses of plates under more complex load applications such as combined biaxial loads, edge shear and lateral pressure.

As an easier alternative approach, Equations (4.49) may be utilized for developing the plate ultimate strength formulations under simpler load applications and a relevant combination of such strength formulations as obtained for various simpler load cases may be adopted to derive the strength formula under all potential load applications.

4.9.2 Combined Longitudinal Axial Load and Lateral Pressure

The maximum and minimum membrane stresses are in this case calculated from Equations (4.18) in terms of σ_{xav} and p together with initial imperfections. Under the present type of load application, the initial yield location at the plate edges may be the longitudinal edges by the nature of the Mises–Hencky yield condition.

By substituting the maximum and minimum membrane stresses into Equation (4.49b), the ultimate longitudinal axial strength, σ_{xu}, is obtained as the solution of the following equation with regard to σ_{xav}, regarding p as a secondary constant load, namely

$$\left(\frac{\sigma_{x\,\max}}{\sigma_Y}\right)^2 - \left(\frac{\sigma_{x\,\max}}{\sigma_Y}\right)\left(\frac{\sigma_{y\,\min}}{\sigma_Y}\right) + \left(\frac{\sigma_{y\,\min}}{\sigma_Y}\right)^2 = 1 \tag{4.50a}$$

where $\sigma_{x\,\max}$ is as defined in Equation (4.18a), $\sigma_{y\,\min}$ as defined in Equation (4.18d).

When the lateral pressure is not involved, the ultimate strength, σ_{xu}, is of course calculated by letting $p = 0$. It is interest that, when the unloaded edges move freely in plane, no membrane stresses develop in the y direction, as shown in Figure 4.6(b). In this case, the ultimate strength formulation, Equation (4.50a), can be simplified to

$$\sigma_{x\,\max} = \sigma_Y \tag{4.50b}$$

Alternatively, using the effective width approach, σ_{xu} is simply given by

$$\sigma_{xu} = \sigma_Y \frac{b_{eu}}{b} \tag{4.50c}$$

where b_{eu} = effective width at the ULS, as defined in Equation (4.21c).

When the plate is subjected to predominantly axial tensile loads, the plate ultimate strength may approximately be taken as $\sigma_{xu} = \sigma_Y$, while the ultimate strength of the plate under combined longitudinal axial tension and lateral pressure loads can also be calculated from Equation (4.50a).

As will be described in Section 4.13, the plate ultimate strength predictions using the formulations, e.g., Equation (4.50a), presented in this chapter are automated using the ALPS/ULSAP computer program. Figure 4.13 compares theoretical results of Equation (4.50a) with the mechanical collapse tests and the nonlinear FEA for long plates with different plate aspect ratios and under longitudinal axial compressive loads. While Equation (4.50a) deals with initial imperfections as direct parameters of influence, the mechanical collapse tests involve various uncertain levels of both initial deflections and residual stresses. For more details of the test data, Ellinas *et al.* (1984) may be referred to. In the FEA, two types of unloaded plate edge condition are applied: (1) the unloaded plate edges move freely in plane, and (2) they are kept straight. For the FEAs, an 'average' level of initial deflections is considered, while the welding residual stresses are not included. The finite element solutions with edge condition (1) are smaller than those with edge condition (2), as would be expected.

4.9.3 Combined Transverse Axial Load and Lateral Pressure

The maximum and minimum membrane stresses are in this case calculated from Equations (4.31) in terms of σ_{yav} and p together with initial imperfections. For the present type of load application, the initial yield location at the plate edges may be the transverse edges by the nature of the Mises–Hencky yield condition.

By substituting the maximum and minimum membrane stresses into Equation (4.49c), the ultimate transverse axial strength, σ_{yu}, is obtained as the solution of the following

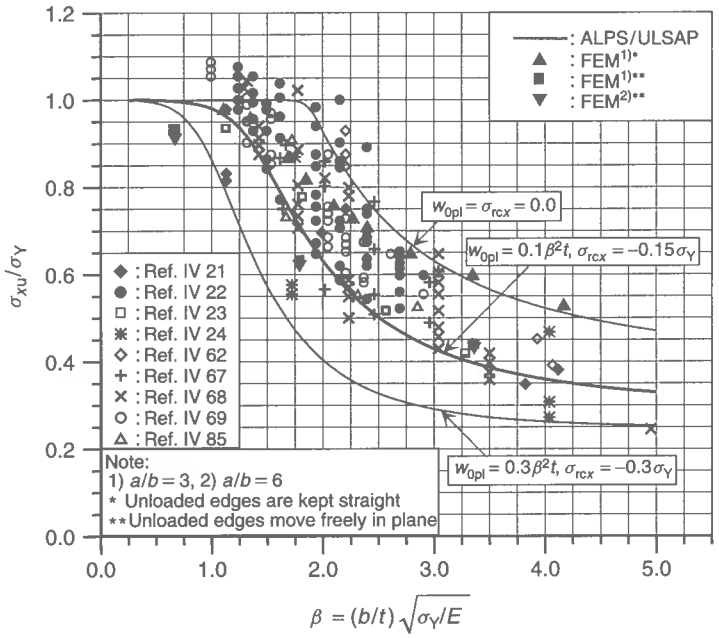

Figure 4.13 Variations of the ultimate strength of steel plates under axial compression as a function of the plate slenderness ratio (reference numbers for test data are taken from Ellinas *et al.* 1984)

equation with regard to σ_{yav}, regarding p as a secondary constant load, namely

$$\left(\frac{\sigma_{x\,\min}}{\sigma_Y}\right)^2 - \left(\frac{\sigma_{x\,\min}}{\sigma_Y}\right)\left(\frac{\sigma_{y\,\max}}{\sigma_Y}\right) + \left(\frac{\sigma_{y\,\max}}{\sigma_Y}\right)^2 = 1 \tag{4.51a}$$

where $\sigma_{x\,\min}$ is as defined in Equation (4.31b), $\sigma_{y\,\max}$ as defined in Equation (4.31c).

When the lateral pressure is not involved, the ultimate strength, σ_{yu}, is of course calculated by letting $p = 0$. When the unloaded edges move freely in plane, no membrane stresses develop in the x direction. Therefore, Equation (4.51a) can in this case be simplified as follows:

$$\sigma_{y\,\max} = \sigma_Y \tag{4.51b}$$

Alternatively, using the effective width approach, σ_{yu} may be given by

$$\sigma_{yu} = \sigma_Y \frac{a_{eu}}{a} \tag{4.51c}$$

where a_{eu} = effective length at the ULS, as defined in Equation (4.34c).

When the plate is subjected to predominantly axial tensile loads, the plate ultimate strength may approximately be taken as $\sigma_{yu} = \sigma_Y$, while the ultimate strength of the plate under combined transverse axial tension and lateral pressure loads can also be calculated from Equation (4.51a). Figure 4.14 compares Equation (4.51a) with nonlinear finite element results. In the FEAs, the plate edges are simply supported, keeping them straight.

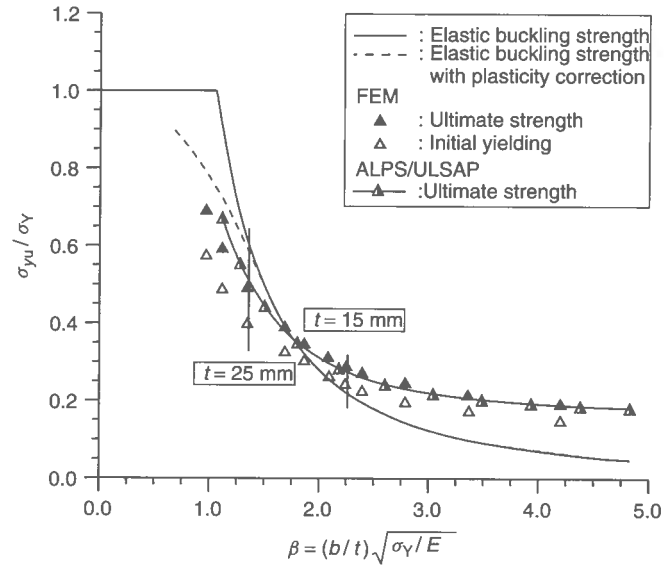

Figure 4.14 Variation of the ultimate transverse compressive strength of a long plate as a function of the reduced slenderness ratio, $a/b = 3$

4.9.4 Lateral Pressure

The ultimate strength, p_{u0}, of plates under lateral pressure alone may be calculated as the lowest value of the three lateral pressures as obtained by satisfying the three conditions of Equations (4.49) when $\sigma_{xav} = \sigma_{yav} = \tau_{av} = 0$.

The static collapse load, p_c, of rectangular plates subject to a uniformly distributed lateral pressure is found between the lower and upper bounds as follows (Jones 1975):

$$\frac{8M_P}{b^2}(1+\alpha+\alpha^2) \le p_c \le \frac{24M_P}{b^2}\frac{1}{(\sqrt{3+\alpha^2}-\alpha)^2} \tag{4.52a}$$

for simply supported plates, and

$$\frac{16M_P}{b^2}(1+\alpha^2) \le p_c \le \frac{48M_P}{b^2}\frac{1}{(\sqrt{3+\alpha^2}-\alpha)^2} \tag{4.52b}$$

for clamped plates, where $M_P = \sigma_Y t^2/4$ is the plastic bending moment per unit breadth that the plate cross-section may carry; $\alpha = b/a$.

Equations (4.52) have been derived using the upper and lower bound theorems for plates made of rigid–plastic material, which obey the Tresca yield criterion. The effect of shear on the yielding has been neglected assuming that the plates are thin.

It is of interest that Equations (4.52) can be simplified for a square plate with $\alpha = 1$ as follows:

$$\frac{24M_P}{b^2} \le p_c \le \frac{24M_P}{b^2} \quad \text{for simply supported plates} \tag{4.53a}$$

$$\frac{32M_P}{b^2} \le p_c \le \frac{48M_P}{b^2} \quad \text{for clamped plates} \tag{4.53b}$$

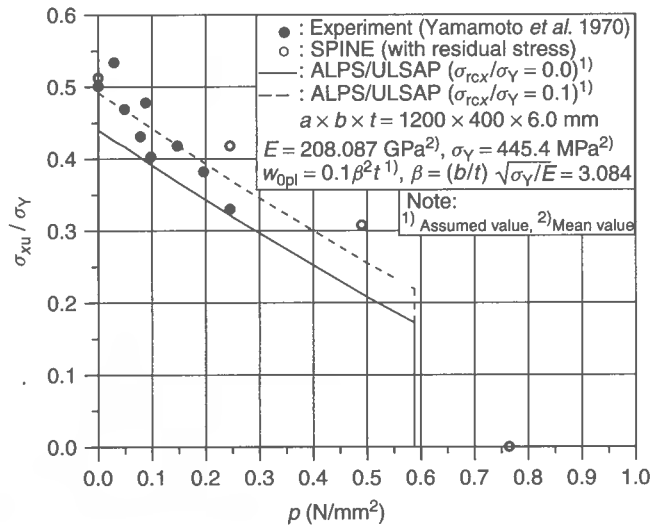

Figure 4.15 Comparison of the ALPS/ULSAP method with the Yamamoto *et al.* collapse test results for plating under combined longitudinal axial compression and lateral pressure loads

It may be seen from Equations (4.53) that the lower and upper limits coincide for simply supported plates, whereas they differ significantly, i.e., 2:3, for clamped plates. In this case, Fox (1974) has shown that the collapse load equals $42.85\,\mathrm{MP}/b^2$.

In this regard, an upper limit, p_{cr}, of the ultimate lateral pressure load for simply supported plates is relevant as follows:

$$p_{cr} = \frac{6t^2\sigma_Y}{b^2}\frac{1}{(\sqrt{3+\alpha^2}-\alpha)^2} \tag{4.54}$$

The ultimate lateral pressure load, p_{u0}, should not be greater than the upper limit, p_{cr}. It is noted that the rigid–plastic theory formulas noted above do not account for the membrane effects and thus they may predict the critical lateral pressure pessimistically. Interestingly, the so-called permanent deflection of the plate under lateral pressure may be defined as the maximum deflection at the ultimate lateral pressure.

Figure 4.15 compares the ALPS/ULSAP results to the corresponding mechanical collapse test results from Yamamoto *et al.* (1970) and SPINE solutions for long plating of $a/b = 3$ under combined longitudinal axial compression and lateral pressure loads. Again, ALPS/ULSAP indicates the results of Equation (4.51a) together with Equation (4.54). The SPINE results were obtained using the semi-analytical method as will be presented in Chapter 11. The model uncertainties for the ALPS/ULSAP method on the basis of the Yamamoto *et al.* testing are mean = 0.967 and COV = 0.064.

4.9.5 Edge Shear

Since the deflection pattern of the plates under edge shear in the post-buckling or large-deflection regime is quite complex, the analytical approach may not be straightforward to

use in evaluating the membrane stress distribution inside the plate buckled in edge shear. In this case, a nonlinear numerical method is more convenient.

In such a case, a series of elastic–plastic large-deflection FEAs for plates under edge shear alone were carried out by Paik *et al.* (2001) varying the plate thickness, the aspect ratio, the boundary condition and the magnitude of post-weld initial deflections. It is assumed that the plate edges remain straight.

Figure 4.16 shows the variation of the plate ultimate edge shear strength for simply supported plates plotted versus the elastic shear buckling stress varying the plate aspect ratio. The dotted line represents the elastic shear buckling strength with plasticity correction using the Johnson–Ostenfeld formula, Equation (2.93). Figure 4.17 shows the effect of the plate aspect ratio on the plate ultimate shear strength. As the plate aspect ratio increases the plate ultimate shear strength tends to decrease. As is apparent from Figure 4.17, however, the ultimate shear strength depends weakly on the plate aspect ratio, especially for relatively thick plates.

By curve fitting based on the computed results, the following empirical formula for the ultimate strength, τ_{u0}, of a plate under edge shear alone may be used:

$$\frac{\tau_{u0}}{\tau_Y} = \begin{cases} 1.324(\tau_E/\tau_Y) & \text{for } 0 < \tau_E/\tau_Y \le 0.5 \\ 0.039(\tau_E/\tau_Y)^3 - 0.274(\tau_E/\tau_Y)^2 + 0.676(\tau_E/\tau_Y) + 0.388 & \text{for } 0.5 < \tau_E/\tau_Y \le 2.0 \\ 0.956 & \text{for } \tau_E/\tau_Y > 2.0 \end{cases} \tag{4.55a}$$

where τ_E is the elastic shear buckling stress of the plate, as defined in Table 3.1 of Chapter 3. Figure 4.16 plots Equation (4.55a).

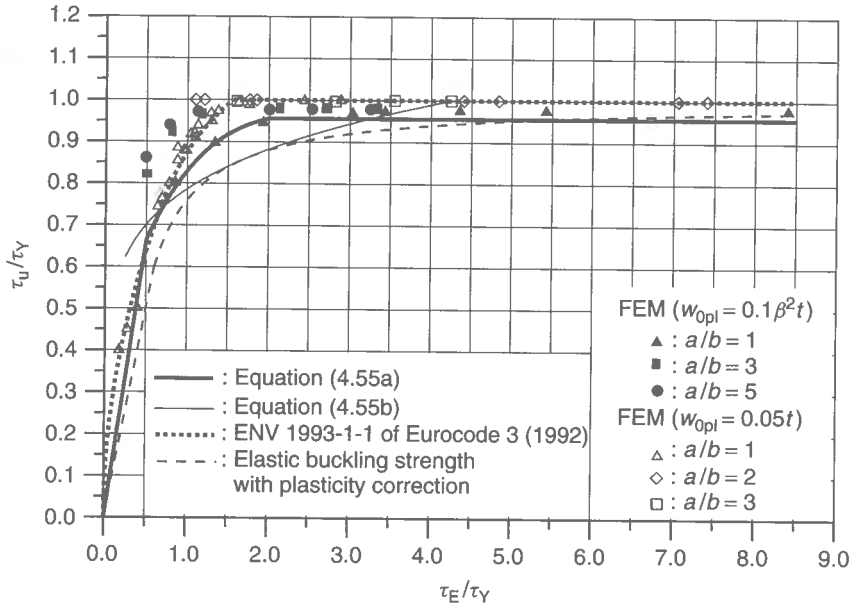

Figure 4.16 The ultimate strength versus the elastic buckling stress of the plate under edge shear (For the formula of ENV 1993-1-1, Equation (7.4) of Chapter 7 is referred to)

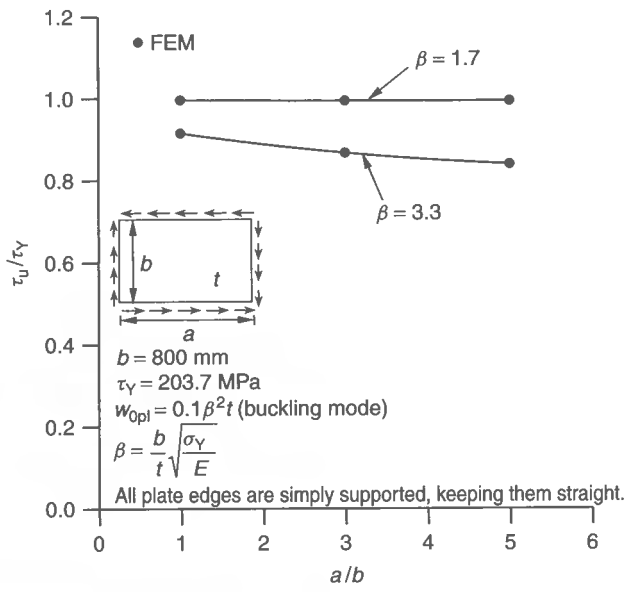

Figure 4.17 Effect of the aspect ratio on the plate ultimate shear strength

Equation (4.55a) has been subdivided into three equations which represent the ultimate edge shear strength of thin plates, medium thickness plates and thick plates, respectively, and shows a modeling error characterized by mean bias = 0.931 and COV = 0.075 when compared to the nonlinear finite element solutions for plates by varying the aspect ratios and initial deflections. In the treatment above, the ultimate strength of a stiffened panel in edge shear is approximately taken as that of plating between stiffeners in edge shear. Any strength reserve due to tension field action where a developing diagonal tension is anchored by the adjoining stiffening is also not included. The approach is thus somewhat pessimistic. Also, implicit in the approach is the (usually reasonable) assumption that the stiffeners of stiffened panels are normally designed such that they will remain straight until the panel buckles in edge shear. Corrections are necessary if this is not the case, as will be described in Chapter 7.

Alternatively, ENV 1993-1-1 (1992) of Eurocode 3 suggests an empirical formula for the plate ultimate shear strength, as defined in Equation (7.4) of Chapter 7. Also, the plate ultimate edge shear strength is often predicted by the plasticity correction of the elastic shear buckling strength using the Johnson–Ostenfeld formula, Equation (2.93). Nara *et al.* (1988) proposed an empirical closed-form expression of the ultimate shear strength of plating obtained by curve fitting based on the nonlinear FEA as follows:

$$\frac{\tau_u}{\tau_Y} = \left(\frac{0.486}{\lambda}\right)^{0.333} \leq 1.0 \text{ for } 0.486 \leq \lambda \leq 2.0 \tag{4.55b}$$

where $\lambda = \sqrt{\tau_Y/\tau_E}$, τ_E = elastic shear buckling stress.

Figure 4.16 compares Equation (4.55a) to more refined nonlinear finite element solutions and other formulations noted above. It is seen from Figure 4.16 that Equation (4.55a) covers a wider range of the plate slenderness ratio with reasonable accuracy.

4.9.6 Combined Edge Shear and Lateral Pressure

While the effect of lateral pressure loads on the ultimate edge shear strength is typically neglected in most current design procedures of steel-plated structures, the lateral pressure loads may in some cases affect (reduce) the plate ultimate edge shear strength.

Figure 4.18 shows the ultimate strength interaction relationship for a plate under combined edge shear and lateral pressure obtained using a semi-analytical method SPINE, as will be described in Chapter 11. It is seen from Figure 4.18 that the ultimate strength interaction between edge shear and lateral pressure is significant and thus cannot be ignored.

From the limited results, it is also observed that their interacting effect tends to become moderate with increase in the plate aspect ratio. As a pessimistic measure, the plate ultimate strength interaction equation between edge shear and lateral pressure may be derived by curve fitting based on the interaction curve of square plates (i.e., with $a/b = 1$) as follows:

$$\left(\frac{\tau}{\tau_{u0}}\right)^{1.5} + \left(\frac{p}{p_{u0}}\right)^{1.2} = 1 \tag{4.56}$$

where τ_{u0} = plate ultimate strength under edge shear alone as defined in Equation (4.55a), p_{u0} = plate ultimate strength under lateral pressure alone.

The ultimate edge shear strength, τ_u, of a plate under combined τ_{av} and p is then obtained as the solution of Equation (4.56) with regard to τ_{av}, treating p as a secondary constant load parameter.

4.9.7 Combined Biaxial Loads, Edge Shear and Lateral Pressure

So far, three sets of the ultimate strength formulations under a primary in-plane load component together with secondary lateral pressure loading have been derived. The ultimate

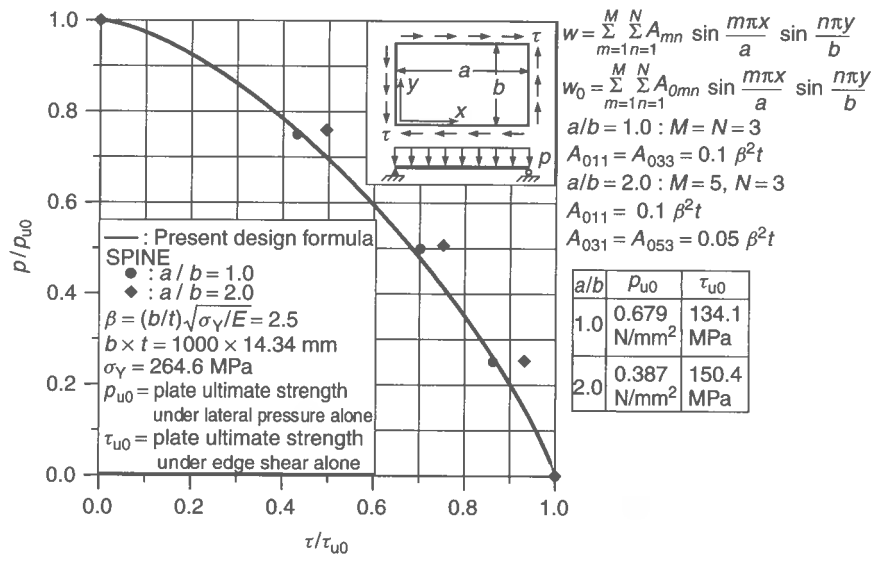

Figure 4.18 Ultimate strength interaction relationship for a simply supported plate subjected to edge shear and lateral pressure

strength formulation under all of the load components involved can now be derived by a relevant combination of individual strength formulas.

While various types of the plate ultimate strength interaction relationships between biaxial compression have been suggested in the literature, most of them may be generalized to the following form:

$$\left(\frac{\sigma_{xav}}{\sigma_{xu}}\right)^{c_1} + \alpha\left(\frac{\sigma_{xav}}{\sigma_{xu}}\right)\left(\frac{\sigma_{yav}}{\sigma_{yu}}\right) + \left(\frac{\sigma_{yav}}{\sigma_{yu}}\right)^{c_2} = 1 \tag{4.57}$$

where σ_{xu}, σ_{yu} are as defined in Section 4.9.2 or 4.9.3 and α, c_1, c_2 are coefficients.

Some examples of the constants used in Equation (4.57) by different investigators are indicated in Table 4.1. Figure 4.19 plots Equation (4.57) with the various constants indicated in Table 4.1. Figure 4.20 compares the ultimate strength interaction curve using

Table 4.1 Examples of the constants used in Equation (4.57) for biaxial compressive loading.

Reference	Constants used in Equation (4.57)
BS 5400 (2000)	$c_1 = c_2 = 2$, $\alpha = 0$; both σ_{xav} and σ_{yav} are compressive
Valsgård (1980)	$c_1 = 1$, $c_2 = 2$, $\alpha = -0.25$ for $a/b = 3$; both σ_{xav} and σ_{yav} are compressive
Dier & Dowling (1980)	$c_1 = c_2 = 2$, $\alpha = 0.45$; both σ_{xav} and σ_{yav} are compressive
Stonor *et al.* (1983)	$c_1 = c_2 = 1.5$, $\alpha = 0$ (lower bound) $c_1 = c_2 = 2$, $\alpha = -1$ (upper bound) Both σ_{xav} and σ_{yav} are compressive
Paik *et al.* (2001)	$c_1 = c_2 = 2$, $\alpha = 0$; both σ_{xav} and σ_{yav} are compressive (negative) $c_1 = c_2 = 2$, $\alpha = -1$; either σ_{xav} or σ_{yav} or both are tensile (positive)

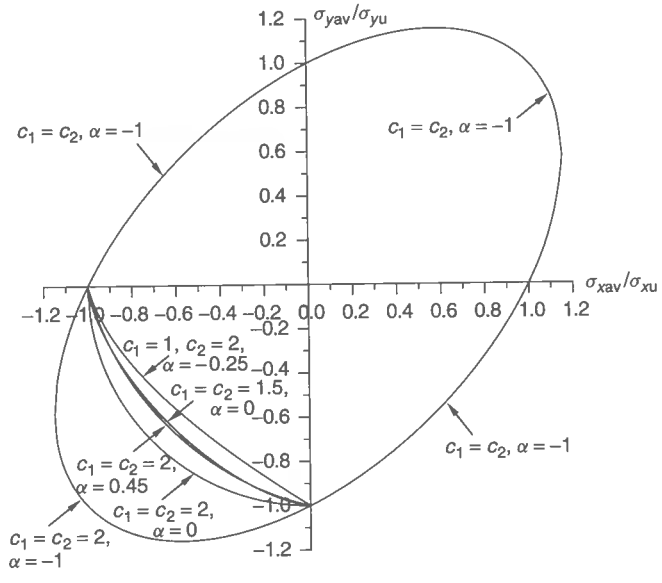

Figure 4.19 Various types of the plate ultimate strength interaction curves under biaxial loads

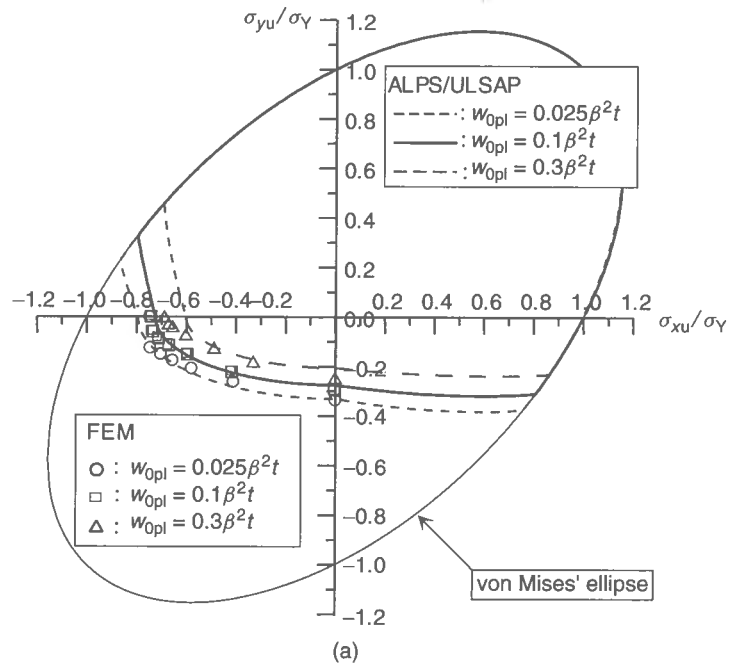

Figure 4.20 Ultimate strength interaction relationship between biaxial compression or tension for a thin plate: $a/b = 3$, $b = 1000\,\text{mm}$, $E = 205.8\,\text{GPa}$, $\sigma_Y = 235.2\,\text{MPa}$: (a) $t = 15\,\text{mm}$; (b) $t = 25\,\text{mm}$

the constants of Paik *et al.* (2001) with nonlinear finite element results for a simply supported plate under biaxial compression or tension.

In general, the plates making up plated structures can sometimes be subjected to axial tension in one direction while axial compression is applied in the other direction. By the nature of the Mises–Hencky yield condition, the biaxial compressive loading condition is not always the most critical, but in some cases the loading condition under axial tension in one direction and axial compression in the other direction could be more important. This implies that the plate ultimate strength interaction relationships should in principle be established by considering any possible combination of axial loads (tensile or compressive), together with edge shear loads.

Based on the insights developed by a series of nonlinear numerical solutions varying the loading ratio and the plate aspect ratio, for instance, the following ultimate strength interaction relationship between biaxial compression/tension, edge shear and lateral pressure may be proposed:

$$\left(\frac{\sigma_{xav}}{\sigma_{xu}}\right)^{c_1} + \alpha\left(\frac{\sigma_{xav}}{\sigma_{xu}}\right)\left(\frac{\sigma_{yav}}{\sigma_{yu}}\right) + \left(\frac{\sigma_{yav}}{\sigma_{yu}}\right)^{c_2} + \left(\frac{\tau_{av}}{\tau_u}\right)^{c_3} = 1 \tag{4.58}$$

where σ_{xu}, σ_{yu} and τ_u should be computed by taking into account the effect of lateral pressure, from Sections 4.9.2, 4.9.3 and 4.9.6, respectively. The coefficients of Equation (4.58) may be taken as $c_1 = c_2 = c_3 = 2$, while $\alpha = 0$ when both σ_{xav} and σ_{yav} are compressive (negative) and $\alpha = -1$ when either σ_{xav} or σ_{yav}, or both, are tensile (positive).

4.10 Post-ultimate Behavior

4.10.1 Average Stress–Strain Relationship

In the post-ultimate regime, the internal stress will decrease as long as the axial compressive displacements continually increase. In this case, the average membrane stress components may be calculated in terms of the plate effective width or length as follows:

$$\sigma_{xav} = \frac{b_e}{b}\sigma^u_{x\,max} \tag{4.59a}$$

$$\sigma_{yav} = \frac{a_e}{a}\sigma^u_{y\,max} \tag{4.59b}$$

where $\sigma^u_{x\,max}$ and $\sigma^u_{y\,max}$ are the maximum membrane stresses of the plate in the x and y directions, immediately after the ultimate strength is reached, i.e., $\sigma^u_{x\,max} = \sigma_{x\,max}$ at $\sigma_{xav} = \sigma_{xu}$ and $\sigma^u_{y\,max} = \sigma_{y\,max}$ at $\sigma_{yav} = \sigma_{yu}$.

The effective width or length of the plate in the post-ultimate strength regime may be defined as follows:

$$\frac{b_e}{b} = \frac{\sigma^*_{xav}}{\sigma^*_{x\,max}} \tag{4.60a}$$

$$\frac{a_e}{a} = \frac{\sigma^*_{yav}}{\sigma^*_{y\,max}} \tag{4.60b}$$

where the asterisk represents a value of the plate in the post-ultimate regime.

As may be surmised from variation of the effective width versus applied loads as shown in Figure 4.9, the effect of initial imperfections and Poisson's ratio is negligibly small in the post-ultimate regime. While the plate effective width will of course decrease in the post-ultimate regime as long as the axial compressive displacements increase, it is assumed that the reduction tendency of the plate effective width or length is similar to that in the pre-ultimate regime.

When initial imperfections are not involved, $\sigma^*_{x\,max}$ in Equation (4.60a) and $\sigma^*_{y\,max}$ in Equation (4.60b) can be determined from $\sigma_{x\,max}$ in Equation (4.20) and $\sigma_{y\,max}$ in Equation (4.33), respectively. For more simplified expressions, the following equations may approximately be relevant with axial compression as negative:

$$\sigma^*_{x\,max} = E\varepsilon_{xav} = 2\sigma^*_{xav} - \sigma_{xE} \tag{4.61a}$$

$$\sigma^*_{y\,max} = E\varepsilon_{yav} = 2\sigma^*_{yav} - \sigma_{yE} \tag{4.61b}$$

where σ_{xE} and σ_{yE} are the elastic compressive buckling stresses in the x and y directions, respectively.

By substituting Equations (4.61) into Equations (4.60), the plate effective width or length can be expressed in terms of strain components as follows:

$$\frac{b_e}{b} = \frac{1}{2}\left(1 + \frac{\sigma_{xE}}{E\varepsilon_{xav}}\right) \tag{4.62a}$$

$$\frac{a_e}{a} = \frac{1}{2}\left(1 + \frac{\sigma_{yE}}{E\varepsilon_{yav}}\right) \tag{4.62b}$$

The average stress–strain relationships in the post-ultimate regime can then be derived by substituting Equations (4.62) into Equations (4.59) as follows:

$$\sigma_{xav} = \frac{1}{2}\left(1 + \frac{\sigma_{xE}}{E\varepsilon_{xav}}\right)\sigma^u_{x\,max} \tag{4.63a}$$

$$\sigma_{yav} = \frac{1}{2}\left(1 + \frac{\sigma_{yE}}{E\varepsilon_{yav}}\right)\sigma^u_{y\,max} \tag{4.63b}$$

The incremental form of Equations (4.63) is then given by

$$\Delta\sigma_{xav} = -\frac{\sigma^u_{x\,max}}{2}\frac{\sigma_{xE}}{E\varepsilon^2_{xav}}\Delta\varepsilon_{xav} \tag{4.64a}$$

$$\Delta\sigma_{yav} = -\frac{\sigma^u_{y\,max}}{2}\frac{\sigma_{yE}}{E\varepsilon^2_{yav}}\Delta\varepsilon_{yav} \tag{4.64b}$$

On the other hand, the shear stress–strain relationship in the post-ultimate regime is given by

$$\Delta\tau_{av} = G^*_e\Delta\gamma_{av} \tag{4.64c}$$

where G^*_e is the tangent shear modulus in the post-ultimate regime, which is often supposed to be $G^*_e = 0$ when the unloading behavior due to shear is not very significant.

In combined load cases, the average stress–strain relationship of the plate in the post-ultimate regime is therefore given from all stress–strain relationship together with Equations (4.64) as follows:

$$\begin{Bmatrix} \Delta\sigma_{xav} \\ \Delta\sigma_{yav} \\ \Delta\tau_{av} \end{Bmatrix} = [D_p]^U \begin{Bmatrix} \Delta\varepsilon_{xav} \\ \Delta\varepsilon_{yav} \\ \Delta\gamma_{av} \end{Bmatrix} \tag{4.65}$$

where

$$[D_p]^U = \begin{bmatrix} A_1 & 0 & 0 \\ 0 & A_2 & 0 \\ 0 & 0 & A_3 \end{bmatrix}$$

is the stress–strain matrix of the plate in the post-ultimate regime, with

$$A_1 = -\frac{\sigma^u_{x\,max}}{2}\frac{\sigma_{xE}}{E\varepsilon^2_{xav}},\ A_2 = -\frac{\sigma^u_{y\,max}}{2}\frac{\sigma_{yE}}{E\varepsilon^2_{yav}},\ A_3 = G^*_e$$

Table 4.2 presents a summary of the average stress–strain relationships for the plate under combined loads until and after the ultimate strength is reached. Note that a bifurcation buckling phenomenon does not occur when initial deflection exists, since the in-plane stiffness progressively decreases from the very beginning as axial compression increases. While the formulations of the average stress–strain relationship of a plate presented in this chapter accommodate combined biaxial loads, edge shear and lateral pressure, some more simplified formulations for plates under uniaxial compressive loads are also available (e.g., Hu & Sun 1999, Rhodes 2002, among others). The average stress–strain relationships of plates indicated in Table 4.2 are incorporated in the ALPS/ISUM program for the progressive collapse analysis of steel-plated structures using the idealized structural unit method (ISUM), as will be described in Chapter 13.

4.10.2 Verification Examples

Figure 4.21 shows the progressive collapse behavior of a steel plate under longitudinal axial compressive loads as obtained by the average stress–strain relationships noted above. It is seen from this figure that the post-ultimate response as well as the pre-ultimate strength behavior significantly depend on the plate dimensions among others, as would be expected.

Table 4.2 A summary of the average stress–strain relationships for a plate under combined loads.

Status	Equation
Linear elastic regime	(3.1)
Post-buckling or elastic large-deflection regime	(4.48)
Ultimate strength	(4.58)
Post-ultimate regime	(4.65)

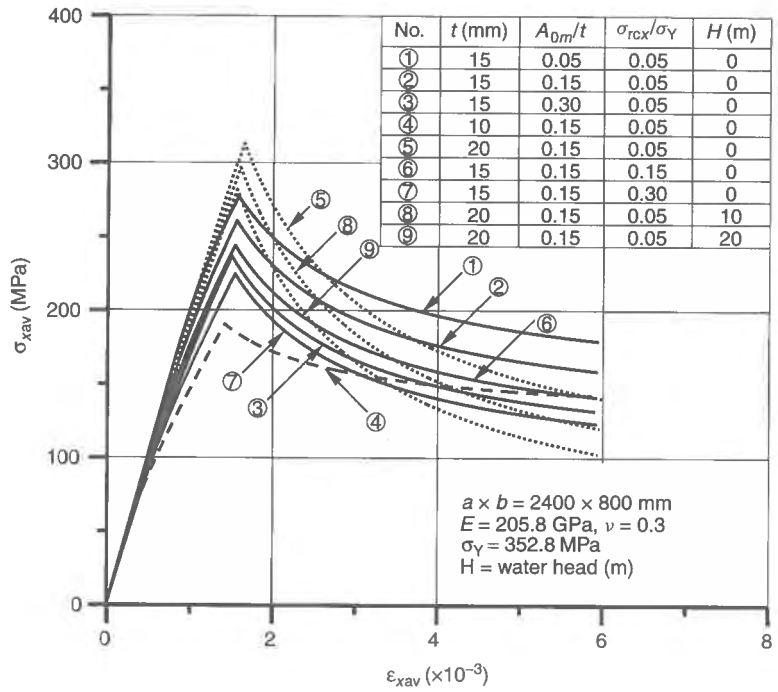

Figure 4.21 The average stress–strain curves of a simply supported steel plate under axial compressive loads

4.11 Effect of Openings

The openings in plates can of course reduce the ultimate strength. In this section, the ultimate strength characteristics of perforated plates are considered and some practical design formulations of plate ultimate strength accounting for the effect of openings are presented. The effect of opening shapes is also described. In all cases of this section, the plate ultimate strengths are computed by elastic–plastic large-deflection FEAs. In these finite element computations, the plate edges are simply supported, keeping them straight.

While Figure 3.16 in Chapter 3 gives the nomenclature of a plate with a centrally located circular hole, Figure 4.22 shows a typical finite element mesh for a plate with a

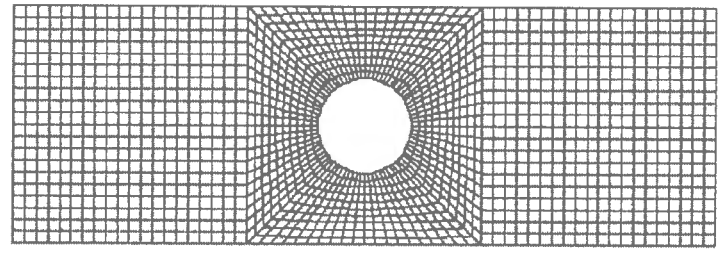

Figure 4.22 A sample of the finite element mesh for a plate with a centrally located circular hole, $a/b = 3$

circular hole. An average level of initial deflection is considered while no residual stresses exist. The strain-hardening effect is not accounted for.

4.11.1 Longitudinal Axial Compression

Figure 4.23 shows typical stress–strain curves of a plate with a centrally located circular hole as shown in Figure 3.16 of Chapter 3 and under longitudinal axial compressive loads, varying the size of hole. It is evident from Figure 4.23 that the opening significantly affects (reduces) the plate ultimate strength.

Figure 4.24 shows the variation of the plate ultimate strength in terms of the size of opening, the plate aspect ratio or the plate thickness. It is seen from Figure 4.24 that both the plate aspect ratio and the plate thickness are not significant parameters affecting the ultimate strength of a long perforated plate under longitudinal axial compression, normalized by that of the perfect plate, i.e., without perforations.

Based on the insights noted above, we may derive an empirical formula of the ultimate strength reduction factor, R_{xu}, as follows:

$$R_{xu} = \frac{\sigma_{xu}}{\sigma_{xu0}} = -0.700\left(\frac{d_c}{b}\right)^2 - 0.365\frac{d_c}{b} + 1.0 \tag{4.66}$$

where σ_{xu}, σ_{xu0} = ultimate strengths with or without an opening.

The accuracy of Equation (4.66) is checked in Figure 4.24(c). Therefore, once the ultimate strength of a plate without an opening is calculated as presented in Section 4.9 of this chapter, the ultimate strength of a plate with a centrally located circular hole

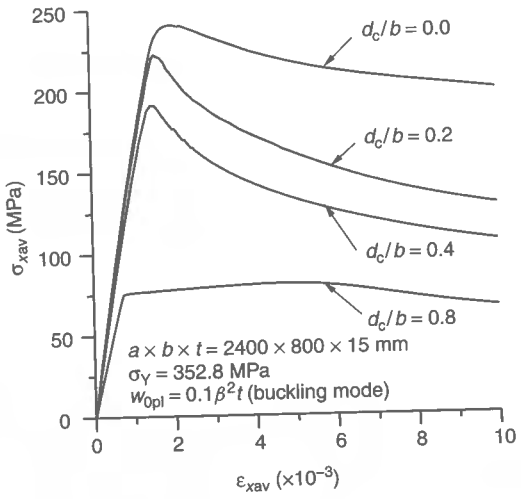

Figure 4.23 Typical stress–strain curves of a plate with a centrally located circular hole and under longitudinal axial compression, varying the size of hole, as obtained by nonlinear FEA, $a/b = 3$, $\beta = 2.2$

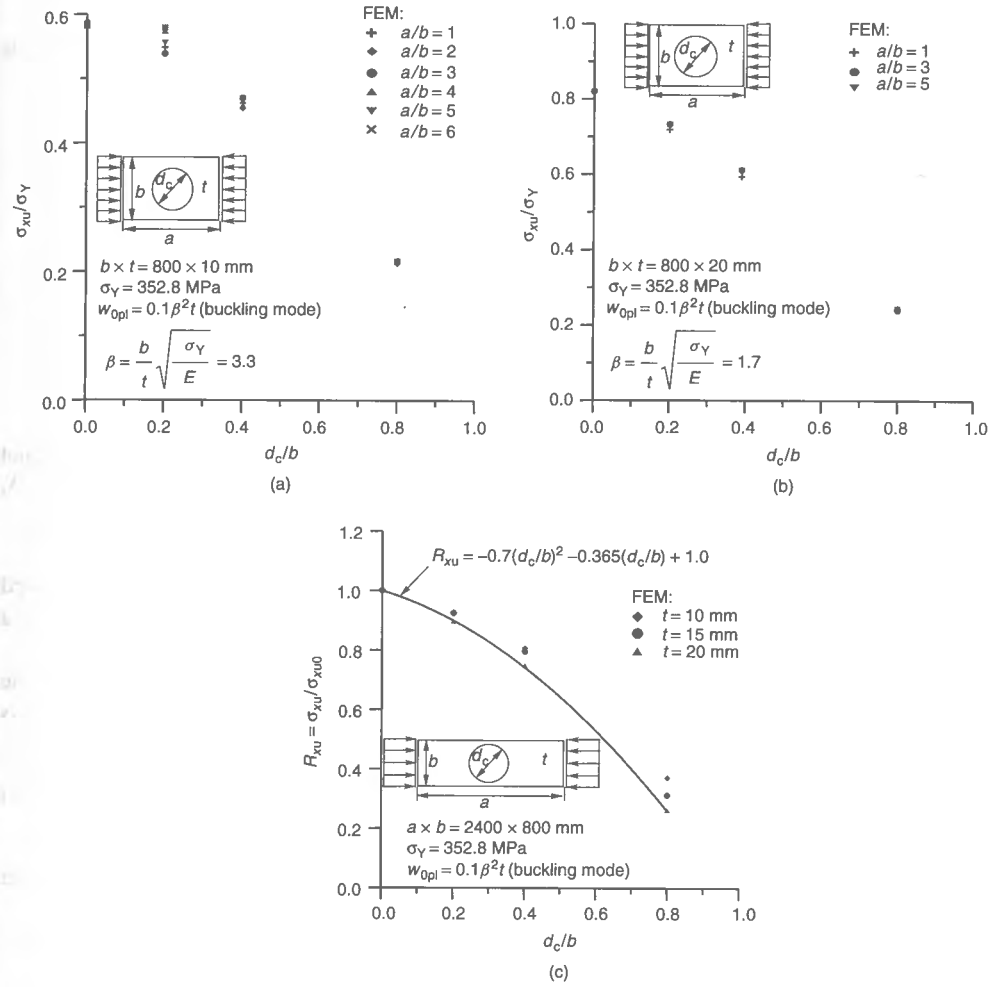

Figure 4.24 Variation of the ultimate strength of plates with a centrally located circular hole and under longitudinal axial compression as a function of the plate aspect ratio and the size of hole: (a) $\beta = 3.3$; (b) $\beta = 1.7$; and (c) as a function of the plate thickness and the size of hole, $a/b = 3$

can be obtained by multiplying it by the strength reduction factor, R_{xu}, as defined in Equation (4.66).

4.11.2 Transverse Axial Compression

Figure 4.25 shows typical stress–strain curves of a plate with a centrally located circular hole and under transverse axial compressive loads, varying the size of hole. Figure 4.26 shows the variation of the plate ultimate strength for transverse axial compression, varying the size of opening, the plate aspect ratio or the plate thickness. It is seen from

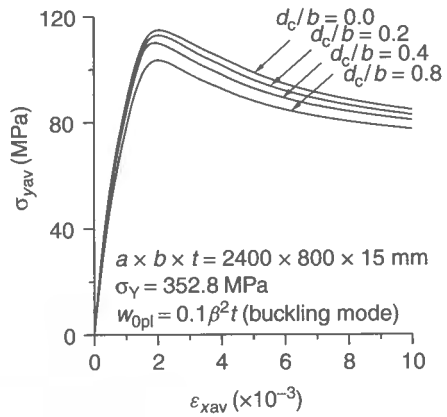

Figure 4.25 Typical stress–strain curves of a plate with a centrally located circular hole and under transverse axial compression, varying the size of hole, as obtained by nonlinear FEA, $a/b = 3$, $\beta = 2.2$

Figure 4.26 that the effect of plate aspect ratio on the ultimate strength of perforated plates under transverse axial compression is significant, while the plate thickness is not a significant parameter.

Based on the insights noted above, the plate ultimate reduction factor, R_{yu}, for transverse axial compression may be empirically derived by curve fitting of the finite element results as follows:

$$R_{yu} = \frac{\sigma_{yu}}{\sigma_{yu0}} = C_1 \left(\frac{d_c}{b}\right)^2 + C_2 \frac{d_c}{b} + 1.0 \tag{4.67}$$

where $\sigma_{yu}, \sigma_{yu0}$ = ultimate strength of a plate with or without an opening and under transverse axial compression,

$$C_1 = \begin{cases} -0.177(a/b)^2 + 1.088\,a/b - 1.671 & \text{for } 1 \le a/b \le 3 \\ 0.0 & \text{for } 3 \le a/b \le 6 \end{cases}$$

$$C_2 = \begin{cases} -0.048(a/b)^2 + 0.252\,a/b - 0.386 & \text{for } 1 \le a/b \le 3 \\ -0.062 & \text{for } 3 \le a/b \le 6 \end{cases}$$

The accuracy of Equation (4.67) is checked in Figures 4.27(a) and (b).

4.11.3 Edge Shear

Figure 4.28 shows typical stress–strain curves of a plate with a centrally located circular hole and under edge shear, varying the size of hole. Figure 4.29 shows the variation of the plate ultimate strength for edge shear, varying the size of opening, the plate aspect ratio or the plate thickness. It is seen from Figure 4.29 that the ultimate shear strength of perforated plates with holding the size of opening constant tends to increase as the plate aspect ratio increases, while the plate thickness is not a significant parameter.

Based on the insights noted above, the plate ultimate reduction factor, $R_{\tau u}$, for edge shear may be empirically derived by curve fitting of the finite element results as follows:

$$R_{\tau u} = \frac{\tau_u}{\tau_{u0}} = C_1 \left(\frac{d_c}{b}\right)^2 + C_2 \frac{d_c}{b} + 1.0 \tag{4.68}$$

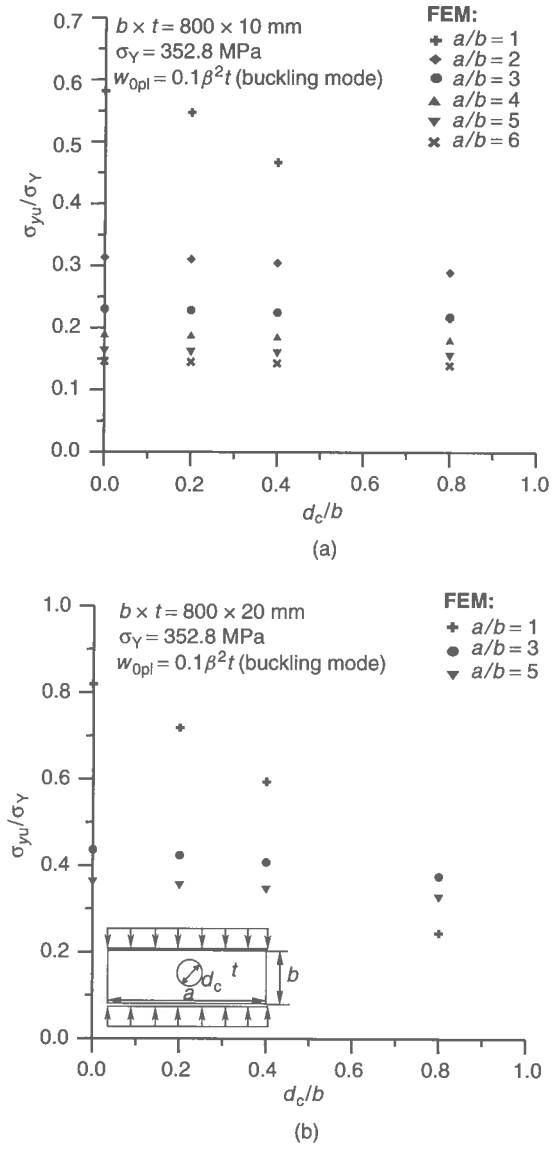

Figure 4.26 Variation of the ultimate strength of plates with a centrally located circular hole and under transverse axial compression as a function of the plate aspect ratio and the size of hole: (a) $\beta = 3.3$; (b) $\beta = 1.7$; and (c) as a function of the plate thickness and the size of hole, $a/b = 3$

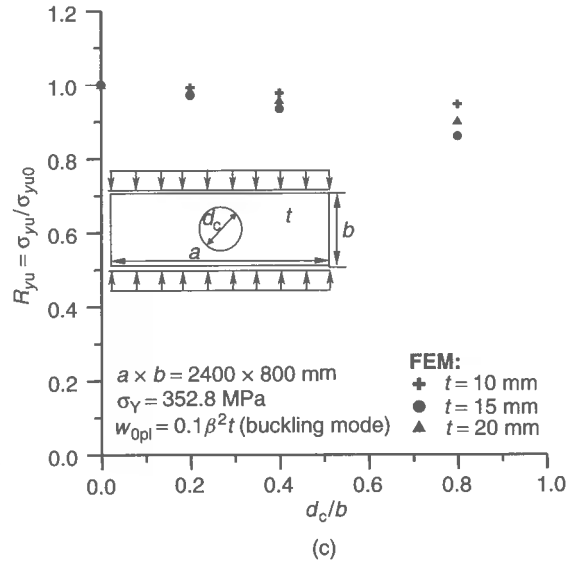

(c)

Figure 4.26 (*continued*)

where τ_u, τ_{u0} = ultimate shear strength of a plate with or without an opening, with

$$C_1 = -0.009\left(\frac{a}{b}\right)^2 - 0.068\left(\frac{a}{b}\right) - 0.415,\ C_2 = -0.025\left(\frac{a}{b}\right)^2 + 0.309\left(\frac{a}{b}\right) - 0.787$$

The accuracy of Equation (4.68) is checked in Figure 4.30.

4.11.4 Combined Loads

Combined Biaxial Compression

Figure 4.31 shows typical stress–strain curves of a plate with a centrally located circular hole and under biaxial compression. Figure 4.32 shows the ultimate strength interaction relationships of the perforated plate under biaxial compression as a function of the plate thickness. The curves in Figure 4.32 are the results obtained by the plate ultimate strength formulations presented in this chapter.

Combined Longitudinal Axial Compression and Edge Shear

Figure 4.33 shows typical stress versus central deflection curves of a plate with a centrally located circular hole and under combined longitudinal axial compression and edge shear. Figure 4.34 shows the ultimate strength interaction relationships of the perforated plate under combined longitudinal axial compression and edge shear as a function of the plate thickness. The curves in Figure 4.34 are the results obtained by the plate ultimate strength formulations presented in this chapter.

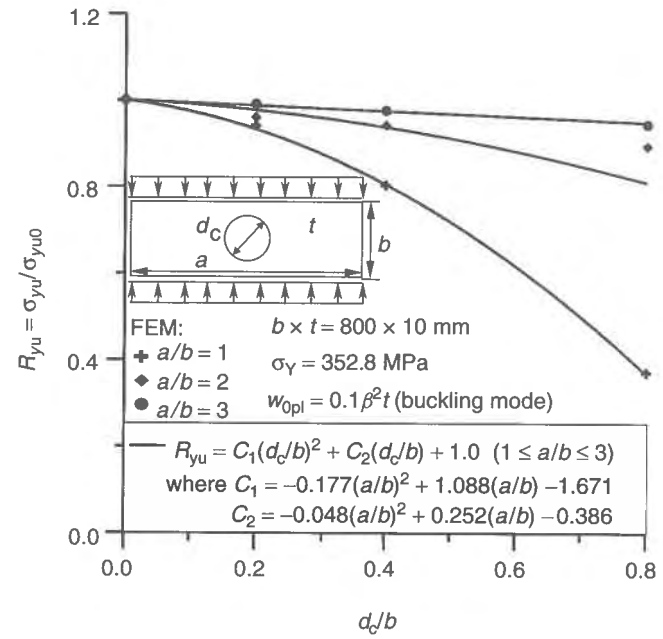

(a)

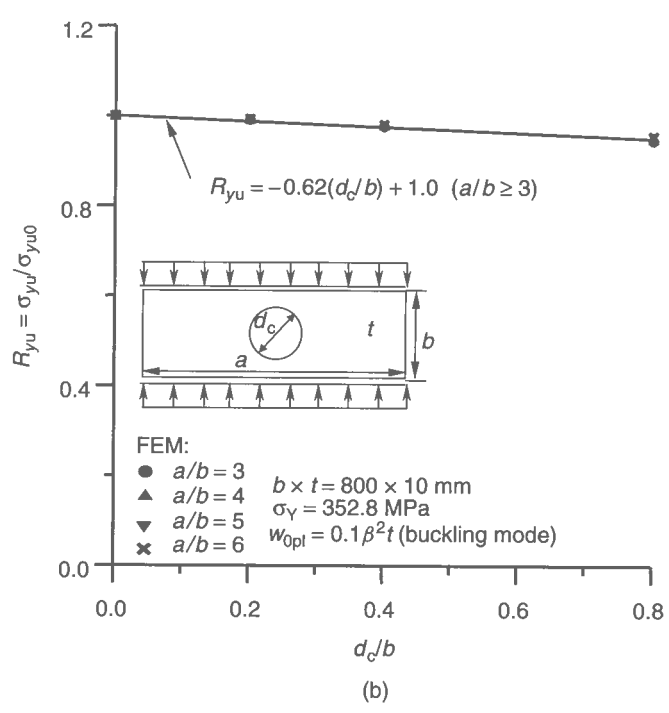

(b)

Figure 4.27 Accuracy of Equation (4.67) for (a) $1 \le a/b \le 3$ and (b) $3 \le a/b \le 6$

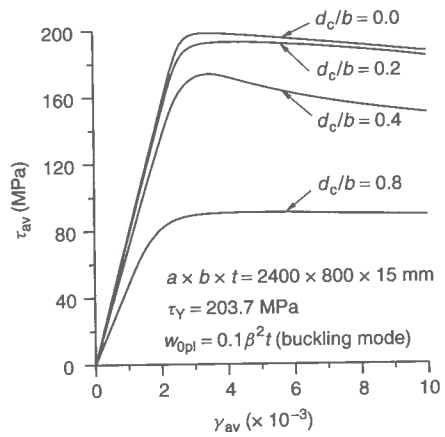

Figure 4.28 Typical stress–strain curves of a plate with a centrally located circular hole and under edge shear, varying the size of hole, as obtained by nonlinear FEA, $a/b = 3$, $\beta = 2.2$

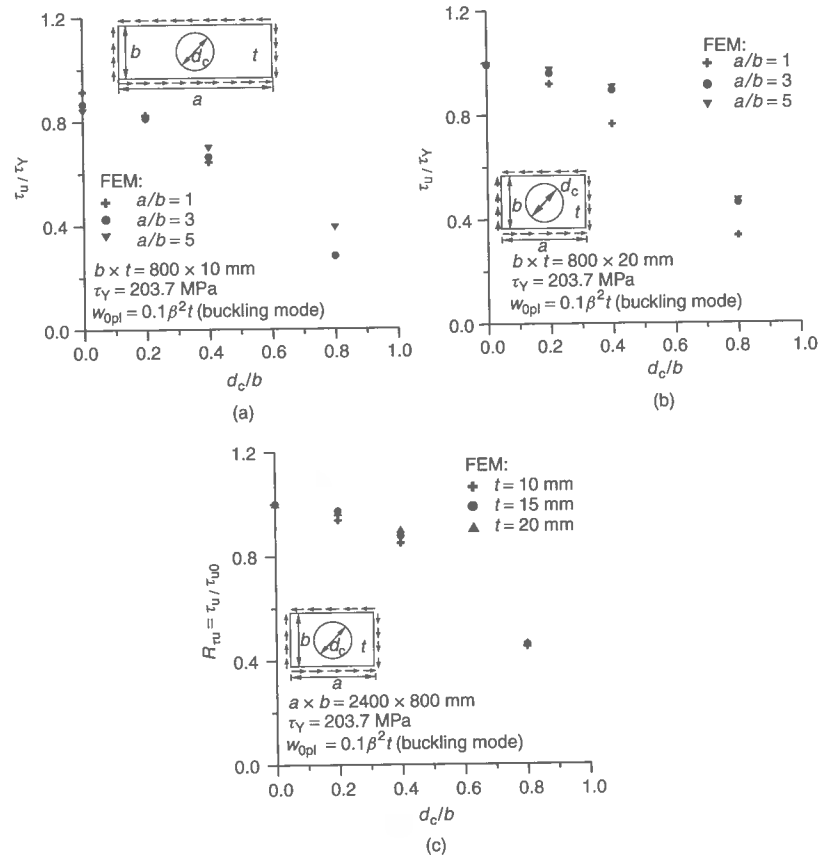

Figure 4.29 Variation of the ultimate strength of plates with a centrally located circular hole and under edge shear as a function of the plate aspect ratio and the size of hole: (a) $\beta = 3.3$; (b) $\beta = 1.7$; and (c) as a function of the plate thickness and the size of hole, $a/b = 3$

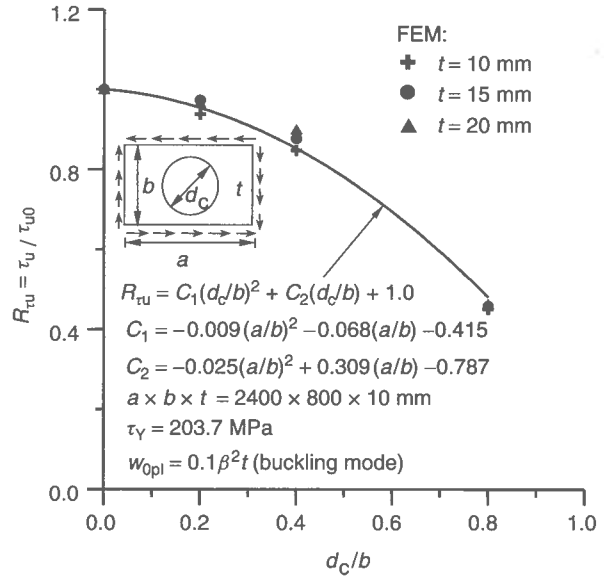

Figure 4.30 Accuracy of Equation (4.68)

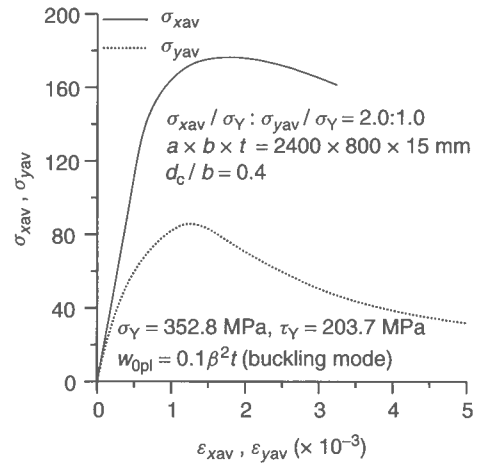

Figure 4.31 Typical stress–strain curves of a plate with a centrally located circular hole and under combined biaxial compressive loads, as obtained by nonlinear FEA, $a/b = 3$, $\beta = 2.2$, $d_c/b = 0.4$

Combined Transverse Axial Compression and Edge Shear

Figure 4.35 shows typical stress versus central deflection curves of a plate with a centrally located circular hole and under combined transverse axial compression and edge shear. Figure 4.36 shows the ultimate strength interaction relationships of the perforated plate under combined transverse axial compression and edge shear as a function of the plate thickness. The curves in Figure 4.36 are the results obtained by the plate ultimate strength formulations presented in this chapter.

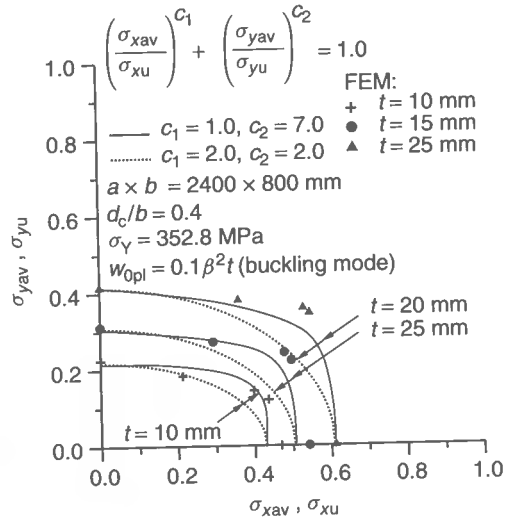

Figure 4.32 Ultimate strength interaction relationship of a plate with a centrally located circular hole and under combined biaxial compressive loads as a function of the plate thickness

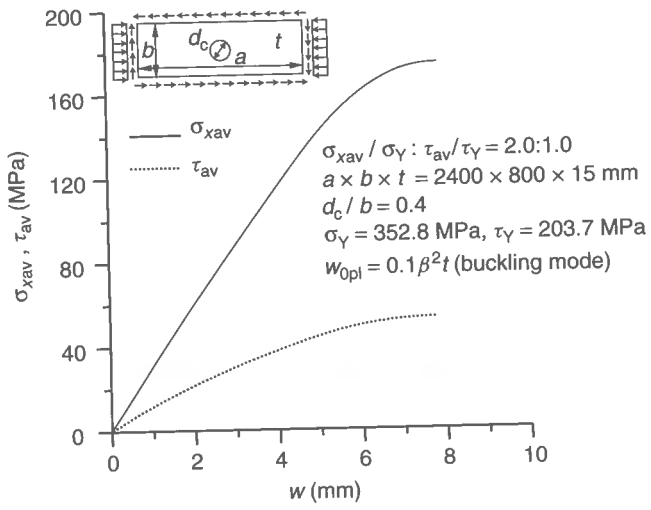

Figure 4.33 Typical stress versus central deflection curves of a plate with a centrally located circular hole and under combined longitudinal axial compression and edge shear, as obtained by nonlinear FEA, $a/b = 3$, $\beta = 2.2$, $d_c/b = 0.4$

4.11.5 Effect of Opening Shapes

In the previous sections, the ultimate strength of plates with circular holes has been considered. This section deals with the effect of opening shapes. Figure 4.37 shows two

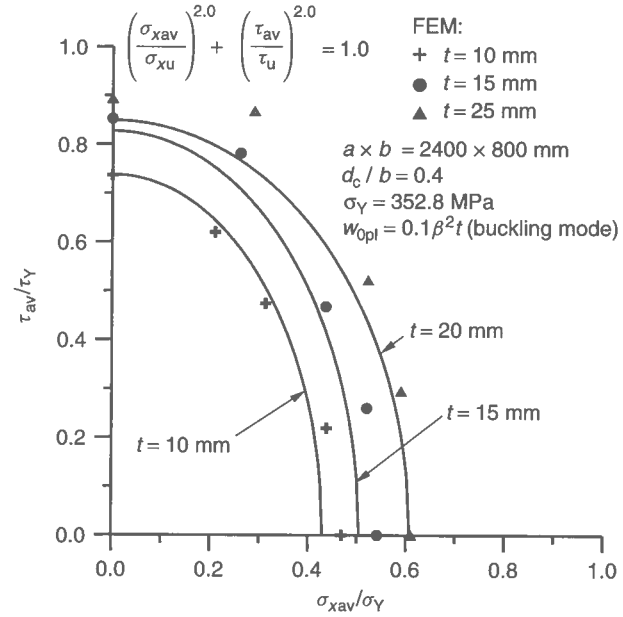

Figure 4.34 Ultimate strength interaction relationship of a plate with a centrally located circular hole and under combined longitudinal axial compression and edge shear as a function of the plate thickness

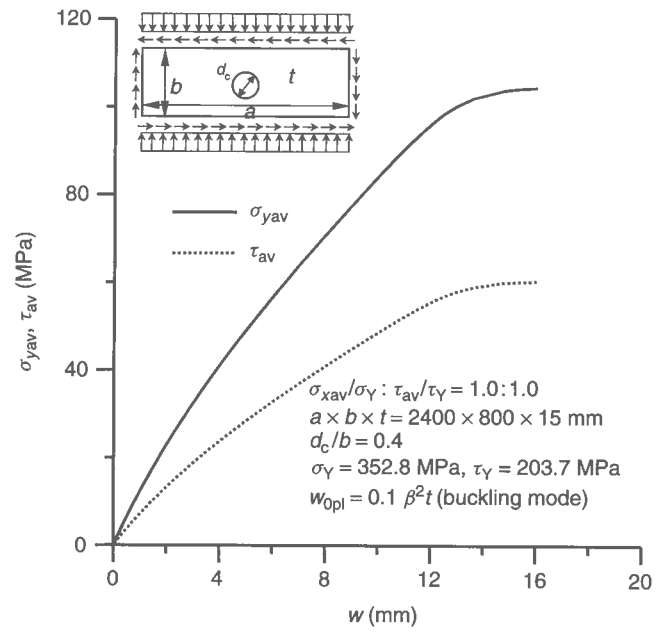

Figure 4.35 Typical stress versus central deflection curves of a plate with a centrally located circular hole and under combined transverse axial compression and edge shear, as obtained by nonlinear FEA, $a/b = 3$, $\beta = 2.2$, $d_c/b = 0.4$

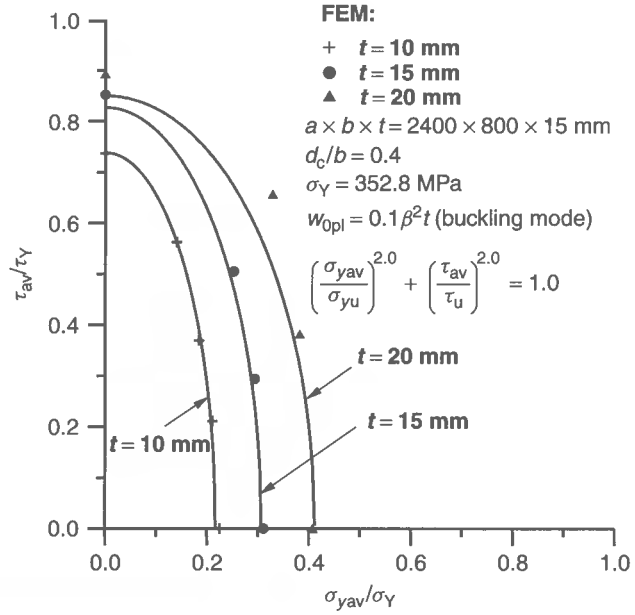

Figure 4.36 Ultimate strength interaction relationship of a plate with a centrally located circular hole and under combined transverse axial compression and edge shear as a function of the plate thickness

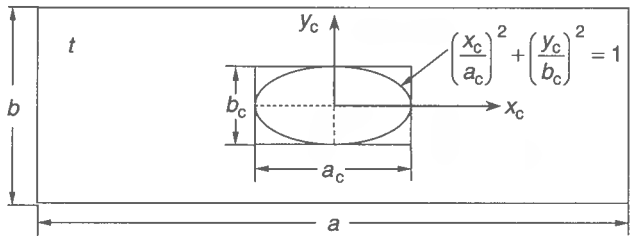

Figure 4.37 Elliptical and rectangular types of opening

types of hole, i.e., with elliptical and rectangular shapes. Figure 4.38 represents samples of the finite element mesh for the plate with elliptical or rectangular holes.

The insights developed by a series of nonlinear FEA for plates with elliptical or rectangular holes, varying the size of holes, the plate aspect ratio or the plate thickness, suggest that the ultimate strength reduction factor formulas derived in the previous sections for plates with a circular hole can also be valid for elliptical or rectangular types of hole, but replacing the parameters in the formulas (Jun 2002). In calculating the plate ultimate strength for longitudinal axial compression, the value of b_c/b is inserted into the parameter d_c/b, while the value of a_c/a is regarded as d_c/b for transverse axial compression. The accuracy of this approximate treatment is checked in Figures 4.39 and 4.40.

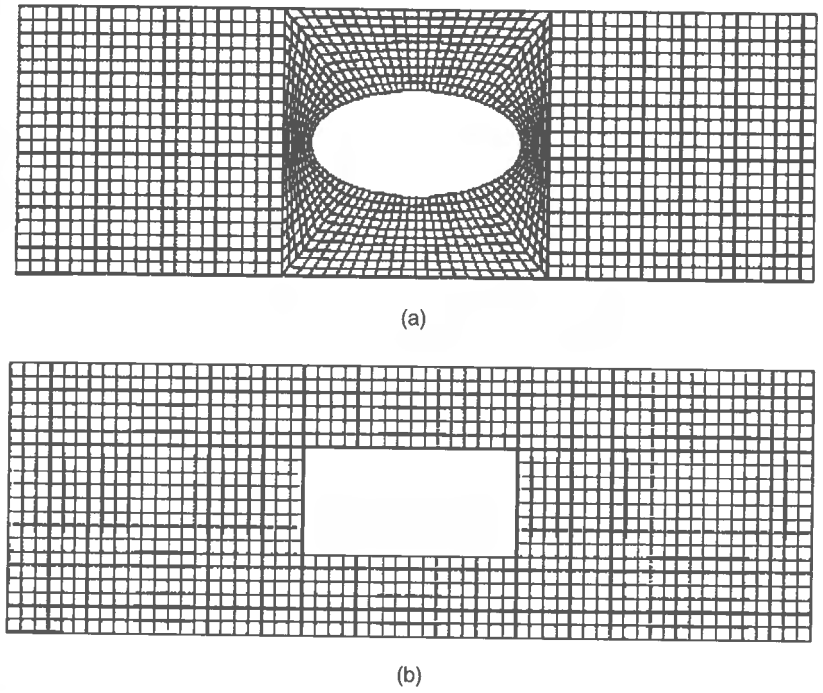

(a)

(b)

Figure 4.38 A sample of the finite element mesh for the plate with (a) a centrally located elliptical hole, $a/b = 3$, and (b) a centrally located rectangular hole, $a/b = 3$

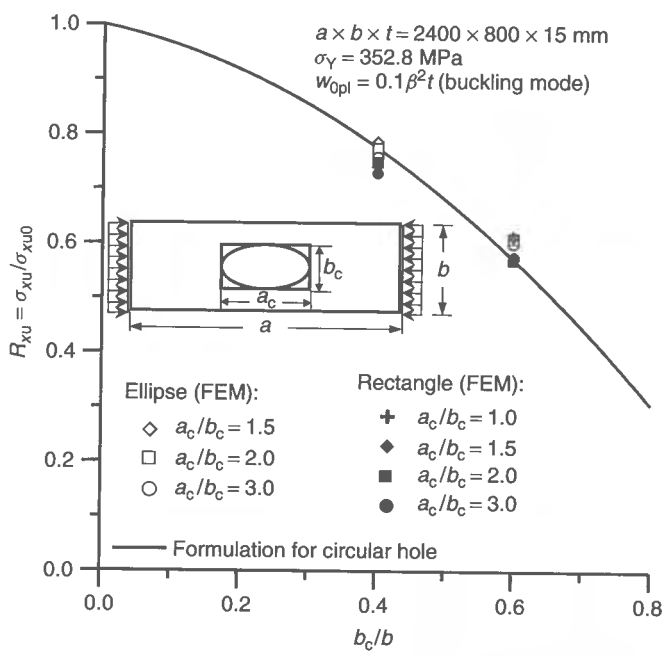

Figure 4.39 A comparison of the theoretical ultimate strength formula with FEA for perforated plates with various shapes of opening and under longitudinal axial compression

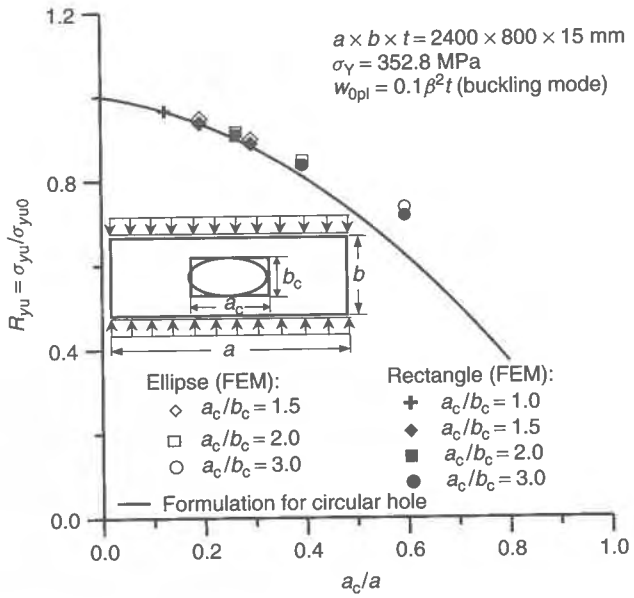

Figure 4.40 A comparison of the theoretical ultimate strength formula with FEA for perforated plates with various shapes of opening and under transverse axial compression

4.12 Effect of Age-related Structural Degradation

4.12.1 Corrosion Damage

Two primary parameters of age-related structural degradation are corrosion and fatigue cracks. As previously described in Section 1.8.1 of Chapter 1, corrosion wear can reduce the ultimate strength of plates. For general (uniform) corrosion which uniformly reduces the plate thickness, the plate ultimate strength calculations are typically carried out by excluding the thickness loss due to corrosion. For localized corrosion such as pitting or grooving, the strength calculation procedure can be more complex, but for a simplified pessimistic treatment, the corroded plates may also be idealized using an equivalent general corrosion.

This section investigates the effect of corrosion on the plate ultimate strength using nonlinear FEA. Two types of corrosion, namely pitting and general (uniform) corrosion, are considered. Figure 4.41(a) shows a schematic of a plate with localized corrosion of rectangular profile, $a_r \times b_r \times t_r$, in size, and Figure 4.41(b) represents a sample of the finite element model. All four edges of the plates are assumed to be simply supported, keeping them straight. While an average level of initial deflection is assumed, no welding residual stresses exist.

In the FEA modeling, the plate thickness is subdivided into several layers and the material properties (e.g., Young's modulus) of the pitting corrosion region are supposed to be zero for reasons of computational efficiency. The validity of this modeling procedure is confirmed for the simpler case of a plate with symmetric pit corrosion by comparing it to another method of modeling which directly cuts out the pitting corrosion regions.

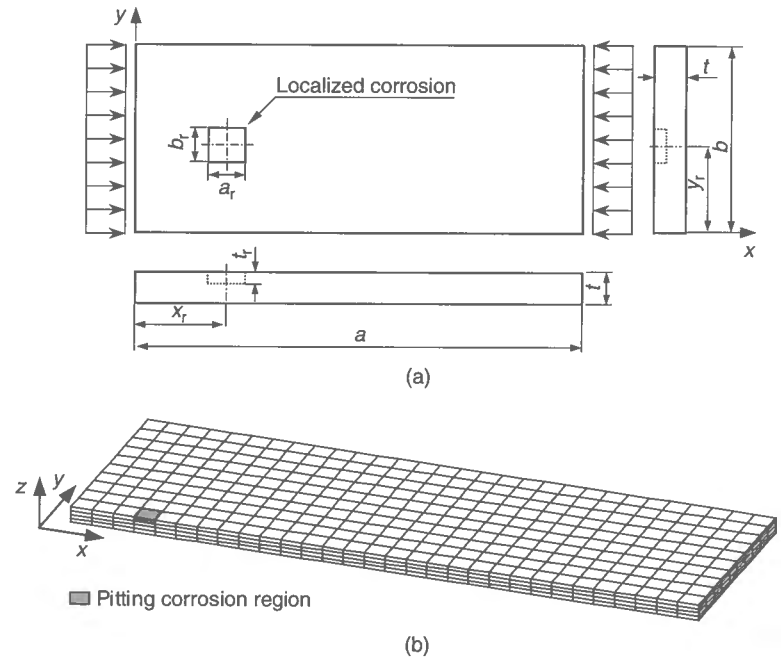

Figure 4.41 (a) A schematic of a plate with localized (unsymmetric) pit corrosion; (b) A sample of the FEA model of a plate with localized (unsymmetric) pit corrosion

The center of the corroded region is located at the coordinates (x_r, y_r). For general corrosion, it is assumed that the depth (diminution) of corrosion, t_r, is uniformly reduced over the entire plate element. Figure 4.42 presents typical average stress–strain curves of the corroded plates under axial compressive loads, varying the location of a small single pitting corrosion or the depth of corrosion, as those obtained by nonlinear FEA. As expected from Figure 4.42, one isolated small corrosion pit located anywhere in the plate may not reduce the plate ultimate compressive strength to any significant extent. However, such a pit does affect the post-ultimate strength behavior of the plate. Specifically, the unloading path of the plate with a through thickness pit in the post-ultimate regime becomes more rapid than that of the general corrosion plate, implying more unstable behavior. This is because of the important role the out-of-plane bending due to eccentric loading around the localized corrosion plays in such a case. The results also suggest that the use of an 'equivalent' general corrosion-based approximation to represent a case of low-intensity pitting may be somewhat pessimistic in terms of the ultimate strength, but it is not always pessimistic in terms of the post-ultimate strength behavior.

Next, the effect of pitting corrosion intensity on the plate ultimate strength in compression is considered. It is known that the shape of pitting corrosion is typically circular and the maximum diameter of one area of localized corrosion may be in the range of 25–80 mm for marine immersion corrosion of steel (Daidola *et al.* 1997), with the lower values being more likely. The calculations here assume that the shape of pitting corrosion is rectangular, and of dimensions $a_r \times b_r = 80 \times 80$ mm, primarily for reasons of computational efficiency. Figure 4.43 shows a schematic distribution of localized corrosion with 30% intensity.

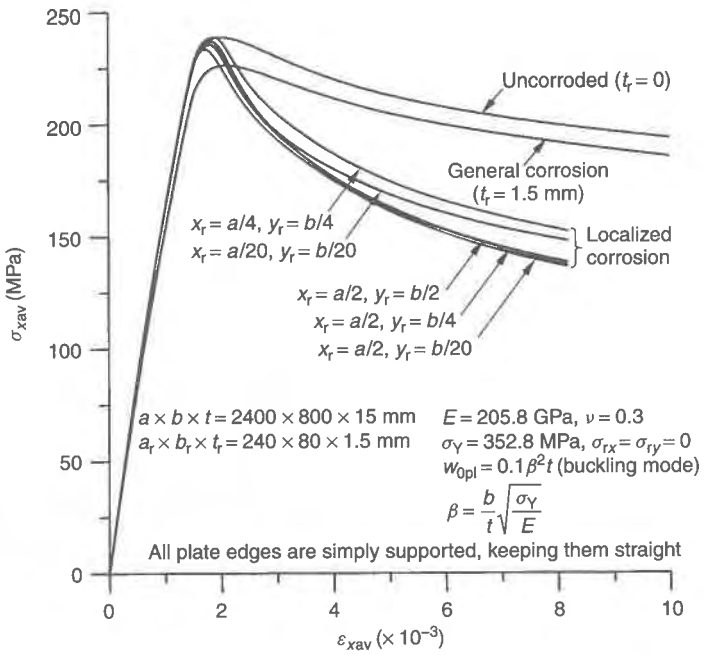

Figure 4.42 Effect of (a) the localized corrosion location and (b) the localized corrosion depth on the plate ultimate strength behavior, as obtained by nonlinear FEA

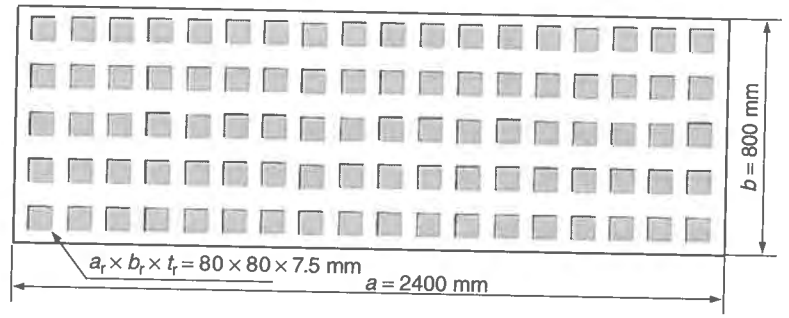

Figure 4.43 A schematic distribution of localized corrosions with 30% intensity

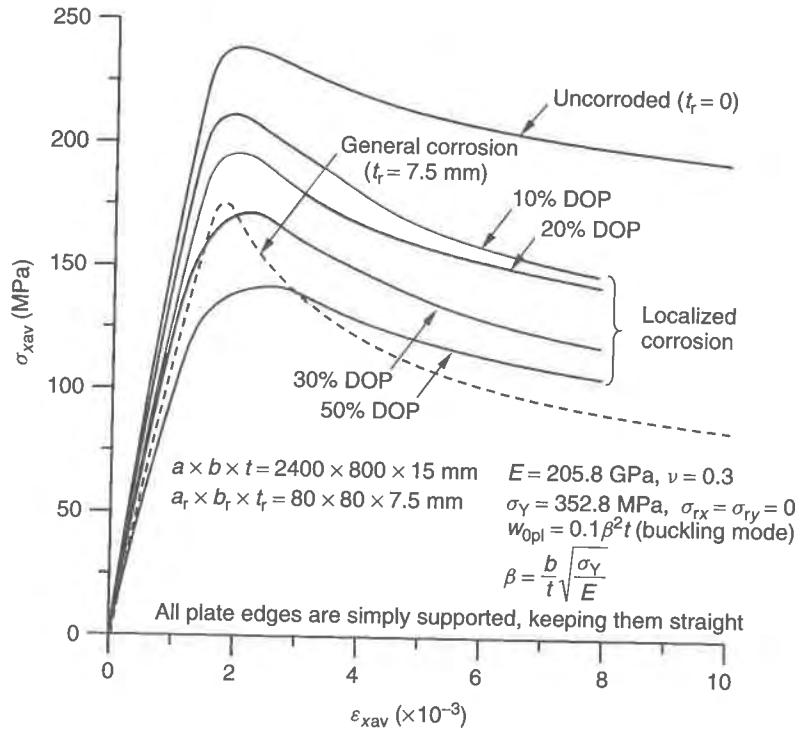

Figure 4.44 Effect of the degree of pitting corrosion intensity on the plate ultimate strength behavior, as obtained by nonlinear FEA (DOP = degree of pitting corrosion intensity)

Figure 4.44 shows the effect of the degree of pitting corrosion on the plate ultimate strength behavior. As the degree of pitting corrosion increases, the plate ultimate strength decreases significantly as would be expected. For the case considered in Figure 4.44, a general corrosion-based prediction of the plate ultimate strength correlates well with that of about 30% degree of pitting corrosion keeping the pit depth the same. Pitting over 30% of the plate surface area would normally be considered unacceptable in practice.

4.12.2 Fatigue Cracks

In aging steel structures, fatigue crack damage is often found and can in some cases significantly affect (reduce) the load-carrying capacity. For the analysis of structural members with existing cracks and under monotonically increasing loads, the theory of fracture mechanics may be used to predict the ULS capacity, as will be described in Chapter 10. However, it is not straightforward to carry out such an analysis for a large structure involving many pre-existing cracks.

As an easier alternative within the current framework of ultimate strength calculation for a complex structural system, the ultimate strength of plates with existing cracks may be predicted on the basis of the reduced cross-sectional area, accounting for the loss of load-carrying material due to the crack damage, as will be described in Section 10.6 of Chapter 10.

4.13 Computer Software ALPS/ULSAP

Ultimate strength formulations of plates presented in this chapter are automated using a computer program called ALPS/ULSAP, which stands for nonlinear analysis of large plated structures/ultimate strength analysis of panels. The ALPS/ULSAP program together with the user's manual can be downloaded from the web site by following the instructions noted in the appendices to this book.

References

BS 5400 (2000). *Steel, concrete and composite bridges. Part 3 code of practice for design of steel bridges*. British Standards Institution, London.

Daidola, J.C., Parente, J., Orisamolu, I.R. & Ma, K.T. (1997). *Residual strength assessment of pitted plate panels*. Ship Structure Committee, SSC-394, Washington, DC.

Dier, A.F. & Dowling, P.J. (1980). Strength of ship's plating – plates under combined lateral loading and biaxial compression. CESLIC Report SP8, Department of Civil Engineering, Imperial College, London.

Ellinas, C.P., Supple, W.J. & Walker, A.C. (1984). *Buckling of offshore structures: a state-of-the-art review*. Gulf Publishing, Houston.

ENV 1993-1-1 (1992). *Eurocode 3: design of steel structures, part 1.1 general rules and rules for buildings*. British Standards Institution, London.

Faulkner, D. (1975). A review of effective plating for use in the analysis of stiffened plating in bending and compression. *Journal of Ship Research*, 19(1): 1–17.

Faulkner, D., Adamchak, J.C., Snyder, G.J. & Vetter, M.F. (1973). Synthesis of welded grillages to withstand compression and normal loads. *Computers & Structures*, 3: 221–246.

Fletcher, C.A.J. (1984). *Computational Galerkin method*. Springer-Verlag, New York.

Fox, E.N. (1974). Limit analysis for plates: the exact solution for a clamped square plate of isotropic homogeneous material obeying the square yield criterion and loaded by a uniform pressure. *Philosophical Transactions of the Royal Society of London, Series A (Mathematical and Physical Sciences)*, 277: 121–155.

Fujita, Y., Nomoto, T., Niho, O. & Yoshie, A. (1979). Ultimate strength of rectangular plates subjected to combined loading (2nd report) – rectangular plates under compression and lateral pressure. *Journal of the Society of Naval Architects of Japan*, 146: 289–297 (in Japanese).

Hu, Y. & Sun, J. (1999). An approximate method to generate average stress–strain curve with the effect of residual stresses for rectangular plates under uniaxial compression in ship structures. *Marine Structures*, 12: 585–603.

Jones, N. (1975). Plastic behavior of beams and plates. Chapter 23 in *Ship Structural Design Concepts*. Cornell Maritime Press, Cambridge, MD, 747–778.

Jones, N. (1989). *Structural impact*. Cambridge University Press, Cambridge.

Jun, M.J. (2002). *Development of buckling and ultimate strength formulations for ship plating with cutout*. Master Thesis, Department of Naval Architecture and Ocean Engineering, Pusan National University, Busan (in Korean).

Marguerre, K. (1938). Zur Theorie der gekreummter Platte grosser Formaenderung. *Proceedings of the 5th International Congress for Applied Mechanics*, Cambridge.

Murray, N.W. (1986). *Introduction to the theory of thin-walled structures*. Clarendon Press, Oxford.

Nara, S., Deguchi, Y. & Fukumoto, Y. (1988). Ultimate strength of steel plate panels with initial imperfections under uniform shearing stress. *Proceedings of the Japan Society of Civil Engineers*, 392/I-9: 265–271 (in Japanese).

Paik, J.K. (1995). A new concept of the effective shear modulus for a plate buckled in shear. *Journal of Ship Research*, 39(1): 70–75.

Paik, J.K. & Pedersen, P.T. (1996). A simplified method for predicting the ultimate compressive strength of ship panels. *International Shipbuilding Progress*, 43(434): 139–157.

Paik, J.K., Thayamballi, A.K. & Kim, B.J. (2001). Advanced ultimate strength formulations for ship plating under combined biaxial compression/tension, edge shear and lateral pressure loads. *Marine Technology*, 38(1): 9–25.

Rhodes, J. (2002). Buckling of thin plates and members – and early work on rectangular tubes. *Thin-Walled Structures*, 40: 87–108.

Stonor, R.W.P., Bradfield, C.D., Moxham, K.E. & Dwight, J.B. (1983). Tests on plates under biaxial compression. Report CUED/D-Struct/TR98, Engineering Department, Cambridge University, Cambridge.

Timoshenko, S.P. & Woinowsky-Krieger, S. (1981). *Theory of plates and shells*, Second Edition, McGraw-Hill, London.

Valsgåard, S. (1980). Numerical design prediction of the capacity of plates in in-plane compression. *Computers & Structures*, 12: 729–739.

Wood, R.H. (1961). *Plastic and elastic design of slabs and plates*. The Ronald Press, New York.

Yamamoto, Y., Matsubara, N. & Murakami, T. (1970). Buckling strength of rectangular plates subjected to edge thrusts and lateral pressure (2nd report). *Journal of the Society of Naval Architects of Japan*, 127: 171–179 (in Japanese).

5 Elastic and Inelastic Buckling of Stiffened Panels and Grillages

5.1 Fundamentals of Stiffened Panel Buckling

As compressive loads increase, a stiffened panel, being an assembly of plating and stiffeners, can buckle if the applied load (or for convenience, stress) reaches a critical value. The buckling patterns of the stiffened panel can normally be categorized into two major groups, namely overall buckling and local buckling, the latter being associated with buckling of either plating or stiffeners. Figure 5.1 shows typical patterns of stiffened panel buckling.

When the stiffeners are 'small', a stiffened panel can buckle together with plating, in a mode that may be termed overall buckling, as shown in Figure 5.1(a). On the other hand, when the stiffeners are relatively strong they remain straight until the plating between them buckles locally, as shown in Figure 5.1(b). If the height of the stiffener web is large or the web thickness is small, the stiffener web can buckle locally much like a plate element, see Figure 5.1(c). When the torsional rigidity of the stiffener is not strong enough, the stiffener can twist sideways, in a mode called lateral–torsional buckling (also called tripping), as shown in Figure 5.1(d). While Figure 5.1 illustrates each buckling pattern separately for convenience, some buckling modes may in some cases interact and occur almost simultaneously.

Unlike columns, a stiffened panel can normally sustain applied loads further even after buckling occurs locally and the stiffened panel ultimate strength is eventually reached by excessive plasticity in the plate field and/or failure of stiffener. However, any occurrence of the elastic overall buckling is generally to be considered a significant instability of the entire structure. In design, therefore, the order of the buckling modes for a stiffened panel or grillage is typically controlled such that the overall buckling mode is prevented prior to local buckling of plating between stiffeners.

The elastic buckling of a stiffened panel is thus a good indication of the required panel strength with regard to the serviceability limit state (SLS) design. To better understand the ultimate limit state (ULS) design procedure, it is also essential to have a basic knowledge of the buckling strength of the stiffened panel.

In the SLS design of stiffened panels using Equation (1.1) of Chapter 1, the design load effects (i.e., stresses) are calculated by the classical theory of structural mechanics

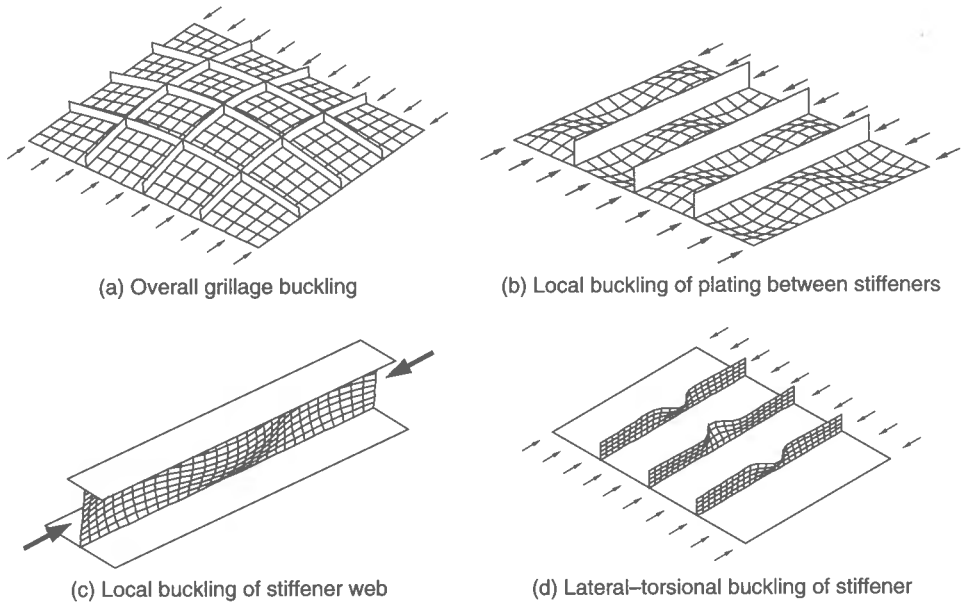

Figure 5.1 Schematics of various types of stiffened panel buckling

or linear elastic finite element analysis, while the design capacity may be determined by relevant buckling strength formulations.

This chapter presents the fundamentals as well as useful elastic buckling strength design formulations for a stiffened panel under combined loads and also under single types of loads. The elastic–plastic buckling strength in such a case may as usual be estimated by correcting the elastic buckling strength using the Johnson–Ostenfeld formula, Equation (2.93), so that the influence of plasticity is approximately accounted for.

5.2 Geometric and Material Properties

Figure 5.2 shows a typical stiffened panel taken from a continuous stiffened plate structure under combined loads. The strength formulations are in principle considered for a panel with stiffeners in both directions since the buckling of a longitudinally or transversely stiffened panel, i.e., with stiffeners in one direction alone, can be considered as a specific case of a cross-stiffened panel (called a grillage).

The length and breadth of the stiffened panel are denoted by L and B, respectively. The thickness of the plate is t. The number of x and y stiffeners is n_{sx} and n_{sy}, respectively. The stiffeners are considered to be arranged with the same spacing in any given direction, the spacing of the stiffeners being denoted by a between y stiffeners, i.e., $a = L/(n_{sy} + 1)$, and b between x stiffeners, i.e., $b = B/(n_{sx} + 1)$.

Figure 5.3 presents the typical geometry of stiffeners in the x or y direction. Stiffeners are attached to one side of the panel, i.e., on the positive side of the z direction. The geometry of the stiffeners in each direction of the panel is considered identical. The stiffened panel is surrounded by longitudinal girders and transverse frames which are heavier than the stiffeners.

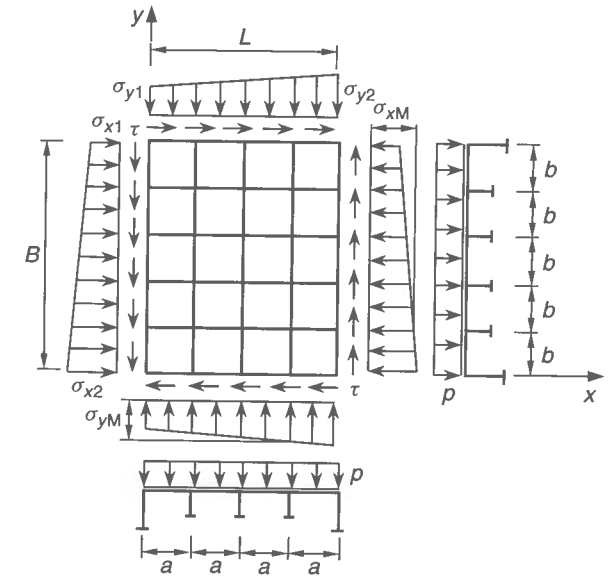

Figure 5.2 A cross-stiffened panel under combined in-plane loads and lateral pressure

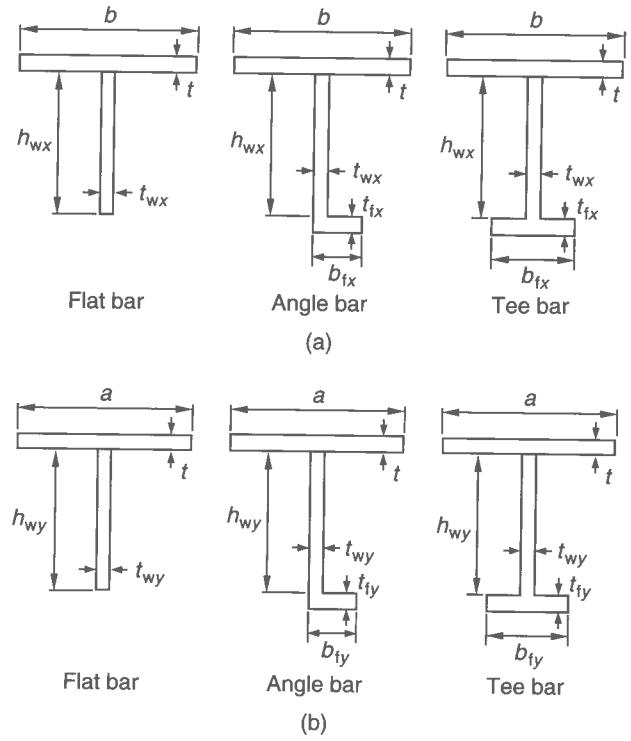

Figure 5.3 Typical cross-section types for (a) longitudinals and (b) transverses

The elastic modulus and Poisson's ratio of both plating and stiffeners are E and ν, respectively. The elastic shear modulus is thus $G = E/[2(1+\nu)]$. The bending rigidity of plating between stiffeners is denoted by $D = Et^3/[12(1-\nu^2)]$. The material yield stress is σ_{Yp} for plating and σ_{Ys} for stiffeners. When the stiffened panel buckles in the overall mode and reaches the ultimate strength primarily by excessive plasticity of the plate, it may be idealized as an 'orthotropic plate'. In this case, it is proposed that an equivalent yield stress, σ_{Yeq}, for the entire stiffened panel may approximately be defined as

$$\sigma_{Yeq} = \begin{cases} \sigma_{Yx} & \text{for longitudinally stiffened panels} \\ \sigma_{Yy} & \text{for transversely stiffened panels} \\ (\sigma_{Yx} + \sigma_{Yy})/2 & \text{for orthogonally stiffened panels} \end{cases} \tag{5.1}$$

where

$$\sigma_{Yx} = \frac{Bt\sigma_{Yp} + n_{sx}A_{sx}\sigma_{Ys}}{Bt + n_{sx}A_{sx}}, \quad \sigma_{Yy} = \frac{Lt\sigma_{Yp} + n_{sy}A_{sy}\sigma_{Ys}}{Lt + n_{sy}A_{sy}}$$

$$A_{sx} = h_{wx}t_{wx} + b_{fx}t_{fx}, \quad A_{sy} = h_{wy}t_{wy} + b_{fy}t_{fy}$$

However, when the panel reaches the ultimate strength subsequent to the more localized failure of the plate or stiffeners, individual yield stresses are to be used for the collapse strength calculation of each part, as will be described in Chapter 6.

5.3 Loads and Load Effects

When a continuous stiffened plate structure is subjected to external loads, the load effects (e.g., stresses, deformations) can be typically analyzed by the linear elastic finite element method or classical theory of structural mechanics. As previously described in Section 3.3 of Chapter 3, the response associated with the primary, secondary and tertiary levels of the structure must be accounted for in determining the characteristic measure of the load effects in a stiffened panel.

As shown in Figure 5.2, the potential stresses acting on stiffened panels are generally of six types as follows:

- longitudinal axial stress;
- transverse axial stress;
- edge shear stress;
- longitudinal in-plane bending stress;
- transverse in-plane bending stress; and
- lateral pressure-related stress.

In this chapter (and Chapter 6), it is taken that compressive stresses are negative and tensile stresses are positive, unless otherwise specified. When the stiffened panels are simultaneously subjected to combined in-plane loads and lateral pressure, the latter is normally considered to be applied first in our treatment, and the other in-plane load components will then be taken to be applied additionally.

In the overall buckling mode, the plating typically deflects together with stiffeners. In this case, the average values of the applied axial stresses are often used as the characteristic measure of the load effects, thus neglecting the influence of in-plane bending as follows:

$$\sigma_{xav} = \frac{\sigma_{x1} + \sigma_{x2}}{2}, \quad \sigma_{yav} = \frac{\sigma_{y1} + \sigma_{y2}}{2} \tag{5.2}$$

where σ_{x1}, σ_{x2}, σ_{y1}, σ_{y2} are as defined in Figure 5.2.

In a local buckling mode, the axial compressive stresses applied at the location of the most highly stressed stiffeners may be used as the stress parameters for local buckling analysis of the stiffeners or plating. The values of the highest applied stresses at the x and y stiffeners are denoted by σ_{xM} and σ_{yM}, respectively, see Figure 5.2. Also, the edge shear stress and uniform lateral pressure loads are denoted by τ_{av} and p, respectively.

5.4 Boundary Conditions

The edges of the stiffened panel extent are usually supported by strong beam members (e.g., girders or frames). The bending rigidities of the boundary support members are normally quite large compared to that of the panel itself. This implies that the normal displacements of the support members in the direction of panel deflections are very small even up to panel collapse. The rotational restraints along the panel edges depend on the torsional rigidities of the support members, and these are neither zero nor infinite.

When predominantly in-plane compressive loads are applied on a continuous plated structure surrounded by support members, the buckling pattern of the panel is expected to be asymmetrical, i.e., one panel will tend to buckle up and the adjacent panel tends to deflect down. In this case, rotational restraints along the panel edges can be considered to be small.

When the plated structure is subjected predominantly to laterally distributed loads, however, the buckling pattern of the structure tends to be symmetrical, at least for large enough pressures, i.e., each adjacent panel may deflect in the direction of lateral pressure loading. In this case, the edge rotational restraints can eventually become large enough so that they correspond to a clamped condition from the beginning of loading in some cases. However, if plasticity occurs earlier along the panel edges where the large bending moments are developed, the rotational restraints at the yielded edges will then be lessened as the applied loads increase.

In a continuous plated structure, the edges of individual stiffened panels are considered to remain almost straight due to the structural response being relative to the adjacent panels even if the panel deflects. In this regard, an idealized condition, i.e., one with zero rotational restraints along the panel edges, has been widely used for practical purposes of analysis.

In this chapter (and Chapter 6), it is also assumed that the panel edges are simply supported, with zero deflection and zero rotational restraints along four edges, with all edges kept straight. In most practical situations, this approximation will lead to adequate results. In contrast, the influence of rotational restraints along the junctions of plate–stiffener and/or stiffener web–flange may need to be accounted for in the calculations of local buckling of either plating between stiffeners or stiffener web.

5.5 Fabrication-related Initial Imperfections

While the fabrication-related initial imperfections in stiffened panels are described in Section 1.7 of Chapter 1, it is assumed for the purposes of this chapter that initial imperfections do not exist, mostly since a bifurcation buckling phenomenon may not appear in a panel that has initial deformations or curvatures. As will be noted later in Chapter 6, however, the influence of initial imperfections on the panel ultimate strength is accounted for.

5.6 Linear Elastic Behavior

When the stiffened panel is subjected to predominantly axial tensile loads, its behavior will remain linear elastic until gross yielding is reached. Also, if the panel does not involve initial imperfections at all, it will under compression show linear elastic behavior until buckling takes place.

In this case, since a stiffened panel is an assembly of plating and stiffeners, its behavior can be represented by the average stress–strain relationships, which are defined by

$$\varepsilon_{xav} = \frac{1}{E_x}\sigma_{xav} - \frac{\nu_y}{E_y}\sigma_{yav} \tag{5.3a}$$

$$\varepsilon_{yav} = -\frac{\nu_x}{E_x}\sigma_{xav} + \frac{1}{E_y}\sigma_{yav} \tag{5.3b}$$

$$\gamma_{av} = \frac{1}{G_{xy}}\tau_{av} \tag{5.3c}$$

where ε_{xav}, ε_{yav}, γ_{av} are the average strain components corresponding to average stress components σ_{xav}, σ_{yav}, τ_{av}, respectively; E_x, E_y, G_{xy} = elastic constants of the stiffened panel as defined in Section 6.4.1 of Chapter 6. Equations (5.3a) to (5.3c) can be rewritten as follows:

$$\sigma_{xav} = \frac{E_x}{1-\nu_x\nu_y}(\varepsilon_{xav} + \nu_y\varepsilon_{yav}) \tag{5.3d}$$

$$\sigma_{yav} = \frac{E_y}{1-\nu_x\nu_y}(\nu_x\varepsilon_{xav} + \varepsilon_{yav}) \tag{5.3e}$$

$$\tau_{av} = G_{xy}\gamma_{av} \tag{5.3f}$$

Equations (5.3d) to (5.3f) can be written in matrix form as follows:

$$\begin{Bmatrix} \sigma_{xav} \\ \sigma_{yav} \\ \tau_{av} \end{Bmatrix} = [D_{sp}]^E \begin{Bmatrix} \varepsilon_{xav} \\ \varepsilon_{yav} \\ \gamma_{av} \end{Bmatrix} \tag{5.4}$$

where

$$[D_{sp}]^E = \begin{bmatrix} A_1 & A_2 & 0 \\ B_1 & B_2 & 0 \\ 0 & 0 & C_1 \end{bmatrix}$$

is the stress–strain matrix of the stiffened panel in the linear elastic regime, with

$$A_1 = \frac{E_x}{1-\nu_x\nu_y}, \quad A_2 = \frac{E_x\nu_y}{1-\nu_x\nu_y}, \quad B_1 = \frac{E_y\nu_x}{1-\nu_x\nu_y}, \quad B_2 = \frac{E_y}{1-\nu_x\nu_y}, \quad C_1 = G_{xy}$$

Since Equation (5.4) is linear with regard to both stress and strain, the incremental form of the average stress–strain relationship with regard to the stress and strain components will be identical to Equation (5.4).

5.7 Overall Buckling Versus Local Buckling

Since any occurrence of the elastic overall panel buckling leads to a significant instability of the entire plated structure, the order of the panel buckling modes is typically controlled such that the overall panel buckling mode is prevented prior to local buckling of plating between stiffeners. Under a multi-axial compressive load situation, the following criterion must then be satisfied so that overall panel buckling may not take place prior to the local buckling of plating between stiffeners, namely

$$K_{OB} \le K_{LB} \tag{5.5a}$$

where K_{LB} and K_{OB} denote the characteristic measures of local plate buckling and overall panel buckling, respectively, which may be given in terms of the applied stresses and the corresponding buckling strength components. For instance, K_{LB} and K_{OB} may be given for a stiffened panel under biaxial compressive loads as follows:

$$K_{OB} = \sqrt{\left(\frac{\sigma_{xav}}{\sigma_{xEO}}\right)^2 + \left(\frac{\sigma_{yav}}{\sigma_{yEO}}\right)^2}, \quad K_{LB} = \sqrt{\left(\frac{\sigma_{xM}}{\sigma_{xEL}}\right)^2 + \left(\frac{\sigma_{yM}}{\sigma_{yEL}}\right)^2} \tag{5.5b}$$

where σ_{xav}, σ_{yav} = average compressive stresses in the x or y direction, σ_{xM}, σ_{yM} = highest compressive stresses in the x or y direction, σ_{xEO}, σ_{yEO} = elastic overall compressive buckling stresses in the x or y direction, σ_{xEL}, σ_{yEL} = elastic compressive buckling stresses of plating between stiffeners in the x or y direction.

For uniaxial compression, the criterion is readily obtained from Equations (5.5a) and (5.5b) so that the overall buckling will not occur prior to local buckling of plating between stiffeners as long as the following condition is satisfied:

$$\frac{\sigma_{xav}}{\sigma_{xEO}} \le \frac{\sigma_{xM}}{\sigma_{xEL}} \quad \text{or} \quad \frac{\sigma_{yav}}{\sigma_{yEO}} \le \frac{\sigma_{yM}}{\sigma_{yEL}} \tag{5.5c}$$

In this regard, Equations (5.5) can be utilized to control the order of the buckling mode for a stiffened panel once the elastic buckling strength components in the local and overall modes are known.

5.8 Elastic Overall Buckling

This section presents the elastic overall buckling strength formulations of a stiffened panel under combined loads as well as single types of loads.

5.8.1 Longitudinal Axial Compression

Longitudinally Stiffened Panels

The overall buckling of a panel with only longitudinal stiffeners and under longitudinal axial compression may approximately be represented by the column buckling of a plate–stiffener combination as previously described in Section 2.8.2 of Chapter 2. In this case, the plate–stiffener combination as representative of the panel is supposed to be simply supported at both ends.

Transversely Stiffened Panels

The overall buckling strength of the panel with only transverse stiffeners and under longitudinal axial compression may be approximately predicted from the corresponding plate buckling strength formula presented in Section 3.6 of Chapter 3, but by assuming that the transverse stiffeners do not exist. It is cautioned that the coordinate system of the panel may need to be rotated since the plate buckling strength formulas presented in Section 3.6 consider only long plates, i.e., $L/B \geq 1$.

Orthogonally Stiffened Panels

When the panel has stiffeners in both the x and y directions and it buckles in the overall mode, the elastic overall buckling strength of the panel can be calculated by solving the nonlinear governing differential equations derived from the elastic large-deflection orthotropic plate theory, as will be described in detail later in Chapter 6. An analytical solution of the elastic overall buckling for a simply supported orthotropic plate under uniaxial compressive loads in the x direction is given by

$$\sigma_{xEO,1} = -\frac{\pi^2}{B^2 t}\left(D_x \frac{m^2 B^2}{L^2} + 2Hn^2 + D_y \frac{n^4 L^2}{m^2 B^2}\right) \equiv -k_{xO}\frac{\pi^2 D}{B^2 t} \tag{5.6}$$

where

$$k_{xO} = \frac{1}{D}\left(D_x \frac{m^2 B^2}{L^2} + 2Hn^2 + D_y \frac{n^4 L^2}{m^2 B^2}\right)$$

is the elastic overall buckling strength coefficient for longitudinal axial compression, D_x, D_y, H are as defined in Section 6.4.1 of Chapter 6, and D is as defined in Section 5.2. The subscript '1' indicates that the number of load components is one. m and n are the overall buckling half-wave numbers of the panel in the x and y directions, respectively.

As long as longitudinal compressive loads are applied, the buckling half-wave number of the orthotropic plate in the direction of the short edge may be taken as 1, which is similar to that of an isotropic plate, namely

$$n = 1 \quad \text{for a long orthotropic plate with } L/B \geq 1 \tag{5.7a}$$

$$m = 1 \quad \text{for a wide orthotropic plate with } L/B < 1 \tag{5.7b}$$

When the cross-stiffened panel surrounded by heavy longitudinal girders and transverse frames is relatively wide, therefore, $m = 1$ may sometimes be used for practical purposes.

In this case, the buckling half-wave number in the y direction may also be taken as $n = 1$ since no axial compressive loads are applied in the y direction.

On the other hand, m must be determined for a long orthotropic plate as a minimum integer satisfying the following condition since $n = 1$, namely

$$\left(\frac{L}{B}\right)^4 \leq \frac{D_x}{D_y} m^2 (m+1)^2 \tag{5.8a}$$

From this, it is evident that the buckling half-wave number of the orthotropic plate is affected by the structural orthotropy as well as the panel aspect ratio. For an isotropic plate, Equation (5.8a) becomes

$$\frac{L}{B} \leq \sqrt{m(m+1)} \tag{5.8b}$$

since $D_x = D_y$.

5.8.2 Transverse Axial Compression

Longitudinally Stiffened Panels

The overall buckling strength of the panel with only longitudinal stiffeners and under transverse axial compression may approximately be predicted from the corresponding plate buckling strength formula presented in Section 3.6 of Chapter 3, but by assuming that the longitudinal stiffeners do not exist. It is again cautioned that the coordinate system of the panel may need to be rotated since the plate buckling strength formulas presented in Section 3.6 consider only long plates, i.e., $L/B \geq 1$.

Transversely Stiffened Panels

The overall buckling of a panel with only transverse stiffeners, and under transverse axial compression, may approximately be represented by the column buckling of the plate–stiffener combination with the simply supported end condition as previously described in Section 2.8.2 of Chapter 2.

Orthogonally Stiffened Panels

The large-deflection orthotropic plate theory can also be applied to calculate the elastic overall buckling of a cross-stiffened panel under axial compression in the y direction, as will be described later in Chapter 6.

In this case, the solution of the nonlinear governing differential equations of the large-deflection orthotropic plate theory under boundary conditions of simple support at all edges gives the elastic overall buckling strength of a stiffened panel under uniaxial compressive loads in the y direction as follows:

$$\sigma_{yEO,1} = -\frac{\pi^2}{B^2 t}\left(D_x \frac{m^4 B^4}{n^2 L^4} + 2H\frac{m^2 B^2}{L^2} + D_y n^2\right) \equiv -k_{yO}\frac{\pi^2 D}{B^2 t} \tag{5.9}$$

where

$$k_{yO} = \frac{1}{D}\left(D_x \frac{m^4 B^4}{n^2 L^4} + 2H\frac{m^2 B^2}{L^2} + D_y n^2\right)$$

is the elastic overall buckling strength coefficient for transverse axial compression, D_x, D_y, H are as defined in Section 6.4.1 of Chapter 6, and D is as defined in Section 5.2. m and n are the buckling half-wave numbers of the panel in the x and y directions, respectively.

As indicated in Equations (5.7), $m = n = 1$ may be taken for a long orthotropic plate (i.e., with $L/B \geq 1$), since no axial compressive loads are applied in the x direction. For a wide orthotropic plate (i.e., with $L/B < 1$), the buckling half-wave number in the y direction may be determined as a minimum integer satisfying the following condition since $m = 1$:

$$\left(\frac{B}{L}\right)^4 \leq \frac{D_y}{D_x} n^2 (n+1)^2 \tag{5.10a}$$

For an isotropic plate, Equation (5.10a) will be simplified to

$$\frac{B}{L} \leq \sqrt{n(n+1)} \tag{5.10b}$$

since $D_x = D_y$.

5.8.3 Edge Shear

The elastic overall buckling of a stiffened panel under edge shear may be determined using the orthotropic plate theory. The elastic overall buckling strength for a simply supported orthotropic plate in edge shear was obtained by Seydel (1933), and is given by

$$\tau_{EO,1} = k_s \frac{\pi^2}{B^2 t} D_x^{1/4} D_y^{3/4} \tag{5.11}$$

where k_s is the shear buckling coefficient which may be determined from Figure 5.4 as a function of the panel aspect ratio and the various structural orthotropy parameters. As may be seen from Figure 5.4, $k_s \approx 9.34$, when $D_x = D_Y = H = D$ and $L/B = 1$, which corresponds to the elastic shear buckling coefficient of an isotropic square plate.

As long as the stiffeners are not very weak and they remain straight, which is the case when there is no development of a significant membrane tension field, the elastic overall shear buckling strength of a stiffened panel can be approximately taken as the elastic shear buckling strength of the simply supported plate between stiffeners with k_τ as defined in Table 3.1 of Chapter 3, as follows:

$$\tau_{EO,1} = k_\tau \frac{\pi^2}{12(1-\nu^2)}\left(\frac{t}{b}\right)^2 \tag{5.12}$$

5.8.4 Combined Biaxial Compression/Tension

The elastic overall post-buckling behavior of a stiffened panel under combined biaxial compression/tension can also be calculated by analytically solving the nonlinear governing

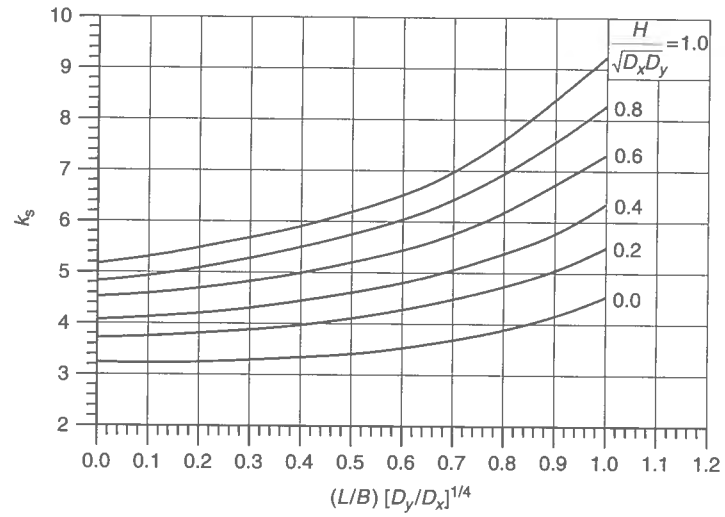

Figure 5.4 Overall buckling coefficient of stiffened panels in edge shear (Allen & Bulson 1980)

differential equation of the large-deflection orthotropic plate theory, as will be described in Chapter 6. Immediately before the bifurcation buckling occurs, the panel lateral deflection must be zero. This results in an overall panel buckling criterion under combined biaxial loads as follows:

$$\frac{m^2 B}{L}\sigma_{xav} + \frac{n^2 L}{B}\sigma_{yav} + \frac{\pi^2}{t}\left(D_x \frac{m^4 B}{L^3} + 2H\frac{m^2 n^2}{LB} + D_y \frac{n^4 L}{B^3}\right) = 0 \tag{5.13}$$

where σ_{xav} and σ_{yav} are the applied axial stresses in the x and y directions; m and n are the buckling half-wave numbers in the x and y directions, respectively.

It is readily seen from Equation (5.13) that Equation (5.6) or (5.9) applicable to the corresponding uniaxial compressive load cases may be obtained by putting the other stress component to zero. By holding the loading ratio, $c = \sigma_{yav}/\sigma_{xav}$, constant, the elastic overall buckling strength components, σ_{xEO} or σ_{yEO}, are in this case calculated by the solution of Equation (5.13) as follows:

$$\sigma_{xEO} = -\frac{\pi^2}{t(m^2 B/L + cn^2 L/B)}\left(D_x \frac{m^4 B^2}{n^2 L^4} + 2H\frac{m^2}{L^2} + D_y \frac{n^2}{B^2}\right) \tag{5.14a}$$

$$\sigma_{yEO} = c\sigma_{xEO} \tag{5.14b}$$

For a long panel (i.e., with $L/B \geq 1$), the buckling half-wave number m in the x direction is determined as a minimum integer satisfying the following equation since $n = 1$ in the direction of short edges:

$$\frac{D_x(m^4 B^2/L^4) + 2H(m^2/L^2) + D_y(1/B^2)}{m^2 B/L + cL/B} \leq \frac{D_x[(m+1)^4 B^2/L^4] + 2H[(m+1)^2/L^2] + D_y(1/B^2)}{(m+1)^2 B/L + cL/B} \tag{5.15}$$

where it is evident that the buckling half-wave number of the panel under biaxial loads is affected by the biaxial loading ratio as well as the structural orthotropy and aspect ratio.

For a wide panel (i.e., with $L/B < 1$), the buckling half-wave number n in the y direction can be determined as the minimum integer satisfying the following equation since $m = 1$ in the direction of short edges:

$$\frac{D_x(B^2/n^2L^4) + 2H(1/L^2) + D_y(n^2/B^2)}{B/L + cn^2L/B} \leq \frac{D_x[B^2/(n+1)^2L^4] + 2H(1/L^2) + D_y[(n+1)^2/B^2]}{B/L + c(n+1)^2L/B} \tag{5.16}$$

5.8.5 Combined Axial Compression and Edge Shear

Following the isotropic buckling strength interaction relationship as previously noted in Chapter 3, the elastic overall buckling strength interaction equations for a stiffened panel under combined uniaxial compression and edge shear are sometimes used for practical design purposes as follows:

$$\frac{\sigma_{xav}}{\sigma_{xEO,1}} + \left(\frac{\tau_{av}}{\tau_{EO,1}}\right)^2 = 1 \tag{5.17a}$$

$$\frac{\sigma_{yav}}{\sigma_{yEO,1}} + \left(\frac{\tau_{av}}{\tau_{EO,1}}\right)^2 = 1 \tag{5.17b}$$

where $\sigma_{xEO,1}$ is as defined in Section 5.8.1, $\sigma_{yEO,1}$ is as defined in Section 5.8.2, and $\tau_{EO,1}$ is as defined in Section 5.8.3.

5.9 Elastic Local Buckling of Plating between Stiffeners

When the stiffeners become stiff, they may remain straight until the plating between them buckles locally. In this case, the local buckling strength of plating can be calculated using the methods for the bare plate element between stiffeners taking into account the influences of various parameters, as previously presented in Chapter 3.

5.10 Elastic Local Buckling of Stiffener Web

The web of a stiffener in a stiffened panel can locally buckle, a possibility that must usually be considered for built-up sections. Such as occurrence of local buckling in the stiffener cross-section can sometimes be quite a sudden phenomenon resulting in subsequent unloading of the stiffened panel, particularly with use of flat-bar stiffeners. In this case, once such stiffener web buckling occurs, the buckled or collapsed plating is left with essentially no stiffening and thus overall stiffened panel collapse may follow with little increase in the loading.

The local buckling of the stiffener web and the buckling/collapse of plating between stiffeners normally interact, and can take place in any order, depending on the dimensions

of plating and stiffener. Clearly, buckling of the stiffener web prior to the inception of buckling in plating between stiffeners is normally an undesirable failure mode.

It is hence usually necessary in design that the stiffener web does not buckle until the plating between stiffeners buckles or collapses. However, the local buckling strength of the stiffener web depends significantly on the torsional rigidities of the adjacent members to which they are attached, among other factors. Since the rotational restraint along any plate–stiffener intersection can be decreased by collapse of the plating involved, local buckling strength of the stiffener web should be calculated by taking into account this effect to the extent it is relevant. As an approximation in such cases, the effective width of plating likely to buckle, as calculated at the ULS, is used for calculating the torsion constants supplied by such plating.

5.10.1 Governing Differential Equation

Figure 5.5 shows a schematic representation of loading and boundary conditions for a plate–stiffener combination model with the attached effective plating between two adjacent transverse frames in a grillage. In this case, the elastic buckling strength for the stiffener web can be analyzed by solving the governing differential equations, see Bleich (1952), among others.

The elastic buckling strength of a stiffener web, which is regarded as a very long plate (strip) under the appropriate edge conditions, may be analytically addressed as a characteristic value problem. The boundary condition of flat-bar stiffener along one edge is free, but for angle-type or Tee-stiffeners it may be assumed that the stiffener flange will not buckle until the inception of local buckling in the stiffener web, while the attached plating of the stiffened panel can itself buckle. This would imply that the rotational restraint at the web–flange junction is fully effective until the stiffener web buckles, while that at the web–panel plating junction takes a value deriving from an effective cross-section.

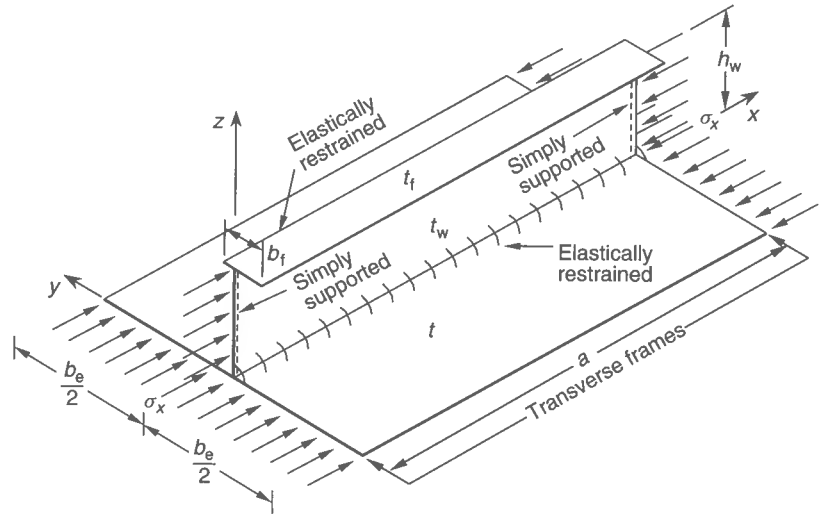

Figure 5.5 Schematic representation of loading and boundary conditions for the plate–stiffener combination model with the attached effective plating between two adjacent transverse frames under axial compression

where it is evident that the buckling half-wave number of the panel under biaxial loads is affected by the biaxial loading ratio as well as the structural orthotropy and aspect ratio.

For a wide panel (i.e., with $L/B < 1$), the buckling half-wave number n in the y direction can be determined as the minimum integer satisfying the following equation since $m = 1$ in the direction of short edges:

$$\frac{D_x(B^2/n^2L^4) + 2H(1/L^2) + D_y(n^2/B^2)}{B/L + cn^2L/B} \leq \frac{D_x[B^2/(n+1)^2L^4] + 2H(1/L^2) + D_y[(n+1)^2/B^2]}{B/L + c(n+1)^2L/B} \tag{5.16}$$

5.8.5 Combined Axial Compression and Edge Shear

Following the isotropic buckling strength interaction relationship as previously noted in Chapter 3, the elastic overall buckling strength interaction equations for a stiffened panel under combined uniaxial compression and edge shear are sometimes used for practical design purposes as follows:

$$\frac{\sigma_{xav}}{\sigma_{xEO,1}} + \left(\frac{\tau_{av}}{\tau_{EO,1}}\right)^2 = 1 \tag{5.17a}$$

$$\frac{\sigma_{yav}}{\sigma_{yEO,1}} + \left(\frac{\tau_{av}}{\tau_{EO,1}}\right)^2 = 1 \tag{5.17b}$$

where $\sigma_{xEO,1}$ is as defined in Section 5.8.1, $\sigma_{yEO,1}$ is as defined in Section 5.8.2, and $\tau_{EO,1}$ is as defined in Section 5.8.3.

5.9 Elastic Local Buckling of Plating between Stiffeners

When the stiffeners become stiff, they may remain straight until the plating between them buckles locally. In this case, the local buckling strength of plating can be calculated using the methods for the bare plate element between stiffeners taking into account the influences of various parameters, as previously presented in Chapter 3.

5.10 Elastic Local Buckling of Stiffener Web

The web of a stiffener in a stiffened panel can locally buckle, a possibility that must usually be considered for built-up sections. Such as occurrence of local buckling in the stiffener cross-section can sometimes be quite a sudden phenomenon resulting in subsequent unloading of the stiffened panel, particularly with use of flat-bar stiffeners. In this case, once such stiffener web buckling occurs, the buckled or collapsed plating is left with essentially no stiffening and thus overall stiffened panel collapse may follow with little increase in the loading.

The local buckling of the stiffener web and the buckling/collapse of plating between stiffeners normally interact, and can take place in any order, depending on the dimensions

of plating and stiffener. Clearly, buckling of the stiffener web prior to the inception of buckling in plating between stiffeners is normally an undesirable failure mode.

It is hence usually necessary in design that the stiffener web does not buckle until the plating between stiffeners buckles or collapses. However, the local buckling strength of the stiffener web depends significantly on the torsional rigidities of the adjacent members to which they are attached, among other factors. Since the rotational restraint along any plate–stiffener intersection can be decreased by collapse of the plating involved, local buckling strength of the stiffener web should be calculated by taking into account this effect to the extent it is relevant. As an approximation in such cases, the effective width of plating likely to buckle, as calculated at the ULS, is used for calculating the torsion constants supplied by such plating.

5.10.1 Governing Differential Equation

Figure 5.5 shows a schematic representation of loading and boundary conditions for a plate–stiffener combination model with the attached effective plating between two adjacent transverse frames in a grillage. In this case, the elastic buckling strength for the stiffener web can be analyzed by solving the governing differential equations, see Bleich (1952), among others.

The elastic buckling strength of a stiffener web, which is regarded as a very long plate (strip) under the appropriate edge conditions, may be analytically addressed as a characteristic value problem. The boundary condition of flat-bar stiffener along one edge is free, but for angle-type or Tee-stiffeners it may be assumed that the stiffener flange will not buckle until the inception of local buckling in the stiffener web, while the attached plating of the stiffened panel can itself buckle. This would imply that the rotational restraint at the web–flange junction is fully effective until the stiffener web buckles, while that at the web–panel plating junction takes a value deriving from an effective cross-section.

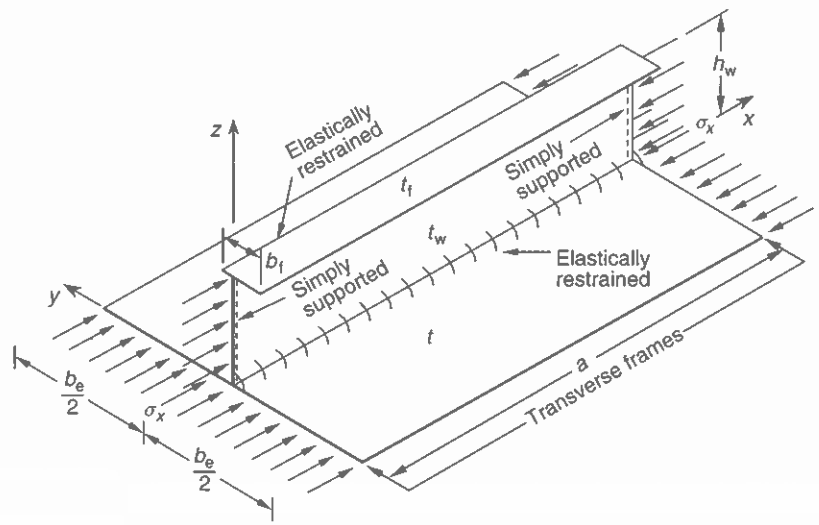

Figure 5.5 Schematic representation of loading and boundary conditions for the plate–stiffener combination model with the attached effective plating between two adjacent transverse frames under axial compression

The fundamental differential equation for the out-of-plane (i.e., sideways) deflection of the stiffener web with zero initial deflection under axial compressive loads can be derived under the assumption that the deflection is small when compared to the thickness of the stiffener web. The applicable equation for the stiffener web is given by (Bleich 1952)

$$D_w\left(\frac{\partial^4 v}{\partial x^4}+2\frac{\partial^4 v}{\partial^2 x\partial^2 z}+\frac{\partial^4 v}{\partial z^4}\right)+t_w\sigma_x\frac{\partial^2 v}{\partial x^2}=0 \tag{5.18}$$

where v = sideways deflection of the stiffener web, $D_w = Et_w^3/[12(1-\nu^2)]$ = bending rigidity of stiffener web.

The solution of the above equation for v will provide the deflected form of the stiffener web under compression σ_x, e.g., $\sigma_x = \sigma_{xM}$ when in-plane bending is applied, or $\sigma_x = \sigma_{xav}$ for uniform compression, which represents equilibrium but in an unstable position. The buckling strength is defined by the load at a bifurcation point where, in addition to the plane equilibrium from $v = 0$, a deflected but unstable form of equilibrium also occurs.

5.10.2 Exact Web Buckling Characteristic Equation

To solve Equation (5.18), the edge conditions for the stiffener web consistent with its support characteristics should be prescribed. The loaded edges of the stiffener web at $x = 0$ and a are normally supported by transverse frames, and can (somewhat pessimistically) be assumed to be simply supported. Hence we have

$$v = 0 \quad \text{at } x = 0 \text{ and } a \tag{5.19a}$$

$$M_z = 0 \quad \text{at } x = 0 \text{ and } a \tag{5.19b}$$

where M_z = bending moment per unit length of stiffener web about the z axis.

In practical cases, since the bending rigidity of plating in the xy plane is normally comparatively very large, the deflection (sideways movement) of the stiffener web along the lower edge, i.e., $z = 0$, relative to transverse frames, can be assumed to be zero, and hence

$$v = 0 \text{ at } z = 0 \tag{5.20}$$

However, the edge of the stiffener web along $z = 0$ where it joins the plating cannot be assumed to rotate freely during buckling. Hence we consider that the lower edge of the stiffener web is rotationally restrained, with the magnitude of the restraint depending on the torsional rigidity of the plating. Along the edge at $z = 0$ the bending moments which appear during buckling of the stiffener web must be equal and opposite to the rate of change of the twisting moments of plating, which gives us the condition that

$$M_x = -\frac{\partial m_x}{\partial x} \text{ at } z = 0 \tag{5.21}$$

where M_x = bending moment per unit length of stiffener web about the x axis, which is taken as

$$M_x = -D_w\left(\frac{\partial^2 v}{\partial z^2}+\nu\frac{\partial^2 v}{\partial x^2}\right)$$

m_x = twisting moment per unit length of plating about the x axis, which may be approximated by neglecting the warping rigidity of the plating as

$$m_x = -GJ_p\frac{\partial^2 v}{\partial x\partial z}$$

$J_p = b_e t^3/3$ = torsion constant of attached effective plating.

The edge condition for the stiffener web at $z = h_w$ will depend on both the bending and torsional rigidities of the stiffener flange. For flat-bar stiffeners which do not have a stiffener flange, the deflection and rotation along the edge at $z = h_w$ will occur freely. On the other hand, for angle or Tee section stiffeners, the stiffener web is elastically restrained by the stiffener flange. Hence the deflection (sideways movement) along this edge is not zero, but equals the deflection of the stiffener flange. The general condition for deflection along the edge at $z = h_w$ can then be expressed by

$$EI_f\frac{\partial^4 v}{\partial x^4} = D_w\left[\frac{\partial^3 v}{\partial z^3}+(2-\nu)\frac{\partial^3 v}{\partial x^2\partial z}\right] \text{ at } z = h_w \tag{5.22}$$

where I_f = moment of inertia of stiffener flange at $z = h_w$ with regard to the z axis, which is taken as $I_f = b_f^3 t_f/3$ in the case of an angle section and $I_f = b_f^3 t_f/12$ in the case of a Tee section.

The rotation along the edge at $z = h_w$ may be restrained due to the torsional rigidity of the stiffener flange, and the bending moments of the stiffener web must be equal to the rate of change of the twisting moment of the stiffener flange, namely

$$M_x = -\frac{\partial m_x}{\partial x} \text{ at } z = h_w \tag{5.23}$$

where M_x is as defined in Equation (5.21),

$$m_x = -GJ_f\frac{\partial^2 v}{\partial x\partial z}$$

$J_f = b_f t_f^3/3$ = torsion constant of stiffener flange.

For flat-bar stiffeners, i.e., with $I_f = 0$ or $J_f = 0$, Equation (5.23) corresponds to the condition that the rotation at $z = h_w$ occurs freely so that no moments develop there.

The general solution of Equation (5.18) satisfying the conditions of simple support at $x = 0$ and a, as expressed by Equation (5.19), can be assumed to be of the following form:

$$v = Z(z)\sin\frac{m\pi x}{a} \tag{5.24}$$

where $Z(z)$ indicates a function of z, and m represents the number of primary buckling half waves for the stiffener web along the x direction.

Substituting Equation (5.24) into Equation (5.18), we can obtain an ordinary differential equation of the fourth order upon replacing σ_x by σ_E^W as follows:

$$\frac{\partial^4 Z}{\partial z^4}-2\left(\frac{m\pi}{a}\right)^2\frac{\partial^2 Z}{\partial z^2}+\left(\frac{m\pi}{a}\right)^4(1-\mu^2)Z = 0 \tag{5.25}$$

where

$$\mu = \frac{a}{mh_w}\sqrt{k_w}, \quad k_w = \sigma_E^W \frac{h_w^2 t_w}{\pi^2 D_w}$$

σ_E^W = elastic local buckling stress of stiffener web. The general solution of Equation (5.25) is given by

$$Z(z) = C_1 e^{-\alpha_1 z} + C_2 e^{\alpha_1 z} + C_3 \cos\alpha_2 z + C_4 \sin\alpha_2 z \tag{5.26}$$

where

$$\alpha_1 = \frac{m\pi}{a}\sqrt{\mu+1}, \quad \alpha_2 = \frac{m\pi}{a}\sqrt{\mu-1}$$

From Equations (5.20) and (5.21), the following relationships between the constants in Equation (5.26) can be obtained:

$$C_1 = \frac{C_3(\alpha_1^2+\alpha_2^2-\alpha_1\alpha_3)}{2\alpha_1\alpha_3} + \frac{C_4\alpha_2}{2\alpha_1}, \quad C_2 = -\frac{C_3(\alpha_1^2+\alpha_2^2+\alpha_1\alpha_3)}{2\alpha_1\alpha_3} - \frac{C_4\alpha_2}{2\alpha_1} \tag{5.27}$$

where

$$\alpha_3 = \frac{GJ_p}{D_w}\left(\frac{m\pi}{a}\right)^2 = h_w\zeta_p\left(\frac{m\pi}{a}\right)^2, \quad \zeta_p = \frac{GJ_p}{h_w D_w}$$

Upon substitution of Equation (5.27) into Equation (5.26), we obtain

$$Z(z) = C_3\left(\cos\alpha_2 z - \cosh\alpha_1 z - \frac{\alpha_1^2+\alpha_2^2}{\alpha_1\alpha_3}\sinh\alpha_1 z\right) + C_4\left(\sin\alpha_2 z - \frac{\alpha_2}{\alpha_1}\sinh\alpha_1 z\right) \tag{5.28}$$

Substitution of Equation (5.28) into Equation (5.24) then yields

$$v = \left[C_3\left(\cos\alpha_2 z - \cosh\alpha_1 z - \frac{\alpha_1^2+\alpha_2^2}{\alpha_1\alpha_3}\sinh\alpha_1 z\right) + C_4\left(\sin\alpha_2 z - \frac{\alpha_2}{\alpha_1}\sinh\alpha_1 z\right)\right]\sin\frac{m\pi x}{a} \tag{5.29}$$

Using the boundary conditions, i.e., Equations (5.22) and (5.23), along the edge of the stiffener web at $z = h_w$, the unknown constants, C_3 and C_4, are determined from

$$\begin{bmatrix} A_{11} & A_{12} \\ A_{21} & A_{22} \end{bmatrix}\begin{pmatrix} C_3 \\ C_4 \end{pmatrix} = 0 \tag{5.30}$$

where

$$A_{11} = h_w\gamma_f\left(\frac{m\pi}{a}\right)^4(\cos\alpha_2 h_w - \cosh\alpha_1 h_w - S\sinh\alpha_1 h_w) - (\alpha_2^3\sin\alpha_2 h_w - \alpha_1^3\sinh\alpha_1 h_w - S\alpha_1^3\cosh\alpha_1 h_w) - (2-\nu)\left(\frac{m\pi}{a}\right)^2(\alpha_2\sin\alpha_2 h_w + \alpha_1\sinh\alpha_1 h_w + S\alpha_1\cosh\alpha_1 h_w)$$

$$A_{12} = h_w\gamma_f\left(\frac{m\pi}{a}\right)^4\left(\sin\alpha_2 h_w - \frac{\alpha_2}{\alpha_1}\sinh\alpha_1 h_w\right) + (\alpha_2^3\cos\alpha_2 h_w + \alpha_1^2\alpha_2\cosh\alpha_1 h_w) + (2-\nu)\left(\frac{m\pi}{a}\right)^2(\alpha_2\cos\alpha_2 h_w - \alpha_2\cosh\alpha_1 h_w)$$

$$A_{21} = h_w\zeta_f\left(\frac{m\pi}{a}\right)^2(\alpha_2\sin\alpha_2 h_w + \alpha_1\sinh\alpha_1 h_w + S\alpha_1\cosh\alpha_1 h_w) + (\alpha_2^2\cos\alpha_2 h_w + \alpha_1^2\cosh\alpha_1 h_w + S\alpha_1^2\sinh\alpha_1 h_w) + \nu\left(\frac{m\pi}{a}\right)^2(\cos\alpha_2 h_w - \cosh\alpha_1 h_w - S\sinh\alpha_1 h_w)$$

$$A_{22} = -h_w\zeta_f\left(\frac{m\pi}{a}\right)^2(\alpha_2\cos\alpha_2 h_w - \alpha_2\cosh\alpha_1 h_w) + (\alpha_2^2\sin\alpha_2 h_w + \alpha_1\alpha_2\sinh\alpha_1 h_w) + \nu\left(\frac{m\pi}{a}\right)^2\left(\sin\alpha_2 h_w - \frac{\alpha_2}{\alpha_1}\sinh\alpha_1 h_w\right)$$

$$S = \frac{\alpha_1^2+\alpha_2^2}{\alpha_1\alpha_3}, \quad \gamma_f = \frac{EI_f}{h_w D_w}, \quad \zeta_f = \frac{GJ_f}{h_w D_w}$$

Equation (5.30) has solutions different from zero only if the determinant, Δ, of the coefficient matrix vanishes. The condition for determinant $\Delta = 0$ of Equation (5.30) then yields

$$\Delta = \begin{vmatrix} A_{11} & A_{12} \\ A_{21} & A_{22} \end{vmatrix} = 0 \quad \text{or} \quad \Delta = A_{11}A_{22} - A_{12}A_{21} = 0 \tag{5.31}$$

Equation (5.31) is the characteristic equation for elastic buckling of the stiffener web with or without a stiffener flange. The solution of Equation (5.31) would then provide the value of the buckling coefficient, k_w, for stiffener web buckling. The elastic local buckling strength of the stiffener web can be obtained by the solution of the characteristic equation, with compressive stress taking a negative sign as follows:

$$\sigma_E^W = -k_w\frac{\pi^2 E}{12(1-\nu^2)}\left(\frac{t_w}{h_w}\right)^2 \tag{5.32}$$

where σ_E^W = elastic buckling strength of stiffener web, k_w = elastic buckling strength coefficient of stiffener web.

To account for the effect of welding residual stress, the web buckling stress computed from Equation (5.32) may be reduced by the compressive residual stress in the stiffener web.

5.10.3 Closed-form Web Buckling Strength Expressions

The task of solving Equation (5.31) in any specific case is not always straightforward, and so it is very desirable for a designer to have a closed-form expression for predicting the local buckling strength of the stiffener web more readily.

Hence an empirical expression may be particularly useful to predict the buckling strength of the stiffener web in terms of the relevant torsional rigidities of the plating and stiffener flange. One such expression for the buckling coefficient, k_w, in Equation (5.32) is given by Paik *et al.* (1998) as follows:

$$k_w = \begin{cases} C_1\zeta_p + C_2 & \text{for } 0 \le \zeta_p \le \eta_w \\ C_3 - 1/(C_4\zeta_p + C_5) & \text{for } \eta_w < \zeta_p \le 60 \\ C_3 - 1/(60C_4 + C_5) & \text{for } 60 < \zeta_p \end{cases} \tag{5.33}$$

where

$$\eta_w = -0.444\zeta_f^2 + 3.333\zeta_f + 1.0$$

$$C_1 = -0.001\zeta_f + 0.303$$

$$C_2 = 0.308\zeta_f + 0.427$$

$$C_3 = \begin{cases} -4.350\zeta_f^2 + 3.965\zeta_f + 1.277 & \text{for } 0 \le \zeta_f \le 0.2 \\ -0.427\zeta_f^2 + 2.267\zeta_f + 1.460 & \text{for } 0.2 < \zeta_f \le 1.5 \\ -0.133\zeta_f^2 + 1.567\zeta_f + 1.850 & \text{for } 1.5 < \zeta_f \le 3.0 \\ 5.354 & \text{for } 3.0 < \zeta_f \end{cases}$$

$$C_4 = \begin{cases} -6.70\zeta_f^2 + 1.40 & \text{for } 0 \le \zeta_f \le 0.1 \\ 1/(5.10\zeta_f + 0.860) & \text{for } 0.1 < \zeta_f \le 1.0 \\ 1/(4.0\zeta_f + 1.814) & \text{for } 1.0 < \zeta_f \le 3.0 \\ 0.0724 & \text{for } 3.0 < \zeta_f \end{cases}$$

$$C_5 = \begin{cases} -1.135\zeta_f + 0.428 & \text{for } 0 \le \zeta_f \le 0.2 \\ -0.299\zeta_f^3 + 0.803\zeta_f^2 - 0.783\zeta_f + 0.328 & \text{for } 0.2 < \zeta_f \le 1.0 \\ -0.016\zeta_f^3 + 0.117\zeta_f^2 - 0.285\zeta_f + 0.235 & \text{for } 1.0 < \zeta_f \le 3.0 \\ 0.001 & \text{for } 3.0 < \zeta_f \end{cases}$$

For flat-bar stiffeners, Equation (5.33) will become much simpler since $\zeta_f = 0$, the computed results being well approximated by

$$k_w = \begin{cases} 0.303\zeta_p + 0.427 & \text{for } 0 \le \zeta_p \le 1 \\ 1.277 - 1/(1.40\zeta_p + 0.428) & \text{for } 1 < \zeta_p \le 60 \\ 1.2652 & \text{for } 60 < \zeta_p \end{cases} \tag{5.34}$$

Figure 5.6(a) shows the variation of the elastic buckling coefficient for a flat-bar stiffener web as a function of the web aspect ratio, a/h_w, and the torsional rigidity of plating. It is seen that with an increase in the torsional rigidity of plating, the web buckling coefficient increases significantly. So accounting for such effects can be important, particularly in cases where stiffener web buckling is a possibility. The effects of the web aspect ratio on the buckling strength of the stiffener web can be ignored in most practical cases.

Figures 5.6(b) and (c) show the variations of the elastic buckling strength coefficient for angle or Tee-section stiffener web as a function of three parameters, namely the aspect ratio of the stiffener web, the torsional rigidity of the plating and the torsional rigidity of the stiffener flange.

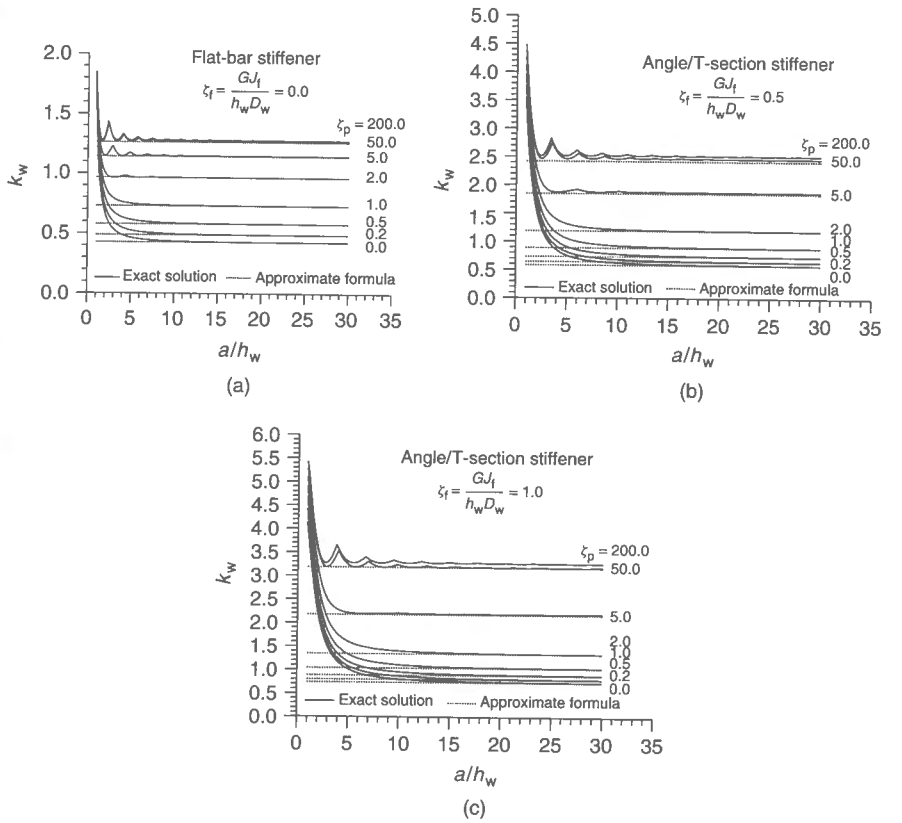

Figure 5.6 Variation of the elastic buckling strength coefficient (a) for a flat-bar stiffener web as a function of the web aspect ratio and torsional rigidity of plating, and (b), (c) for angle or Tee-section stiffener web as a function of the web aspect ratio and torsional rigidities of plating or stiffener flange

The results are shown in the practical ranges of parameters applicable to merchant ship steel stiffened panels. With an increase in the torsional rigidities of the stiffener flange and/or plating, the elastic buckling strength of the stiffener web increases significantly, while the influence of the web aspect ratio on the buckling strength of the stiffener web can again ignored for most practical purposes.

The dotted lines in Figure 5.6 represent the approximate solutions for the web buckling coefficient, as given by Equations (5.33) or (5.34). These may be compared with the solid lines in the figure which represent the exact results computed by directly solving the characteristic buckling equation, Equation (5.31). Equation (5.32) together with Equations (5.33) or (5.34) provides reasonably accurate predictions for the elastic buckling strength of the stiffener web with or without a stiffener flange.

5.11 Elastic Local Buckling of Stiffener Flange

The local buckling of the stiffener flange prior to buckling of the plating between stiffeners is also an undesirable failure mode. In design, stiffener flange buckling must be prevented

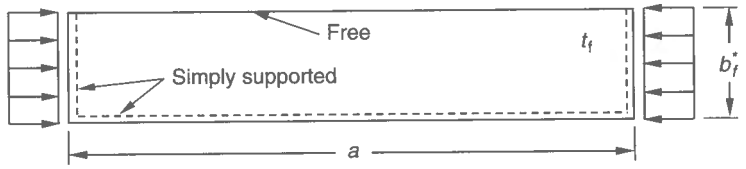

Figure 5.7 A stiffener flange with three simply supported edges and one free edge

until the stiffened panel reaches the ULS. For practical pessimistic assessment, the elastic local compressive buckling strength, σ_E^F, of the stiffener flange is often estimated using a plate idealization in which three edges are simply supported and one edge is free, as shown in Figure 5.7, with results as follows:

$$\sigma_E^F = k_f \frac{\pi^2 E}{12(1-\nu^2)} \left(\frac{t_f}{b_f^*}\right)^2 \tag{5.35}$$

where $k_f = 0.425 + \left(b_f^*/a\right)^2$, $b_f^* = b_f$ for unsymmetric angle stiffeners and $b_f^* = 0.5b_f$ for symmetric Tee-stiffeners.

To prevent the compression flange buckling, the requirements of Equation (7.14) in Chapter 7 may need to be satisfied.

5.12 Lateral–Torsional Buckling of Stiffeners

5.12.1 Fundamentals of Lateral–Torsional Buckling

The lateral–torsional buckling (also called tripping) of stiffeners is a phenomenon in which the failure of a stiffened panel occurs subsequent to the stiffener twisting sideways about the edge of the stiffener web attached to the plating. When the torsional rigidity of the stiffener is small or the stiffener flange is weak, this phenomenon is more likely to take place.

Like the stiffener web buckling previously described in Section 5.10, tripping can be a relatively sudden phenomenon resulting in subsequent unloading of the stiffened panel. Once tripping occurs, the buckled or collapsed plating is left with essentially much reduced stiffening and thus overall collapse may follow.

A plate–stiffener combination with the attached effective plating under combined axial compression and lateral line loads is typically considered to collapse if tripping occurs after the plating between stiffeners collapses.

In a continuous steel stiffened panel, tripping may generally involve a coupling of sideways and vertical deflection and rotation of the stiffener web together with local buckling of the attached plating, as shown in Figure 5.8(a). Unlike an ordinary beam–column in steel-framed structures, the attached plating of a plate–stiffener combination in steel-plated structures is restricted from deflecting sideways, while the beam (stiffener) flange is relatively free to deflect sideways and vertically.

For unsymmetric section profiles (e.g., angle section), vertical bending, sideways bending and torsion are typically coupled, while for symmetric section profiles (e.g., Tee section), only sideways bending and torsion are normally coupled. This implies that the

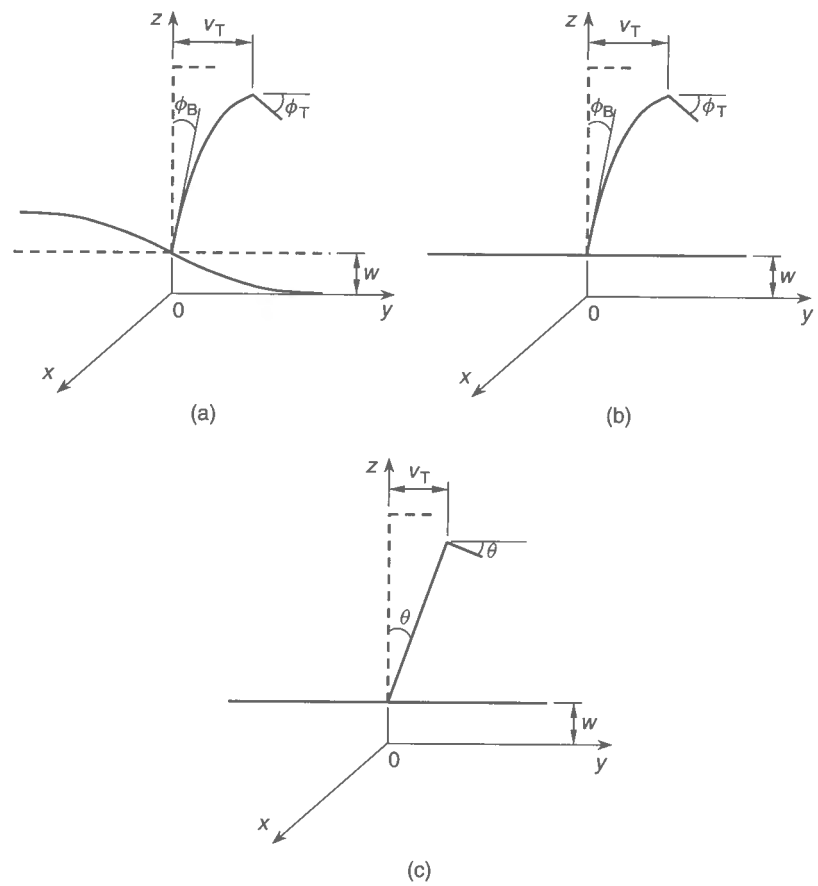

Figure 5.8 General and idealized tripping deformations of a plate–beam combination: (a) general deformations of flexible stiffener web with plate rotational restraints; (b) simplified deformations of flexible stiffener web without plate rotational restraints; (c) simplified deformations of rigid stiffener web without plate rotational restraints

overall flexural Euler buckling and lateral–torsional buckling can sometimes be closely coupled for plate–stiffener combinations.

Many researchers have studied the tripping of stiffeners theoretically, numerically and experimentally. Earlier work that used the classical theory of thin-walled bars has been summarized by Bleich (1952). During the 1970s and 1980s, further studies were undertaken by Faulkner *et al.* (1973), Smith (1976), Adamchak (1979) and Faulkner (1975, 1987), among others. Hughes (1986) has reviewed and summarized some of these studies. During the 1990s, in addition to the tripping problem under axial compression alone (Danielson *et al.* 1990, Danielson 1995, Hu *et al.* 1997), the effect of combined axial compression and lateral loads was studied by Hughes & Ma (1996a, 1996b) and Hu *et al.* (2000), among others.

While nonlinear finite element methods can accurately analyze the tripping behavior in any specific case, it is not straightforward to derive theoretical solutions of the tripping strength for a plate–stiffener combination considering the general section deformations

depicted in Figure 5.8(a). For practical design purposes, however, it would be more desirable to use a closed-form expression of the tripping strength which is based on the corresponding analytical solutions.

Related to this problem, different idealizations of the tripping deformations may be made as approximations to the most general case of tripping deformations as shown in Figure 5.8(a), all potentially taking into account the coupling effect between the flexural column buckling and lateral–torsional buckling. Three possible idealizations are as follows:

- flexible web without the plate rotational restraint, see Figure 5.8(b);
- rigid web with the plate rotational restraint; and
- rigid web without the plate rotational restraint, see Figure 5.8(c).

While the rotational restraints between the stiffener web and the attached plating may generally play an important role in the tripping behavior or local buckling of the stiffener web (the latter being previously discussed in Section 5.10), rotational restraint effects from the plating may be ignored if the plating between stiffeners buckles prior to tripping, implying that the contribution of the attached plating to restrict the rotation of the stiffener web about the plate–web junction is small, and thus it may be considered that the stiffener and the attached plating are pin-joined.

This assumption will arguably result in a lower bound solution of the tripping strength since plate rotational restraints will always exist to some extent, while the effect of buckled plating may approximately be incorporated within the effective plate width in the sectional properties of the plate–stiffener combination with the axis of rotation unchanged. Solutions using such an approach may typically be used when the ratio of the stiffener web height to the web thickness (i.e., h_w/t_w) is smaller than 20 (Hughes & Ma 1996a).

On the other hand, as the height of the stiffener web increases, the stiffener web is likely to deflect sideways and local 'web plate' buckling can in some cases occur. Since this type of failure is in principle considered in Section 5.10, it is assumed for tripping analysis herein that the cross-section of the stiffener web does not deflect locally, similar to the assumption of ordinary beam–column theory, while it can twist sideways. This assumption may result in an optimistic strength prediction, particularly when the ratio of the stiffener web height to the web thickness is very large so that the local web buckling can take place. The tripping strength of a flat-bar stiffener may be considered to be equal to the local web buckling strength of the stiffener as presented in Section 5.10.

5.12.2 Closed-form Tripping Strength Expressions

To derive a closed-form analytical solution of the tripping strength, therefore, the rigid-web case without the plate rotational restraints as shown in Figure 5.8(c) may be adopted. As may be seen later in Figure 5.9, the results obtained using this idealization are comparable to those from more refined solution procedures. By inclusion of the rotational restraint effect along the web–plate junction, the elastic tripping strength will be increased further (Hu *et al.* 2000).

The elastic tripping strength of angle or Tee-type stiffeners under combined axial compression, σ_x ($= \sigma_{xM}$ or σ_{xav}), and uniform lateral pressure line load, $q = pb$ (a line force obtained by multiplication of the uniform lateral pressure, p, and the breadth, b, of plating between stiffeners, as shown in Figure 2.5 of Chapter 2) in the x direction, can be calculated by applying the principle of minimum potential energy.

The strain energy, U, of the plate–stiffener combination (i.e., with associated effective plating) stored during the tripping can in this case be given with $v_w = z\theta$(= sideways deflection of the web), $v_T = h_w\theta$(= maximum value of v_w) and $\phi_B = \phi_T = \theta$, resulting in

$$U = \frac{E}{2}\int_0^a I\left(\frac{\partial^2 w}{\partial x^2}\right)^2 \mathrm{d}x + \frac{E}{2}\int_0^a I_z h_w^2\left(\frac{\partial^2 \theta}{\partial x^2}\right)^2 \mathrm{d}x + \frac{E}{2}\int_0^a 2I_{zy}h_w\frac{\partial^2 w}{\partial x^2}\frac{\partial^2 \theta}{\partial x^2}\,\mathrm{d}x + \frac{G}{2}\int_0^a (J_w + J_f)\left(\frac{\partial \theta}{\partial x}\right)^2 \mathrm{d}x \tag{5.36}$$

where I = moment of inertia of stiffener and attached effective width of plating with regard to the y axis, given by

$$I = b_e\int_{-t/2}^{t/2}(z_p - z)^2\,\mathrm{d}z + t_w\int_{-h_w/2}^{h_w/2}\left(z_p - \frac{t}{2} - \frac{h_w}{2} - z\right)^2\mathrm{d}z + b_f\int_{-t_f/2}^{t_f/2}\left(z_p - \frac{t}{2} - h_w - \frac{t_f}{2} - z\right)^2\mathrm{d}z$$

I_z = moment of inertia of the panel with respect to the z axis, given by

$$I_z = t\int_0^{b_e} y_o^2\,\mathrm{d}y + h_w\int_0^{t_w} y_o^2\,\mathrm{d}z + t_f\int_0^{b_f}(y_o - y)^2\,\mathrm{d}z$$

I_{zy} = product of inertia of panel with respect to the yz plane, given by

$$I_{zy} = \int_0^{b_e}\int_{-t/2}^{t/2}(z_p - z)\,y_o\,\mathrm{d}z\,\mathrm{d}y + \int_0^{t_w}\int_{-h_w/2}^{h_w/2}\left(z_p - \frac{t}{2} - \frac{h_w}{2} - z\right)y_o\,\mathrm{d}z\,\mathrm{d}y + \int_0^{b_f}\int_{-t_f/2}^{t_f/2}\left(z_p - \frac{t}{2} - h_w - \frac{t_f}{2} - z\right)(y_o - y)\,\mathrm{d}z\,\mathrm{d}y$$

J_w = torsion constant for the web, given by

$$J_w = \frac{1}{3}t_w^3 h_w\left(1 - \frac{192}{\pi^5}\frac{t_w}{h_w}\sum_{n=1,3,5}^{\infty}\frac{1}{n^5}\tanh\frac{n\pi h_w}{2t_w}\right)$$

J_f = torsion constant for the flange, given by

$$J_f = \frac{1}{3}t_f^3 b_f\left(1 - \frac{192}{\pi^5}\frac{t_f}{b_f}\sum_{n=1,3,5}^{\infty}\frac{1}{n^5}\tanh\frac{n\pi b_f}{2t_f}\right)$$

z_p = distance from the middle plane of the attached plating to the elastic horizontal neutral axis with attached effective plating, y_0 = distance from the middle plane of the web to the elastic vertical neutral axis with attached effective plating.

In Equation (5.36), w is the deflection of the stiffener in the z direction, and θ is the rotation of the stiffener with regard to the x axis. The moments of inertia and other geometric constants used in Equation (5.36) are calculated for the stiffener with attached effective plating which approximately accommodates the effect of plate buckling.

On the other hand, the external potential energy, W, done during the tripping is given by

$$W = -\frac{1}{2}\int_{A_p}\sigma_p\int_0^a\left(\frac{\partial w}{\partial x}\right)^2 \mathrm{d}x\,\mathrm{d}A - \frac{1}{2}\int_{A_w}\sigma_w\int_0^a\left[\left(\frac{\partial w}{\partial x}\right)^2 + z^2\left(\frac{\partial \theta}{\partial x}\right)^2\right]\mathrm{d}x\,\mathrm{d}A$$
$$-\frac{1}{2}\int_{A_f}\sigma_f\int_0^a\left[h_w^2\left(\frac{\partial \theta}{\partial x}\right)^2 + \left(\frac{\partial w}{\partial x}\right)^2 - 2y\frac{\partial w}{\partial x}\frac{\partial \theta}{\partial x} + y^2\left(\frac{\partial \theta}{\partial x}\right)^2\right]\mathrm{d}x\,\mathrm{d}A \quad (5.37)$$

where σ_p, σ_w and σ_f are the axial stresses in the plate, web and flange, respectively. $\int_{A_p}()\mathrm{d}A$, $\int_{A_w}()\mathrm{d}A$ and $\int_{A_f}()\mathrm{d}A$ indicate the integration for the corresponding section area of plating (i.e., $A_p = b_e t$), web (i.e., $A_w = h_w t_w$) and flange (i.e., $A_f = b_f t_f$), respectively.

The total potential energy, Π, is then obtained from the sum of U in Equation (5.36) and W in Equation (5.37). When the plate–stiffener combination which is assumed to be simply supported at both ends is subjected to combined axial compressive stress, σ_x, and uniform lateral line load, $q = pb$, the axial stresses at the plate (i.e., σ_p), web (i.e., σ_w) and flange (i.e., σ_f) can be calculated for the stiffener with the associated effective plating as follows:

$$\sigma_p = \sigma_x - \frac{q}{I}z_p\frac{x(L-x)}{2}, \quad \sigma_w = \sigma_x - \frac{q}{I}(z_p - z)\frac{x(a-x)}{2},$$
$$\sigma_f = \sigma_x - \frac{q}{I}(z_p - h_w)\frac{x(a-x)}{2} \quad (5.38)$$

The displacement functions of the stiffener due to tripping are assumed (since the stiffener web does not deflect locally and the end conditions are simply supported) as follows:

$$w = \sum_{m=1} A_m \sin\frac{m\pi x}{a}, \quad \theta = \sum_{m=1} B_m \sin\frac{m\pi x}{a} \quad (5.39)$$

where A_m and B_m are unknown constants.

In typical steel-plated structures, a stiffened panel is usually a multi-bay structure supported by transverse frames or brackets. Therefore, Equation (5.39) may be simplified further by taking only the predominant tripping half-wave number of the stiffener between two transverse frames or brackets, as for the post-buckling behavior of plating. Usually the primary tripping half-wave number is not known beforehand, but it can be determined so that the resulting tripping strength must be the smallest among those obtained for potential half-wave numbers.

Substituting Equation (5.39) into the total potential energy equation, Π, and applying the principle of minimum potential energy, the characteristic equation for elastic tripping buckling of the stiffener is calculated. The elastic tripping stress, σ_E^T, of the plate–stiffener combination is then obtained by solution of the characteristic equation with regard to the axial compressive stress, while lateral pressure is regarded as a given constant load.

For unsymmetric angle stiffeners, a closed-form expression of the elastic tripping strength can be obtained with compressive stress taken as negative as follows:

$$\sigma_E^T = (-1)\min_{m=1,2,3\ldots}\left|\frac{C_2 + \sqrt{C_2^2 - 4C_1C_3}}{2C_1}\right| \quad (5.40)$$

where

$$C_1 = (b_e t + h_w t_w + b_f t_f)I_p - S_f^2$$

$$C_2 = -I_p\left[EI\left(\frac{m\pi}{a}\right)^2 - \frac{qa^2}{12}\frac{S_1}{I}\left(1 - \frac{3}{m^2\pi^2}\right)\right] - (b_e t + h_w t_w + b_f t_f)$$
$$\times\left[G(J_w + J_f) + EI_z h_w^2\left(\frac{m\pi}{a}\right)^2 - \frac{qa^2}{12}\frac{S_2}{I}\left(1 - \frac{3}{m^2\pi^2}\right)\right]$$
$$+ 2S_f\left[EI_{zy}h_w\left(\frac{m\pi}{a}\right)^2 - \frac{qa^2}{12}\frac{S_3}{I}\left(1 - \frac{3}{m^2\pi^2}\right)\right]$$

$$C_3 = \left[EI\left(\frac{m\pi}{a}\right)^2 - \frac{qa^2}{12}\frac{S_1}{I}\left(1 - \frac{3}{m^2\pi^2}\right)\right]$$
$$\times\left[G(J_w + J_f) + EI_z h_w^2\left(\frac{m\pi}{a}\right)^2 - \frac{qa^2}{12}\frac{S_2}{I}\left(1 - \frac{3}{m^2\pi^2}\right)\right]$$
$$-\left[EI_{zy}h_w\left(\frac{m\pi}{a}\right)^2 - \frac{qa^2}{12}\frac{S_3}{I}\left(1 - \frac{3}{m^2\pi^2}\right)\right]^2$$

$$S_f = -\frac{t_f b_f^2}{2}$$

$$S_1 = -(z_p - h_w)t_f b_f - b_e t z_p - h_w t_w\left(z_p - \frac{h_w}{2}\right)$$

$$S_2 = -(z_p - h_w)t_f\left(h_w^2 b_f + \frac{b_f^3}{3}\right) - h_w^3 t_w\left(\frac{1}{3}z_p - \frac{h_w}{4}\right)$$

$$S_3 = (z_p - h_{\dot{w}})\frac{b_f^2 t_f}{2}$$

$$I = \frac{b_e t^3}{12} + A_p z_p^2 + \frac{t_w h_w^3}{12} + A_w\left(z_p - \frac{t}{2} - \frac{h_w}{2}\right)^2 + \frac{b_f t_f^3}{12} + A_f\left(z_p - \frac{t}{2} - h_w - \frac{t_f}{2}\right)^2$$

$$I_z = A_p y_0^2 + A_w y_0^2 + A_f\left(y_0^2 - b_f y_0 + \frac{b_f^2}{3}\right)$$

$$I_{zy} = A_p z_p y_0 + A_w\left(z_p - \frac{t}{2} - \frac{h_w}{2}\right)y_0 + A_f\left(z_p - \frac{t}{2} - h_w - \frac{t_f}{2}\right)\left(y_0 - \frac{b_f}{2}\right)$$

I_p = polar moment of inertia of stiffener about toe, given by

$$I_p = \frac{t_w h_w^3}{3} + \frac{t_w^3 h_w}{3} + \frac{b_f^3 t_f}{3} + \frac{b_f t_f^3}{3} + A_f h_w^2$$

$$z_p = \frac{0.5A_w(t + h_w) + A_f(0.5t + h_w + 0.5t_f)}{b_e t + h_w t_w + b_f t_f}$$

$$y_o = \frac{b_f^2 t_f}{2(b_e t + h_w t_w + b_f t_f)}$$

q = equivalent line pressure ($q = pb$), m = tripping half-wave number of the stiffener.

For symmetric Tee-stiffeners, a closed-form expression of the elastic tripping strength can be obtained with compressive stress taken as negative as follows:

$$\sigma_E^T = (-1) \min_{m=1,2,3\ldots} \left| -\frac{a^2 G(J_w + J_f) + E I_f h_w^2 m^2 \pi^2}{I_p a^2} + \frac{qa^2}{12} \frac{S_4}{I I_p} \left(1 - \frac{3}{m^2 \pi^2}\right) \right| \quad (5.41)$$

where

$$S_4 = -(z_p - h_w) t_f \left(h_w^2 b_f + \frac{b_f^3}{12}\right) - h_w^3 t_w \left(\frac{1}{3} z_p - \frac{h_w}{4}\right)$$

$$I_p = \frac{t_w h_w^3}{3} + \frac{t_w^3 h_w}{12} + \frac{b_f t_f^3}{3} + \frac{b_f^3 t_f}{12} + A_f h_w^2,\ I_f = \frac{b_f^3 t_f}{12}$$

To account for the effect of welding residual stresses, the tripping stress computed above is typically reduced by an effective compressive residual stress, σ_{rs}^*. Danielson (1995) suggests an empirical formula of σ_{rs}^* as follows:

$$\sigma_{rs}^* = \sigma_{rc} \left(1 + \frac{2\pi^2 I}{b^3 t}\right) \quad (5.42)$$

where σ_{rc} = compressive residual stress in the stiffener web, I = moment of inertia for the full section of the plate–stiffener combination, refer to Table 2.1 in Chapter 2.

As previously noted, the elastic tripping strength of flat-bar stiffeners is approximately taken as being equal to the local buckling strength, σ_E^W, of the stiffener web as defined in Equation (5.32), i.e., $\sigma_E^T = \sigma_E^W$.

5.12.3 Verification Examples

Figure 5.9 shows the effect of the h_w/t_w ratio on the tripping strength for a particular plate–stiffener combination. The two types of idealizations, i.e., one for a flexible web as given by Hughes & Ma (1996a) using a simplified numerical method and the other for a rigid web as predicted by Equations (5.40) and (5.41), both without the plate rotational restraints, are considered. The more refined eigenvalue finite element solutions are also compared in the figure. As will be described in Section 5.13 of this chapter, the inelastic tripping strengths were estimated by plasticity correction of the corresponding elastic tripping strengths using the Johnson–Ostenfeld formula, Equation (2.93), where needed.

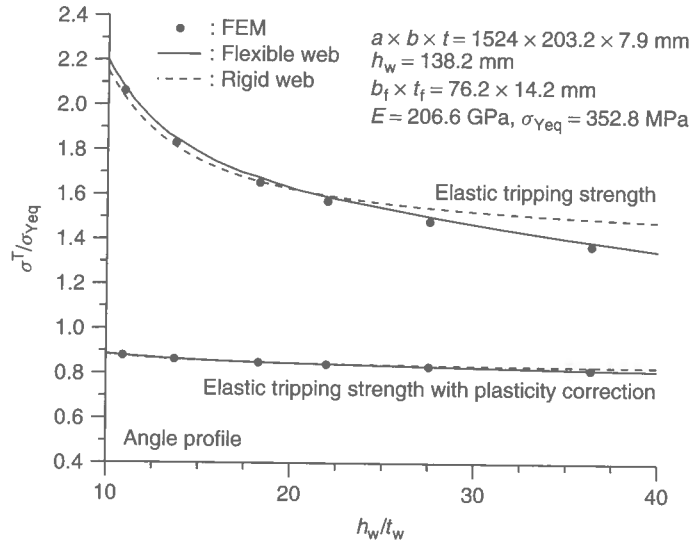

(a) Angle section stiffener with attached effective plating

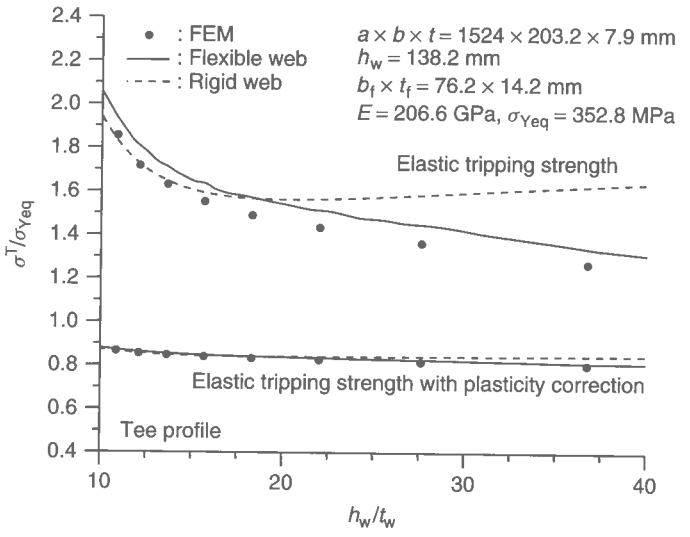

(b) Tee section stiffener with attached effective plating

Figure 5.9 Effect of the h_w/t_w ratio on the tripping strength of a plate and flange–stiffener combination without considering the plate rotational restraints (σ_{Yeq} = equivalent yield strength of the plate–stiffener combination)

It is seen from Figure 5.9 that the effect of stiffener web deflection can be ignored when the h_w/t_w ratio is small, but the rigid-web approximation neglecting the effect of stiffener web deflection can result in the overestimation of the elastic tripping strength for larger h_w/t_w ratios. The elastic tripping strength will also increase further because of the rotational restraint effect along the web–plate intersection (Hu *et al.* 2000). As is evident from Figure 5.9, however, the inelastic tripping strength may not be significantly affected

by the stiffener web deflection and hence Equations (5.40) and (5.41) will be useful for practical purposes of stiffener tripping design.

5.13 Elastic–Plastic Buckling

The stocky stiffened panel will buckle in the inelastic regime with a certain degree of plasticity. While the nonlinear finite element method can deal accurately with this behavior, it is computing and labor intensive.

For practical design purposes, an easier alternative to account for the influence of plasticity is to make the plasticity correction of the elastic buckling strength using the Johnson–Ostenfeld formulation as indicated in Equation (2.93) of Chapter 2. Some examples of the application of the Johnson–Ostenfeld formula to the inelastic buckling strength of plates are shown in Chapter 3. As a point of interest, it is also known that the use of the Johnson–Ostenfeld formula is not appropriate for inelastic buckling strength of perforated plates. For inelastic lateral–torsional buckling strength of stiffeners, the Johnson–Ostenfeld formula has again been used (Adamchak 1979).

The elastic–plastic buckling strength of the stiffened panel under single types of loads may then be approximately estimated by substituting the corresponding elastic buckling strength into Equation (2.93) in Chapter 2. For combined loading, a relevant interaction relationship between the inelastic buckling strength components may be adopted using a method similar to that for plating as previously described in Chapter 3.

5.14 Computer Software ALPS/BUSAP

As previously noted in Section 3.15 of Chapter 3, ALPS/BUSAP also automates the buckling strength computations of the stiffened panels presented in this chapter. The lateral–torsional buckling strength of stiffeners and local buckling strength of stiffener webs, as well as local buckling strength of plating between stiffeners, are computed. This program can be downloaded from the web site by following the instructions given in the appendices to this book.

References

Adamchak, J.C. (1979). *Design equations for tripping of stiffeners under inplane and lateral loads*. DTNSRDC-79/064, Naval Surface Warfare Center, Washington, DC, October.
Allen, H.G. & Bulson, P.S. (1980). *Background to buckling*. McGraw-Hill, London.
Bleich, F. (1952). *Buckling strength of metal structures*. McGraw-Hill, New York.
Danielson, D.A. (1995). Analytical tripping loads for stiffened plates. *International Journal of Solids and Structures*, 32(8/9): 1317–1328.
Danielson, D.A., Kihl, D.P. & Hodges, D.H. (1990). Tripping of thin-walled plating stiffeners in axial compression. *Thin-Walled Structures*, 10(2): 121–142.
Faulkner, D. (1975). in Chapter 21 Compression strength of welded grillages. *Ship Structural Design Concepts*, Cornell Maritime Press, Cambridge, MD, 633–712.
Faulkner, D. (1987). Toward a better understanding of compression induced tripping. In *Steel Structures*, Elsevier Applied Science, London, 159–175.
Faulkner, D., Adamchak, J.C., Snyder, G.J. & Vetter, M.R. (1973). Synthesis of welded grillages to withstand compression and normal loads. *Computers & Structures*, 3: 221–246.

Hu, S.Z., Chen, Q., Pegg, N. & Zimmerman, T.J.E. (1997). Ultimate collapse tests of stiffened plate ship structural units. *Marine Structures*, 10: 587–610.
Hu, Y., Chen, B. & Sun, J. (2000). Tripping of thin-walled stiffeners in the axially compressed stiffened panel with lateral pressure. *Thin-Walled Structures*, 37: 1–26.
Hughes, O.F. (1986). *Ship structural design: a rationally-based, computer-aided, optimization approach*. The Society of Naval Architects and Marine Engineers, Jersey City, NJ.
Hughes, O.F. & Ma, M. (1996a). Elastic tripping analysis of asymmetrical stiffeners. *Computers & Structures*, 60(3): 369–389.
Hughes, O.F. & Ma, M. (1996b). Inelastic analysis of panel collapse by stiffener buckling. *Computers & Structures*, 61(1): 107–117.
Paik, J.K., Thayamballi, A.K. & Park, Y.I. (1998). Local buckling of stiffeners in ship plating. *Journal of Ship Research*, 42(1): 56–67.
Seydel, E. (1933). Uber das Ausbeulen von rechteckigen Isotropen oder orthogonal-anisotropen Platten bei Schubbeanspruchung. *Ingenieur-Archiv*, 4: 169 (in German).
Smith, C.S. (1976). Compressive strength of welded steel ship grillages. *RINA Transactions*, 118: 325–359.

6 Post-buckling and Ultimate Strength Behavior of Stiffened Panels and Grillages

6.1 Fundamentals of Stiffened Panel Collapse Behavior

A stiffened panel is an assembly of the plating and stiffeners (support members). Even if the stiffened panel or its parts initially buckle in the elastic or even inelastic regime, the stiffened panel will normally be able to sustain further applied loads. The ultimate strength of the stiffened panel is eventually reached by excessive plasticity and/or stiffener failure. Figure 4.1 in Chapter 4 may be referred to for the collapse behavior of the stiffened panel subject to predominantly axial compressive loads.

A method for the prediction of stiffened panel ultimate strength has its own level of accuracy. Apart from the inherent variability in the structural properties and phenomena involved, the following four aspects are the primary reasons for such differences:

- the finite number of collapse modes that are considered, the way they are idealized for consideration, and the effects of failure mode interactions that may be neglected;
- differences in treatment of the effective width of plating between stiffeners;
- consideration of post-weld initial imperfections;
- consideration of rotational restraints between plating and stiffeners and/or between stiffener web and flange.

First, not all theoretically possible collapse modes are usually considered in the development of any particular design-oriented strength prediction method. Second, it is important to accurately predict the effective width of plating in calculating the effective cross-sectional area of a plate–stiffener combination. As the compressive loads increase, the effective width of the buckled plating would, by definition, vary because it is a function of the applied compressive stresses. However, most simplified methods assume that the effective width of plating does not depend on the applied compressive loads, the ultimate effective width of plating being used instead as a convenient 'constant'. Third, initial

deflections and welding-induced residual stresses are not always treated as parameters of influence in the development of the method. Most methods take into account the influence of initial imperfections for the plating between stiffeners, but only some of them include the initial imperfection effects for the stiffener. Finally, the stiffener has some rotational restraints at its line of attachment to the plating and/or along the stiffener web–flange intersection. Such restraint affects the failure of the stiffener, but most methods neglect this effect.

In the ultimate limit state (ULS) design of stiffened panels using Equation (1.1) in Chapter 1, the capacity indicates the ultimate strength which may be determined by relevant ultimate strength formulations, while the demand represents the extreme value of the load effects (stresses) which are calculated by the classical theory of structural mechanics or linear elastic finite element analysis (FEA) once the overall loads are known, as noted in Section 5.3 of Chapter 5.

This chapter presents the ultimate strength formulations for stiffened panels and grillages. The formulations presented are designed to be more sophisticated than previous theoretically based simplified procedures. The average stress–strain relationships for the stiffened panel are also presented to characterize the behavior until and after the ultimate strength is reached.

6.2 Classification of Panel Collapse Modes

When subjected to predominantly axial tension, the stiffened panel may fail by gross yielding. On the other hand, the stiffened panel under predominantly compressive loads may potentially show a variety of failure modes until the ultimate strength is reached, as shown in Figure 6.1. The primary modes of overall failure for a stiffened panel subject to predominantly compressive loads will be considered as categorized into the following six types:

- Mode I: overall collapse of plating and stiffeners as a unit;
  - — Mode I-1: Mode I for uniaxially stiffened panels, see Figure 6.1(a)
  - — Mode I-2: Mode I for cross-stiffened panels, see Figure 6.1(b)
- Mode II: biaxial compressive collapse, see Figure 6.1(c);
- Mode III: beam–column-type collapse, see Figure 6.1(d);
- Mode IV: local buckling of stiffener web, see Figure 6.1(e);
- Mode V: tripping of stiffener, see Figure 6.1(f); and
- Mode VI: gross yielding.

Mode I typically represents the collapse pattern when the stiffeners are relatively weak. In this case, the stiffeners can buckle together with plating as a unit, the overall buckling behavior initially being elastic. The stiffened panel can normally sustain further loading even after overall buckling in the elastic regime occurs and the ultimate strength is eventually reached by formation of a large yield region inside the panel and/or along the panel edges. In Mode I, the collapse behavior of a uniaxially stiffened panel termed Mode I-1 is slightly different from that of a cross-stiffened panel termed Mode I-2. The former is in fact initiated by the beam–column-type failure, while the latter failure resembles that of an 'orthotropic plate'.

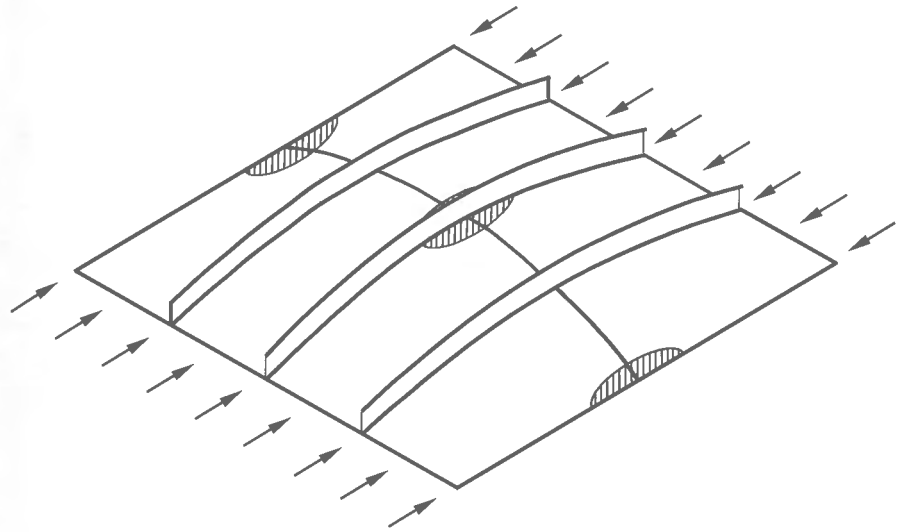

(a)

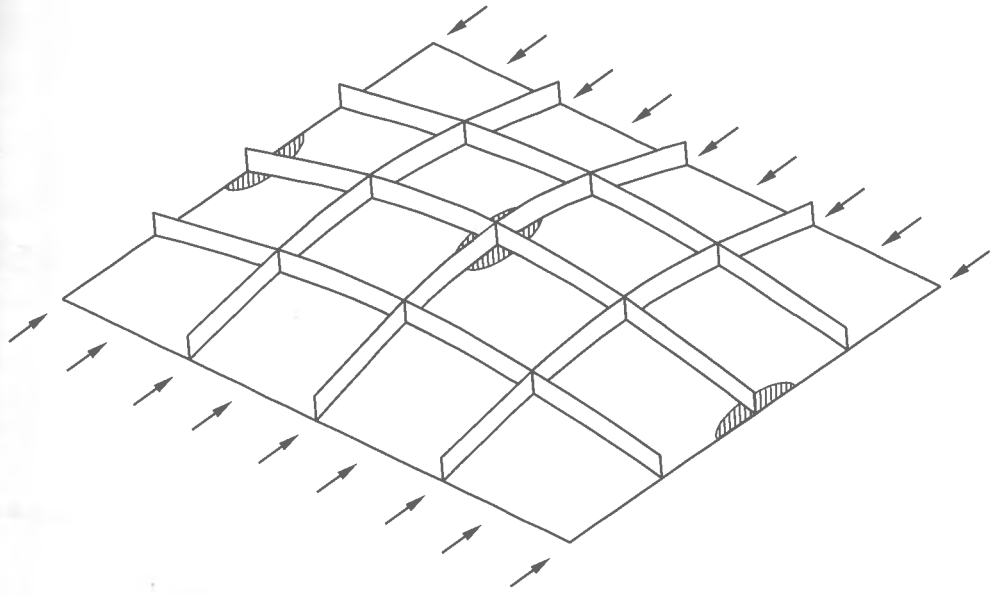

(b)

Figure 6.1 Failure modes (shaded areas represent yielded region). (a) Mode I-1: overall collapse of a uniaxially stiffened panel; (b) Mode I-2: overall collapse of a cross-stiffened panel; (c) Mode II: biaxial compressive collapse; (d) Mode III: beam–column-type collapse; (e) Mode IV: collapse by local buckling of stiffener web; (f) Mode V: collapse by tripping of stiffener

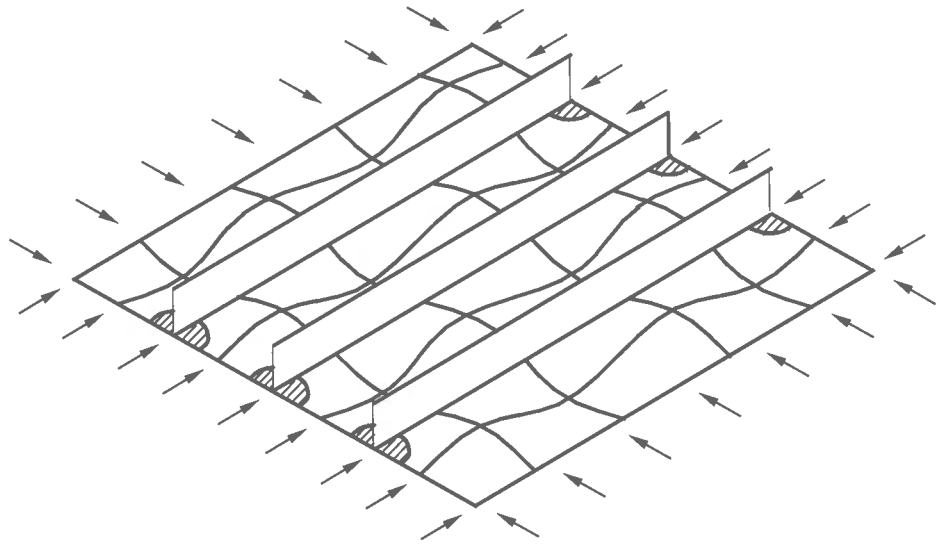

(c)

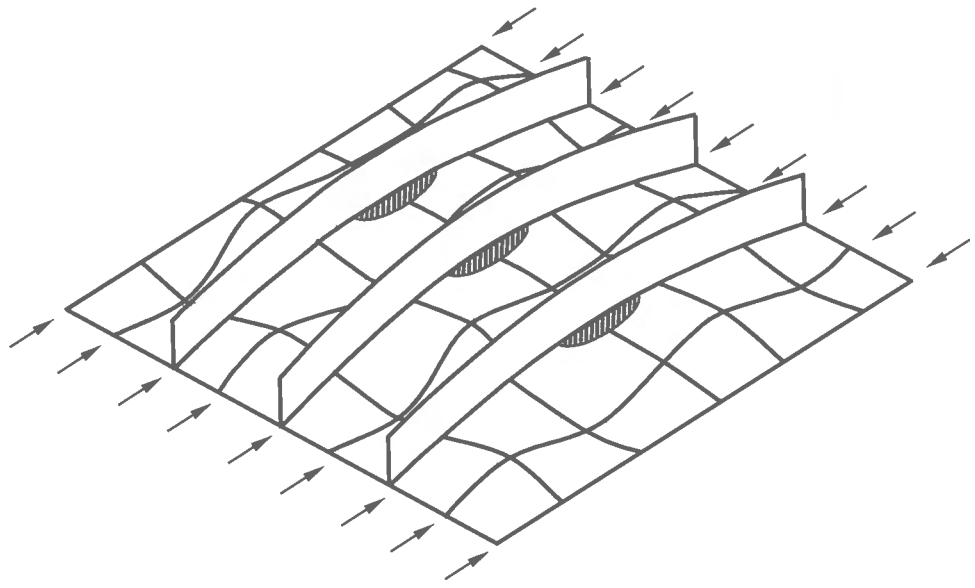

(d)

Figure 6.1 (*continued*)

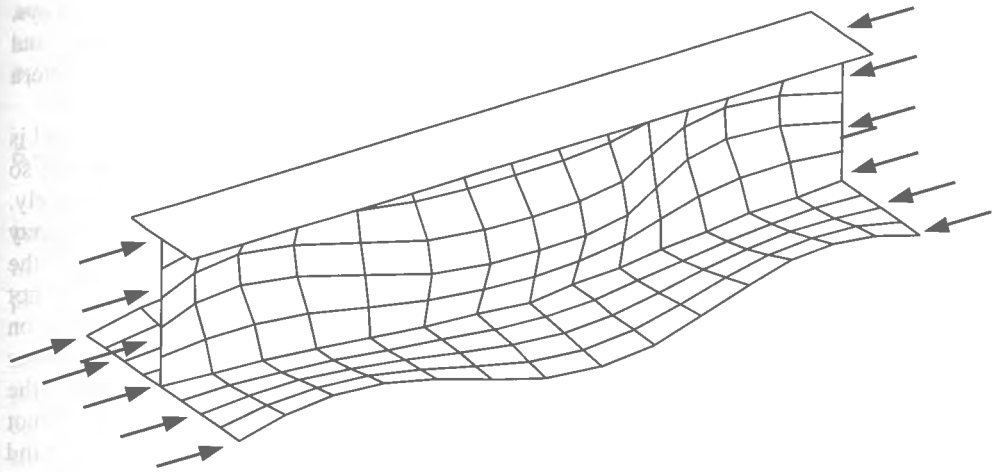

(e)

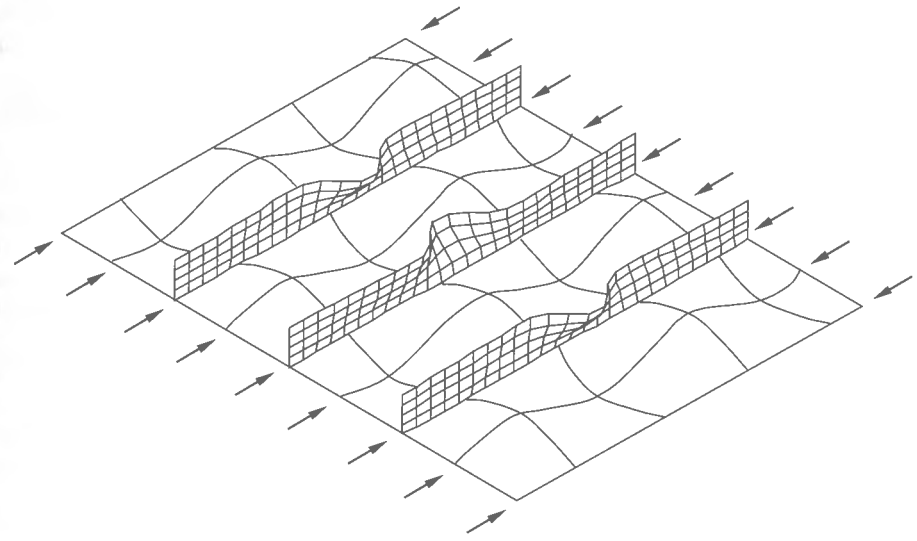

(f)

Figure 6.1 (*continued*)

Mode II represents the collapse pattern wherein the panel collapses by yielding along the plate–stiffener intersection at the panel edges, with no stiffener failure. This type of collapse can be important in some cases when the panel is predominantly subjected to biaxial compressive loads and/or when the plating is stocky.

Mode III indicates a failure pattern in which the ultimate strength is reached by yielding of the plate–stiffener combination at mid-span. Mode III failure typically occurs when the dimensions of the stiffeners are intermediate, i.e., neither weak nor very strong.

Modes IV and V typically arise from stiffener-induced failure when the ratio of stiffener web height to stiffener web thickness is large and/or when the type of the stiffener flange

is inadequate to remain straight so that the stiffener web buckles or twists sideways. Mode V can occur when the ultimate strength is reached subsequent to lateral–torsional buckling (also called tripping) of the stiffener, while Mode IV represents a failure pattern in which the panel collapses by local compressive buckling of the stiffener web.

Mode VI typically takes place when the panel slenderness is very small (i.e., the panel is very stocky) and/or when the panel is predominantly subjected to axial tensile loading so that neither local nor overall buckling occurs until the panel cross-section yields entirely.

While Figure 6.1 illustrates each collapse pattern separately, some collapse modes may in some cases interact and occur simultaneously. It is also important to realize that the division of behavior of a stiffened panel as illustrated above is (1) artificial, and (2) not necessarily completely descriptive of all anticipated actual behavior, although based on the insights and experiences such division is thought to be adequate for design purposes in steel-plated structures. Further, even accepting these idealizations of behavior, the calculation of the ultimate strength of the stiffened panel under combined loads is not straightforward, because of the interplay of the various factors such as geometric and material properties, loading, post-weld initial imperfections (i.e., initial deflection and welding-induced residual stresses) and boundary conditions.

For practical design purposes, therefore, it is typically considered that the collapse of stiffened panels occurs at the lowest value among the various ultimate loads calculated considering each of the above collapse patterns separately.

6.3 Modeling of Stiffened Panels

The applicable geometric and material properties of the stiffened panel are as defined in Section 5.2 of Chapter 5. In calculations of the panel ultimate strength, the effective width, b_e, and effective 'length', a_e, of plating between stiffeners as described in Chapter 4 will be used. The characteristics of load effects on the stiffened panel are modeled as indicated in Section 5.3. The number of potential stress components acting on a stiffened panel is generally six, namely longitudinal axial stress, transverse axial stress, edge shear, longitudinal in-plane bending, transverse in-plane bending and lateral pressure, see Figure 5.2 in Chapter 5. It is considered that the compressive stress is negative and the tensile stress is positive, unless otherwise specified. That is, the longitudinal axial load has a negative value when the corresponding load is compressive, and vice versa.

As noted in Section 5.4, the edges of the stiffened panel bounded by longitudinal girders and transverse frames are considered to be simply supported, with zero deflection and zero rotational restraints along four edges, with all edges kept straight. This approximation will lead to some pessimistic, but adequate, results for practical design purposes of a stiffened panel in a continuous stiffened plate structure. The level of fabrication-related initial imperfections may sometimes be of significance and can reduce the ultimate load-carrying capacity of the structure. The characteristics of these initial imperfections are idealized as previously noted in Section 1.7 of Chapter 1.

6.4 Nonlinear Governing Differential Equations of Stiffened Panels

The nonlinear governing differential equations of stiffened panels may be divided into two groups depending on the buckling modes, namely those for the overall panel buckling

and those for local plate buckling. The former type of post-buckling behavior may be analyzed by the large-deflection orthotropic plate theory, while the latter type is analyzed by the large-deflection isotropic plate theory.

6.4.1 Large-deflection Orthotropic Plate Theory after Overall Grillage Buckling

When the stiffeners are relatively small, overall buckling may take place, see Figure 5.1(a) in Chapter 5. In this case, the cross-stiffened panel may be idealized as an orthotropic plate, where the stiffeners are in a sense smeared into the plating.

The orthotropic plate approach implies that stiffeners are relatively numerous and small so as to deflect together with the plating, and that the physical stiffeners remain stable through the ranges of orthotropic plate behavior. It has been said that the application of the orthotropic plate theory to cross-stiffened panels must be restricted to stiffened panels with more than three stiffeners in each direction (Smith 1966, Troitsky 1976, Mansour 1977). In addition, stiffeners in a given direction must be similar. For an approximation, however, the post-buckling behavior of steel panels with numerous small stiffeners in one direction may also be analyzed by the large-deflection orthotropic plate theory.

The overall buckling behavior of the panel can then be analyzed by solving the nonlinear governing differential equations of the large-deflection orthotropic plate theory, which are two, namely the equilibrium equation and the compatibility equation (e.g., Troitsky 1976). By taking into account the effect of initial deflections, the two governing differential equations for the cross-stiffened panel (i.e., having stiffeners in both the x and y directions) can be written as follows:

$$D_x\frac{\partial^4 w}{\partial x^4}+2H\frac{\partial^4 w}{\partial x^2\partial y^2}+D_y\frac{\partial^4 w}{\partial y^4} - t\left[\frac{\partial^2 F}{\partial y^2}\frac{\partial^2(w+w_0)}{\partial x^2}-2\frac{\partial^2 F}{\partial x\partial y}\frac{\partial^2(w+w_0)}{\partial x\partial y}+\frac{\partial^2 F}{\partial x^2}\frac{\partial^2(w+w_0)}{\partial y^2}+\frac{p}{t}\right]=0 \quad (6.1a)$$

$$\frac{1}{E_y}\frac{\partial^4 F}{\partial x^4}+\left(\frac{1}{G_{xy}}-2\frac{\nu_x}{E_x}\right)\frac{\partial^4 F}{\partial x^2\partial y^2}+\frac{1}{E_x}\frac{\partial^4 F}{\partial y^4} - \left[\left(\frac{\partial^2 w}{\partial x\partial y}\right)^2-\frac{\partial^2 w}{\partial x^2}\frac{\partial^2 w}{\partial y^2}+2\frac{\partial^2 w_0}{\partial x\partial y}\frac{\partial^2 w}{\partial x\partial y}-\frac{\partial^2 w_0}{\partial x^2}\frac{\partial^2 w}{\partial y^2}-\frac{\partial^2 w}{\partial x^2}\frac{\partial^2 w_0}{\partial y^2}\right]=0 \quad (6.1b)$$

where w_0 and w are the initial and added deflection functions for the orthotropic plate, respectively, and F is Airy's stress function. E_x and E_y are the elastic moduli of the orthotropic plate in the x and y directions, respectively. G_{xy} is the elastic shear modulus of the orthotropic plate which can be approximately taken as follows:

$$G_{xy}=\frac{E_xE_y}{E_x+(1+2\sqrt{\nu_x\nu_y})E_y}\approx\frac{\sqrt{E_xE_y}}{2(1+\sqrt{\nu_x\nu_y})} \quad (6.2)$$

D_x and D_y in Equation (6.1a) are the flexural rigidities of the orthotropic plate in the x and y directions, respectively. H is the effective torsional rigidity of the orthotropic

plate. Once Airy's stress function, F, and the added deflection, w, are known, the stresses inside the panel can be calculated as follows:

$$\sigma_x = \frac{\partial^2 F}{\partial y^2} - \frac{E_x z}{1-\nu_x\nu_y}\left(\frac{\partial^2 w}{\partial x^2} + \nu_y \frac{\partial^2 w}{\partial y^2}\right) \tag{6.3a}$$

$$\sigma_y = \frac{\partial^2 F}{\partial x^2} - \frac{E_y z}{1-\nu_x\nu_y}\left(\frac{\partial^2 w}{\partial y^2} + \nu_x \frac{\partial^2 w}{\partial x^2}\right) \tag{6.3b}$$

$$\tau = -\frac{\partial^2 F}{\partial x \partial y} - 2G_{xy} z \frac{\partial^2 w}{\partial x \partial y} \tag{6.3c}$$

where σ_x and σ_y are the axial stresses in the x and y directions, respectively, and τ is the edge shear stress. z is the axis in the plate thickness direction with $z = 0$ at the mid-thickness.

The reliability of orthotropic plate analysis depends significantly on various elastic constants that need to be determined when a stiffened panel is replaced by an equivalent orthotropic plate. In the following, the large-deflection orthotropic plate theory constants developed by Paik *et al.* (2001) are introduced.

For an isotropic plate, the number of independent elastic constants is two, namely the elastic modulus, E, and the Poisson ratio, ν. For the orthotropic plate, four elastic constants, namely E_x, E_y, ν_x and ν_y, are required to describe the orthotropic stress–strain relationship of the plate.

In real stiffened panels, the anisotropy in the two mutually perpendicular directions arises from different properties of the geometry rather than from different properties of the material which itself is inherently isotropic. In this case, the corresponding orthotropic constants of the elastic moduli can be approximately given by

$$E_x = E\left(1 + \frac{n_{sx}A_{sx}}{Bt}\right), \quad E_y = E\left(1 + \frac{n_{sy}A_{sy}}{Lt}\right) \tag{6.4}$$

where the geometric parameters are defined in Section 5.2 of Chapter 5.

Also, the flexural and torsional rigidities of the orthotropic plate can be approximately expressed by

$$D_x = \frac{Et^3}{12(1-\nu_x\nu_y)} + \frac{Etz_{0x}^2}{1-\nu_x\nu_y} + \frac{EI_x}{b} \tag{6.5a}$$

$$D_y = \frac{Et^3}{12(1-\nu_x\nu_y)} + \frac{Etz_{0y}^2}{1-\nu_x\nu_y} + \frac{EI_y}{a} \tag{6.5b}$$

$$H = \frac{1}{2}\left(\nu_y D_x + \nu_x D_y + G_{xy}\frac{t^3}{3}\right) \tag{6.5c}$$

where

$$I_x = \frac{t_{wx}h_{wx}^3}{12} + t_{wx}h_{wx}\left(\frac{h_{wx}}{2} + \frac{t}{2} - z_{0x}\right)^2 + \frac{b_{fx}t_{fx}^3}{12} + b_{fx}t_{fx}\left(\frac{t_{fx}}{2} + h_{wx} + \frac{t}{2} - z_{0x}\right)^2$$

$$I_y = \frac{t_{wy}h_{wy}^3}{12} + t_{wy}h_{wy}\left(\frac{h_{wy}}{2} + \frac{t}{2} - z_{0y}\right)^2 + \frac{b_{fy}t_{fy}^3}{12} + b_{fy}t_{fy}\left(\frac{t_{fy}}{2} + h_{wy} + \frac{t}{2} - z_{0y}\right)^2$$

$$z_{0x} = \frac{h_{wx}t_{wx}(h_{wx}/2 + t/2) + b_{fx}t_{fx}(t_{fx}/2 + h_{wx} + t/2)}{bt + h_{wx}t_{wx} + b_{fx}t_{fx}}$$

$$z_{0y} = \frac{h_{wy}t_{wy}(h_{wy}/2 + t/2) + b_{fy}t_{fy}(t_{fy}/2 + h_{wy} + t/2)}{at + h_{wy}t_{wy} + b_{fy}t_{fy}}$$

For an isotropic plate, the flexural rigidities will of course simplify to the following well-known expression:

$$D_x = D_y = H = D = \frac{Et^3}{12(1-\nu^2)} \tag{6.6}$$

To determine the various elastic constants indicated above, Poisson's ratios ν_x and ν_y due to structural orthotropy and which are not material properties but rather elastic constants corresponding to the given geometrical configuration should be known in advance. Based on Betti's reciprocity theorem, the following two requirements are then pertinent:

$$\nu_x E_y = \nu_y E_x, \quad \nu_x D_y = \nu_y D_x \tag{6.7}$$

Substitution of Equations (6.4), (6.5a) and (6.5b) into Equation (6.7) leads to

$$\left[\frac{EI_x}{b}\left(\frac{E_y}{E_x}\right)^2 - \frac{EI_y}{a}\left(\frac{E_y}{E_x}\right)\right]\nu_x^3 - \left[\frac{E_y}{E_x}\left(\frac{Et^3}{12} + Etz_{0x}^2 + \frac{EI_x}{b}\right) - \frac{Et^3}{12} - Etz_{0y}^2 - \frac{EI_y}{a}\right]\nu_x = 0 \tag{6.8}$$

The solution of Equation (6.8) together with Equation (6.7) results in the effective Poisson ratios in the x and y directions, namely

$$\nu_x = c\left[\frac{(E_y/E_x)(Et^3/12 + Etz_{0x}^2 + EI_x/b) - Et^3/12 - Etz_{0y}^2 - EI_y/a}{(EI_x/b)(E_y/E_x)^2 - (EI_y/a)(E_y/E_x)}\right]^{0.5} \tag{6.9a}$$

$$\nu_y = \frac{E_y}{E_x}\nu_x = c\frac{E_y}{E_x}\left[\frac{(E_y/E_x)(Et^3/12 + Etz_{0x}^2 + EI_x/b) - Et^3/12 - Etz_{0y}^2 - EI_y/a}{(EI_x/b)(E_y/E_x)^2 - (EI_y/a)(E_y/E_x)}\right]^{0.5} \tag{6.9b}$$

where c is a correction factor to correlate Poisson's ratios with $\nu_x = \nu_y = \nu$ for an isotropic plate, which may approximately be taken as $c = \nu/0.86$. Note also that $\nu_x = \nu_y = \nu$ if

$$\frac{EI_x}{b}\left(\frac{E_y}{E_x}\right)^2 = \frac{EI_y}{a}\left(\frac{E_y}{E_x}\right) \quad \text{or} \quad \frac{E_x}{E_y} = \frac{a}{b}\frac{I_x}{I_y}$$

6.4.2 Large-deflection Isotropic Plate Theory after Local Plate Buckling

When the stiffeners are strong enough, they will not fail prior to buckling of plating between them. In this case, the large-deflection behavior (including buckling) of plating between stiffeners is of primary concern and can be analyzed by solving the nonlinear governing differential equations of the large-deflection isotropic plate theory, see Section 4.7 in Chapter 4.

6.5 Elastic Large-deflection Behavior after Overall Grillage Buckling

6.5.1 Combined Longitudinal Axial Load and Lateral Pressure

The elastic large-deflection behavior of the stiffened panel following the overall buckling mode is now studied when the panel is subjected to combined σ_{xav} (either compressive or tensile) and p, the latter being regarded as a secondary load component. To analytically solve the nonlinear governing differential equations, Equations (6.1), it is desirable to use simplified initial and added deflection functions which involve only one deflection term.

For a panel under predominantly longitudinal compressive axial loads, the deflection term associated with the buckling mode normally plays a dominant role in the elastic large-deflection response. For the purposes of the current task where the orthotropic plate deflection itself is not of primary interest but the membrane stress distribution of the orthotropic plate under σ_{xav} and p is needed, the orthotropic plate initial and added deflection functions are further simplified by including only the predominant buckling mode term as follows:

$$w_0 = A_{0m} \sin\frac{m\pi x}{L} \sin\frac{\pi y}{B} \tag{6.10a}$$

$$w = A_m \sin\frac{m\pi x}{L} \sin\frac{\pi y}{B} \tag{6.10b}$$

where one half-wave mode is assumed in the unloaded (y) direction. m is the half-wave number in buckling when σ_{xav} is compressive, while $m = 1$ is taken when σ_{xav} is predominantly tensile. A_{0m} is the amplitude of the buckling mode initial deflection, while A_m is the unknown amplitude of the added deflection function. As will be seen later, the buckling mode, m, depends on the structural orthotropy as well as the panel aspect ratio. $A_{0m} = 0$ is assumed when σ_{xav} is tensile.

It is important to realize that the deflection functions, Equations (6.10), are used for the purpose of the membrane stress distribution analysis only. A greater number of deflection terms should in principle be included for calculating the shape of the panel deflection itself that should be of interest.

Considering the idealized initial imperfections, boundary conditions and load application, the membrane stress distribution inside the stiffened panel after overall buckling can be obtained as the solutions of the nonlinear governing differential equations, Equations (6.1). To do this, one should start by determining A_m in Equation (6.10b) under the applied loading. Substitution of Equations (6.10) into Equation (6.1b) results in

$$\frac{1}{E_y}\frac{\partial^4 F}{\partial x^4} + \left(\frac{1}{G_{xy}} - 2\frac{\nu_x}{E_x}\right)\frac{\partial^4 F}{\partial x^2 \partial y^2} + \frac{1}{E_x}\frac{\partial^4 F}{\partial y^4} = \frac{m^2\pi^4}{2L^2B^2}A_m(A_m + 2A_{0m})\left(\cos\frac{2m\pi x}{L} + \cos\frac{2\pi y}{B}\right) \tag{6.11}$$

The particular solution, F_P, of Airy's stress function, F, is obtained by solving Equation (6.11) as follows:

$$F_P = \frac{A_m(A_m + 2A_{0m})}{32}\left(E_y\frac{L^2}{m^2B^2}\cos\frac{2m\pi x}{L} + E_x\frac{m^2B^2}{L^2}\cos\frac{2\pi y}{B}\right) \tag{6.12}$$

The homogeneous solution, F_H, of Airy's stress function, F, which satisfies the applied loading condition is given by

$$F_H = \sigma_{xav}\frac{y^2}{2} \tag{6.13}$$

The applicable stress function solution, F, may then be expressed as the sum of F_P and F_H as follows:

$$F = \sigma_{xav}\frac{y^2}{2} + \frac{A_m(A_m + 2A_{0m})}{32}\left(E_y\frac{L^2}{m^2B^2}\cos\frac{2m\pi x}{L} + E_x\frac{m^2B^2}{L^2}\cos\frac{2\pi y}{B}\right) \tag{6.14}$$

By substituting Equations (6.10) and (6.14) into Equation (6.1a) and applying the Galerkin method, we will get the following equation:

$$\int_0^L\int_0^B \left\{D_x\frac{\partial^4 w}{\partial x^4} + 2H\frac{\partial^4 w}{\partial x^2\partial y^2} + D_y\frac{\partial^4 w}{\partial y^4} - t\left[\frac{\partial^2 F}{\partial y^2}\frac{\partial^2(w+w_0)}{\partial x^2} - 2\frac{\partial^2 F}{\partial x\partial y}\frac{\partial^2(w+w_0)}{\partial x\partial y} + \frac{\partial^2 F}{\partial x^2}\frac{\partial^2(w+w_0)}{\partial y^2} + \frac{p}{t}\right]\right\} \sin\frac{m\pi x}{L}\sin\frac{\pi y}{B}dx\,dy = 0 \tag{6.15}$$

By performing the integration of Equation (6.15) over the entire panel, a third-order equation with respect to A_m is obtained. This results in

$$C_1A_m^3 + C_2A_m^2 + C_3A_m + C_4 = 0 \tag{6.16}$$

where

$$C_1 = \frac{\pi^2}{16}\left(E_x\frac{m^4B}{L^3} + E_y\frac{L}{B^3}\right), \quad C_2 = \frac{3\pi^2A_{0m}}{16}\left(E_x\frac{m^4B}{L^3} + E_y\frac{L}{B^3}\right)$$

$$C_3 = \frac{\pi^2A_{0m}^2}{8}\left(E_x\frac{m^4B}{L^3} + E_y\frac{L}{B^3}\right) + \frac{m^2B}{L}\sigma_{xav} + \frac{\pi^2}{t}\left(D_x\frac{m^4B}{L^3} + 2H\frac{m^2}{LB} + D_y\frac{L}{B^3}\right)$$

$$C_4 = A_{0m}\frac{m^2B}{L}\sigma_{xav} - \frac{16LB}{\pi^4t}p$$

For the integration of Equation (6.15), it was approximated that the contribution of lateral pressure to nonlinear membrane stresses would arise from the deflection component of $m = 1$ only and it was linearly superposed to those by in-plane loads. The solution of Equation (6.16) can be obtained in an explicit form using the Cardano method as indicated in Equation (4.12) of Chapter 4. If the axial compressive stress reaches the buckling stress, the perfect orthotropic panel (i.e., without initial deflection) buckles, while no similar bifurcation phenomenon occurs in the plate with initial deflection. The bifurcation overall buckling strength equation of the perfect panel under σ_{xav} in compression can then be derived for the case with $p = 0$. When the initial deflection does not exist, i.e., $A_{0m} = 0, C_2 = C_4 = 0$. Thus Equation (6.16) will be given (since the lateral deflection immediately before the panel buckles must in this case be zero, i.e., $A_m = 0$) as follows:

$$A_m = \sqrt{-\frac{C_3}{C_1}} = 0 \tag{6.17}$$

where

$$C_1 = \frac{\pi^2}{16}\left(E_x\frac{m^4B}{L^3} + E_y\frac{L}{B^3}\right), C_3 = \frac{m^2B}{L}\sigma_{xav} + \frac{\pi^2}{t}\left(D_x\frac{m^4B}{L^3} + 2H\frac{m^2}{LB} + D_y\frac{L}{B^3}\right)$$

The solution of Equation (6.17) results in either $C_3 = 0$ or the following equation:

$$\frac{m^2B}{L}\sigma_{xav} + \frac{\pi^2}{t}\left(D_x\frac{m^4B}{L^3} + 2H\frac{m^2}{LB} + D_y\frac{L}{B^3}\right) = 0 \tag{6.18}$$

Hence the elastic overall buckling strength, σ_{xEO}, of the stiffened panel under σ_{xav} in compression is given from Equation (6.18) upon replacing σ_{xav} with σ_{xEO} as follows:

$$\sigma_{xEO} = -\frac{\pi^2}{t}\left(D_x\frac{m^2}{L^2} + 2H\frac{1}{B^2} + D_y\frac{L^2}{m^2B^4}\right) \tag{6.19}$$

Using Equation (6.19), the buckling half-wave number, m, can be determined as the minimum integer satisfying the following condition since buckling load must be identical at the transition of buckling half waves, namely

$$D_x\frac{m^2}{L^2} + 2H\frac{1}{B^2} + D_y\frac{L^2}{m^2B^4} \le D_x\frac{(m+1)^2}{L^2} + 2H\frac{1}{B^2} + D_y\frac{L^2}{(m+1)^2B^4} \tag{6.20a}$$

or, more simply,

$$\left(\frac{L}{B}\right)^4 \le \frac{D_x}{D_y}m^2(m+1)^2 \tag{6.20b}$$

It is evident from Equation (6.20b) that the buckling mode depends on both the plate aspect ratio and the structural orthotropy. For an isotropic plate under σ_{xav} in compression, Equation (6.20b) will of course simplify to the well-known condition since $D_x = D_y$, as follows:

$$\frac{L}{B} \le \sqrt{m(m+1)} \tag{6.20c}$$

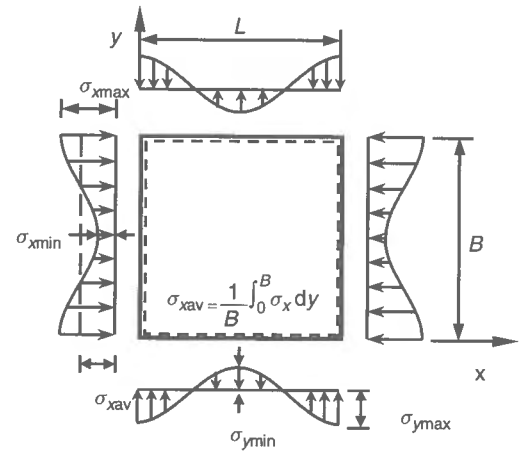

Figure 6.2 Membrane stress distribution inside an orthotropic plate under predominantly longitudinal axial compressive loads

Once A_m is determined as the solution of Equation (6.16) for the given values of σ_{xav} and p, the stresses inside the panel can then be computed by substituting Equations (6.10) and (6.14) into Equations (6.3). The membrane stress distribution inside the panel is non-uniform after large-deflection behavior occurs as shown in Figure 6.2. The maximum or minimum membrane stresses in the x and y directions are given from Equations (6.3) at $z = 0$ as follows:

$$\sigma_{x\,max} = \sigma_{xav} - \rho_x\frac{m^2\pi^2E_xA_m(A_m + 2A_{0m})}{8L^2} \tag{6.21a}$$

$$\sigma_{x\,min} = \sigma_{xav} + \rho_x\frac{m^2\pi^2E_xA_m(A_m + 2A_{0m})}{8L^2} \tag{6.21b}$$

$$\sigma_{y\,max} = -\rho_x\frac{\pi^2E_yA_m(A_m + 2A_{0m})}{8B^2} \tag{6.21c}$$

$$\sigma_{y\,min} = \rho_x\frac{\pi^2E_yA_m(A_m + 2A_{0m})}{8B^2} \tag{6.21d}$$

where A_m is obtained by the solution of Equation (6.16); ρ_x is the correction factor.

As previously noted in Chapter 4 for isotropic plates, the lateral deflection of a wide orthotropic plate under σ_{xav} in compression may be somewhat different from the sinusoidal pattern assumed by Equations (6.10) in that it takes a 'bath tub' shape around the orthotropic plate edges while the deflected shape in the middle part of the plate is more flat, see Figure 4.8(a) in Chapter 4. As a result, the deflection around the panel edges is normally larger than the case considering the sinusoidal pattern of deflection so that the membrane stresses become larger. To account for this effect of the bath tub shape deflection, the stress term related to the large-deflection effect is amplified by multiplying the correction factor, ρ_x. In the case of such an approximation, the correction factor, ρ_x, may be empirically derived for the orthotropic plate under σ_{xav} in compression as a function of the structural orthotropy. For instance, based on the insights developed by a series

of nonlinear finite element computations, varying the dimensions and aspect ratio of the stiffened panel, the following approximation has been suggested by Paik *et al.* (2001):

$$\rho_x = \begin{cases} \rho_x^* & \text{for } (L/B)^4 \geq D_y/(4D_x) \\ 2\rho_x^* & \text{for } (L/B)^4 < D_y/(4D_x) \end{cases} \tag{6.22}$$

where

$$\rho_x^* = \begin{cases} 1.0 & \text{for } H/D < 1.3569 \\ 0.0894(H/D - 1.3569) + 1.0 & \text{for } H/D \geq 1.3569 \end{cases}$$

Equation (6.22) implies that due to the effect of the bath tub shape deflection, the large-deflection-related terms of the maximum and minimum membrane stresses are amplified. When σ_{xav} is tensile, $\rho_x = 1.0$ can be used.

6.5.2 Combined Transverse Axial Load and Lateral Pressure

The elastic large-deflection behavior is now considered when the panel is subjected to combined σ_{yav} (either compressive or tensile) and p, the latter being regarded as a secondary load component. The dominant term of the initial and added deflection functions of the panel under σ_{yav} and p can be assumed by considering only the buckling mode as follows:

$$w_0 = A_{0n} \sin\frac{\pi x}{L} \sin\frac{n\pi y}{B} \tag{6.23a}$$

$$w = A_n \sin\frac{\pi x}{L} \sin\frac{n\pi y}{B} \tag{6.23b}$$

where A_n is the unknown amplitude of the added deflection function, while A_{0n} is the initial deflection amplitude. The half-wave number in the unloaded (x) direction is taken as one, while n is the buckling half-wave number in the loading (y) direction. As will be seen later, the buckling half-wave mode, n, depends on the structural orthotropy as well as the aspect ratio. When σ_{yav} is tensile, $n = 1$ and $A_{0n} = 0$ are normally assumed.

By solving the nonlinear governing differential equations, Equations (6.1), together with Equations (6.23) in a similar manner to that of Section 6.5.1, A_n in Equation (6.23b) can be obtained as the solution of the following equation:

$$C_1 A_n^3 + C_2 A_n^2 + C_3 A_n + C_4 = 0 \tag{6.24}$$

where

$$C_1 = \frac{\pi^2}{16}\left(E_x\frac{B}{L^3} + E_y\frac{n^4 L}{B^3}\right), \quad C_2 = \frac{3\pi^2 A_{0n}}{16}\left(E_x\frac{B}{L^3} + E_y\frac{n^4 L}{B^3}\right)$$

$$C_3 = \frac{\pi^2 A_{0n}^2}{8}\left(E_x\frac{B}{L^3} + E_y\frac{n^4 L}{B^3}\right) + \frac{n^2 L}{B}\sigma_{yav} + \frac{\pi^2}{t}\left(D_x\frac{B}{L^3} + 2H\frac{n^2}{LB} + D_y\frac{n^4 L}{B^3}\right)$$

$$C_4 = A_{0n}\frac{n^2 L}{B}\sigma_{yav} - \frac{16LB}{\pi^4 t}p$$

Again, it was approximated that the contribution of lateral pressure to nonlinear membrane stresses would arise from the deflection component of $n = 1$ only. Equation (6.24)

can be solved with regard to A_n by applying Equation (4.12) of Chapter 4. For a perfect orthotropic plate (i.e., without initial deflections), the elastic overall buckling strength under σ_{yav} in compression can be obtained, since A_n must be zero immediately before buckling occurs, as follows:

$$\sigma_{yEO} = -\frac{\pi^2}{t}\left(D_x\frac{B^2}{n^2 L^4} + 2H\frac{1}{L^2} + D_y\frac{n^2}{B^2}\right) \tag{6.25}$$

The buckling half-wave number, n, can in this case be determined as the minimum integer satisfying the following equation:

$$\left(\frac{B}{L}\right)^4 \leq \frac{D_y}{D_x}n^2(n+1)^2 \tag{6.26a}$$

As is apparent from Equation (6.26a), the buckling half mode depends on both the aspect ratio and the structural orthotropy. For an isotropic plate under σ_{xav} in compression, Equation (6.26a) will of course simplify to the well-known equation, since $D_x = D_y$, as follows:

$$\frac{B}{L} \leq \sqrt{n(n+1)} \tag{6.26b}$$

Applying an approach similar to that described in Section 6.5.1, the maximum and minimum membrane stress components at $z = 0$ are then given, by accounting for the effect of bath tub shape deflection, as follows:

$$\sigma_{x\,\max} = -\rho_y\frac{\pi^2 E_x A_n(A_n + 2A_{0n})}{8L^2} \tag{6.27a}$$

$$\sigma_{x\,\min} = \rho_y\frac{\pi^2 E_x A_n(A_n + 2A_{0n})}{8L^2} \tag{6.27b}$$

$$\sigma_{y\,\max} = \sigma_{yav} - \rho_y\frac{n^2\pi^2 E_y A_n(A_n + 2A_{0n})}{8B^2} \tag{6.27c}$$

$$\sigma_{y\,\min} = \sigma_{yav} + \rho_y\frac{n^2\pi^2 E_y A_n(A_n + 2A_{0n})}{8B^2} \tag{6.27d}$$

where A_n is obtained by the solution of Equation (6.24). ρ_y is the correction factor accounting for the effect of bath tub shape deflection, which may be approximated in a fashion similar to that of Equation (6.22) as follows:

$$\rho_y = \begin{cases} \rho_y^* & \text{for } (L/B)^4 \leq 4D_x/D_y \\ 2\rho_y^* & \text{for } (L/B)^4 > 4D_x/D_y \end{cases} \tag{6.28}$$

where

$$\rho_y^* = \begin{cases} 1.0 & \text{for } H/D < 1.3569 \\ 0.0894(H/D - 1.3569) + 1.0 & \text{for } H/D \geq 1.3569 \end{cases}$$

It is noted that when σ_{yav} is tensile, $\rho_y = 1.0$ is to be used.

6.5.3 Average Stress–Strain Relationship under Combined Loads

When the progressive collapse behavior of a large complex plated structure that is composed of individual stiffened panel elements is considered, it is necessary to investigate the behavior of each panel component as external loads increase. The post-buckling or large-deflection behavior of an orthotropic plate under combined biaxial loads and edge shear until the ultimate strength is reached may be represented by the average stress–strain relationship, which is given by

$$\varepsilon_{xav} = \frac{1}{E_x}\sigma_{x\,max} - \frac{\nu_y}{E_y}\sigma_{yav} \tag{6.29a}$$

$$\varepsilon_{yav} = -\frac{\nu_x}{E_x}\sigma_{xav} + \frac{1}{E_y}\sigma_{y\,max} \tag{6.29b}$$

$$\gamma_{av} = \frac{1}{G_{xye}}\tau_{av} \tag{6.29c}$$

where $\sigma_{x\,max}, \sigma_{y\,max}$ = maximum membrane stresses in the x or y direction. G_{xye} is the effective shear modulus of the orthotropic plate, which may approximately be defined from Equations (4.45), but replacing G and G_e by G_{xy} and G_{xye}, respectively.

The incremental form of the above stress–strain relationship is obtained by differentiating Equations (6.29) with regard to the corresponding stress components as follows:

$$\Delta\varepsilon_{xav} = \frac{1}{E_x}\frac{\partial\sigma_{x\,max}}{\partial\sigma_{xav}}\Delta\sigma_{xav} - \left(\frac{\nu_y}{E_y} - \frac{1}{E_x}\frac{\partial\sigma_{x\,max}}{\partial\sigma_{yav}}\right)\Delta\sigma_{yav} \tag{6.30a}$$

$$\Delta\varepsilon_{yav} = -\left(\frac{\nu_x}{E_x} - \frac{1}{E_y}\frac{\partial\sigma_{y\,max}}{\partial\sigma_{xav}}\right)\Delta\sigma_{xav} + \frac{1}{E_y}\frac{\partial\sigma_{y\,max}}{\partial\sigma_{yav}}\Delta\sigma_{yav} \tag{6.30b}$$

$$\Delta\gamma_{av} = \frac{1}{G_{xye}}\left(1 - \frac{\tau_{av}}{G_{xye}}\frac{\partial G_{xye}}{\partial\tau_{av}}\right)\Delta\tau_{av} \tag{6.30c}$$

Equations (6.30) can be rewritten in matrix form as follows:

$$\begin{Bmatrix}\Delta\sigma_{xav}\\ \Delta\sigma_{yav}\\ \Delta\tau_{av}\end{Bmatrix} = [D_{sp}]_O^B \begin{Bmatrix}\Delta\varepsilon_{xav}\\ \Delta\varepsilon_{yav}\\ \Delta\gamma_{av}\end{Bmatrix} \tag{6.31}$$

where

$$[D_p]_O^B = \frac{1}{A_1B_2 - A_2B_1}\begin{bmatrix} B_2 & -A_2 & 0\\ -B_1 & A_1 & 0\\ 0 & 0 & 1/C_1\end{bmatrix}$$

is the pre-ultimate stress–strain matrix of a stiffened panel element following the overall buckling mode, with

$$A_1 = \frac{1}{E_x}\frac{\partial\sigma_{x\,max}}{\partial\sigma_{xav}}, \quad A_2 = -\frac{\nu_y}{E_y} + \frac{1}{E_x}\frac{\partial\sigma_{x\,max}}{\partial\sigma_{yav}}, \quad B_1 = -\frac{\nu_x}{E_x} + \frac{1}{E_y}\frac{\partial\sigma_{y\,max}}{\partial\sigma_{xav}}$$

$$B_2 = \frac{1}{E_y}\frac{\partial\sigma_{y\,max}}{\partial\sigma_{yav}} \quad \text{and} \quad C_1 = \frac{1}{G_{xye}}\left(1 - \frac{\tau_{av}}{G_{xye}}\frac{\partial G_{xye}}{\partial\tau_{av}}\right)$$

When the interaction effect between combined in-plane loads on the maximum membrane stresses is neglected, $\sigma_{x\,max}$ and $\sigma_{y\,max}$ can be obtained from Equations (6.21a) and (6.27c), respectively. In this case,

$$\frac{\partial\sigma_{x\,max}}{\partial\sigma_{yav}} = \frac{\partial\sigma_{y\,max}}{\partial\sigma_{xav}} = 0$$

6.6 Elastic Large-deflection Behavior after Local Plate Buckling

As previously presented in Chapter 5, three primary types of local buckling modes may typically be relevant for a stiffened panel, namely local buckling of plating (between stiffeners), local buckling of stiffener web and lateral–torsional buckling of stiffener.

Once the last two types of local buckling modes occur, the plating between stiffeners will be left with little stiffening and thus the entire stiffened panel may be considered to immediately reach the ULS following overall collapse mode. On the other hand, after local buckling of plating between stiffeners takes place, the stiffened panel may have some residual strength to sustain external loads until it collapses.

Hence only the first type of local buckling mode may be meaningful where the elastic large-deflection behavior of a stiffened panel subsequent to local buckling is concerned before the ultimate strength is reached. For this case, the behavior of the stiffened panel will be represented by an assembly of the buckled or deflected plating (between stiffeners) and the stiffeners themselves.

6.6.1 Combined Longitudinal Axial Load and Lateral Pressure

In this case, the elastic large-deflection behavior of plating (between stiffeners) can be evaluated as described in Section 4.8.1 of Chapter 4. Further, it may be assumed that stiffeners remain straight as long as the column-type initial deflections of stiffeners are not very large. The incremental form of the axial stress–strain relationship of longitudinal stiffeners without attached plating may in this case be approximately computed by

$$\Delta\sigma_{xav} = \frac{a}{A_{sx}}K_{Ex}\Delta\varepsilon_{xav} \tag{6.32}$$

where K_{Ex} = stiffness matrix of a longitudinal stiffener without attached plating, which may be calculated using Equation (2.110) in Chapter 2; $A_{sx} = h_{wx}t_{wx} + b_{fx}t_{fx}$.

6.6.2 Combined Transverse Axial Load and Lateral Pressure

The elastic large-deflection behavior of plating (between stiffeners) can in this case be evaluated as described in Section 4.8.2 of Chapter 4. The incremental form of the axial stress–strain relationship of transverse stiffeners may be approximately given by

$$\Delta\sigma_{yav} = \frac{b}{A_{sy}}K_{Ey}\Delta\varepsilon_{yav} \tag{6.33}$$

where K_{Ey} = stiffness matrix of a transverse stiffener without attached plating, which may be calculated using Equation (2.110) of Chapter 2; $A_{sy} = h_{wy}t_{wy} + b_{fy}t_{fy}$.

6.6.3 Average Stress–Strain Relationship under Combined Loads

The behavior of a stiffened panel subject to local buckling can be represented using an assembly of plating and stiffeners. The stress–strain relationships for the buckled plate part are given by Equation (4.48) in Chapter 4, while those for stiffeners are obtained from Equations (6.32) and (6.33).

Considering that the stresses are composed of two parts, namely for plating and stiffeners, the stress–strain relationship of a stiffened panel in the local buckling mode can then be given in incremental matrix form as follows:

$$\begin{Bmatrix} \Delta\sigma_{xav} \\ \Delta\sigma_{yav} \\ \Delta\tau_{av} \end{Bmatrix} = [D_{sp}]_L^B \begin{Bmatrix} \Delta\varepsilon_{xav} \\ \Delta\varepsilon_{yav} \\ \Delta\gamma_{av} \end{Bmatrix} \tag{6.34}$$

where $[D_{sp}]_L^B = [D_p]^B + [D_s]^B$ = pre-ultimate stress–strain matrix of a stiffened panel following the local plate buckling mode, $[D_p]^B$ = pre-ultimate stress–strain matrix of plating as defined in Equation (4.48), and

$$[D_s]^B = \begin{bmatrix} d_1 \\ d_2 \\ 0 \end{bmatrix}$$

is the pre-ultimate stress–strain matrix of stiffener with

$$d_1 = \frac{a}{A_{sx}} K_{Ex} \quad \text{and} \quad d_2 = \frac{b}{A_{sy}} K_{Ey}$$

6.7 Ultimate Strength

The ultimate strength formulations for the stiffened panel under combined in-plane and lateral pressure loads are now presented for all potential collapse modes noted in Section 6.2. The minimum strength is then taken as the real ULS.

6.7.1 Overall Collapse (Mode I)

Strictly speaking, the collapse behavior for Mode I-1 is different from that of Mode I-2 although both represent the collapse of plating together with stiffeners as a unit. The former is initiated by beam–column-type failure, while the latter resembles the orthotropic plate behavior. As an approximation, however, Mode I-1 for a panel with stiffeners in one direction may be treated as a specific case of Mode I-2 for a panel with stiffeners in both directions.

For the purposes of obtaining Mode I strength of a panel that may be reasonably modeled as an orthotropic plate for buckling and ultimate strength estimation, only the four load components, namely σ_{xav}, σ_{yav}, τ_{av} and p, are considered. Also, the orthotropic plate is considered to have welding-induced initial deflections, but the influence of the residual stresses is ignored, and hence must be otherwise adjusted for, perhaps as a few percent reduction in the computed strength. This is because in a panel with numerous

small stiffeners the effect of tensile and compressive residual stresses on the collapse load may be offset.

The effect of in-plane bending moment on the ultimate strength of the orthotropic plate is also neglected. This is usually not a serious limitation because in such cases some of the panel may be subjected to axial tension while axial compression is applied to the other parts, and the analyst usually has some flexibility in selecting the particular boundaries of a cross-stiffened panel during strength assessment. It is emphasized, however, that in-plane bending is an important factor in the ultimate strength calculations for a panel that collapses by failure of the stiffeners, and must be accounted for in such a case. For the purposes of ultimate strength predictions, large-deflection orthotropic plate theory is used as described in Section 6.4.

Combined Longitudinal Axial Load and Lateral Pressure

The ultimate longitudinal axial strength based on Mode I-1 or I-2 is denoted by σ_{xu}^{I}. The panel is considered to be predominantly subjected to σ_{xav} with $\sigma_{yav} = \tau_{av} = 0$, while p is regarded as the secondary load component.

With increasing panel deflection, the upper and/or lower fibers in the mid-region of the panel will initially yield by the action of bending. Applying the Mises–Hencky yield criterion, the first yield condition of the outer surface of the orthotropic plate may be given by (for the symbols used below, Sections 6.4.1 and 6.5.1 are referred to)

$$\left(\frac{\sigma_{xb}}{\sigma_{Yeq}}\right)^2 - \left(\frac{\sigma_{xb}}{\sigma_{Yeq}}\right)\left(\frac{\sigma_{yb}}{\sigma_{Yeq}}\right) + \left(\frac{\sigma_{yb}}{\sigma_{Yeq}}\right)^2 = 1 \tag{6.35}$$

where σ_{Yeq} = equivalent yield stress as defined in Equation (5.1) of Chapter 5,

$$\sigma_{xb} = \sigma_{xav} - \rho_x \frac{m^2\pi^2 E_x A_m (A_m + 2A_{0m})}{8L^2} - E_x \frac{t_{eq}}{2} \frac{A_m}{1 - \nu_x \nu_y} \left[\left(\frac{m\pi}{L}\right)^2 + \nu_y \left(\frac{\pi}{B}\right)^2\right]$$

$$\sigma_{yb} = -\rho_x \frac{\pi^2 E_y A_m (A_m + 2A_{0m})}{8B^2} - E_y \frac{t_{eq}}{2} \frac{A_m}{1 - \nu_x \nu_y} \left[\nu_x \left(\frac{m\pi}{L}\right)^2 + \left(\frac{\pi}{B}\right)^2\right]$$

t_{eq} = equivalent plate thickness which may be taken as

$$t_{eq} = \frac{t_{xeq} + t_{yeq}}{2}$$

with

$$t_{xeq} = t + \frac{n_{sx} A_{sx}}{B}, \quad t_{yeq} = t + \frac{n_{sy} A_{sy}}{L}$$

The stiffened panel, specifically with stiffeners in one direction only, may reach the ultimate strength if Equation (6.35) is satisfied. However, the panel may not collapse as long as it is possible to redistribute the applied loads to the straight panel boundaries by the membrane action. Collapse will then occur when the most stressed boundary locations yield, because the panel boundaries can no longer be kept straight, resulting in a rapid

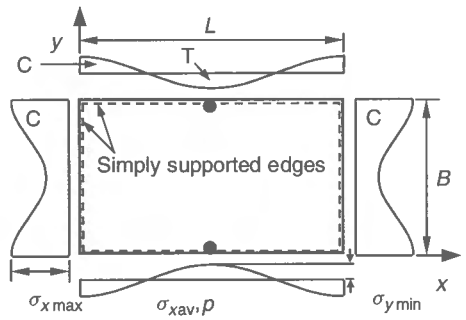

Figure 6.3 Plasticity at panel longitudinal edges for a combined σ_{xav} and p (●, expected yielding locations; C, compression; T, tension)

increase of lateral deflection. The criterion based on the initial plastic yield at the panel longitudinal edges as shown in Figure 6.3 is given by

$$\left(\frac{\sigma_{x\max}}{\sigma_{Yeq}}\right)^2 - \left(\frac{\sigma_{x\max}}{\sigma_{Yeq}}\right)\left(\frac{\sigma_{y\min}}{\sigma_{Yeq}}\right) + \left(\frac{\sigma_{y\min}}{\sigma_{Yeq}}\right)^2 = 1 \tag{6.36}$$

where $\sigma_{x\max}$, $\sigma_{y\min}$ are as defined in Equations (6.21a) and (6.21d).

The ultimate longitudinal axial strength, σ_{xu}^{I}, may be obtained as the solution of Equation (6.35) or (6.36) with regard to σ_{xav}, which is implicit within the stress components. It is noted that the panel ultimate strength value so obtained should of course be greater than the ultimate strength of the entire panel excluding stiffeners, which can be calculated as for an isotropic plate as presented in Chapter 4.

Combined Transverse Axial Load and Lateral Pressure

The ultimate transverse axial strength, σ_{yu}^{I}, based on Mode I is now presented when the panel is predominantly subjected to σ_{yav} with $\sigma_{xav} = \tau_{av} = 0$, while p is regarded as the secondary load component. A similar approach as for the longitudinal compression and pressure case is again used.

In this case, the first yield condition at the outer surface of the orthotropic plate is also given by Equation (6.35), but by replacing the surface stress components with those given by (for the symbols used below, Sections 6.4.1 and 6.5.2 are referred to)

$$\sigma_{xb} = -\rho_y \frac{\pi^2 E_x A_n (A_n + 2A_{0n})}{8L^2} - E_x \frac{t_{eq}}{2} \frac{A_n}{1 - \nu_x \nu_y}\left[\left(\frac{\pi}{L}\right)^2 + \nu_y \left(\frac{n\pi}{B}\right)^2\right] \tag{6.37a}$$

$$\sigma_{yb} = \sigma_{yav} - \rho_y \frac{n^2 \pi^2 E_y A_n (A_n + 2A_{0n})}{8B^2} - E_y \frac{t_{eq}}{2} \frac{A_n}{1 - \nu_x \nu_y}\left[\nu_x \left(\frac{\pi}{L}\right)^2 + \left(\frac{n\pi}{B}\right)^2\right] \tag{6.37b}$$

Also, the initial yield condition at the panel transverse edges as shown in Figure 6.4 is given by

$$\left(\frac{\sigma_{x\min}}{\sigma_{Yeq}}\right)^2 - \left(\frac{\sigma_{x\min}}{\sigma_{Yeq}}\right)\left(\frac{\sigma_{y\max}}{\sigma_{Yeq}}\right) + \left(\frac{\sigma_{y\max}}{\sigma_{Yeq}}\right)^2 = 1 \tag{6.38}$$

where $\sigma_{x\min}$, $\sigma_{y\max}$ are as defined in Equation (6.27b) or (6.27c).

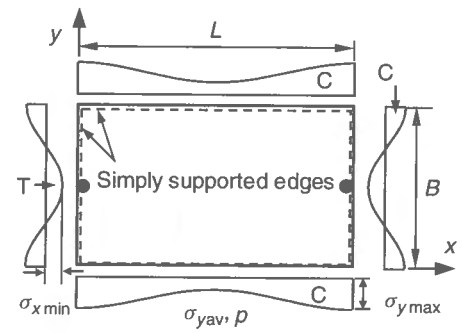

Figure 6.4 Plasticity at panel transverse edges for a combined σ_{yav} and p (●, expected yielding locations; C, compression; T, tension)

The ultimate transverse axial strength, σ_{yu}^{I}, may be obtained as the solution of Equation (6.35) or (6.38) with regard to σ_{yav}, the former being given with the stress components by Equations (6.37). It is again noted that the panel ultimate strength value so obtained should be greater than the ultimate strength of the entire panel excluding stiffeners, which can be calculated as for an isotropic plate as presented in Chapter 4.

Combined Edge Shear and Lateral Pressure

The ultimate pressure load, p_{u0}, for the orthotropic plate under lateral pressure alone is calculated as the smaller value of the two solutions obtained from the previous two subsections with regard to p, assuming one half-wave collapse pattern in both directions, i.e., $m = n = 1$ since $\sigma_{xav} = \sigma_{yav} = 0$. Also, the so-called permanent deflection of the panel under lateral pressure loads may be defined as the maximum deflection at the ultimate lateral pressure.

Next, as a first approximation the ultimate edge shear strength of stiffened panels may be predicted by the empirical formula, Equation (4.55a) of Chapter 4, for the ultimate strength of plating (between stiffeners) under edge shear alone. On the other hand, Mikami *et al.* (1989) proposed an empirical ultimate shear strength formula of a cross-stiffened panel which was originally aimed at designing the plate girder web under shearing force as follows:

$$\frac{\tau_u}{\tau_Y} = \begin{cases} 1.0 & \text{for } \lambda \le 0.6 \\ 1.0 - 0.614(\lambda - 0.6) & \text{for } 0.6 < \lambda \le \sqrt{2} \\ 1/\lambda^2 & \text{for } \lambda > \sqrt{2} \end{cases} \tag{6.39}$$

where $\lambda = \sqrt{(\tau_E/\tau_Y)}$, τ_E = elastic shear buckling stress, $\tau_Y = \sigma_Y/\sqrt{3}$.

For combined edge shear and lateral pressure loading, Equation (4.56) in Chapter 4 may be adopted for the ultimate strength interaction equation for an orthotropic plate, but replacing τ_{u0} and p_{u0} by the corresponding orthotropic plate strength values. Further study is recommended for a more elaborate and better description, and it is also to be noted that these approximations may provide somewhat pessimistic evaluations of the panel ultimate strength.

Combined Biaxial Loads, Edge Shear and Lateral Pressure

The following ultimate strength interaction equation may be used for Mode I failure of a stiffened panel under combined σ_{xav}, σ_{yav}, τ and p, using the Mode I ultimate strength components obtained so far, namely

$$\left(\frac{\sigma_{xav}}{\sigma_{xu}^{I}}\right)^{c_1} - \alpha\left(\frac{\sigma_{xav}}{\sigma_{xu}^{I}}\right)\left(\frac{\sigma_{yav}}{\sigma_{yu}^{I}}\right) + \left(\frac{\sigma_{yav}}{\sigma_{yu}^{I}}\right)^{c_2} + \left(\frac{\tau}{\tau_{u}^{I}}\right)^{c_3} = 1 \tag{6.40}$$

where α is an interaction constant as described in Section 4.9.7 of Chapter 4. The coefficients c_1–c_3 are often taken such that $c_1 = c_2 = c_3 = 2$. Following the approach used for the interaction equation for plating alone, α may be taken as $\alpha = 0$ when both σ_{xav} and σ_{yav} are compressive (negative), while $\alpha = 1$ when either σ_{xav} or σ_{yav}, or both, are tensile (positive). Equation (6.40) is similar in form to the Mises–Hencky yield function, and has been established on the basis of curve fits to the corresponding nonlinear numerical finite element solutions or experimental data (Furuta *et al.* 1991, Kitada *et al.* 1991a, 1991b).

6.7.2 Biaxial Compressive Collapse (Mode II)

A panel with relatively thick plating and under predominantly biaxial compressive stresses may collapse if the plate–stiffener intersection yields at the corners of plating between stiffeners, as shown in Figure 6.1(c). This is because if the plate corners which are most highly compressed in both directions yield, the panel may follow the collapse with little increase in the loading since the stiffeners may become unstable immediately. It is noted that the biaxial compressive stress situation at the corners of plating between stiffeners is also of importance when the panel is subjected to large lateral pressure loads.

In this case, of primary concern is the collapse of plating which is most highly stressed in a stiffened panel under in-plane compressive loads including bending. It is thus considered that the plating between stiffeners is subjected to the four stress components, namely σ_{xM}, σ_{yM}, τ_{av} and p, where σ_{xM} and σ_{yM} are the highest stresses in the x or y direction, as shown in Figure 5.2 of Chapter 5. Also, the post-weld initial imperfections of the plating in the form of initial deflection and residual stress are idealized as noted in Section 1.7 of Chapter 1. The membrane stress distribution inside the plating under combined loads, obtained by solving the nonlinear governing differential equations of the large-deflection isotropic plate theory presented in Chapter 4, provides the basic input necessary to check yielding.

Combined Longitudinal Axial Load and Lateral Pressure

The ultimate longitudinal axial strength, σ_{xu}^{II}, based on Mode II is considered for the most highly stressed plating between stiffeners under combined σ_{xM} and p when $\sigma_{yM} = \tau = 0$. The applicable maximum and minimum membrane stress components for plating between stiffeners can be calculated by solving the nonlinear governing differential equations of the large-deflection isotropic plate theory, as described in Chapter 4. The stiffened panel is then considered to collapse in Mode II if the plate corner yields. This results in the condition in Equation (4.49a) of Chapter 4. In this case, $\sigma_{x\,max}$ and $\sigma_{y\,max}$ are functions of σ_{xM} and p as well as the post-weld initial imperfections.

The panel ultimate longitudinal axial strength, σ_{xu}^{II}, based on Mode II, is then obtained by the solution of Equation (4.49a) with regard to σ_{xM} by substituting the maximum and minimum membrane stress components, Equations (4.18), upon replacing σ_{xav} with σ_{xM}. The approach used is quite similar to that for Mode I based on the initial yield at the panel boundaries, except for (1) inclusion of both post-weld residual stresses and initial deformations, and (2) yielding being considered to occur at the plate corners.

Combined Transverse Axial Load and Lateral Pressure

For combined σ_{yM} and p, the panel ultimate transverse axial strength, σ_{yu}^{II}, based on Mode II, is obtained by the solution of Equation (4.49a) with regard to σ_{yM}, but by substituting the maximum and minimum membrane stress components, Equations (4.31), into Equation (4.49a). As before, these membrane stress components are derived by solving the nonlinear governing differential equations of the large-deflection isotropic plate theory, as presented in Section 4.8.2 of Chapter 4. In this case, $\sigma_{x\,max}$ and $\sigma_{y\,max}$ are functions of σ_{yM} and p as well as initial imperfections.

Combined Edge Shear and Lateral Pressure

When the stiffeners are relatively strong (the plating fails prior to the stiffeners), the ultimate lateral pressure load, p_{u0}, may for this case be calculated as presented in Section 4.9.4 of Chapter 4. In this case, one half-wave collapse pattern is assumed in both directions (i.e., $m = n = 1$), when $\sigma_{xM} = \sigma_{yM} = 0$ and the plate edges yield.

Two upper limits of the ultimate lateral pressure load are also typically relevant. The first upper limit is given as ultimate lateral pressure load as previously described in the third subsection of Section 6.7.1 for Mode I overall collapse. The second upper limit is the 'critical' lateral pressure, p_{cr}, of plating (between stiffeners), as obtained by the rigid–plastic theory, which is given by Equation (4.54) in Chapter 4. Thus, p_{u0} should not be greater than the two upper limits noted above.

Equation (4.56) in Chapter 4 is again to be adopted for the ultimate strength interaction relationship between edge shear and lateral pressure of the stiffened panel following Mode II, but using the corresponding value of p_{u0} based on Mode II behavior, while the ultimate edge shear strength is again calculated from Equation (4.55a).

Combined Biaxial Loads, Edge Shear and Lateral Pressure

An expression similar to Equation (6.40) is used for the Mode II ultimate strength interaction equation for a stiffened panel under combined σ_{xM}, σ_{yM}, τ and p, using the Mode II ultimate strength components obtained so far. The applicable expression is as follows:

$$\left(\frac{\sigma_{xM}}{\sigma_{xu}^{II}}\right)^{c_1} - \alpha\left(\frac{\sigma_{xM}}{\sigma_{xu}^{II}}\right)\left(\frac{\sigma_{yM}}{\sigma_{yu}^{II}}\right) + \left(\frac{\sigma_{yM}}{\sigma_{yu}^{II}}\right)^{c_2} + \left(\frac{\tau}{\tau_{u}^{II}}\right)^{c_3} = 1 \tag{6.41}$$

where $\alpha = 0$ when both σ_{xM} and σ_{yM} are compressive (negative), while $\alpha = 1$ when either σ_{xM} or σ_{yM}, or both, are tensile (positive). The coefficients c_1–c_3 are taken as those of Equation (6.40).

6.7.3 Beam–Column-type Collapse (Mode III)

For collapse mode III, the plate–stiffener combination approach is applied using the modified Perry–Robertson formula as previously described in Section 2.9.1 of Chapter 2. In this case, the ultimate strength is considered to be reached if the extreme fibers of the cross-section (at mid-span in the simply supported case) yield; that is, when the axial stress at the outmost section reaches the yield stress either on the stiffener or the plate side, the former being called 'stiffener-induced failure' and the latter being called 'plate-induced failure'.

As described in Section 2.11.4 of Chapter 2, however, it is recognized that the Perry–Robertson stiffener-induced failure mode predictions are too pessimistic in comparison to actual test data or nonlinear FEA when the stiffeners are relatively small. This is because, while the original idea of the Perry–Robertson formula assumes that the stiffener-induced failure occurs if the tip of the stiffener yields, plasticity may grow into the stiffener web as long as lateral–torsional buckling or stiffener web buckling does not take place, so that the stiffener may resist the further loading even after the first yielding occurs at the extreme fiber of the stiffener.

Hence in such cases one may exclude the stiffener induced failure condition (i.e., yielding at the tip of the stiffener) from Mode III panel ultimate strength calculations. The possibility of the stiffener-induced failure mode due to local buckling of the stiffener web or lateral–torsional buckling of the stiffener is dealt with in Modes IV or V, respectively, later on.

It is considered that the most highly stressed stiffener in the x and y directions is subjected to the four stress components, namely $\sigma_{x\mathrm{M}}$, $\sigma_{y\mathrm{M}}$, τ_{av} and p. Normally, the effectiveness of plating between stiffeners progressively decreases until the plating collapses. The effectiveness of the plating between stiffeners is evaluated by taking into account the influence of the post-weld initial imperfections in the form of initial deflection and residual stresses.

Combined Longitudinal Axial Load and Lateral Pressure

The Mode III panel ultimate longitudinal axial strength, $\sigma_{xu}^{\mathrm{III}}$, is now considered when the panel is subjected to combined $\sigma_{x\mathrm{M}}$ and p, using a representative plate–stiffener combination under axial stress, $\sigma_{x\mathrm{M}}$, plus lateral line load $q = pb$ (i.e., multiplied by the uniform lateral pressure, p, and the breadth, b, of plating between longitudinal stiffeners).

(1) Effective width of plating between longitudinals: It is considered that the isotropic plating between stiffeners collapses locally when the plate longitudinal edges yield, as shown in Figure 4.12(b) of Chapter 4. The plate ultimate strength condition is in this case given by Equation (4.50a) with $\sigma_{\mathrm{Y}} = \sigma_{\mathrm{Yp}}$.

The ultimate longitudinal axial strength of the plating between stiffeners, σ_{xu}^{L}, is then calculated by the solution of Equation (4.50a) with regard to $\sigma_{x\mathrm{M}}$, but more approximate approaches may typically be used to calculate σ_{xu}^{L}, as described in Section 4.9.2 of Chapter 4. As presented in the second subsection of Section 4.8.1, the effective width of the plating between the most highly compressed longitudinal stiffeners can be calculated by taking into account the effects of the combined loads involved as well as the post-weld initial imperfections.

(2) Collapse strength of a plate–stiffener combination: Under combined $\sigma_{x\mathrm{M}}$ and $q = pb$, the ultimate strength of a plate–stiffener combination can be calculated using the modified Perry–Robertson formula. While a more elaborate description may be found in Section 2.9.1 of Chapter 2, a closed-form expression of the ultimate strength for the plate–stiffener combination under combined $\sigma_{x\mathrm{M}}$ (compression) and q accounting for the effect of initial deflection is given by Equations (2.108).

It is important to realize that Equations (2.108) do not involve local buckling of stiffener web or tripping of stiffener. Since compression is defined as negative, $\sigma_{xu}^{\mathrm{III}}$ will eventually take a negative value for $\sigma_{x\mathrm{M}}$ in compression. For $\sigma_{x\mathrm{M}}$ in tension, the panel ultimate strength will approximately equal the equivalent yield strength, i.e., $\sigma_{xu}^{\mathrm{III}} = \sigma_{\mathrm{Y}x}$, where $\sigma_{\mathrm{Y}x}$ is defined in Equation (5.1) of Chapter 5.

It has been recognized that for panels with relatively weak stiffeners the modified Perry–Robertson approach can apparently predict an ultimate axial compressive strength which is in some cases even less than that of the bare plate (i.e., panel without stiffeners), while the orthotropic plate approach gives the value which is greater than the real panel ultimate strength. In this regard, a lower limit of the panel ultimate strength following Mode III, given by the weighted average of the bare plate ultimate strength and the orthotropic plate ultimate strength as long as $\sigma_{x\mathrm{M}}$ is compressive, may be used, namely

$$\left|\sigma_{xu}^{\mathrm{III}}\right| \geq \left|\frac{t\sigma_{xu}^{\mathrm{GB}} + t_{x\mathrm{eq}}\sigma_{xu}^{\mathrm{GO}}}{t + t_{x\mathrm{eq}}}\right| \tag{6.42}$$

where $\sigma_{xu}^{\mathrm{GB}}$ and $\sigma_{xu}^{\mathrm{GO}}$ are the ultimate strengths for the bare plate and the orthotropic plate under $\sigma_{x\mathrm{M}}$ plus p, respectively, the latter being calculated from the panel ultimate strength equation for Mode I, and the former being also calculated from the same equation but hypothetically removing stiffeners from the entire panel; $t_{x\mathrm{eq}}$ is as defined in Equation (6.35). In this chapter, this fictitious collapse pattern is denoted as 'Mode I (mean)' for reference purposes.

Combined Transverse Axial Load and Lateral Pressure

When the panel is subjected to combined $\sigma_{y\mathrm{M}}$ and p, the Mode III panel ultimate transverse axial strength, $\sigma_{yu}^{\mathrm{III}}$, can be calculated in a manner similar to that under combined $\sigma_{x\mathrm{M}}$ and p using a representative of the plate–stiffener combination under axial stress, $\sigma_{y\mathrm{M}}$, plus lateral line load, $q = pa$ (i.e., multiplied by the uniform lateral pressure, p, and the length, a, of plating between transverse stiffeners). Relevant details are as follows.

(1) Effective length of plating between transverses: The plating between stiffeners collapses locally if the plate transverse edges yield similar to that shown in Figure 4.12(c). The plate ultimate strength condition is in this case given by Equation (4.51a).

While the ultimate strength, σ_{yu}^{L}, of plating between transverse stiffeners under combined $\sigma_{y\mathrm{M}}$ and p can in principle then be obtained as the solution of Equation (4.51a) with regard to $\sigma_{y\mathrm{M}}$, in typical practice more approximate approaches are often used, as presented in Section 4.9.3 of Chapter 4. The effective length of the plating between the most highly compressed transverse stiffeners can again be evaluated, by taking into account the effects of combined loads ($\sigma_{y\mathrm{M}}$ plus p) as well as the post-weld initial imperfections as presented in the second subsection of Section 4.8.2 in Chapter 4.

(2) Collapse strength of a plate–stiffener combination: Under combined σ_{yM} and $q = pa$, the ultimate strength, σ_{yu}^{III}, of a plate–stiffener combination accounting for the influence of initial deflection can also be calculated using the modified Perry–Robertson approach, i.e., Equations (2.108) for the plate–stiffener combination in the y direction (when compression is taken as positive). Since compression is taken as negative, σ_{yu}^{III} will eventually take a negative value for σ_{yM} in compression. On the other hand, for σ_{yM} in tension, the ultimate strength will approximately equal the equivalent yield strength, i.e., $\sigma_{yxu}^{III} = \sigma_{Yy}$, where σ_{Yy} is defined in Equation (5.1). A lower limit of σ_{yu}^{III} similar to Equation (6.42) is again used (as long as σ_{yM} is compressive stress) as follows:

$$\left|\sigma_{yu}^{III}\right| \geq \left|\frac{t\sigma_{yu}^{GB} + t_{yeq}\sigma_{yu}^{GO}}{t + t_{yeq}}\right| \tag{6.43}$$

where σ_{yu}^{GB} and σ_{yu}^{GO} are the ultimate strengths for the bare plate and the orthotropic plate under σ_{yM} plus p, respectively, the latter being calculated from the panel ultimate strength equation for Mode I while the former is also calculated from the same equation but removing stiffeners from the entire panel; t_{yeq} is as defined in Equation (6.35). In this chapter, this fictitious collapse pattern is denoted as 'Mode I (mean)' for reference purposes.

Combined Edge Shear and Lateral Pressure

In Mode III, the ultimate lateral load, p_{uo}, and the ultimate shear strength, τ_{uo}, are defined as the same as those of Mode II. Also, the ultimate strength interaction relation between τ and p is given by Equation (4.56) of Chapter 4, but using the corresponding p_{uo} and τ_{uo}. Thus τ_u^{III} is obtained as the solution of Equation (4.56) with regard to τ_{av}, it also being taken that $\tau_u^{III} = \tau_u^{II}$.

Combined Biaxial Loads, Edge Shear and Lateral Pressure

An expression similar to Equation (6.40) or (6.41) is employed to describe the Mode III ultimate strength interaction relationship for a stiffened panel under combined σ_{xM}, σ_{yM}, τ and p. Using the Mode III ultimate strength components obtained so far, the applicable result is as follows:

$$\left(\frac{\sigma_{xM}}{\sigma_{xu}^{III}}\right)^{c_1} - \alpha\left(\frac{\sigma_{xM}}{\sigma_{xu}^{III}}\right)\left(\frac{\sigma_{yM}}{\sigma_{yu}^{III}}\right) + \left(\frac{\sigma_{yM}}{\sigma_{yu}^{III}}\right)^{c_2} + \left(\frac{\tau}{\tau_u^{III}}\right)^{c_3} = 1 \tag{6.44}$$

where $\alpha = 0$ when both σ_{xM} and σ_{yM} are compressive (negative), while $\alpha = 1$ when either σ_{xM} or σ_{yM}, or both, are tensile (positive). The coefficients c_1–c_3 are taken as those of Equation (6.40).

6.7.4 Collapse by Local Buckling of Stiffener Web (Mode IV)

If the height of the stiffener web increases in comparison to its thickness, the stiffener web is likely to deform and local buckling can in some cases occur. Once web buckling occurs, the buckled or collapsed plating may be left with essentially little stiffening, subsequent to overall grillage collapse. In Mode IV, therefore, it is considered that the stiffened panel reaches the ULS immediately after local buckling of the stiffener web at its most highly stressed location.

The Mode IV ultimate strength may be estimated from the local buckling strength of the stiffener web taking into account the influence of rotational restraints along the plate–stiffener and stiffener web–flange junctions. This is, however, likely to be pessimistic, a perhaps better approximation being to take the panel ultimate strength as the average of the applicable plate and stiffener web ultimate strengths.

It is idealized that the most highly stressed stiffeners are subjected to combined σ_{xM}, σ_{yM}, τ and p. The post-weld initial imperfections in the form of initial deflection and residual stress in the plating around those stiffeners are considered as parameters of influence.

Combined Longitudinal Axial Load and Lateral Pressure

The Mode IV panel ultimate longitudinal axial strength, σ_{xu}^{IV}, is considered when the panel is subjected to combined σ_{xM} and p. The ultimate strength and effective width of the most highly stressed plating between stiffeners in the x direction, the stress being denoted by σ_{xu}^{L}, can in this case be taken as the same values calculated for combined σ_{xM} and p following Mode III.

(1) Local buckling strength of longitudinal stiffener web: The local buckling strength of the stiffener web depends significantly on the torsional rigidities along the plate–stiffener or stiffener web–flange intersection, among other factors. A detailed description is given in Section 5.10 of Chapter 5, the elastic buckling strength for the stiffener web considering rotational restraints between plating and stiffeners or between stiffener web and flange being given by Equation (5.32) since compression is taken as negative.

A stocky stiffener web may buckle in the elastic–plastic regime. To account for the effect of plasticity, the Johnson–Ostenfeld formula, Equation (2.93), based on the yield stress of the stiffener (i.e., σ_{Ys}) is used, and the collapse strength, σ_{xu}^{W}, of the x-stiffener web is thus obtained. In using Equation (2.93), the stress sign needs to be converted to positive for compression as well. When σ_{xM} is tensile, $\sigma_{xu}^{W} = \sigma_{Ys}$ is used. When x-stiffeners do not exist, σ_{xu}^{W} must be zero as well.

(2) Panel ultimate strength: The panel ultimate longitudinal axial strength, σ_{xu}^{IV}, accounting for stiffener web buckling at the most highly stressed x-stiffener, can be obtained by the weighted average of the following two cases: (i) the ultimate strength of the plating between stiffeners, and (ii) the ultimate strength of the x-stiffener web. This approximation can be expressed as follows:

$$\sigma_{xu}^{IV} = \frac{\sigma_{xu}^{L} bt + \sigma_{xu}^{W} A_{sx}}{bt + A_{sx}} \tag{6.45}$$

where σ_{xu}^{L} = ultimate strength of plating between x-stiffeners under combined σ_{xM} and p.

Combined Transverse Axial Load and Lateral Pressure

The Mode IV panel ultimate transverse axial strength, σ_{yu}^{IV}, is now considered when the panel is subjected to combined σ_{yM} and p. The treatment is in principle quite similar to

that of the first subsection in Section 6.7.4, and so some of the applicable detail has been omitted below. In this case, the ultimate strength, σ_{yu}^{L}, and effective length, a_e, of the most highly stressed plating between stiffeners in the y direction can again be taken as the same value calculated for Mode III as previously described.

(1) Local buckling strength of transverse stiffener web: The buckling strength, σ_{yu}^{W}, of the y-stiffener web can also be obtained by a method similar to that used for the x-stiffener web. When the y-stiffener web is subjected to axial tensile loads, it may be assumed that σ_{yu}^{W} equals the yield stress of the stiffener (i.e., σ_{Ys}). Also, $\sigma_{yu}^{W} = 0$ when there are no stiffeners in the y direction.
(2) Panel ultimate strength: The ultimate transverse axial strength, σ_{yu}^{IV}, of the entire panel, because of the web buckling of the most highly stressed y-stiffener, is approximated by the average of the applicable plate and stiffener strengths similarly as before:

$$\sigma_{yu}^{IV} = \frac{\sigma_{yu}^{L} at + \sigma_{yu}^{W} A_{sy}}{at + A_{sy}} \tag{6.46}$$

where σ_{yu}^{L} = ultimate strength of plating between y-stiffeners under combined σ_{yM} and p.

Combined Edge Shear and Lateral Pressure

The panel ultimate shear strength considering the lateral pressure load effects for Mode IV is given by that for Modes II or III, taking $\tau_u^{IV} = \tau_u^{II} = \tau_u^{III}$.

Combined Biaxial Loads, Edge Shear and Lateral Pressure

An expression similar to Equation (6.40) or (6.41) or (6.44) is employed for the Mode IV ultimate strength interaction relationship for a stiffened panel subjected to combined $\sigma_{xM}, \sigma_{yM}, \tau$ and p. Using the Mode IV ultimate strength components obtained so far, the applicable expression is as follows:

$$\left(\frac{\sigma_{xM}}{\sigma_{xu}^{IV}}\right)^{c_1} - \alpha\left(\frac{\sigma_{xM}}{\sigma_{xu}^{IV}}\right)\left(\frac{\sigma_{yM}}{\sigma_{yu}^{IV}}\right) + \left(\frac{\sigma_{yM}}{\sigma_{yu}^{IV}}\right)^{c_2} + \left(\frac{\tau_{av}}{\tau_u^{IV}}\right)^{c_3} = 1 \tag{6.47}$$

where $\alpha = 0$ when both σ_{xM} and σ_{yM} are compressive (negative), while $\alpha = 1$ when either σ_{xM} or σ_{yM}, or both, are tensile (positive). The coefficients c_1–c_3 are taken as those of Equation (6.40).

6.7.5 Collapse by Tripping of Stiffener (Mode V)

The lateral–torsional buckling (also called tripping) of stiffeners is a phenomenon in which the failure of a stiffened panel occurs subsequent to the stiffener twisting sideways about the edge of the stiffener web attached to the plating. When the torsional rigidity of the stiffener is small or the stiffener flange is weak, this phenomenon is more likely to take place.

Like the stiffener web buckling previously described, tripping can be a relatively sudden phenomenon resulting in subsequent unloading of the stiffened panel. Once tripping occurs, the buckled or collapsed plating is left with little stiffening and thus overall collapse may follow. In Mode V, the stiffened panel is considered to collapse if tripping occurs.

Local buckling of the stiffener web is treated in Mode IV, and thus for the purposes of Mode V, we consider a type of tripping wherein the cross-section of the stiffener web does not deform locally, consistent with a similar assumption used in ordinary beam–column theory. It therefore follows that the tripping strength of the flat-bar type of stiffener equals the local buckling of the stiffener web, and such a case is to be treated as part of Mode IV and not Mode V.

Similar to Mode IV, it is idealized that the most highly stressed stiffener being considered is subjected to combined σ_{xM}, σ_{yM}, τ and p. The post-weld initial imperfections in the form of initial deflection and residual stress in the plating are included as parameters of influence.

The ultimate strength of the stiffened panel is then approximated as a weighed average of the ultimate strengths of the plating and the tripping strength of the stiffener. The intention behind the averaging proposed is to avoid an overly pessimistic estimate of the stiffened panel ultimate strength.

Combined Longitudinal Axial Load and Lateral Pressure

The panel ultimate longitudinal axial strength, σ_{xu}^{V}, based on Mode V, is presented with the panel subjected to combined σ_{xM} and p. The ultimate strength and effective width of the most highly stressed plating between stiffeners in the x direction can in this case be taken as the same values calculated for Mode III as previously described.

(1) Tripping strength of longitudinal stiffener: Following an elaborate description made in Section 5.12 of Chapter 5, the elastic tripping strength, σ_{xE}^{T}, of the longitudinal stiffener can be calculated by Equation (5.40) for unsymmetric angle stiffeners and Equation (5.41) for symmetric Tee-stiffeners. The effect of plasticity is then incorporated by using the Johnson–Ostenfeld formula, Equation (2.93), resulting in the inelastic tripping strength, σ_{xu}^{T}. In the usage of Equation (2.93), the stress sign needs to be converted to positive for compression. When σ_{xM} is tensile, $\sigma_{xu}^{T} = \sigma_{Ys}$ may be used. Also, $\sigma_{xu}^{T} = 0$ is used when the panel does not have stiffeners in the x direction.
(2) Panel ultimate strength: Applying an argument similar to that used for Mode IV, the ultimate longitudinal axial strength, σ_{xu}^{V}, of the stiffened panel subsequent to tripping is approximated by the weighted average of the local collapse strength of plating and the stiffener tripping strength in the x direction as follows:

$$\sigma_{xu}^{V} = \frac{\sigma_{xu}^{L} bt + \sigma_{xu}^{T} A_{sx}}{bt + A_{sx}} \tag{6.48}$$

where σ_{xu}^{L} = ultimate strength of plating between x-stiffeners under combined σ_{xM} and p.

Combined Transverse Axial Load and Lateral Pressure

When the panel is subjected to combined σ_{yM} and p, the panel ultimate transverse axial strength, σ_{yu}^{V}, based on Mode V, can be obtained in a way similar to that under σ_{xM} and p. In this case, the ultimate strength, σ_{yu}^{L}, and effective length, a_e, of the most highly stressed plating between stiffeners in the y direction can be taken as the same as the value calculated for Mode III as previously described.

(1) Tripping strength of transverse stiffener: Using a method similar to that for the x-stiffener, the tripping strength, σ_{yu}^{T}, of the y-stiffener can be calculated. When σ_{yM} is tensile, $\sigma_{yu}^{T} = \sigma_{Ys}$ is used. Also, $\sigma_{yu}^{T} = 0$ is used when the panel does not have stiffeners in the y direction.
(2) Panel ultimate strength: The ultimate transverse axial strength, σ_{yu}^{V}, of the panel, because of tripping, is approximated by the weighted average of the local collapse strength of plating and the stiffener tripping strength in the y direction as follows:

$$\sigma_{yu}^{V} = \frac{\sigma_{yu}^{L} at + \sigma_{yu}^{T} A_{sy}}{at + A_{sy}} \tag{6.49}$$

where σ_{yu}^{L} = ultimate strength of plating between y-stiffeners under combined σ_{yM} and p.

Combined Edge Shear and Lateral Pressure

The panel ultimate shear strength, considering the lateral pressure load effects for Mode V, is given by that for Mode II or III or IV, taking $\tau_u^{V} = \tau_u^{II} = \tau_u^{III} = \tau_u^{IV}$.

Combined Biaxial Loads, Edge Shear and Lateral Pressure

An expression similar to Equation (6.40) or (6.41) or (6.44) or (6.47) is employed for the Mode V ultimate strength interaction relationship for a stiffened panel under combined σ_{xM}, σ_{yM}, τ and p. Using the Mode V ultimate strength components obtained so far, the applicable expression is as follows:

$$\left(\frac{\sigma_{xM}}{\sigma_{xu}^{V}}\right)^{c_1} - \alpha\left(\frac{\sigma_{xM}}{\sigma_{xu}^{V}}\right)\left(\frac{\sigma_{yM}}{\sigma_{yu}^{V}}\right) + \left(\frac{\sigma_{yM}}{\sigma_{yu}^{V}}\right)^{c_2} + \left(\frac{\tau}{\tau_u^{V}}\right)^{c_3} = 1 \tag{6.50}$$

where $\alpha = 0$ when both σ_{xM} and σ_{yM} are compressive (negative), while $\alpha = 1$ when either σ_{xM} or σ_{yM}, or both, are tensile (positive). The coefficients c_1–c_3 are taken as those of Equation (6.40).

6.7.6 Gross Yielding (Mode VI)

In Mode VI, the panel reaches the ultimate strength by gross yielding of the cross-section without either local or overall (grillage) buckling. The applicable ultimate strength interaction relationship for a stiffened panel under combined loads is in this case similar in

form to the Mises–Hencky yield condition, as follows:

$$\left(\frac{\sigma_{xM}}{\sigma_{xu}^{VI}}\right)^{c_1} - \left(\frac{\sigma_{xM}}{\sigma_{xu}^{VI}}\right)\left(\frac{\sigma_{yM}}{\sigma_{yu}^{VI}}\right) + \left(\frac{\sigma_{yM}}{\sigma_{yu}^{VI}}\right)^{c_2} + \left(\frac{\tau}{\tau_u^{VI}}\right)^{c_3} = 1 \tag{6.51}$$

where $\sigma_{xu}^{VI} = \pm\sigma_{Yx}$(+ for σ_{xM} in tension, − for σ_{xM} in compression), $\sigma_{yu}^{VI} = \pm\sigma_{Yy}$ (+ for σ_{yM} in tension, − for σ_{yM} in compression), $\tau_u^{VI} = \sigma_{Yeq}/\sqrt{3}$, σ_{Yeq}, σ_{Yx}, σ_{Yy} are as defined in Equation (5.1). The coefficients c_1–c_3 are taken as those of Equation (6.40).

6.8 Post-ultimate Behavior

As will be presented in Chapter 13, the post-ultimate strength of a large plated structure composed of a number of stiffened panel elements can be affected by the post-ultimate behavior of any individual component element. In the post-ultimate regime under predominantly axial tensile loads, the internal stress may not change at the level of gross yielding. However, the internal stress typically decreases as long as predominantly axial compressive displacements continually increase.

While two groups of stiffened panel buckling modes, namely overall panel buckling and local plate buckling, may be relevant until the ultimate strength is reached, the post-ultimate behavior of a stiffened panel may also be approximately described by the two groups to the extent it may be of interest. The two groups of panel buckling modes may be distinguished from Equations (5.5) in Chapter 5.

For a stiffened panel following the overall collapse mode, the post-ultimate behavior may be approximately represented by that of an orthotropic plate. On the other hand, the post-ultimate behavior of a stiffened panel following the local plate collapse mode may be expressed by that of plating alone since the contribution of stiffeners is very small in this regime.

6.8.1 Average Stress–Strain Relationship

Overall Grillage Collapse Mode

A similar approach to isotropic plating as presented in Section 4.10 of Chapter 4 may be applied. The effect of initial imperfections and Poisson's ratios may then be neglected in the post-ultimate regime of the stiffened panel. The average stress–strain relationships of the orthotropic plate in the post-ultimate strength regime may thus approximately be determined by

$$\sigma_{xav} = \frac{1}{2}\left(1 + \frac{\sigma_{xEO}}{E_x \varepsilon_{xav}}\right)\sigma_{x\,max}^{u} \tag{6.52a}$$

$$\sigma_{yav} = \frac{1}{2}\left(1 + \frac{\sigma_{yEO}}{E_y \varepsilon_{yav}}\right)\sigma_{y\,max}^{u} \tag{6.52b}$$

where $\sigma_{x\,max}^{u}$ and $\sigma_{y\,max}^{u}$ are the maximum membrane stresses of the panel in the x and y directions immediately after the ultimate strength is reached. σ_{xEO} and σ_{yEO} are defined

in Equation (5.6) for longitudinal axial compression or Equation (5.9) for transverse axial compression, respectively.

The incremental form of Equations (6.52) can be given by

$$\Delta\sigma_{xav} = -\frac{\sigma^{u}_{x\,max}}{2}\frac{\sigma_{xEO}}{E_x\varepsilon^2_{xav}}\Delta\varepsilon_{xav} \tag{6.53a}$$

$$\Delta\sigma_{yav} = -\frac{\sigma^{u}_{y\,max}}{2}\frac{\sigma_{yEO}}{E_y\varepsilon^2_{yav}}\Delta\varepsilon_{yav} \tag{6.53b}$$

On the other hand, when the tangent shear modulus of the panel in the post-ultimate strength regime is denoted by G^*_{xye}, which may sometimes be taken as $G^*_{xye} = 0$, the edge shear stress–strain relationship in the incremental form may be given by

$$\Delta\tau_{av} = G^*_{xye}\Delta\gamma_{av} \tag{6.53c}$$

Equations (6.53) can be rewritten in matrix form as follows:

$$\begin{Bmatrix}\Delta\sigma_{xav}\\ \Delta\sigma_{yav}\\ \Delta\tau_{av}\end{Bmatrix} = [D_{sp}]^{U}_{O}\begin{Bmatrix}\Delta\varepsilon_{xav}\\ \Delta\varepsilon_{yav}\\ \Delta\gamma_{av}\end{Bmatrix} \tag{6.54}$$

where

$$[D_{sp}]^{U}_{O} = \begin{bmatrix}A_1 & 0 & 0\\ 0 & A_2 & 0\\ 0 & 0 & A_3\end{bmatrix}$$

is the post-ultimate stress–strain matrix of a stiffened panel following overall grillage collapse mode, with

$$A_1 = -\frac{\sigma^{u}_{x\,max}}{2}\frac{\sigma_{xEO}}{E_x\varepsilon^2_{xav}},$$

$$A_2 = -\frac{\sigma^{u}_{y\,max}}{2}\frac{\sigma_{yEO}}{E_y\varepsilon^2_{yav}} \quad \text{and} \quad A_3 = G^*_{xye}$$

Local Plate Collapse Mode

The post-ultimate behavior of a stiffened panel following the local plate collapse mode is represented by that of plating, as previously noted in Section 4.10 of Chapter 4. The stress–strain relationship is thus given by

$$\begin{Bmatrix}\Delta\sigma_{xav}\\ \Delta\sigma_{yav}\\ \Delta\tau_{av}\end{Bmatrix} = [D_{sp}]^{U}_{L}\begin{Bmatrix}\Delta\varepsilon_{xav}\\ \Delta\varepsilon_{yav}\\ \Delta\gamma_{av}\end{Bmatrix} \tag{6.55}$$

where $[D_{sp}]^{U}_{L} = [D_p]^{U}$ is as defined in Equation (4.65) of Chapter 4.

Table 6.1 summarizes the formulations or procedures for the analysis of the progressive collapse behavior of a stiffened panel. As will be presented in Chapter 13, these formulations are incorporated into the ALPS/ISUM computer program.

Table 6.1 Summary of the formulations for the panel progressive collapse behavior.

Status	Formulation
Pre-collapse regime	Equation (6.31) for overall (grillage) buckling mode Equation (6.34) for local plate buckling mode
Ultimate strength	Section 6.7
Post-ultimate regime	Equation (6.54) after overall (grillage) collapse Equation (6.55) after local plate collapse

6.8.2 Verification Examples

Figure 6.5 shows sample stress–strain curves of a stiffened panel in a continuous plate structure as considered in Section 2.11.4 of Chapter 2. In addition to the theory presented in this chapter, seven types of computations as indicated in Section 2.11.4 are considered. The curves cover the entire history before and after the ULS is reached. In Figures 6.5(a) and (b), the theoretical formulations of the stiffened panel model (SPM) presented in this chapter (denoted by number 8) are compared to more refined finite element results as well as the theory of the plate–stiffener combination (PSC) presented in Chapter 2, i.e., denoted by number 7. The panel collapse modes were predicted by the present theory as Modes I-1

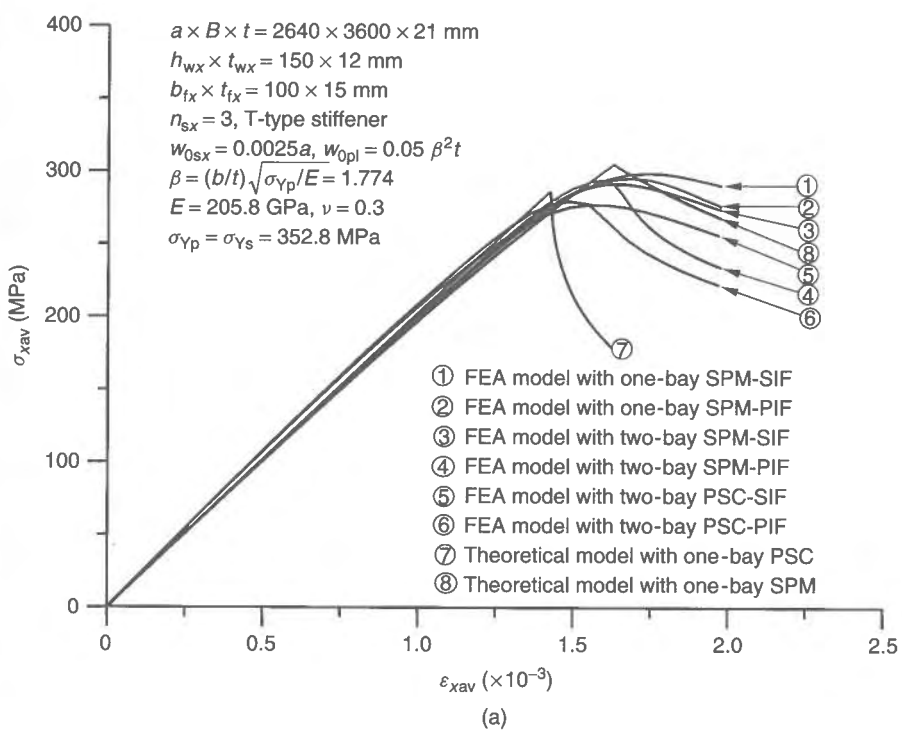

Figure 6.5 A comparison of the average stress–strain curves for a stiffened panel with (a) $h_{wx} = 150$ mm and (b) $h_{wx} = 210$ mm, refer to Section 2.11.4 in Chapter 2; (c) average stress–strain curves for a stiffened panel obtained by the theoretical formulations for the stiffened panel element

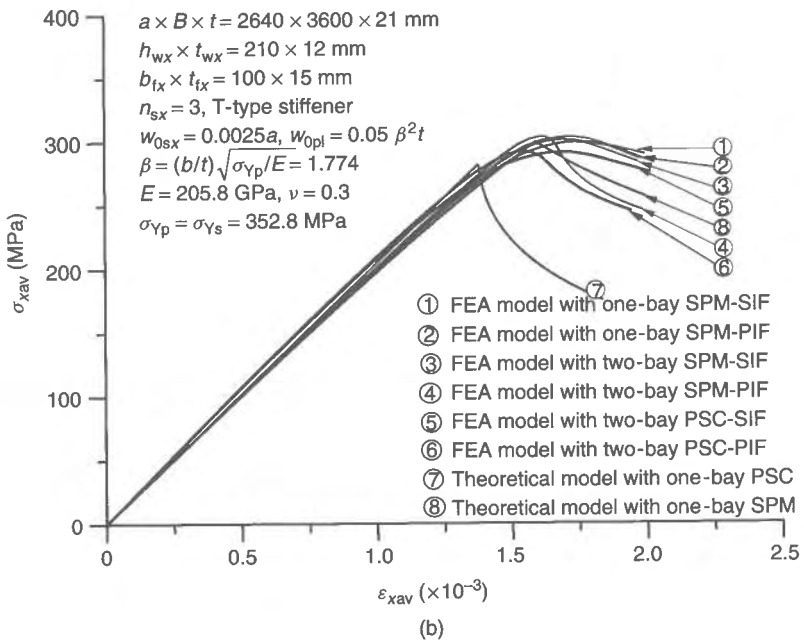

(b)

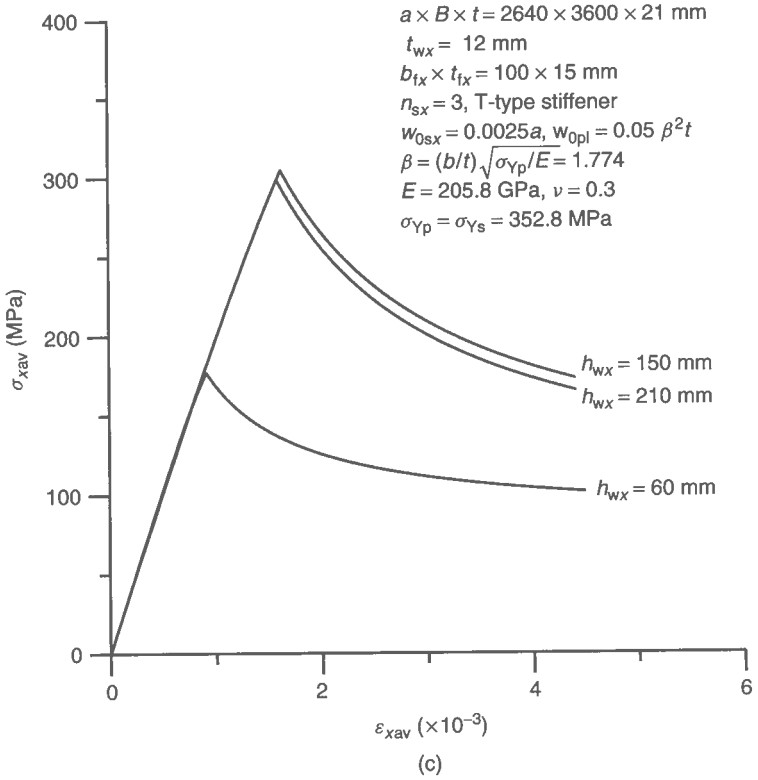

(c)

Figure 6.5 (*continued*)

(overall collapse), III (beam–column-type collapse) and V (tripping) for $h_w = 60$ mm, 150 mm and 210 mm, respectively, and they correspond to those by FEA. Also of interest from Figure 6.5(c), the panel ultimate strength for $h_{wx} = 210$ mm is smaller than that for $h_{wx} = 150$ mm. This is because the former panel collapses by tripping of the stiffener, while the latter reaches the ultimate strength by beam–column-type collapse and the former panel provides a lower load-carrying capacity as shown later in Figure 6.6(c). The progressive collapse behavior predicted by the present theory correlates well with the FEAs.

6.9 Computer Software ALPS/ULSAP

6.9.1 Outline of the Computer Software

The ultimate strength formulations for stiffened panels as presented in this chapter are automated within the computer program ALPS/ULSAP, which stands for nonlinear analysis of large plated structures/ultimate strength analysis of panels. The ALPS/ULSAP program together with the user's manual can be downloaded from the web site given in the appendices to this book.

6.9.2 Application Examples

The ALPS/ULSAP method is now applied to the ultimate strength predictions of a continuous stiffened plate structure. The principal dimensions and material properties of the structure are the same as considered in Section 2.11.4 of Chapter 2, while the stiffener type and web height are varied in the present examples. The yield stress of stiffeners is taken as equal to that of the plating, i.e., $\sigma_{Ys} = \sigma_{Yp}$. The panel has three stiffeners in the longitudinal direction. The ALPS/ULSAP predictions are then compared to the nonlinear FEAs obtained using the two-bay stiffened panel models as described in Section 2.11.4. In the analyses, it is considered that the welding residual stresses do not exist, while the stiffeners have an 'average' level of column-type initial deflection, i.e., $w_{0sx} = 0.0025a = 6.6$ mm, and the plating between stiffeners has a 'slight' level of (buckling mode) initial deflection, i.e., $w_{0pl} = 0.05\beta^2 t = 3.3$ mm.

Figure 6.6 shows the variation of the ultimate strength of the longitudinally stiffened panel under axial compression, as a function of the ratio of stiffener web height to web thickness. In Figure 6.6, Mode I ultimate strength predictions were made so that the stiffened panel was considered to collapse if the panel edges yielded. Figures 6.6(a) to 6.6(c) represent the variation in the ultimate strengths as obtained for each collapse mode of the panel with flat-bar, angle or Tee-type stiffeners, respectively. The minimum values are in effect the ultimate strength as would be predicted by ALPS/ULSAP. The Perry–Robertson formula predictions by yielding at the tip of the stiffener (without either local buckling of the stiffener web or tripping of the stiffener) are also shown for comparison. The more refined finite element results obtained using two-bay stiffened panel models, see Section 2.11.4 in Chapter 2, are compared.

It is evident from Figure 6.6 that as the height of the stiffener web increases, the panel ultimate strength increases. When the stiffeners are relatively small, they buckle together with the plating showing Mode I failure. When the stiffeners become stiff, the plating between them buckles while they remain straight, and the ultimate strength is

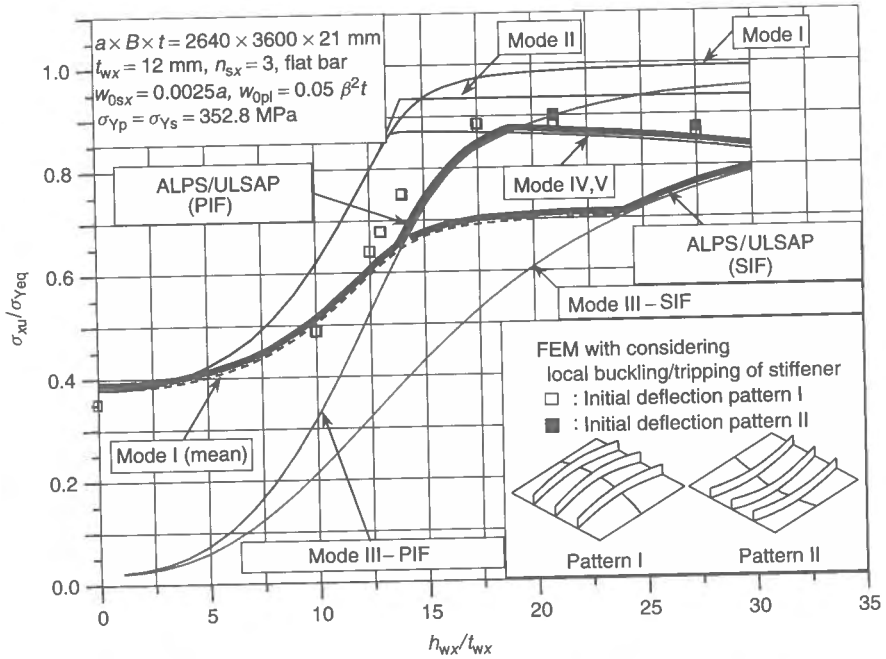

Figure 6.6 Ultimate strengths of longitudinally stiffened panels with (a) three flat bars; (b) three angle bars and (c) three Tee-stiffeners under uniaxial compression, varying the ratio of stiffener web height to web thickness (PIF = plate-induced failure, SIF = stiffener-induced failure)

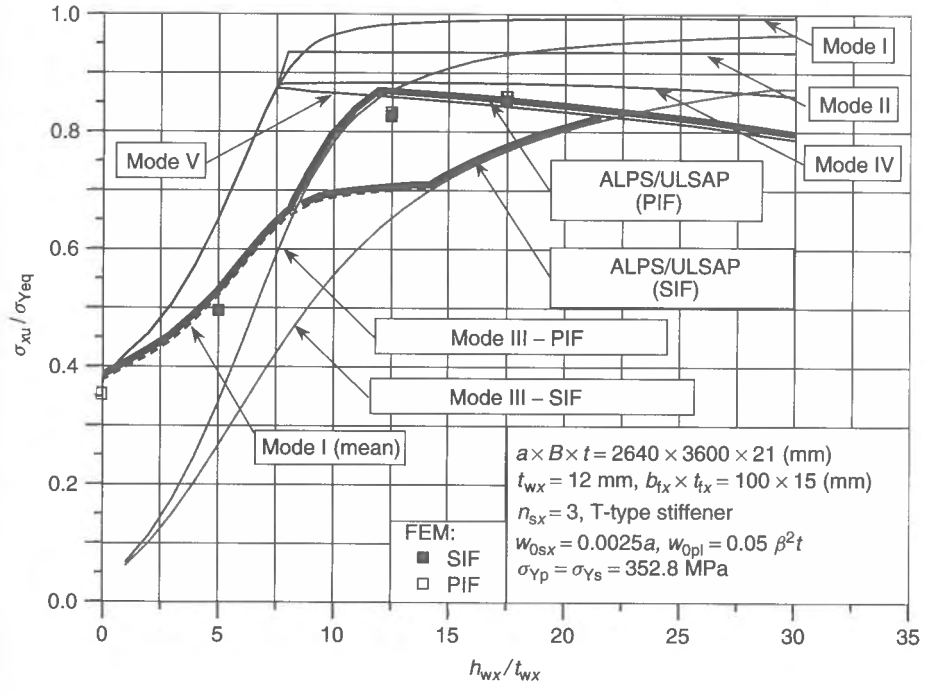

Figure 6.6 (*continued*)

eventually reached by the beam–column-type collapse involving Mode III. If the height of the stiffener web exceeds a critical value, however, the ultimate strength tends to flatten out. This is because the stiffener web buckles locally or twists sideways when the height of the stiffener web is large.

It is also seen that the Perry–Robertson formula predictions by the condition of both PIF and SIF are too pessimistic when the stiffeners are small, since they are even smaller than the bare panel excluding stiffeners. This pessimism aspect needs further investigation, and the stiffener-induced failure mode predictions by the Perry–Robertson formula are currently excluded from the ALPS/ULSAP as previously noted. The Mode III panel ultimate strength is then predicted based on the PIF condition, but with the lower limits of Equation (6.42) in this specific case.

Mode I ultimate strength prediction may sometimes be made from Equation (6.35) based on the initial yield at the outer surface of the panel, while Equation (6.36) is based on the initial yield at the panel boundaries. Figure 6.7 compares Equation (6.35) with Equation (6.36) for the ultimate strength predictions of the panel with three Tee-stiffeners as noted above. It is observed that Equation (6.35) may be more relevant for panels with very small stiffeners since the ultimate strength predicted by Equation (6.35) is on the conservative side.

The performance of the ALPS/ULSAP method as applied to steel grillage is now considered using test data and related numerical results pertaining to an extensive series of mechanical tests performed and reported by Smith (1976). The test grillages were stiffened with flat-bar, angle or T-type stiffeners in both longitudinal and transverse directions. Such

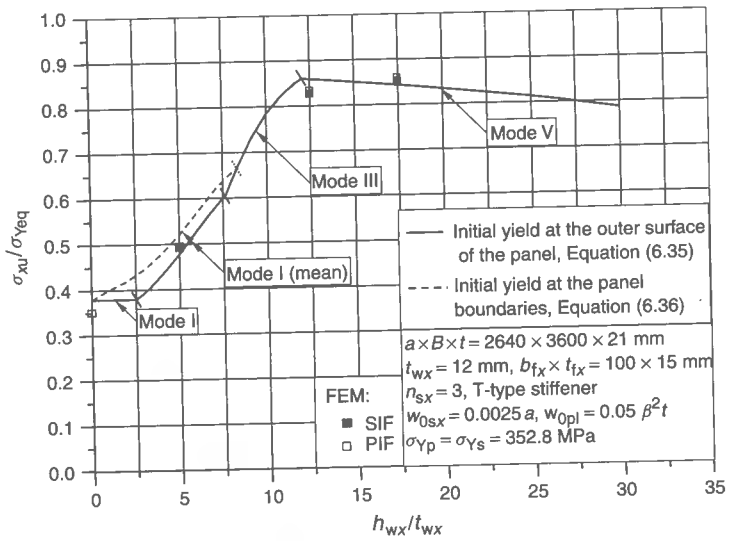

Figure 6.7 A comparison of Equation (6.35) with Equation (6.36) for the ultimate strength predictions of the panel with three Tee-stiffeners

cross-stiffened panels are particularly relevant to the design of naval vessels, small craft and high-speed vessels. In this section, the Smith test data are recorded for the sake of completeness. In some cases what is given here regarding the Smith data are the interpretations of material presented by Smith from more than one source. The interested reader is thus cautioned to rely on Smith's original publications as the definitive ones.

Smith (1976) carried out a series of collapse tests using a total of 11 full-scale welded steel grillages representing typical warship deck structures under axial compression, or bottom structures under combined axial compression and lateral pressure. The test structures include four pairs of nominally identical grillages (numbers 1a, 1b, 2a, 2b, 3a, 3b, 4a, 4b) representing a ship bottom configuration, together with two grillages (numbers 5, 7) representing frigate strength decks and one grillage (number 6) corresponding to a light superstructure deck. The typical grillage model that Smith tested is as that shown in Figure 6.8.

Smith *et al.* (1992) later computed the ultimate strengths of the Smith test grillages using the nonlinear finite element method as well, where they used the two-bay beam–column model as representative of the grillages. The overall dimensions of each grillage were $L = 6096$ mm long by $B = 3048$ mm wide, excluding the panel ends which are bolted to the test frames along the edges. Except for numbers 4a and 4b, which have both large girders and small stiffeners in the longitudinal direction, all test grillages have identical T-type longitudinal stiffeners and identical T-type transverse frames.

Table 6.2 indicates the geometric properties of longitudinals and transverses and the material yield stresses for the plating and stiffeners, where numbers 4a and 4b are represented by the longitudinally stiffened panel between two adjacent longitudinal girders and two adjacent transverse frames. Table 6.3 presents the important ultimate-strength-related geometric characteristics for each grillage. The initial deflections of plating, longitudinals or transverses were measured in these tests. There was reportedly a high degree of

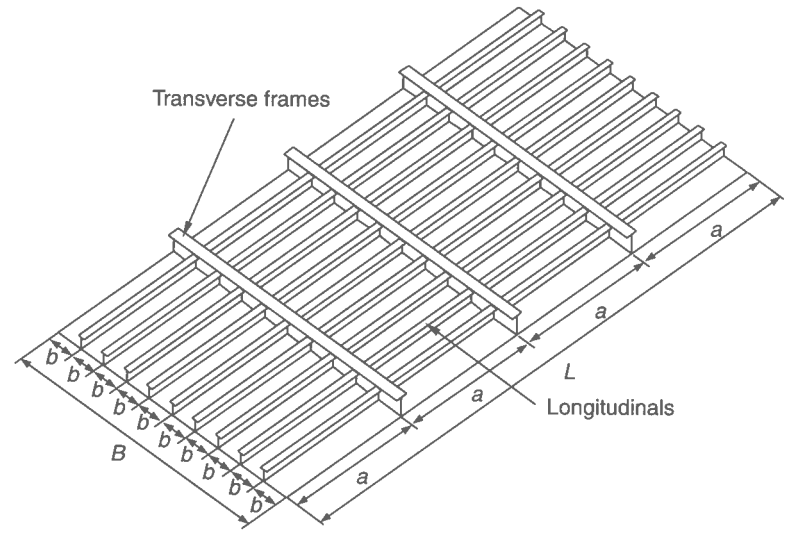

Figure 6.8 A schematic of the Smith test grillage

variability associated with the plate initial deflection measurements, with the COVs of w_{0pl} and w_{0sx} in the range of 0.22–0.63 and 0.29–1.04, respectively. Specifically, it is reportedly observed that plating and stiffener imperfections for model number 3b were abnormally large, with an 'unfavorable' relative stiffener distortion as well. Also, number 6, representing a light superstructure deck, had a 'serious level' of initial imperfections which would be untypical in a real structure. The welding-induced residual stresses of plating were also measured for selected grillages. The corresponding COV of the compressive residual stress, σ_{rcx}, in the longitudinal direction was in the range of 0.12–0.52. The residual stresses of longitudinals or transverses were neither measured nor reported.

Table 6.4 summarizes the initial imperfections of plating and stiffeners for each grillage, on the basis of the measurements and insights provided in Smith (1976) and Smith *et al.* (1992). Based on the measured initial deflection patterns of plating, Table 6.4 represents the buckling mode initial deflection component of each grillage also. It is noted that in the FEA of Smith *et al.* (1992), two types of computations were tried with different levels of initial deflections, namely FEA-1 with average initial imperfections and FEA-2 with actual initial imperfections.

Table 6.5 compares the present design procedure predictions from ALPS/ULSAP with the Smith mechanical test results. In the ALPS/ULSAP ultimate strength calculations of individual test grillages, an entire grillage was considered, i.e., including transverse frames as well as longitudinals, except for test numbers 4a and 4b. Also, Mode I predictions were made based on the yield of the panel edges.

Figure 6.9 shows the correlation of the theoretical solutions and experimental results. The collapse modes predicted by ALPS/ULSAP and the experiments are also indicated in Table 6.5. Collapse of most test models is predicted to involve the lateral–torsional buckling of longitudinals (Mode V) as was observed in the experiments. ALPS/ULSAP predicts the panel collapse modes reasonably well. It also compares fairly well with the more refined data of the ultimate strengths in most cases.

Table 6.2 Mean values of geometric properties and material yield stresses for the Smith test grillages.

Grillage no.	L (mm)	B (mm)	t (mm)	n_{sx}	h_{wx} (mm)	t_{wx} (mm)	b_{fx} (mm)	t_{fx} (mm)	n_{sy}	h_{wy} (mm)	t_{wy} (mm)	b_{fy} (mm)	t_{fy} (mm)	σ_{Yp} (MPa)	σ_{Ys} (MPa)	σ_{Yeq} (MPa)
1a	6096	3048.0	8.00	4	153.67	7.21	78.99	14.22	4	257.56	9.37	125.48	18.29	249.1	253.7	250.4
1b	6096	3048.0	7.87	4	152.40	7.11	76.20	14.22	4	254.00	9.14	127.00	18.29	252.2	252.4	252.3
2a	6096	3048.0	7.72	9	115.57	5.44	45.97	9.53	3	204.98	8.31	102.62	16.26	261.3	268.9	263.1
2b	6096	3048.0	7.37	9	114.30	5.38	44.70	9.53	3	203.71	8.33	102.62	16.26	259.7	274.9	263.3
3a	6096	3048.0	6.38	9	77.72	4.52	25.91	6.35	3	156.21	6.81	78.99	14.22	250.6	227.9	246.8
3b	6096	3048.0	6.40	9	77.22	4.65	27.94	6.35	3	153.92	6.88	79.25	14.22	252.2	223.3	247.3
4a	1219.2	1016.0	6.43	3	76.71	4.85	27.69	6.35	–	–	–	–	–	259.7	223.9	252.5
4b	1219.2	1016.0	6.40	3	76.96	4.55	26.16	6.35	–	–	–	–	–	264.3	227.9	257.3
5	6096	3048.0	6.43	4	116.08	5.33	46.23	9.53	3	154.18	6.76	77.22	14.22	247.6	230.9	244.9
6	6096	3048.0	6.32	4	76.20	4.55	27.43	6.35	4	114.55	5.36	46.23	9.53	256.7	241.5	255.2
7	6096	3048.0	6.30	4	115.06	5.16	45.21	9.53	3	153.92	6.65	78.74	14.22	290.1	305.3	303.3

Notes: Grillage Numbers 4a and 4b represent longitudinally stiffened panels between two adjacent longitudinal girders and two adjacent transverse frames, $\nu = 0.3$, $E = 205.8$ GPa.

Table 6.3 Other geometric characteristics of the Smith test grillages.

Grillage no.	$\frac{b}{t}$	β	$\frac{a}{r}$	λ	$\frac{A_{sx}}{bt}$
1a	76.2	2.67	21	0.24	0.42
1b	77.4	2.72	21	0.23	0.43
2a	39.5	1.42	36.5	0.42	0.40
2b	41.4	1.48	36	0.42	0.42
3a	47.8	1.68	66	0.70	0.24
3b	47.6	1.68	66	0.70	0.24
4a	39.5	1.41	50	0.54	0.28
4b	39.7	1.43	50	0.53	0.28
5	94.9	3.31	42	0.45	0.24
6	96.4	3.42	68	0.75	0.12
7	96.8	3.65	42	0.52	0.24

Note: $\gamma, \beta, \lambda =$ as defined in Table 2.1 of Chapter 2.

Table 6.4 Initial imperfections of plating, longitudinals and transverses for the Smith test grillages.

Grillage no.	$\frac{w_{0pl}}{b}$	$\frac{w_{0sx}}{a}$	$\frac{w_{0sy}}{w_{0sx}}$	$\frac{\sigma_{rcx}}{\sigma_{Yp}}$	$\frac{\sigma_{rcy}}{\sigma_{rcx}}$	$\frac{\sigma_{rsx}}{\sigma_{Ys}}$	$\frac{\sigma_{rsy}}{\sigma_{rsx}}$	$\frac{A_{0m}}{w_{0pl}}$
1a	0.0060	0.0007	0.7	–	–	–	–	0.1
1b	0.0077	0.0011	–	–	–	–	–	0.1
2a	0.0044	0.0025	–	0.48	0.10	–	–	0.1
2b	0.0060	0.0010	–	0.33	0.10	–	–	1.0
3a	0.0093	0.0028	0.2	0.38	0.10	–	–	0.7
3b	0.0150	0.0019	0.8	0.43	0.10	–	–	1.0
4a	0.0081	0.0023	0.5	0.38	0.10	–	–	0.8
4b	0.0063	0.0008	0.5	0.41	0.10	–	–	0.7
5	0.0100	0.0008	−0.4	0.16	0.10	–	–	0.1
6	0.0125	0.0020	0.4	0.31	0.10	–	–	1.0
7	0.0094	0.0007	–	0.08	0.10	–	–	0.1

Sources: Smith (1976) and Table 3 of Smith *et al.* (1992).
Note: A_{0m} = buckling mode initial deflection.

Table 6.5(a) Comparison of the Smith FEA with the experiment for ultimate strength of grillages.

Grillage no.	p (MPa)	$\left(\frac{\sigma_{xu}}{\sigma_{Yeq}}\right)_{Exp}$	$\left(\frac{\sigma_{xu}}{\sigma_{Yeq}}\right)_{FEA-1}$	$\left(\frac{\sigma_{xu}}{\sigma_{Yeq}}\right)_{FEA-2}$	$\frac{(\sigma_{xu})_{FEA-1}}{(\sigma_{xu})_{Exp}}$	$\frac{(\sigma_{xu})_{FEA-2}}{(\sigma_{xu})_{Exp}}$
1a	0	0.76	0.65	0.69	0.855	0.908
1b	0.103(15 psi)	0.73	0.57	0.57	0.781	0.781
2a	0.048(7 psi)	0.91	0.81	0.81	0.890	0.890
2b	0	0.83	0.82	0.82	0.988	0.988
3a	0.021(3 psi)	0.69	0.69	0.63	1.000	0.913
3b	0	0.61	0.71	0.60	1.164	0.984
4a	0	0.82	0.80	0.75	0.976	0.915
4b	0.055(8 psi)	0.83	0.73	0.76	0.880	0.916
5	0	0.72	0.51	0.55	0.708	0.764
6	0	0.49	–	–	–	–
7	0	0.65	0.49	0.53	0.754	0.815
				Mean	0.900	0.887
				COV	0.152	0.087

Notes: FEA − 1 = with average imperfections, FEA − 2 = with actual imperfections.

Table 6.5(b) Comparison of ALPS/ULSAP with the Smith experiments and FEA for ultimate strength of grillages.

Grillage no.	p (MPa)	$\left(\frac{\sigma_{xu}}{\sigma_{Yeq}}\right)_{ULSAP}$	$\frac{(\sigma_{xu})_{ULSAP}}{(\sigma_{xu})_{Exp}}$	$\frac{(\sigma_{xu})_{ULSAP}}{(\sigma_{xu})_{FEA-1}}$	$\frac{(\sigma_{xu})_{ULSAP}}{(\sigma_{xu})_{FEA-2}}$	Collapse modes: Exp	Collapse modes: ULSAP
1a	0	0.76	1.000	1.169	1.101	V	V
1b	0.103	0.62	0.849	1.088	1.088	V	V
2a		0.79	0.868	0.975	0.975	III + V	I
	0.048	(0.86)	(0.945)	(1.062)	(1.062)		III
		(0.90)	(0.989)	(1.111)	(1.111)		V
2b	0	0.79	0.952	0.963	0.963	III + V	V
3a	0.021	0.69	1.000	1.000	1.095	III + V	V
3b	0	0.58	0.951	0.817	0.967	III + V	V
4a	0	0.80	0.976	1.000	1.067	III + V	V
4b	0.055	0.81	0.976	1.110	1.066	III + V	V
5	0	0.52	0.722	1.020	0.945	III + V	V
6	0	0.37	0.755	–	–	I + V	V
7	0	0.52	0.800	1.061	0.981	III + V	V
		Mean	0.895	1.020	1.025		
		COV	0.113	0.095	0.062		

Notes: I + V or III + V indicates that the grillage collapsed in Mode I or III together with Mode V. The values in brackets are given for comparisons when the ALPS/ULSAP method predicted a collapse mode different from the experiment.

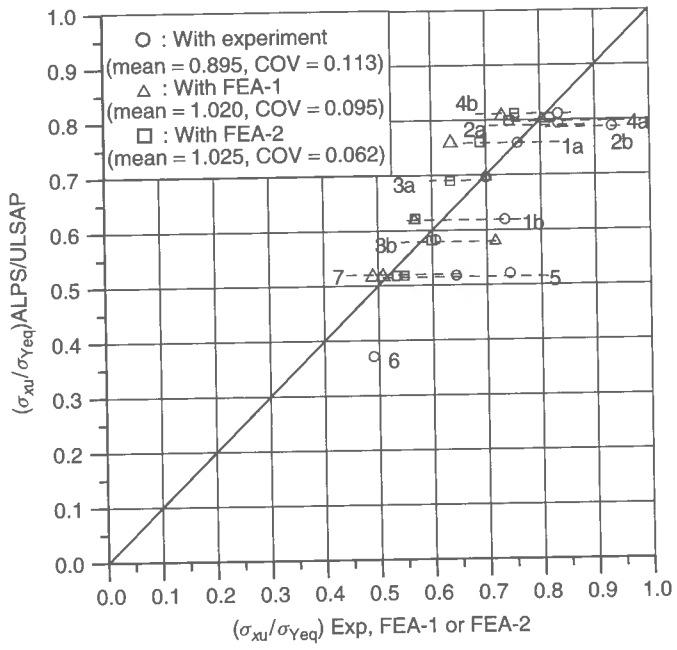

Figure 6.9 Correlation of the ALPS/ULSAP method with the experimental data and finite element solutions for the Smith test grillages

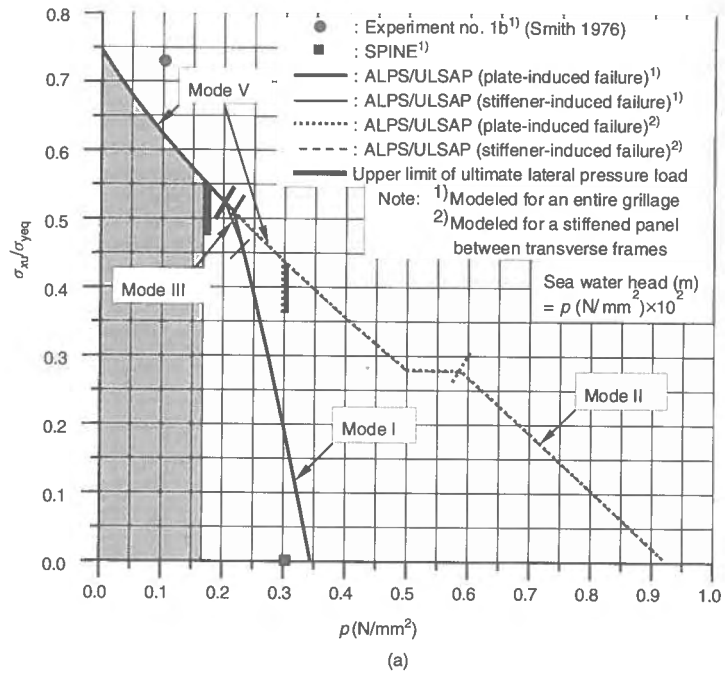

Figure 6.10 Comparison of ALPS/ULSAP with the Smith test grillage (a) number 1b; (b) number 2a and (c) number 3a under combined axial compression and lateral pressure. Reprinted from *Thin Walled Structures*, Vol. 40, Paik, J.K. & Kim, B.J. Ultimate strength formulations for stiffened panels under combined axial load, in-plane bending and lateral pressure: a benchmark study, 45–83, 2002, with permission from Elsevier Science

Figure 6.10 compares the ALPS/ULSAP predictions with the Smith collapse test results or SPINE semi-analytical solutions for three grillages that Smith tested under combined axial compression and lateral pressure; refer to the related data tables above and Chapter 11 for the SPINE method. The Perry–Robertson formula predictions based on the SIF condition for Mode III are also shown for comparison, although they are not included in the ALPS/ULSAP ultimate strength computations. The Mode I ultimate strength prediction is again made based on the yield of the panel edges. The upper limit of the 'critical' lateral pressure is also given in Figure 6.10. The real panel ultimate strength is then represented by the thicker solid line of Figure 6.10 inside the upper limit of the critical lateral pressure.

While the experiments and SPINE analyses were undertaken for the models of the entire grillages, i.e., including both longitudinal and transverse frames, two kinds of modeling with regard to the extent of calculation were considered for the ALPS/ULSAP ultimate strength predictions, namely one for an entire grillage and the other for a longitudinally stiffened panel between two adjacent transverse frames. The real ultimate strength is taken as the smaller value of the two results. The latter calculation model significantly overestimates the ultimate strength compared to the former, particularly when the magnitude of lateral pressure loads is large. The ultimate strength characteristics of ship grillages depend on the dimensions of transverse frames as well as those of longitudinals.

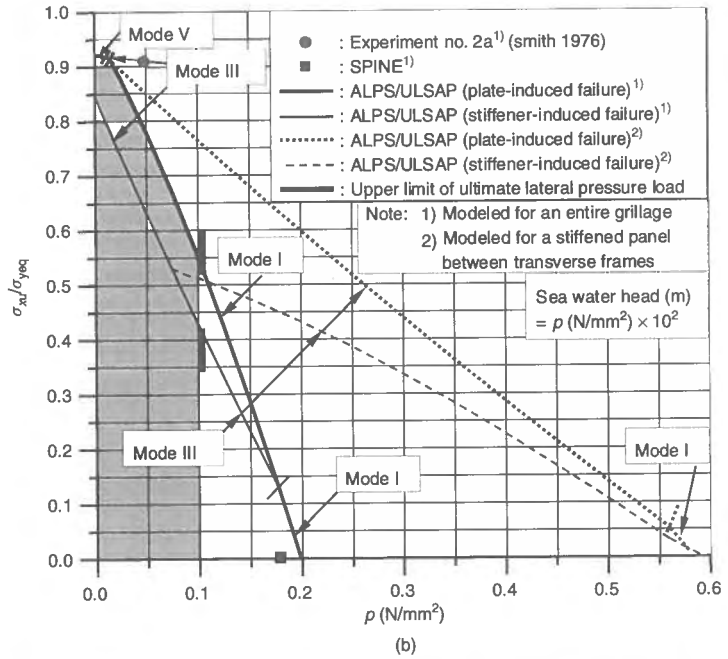

Figure 6.10 (*continued*)

When a larger magnitude of lateral pressure loads is applied, the relatively weak transverse frames in the grillage can fail and do not continue to support the related panel, and therefore the latter type of modeling, i.e., only for a stiffened panel between two adjacent transverse frames which are assumed to remain straight or not to fail, may provide quite optimistic ultimate strength predictions of the grillage. The grillages fail in the overall collapse mode I as the lateral pressure loads are dominant. The ALPS/ULSAP method with the former type of modeling predicts the ultimate strength reasonably well for the entire range of lateral pressure considered in the Smith collapse test data used. It is also noted that the SIF-based Mode III predictions using the Perry–Robertson formula are too pessimistic compared to the test results, and thus they are excluded from the ALPS/ULSAP panel ultimate strength calculations. In Figure 6.10, the shaded areas represent the safe zone of the structure against the applied loading.

References

Furuta, T., Kitada, T. & Nakai, H. (1991). A design of stiffened steel plates subjected to biaxial in-plane forces. *Proceedings of the International Conference on Steel and Aluminum Structures (ICSAS'91)*, Singapore, May 22–24, 481–490.

Kitada, T., Nakai, H. & Furuta, T. (1991a). Ultimate strength and interaction curve of stiffened plates subjected to biaxial in-plane forces. *Structural Engineering/Earthquake Engineering*, 8(3): 113–122.

Kitada, T., Nakai, H. & Furuta, T. (1991b). Experimental study on ultimate strength of stiffened plates subjected to longitudinal tension and transverse compression. *Journal of Constructional Steel Research*, 19: 203–212.

Mansour, A.E. (1977). *Gross panel strength under combined loading*. Ship Structure Committee, SSC-270, Washington, DC.

Mikami, I., Kimura, T. & Yamazato, Y. (1989). Prediction of ultimate strength of plate girders for design. *Journal of Structural Engineering*, 35A: 511–522 (in Japanese).

Paik, J.K., Thayamballi, A.K. & Kim, B.J. (2001). Large deflection orthotropic plate approach to develop ultimate strength formulations for stiffened panels under combined biaxial compression/tension and lateral pressure. *Thin-Walled Structures*, 39: 215–246.

Smith, C.S. (1966). Elastic analysis of stiffened plating under lateral loading. *RINA Transactions*, 108(2): 113–131.

Smith, C.S. (1976). Compressive strength of welded steel ship grillages. *RINA Transactions*, 118: 325–359.

Smith, C.S., Anderson, N., Chapman, J.C., Davidson, P.C. & Dowling, P.J. (1992). Strength of stiffened plating under combined compression and lateral pressure. *RINA Transactions*, 134: 131–147.

Troitsky, M.S. (1976). *Stiffened panels: bending, stability and vibrations*. Elsevier Scientific Publishing Company, Amsterdam.

7 Ultimate Strength of Plate Assemblies: Plate Girders, Box Columns/Girders and Corrugated Panels

7.1 Introduction

Units of plate assemblies often constitute primary strength parts in building steel-plated structures. These include plate girders, box columns/girders and corrugated plate panels. This chapter is a classical first principles based treatment of the ultimate strength of plate assemblies. In usual design practice today, the design of such assemblies relies largely on structural codes, which contain a wealth of varying approaches to the strength treatment of these members, some based on classical theory and others based on results of structural model testing. In this regard, the interested reader may consult ECCS (1978), Allen & Bulson (1980) and ENV 1993-1-1 (1992) of Eurocode 3, among others.

Welded plate girders, which are one major type of plate assembly of interest, are primary strength members in industrial buildings, bridges, ships and offshore platforms. They are typically used to resist bending about their strong axis. The flanges of a plate girder are designed so that they effectively sustain bending stresses, while the web is designed to resist stresses due to the shearing forces.

In buildings, especially for fabrication of portal frames in the competitive industrial sector, the web of plate girders is sometimes not stiffened, except at the bearings or at locations where point loads are applied. A slender web may buckle in the elastic regime. To improve the load-carrying capacity of plate girders, therefore, the web should be stiffened in the longitudinal and/or transverse directions to the extent required, with longitudinal stiffeners located in the compression zone of the web in particular.

In the past, when the linear theory of plate buckling was used for the design of large steel-plate girders, longitudinal stiffeners were invariably used, but it has been realized that in many cases unstiffened webs could be more economical than stiffened webs

(Maquoi 1992). That plate girder webs without stiffeners will be necessarily stocky is not always true in the field of buildings. For instance, many industrial buildings for warehouses are nowadays erected using deep girders with unstiffened slender webs of which the slenderness ratio (i.e., the ratio of the girder depth to the web thickness) is sometimes up to 300.

The webs of plate girders are normally welded to each flange by a single-sided butt weld. When the web has stiffeners in both longitudinal and transverse directions, longitudinal stiffeners may be welded on one side of the web, while transverse stiffeners are located on the other side. Because of extensive welding processes employed during fabrication of plate girders, initial imperfections in the form of initial deflection and residual stress normally develop and may affect the ultimate strength.

Welded built-up box columns/girders with relatively large sizes are commonly used in offshore structures, building frames and other civil engineering structures. Box columns are predominantly subjected to axial compressive loads, while box girders are used to sustain predominantly bending. Box girders can have a variety of cross-sectional shapes ranging from a deep narrow box to a wide shallow box. The flanges of box girders are normally wider and more slender than those of plate girders, while the webs of box girders are of comparable slenderness to those of plate girders. These are, however, generalizations that may not always be true in specific cases. The relative distribution of material in a plated beam or column unit is, however, usually driven by cost and arrangement considerations.

Corrugated panels are typically seen at transverse bulkheads of merchant ships which carry bulk cargoes such as iron ore or coal. In civil engineering structures, the webs of plate girders are sometimes constructed of corrugated plate panels. Corrugated panels in transverse bulkheads of merchant ships are likely to be subjected to lateral pressure and axial loads, while they are typically subjected to axial loads and shearing forces in civil engineering structures.

This chapter deals with the ultimate strength formulations for selected types of plate assemblies, while some others are described in the other chapters of this book. With the load effects computed by the usual linear elastic finite element method or classical theory of structural mechanics, the ultimate limit state (ULS) design of such plate assemblies is undertaken so that Equation (1.1) in Chapter 1 is satisfied.

7.2 Ultimate Strength of Plate Girders

Figure 7.1 shows a plate girder with transverse stiffeners under combined bending moments and shearing forces. This section presents the ultimate strength formulations of such plate girders under bending moment, shearing force, patch load and combinations thereof. For more elaborate guidelines for the ULS design of plate girders, Maquoi (1992) and Kitada & Dogaki (1997), among others, may be referred to.

7.2.1 Ultimate Strength under Shearing Force

A stocky plate girder web under shearing force may not fail until the following upper limit of the load-carrying capacity is reached, namely

$$V_P = h t_w \tau_Y \tag{7.1}$$

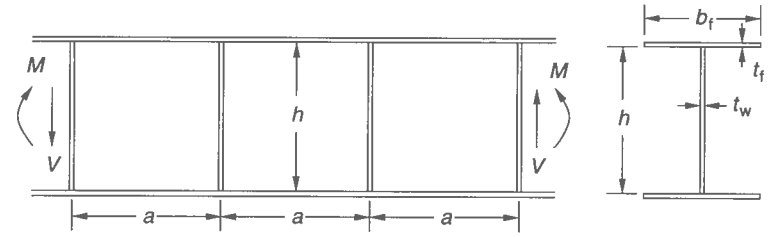

Figure 7.1 A plate girder under longitudinal bending and shearing forces

where $\tau_Y = \sigma_{Yw}/\sqrt{3}$ = shear yield stress, σ_{Yw} = web yield stress, V_P = plastic shear strength.

However, a slender web can buckle before it reaches the ultimate strength. It is considered that the shear buckling may take place if the following criteria are satisfied (ENV 1993-1-1 1992):

$$\frac{h}{t_w} > 69\varepsilon \text{ for an unstiffened web} \tag{7.2a}$$

$$\frac{h}{t_w} > 30\varepsilon\sqrt{k_s} \text{ for a stiffened web} \tag{7.2b}$$

where $\varepsilon = \sqrt{(235/\sigma_{Yw})}$, σ_{Yw} = web yield stress in N/mm^2, k_s = web shear buckling coefficient which is given by $k_s = 5.34$ for webs with transverse stiffeners at the supports but no intermediate transverse stiffeners; $k_s = 4.0 + 5.34(h/a)^2$ for webs with transverse stiffeners at the supports and intermediate transverse stiffeners with $a/h < 1$; $k_s = 5.34 + 4.0(h/a)^2$ for webs with transverse stiffeners at the supports and intermediate transverse stiffeners with $a/h \geq 1$.

Equation (7.2a) implies that all webs with h/t_w greater than 69ε may be designed to have transverse stiffeners at the supports. The shear buckling strength of a web depends on the h/t_w ratio and the spacing, a, of any intermediate web stiffeners. The shear buckling strength may also be affected by the anchorage of tension fields associated with end stiffeners or flanges. The anchorage provided by flanges will normally be reduced by longitudinal stresses due to bending moment and axial load.

For shear buckling strength estimation of plate girder webs without intermediate transverse stiffeners or of webs with transverse stiffeners only, the following two methods are useful (ENV 1993-1-1 1992):

(1) The simple post-elastic critical buckling strength method, which can be used for webs of plate girders, with or without intermediate transverse stiffeners, provided that the web has transverse stiffeners at the supports, but only for webs with $a/h \geq 3.0$. It has been found that the simple post-critical method tends to underestimate the strength for $a/h < 3.0$.
(2) The tension field method, which may be used for webs with transverse stiffeners at the supports plus intermediate transverse stiffeners, provided that adjacent panels or end posts provide anchorage for the tension fields, but only for webs with $a/h < 3.0$. It is found that the tension field method tends to underestimate the strength for the webs with $a/h \geq 3.0$.

For both methods noted above, it is considered that the transverse stiffeners are stiff enough so that they remain straight until the web buckles. In this regard, ENV 1993-1-1 (1992) of Eurocode 3 suggests that the following stiffness criterion for the transverse stiffeners must be satisfied:

$$I_s \geq \begin{cases} 1.5h^3t_w^3/a^2 & \text{for } a/h < \sqrt{2} \\ 0.75ht_w^3 & \text{for } a/h \geq \sqrt{2} \end{cases} \tag{7.3}$$

where I_s = moment of inertia of the transverse stiffener.

Simple Post-critical Buckling Method

In this method, the ultimate shear load of a web is calculated as follows

$$V_u = ht_w\tau_u \tag{7.4}$$

where τ_u = simple post-critical shear strength which is taken as Equation (4.55a) or the formula of ENV 1993-1-1 (1992), namely

$$\tau_u = \begin{cases} \tau_Y & \text{for } \lambda \leq 0.8 \\ [1 - 0.625(\lambda - 0.8)]\tau_Y & \text{for } 0.8 < \lambda < 1.2 \\ 0.9/\lambda\tau_Y & \text{for } \lambda \geq 1.2 \end{cases}$$

where

$$\lambda = \sqrt{\frac{\tau_Y}{\tau_E}} = \frac{h}{t_w}\frac{1}{37.4\varepsilon\sqrt{k_s}}$$

τ_E = elastic web shear buckling stress, k_s and ε are as defined in Equations (7.2).

Tension Field Method

The plate girder with intermediate transverse stiffeners has normally a significant reserve strength after the web buckles in shear. This is because the so-called tension field effect appears in the web, as shown in Figure 7.2(a). As applied loads increase, the stress inside the web is redistributed so that the diagonal tensile stresses continue to increase with the applied shear, while the diagonal compressive stresses remain substantially unchanged. In this regard, the web ultimate shear load, V_u, is typically given as a sum of the three contributions, namely

$$V_u = V_{cr} + V_t + V_f \tag{7.5}$$

where V_{cr} = beam-action strength, V_t = tension field strength, V_f = frame-action strength.

For practical purposes, the frame-action strength is often neglected, i.e., $V_f = 0$. The beam-action strength, V_{cr}, is obtained by

$$V_{cr} = ht_w\tau_{cr} \tag{7.6}$$

where τ_{cr} is the critical shear buckling stress which can be obtained by substituting the elastic shear buckling stress, τ_E, into the Johnson–Ostenfeld formula, Equation (2.93), and

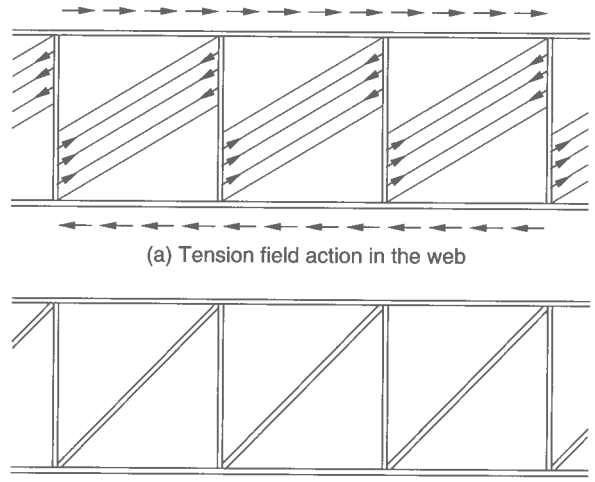

(a) Tension field action in the web

(b) Truss-like structure

Figure 7.2 Tension field action in the web of a plate girder under shearing force

τ_E is often estimated assuming that all four web edges are simply supported, given by

$$\tau_E = k_s\frac{\pi^2 E}{12(1-\nu^2)}\left(\frac{t_w}{h}\right)^2 \tag{7.7a}$$

with E = Young's modulus, ν = Poisson's ratio, k_s = elastic shear buckling coefficient for the web with intermediate transverse stiffeners as defined in Equations (7.2) or

$$k_s = \begin{cases} 5.34 + 4(h/a)^2 & \text{for } a/h \geq 1 \\ 4.0 + 5.34(h/a)^2 & \text{for } a/h < 1 \end{cases} \tag{7.7b}$$

For the strength predictions related to the tension field action, two models are typically adopted, namely the so-called Basler model (Basler 1961) and the so-called Cardiff model (Porter *et al.* 1975). In the Basler model, the flanges are assumed to be too flexible to support any lateral loading induced by the tension field. The yield band which determines the tension field strength is resisted by the transverse stiffeners alone. The width of the tensile band depends on the slope of the band which is chosen to maximize the shear strength. The Basler model may be considered to provide a lower bound to the web ultimate shear strength.

It is considered that the plate girder subject to a tension field behaves as a truss structure together with the flanges and vertical stiffeners to transfer additional shearing force as shown in Figure 7.2(b).

However, the plate girder may not sustain further increase of shear if the tension field material yields. The contribution due to the tension field action to the load-carrying capacity is then given by

$$V_t = ht_w\tau_{tf} \tag{7.8}$$

where τ_{tf} = shear strength due to the tension field contribution.

Using the Basler model, τ_{tf} can be approximately calculated based on the model of the truss-like structure which neglects the contribution made by the bending resistance of the flanges, with results as follows:

$$\tau_{tf} = \frac{\sigma_{Yw}}{2} \frac{1 - \tau_{cr}/\tau_Y}{\sqrt{1 + (a/h)^2}} \tag{7.9}$$

where τ_{cr} is as defined in Equation (7.6).

It is noted that the transverse stiffeners in such a case where the tension field is taken advantage of in design should be strong enough so that they can sustain and transmit the forces caused by the tension field action in the web. To achieve this, the following criteria need to be satisfied:

$$A_s \geq \frac{P_s}{\sigma_{Yw}}, \quad I_s \geq \frac{P_s h^2}{\pi^2 E} \tag{7.10a}$$

where A_s, I_s = cross-sectional area or moment of inertia of the transverse stiffener, which is similar to Equation (7.3), P_s = stiffener force due to the tension field action, given by (Trahair & Bradford 1988)

$$P_s = \frac{\sigma_{Yw} h t_w}{2} \left(1 - \frac{\tau_{cr}}{\tau_Y}\right) \left[\frac{a}{h} - \frac{(a/h)^2}{\sqrt{1 + (a/h)^2}}\right] \tag{7.10b}$$

Some valuable improvements to the Basler model were made by Rockey and his colleagues at University College, Cardiff (Porter *et al.* 1975) and the result is often called the Cardiff model. The Cardiff model takes into account the effect of the bending stiffness of the flanges on the width of the diagonal tension band. While the diagonal tension band is composed of three parts as shown in Figure 7.2(a), the central part anchors on the transverse stiffeners and the two parts anchor on the lower and upper flanges. Therefore, the strength related to the tension field action is determined by the vertical component of the force in the band at collapse. If the flanges have an infinite flexural stiffness for bending in the plane of the web, a pure tension field will develop. In this case, the anchorage lengths on the flanges become equal to the spacing, a, of the intermediate transverse stiffeners (or the web length). For very flexible flanges, the tension field anchors on the adjacent webs only. In practice, the anchorage lengths will only span part of the web length since the flanges have a finite flexural rigidity. For an elaborate description of the Basler and Cardiff models, the interested reader may refer to Maquoi (1992). The descriptions above are only for internal webs. Maquoi (1992) is also referred to for end webs.

7.2.2 Ultimate Strength under Bending Moment

In this section, the ultimate bending strength formulations of a plate girder with the section symmetrical with respect to the web are presented. The collapse behavior of a plate girder under bending is governed by buckling of the web and the compression flange. The elastic buckling stress, σ_{bE}, of the plate girder web under longitudinal bending may be calculated from Equation (3.2) in Chapter 3, considering that all four web edges are

simply supported as follows:

$$\sigma_{bE} = k_b \frac{\pi^2 E}{12(1 - \nu^2)} \left(\frac{t_w}{h}\right)^2 \tag{7.11}$$

where

$$k_b = \begin{cases} 23.9 & \text{for } a/h \geq \frac{2}{3} \\ 15.9 + 1.87(h/a)^2 + 8.6(a/h)^2 & \text{for } a/h < \frac{2}{3} \end{cases}$$

The inelastic (or critical) buckling strength, σ_{bcr}, of the web under bending is then estimated by plasticity correction of the elastic buckling strength using the Johnson–Ostenfeld formula, Equation (2.93). When the web buckles in bending, the corresponding critical bending moment, M_{wcr}, for the plate girder is given by

$$M_{wcr} = \frac{2I}{h} \sigma_{bcr} \tag{7.12}$$

where I = moment of inertia of the plate girder cross-section.

Under longitudinal bending, M, the compression flange is subjected to the axial compressive stress, given by

$$\sigma_f = -\frac{M}{2I}(h + t_f) \tag{7.13}$$

The compression flange may buckle before or after the web fails, while the failure pattern of the former type, i.e., buckling of the compression flange prior to failure of the web, is quite undesirable. The buckling of the compression flange may be estimated from Equation (5.35) in Chapter 5 considering the half flange with regard to the web which has the boundary conditions simply supported at three edges and free at one edge, as shown in Figure 5.7. The critical buckling strength, σ_{fcr}, of the compression flange is then approximately computed by substituting the corresponding elastic buckling strength into the Johnson–Ostenfeld formula, Equation (2.93) of Chapter 2.

To prevent the possibility of the compression flange buckling in the plane of the plate girder web, the following criterion needs to be satisfied (ENV 1993-1-1 1992):

$$\frac{h}{t_w} \leq 0.55 \frac{E}{\sigma_{Yf}} \sqrt{\frac{A_w}{A_{fc}}} \tag{7.14}$$

where A_w = area of the web, A_{fc} = area of the compression flange, σ_{Yf} = yield stress of the compression flange.

The critical bending moment at buckling of the compression flange may be given by

$$M_{fcr} = \frac{2I\sigma_{fcr}}{h + t_f} \tag{7.15}$$

For a plate girder with unequal flanges, the buckling of the flanges may be checked for the weaker flange. The plastic bending moment of the plate girder without local buckling is given by

$$M_P = M_{Pw} + M_{Pf} \tag{7.16}$$

where $M_{Pf} = hb_f t_f \sigma_{Yf}$ = plastic moment of the flanges, $M_{Pw} = (h^2 t_w/4)\sigma_{Yw}$ = plastic moment of the web.

In practice, the flanges are normally designed so that they do not buckle until the plate girder reaches the ultimate strength. In this case, the ultimate strength behavior of the plate girder is primarily governed by buckling of the web. Therefore, two types of failure regimes are to be considered for the calculation of the ultimate strength, depending on flange failure either before or after buckling of the web.

Mode I

If $M_{wcr} > M_Y$, the web may not buckle until the flange fails or yields. In this case, it is considered that the plate girder reaches the ultimate strength if the compression flange yields. This results in

$$M_u = M_Y \tag{7.17}$$

where M_u = ultimate bending moment of the plate girder, $M_Y = (2I/h)\sigma_{Yf}$ = critical bending moment at yielding of the compression flange.

Mode II

The axial stress distribution over the plate girder cross-section immediately after the web buckles in bending may be idealized as shown in Figure 7.3. The plate girder may sustain further increase of bending, but only the flange and the web with the effective section will be available in the compression zone while all sections in the tension side are still fully effective, as shown in Figure 7.3. The axial stress, σ_{fc}, of the compression flange is then computed by (for the symbols used below, Figure 7.3 is referred to)

$$\sigma_{fc} = -\frac{h + t_f}{2}\left[\frac{M_{wcr}}{I} + \frac{M - M_{wcr}}{I_e}(1 + 2e)\right] \tag{7.18}$$

where

$$I_e = \left(\frac{1}{2} + 2e^2\right)h^2 b_f t_f + \frac{1}{3}h^3 t_w\left[\frac{1}{4} + 3e^2 - \left(\frac{1}{2} + e - c\right)^3\right]$$

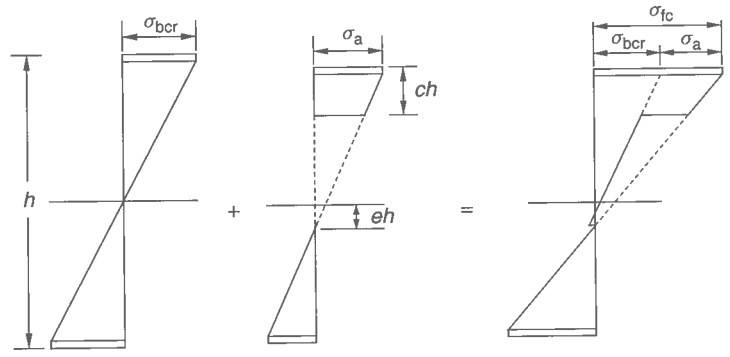

Figure 7.3 Idealized stress distribution over the plate girder cross-section under bending after buckling of the web (c = effective section coefficient)

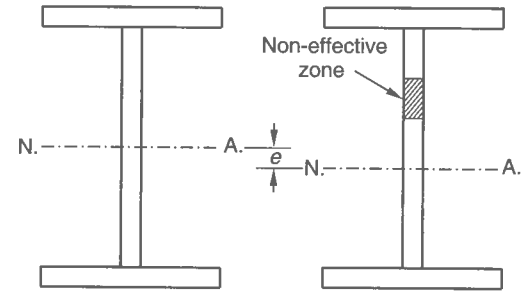

Figure 7.4 Effective cross-section of a plate girder

is the effective moment of inertia of the plate girder cross-section, with

$$e = \left(\frac{1}{2} + c + 2\frac{b_f t_f}{h t_w}\right) - \sqrt{2\left(1 + 2\frac{b_f t_f}{h t_w}\right)\left(c + \frac{b_f t_f}{h t_w}\right)}$$

The plate girder is considered to collapse if the axial stress of the compression flange equals the yield stress, namely $\sigma_{fc} = -\sigma_{Yf}$. This results in

$$M_u = M_{wcr} + (M_Y - M_{wcr})\frac{I_e}{I}\frac{1}{1 + 2e} \tag{7.19}$$

In Europe, the ultimate bending strength predictions are typically made by applying the concept of the effective cross-section associated with the effective width of the compression elements. The plastic bending capacity is then calculated as for the procedure noted in Section 2.6.3 of Chapter 2 but with the effective cross-sections, as shown in Figure 7.4. It is noted that even for uniaxial compressive loading the additional moment induced by the shift of the neutral axis can develop in the effective cross-section and must be accounted for in the strength calculations.

The shear lag effects in flanges may be neglected if the flange breadth is less than 10% of the length between points of zero moment for internal elements or if the outstand is less than 5% of the length between points of zero moment for outstand elements. When these limits are exceeded the shear lag effects cannot be neglected and an effective breadth of the flanges should be used. For more elaborate descriptions of the possible interaction between shear lag and plate buckling, Section 2.5.3 in Chapter 2 may be referred to.

For other types of ultimate bending strength design formulations for plate girders with stiffened webs, Kitada & Dogaki (1997) may be referred to.

7.2.3 Ultimate Strength under Combined Shearing Force and Bending Moment

Plate girders are likely to be subjected to combined bending and shearing forces. For plate girders with slender webs, the ultimate strength may be reached after buckling of the webs. The ultimate strength interaction relationship of such plate girders under

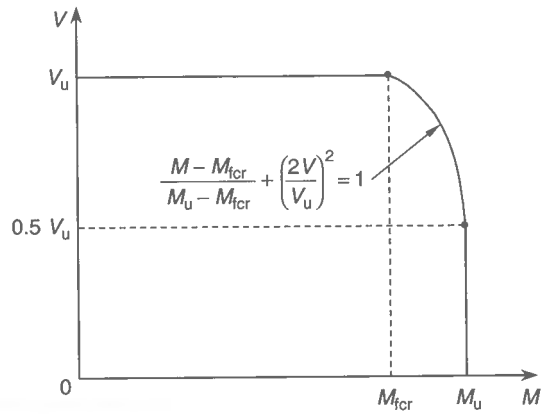

(a) Simple post-critical buckling method basis

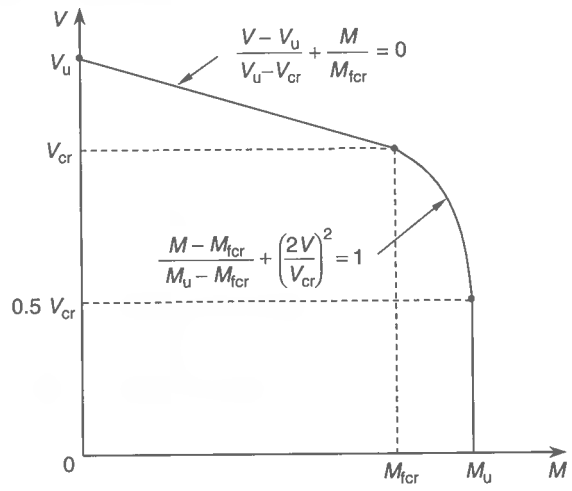

(b) Tension field method basis

Figure 7.5 A schematic of the ultimate strength relationship of plate girders under combined bending and shearing forces

combined bending and shearing forces is often represented by a piecewise linear curve as shown in Figure 7.5 (ENV 1993-1-1 1992).

It is more convenient to have a closed-form expression of the ultimate strength interaction relationship for plate girders under combined bending and shearing force. For this purpose, the following formula may be used:

$$\left(\frac{M}{M_u}\right)^4+\left(\frac{V}{V_u}\right)^4=1 \tag{7.20}$$

where V_u = ultimate shear force as defined in Section 7.2.1, M_u = ultimate bending moment as defined in Section 7.2.2. The validity of Equation (7.20) has been confirmed

by comparing to the test results on plate girders under combined bending and shearing force (Fukumoto *et al.* 1985, Mikami *et al.* 1991). It was found that Equation (7.20) agreed well with the lower limit of the test results, with related modeling error given by mean = 0.856 and COV = 0.08 for $\sigma_{uf} \le \sigma_{uw}$ and mean = 0.926 and COV = 0.05 for $\sigma_{uf} > \sigma_{uw}$, where σ_{uf} = ultimate strength of compression flange, σ_{uw} = ultimate strength of web.

7.2.4 Ultimate Strength under Patch Load

Plate girders used in the field of civil engineering are sometimes subjected to patch loads, as shown in Figure 7.6. The collapse strength of an unstiffened web subject to patch (transverse) loads applied through a plate girder flange is governed by one of the following three failure modes (ENV 1993-1-1 1992):

- crushing of the web close to the flange, accompanied by plastic deformation of the flange;
- crippling of the web in the form of localized buckling and crushing of the web close to the flange, accompanied by plastic deformation of the flange; and
- buckling of the web over most of the depth of the plate girder.

Two types of load application are normally considered: (1) forces applied through one flange and resisted by shear forces in the web; or (2) forces applied to one flange and transferred through the web directly to the other flange. For load type (1), the capacity of the web to lateral forces may be determined as the smaller value of the two strengths due to crushing and crippling. For load type (2), the web capacity may be taken as the smaller value of the two strengths due to crushing and buckling. The crippling strength of a web with intermediate transverse stiffeners is similar to that of an unstiffened web, with the increase due to the stiffeners.

Dogaki *et al.* (1992a) studied the ultimate strength of longitudinally stiffened plate girders under patch loading. They concluded that the optimum location of the longitudinal stiffener close to the plate girder flange under patch loading is about $b_w = 0.15h_w$, see Figure 7.6. Dogaki *et al.* (1992b) then proposed an empirical expression of the ultimate strength, P_u, of plate girders under (concentrated) patch loading by curve fitting based on their own test results, as follows:

$$\frac{P_u}{2V_P}=\frac{0.594}{\lambda}+0.069 \tag{7.21}$$

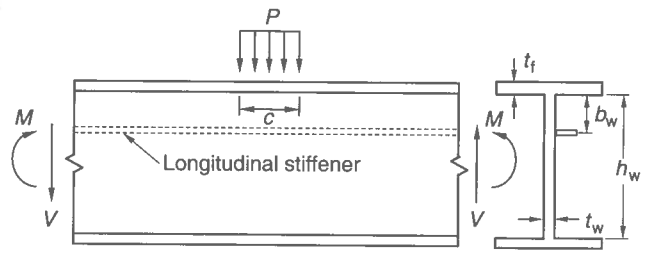

Figure 7.6 A plate girder with the unstiffened web under patch load

where V_P is as defined in Equation (7.1), $\lambda = \sqrt{(2V_P/P_E)}$ = buckling parameter, P_E = elastic buckling strength of plate girder web under patch loading, taking into account the effects of flexural and torsional rigidities of the flange.

For plate girders without longitudinal stiffeners under patch loading, Takimoto (1994) proposed a closed-form expression of the ultimate strength, P_u, as follows (for the symbols used below, refer to Figure 7.6):

$$P_u = (25t_w^2\sigma_{Yw} + 4t_w t_f \sigma_{Yf})\left(1 + \frac{c + 2t_f}{2h_w}\right) \tag{7.22}$$

The mean and COV of the accuracy of Equation (7.22) when compared to the test results for 143 specimens on plate girders under patch loading were 0.984 and 0.15, respectively. For more details on the ULS design of plate girder webs to patch loading, Granath *et al.* (2000) or ENV 1993-1-1 (1992) may be referred to.

7.2.5 Ultimate Strength under Combined Patch Load, Shearing Force and Bending Moment

An ultimate strength interaction relationship for the plate girders under combined patch load, bending moment and shearing force has been proposed by Takimoto (1994) as follows:

$$\left(\frac{P}{P_u}\right)^2 + \left(\frac{M}{M_u}\right)^4 + \left(\frac{V}{V_u}\right)^4 = 1 \tag{7.23}$$

where V_u is as defined in Section 7.2.1, M_u is as defined in Section 7.2.2 and P_u is as defined in Section 7.2.4.

7.3 Ultimate Strength of Box Columns/Girders

When a thin-walled structure with a box-type cross-section is subjected to predominantly axial compression, it is called a box column, while it is termed a box girder when bending is a predominant loading component. This section presents the ultimate strength formulations of box columns/girders with diaphragms under axial compression, bending and their combination, as shown in Figure 7.7. Kitada & Dogaki (1997) and Dowling & Harding (1992), among others, may be referred to for more elaborate guidelines on the ULS design of such box girders.

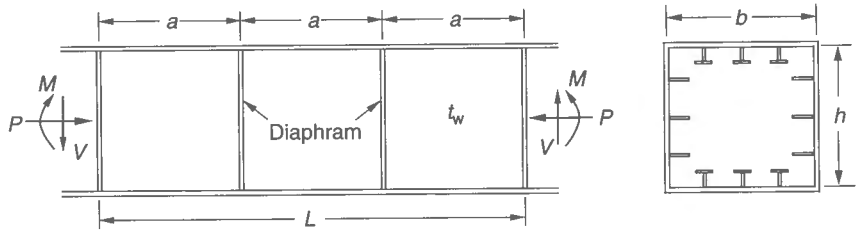

Figure 7.7 A box column/girder under combined axial compression, shearing force and bending

7.3.1 Ultimate Strength under Axial Compression

The ultimate strength of a box column may be obtained as the sum of the strengths of individual flanges or webs. In this case, the interacting effect between the webs and flanges may be negligible and their edges are considered to be simply supported.

For short box columns, the ultimate strength is governed by local buckling of flanges or webs, while for slender box columns it is affected by both global buckling of the box column and the local buckling of its components.

The ultimate strength, σ_{uL}, of a short box column under axial compression considering the local buckling and collapse of component elements may therefore be obtained by

$$\sigma_{uL} = \frac{1}{A_t}\sum_{i=1}^{4} A_i \sigma_{upi} \tag{7.24}$$

where A_i, σ_{upi} = cross-sectional area and the ultimate compressive strength of the ith panel (i.e., flange or web panels), A_t = total cross-sectional area.

The ultimate strength, σ_{uG}, of a long box column (without considering local buckling) in the global collapse mode may be obtained by the plasticity correction of the corresponding Euler buckling strength, σ_{EG}, using the Johnson–Ostenfeld formula, Equation (2.93). The Euler global buckling stress, σ_{EG}, is given for a box column simply supported at both ends as follows:

$$\sigma_{EG} = \frac{\pi^2 EI}{L^2} \tag{7.25}$$

where I = moment of inertia of the cross-section with regard to the weaker axis, L = length of the box column, E = Young's modulus.

The global buckling strength of a box column with initial imperfections may be calculated by the Perry–Robertson formula presented in the second subsection of Section 2.8.5 of Chapter 2.

For a box column with a 'medium' length, the interacting effect between local and overall buckling may play a significant role. In this case, the ultimate strength, σ_u, of the box column may be estimated from the Johnson–Ostenfeld formula, but by correcting the yield stress, σ_Y, as follows (AISC 1969):

$$\sigma_u = \begin{cases} \sigma_{EG} & \text{for } \sigma_{EG} \le 0.5c\sigma_Y \\ c\sigma_Y\,(1 - c\sigma_Y/4\sigma_{EG}) & \text{for } \sigma_{EG} > 0.5c\sigma_Y \end{cases} \tag{7.26a}$$

where c is a knock-down factor applied to the yield stress, being defined as follows:

$$c = \frac{\sigma_{uL}}{\sigma_Y} \tag{7.26b}$$

Alternatively, the ultimate strength of a box column taking into account the effect of local buckling may be calculated using the reduced cross-section associated with the effective width of plate elements (ENV 1993-1-1 1992).

It is of interest to note that a 'uniform' box column may generally buckle in the global mode when the elastic buckling stress, σ_{EL}, of individual plate elements is greater than the global elastic buckling stress, σ_{EG}, of the box column, and vice versa for the local

buckling mode. The transition from the local buckling mode to the global buckling mode may take place when σ_{EL} equals σ_{EG}, namely

$$\sigma_{EL} = \sigma_{EG} \tag{7.27a}$$

For a square cross-section uniform box column without stiffeners simply supported at both ends, for instance, we have

$$\sigma_{EL} = \frac{4\pi^2 E}{12(1-\nu^2)}\left(\frac{t}{b}\right)^2, \quad \sigma_{EG} = \frac{\pi^2 EI}{A_t L^2}, \quad A_t = 4bt, \quad I = \frac{2}{3}b^3 t \tag{7.27b}$$

where ν = Poisson's ratio.

Substitution of Equation (7.27b) into Equation (7.27a) yields

$$\frac{L}{b} = \sqrt{\frac{1-\nu^2}{2}}\frac{b}{t} \approx 0.675\frac{b}{t} \tag{7.27c}$$

when $\nu = 0.3$. From Equation (7.27c), one may say that the global buckling mode will take place when L/b is larger than $0.675b/t$ for a square-section uniform box column (without stiffeners) that is simply supported at both ends.

7.3.2 Ultimate Strength under Bending Moment

The ultimate strength behavior of a box girder under bending will be governed by buckling of the compression flange. The buckled flange will lose effectiveness as depicted by Figure 7.8. The box girder can normally sustain further increase of bending even after buckling of the compression flange and will be considered to collapse if the compressive stress at the buckled flange reaches the yield stress.

The ultimate bending capacity, M_u, can then be calculated by integrating the bending stress distribution over the effective cross-section with regard to the neutral axis. As an example, Figure 7.9 shows an idealized bending stress distribution over the box girder cross-section composed of unstiffened plate elements at the ULS. In this case, the compression flange has the effective width, b_e, since it has buckled. The ultimate bending capacity is thus calculated as follows:

$$\frac{M_u}{M_Y} = \frac{(2+3b/h)b_e/b + 2 + h/b}{4 + 3b/h + h/b} \tag{7.28}$$

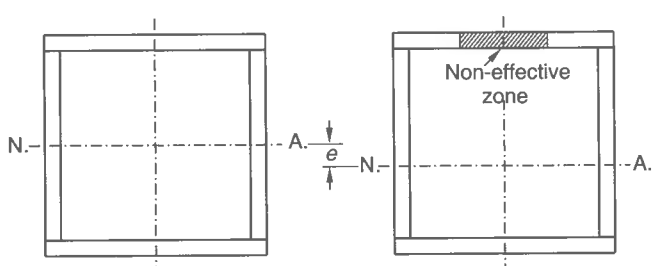

Figure 7.8 Effective cross-section of a box girder

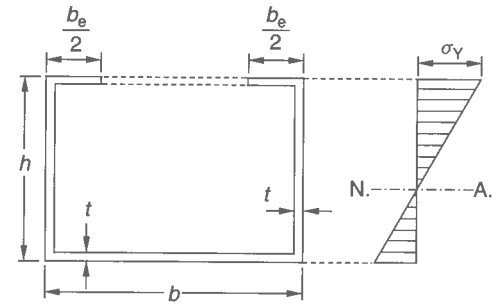

Figure 7.9 Idealized bending stress distribution over a box girder with the effective cross-section at the ULS

where b_e = effective width of the compression flange, which may be obtained as noted in Section 2.5 of Chapter 2, M_Y = first yield bending moment without local buckling.

For the ultimate strength design formulations of longitudinally stiffened box girders under bending, Section 8.5 of Chapter 8 or Kitada & Dogaki (1997) and Dowling & Harding (1992) may be referred to. For the ultimate strength of box girders under combined axial compression and bending, Kitada *et al.* (1989) is referred to.

In calculating the ultimate strength of a box girder under bending, the influence of shear lag on the compression flange buckling may play an important role. As shown in Figure 2.6 of Chapter 2, the stress distribution is not uniform in the wide compression flange of a box girder because of the shear lag effect. However, it is known that the shear lag effect may be neglected when the average stress is greater than two-thirds of the maximum stress (Kitada *et al.* 1992).

On the other hand, Dowling & Burgan (1987) proposed an approximate expression for predicting the ultimate strength, σ_u, of a stiffened compression flange taking into account the shear lag effect, as follows:

$$\frac{\sigma_u}{\sigma_Y} = \frac{\sigma_{u0}}{\sigma_Y}\left(\frac{b_e}{b}\right)^c \tag{7.29}$$

where σ_{u0} = ultimate strength neglecting the shear lag effect, b_e = effective breadth due to shear lag, $c = b/(2L)$, L = span length.

7.3.3 Ultimate Strength under Shearing Force

An approach similar to that for a plate girder under shearing force can also be used in this case. Applying the tension field method based on the Basler model, the ultimate shear strength, V_u, of a symmetric box girder section with intermediate transverse stiffeners but without longitudinal stiffeners can be calculated as follows (Wolchuk & Mayrbourl 1980):

$$V_u = 2(V_{cr} + V_t) \tag{7.30}$$

where $V_{cr} = ht_w\tau_{cr}$, $V_t = ht_w\tau_{tf}/[2(\sqrt{1+\alpha^2}+\alpha)]$, h = depth of web between flanges, measured along webs, t_w = web thickness, $\alpha = a/h$, a = spacing of transverse stiffeners

(or diaphragms), τ_{cr} = critical shear buckling stress of web as defined in Equation (7.6), τ_{tf} = tension field shear stress as defined in Equation (7.9).

7.3.4 Ultimate Strength under Combined Shearing Force and Bending Moment

The ultimate strength interaction relationship for a box girder without longitudinal stiffeners under combined shearing force and bending moment may be expressed in a manner similar to that for a plate girder as noted in Section 7.2.3.

7.4 Ultimate Strength of Corrugated Panels

This section presents the ultimate strength formulations of a corrugated panel under some typical types of load application. Figure 7.10 shows a schematic of the corrugated panel considered.

7.4.1 Ultimate Strength under Axial Compression

The ultimate strength of the corrugated panel under axial compressive loads may be obtained as the sum of the ultimate compressive strengths for individual walls of the corrugations, i.e., flanges and webs. In this case, all four edges of each plate may be assumed to be simply supported. The ultimate strength formulations of individual plate elements presented in Chapter 4 can be used for this purpose.

7.4.2 Ultimate Strength under Shearing Force

Due to corrugations, the shear strength of a corrugated panel is greater than that of a similar flat plate with the same thickness and overall dimensions. Under shearing force, two distinct buckling modes are normally relevant (Maquoi 1992), namely (1) shear buckling

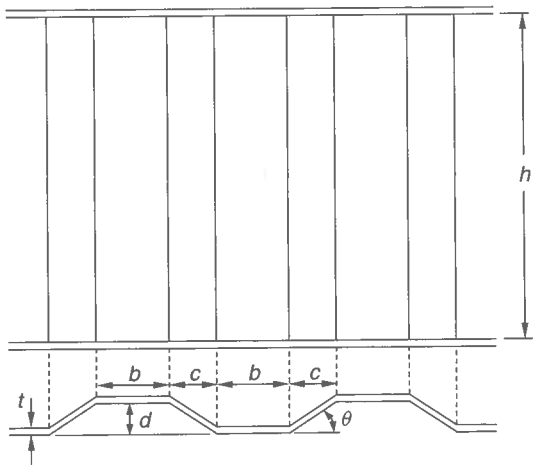

Figure 7.10 Schematic of the corrugated panel

that occurs locally in the largest plane wall element of the folds and is restricted to that region only, and (2) global shear buckling generally involving several folds that may occur with snap-through and causes yield lines to cross these folds, resulting in an appropriate change in the panel configuration.

In contrast to the plane webs, the corrugated webs do not usually exhibit a significant strength reserve after shear buckling. Hence the corrugated panel may be taken to reach the ULS if the wall of the corrugation buckles. For this case, the elastic local shear buckling strength may be calculated for the corrugation flange (plate) with the condition of simple supports at all four edges. As shown in Figure 7.10, the length, breadth and thickness of the plate are denoted by h, b and t, respectively. The critical local shear buckling strength, τ_L, may be estimated by the plasticity correction of the corresponding elastic stress using the Johnson–Ostenfeld formula, Equation (2.93).

The elastic global shear buckling strength, τ_G^*, of the corrugated panel may be given by (Maquoi 1992)

$$\tau_G^* = \frac{36}{h^2 t}\sqrt[4]{D_x D_y^3} \tag{7.31}$$

where

$$D_x = \frac{Et^3}{12(1-\nu^2)}\frac{b+c}{b+c/\cos\theta}, \quad D_y = \frac{Ed^2 t}{12(1-\nu^2)}\frac{3b+c/\cos\theta}{b+c}$$

E = Young's modulus, ν = Poisson's ratio.

The critical global shear buckling strength, τ_G, is then estimated by the plasticity correction of τ_G^* using the Johnson–Ostenfeld formula. In reality, the corrugated panel collapse may involve the two buckling modes together. In this case, Maquoi (1992) suggests the following simple expression for the ultimate shear strength, τ_u, of the corrugated panel, taking into account the interacting effect between the buckling modes, namely

$$\tau_u = 1.3\frac{\tau_L \tau_G}{\tau_L + \tau_G} \tag{7.32}$$

where τ_u should not be greater than either τ_L or τ_G as well.

Equation (7.32) does not have a physical meaning, but serves to interpolate between the local and global buckling strengths.

7.4.3 Ultimate Strength under Lateral Pressure

The corrugated transverse bulkheads of merchant ships such as bulk carriers are often arranged to efficiently sustain large lateral pressure loads. Because of the importance of such members to the integrity of ships carrying dense bulk cargoes, the ultimate strength of corrugated panels under lateral pressure loads has been studied by many investigators (Caldwell 1955, Paik *et al.* 1997, Ji *et al.* 2001, among others).

According to the insights developed by the experiments (Caldwell 1955, Paik *et al.* 1997), an important one is that each corrugation of the corrugated panel deforms similarly (or can normally be designed to deform similarly) under a similar distribution of pressure, implying therefore that the behavior of a single central corrugation could be used as nearly representative of an entire corrugated panel.

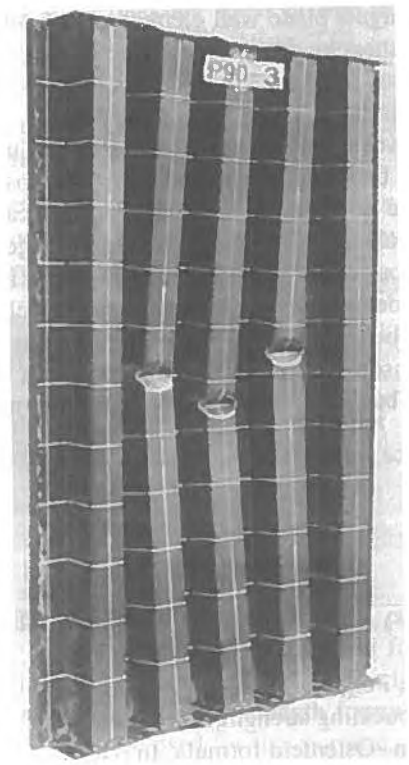

Figure 7.11 A typical collapse pattern of the corrugated panel under lateral pressure (Paik *et al.* 1997)

Figure 7.11 is a picture representing a typical collapse pattern of a corrugated panel under uniform lateral pressure as obtained by an experiment (Paik *et al.* 1997). Given such behavior, the ultimate strength of a corrugated panel under lateral pressure loads, p, may be estimated for an equivalent beam with the single corrugation cross-section and under a line load, i.e., $q = p(b + c)$, which is multiplied by p with the breadth (i.e., $b + c$) of the beam.

For a single corrugation beam simply supported at both ends and under a triangular type of lateral line loading as indicated in Figure 2.17(c) of Chapter 2, for instance, the ultimate strength is given by replacing the plastic bending moment with the ultimate bending moment in the same figure, as follows:

$$q_u = \frac{9\sqrt{3}}{h^2} M_u \tag{7.33}$$

where M_u = ultimate bending moment of the single corrugation beam.

For other types of end conditions or line load applications, a similar procedure can be applied by replacing the plastic bending capacity with the relevant ultimate bending capacity as presented in Section 2.7 of Chapter 2.

When a single corrugation is subjected to lateral pressure loads as shown in Figure 7.12, M_u in Equation (7.33) may in the limit be estimated by considering a relevant bending

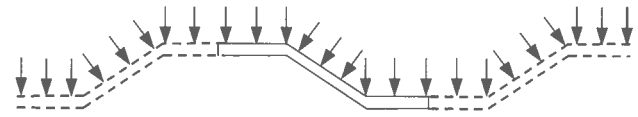

Figure 7.12 A single corrugation under lateral pressure load

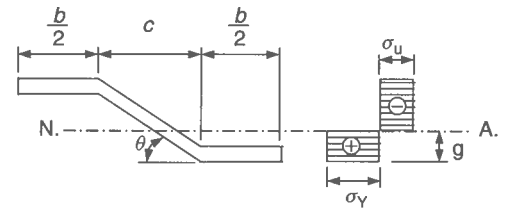

Figure 7.13 Idealized stress distribution at a plastic hinge in a single corrugation cross-section

stress distribution at a plastic hinge condition, representing that all parts in compression reach the ultimate compressive stress while all parts in tension reach the yield stress, as shown in Figure 7.13. This accommodates local buckling in the compressed part of the corrugation. In this case, M_u is given by (Paik *et al.* 1997)

$$M_u = \sigma_Y \left(A_f g + A_w \frac{g^2}{d} \sin\theta \right) + \sigma_u (d - g) \left(A_f + A_w \frac{d - g}{d} \sin\theta \right) \tag{7.34}$$

where $A_w = ct/\cos\theta$, $A_f = bt$, $g = d[2\sigma_u A_w \sin\theta - (\sigma_Y - \sigma_u)A_f]/[2(\sigma_u + \sigma_Y)A_w \sin\theta]$, σ_Y = yield stress, t, d = as defined in Figure 7.10, σ_u = ultimate compressive stress of the corrugation flange accounting for buckling, refer to Section 7.4.1.

References

AISC (1969). *Specification for the design, fabrication and erection of structural steel for buildings*. American Institute of Steel Construction, Chicago.

Allen, H.G. & Bulson, P.S. (1980). *Background to buckling*. McGraw-Hill, London.

Basler, K. (1961). Strength of plate girders in shear. *ASCE Journal of the Structural Division*, 87(ST7): 151–180.

Caldwell, J.B. (1955). The strength of corrugated plating for ships' bulkheads. *RINA Transactions*, 97: 495–522.

Dogaki, M., Yonezawa, H. & Tanabe, T. (1992a). Ultimate strength of plate girders with longitudinal stiffeners under patch loading. *Proceedings of the 3rd Pacific Structural Steel Conference*, The Japan Society of Steel Construction, Tokyo, October 26–28, 507–514.

Dogaki, M., Nishijima, Y. & Yonezawa, H. (1992b). Nonlinear behaviour of longitudinally stiffened webs in combined patch loading and bending. *Constructional Steel Design: World Developments*, Elsevier Applied Science, London, 141–150.

Dowling, P.J. & Burgan, B.A. (1987). Shear lag in steel and composite structures, a state of the art review. *Composite Steel Structures: Advances, Design and Construction*, Elsevier Applied Science, London, 1–23.

Dowling, P.J. & Harding, J.E. (1992). Box girders. Chapter 2.7 in *Constructional Steel Design – An International Guide*, Elsevier Applied Science, London, 175–195.

ECCS (1978). European recommendations for steel construction. European Convention for Constructional Steelwork, ECCS-EG 77–2E, March.

ENV 1993-1-1 (1992). *Eurocode 3: Design of steel structures, part 1.1 general rules and rules for buildings*. British Standards Institution, London.
Fukumoto, Y., Maegawa, K., Itoh, Y. & Asari, Y. (1985). Lateral–torsional buckling tests of welded I-girders under moment gradient. *Proceedings of the Japan Society of Civil Engineers*, 362: 323–332 (in Japanese).
Granath, P., Thorsson, A. & Edlund, B. (2000). I-shaped steel girders subjected to bending moment and travelling patch loading. *Journal of Constructional Steel Research*, 54: 409–421.
Ji, H.D., Cui, W.C. & Zhang, S.K. (2001). Ultimate strength analysis of corrugated bulkheads considering influence of shear force and adjoining structures. *Journal of Constructional Steel Research*, 57: 525–545.
Kitada, T. & Dogaki, M. (1997). Plate and box girders. Chapter 6 in *Structural Stability Design: Steel and Composite Structures*, Pergamon Press, Oxford, 185–228.
Kitada, T., Nakai, H. & Kunihiro, M. (1989). Ultimate strength of box stub columns under combined actions of compression, bending and torsion. *Journal of Constructional Steel Research*, 13: 153–168.
Kitada, T., Nakai, H. & Furuta, T. (1992). Ultimate strength of longitudinally stiffened plates subjected to transverse compression. *Proceedings of the Japan Society of Civil Engineers*, 446: 137–146 (in Japanese).
Maquoi, R. (1992). Plate girders. Chapter 2.6 in *Constructional Steel Design – An International Guide*, Elsevier Applied Science, London, 133–173.
Mikami, I., Harimoto, S., Yamasato, Y. & Yoshimura, F. (1991). Ultimate strength tests of steel plate girders under repetitive shear. *Technical Report of the Kansai University*, Japan, 33: 145–164.
Paik, J.K., Thayamballi, A.K. & Chun, M.S. (1997). Theoretical and experimental study on the ultimate strength of corrugated bulkheads. *Journal of Ship Research*, 41(4): 301–317.
Porter, D.M., Evans, H.R. & Rockey, K.C. (1975). The collapse behavior of plate girders loaded in shear. *The Structural Engineer*, 53: 313–325.
Takimoto, T. (1994). Plate girders under patch loading. *Ultimate Strength and Design of Steel Structures*, The Japan Society of Civil Engineers, Tokyo, 122–127 (in Japanese).
Trahair, N.S. & Bradford, M.A. (1988). *The behaviour and design of steel structures*. Chapman and Hall, London and New York.
Wolchuck, R. & Mayrbourl, R.M. (1980). Proposed design specification for steel box girder bridges. Report No. FHWA-TS 80-205, US Department of Transportation, Federal Highway Administration, Washington, DC.

8 Ultimate Strength of Ship Hulls

8.1 Fundamentals of Hull Girder Collapse

Overall collapse of a ship's hull rarely occurs. Figure 8.1 shows an example of such an accident to a ship. In this case, a Capesize bulk carrier collapsed due to human error during discharge in port of its 126 000 tonnes of iron ore cargo. While this 23-year-old 139 800 dwt ship did not separate into two, the bottom of its mid-body reportedly touched the sea bed, and the hull girder, in fact, collapsed. After having emptied the fore and aft holds among the five cargo holds, buckling collapse took place in the vessel's deck while the central hold was still full.

It is clear that this incident was primarily a result of improper unloading of the cargo from the ship. But it does serve to indicate that a ship, like any other structure, has a finite strength, and whether for routine design purposes, damage investigations, or to determine the ongoing effects of age-related structural degradation, relevant procedures to compute that strength accurately are a necessity. The present chapter considers the ultimate strength prediction of the entire ship hull girder taken as a unit.

A ship hull in an intact condition will sustain applied loads smaller than the design loads, and in normal seagoing and approved cargo loading conditions it will not suffer any structural damage such as buckling and collapse. However, the loads acting on the ship hull are uncertain both because of the nature of rough seas and because of possibly unusual loading/unloading of cargo, the latter due to human error. In rare cases, applied loads may hence exceed design loads and the ship hull may collapse globally. Since aging ships may have suffered structural deterioration due to corrosion and fatigue, related weakening in their structural resistance may play a part as well.

As applied loads increase beyond the design loads, structural members of the ship hull will buckle in compression and yield in tension. A ship hull can normally carry further loading beyond the onset of limited member buckling or yielding, but the structural effectiveness of any such failed members clearly decreases and its individual stiffness can even become 'negative', with their internal stress being redistributed to adjacent intact members. The most highly compressed member will, deterministically speaking, collapse earlier and the stiffness of the overall hull will decrease gradually. As loads continue to increase, buckling and collapse of more structural members will occur progressively until the ultimate limit state (ULS) is reached for the hull girder as a whole. When

Figure 8.1 A ship hull collapse that occurred during unloading of cargo at port

the structural safety of a ship hull is considered, the ultimate hull girder strength must then be accurately evaluated. It is also helpful in this regard if one can derive simple expressions for calculation of the hull ultimate strength so that these can be used for the ready formulation of failure functions to be used in reliability analysis, and in the early stages of structural design.

Most classification society criteria and procedures for ship structural design have been based on the first yield of hull structures together with buckling checks for structural components (i.e., not for the whole hull structure). These methods have proven themselves to be effective for intact vessels in normal seas and loading conditions. However, their applicability to assess the survivability of vessels in damaged or accidental situations, i.e., deterioration due to corrosion, fatigue, collisions, grounding or overloading, is somewhat less certain. In these cases, it is necessary to account more precisely for the interacting effects between yielding, buckling and, sometimes, rupture of local components and the related effects on the global behavior of the structural system.

While service proven, the traditional design criteria and associated linear elastic stress calculations do not necessarily define the true ULS which is the limiting condition beyond which a ship hull will fail to perform its function. Neither do such procedures help understanding of the likely sequence of local failure prior to reaching the ULS. It is of course important to determine the true ultimate strength if one is to obtain consistent measures of safety which can form a fairer basis for comparisons of vessels of different sizes and types. An ability to better assess the true margin of safety should also inevitably lead to improvements in regulations and design requirements.

A consequence of present-day design procedures is that in some ships the ultimate hogging moment is not always greater than the ultimate sagging moment, even if the section modulus at the bottom is larger than that at the deck. This is the case in some bulk carriers where the deck panels are sturdier than the bottom panels. One might of course presume (incorrectly) that, as long as the section modulus at the bottom is greater than that at the deck, the ultimate hull girder strength in hogging will be greater than that in sagging. But this is not always true. Such differences will of course be better detected and corrected if one undertakes ultimate-strength-based design.

This indicates the disadvantage of conventional structural design procedures for ships based on the allowable stress. The ULS design procedure can avoid such difficulties, and facilitate the determination of the real safety margin of the structure.

In the ULS design of ship hulls using Equation (1.1) in Chapter 1, the capacity is taken to be the relevant ultimate strength, while the demand is given in terms of the hull girder loads which may be calculated by the design rules of classification societies or by direct methods. This chapter presents relevant approaches to calculate the ship hull girder loads and the related ultimate strength.

8.2 Hull Girder Loads

8.2.1 Characteristics of Ship Structural Loads

Ship structures are subjected to various types of loads, which may be grouped according to their characteristics in time: static loads, low-frequency dynamic loads, high-frequency dynamic loads and impact loads (Paulling 1988).

Static loads are those arising from the weight and buoyancy of the ship. Low-frequency dynamic loads occur at frequencies which are sufficiently low compared to the frequencies of the vibratory response of the ship hull (and its parts as the case may be) so that the resulting dynamic effects on the structural response are relatively small. Such loads include hull pressure variations induced by waves or oscillatory ship motions, and inertial reaction forces resulting from the acceleration of the mass of the ship and its cargo or ballast water. High-frequency dynamic loads have frequencies that approach or exceed the lowest natural frequency of the hull girder. A typical example is wave-induced 'springing' (flexural vibration of the hull girder) which may occur when the natural period of the hull girder is close to the period of shorter components of the encountered waves. Since steady-state springing occurs at a higher frequency than that of ordinary wave-induced bending, it increases the number of stress cycles during the ship's lifetime, thus possibly increasing the hull girder fatigue damage. Impact loads are those whose duration is even shorter than the period of the high-frequency dynamic loads. Examples of impact loads are slamming and green water impact on deck. Slamming causes a sudden upward acceleration and deflection of the bow and excites hull girder flexural vibration in the first two or three modes, typically with a period in the range of 0.5–2 seconds. This transient slam-induced vibration is termed 'whipping'.

In ship structural analysis and design, the most common loads are the static and low-frequency dynamic loads, the latter usually being treated as static or quasi-static loads. The high-frequency dynamic loads can be important in specific design cases such as the long and slender Great Lakes vessels. The local effect of impact loads, particularly pressure, must usually be considered in some manner in most cases.

Since the characteristics of ship structural loads vary significantly depending on loading, operating conditions and sea states, all potential conditions during the ship's lifetime must be taken into account in the analysis and design of ship structures. Flooding and damaged conditions should also hence be considered.

8.2.2 Calculations of Hull Girder Loads

The important components of hull girder loads are vertical bending, horizontal bending, sectional shear and torsional moment as shown in Figure 8.2. These arise from the distribution of local pressures including sea and cargo loads. The basic theory to calculate hull girder loads may be found in textbooks such as Paulling (1988) and Hughes (1988). For calculating the design hull girder loads of merchant ships the classification societies provide simplified formulas or guidelines, with a direct calculation of hull girder loads from first principles being usually recommended in cases involving unusual structures, patterns of loading or operational conditions.

As the most important hull girder load component, the total vertical bending moment, M_t, for a ship hull is defined as the extreme algebraic sum of still-water moment, M_{sw},

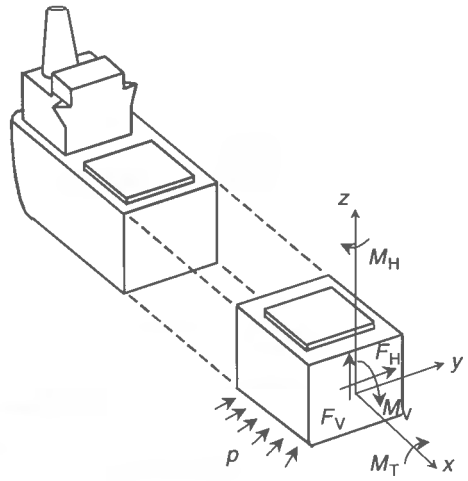

Figure 8.2 Hull girder sectional load components

and wave-induced moment, M_w, as follows:

$$M_t = M_{sw} + M_w \tag{8.1}$$

where M_{sw} is taken as the maximum value of the still-water bending moment resulting from the worst load condition on the ship considering both hogging and sagging. For merchant ships, the design value of M_{sw} may be taken as the maximum allowable still-water bending moment approved by a ship classification society. M_w is taken as the extreme wave-induced bending moment which the ship is likely to encounter during its lifetime.

For the safety and reliability assessment of damaged ship structures, hydrodynamic 'strip' theory (so called because the hull is idealized as a series of short prismatic sections, or girthwise 'strips') may be used to determine M_w. For long-term prediction of wave-induced loads, loads that are likely to be exceeded only once during the vessel's design lifetime are considered, including all sea states that may be encountered, while short-term prediction is carried out based on a ship encountering a storm of a specific persistence or duration (e.g., 3 hours).

Conventionally, a long-term analysis has been normally employed to determine M_w for the design of newly built ships, while a short-term analysis is typically necessary to predict M_w for ships in specific sea conditions, such as for damaged ships. In calculating M_w, a second-order strip theory may be used where it is necessary to distinguish between sagging and hogging wave-induced bending moments.

To approximately take into account the correlation between still-water and wave-induced bending moments, the following type of equation can be used for calculating the total bending moment:

$$M_t = k_{sw}M_{sw} + k_wM_w \tag{8.2}$$

where k_{sw} and k_w are load combination factors for still-water and wave-induced bending moments, respectively. These account for the non-simultaneous occurrence of extreme still-water and wave-induced loads.

To consider dynamic load effects, the total bending moment may be given by

$$M_t = k_{sw}M_{sw} + k_w(M_w + k_dM_d) \tag{8.3}$$

where k_d is the load combination factor related to the dynamic bending moment, M_d, arising from either slamming or whipping. M_d is taken as the extreme dynamic bending moment in the same wave condition (e.g., sea state) as the wave-induced bending moment, while the effect of ship hull flexibility is accounted for in the computation of M_d. In very high sea states, M_d is normally ignored because the possibility of whipping is usually low. For considering the hull girder effects of slamming in oceangoing merchant ships, it has been suggested that $M_d = 0.15M_w$ may be used for tankers in sagging, but $M_d = 0$ in hogging (Mansour & Thayamballi 1994).

While external pressure loads imposed on the ship hull in seaways can be calculated in terms of sea water heads, the internal pressure loads must be determined for each fully loaded cargo hold and ballast tank, as caused by the dominating ship motions (pitch and roll) and the resulting accelerations. The relative phasing of all such dynamic loads is important in defining the total load.

Still-water Loads

A detailed distribution of the still-water moment along the ship's length can be calculated by a double integration of the difference between the weight force and the buoyancy force, using simple beam theory.

The sectional shear force, $F(x_1)$, at location x_1 is estimated by the integral of the load curve which represents the difference between the weight and buoyancy curves, namely

$$F(x_1) = \int_0^{x_1} f(x)\,dx \tag{8.4a}$$

where $f(x) = b(x) - w(x)$ = net load per unit length in still water, $b(x)$ = buoyancy per unit length, $w(x)$ = weight per unit length.

The bending moment, $M(x_1)$, at location x_1 is estimated as the integral of the shear curve indicated in Equation (8.4a) as follows:

$$M(x_1) = \int_0^{x_1} F(x)\,dx \tag{8.4b}$$

Long-term Wave-induced Loads–IACS Unified Formulas

Ship classification societies had over time established their own individual design guidelines, based on their own studies and experience. This resulted in a variety of different requirements for ship hull girder structural design. The International Association of Classification Societies (IACS) has now unified these requirements in the case of the hull girder longitudinal strength.

This is important because the longitudinal strength of a ship governs basic scantlings of primary strength members such as strength decks, side shells, bottom structures and longitudinal bulkheads, thereby resulting in a great impact upon hull weight, cargo deadweight

and ship price. The unified standard for a ship's longitudinal strength was approved by the IACS in May 1989, and it is now implemented as the longitudinal strength requirement of most classification societies.

In the IACS unified requirements, while the design still-water vertical bending moment, M_{sw}, is calculated as usual, by considering all appropriate loading conditions, the design wave-induced vertical bending moment, M_w, is given by unified formulas representing a once in 20 year occurrence under North Atlantic wave conditions. With the hogging moment taken as positive and the sagging moment taken as negative, the applicable formulas are as follows:

$$M_w = +0.19C_1C_2L^2BC_b \quad \text{(kN m)} \qquad \text{for hogging} \tag{8.5a}$$

$$M_w = -0.11C_1C_2L^2B(C_b + 0.7) \quad \text{(kN m)} \qquad \text{for sagging} \tag{8.5b}$$

where L = ship length in m, B = ship breadth in m, C_b = block coefficient (which is taken in Equations (8.5) such that $C_b = 0.6$ when C_b is smaller than 0.6).

While the coefficient C_2 is taken as $C_2 = 1.0$ around the mid-ship location, i.e., between $0.4L$ and $0.65L$ measured from the after-perpendicular of the ship, a value smaller than 1.0 is used to represent the distribution at the other locations. The coefficient C_1 in Equations (8.5) is determined as a function of vessel length in meters as follows:

$$C_1 = \begin{cases} 10.75 - [(300 - L)/100]^{1.5} & \text{for } 90 \le L \le 300 \\ 10.75 & \text{for } 300 < L \le 350 \\ 10.75 - [(L - 350)/150]^{1.5} & \text{for } 350 < L \le 500 \end{cases} \tag{8.5c}$$

Long-term Wave-induced Loads–Direct Calculations

As previously stated, using a direct method such as strip theory or panel theory, detailed information as to the values and distribution of long-term wave-induced loads along the ship length can be estimated for the anticipated environmental conditions.

The calculation of the hull girder loads in waves requires information related to the time-variant distribution of fluid forces over the wetted surface of the ship hull together with the distribution of the inertia forces. The time-variant fluid forces depend on the wave-induced motions of the water and the corresponding motions of the ship. The distribution of inertia forces is estimated by multiplying the local mass of the ship with the local absolute value of acceleration.

The shear force and bending moment are then obtained at any instant by computing the first and second integrals of the distribution of sectional force per unit length along the ship length, respectively. The wave-induced sectional shear force, $F_w(x_1)$, at location x_1 is then given by

$$F_w(x_1) = \int_0^{x_1} f_w(x)\,dx \tag{8.6a}$$

where $f_w(x) = d_f(x) - d_i(x)$ = net load per unit length in waves, $d_f(x)$ = time-variant fluid force per unit length, $d_i(x)$ = inertia force per unit length.

The wave-induced bending moment is then obtained by the integral of the wave-induced shear force as follows:

$$M_w(x_1) = \int_0^{x_1} F_w(x)\,dx \tag{8.6b}$$

To obtain a part of the time-variant fluid forces and the inertia forces, the wave-induced motions of the ship should be analyzed in advance of the loads themselves. The solutions for these ship motions and the resulting forces are normally obtained using the so-called strip theory. Related procedures may be found in most classification society guidance, and in standard textbooks, e.g., Paulling (1988) and Jensen (2001). The total hull girder loads are then obtained by a relevant sum of the still-water and wave-induced loads as previously noted.

Short-term Wave-induced Loads–Simplified Direct Calculations Using Parametric Seakeeping Tables

The calculations of the extreme wave-induced loads of a ship during a short-term sea state may also be calculated using direct methods. In many cases and within predefined ranges

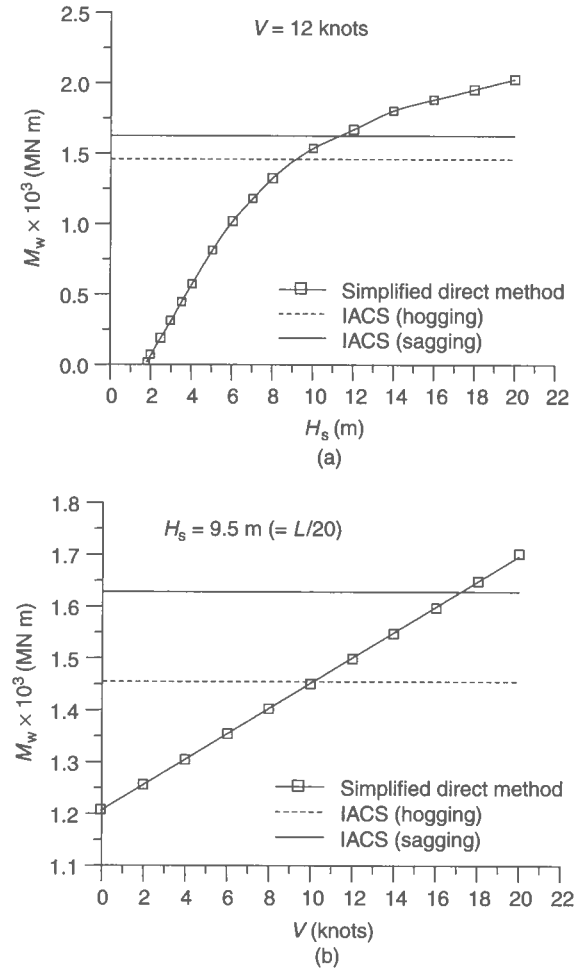

Figure 8.3 Variation of the wave-induced bending moments for a very large crude oil carrier in a 3 hour storm, with increase in (a) the significant wave height and (b) the ship speed as obtained by the simplified direct method (Paik *et al.* 1998)

of validity, time savings in this regard can be achieved by use of parametric seakeeping tables considering variations in ship size, significant wave height and ship speed, such as those developed by Loukakis–Chryssostomidis (1975). The Loukakis-Chryssostomidis seakeeping tables are designed to efficiently determine the rms (root-mean-square) value of the wave-induced bending moment given the values of significant wave height (H_s), B/T ratio (B = ship beam, T = ship draft), L/B ratio (L = ship length), ship operating speed (V), the block coefficient (C_b) and sea-state persistence time.

The most probable extreme value of the wave-induced loads, M_w, i.e., mode, which we may refer to as a mean for convenience, and its standard deviation, σ_w can then be computed based on upcrossing analysis as follows:

$$M_w = \sqrt{2\lambda_0 \ln N} + \frac{0.5772}{\sqrt{2\lambda_0 \ln N}}, \sigma_w = \frac{\pi}{\sqrt{6}}\sqrt{\frac{\lambda_0}{2 \ln N}} \tag{8.7}$$

where $\sqrt{\lambda_0}$ is the rms value of the short-term wave-induced bending moment process; N is the expected number of wave bending peaks. For example, if a peak normally occurs once in every 6–10 seconds, and hence in a 3 hour storm, $N = 3 \times 60 \times 60/10 \approx 1000$.

Figure 8.3 shows an example of the wave-induced bending moment for a very large crude oil carrier obtained by the simplified direct method, varying the effective wave height or the ship speed. The IACS design wave-induced moment values are also compared. It is seen from Figure 8.3(a) that the wave-induced bending moment can theoretically be forced to exceed the IACS design value if the significant wave height is continually increased and the vessel's speed is kept high, which of course are unrealistic assumptions. Figure 8.3(b) shows that the wave-induced bending moments increase nearly linearly with increase in the ship speed. Further, the figure shows that for the present hypothetical ship, the wave-induced bending moment should never exceed the IACS design value for reasonable ship speeds and significant wave heights.

8.3 Basic Properties of Ship Hull Cross-sections

8.3.1 Section Moduli

Since the section modulus of a ship is indicative of the ship's longitudinal strength, all classification societies have established relevant requirements so that the section modulus should be greater than a prescribed value.

Figure 8.4 shows mid-ship cross-sections of typical merchant ships. It is seen that the ship structural characteristics vary significantly depending on the cargo types or missions, among other factors. The classical theory for strength of materials can be used for calculating the elastic section modulus of the ship hull cross-section. In structural modeling, the ship hull cross-section may be regarded as an assembly of a number of either plate–stiffener combination models as shown in Figure 2.2(a) of Chapter 2 or plate–stiffener separation models as shown in Figure 2.2(b).

The section moduli of a ship are often calculated for the two cases, i.e., one with a fully effective section and the other with a partially effective section.

Fully Effective Section

In this case, the neutral axis, g, of the hull cross-section above the base line can be obtained by assuming that all longitudinal strength members are fully effective as follows:

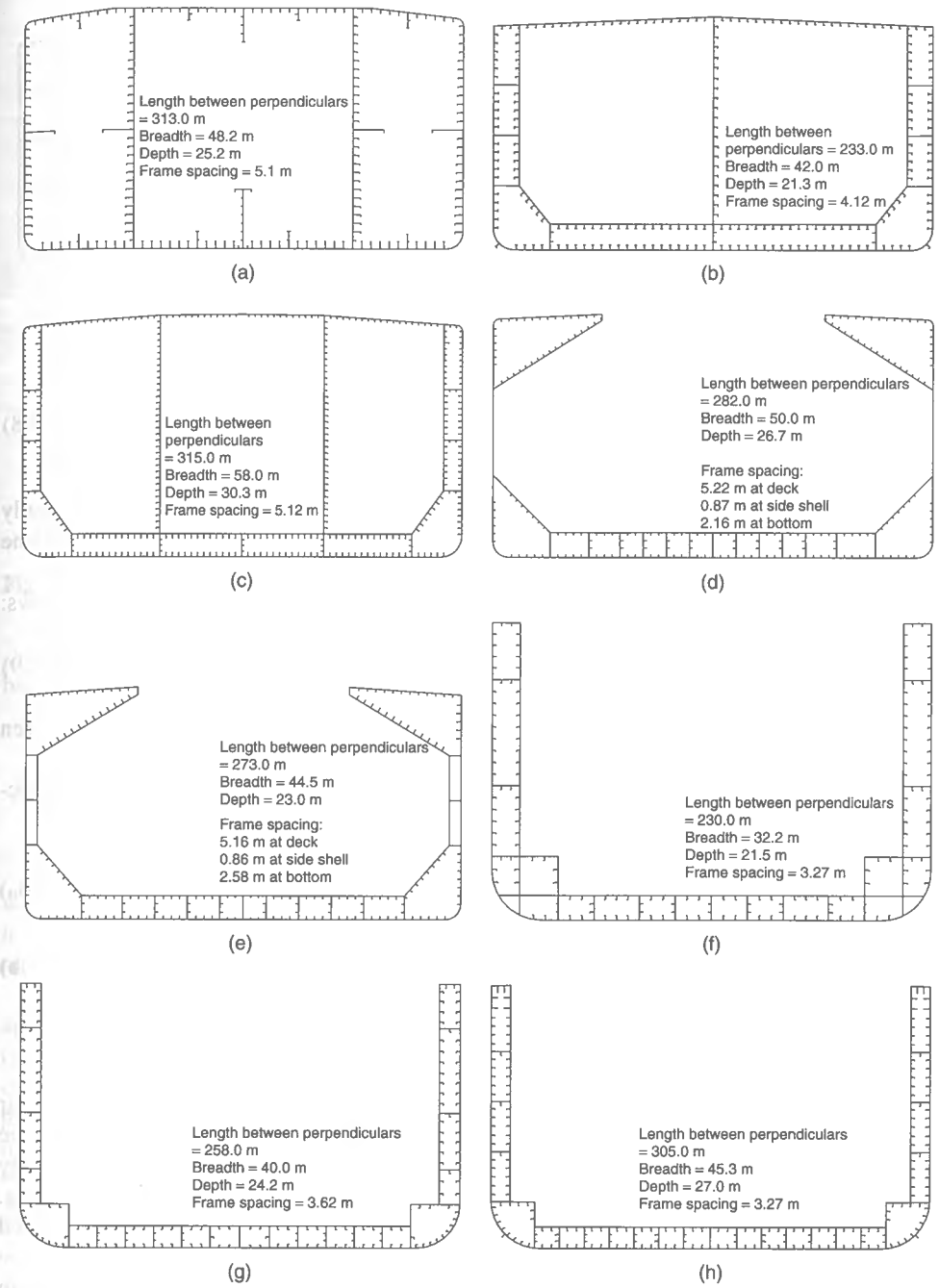

Figure 8.4 Schematic representation of mid-ship sections (TEU = twenty foot equivalent unit): (a) A 254 000 dwt single hull tanker; (b) A 105 000 dwt double hull tanker with one center–longitudinal bulkhead; (c) A 313 000 dwt double hull tanker with two side–longitudinal bulkheads; (d) A 170 000 dwt single skin-sided bulk carrier; (e) A 169 000 dwt double skin-sided bulk carrier; (f) A 3500 TEU container; (g) A 5500 TEU container; (h) A 9000 TEU container; (i) A 113 000 dwt FPSO (floating production storage offloading unit); (j) A 165 000 dwt shuttle tanker

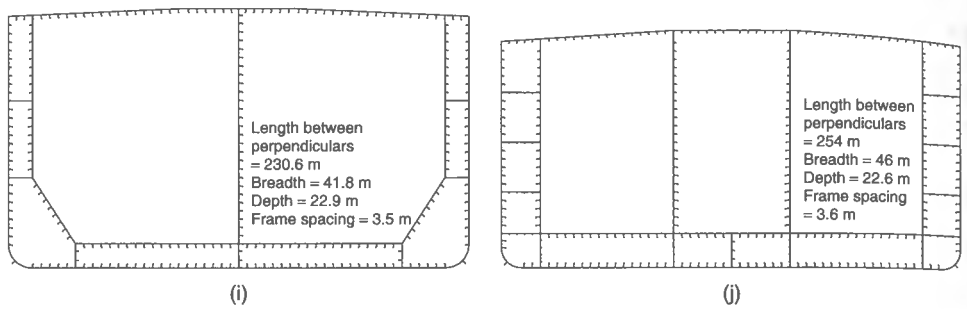

Figure 8.4 (*continued*)

$$g = \frac{\sum A_i z_i}{\sum A_i} \tag{8.8}$$

where A_i = cross-sectional area of the ith plate–stiffener combination member with fully effective attached plating, z_i = coordinate of the ith member measured from the base line to the deck since $z = 0$ is taken at the base line.

Therefore, the moment of inertia, I_y, of the hull cross-section is calculated as follows:

$$I_y = \sum A_i (z_i - g)^2 + \sum i_{yi} \tag{8.9}$$

where i_{yi} = local moment of inertia for each member (e.g., stiffener, plating between stiffeners) with regard to its own neutral axis.

The section moduli at the deck or bottom shells, being denoted by Z_D or Z_B, respectively, can then be given by

$$Z_D = \frac{I_y}{D - g} \tag{8.10a}$$

$$Z_B = \frac{I_y}{g} \tag{8.10b}$$

Partially Effective Section

As the design hull girder loads increase, some structural members may typically lose their effectiveness because of buckling. To account for this effect, the section moduli can be computed using an effective hull cross-section that represents the load-carrying capacity given the buckled state of one or more of the members depending on the applied loading.

When a vertical bending moment is applied with regard to the neutral axis, g, as defined in Equation (8.8), the longitudinal stress distribution over the hull cross-section may be obtained as shown in Figure 8.5. Because of the nature of vertical bending, the stress in one part is tensile while that in the other part is compressive. In a sagging condition, for instance, the upper part, i.e., above the neutral axis, is in compression, while the corresponding lower part, i.e., below the neutral axis, is in tension, and vice versa in hogging. It is considered that the effectiveness of the compressed members may be possibly reduced, while the structural members subject to tension may keep full effectiveness.

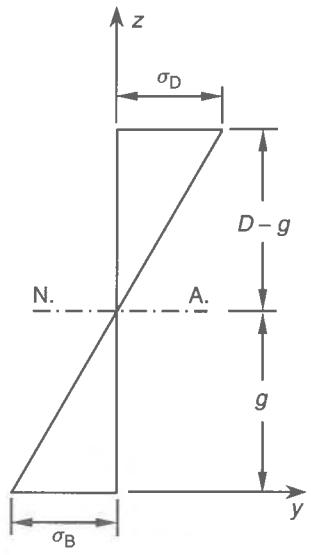

Figure 8.5 Idealized longitudinal stress distribution in a hull section

In this case, the neutral axis, g_e, of the partially effective hull cross-section above the base line can be obtained by

$$g_e = \frac{\sum_C A_{ei} z_i + \sum_T A_j z_j}{\sum_C A_{ei} + \sum_T A_j} \tag{8.11}$$

where A_{ei} = effective cross-sectional area of the ith member, A_j, z_i or z_j are as defined in Equation (8.8), $\sum_C (\,)$, $\sum_T (\,)$ = summation for the part in compression or tension, respectively.

In calculating Equation (8.11), A_{ei} may be calculated using the effective plate width approach. For this purpose, most ship classification societies have employed the Faulkner-type effective width formula, Equation (4.21c), in Chapter 4. For ship structures with certain types of degradation (e.g., collision or grounding damage) which may result in parts of the structure being entirely ineffective for sustaining external loads, the section modulus calculations may be made by excluding the damaged members located in both the tension and compression parts.

For the effective hull cross-section, the moment of inertia, I_{ey}, is then given by

$$I_{ey} = \sum_C A_{ei} (z_i - g_e)^2 + \sum_T A_j (z_j - g_e)^2 + \sum i_{eyi} \tag{8.12a}$$

where i_{eyi} = effective local moment of inertia for each member with regard to its own neutral axis.

In design, the moment of inertia calculated from Equation (8.12a) must be greater than the prescribed minimum requirement value, which is given by IACS only for an intact

section as follows:

$$I_{\min} = 3C_1 L^3 B(C_b + 0.7)(\text{cm}^4) \tag{8.12b}$$

where L, B, C_1, C_b are as defined in Equations (8.5).

The effective section moduli at the deck or bottom plating, being denoted by Z_{De} or Z_{Be}, respectively, can be obtained by

$$Z_{De} = \frac{I_{ey}}{D - g_e} \tag{8.13a}$$

$$Z_{Be} = \frac{I_{ey}}{g_e} \tag{8.13b}$$

With the allowable bending stress limited to $175/K$(MPa) considering the various loading conditions and the associated total bending moment, the smaller value of the two section moduli above is taken as the reference section modulus of the ship which is required to be greater than the IACS minimum requirement value, $Z_{\min}$, given for an intact section as follows:

$$Z_{\min} = C_1 L^2 B(C_b + 0.7)K(\text{cm}^3) \tag{8.13c}$$

where K = high tensile steel factor which is taken as $K = 1.0$ for ordinary mild steel, $K = 0.78$ for grade H32 high tensile steel, $K = 0.72$ for grade H36 high tensile steel and $K = 0.68$ for grade H40 high tensile steel per IACS unified requirements.

8.3.2 Full Plastic Bending Capacity

It is sometimes of interest to know the full plastic bending capacity of the ship hull cross-section, although this is largely a seldom realized property. The axial stress distribution over the hull cross-section at the fully plastic state is similar to that of the plate–stiffener combination shown in Figure 2.9 of Chapter 2.

Under pure vertical bending, the following condition must be satisfied since no net axial force acts on the hull, namely

$$\int \sigma_x \, dA = 0 \tag{8.14a}$$

where σ_x = longitudinal axial stress over the elemental area, dA.

The neutral axis, g_p, of the fully plastic cross-section above the base line can then be obtained as follows:

$$g_p = \frac{\sum A_i \sigma_{Yi} z_i}{\sum A_i \sigma_{Yi}} \tag{8.14b}$$

where σ_{Yi} = yield stress of the ith member.

The full plastic bending capacity, M_p, of the ship hull cross-section is then calculated as follows:

$$M_p = \sum A_i \sigma_{Yi} |z_i - g_p| \tag{8.14c}$$

For damaged ship hulls, the procedure noted above may use the reference axis that is parallel to the original principal axis in the undamaged condition, because the strength safety checks normally involve moments taken about those orientations. But such a use, while adequate for both symmetric cases of damage and cases involving limited amounts of unsymmetric damage, may require appropriate modification where there is extensive unsymmetrical damage, see Maestro & Marino (1988).

8.4 Progressive Collapse Behavior of Ship Hulls

The approaches for the progressive collapse analysis of ship hull structures may be classified into two groups, namely

- the conventional nonlinear finite element method
- the simplified (special purpose) nonlinear finite element method.

The conventional nonlinear finite element method which will be presented later in Chapter 12 can be used to analyze the detailed nonlinear response of ship structures which involves both geometric and material nonlinearities until and after the overall hull girder collapse is reached. While the application of the conventional nonlinear finite element method to the progressive collapse analysis of ship hulls is not difficult, it is usually impractical on a routine basis because of the huge amount of computational cost involved.

An alternative to reduce modeling efforts and computing time in nonlinear finite element analyses is to reduce the number of degrees of freedom. Modeling the object structure with very large-sized structural units is perhaps the best way to do that. Properly formulated structural units in such an approach can then be used to efficiently model the actual nonlinear behavior of large structural units. Ueda & Rashed (1974, 1984), who suggested this idea, called it the idealized structural unit method (ISUM) when they attempted to analyze the ultimate strength of a ship transverse-framed structure using the so-called deep girder unit. As will be presented later in Chapter 13, several different types of ISUM units such as the beam–column unit (also called the plate–stiffener combination unit), the rectangular plate unit and the stiffened panel unit have so far been developed. Smith (1977) has also developed a related method.

As will be presented in Chapter 13, the ISUM theory to analyze the progressive collapse behavior of ship hulls is automated within the computer program ALPS/HULL. This section deals with the progressive collapse behavior of different types of ship hulls shown in Figure 8.4, as calculated by ALPS/HULL. For more details see Paik *et al.* (2002).

8.4.1 Single Hull Tanker

Figure 8.6(a) shows the ALPS/HULL model for a hypothetical 254 000 dwt single hull tanker shown in Figure 8.4(a). The model in this case extends between web frames. While it would be more relevant to take the hull module between transverse bulkheads as the extent of the analysis, the present simpler model between web frames may also be appropriate as long as the transverse frames are strong enough so that they would not fail prior to the longitudinal members. This assumption is usually adequate for the hull of a

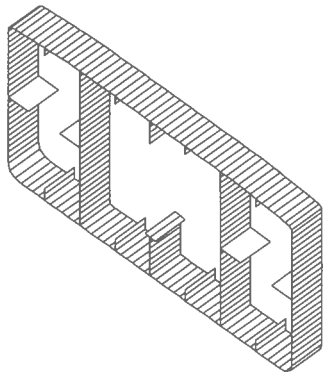

(a)

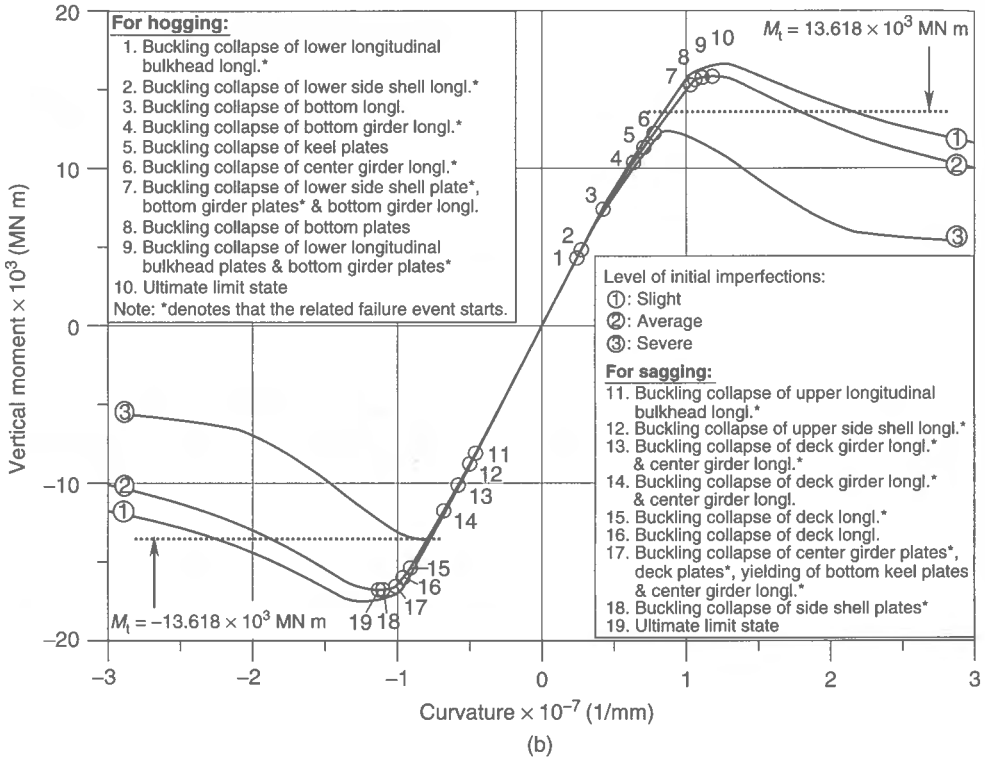

(b)

Figure 8.6 (a) ALPS/HULL model for the single hull tanker (number of plate units = 237, number of stiffened panel units = 2, number of beam–column units = 210); (b) Progressive collapse behavior of a 254 000 dwt single hull tanker under vertical moment, varying the level of initial imperfections, as obtained by ALPS/HULL (M_t = total extreme bending moment predicted by the IACS formula); (c) Variation of the neutral axis due to structural failure for a 254 000 dwt single hull tanker, as obtained by ALPS/HULL (for numerals, see Figure 8.6(b))

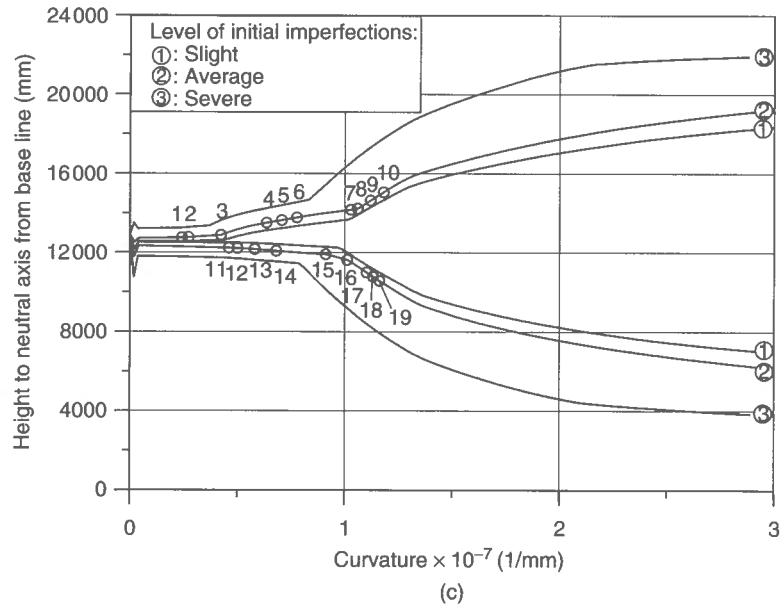

(c)

Figure 8.6 (*continued*)

predominantly longitudinally framed vessel under a vertical bending moment, as will be described in Section 13.11.2 of Chapter 13.

In the ALPS/HULL computations, deck or bottom stiffened panels as well as vertical members (i.e., side shells and longitudinal bulkheads) are modeled by plate–stiffener separation models as assemblies of the ISUM rectangular plate units and the ISUM beam–column units, the latter being used without attached plating, as shown in Figure 8.6(a). This modeling method more accurately represents the vertical bending stress distribution at vertical members or the horizontal bending stress distribution at horizontal members (i.e., deck or bottom panels), since plating between longitudinal support members in typical merchant ship structures may normally fail prior to longitudinal support members. In Figure 8.6(a), the beam–column units are depicted by lines. However, bottom keel plates with stiffeners are modeled by ISUM stiffened panel units. The total numbers of the ISUM plate units, stiffened panel units and beam–column units are 237, 2 and 210, for this specific single skin tanker hull, respectively.

It is considered in the calculations that the structural units have fabrication-related initial imperfections (weld distortions and residual stresses). The longitudinal stiffeners have initial imperfections which are considered to be $w_{0sx} = 0.0015a$ and $\sigma_{rsx} = 0.0$, where w_{0sx} = maximum initial deflection of longitudinal stiffeners, a = length of the stiffener (between transverse frames), σ_{rsx} = residual stress of the stiffener. For plating between longitudinal stiffeners, the level of initial imperfections is varied for three levels, namely 'slight', 'average' and 'severe', as defined in Equations (1.11d) and (1.15) of Chapter 1.

Figure 8.6(b) represents the progressive collapse behavior of the single skin tanker hull under vertical hogging or sagging moment, varying the level of initial imperfections. Some selected typical failure events are represented in the figure. Figure 8.6(c)

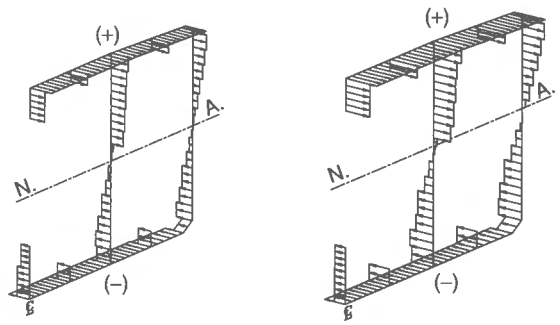

(a) Loading step 1 (b) Loading step 10

Figure 8.7 Variation of the longitudinal stress distribution during the progressive collapse under hogging moment (+, tension; −, compression), as obtained by ALPS/HULL

shows the variation of the neutral axis of the ship hull due to structural failure. The numerals in Figures 8.6(b) and (c) represent the onset of the failure events as predicted by ALPS/HULL.

It is apparent from Figure 8.6(b) that the collapse of the compression flange of the ship hull takes place prior to the yielding of the tension flange as expected. The initial imperfections can measurably affect the progressive collapse behavior of the ship hull. Also, there is still some residual strength even after some buckling collapse of the compression flange. This is due to a shift of the neutral axis toward the tension flange, resulting from loss of effectiveness of the collapsed compression flange as shown in Figure 8.6(c). It is of interest that, as the bending moment increases, the neutral axial position is changed quickly and becomes stable, as shown in Figure 8.6(c). The effective neutral axis is calculated for the partially effective hull cross-section after the bending moment is applied and loss of effectiveness occurs in the cross-section, while it is estimated for the fully effective cross-section before loading. This implies that the section moduli calculated for the fully effective hull cross-section may not always be a real indication of the ship hull sectional resistance. The ultimate hogging moment of the tanker hull is larger than the ultimate sagging moment as usual, since the bottom part is heavier than the deck part.

Figure 8.7 shows examples of the variation of the hull girder longitudinal stress distribution during the progressive collapse. It is generally observed that the ship reaches its ULS if both collapse of the flange and side shell in compression and yielding of the other flange in tension occur. In this situation, the side shell in the vicinity of the neutral axis can still remain in a linear elastic state. It is also noted that first yielding can in some cases occur after the buckling of the compression flange, depending on the specifics of the design.

8.4.2 Double Hull Tanker with Two Side–Longitudinal Bulkheads

Figure 8.8(a) shows the ALPS/HULL model for a hypothetical 313 000 dwt double hull tanker with two side–longitudinal bulkheads as shown in Figure 8.4(c). The method for structural modeling including initial imperfections is similar to that of the single hull tanker described in Section 8.4.1. The total numbers of ISUM plate units and beam–column units are 440 and 392, respectively.

Figure 8.8(b) represents the progressive collapse behavior of the ship hull under vertical moments, varying the level of initial imperfections. Some selected typical failure events

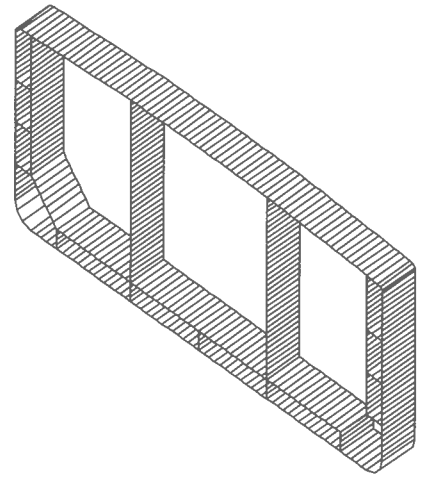

(a)

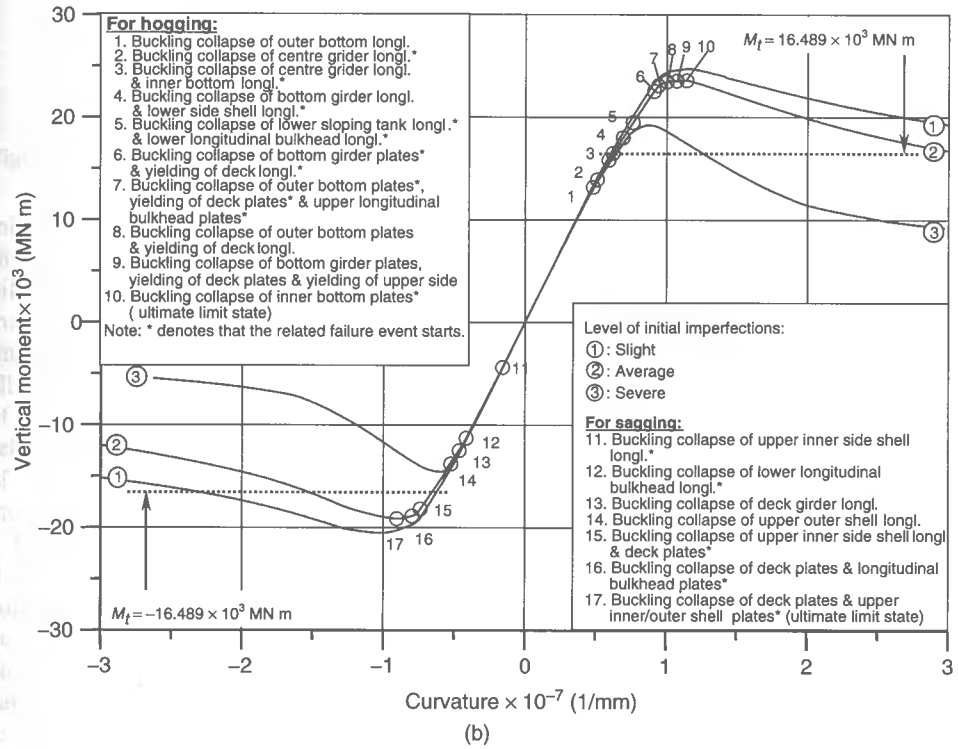

(b)

Figure 8.8 (a) ALPS/HULL model for a 313 000 dwt double hull tanker with two side–longitudinal bulkheads (number of plate units = 440, number of beam–column units = 392); (b) Progressive collapse behavior of a 313 000 dwt double hull tanker with two side–longitudinal bulkheads under vertical moment, varying the level of initial imperfections, as obtained by ALPS/HULL (M_t = total extreme bending moment predicted by the IACS formula)

are represented in the figure. As is apparent from Figure 8.8(b), buckling collapse of the compression flange takes place prior to yielding of the tension flange.

8.4.3 Single Skin-sided Bulk Carrier

Figure 8.9(a) shows the ALPS/HULL model for a hypothetical 170 000 dwt single skin-sided bulk carrier as shown in Figure 8.4(d). The method for structural modeling including

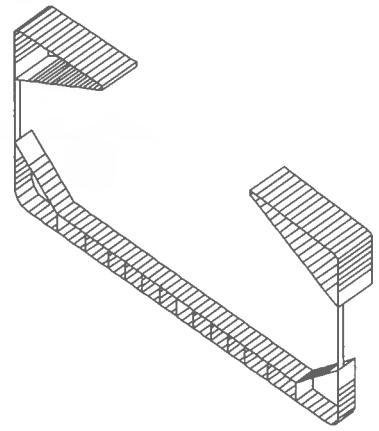

(a)

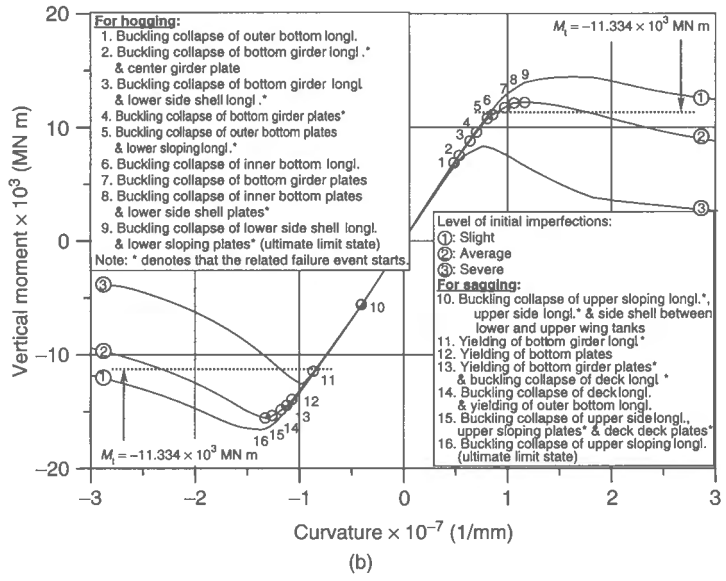

(b)

Figure 8.9 (a) ALPS/HULL model for a 170 000 dwt single skin-sided bulk carrier, the transverse frame spacing being different at deck, side and bottom (number of plate units = 245, number of stiffened panel units = 3, number of beam–column units = 392); (b) Progressive collapse behavior of a 170 000 dwt single skin-sided bulk carrier under vertical moment, varying the level of initial imperfections, as obtained by ALPS/HULL (M_t = total extreme bending moment predicted by the IACS formula); (c) Variation of the neutral axis due to structural failure for a 170 000 dwt single skin-sided bulk carrier, as obtained by ALPS/HULL

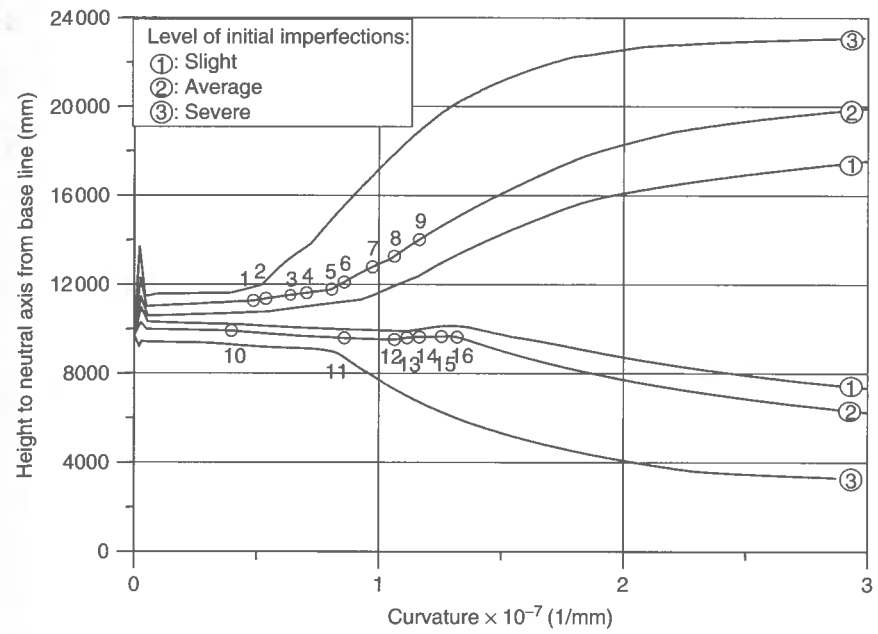

(c)

Figure 8.9 (*continued*)

initial imperfections is similar to that of the single hull tanker described in Section 8.4.1. In bulk carriers, however, the spacing of transverse frames (or floors) at the bottom part is different from that at the deck or at side shells. Thus the length of the related ISUM units may differ, as is evident in Figure 8.9(a). It is assumed that the ISUM units have initial imperfections in the form of initial deflection and welding residual stresses, again applied to all structural members. Figure 8.9(b) represents the predicted progressive collapse behavior of the ship hull under vertical moments, varying the level of initial imperfections. Some selected typical failure events are represented in the figure. Figure 8.9(c) shows the variation of the neutral axis position due to the structural failure events as the applied bending moment increases.

In contrast to the tanker hulls described in Sections 8.4.1 and 8.4.2, the tension flange (i.e., bottom plates) of the bulk carrier hull under sagging moment yields prior to buckling collapse of the compression flange (i.e., deck plates). In the hogging condition, however, buckling collapse of the compression flange (i.e., bottom plates) takes place prior to yielding of the tension flange (i.e., deck plates). This is because the deck panels of this particular bulk carrier are sturdier than the bottom panels. Regardless of this, the elastic section modulus at the bottom is of course much larger than that at the deck, in part because the bulk carrier has large deck openings. It is, however, less consistent with the ultimate strength characteristics.

8.4.4 9000 TEU Container

Figure 8.10(a) shows the ALPS/HULL model for a hypothetical 9000 TEU container as shown in Figure 8.4(h). The method for structural modeling including initial imperfections

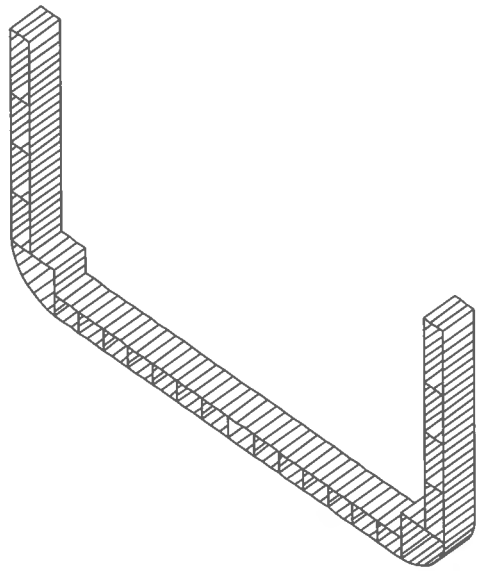

(a)

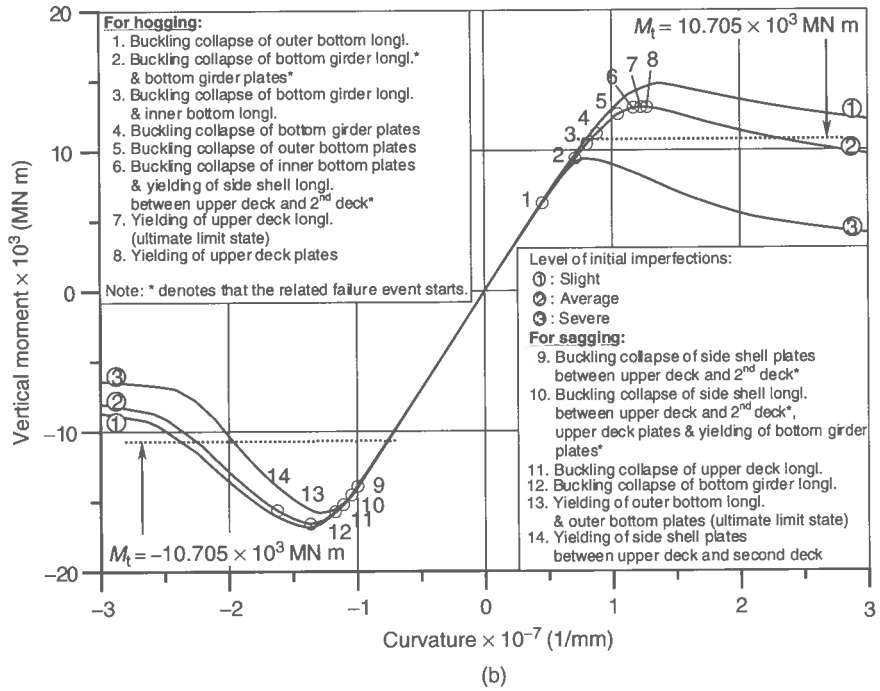

(b)

Figure 8.10 (a) ALPS/HULL model for a 9000 TEU container (number of plate units = 277, number of stiffened panel units = 2, number of beam–column units = 206); (b) Progressive collapse behavior of a 9000 TEU container under vertical moment, varying the level of initial imperfections, as obtained by ALPS/HULL (M_t = total extreme bending moment predicted by the IACS formula); (c) Variation of the neutral axis due to structural failure for a 9000 TEU container, as obtained by ALPS/HULL

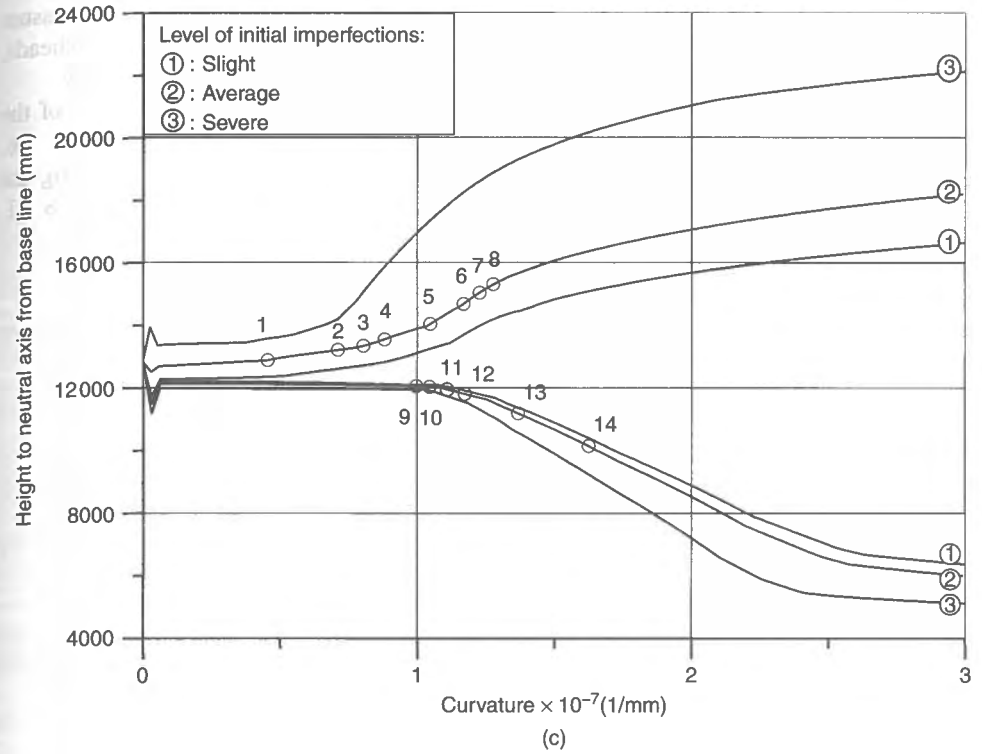

(c)

Figure 8.10 (*continued*)

is similar to that of the single hull tanker described in Section 8.4.1. The total numbers of ISUM plate units, stiffened panel units and beam–column units are 277, 2 and 206, respectively.

Figure 8.10(b) represents the predicted progressive collapse behavior of the ship hull under vertical moments, varying the level of initial imperfections. Some selected failure events are represented in the figure. In contrast to the usual behavior of tanker structures, it was observed that the deck panels under axial compressive loads in the sagging condition did not buckle and reach the ultimate strength by gross yielding. This is because the deck panels are very stocky with large plate thickness. Figure 8.10(c) shows the variation of the neutral axis position due to structural failure events as the bending moment increases.

8.4.5 Effect of Lateral Pressure on Ultimate Vertical Moment

The effect of lateral pressure on the ultimate hull girder strength is now investigated for selected ship hulls under vertical moment. The ALPS/HULL models previously used for progressive collapse analysis without lateral pressure are employed. The outer water pressure applied is calculated from the class society design rules (ABS 2000) using the heavy ballast condition, taking into account the dynamic load effects in a head sea state. The effects of water pressure inside the ballast tanks are not considered for convenience of the present calculations.

Figures 8.11(a) to (c) show schematic representations of the applied water pressure distributions for the 313 000 dwt double hull tanker with two side–longitudinal bulkheads, the 170 000 dwt single-sided bulk carrier and the 9000 TEU container, respectively.

To illustrate the effects of water pressure on the progressive collapse behavior of the ship hulls under vertical moments, the level of water pressure is artificially varied at 0%, 100% and 200% of the design water pressure. The initial imperfections for plating are fixed at the 'average' level, while those for stiffeners are taken as defined in Section 8.4.1.

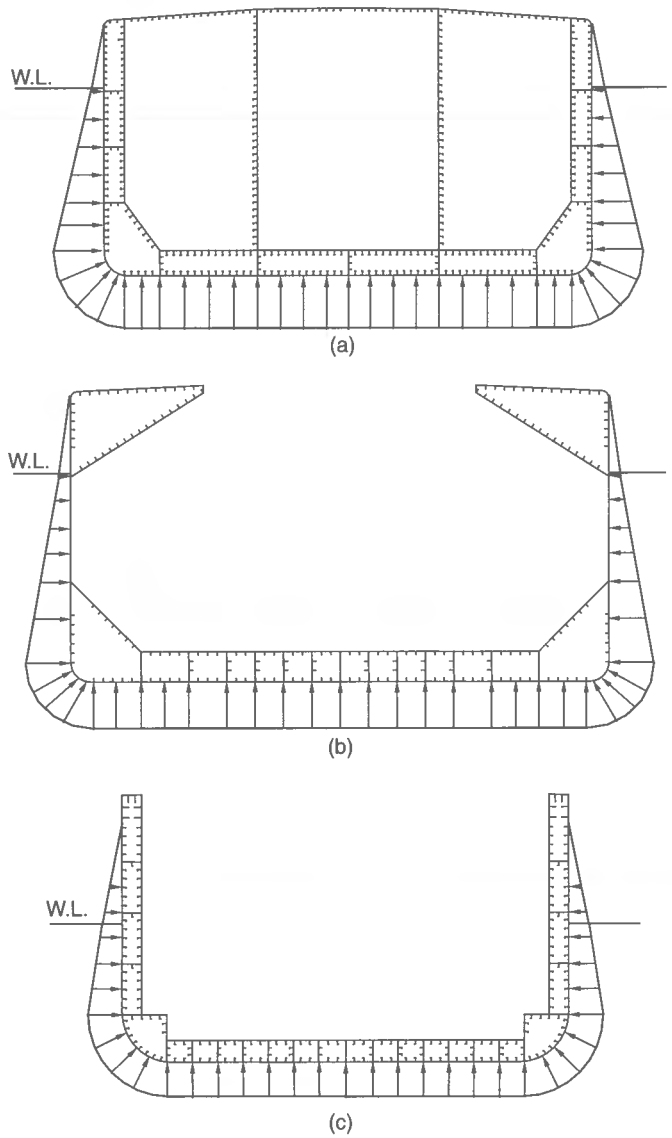

Figure 8.11 (a) 313 000 dwt double hull tanker with two side–longitudinal bulkheads; (b) 170 000 dwt single skin-sided bulk carrier; (c) 9000 TEU container – schematics of design water pressure distributions in the heavy ballast condition in a head sea state (W.L. = water line)

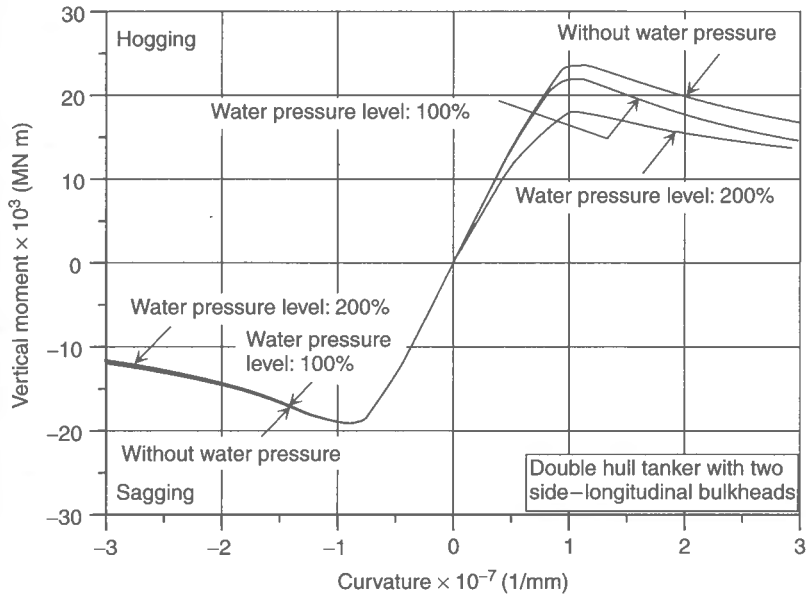

(a)

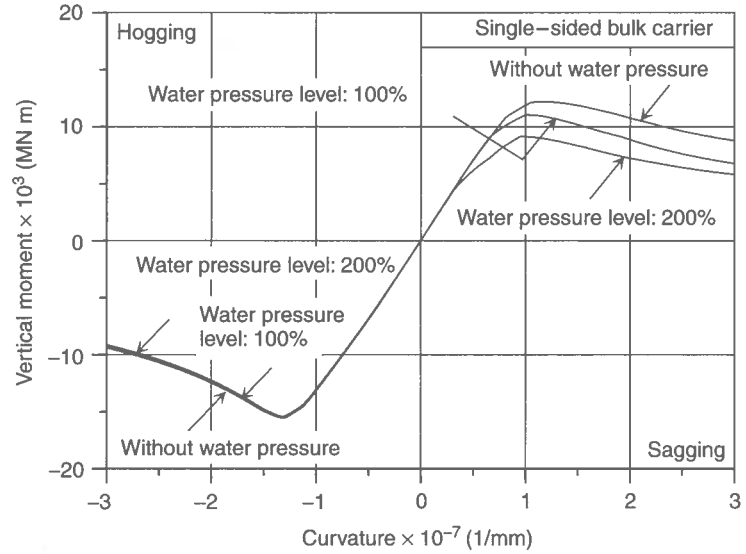

(b)

Figure 8.12 (a) Progressive collapse behavior of the 313 000 dwt double hull tanker with two side–longitudinal bulkheads under vertical moment, varying the magnitude of water pressure, as obtained by ALPS/HULL; (b) Progressive collapse behavior of the 170 000 dwt single skin-sided bulk carrier under vertical moment, varying the magnitude of water pressure, as obtained by ALPS/HULL; (c) Progressive collapse behavior of the 9000 TEU container under vertical moment, varying the magnitude of water pressure, as obtained by ALPS/HULL; (d) Variation of the ultimate hull girder strengths as a function of the magnitude of water pressure

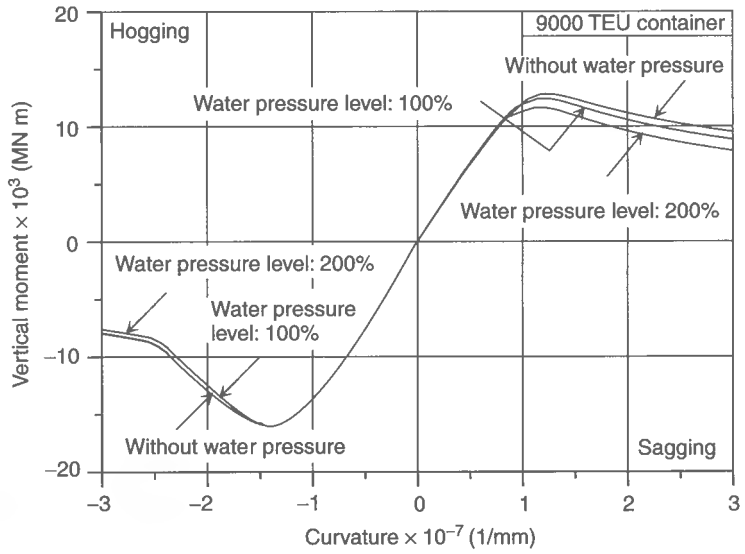

(c)

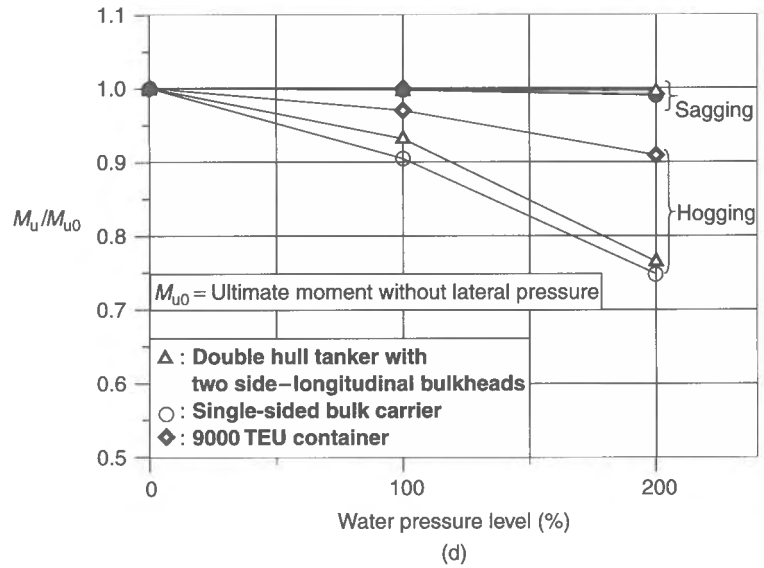

(d)

Figure 8.12 (*continued*)

In the present ALPS/HULL calculations, it is assumed that the lateral pressure is applied to the individual structural members in the same direction as the initial deflections.

Figures 8.12(a) to (c) show the predicted progressive collapse behavior of the three ship hulls under the vertical moment, varying the lateral pressures, sometimes at unrealistic levels as previously noted. Figure 8.12(d) represents the variation of the ultimate hull girder strengths as a function of the water pressure magnitude applied. The effectiveness of plates under compression is normally reduced by lateral pressure loading. In the case

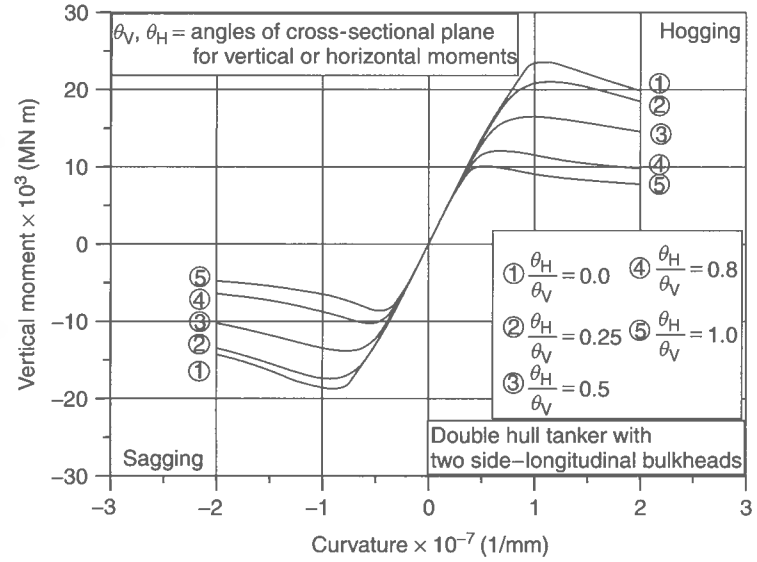

(a)

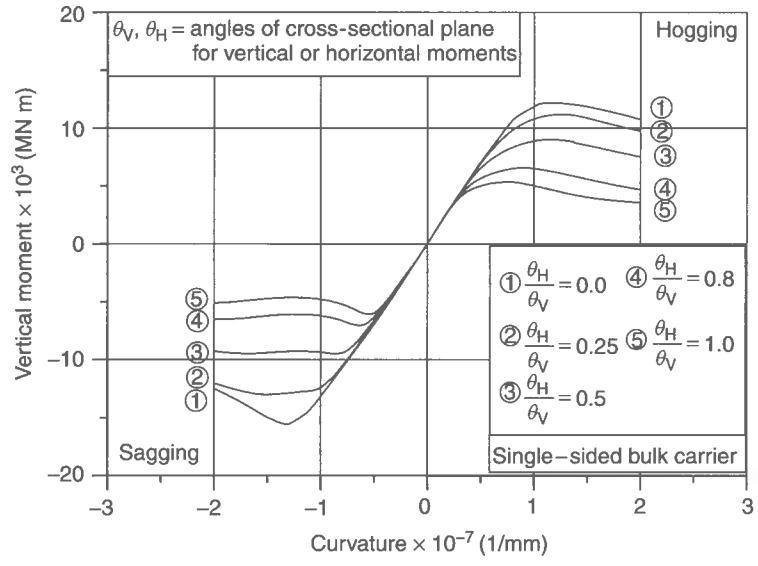

(b)

Figure 8.13 (a) Progressive collapse behavior of the 313 000 dwt double hull tanker with two side–longitudinal bulkheads under combined vertical and horizontal moments, as obtained by ALPS/HULL; (b) Progressive collapse behavior of the 170 000 dwt single skin-sided bulk carrier under combined vertical and horizontal moments, as obtained by ALPS/HULL; (c) Progressive collapse behavior of the 9000 TEU container under combined vertical and horizontal moments, as obtained by ALPS/HULL; (d) Ultimate hull girder strength interaction relationships between vertical and horizontal moments (symbols: ultimate strength obtained by ALPS/HULL)

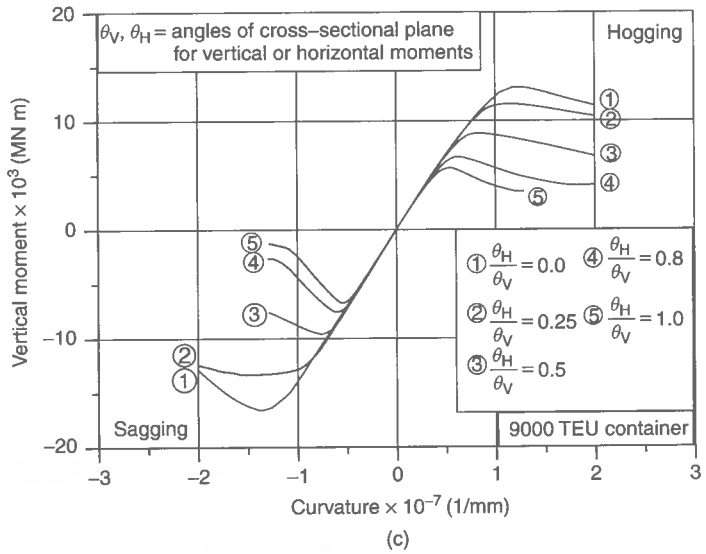

(c)

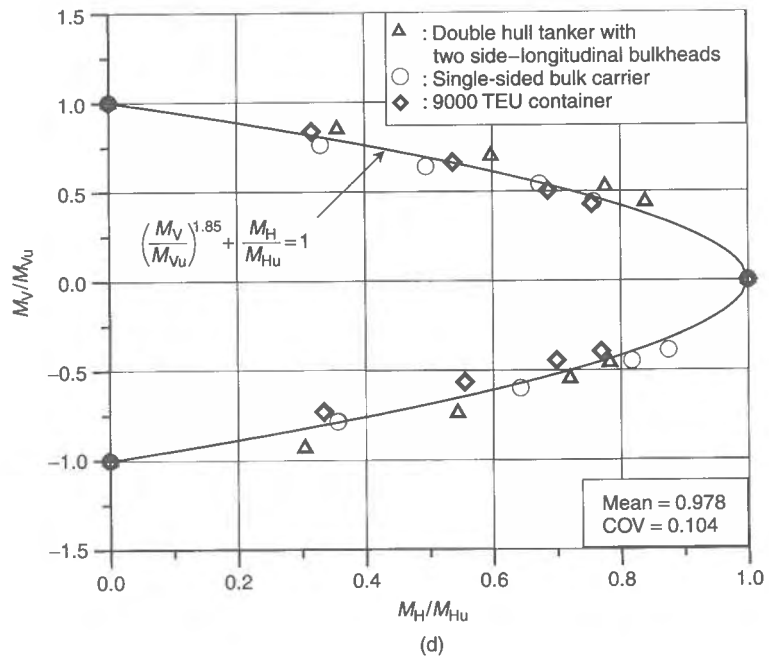

(d)

Figure 8.13 (*continued*)

of the hull girder, this is primarily due to the shear lag effect. When the amount of lateral pressure is large, therefore, the ultimate strength of ship hulls can be possibly smaller than that without lateral pressure.

In calculating the ultimate capacity of ship hulls, the lateral-pressure-related shear lag effect can approximately be taken into account so that the ultimate stress or the effectiveness (i.e., effective width/breadth) of individual structural members is predicted

considering lateral pressure as another load component, see Section 2.5 in Chapter 2 or the second subsection in Section 4.8.1 in Chapter 4.

The effect of lateral water pressure on the ultimate hull girder capacity under hogging moment can be of significance, while under sagging moment the effects appear to be small. This is because sea water is applied mainly to ship bottom or lower side structures which are compressed in hogging in the present calculations. For different loading conditions, the distributions of internal pressure as well as external pressure may be varied so that their effects on the progressive collapse behavior of ship hulls will of course be different.

8.4.6 Effect of Horizontal Moment on Ultimate Vertical Moment

The effect of horizontal moment on the ultimate hull girder strength is now investigated for selected hypothetical ship hulls. The initial imperfections for plating are fixed at the 'average' level, while those for stiffeners are taken as previously defined in Section 8.4.1. Water pressure is not applied.

Figures 8.13(a) to (c) show the progressive collapse behavior of the 313 000 dwt double hull tanker with two side–longitudinal bulkheads, the 170 000 dwt single skin-sided bulk carrier and the 9000 TEU container, respectively. Figure 8.13(d) represents the ultimate hull girder interaction relationship between vertical and horizontal moments so obtained. It is seen that the influence of horizontal moment on the ultimate vertical bending capacity is of significance.

8.5 Closed-form Ultimate Hull Girder Strength Design Formulations

While the nonlinear analysis approaches noted in Section 8.4 may be more relevant for the detailed calculation of the ultimate hull girder strengths in specific cases, closed-form expressions are always beneficial for the more efficient implementation of the ULS design and for the reliability analysis.

8.5.1 Ultimate Vertical Moment

Many ultimate hull strength design formulations under vertical bending have been suggested in the literature. Existing studies on the development of a design formula for the ultimate hull strength prediction may be classified into three approaches, namely

- the analytical approach
- the empirical approach
- the linear (knock-down factor) approach.

The analytical approach is based on an assumed stress distribution over the hull section, from which the moment of resistance of the hull is theoretically calculated taking into account buckling in the compression flange and yielding in the tension flange. In the empirical approach, an expression for strength is derived on the basis of experimental or numerical data for hull models. In the linear approach, the behavior of the hull up to collapse of the compression flange is assumed to be linear, and the ultimate moment

capacity of the hull is basically expressed as the ultimate strength of the compression flange multiplied by the elastic section modulus with a simple correction for buckling and yielding.

The linear (knock-down factor) approach is quite simple, but its accuracy may not always be good because after buckling of the compression flange, the behavior of the hull is then no longer necessarily linear and the neutral axis changes position. Empirical formulations may provide reasonable solutions for conventional ship hulls, but one has to be careful in using empirical formulations for new or unusual hull types and characteristics since they are usually derived on the basis of limited data. On the other hand, analytical formulations can be applied with somewhat greater certainty to new or general hulls because they include section geometry and other effects more precisely.

Linear Approach

It is assumed that the ship hull would reach the ULS when the compression flange, i.e., the upper deck in the sagging condition or the bottom plating in the hogging condition, collapses, and that the relationship between the bending moment and curvature is linear. On the basis of these assumptions, the following expression for predictions of the hull girder ultimate strength, M_u, is given as follows:

$$M_u = kZ\sigma_u \tag{8.15}$$

where σ_u = ultimate stress of the compressed flange, Z = section modulus of the hull at the compressed flange (i.e., deck in sagging or bottom in hogging), k = coefficient accounting for the shift of the neutral axis by local buckling or other factors (usually obtained by correlation with more sophisticated analyses).

Empirical Approach

The hull girder ultimate strength formula is derived by curve fitting based on the relevant existing data for the ultimate strength of ships. One such empirical formulation was derived by Frieze & Lin (1991) as a function of the ultimate strength of the compressed flange as follows:

$$\frac{M_u}{M_p} = C_1 + C_2\frac{\sigma_u}{\sigma_Y} + C_3\left(\frac{\sigma_u}{\sigma_Y}\right)^2 \tag{8.16a}$$

where M_p is as defined in Equation (8.14c), σ_u = ultimate stress of the compression flanges, σ_Y = yield stress.

On the basis of experimental and numerical results for scaled hull models, the coefficients C_1–C_3 were given depending on the mode of vertical bending as follows:

$$C_1 = -0.172, \quad C_2 = 1.548, \quad C_3 = -0.368 \quad \text{for sagging} \tag{8.16b}$$

$$C_1 = \quad 0.003, \quad C_2 = 1.459, \quad C_3 = -0.461 \quad \text{for hogging} \tag{8.16c}$$

Analytical Approach

In this approach, an appropriate distribution of longitudinal stresses in the ship hull cross-section at the state of overall hull girder collapse is first assumed. The ultimate moment

capacity is then obtained by integrating the first moment of the longitudinal stresses with regard to the neutral axis.

There have been several suggestions related to the assumption of the longitudinal stress distribution over the ship hull cross-section at the ULS. For instance, Caldwell (1965) made an assumption that the material in compression has reached its ultimate buckling strength, while that in tension has sustained full yielding. (The ultimate strength of the compressed flange is not necessarily the same as that of the side shell.)

As previously noted in Section 8.4, however, it has been recognized that the ship hull reaches the ULS even before the material in tension yields fully or that in compression collapses entirely. Although the overall collapse of a ship hull under vertical bending moment is initiated and governed by collapse of the compression flange, there can still be some reserve strength beyond collapse of the compression flange. This is because, after buckling of the compression flange occurs, the neutral axis of the hull cross-section moves toward the tension flange and a further increase of the applied bending moment is normally sustained until the tension flange yields. At later stages of this process, the side shell around the compression and the tension flanges will also fail. Therefore, Caldwell's pioneering suggestion for the longitudinal stress distribution at the hull girder ULS may overestimate the actual ultimate bending capacity of a ship hull.

Paik & Mansour (1995) proposed a more refined suggestion for the longitudinal stress distribution over a ship hull cross-section at the state of overall collapse as that shown in Figure 8.14. The longitudinal stress distribution shown in Figure 8.14 resembles that of Figure 8.7(b) obtained for a single hull tanker. As may be seen from Figures 8.7(b) and 8.14, the compression flange has collapsed and the tension flange has yielded at the moment the ultimate strength is reached, but the side shell in the vicinity of the neutral axis is still intact (linear elastic).

From Figure 8.5, the longitudinal axial strain of the ith longitudinal strength member in the effective hull cross-section which is assumed to remain plane may be given by one

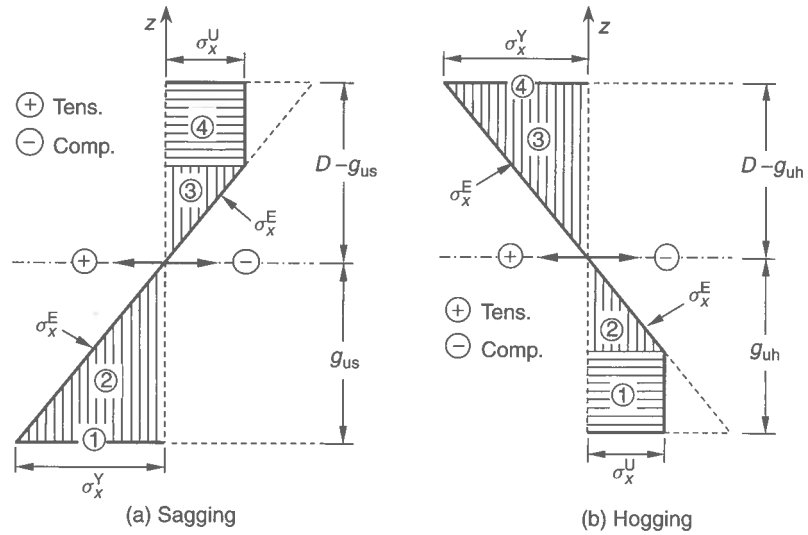

Figure 8.14 Longitudinal stress distribution over the hull cross-section at the overall collapse state as suggested by Paik & Mansour (1995)

of the following two equations which are in fact identical:

$$\varepsilon_{xi} = \frac{\sigma_B}{E_i}\left(1 - \frac{z_i}{g_e}\right) \tag{8.17a}$$

$$\varepsilon_{xi} = \frac{\sigma_D}{E_i(D - g_e)}(z_i - g_e) \tag{8.17b}$$

where g_e is as defined in Equation (8.11), σ_B, σ_D = axial stresses at the bottom or deck plating, E_i, ε_{xi} = Young's modulus or axial strain of the ith longitudinal strength member.

Once the axial strain, ε_{xi}, is determined, the longitudinal axial stresses, σ_{xi}, of the ith longitudinal strength member may be obtained as follows:

$$\sigma_{xi} = E_i\varepsilon_{xi} \le \sigma_{Yi} \tag{8.18}$$

It is assumed that overall collapse of a ship hull girder takes place when the axial stress at the tension flange (i.e., either bottom plating in sagging or deck plating in hogging) reaches the material yield stress, while the region in compression has collapsed. The longitudinal stress distribution at the ULS may thus be divided into four regions, namely (1) the yielded region, (2) the elastic tension region, (3) the elastic compression region and (4) the collapsed compression region, as shown in Figure 8.14.

In the sagging condition as shown in Figure 8.14(a), the neutral axis, g_{us}, above the base line at the ULS can be calculated as follows:

$$g_{us} = \frac{\sum_1 \sigma_{xi}^Y A_i z_i + \sum_2 \sigma_{xj}^E A_j z_j + \sum_3 \sigma_{xk}^E A_{ek} z_k + \sum_4 \sigma_{xl}^U A_{el} z_l}{\sum_1 \sigma_{xi}^Y A_i + \sum_2 \sigma_{xj}^E A_j + \sum_3 \sigma_{xk}^E A_{ek} + \sum_4 \sigma_{xl}^U A_{el}} \tag{8.19a}$$

where σ_x is calculated from Equation (8.18) together with Equation (8.17a) when σ_B just reaches the equivalent yield stress of bottom stiffened panels which is defined by Equation (5.1) in Chapter 5. The superscripts Y, E and U represent the yield stress, elastic stress and ultimate stress, respectively. The subscript, e, indicates the effective section. $\sum_1(\,), \sum_2(\,), \sum_3(\,), \sum_4(\,)$ = summations for members in the regions 1, 2, 3 or 4, respectively.

The ultimate hull girder sagging moment, M_{us}, can then be calculated, with the sagging moment or the compressive stress taken as negative while the hogging moment or the tensile stress is taken as positive, as follows:

$$M_{us} = -\sum_1 \sigma_{xi}^Y A_i (g_{us} - z_i) - \sum_2 \sigma_{xj}^E A_j (g_{us} - z_j) + \sum_3 \sigma_{xk}^E A_{ek} (z_k - g_{us}) + \sum_4 \sigma_{xl}^U A_{el} (z_l - g_{us}) \tag{8.19b}$$

where g_{us} is as defined in Eq. (8.19a)

Similarly, in the hogging condition as shown in Figure 8.14(b), the neutral axis position above the base line at the ULS can be calculated as follows:

$$g_{uh} = \frac{\sum_1 \sigma_{xi}^U A_{ei} z_i + \sum_2 \sigma_{xj}^E A_{ej} z_j + \sum_3 \sigma_{xk}^E A_k z_k + \sum_4 \sigma_{xl}^Y A_l z_l}{\sum_1 \sigma_{xi}^U A_{ei} + \sum_2 \sigma_{xj}^E A_{ej} + \sum_3 \sigma_{xk}^E A_k + \sum_4 \sigma_{xl}^Y A_l} \tag{8.20a}$$

where σ_x is calculated from Equation (8.18) together with Equation (8.17b) when σ_D just reaches the equivalent yield stress of the deck stiffened panels which can be defined by Equation (5.1) in Chapter 5.

The ultimate hull girder hogging moment, M_{uh}, can then be calculated as follows:

$$M_{uh} = -\sum_1 \sigma_{xi}^U A_{ei} (g_{uh} - z_i) - \sum_2 \sigma_{xj}^E A_{ej} (g_{uh} - z_j) + \sum_3 \sigma_{xk}^E A_k (z_k - g_{uh}) + \sum_4 \sigma_{xl}^Y A_l (z_l - g_{uh}) \tag{8.20b}$$

where g_{uh} is as defined in Equation (8.20a).

In calculating Equations (8.19) or (8.20), the longitudinal axis stress for individual structural elements (i.e., either plating or stiffeners) must be taken as a value smaller than either the ultimate stress or the material yield stress, the former being predicted using the closed-form expressions such as those noted in Chapter 2 for stiffeners (with or without attached plating) or those noted in Chapter 4 for plating between stiffeners.

Figure 8.15(a) plots the correlation between ALPS/HULL results and the closed-form expressions of the ultimate bending moments for the 10 ships of various types indicated in Figure 8.4. The mean and COV of the present closed-form expression predictions against the ALPS/HULL progressive collapse analyses for ship hulls with initial imperfections at an 'average' level are 0.996 and 0.082, respectively. Figure 8.15(b) represents the applicability of the hull girder ultimate strength design formula presented in this section when $\gamma_M = 1.15$ in Equation (1.1) of Chapter 1 is adopted. In Figure 8.15(b), the cases with the 'severe' level of initial imperfections were excluded. It is seen from Figure 8.15(b) that the closed-form ultimate hull girder strength expression with $\gamma_M = 1.15$ provides a mean = 0.850 and a COV = 0.086 when measured against the corresponding set of ALPS/HULL progressive collapse analyses.

8.5.2 Ultimate Horizontal Moment

Figure 8.16 shows an example longitudinal axial stress distribution of a single hull tanker under horizontal bending. Using such a distribution as the starting point, an approach that is similar to the case of vertical bending can be applied to derive the ultimate horizontal bending capacity, M_{Hu}, of the ship hull.

8.5.3 Ultimate Vertical Sectional Shear

Figure 8.17 shows the shear stress distribution over a ship hull cross-section under sectional shear at the state of overall collapse. As is apparent from Figure 8.17, most of the

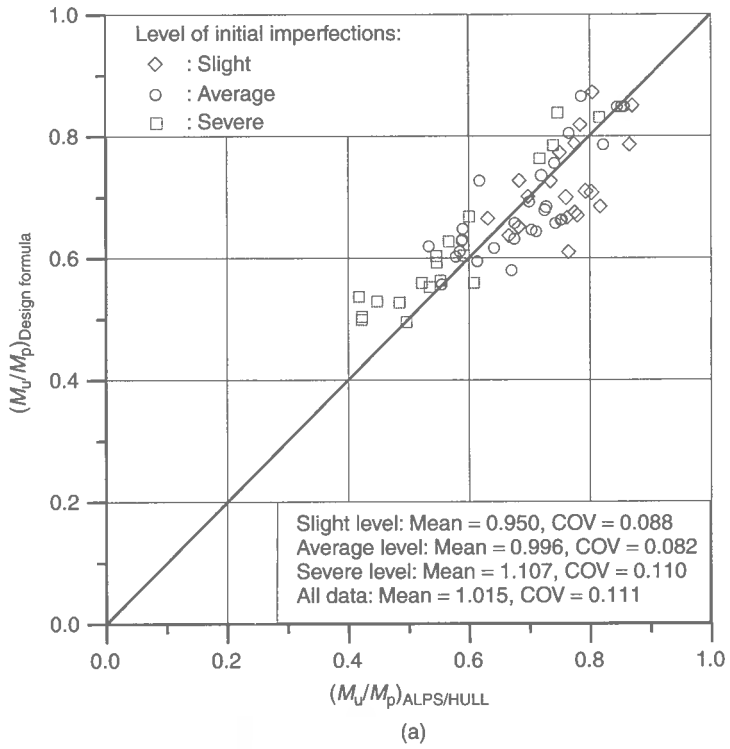

(a)

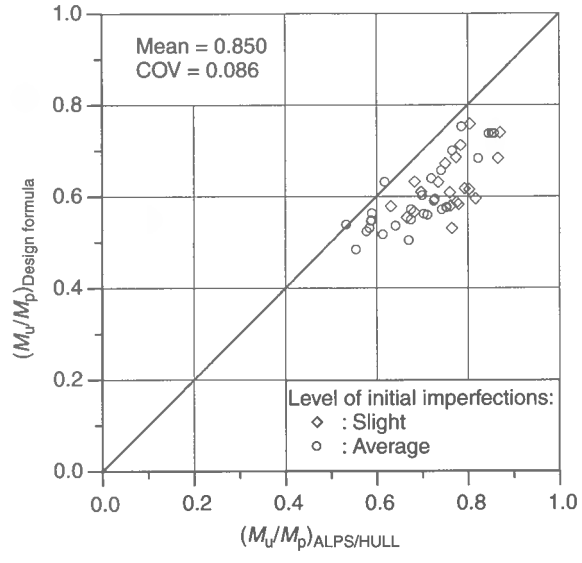

(b)

Figure 8.15 (a) Correlation between ALPS/HULL progressive collapse analyses and closed-form expression predictions, varying the level of initial imperfections; (b) Applicability of the closed-form expression for the ULS design of ship hulls with the capacity factor $\gamma_M = 1.15$

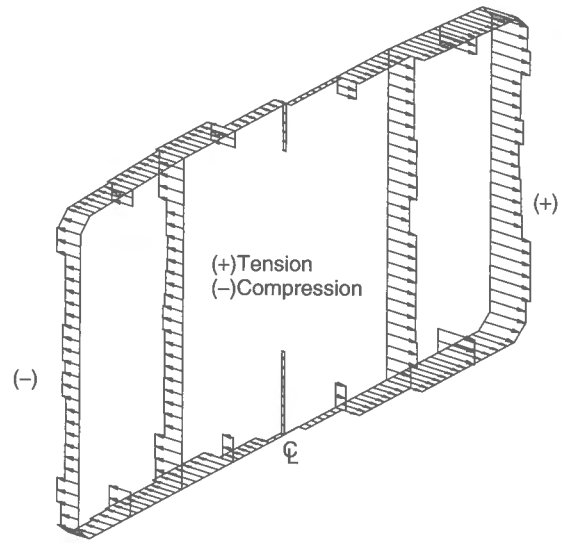

Figure 8.16 Axial stress distribution for a typical single hull tanker at the ultimate collapse state under horizontal moment

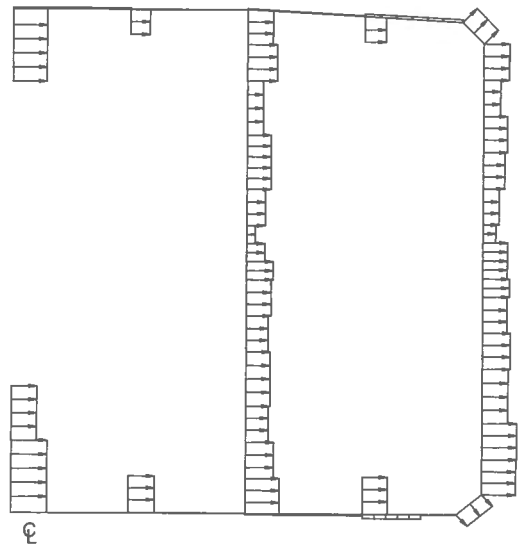

Figure 8.17 Shear stress distribution for a typical single hull tanker at the ultimate collapse state under shear

shearing forces are carried by side shells (or vertical members). The margin plates around the bilge corner are also important members sustaining the shearing force. The total shear load carried by the horizontal members, i.e., deck or bottom panels, is relatively very small and so their contribution may be neglected. Therefore, the ultimate capacity of a ship hull under sectional shear, F_u, may approximately be calculated by

$$F_u = \sum A_{si}\tau_{ui} \tag{8.21}$$

where A_{si} = cross-sectional area of vertical member plating (excluding stiffeners), τ_{ui} = ultimate shear stress of vertical member plating between stiffeners which may be computed from Equation (4.55a) in Chapter 4.

8.5.4 Ultimate Strength under Combined Hull Girder Loads

To obtain a complete picture of hull girder collapse behavior, several combined load conditions may need to be considered in a consistent manner in any first-principles-based procedure for hull girder strength analysis. This section presents an approach to the ultimate strength interaction formulations for ship hulls under combined loads.

Ultimate Strength under Combined Vertical and Horizontal Moments

For the ultimate strength interaction relationship between vertical and horizontal bending moments, the following simple expression is used:

$$\left(\frac{M_V}{M_{Vu}}\right)^{c_1} + \left(\frac{M_H}{M_{Hu}}\right)^{c_2} = 1 \tag{8.22}$$

where M_V, M_{Vu} = applied vertical bending moment and the corresponding capacity, M_H, M_{Hu} = applied horizontal bending moment and the corresponding capacity.

It is noted that M_{Vu} in sagging is normally different from that in hogging. The coefficients c_1 and c_2 may be obtained by curve fitting based on numerical computations. Since the geometric characteristics of ship structures may be accommodated in the expressions for M_{Vu} or M_{Hu}, the coefficients c_1 and c_2 may possibly be determined to account for the interacting effect between M_V and M_H. Strictly speaking, the coefficients c_1 and c_2 may not be identical for different types of ships, but for usual merchant ships, they may be determined as $c_1 = 1.85$ and $c_2 = 1.0$, which reasonably represent the interaction relationship between vertical and horizontal moments for the set of ultimate strength data shown in Figure 8.18 (Paik *et al.* 1996) and Figure 8.13(d).

Ultimate Strength under Combined Vertical Moment and Sectional Shear

A similar interaction expression for the ship hull girder collapse under combined vertical bending, M_V, and shearing forces, F, may be suggested as follows:

$$\left(\frac{M_V}{M_{Vu}}\right)^{c_3} + \left(\frac{F}{F_u}\right)^{c_4} = 1 \tag{8.23}$$

where c_3 and c_4 are empirical constants which may be determined by curve fitting of results based on numerical computations. Figure 8.19 shows that the interaction relationship of Equation (8.23) with $c_3 = 2.0$ and $c_4 = 5.0$ fits a set of available numerical data reasonably well (Paik *et al.* 1996).

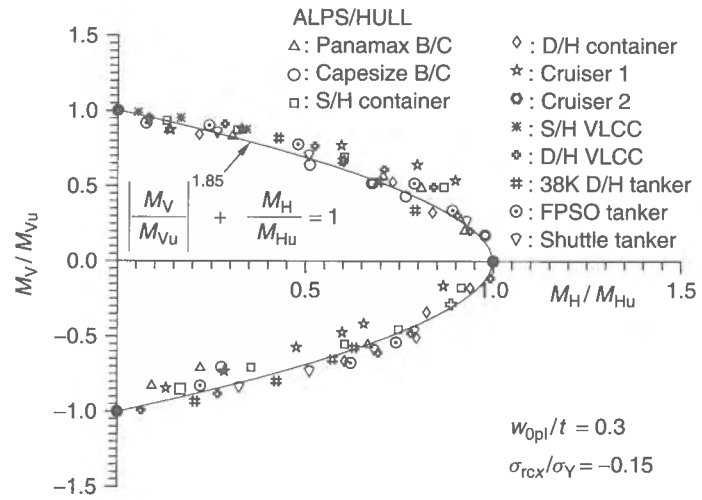

Figure 8.18 A sample interaction relationship for ship hull girder collapse under combined vertical and horizontal moments (Paik *et al.* 1996) (B/C = bulk carrier; S/H = single hull; D/H = double hull; VLCC = very large crude oil carrier; FPSO = floating, production, storage and offloading unit)

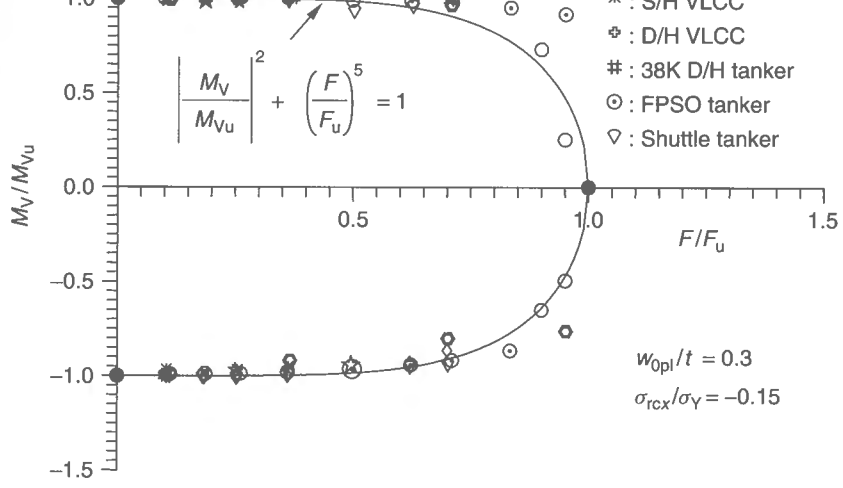

Figure 8.19 A sample interaction relationship for ship hull girder collapse under combined vertical moment and shearing force (Paik *et al.* 1996) (B/C = bulk carrier; S/H = single hull; D/H = double hull; VLCC = very large crude oil carrier; FPSO = floating, production, storage and offloading unit)

Ultimate Strength under Combined Horizontal Moment and Sectional Shear

For the ultimate strength interaction between combined horizontal bending, F_H, and shearing force, F, the following simple expression may be suggested:

$$\left(\frac{M_H}{M_{Hu}}\right)^{c_5} + \left(\frac{F}{F_u}\right)^{c_6} = 1 \tag{8.24}$$

where c_5 and c_6 are empirical constants. Figure 8.20 indicates that $c_5 = 2.5$ and $c_6 = 5.5$ provide a reasonable fit to the corresponding numerical data (Paik *et al.* 1996).

Ultimate Strength under Combined Vertical Moment, Horizontal Moment and Sectional Shear

Applying an approach similar to that presented in Section 3.8 of Chapter 3, an interaction relationship involving the three load components, namely vertical bending, horizontal bending and shearing forces, can be derived based on three sets of the interaction relationships between two load components each, i.e., $M_V - M_H$ relationship, $M_V - F$ relationship and $M_H - F$ relationship. Figure 8.21 shows a schematic representation of the process for deriving the interaction relationship between three load components. The resulting interaction equation is then given by

$$\Gamma u = \left(\frac{M_V}{M_{Vu} F_{VR}}\right)^{c_1} + \left(\frac{M_H}{M_{Hu} F_{HR}}\right)^{c_2} - 1 = 0 \tag{8.25}$$

where $F_{VR} = [1 - (F/F_u)^{c_4}]^{1/c_3}$, $F_{HR} = [1 - (F/F_u)^{c_6}]^{1/c_5}$.

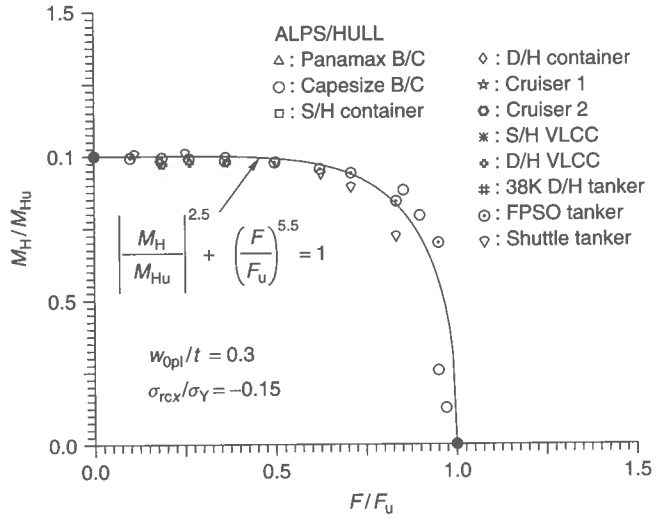

Figure 8.20 A sample interaction relationship for ship hull girder collapse under combined horizontal moment and shearing force (Paik *et al.* 1996)(B/C = bulk carrier; S/H = single hull; D/H = double hull; VLCC = very large crude oil carrier; FPSO = floating, production, storage and offloading unit)

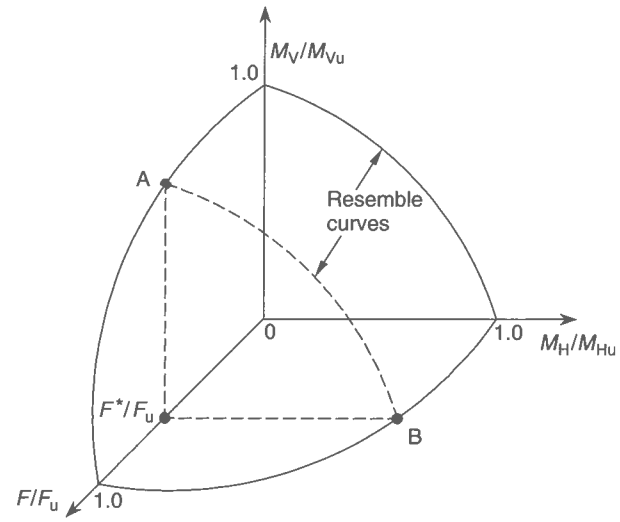

Figure 8.21 A schematic representation of the derivation of the interaction relationship involving three load components

Γ_u thus represents the ship hull collapse function, where F_{VR} and F_{HR} indicate reduction factors due to the shearing force. If the value of Γ_u is less than zero, i.e., $\Gamma_u < 0$, then the ship hull is considered to be in a collapse-free condition, but it will possibly collapse if $\Gamma_u \geq 0$.

For instance, when we take $c_1 = 1.85$, $c_2 = 1.0$, $c_3 = 2.0$, $c_4 = 5.0$, $c_5 = 2.5$ and $c_6 = 5.5$, Equation (8.25) would become

$$\Gamma_u = \left(\frac{M_V}{M_{Vu} F_{VR}}\right)^{1.85} + \frac{M_H}{M_{Hu} F_{HR}} - 1 = 0 \tag{8.26}$$

where $F_{VR} = [1 - (F/F_u)^{5.0}]^{0.5}$, $F_{HR} = [1 - (F/F_u)^{5.5}]^{0.4}$.

8.5.5 Effect of Torsion on Ultimate Vertical Moment

For a ship hull with large deck openings such as container vessels and some large bulk carriers, the analysis of warping stresses and hatch opening deformations is an essential part of ship structural response analysis. For a thin-walled beam with an open cross-section, the torsional stiffness is much less than that with a closed section. This implies that for a given level of torsion, the open section may twist much more due to its low torsional rigidity.

In contrast to the uniform (i.e., St. Venant) torsion of solid beams and a rather special class of warping-free thin-walled beams, non-uniform axial deformation (i.e., warping) usually occurs in the case of thin-walled beams with open sections such that an initially plane cross-section will no longer remain plane. This would mean that torsion will develop axial (warping) stresses as well as shear stresses when the warping displacements are restrained as shown in Figure 8.22.

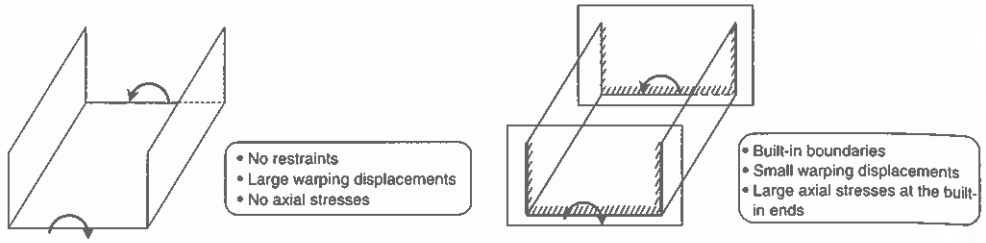

Figure 8.22 Warping displacements and stresses for an open cross-section thin-walled beam under torsion due to end restraints

In actual ship structures, warping displacements are normally only partly restrained and thus the analysis of warping stresses as well as hatch opening deformations is in principle an essential part of the response analyses of ships.

When the cross-sections are free to warp, warping stresses normal to the cross-section will not be introduced. However, at cross-sectional discontinuities such as at the transition between the cargo area and the engine room, or between the cargo area and the fore body, and at heavy cross-deck beams, the warping deformations will be restrained to varying degrees. The restraint at these locations induces warping stresses, which for ships with large deck openings are significant, and so the warping stresses and the associated deformations (e.g., hatch opening distortions) must be accounted for in design.

Related to the effect of torsion on vertical bending capacity, however, it has been shown that torsion is not a very sensitive load component affecting the ultimate vertical bending moment of ship hulls as long as the magnitude of torsion is not predominant (Paik *et al.* 2001). However, it should also be noted that the ultimate bending strength of ship hulls with low torsional rigidity can be reduced significantly when torsion loads are large.

As shown in Figure 8.23, the following formulations may fit the ultimate hull strength interaction relationship for an example container vessel under combined torsion, M_T, and vertical bending, M_V, reasonably well, namely

$$\left(\frac{M_V}{M_{Vu}}\right)^{3.7} + \left(\frac{M_T}{M_{Tu}}\right)^{3.7} = 1 \quad \text{for hogging} \tag{8.27a}$$

$$\left(\frac{M_V}{M_{Vu}}\right)^{3.1} + \left(\frac{M_T}{M_{Tu}}\right)^{3.1} = 1 \quad \text{for sagging} \tag{8.27b}$$

where M_{Tu} = ultimate torsional moment of the ship hull.

8.5.6 Effect of Age-related Structural Degradation on Ultimate Vertical Moment

Aging ships may have suffered structural degradation such as corrosion and fatigue cracks over time. For general corrosion which uniformly reduces the wall thickness of structural members, the ultimate stress or effectiveness of primary strength members may be evaluated by excluding the corrosion diminution (reduction in thickness). For structural members with fatigue cracks, the cross-sectional area associated with the cracking damage may in turn be reduced in strength calculations, as will be presented later in Section 10.6 of Chapter 10.

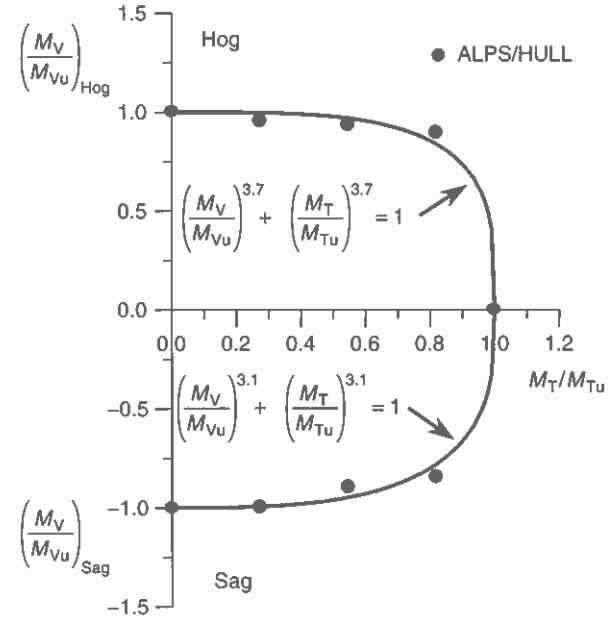

Figure 8.23 Ultimate strength interaction relationship for a container vessel under combined torsion and vertical bending (Paik *et al.* 2001)

In this section, the progressive collapse behavior of a damaged tanker hull under sagging moment is considered, based on ALPS/HULL calculations. A hull module between web frames is taken as the extent of the analysis since the transverse frames are considered to be strong enough so that they would not fail prior to the longitudinal members. An 'average' level of initial imperfections for individual structural members is assumed.

The ship is considered to be 15 years old and the amount of corrosion damage has been assumed to be measured. The ship will have suffered different levels of corrosion damage in the different member locations/categories. Because of heavy corrosion or other damage, either deck girder or deck longitudinals have been considered to have been detached. A total of four hypothetical damage cases and the intact ship are analyzed as follows:

- case 1: intact
- case 2: intact–deck girder detached
- case 3: corroded
- case 4: corroded–deck girder detached
- case 5: corroded–deck girder and deck longitudinals (in port tank) detached.

Figures 8.24(a) to (c) show the related ALPS/HULL models. In the analysis, the thickness of plates or stiffeners is uniformly reduced by the corrosion diminution assumed to have been measured. Figure 8.25 indicates the sagging bending moment versus curvature curves for the five cases. It is apparent that the corrosion damage can significantly reduce the vertical bending capacity of ships.

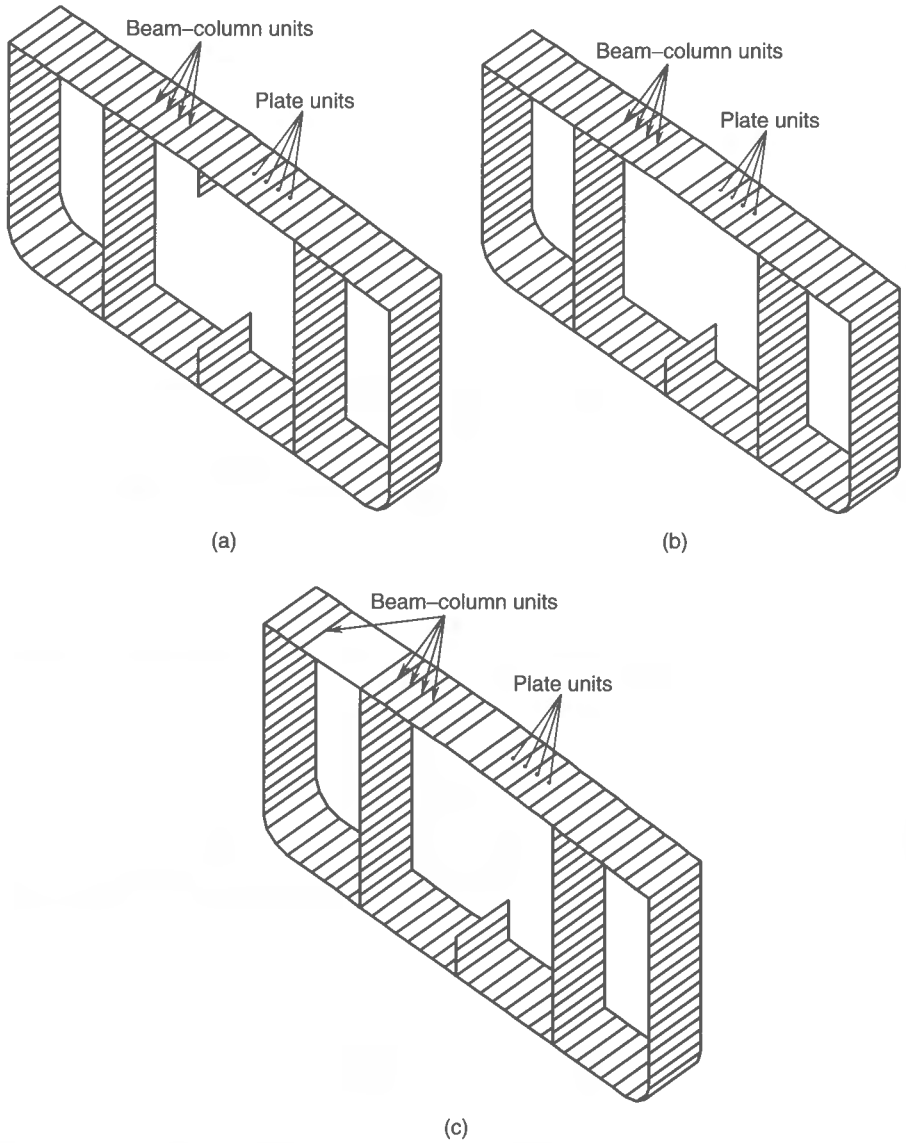

Figure 8.24 ALPS/HULL model for damage cases (a) 1 and 3; (b) 2 and 4; (c) 5

8.5.7 *Effect of Accident-related Structural Damage on Ultimate Vertical Moment*

As noted in the second subsection of Section 8.3.1, the effect of accident-related structural damage such as that due to collision or grounding can approximately be accounted for by excluding the damaged parts from the calculations of effective plate width and the ultimate strength of individual members. Similar exclusion may be applied even for structural members subject to tension as long as they have suffered serious structural damage.

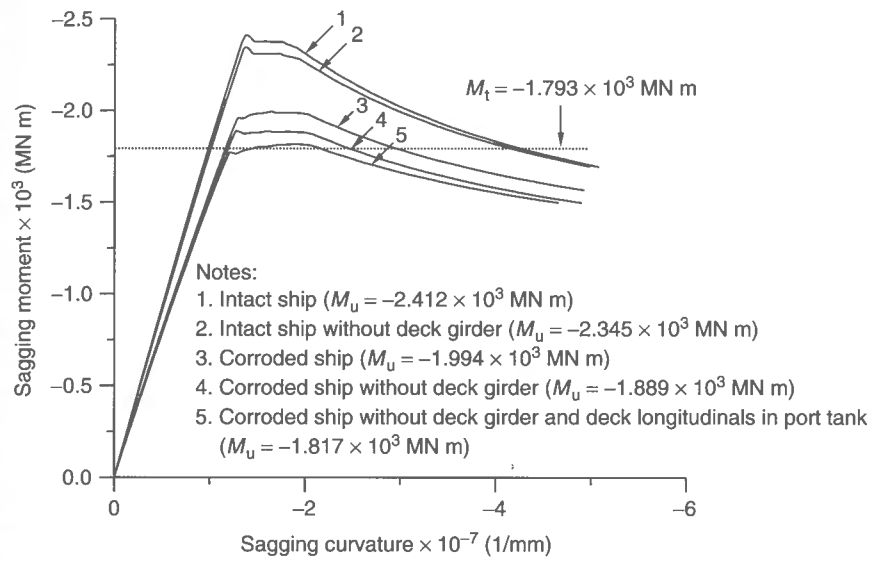

Figure 8.25 The sagging moment versus curvature relationships for a hypothetical corroded/damaged tanker hull, as obtained by ALPS/HULL (M_t = total extreme sagging moment)

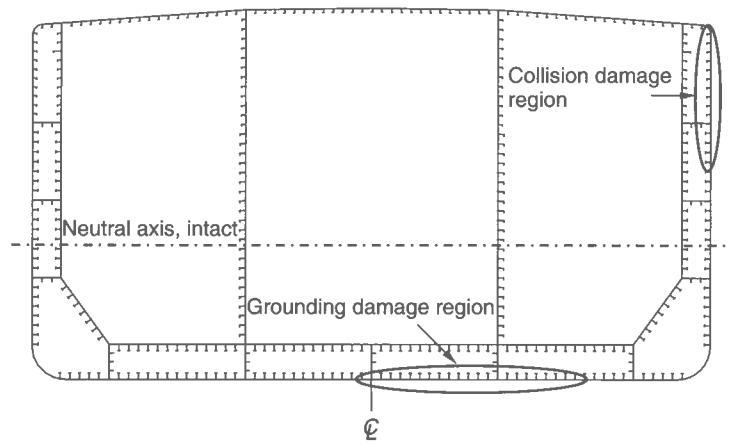

Figure 8.26 Ship hull cross-section with collision or grounding damage

Figure 8.26 represents a ship hull cross-section with collision- or grounding-induced damage. While the grounding damage is present in bottom structures, the collision damage exists from the upper side shell to a known or predefined extent. In this case, the residual strength ratio can be defined as the ratio of the strength measure of the damaged ship to that of the intact ship. For the strength measure, either the section modulus or the ultimate hull girder strength can be used.

Figure 8.27 shows the variation of the residual strength ratio for a hypothetical 307 000 dwt double hull tanker as a function of such grounding or collision damage amount, as obtained by Wang *et al.* (2002). The section moduli of the damaged ship were

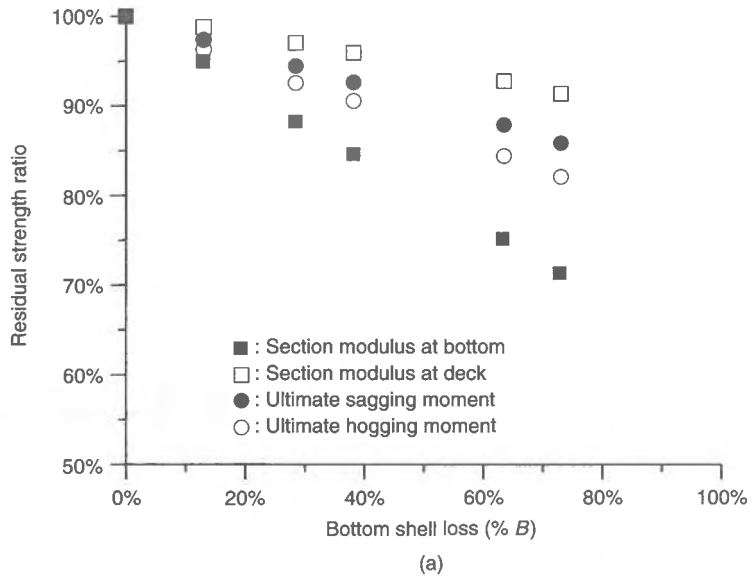

(a)

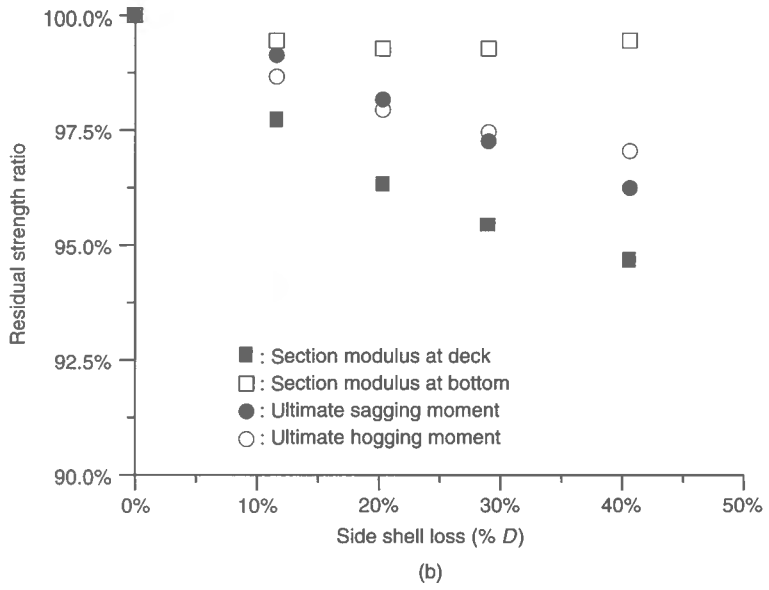

(b)

Figure 8.27 Variation of residual strength of a 307 000 dwt double hull tanker hull as a function of (a) grounding damage amount and (b) collision damage amount

calculated by excluding the damaged members in both the tension and compression parts, while all other members were supposed to be fully effective. The residual strength ratio based on the ultimate hull girder strength was computed by the ALPS/HULL program. These results were obtained subject to the assumption that the damaged neutral axis is parallel to the original, and should thus be viewed as notional, especially for any significant amount of damage.

Some observations noted by Wang *et al.* (2002) using the above parametric results for a double hull tanker are as follows:

(1) The section modulus to the bottom is the most sensitive indicator of the bottom grounding damage, followed by hull girder ultimate strength for hogging, hull girder ultimate strength for sagging, and the section modulus to the deck is the least sensitive, see Figure 8.27(a).
(2) A hull girder with bottom grounding damage exhibits more apparent reserve in the section modulus at the deck than in the hull girder ultimate strength for sagging. The hull with bottom damage shows less apparent reserve in the section modulus to the bottom than in the hull girder ultimate strength for hogging.
(3) For a grounded ship, using the section modulus to the deck is more optimistic to evaluate the residual strength than using the hull girder ultimate strength under sagging; and using the section modulus to the bottom is more conservative than using the hull girder ultimate strength for hogging.
(4) The section modulus to the deck is the most sensitive indicator of the side collision damage, and the section modulus to the bottom is the least sensitive, see Figure 8.27(b). Hull girder ultimate strength for hogging and sagging fall in between these two extremes.
(5) A hull girder with side collision damage exhibits less reserve in the section modulus to the deck than in the hull girder ultimate strength for sagging. The hull with side damage shows more reserve in the section modulus to the bottom than in the hull girder ultimate strength for hogging.
(6) For a ship in collision, using the section modulus to the deck is more conservative to evaluate the residual strength than using the hull girder ultimate strength under sagging; and using the section modulus to the bottom is more optimistic than using the hull girder ultimate strength for hogging.

The reason why the elastic section modulus predictions are compared to the ultimate strength in the above exercise is because some existing rule residual strength calculation procedures for collision and grounding accidents use the elastic section modulus as the parameter characterizing the residual strength with a part of the hull damaged. It is of course preferable to use ultimate strength predictions of ship hull girder residual strength in such cases (Paik *et al.* 1998).

8.6 Computer Software ALPS/USAS

The procedures noted above are automated within the computer program ALPS/USAS, which stands for nonlinear analysis of large plated structures/ultimate strength analysis of intact/damaged ships. ALPS/USAS computes the hull girder loads, the ultimate hull girder strength and the ship hull safety measure.

In ALPS/USAS, the module for the calculation of ship hull girder loads facilitates the computation of the following hull girder load components:

- the distribution of still-water sectional shearing forces and bending moments, using the theory described or referred to in the first subsection of Section 8.2.2 above, given weight and buoyancy distribution data;

- the distribution of long-term wave-induced sectional shearing forces and bending moments using the IACS unified formulas, given the ship's principal dimensions;
- the distribution of short-term wave-induced shearing forces and bending moments using the parametric seakeeping tables referred to in the fourth subsection of Section 8.2.2 above, given the ship's principal dimensions and operating speed, significant wave height, block coefficient, and sea state persistence time.

The ALPS/USAS program also computes effective/full section moduli, full plastic bending moments and ultimate strength of ship hulls using the related closed-form expressions presented in this chapter. The effects of structural damage are taken into account in the calculations. The safety measure of a ship hull is then calculated as follows:

$$\text{Safety measure} = \frac{M_u}{\gamma_M} \frac{1}{\gamma_0 M_t} \tag{8.28}$$

where γ_M, γ_0 = partial safety factors as defined in Equation (1.1), M_u = characteristic ultimate hull girder strength, M_t = characteristic extreme hull girder load.

For ship safety and reliability together with its target measures, Paik & Frieze (2001), among others, may be referred to. To be safe, the value of the safety measure of the ship hull must be greater than 1.0. The program together with the user's manual can be downloaded from the web site given in the appendices to this book.

References

ABS (2000). *Rules for building and classing steel vessels*. American Bureau of Shipping, Houston, TX.

Caldwell, J.B. (1965). Ultimate longitudinal strength. RINA Transactions, 107: 411–430.

Frieze, P.A. & Lin, Y.T. (1991). Ship longitudinal strength modeling for reliability analysis. *Proceedings of Marine Structural Inspection, Maintenance and Monitoring Symposium, Ship Structure Committee and the Society of Naval Architects and Marine Engineers, Arlington, Virginia, March*, III.B.1–III.B.19.

Hughes, O.F. (1988). *Ship structural design: a rationally-based, computer-aided optimization approach*. The Society of Naval Architects and Marine Engineers, Jersey city, NJ.

Jensen, J.J. (2001). *Load and global response of ships*. Elsevier, London.

Loukakis, T.A. & Chryssostomidis, C. (1975). Seakeeping standard series for cruiser-stern ships. *SNAME Transactions*, 83: 67–127.

Maestro, M. & Marino, A. (1988). An assessment of the structural capacity of damaged ships: the plastic approach in longitudinal unsymmetrical bending and the influence of buckling. *International Shipbuilding Progress*, 36(408): 255–265.

Mansour, A.E. & Thayamballi, A.K. (1994). Probability based ship design; loads and load combination. Ship Structure Committee, SSC-373, Washington, DC.

Paik, J.K. & Frieze, P.A. (2001). Ship structural safety and reliability. Progress in Structural Engineering and Materials, 3(2): 198–210.

Paik, J.K. & Mansour, A.E. (1995). A simple formulation for predicting the ultimate strength of ships. *Journal of Marine Science and Technology*, 1(1): 52–62.

Paik, J.K., Thayamballi, A.K. & Che, J.S. (1996). Ultimate strength of ship hulls under combined vertical bending, horizontal bending and shearing forces. *SNAME Transactions*, 104: 31–59.

Paik, J.K., Thayamballi, A.K. & Yang, S.H. (1998). Residual strength assessment of ships after collision and grounding. *Marine Technology*, 35(1): 38–54.

Paik, J.K., Thayamballi, A.K., Pedersen, P.T. & Park, Y.I. (2001). Ultimate strength of ship hulls under torsion. *Ocean Engineering*, 28: 1097–1133.

Paik, J.K., Wang, G., Kim, B.J. & Thayamballi, A.K. (2002). Ultimate limit state design of ship hulls. Presented at the SNAME annual meeting (SNAME Transactions, 110), Boston, MA, October 24–27.

Paulling, J.R. (1988). Strength of ships. Chapter IV. in *Principles of Naval Architecture*. The Society of Naval Architects and Marine Engineers, Jersey city, NJ, 205–299.

Smith, C.S. (1977). Influence of local compressive failure on ultimate longitudinal strength of ship's hull. *Proceedings of the International Symposium on Practical Design in Shipbuilding, Tokyo*, 73–79.

Ueda, Y. & Rashed, S.M.H. (1974). An ultimate transverse strength analysis of ship structure. *Journal of the Society of Naval Architects of Japan, Tokyo*, 136: 309–324 (in Japanese).

Ueda, Y. & Rashed, S.M.H. (1984). The idealized structural unit method and its application to deep girder structures. *Computers & Structures*, 18(2): 277–293.

Wang, G., Chen, Y., Zhang, H. & Peng, H. (2002). Longitudinal strength of ships with accidental damages. *Marine Structures*, 15(2): 119–138.

9 Impact Mechanics and Structural Design for Accidents

9.1 Fundamentals of Structural Impact Mechanics

Steel structures can be subjected to dynamic or impact loads while in service. Any loading which gives rise to a time-dependent structural response is in this chapter termed dynamic or impact loading. Three types of dynamic or impact loadings are normally considered, namely impact, dynamic pressure and impulsive loading (Jones 1997a). In some cases, objects may be dropped from a crane, for instance, on to the deck plating of an offshore platform. The striking mass dropped from a height, h, is often fairly large and travels at a relatively low velocity, $V_0 = \sqrt{(2gh)}$, which may be up to 10–15 m/s. In other cases, a mass, W, may be struck at much higher velocities by a gas explosion on an offshore platform. This class of loading is typically called impact, and the total impact energy of the striking mass travelling with an initial velocity, V_0, is given by sum of the initial kinetic energy ($=WV_0/2$) plus the additional potential energy of the striking mass travelling through the permanent displacement of the struck structure. Water impacts and explosive events which give rise to a pressure-time history acting on the exposed area of a structure is termed 'dynamic pressure'. When the magnitude of the dynamic pressure is very large and the duration is very short, the dynamic pressure can be idealized as the impulsive loading.

The mechanical properties of structural steels are significantly affected by loading speed or strain rate, $\dot{\varepsilon}$, the latter being defined as a relevant ratio of loading speed to structural displacement measured between two reference points, i.e., $\dot{\varepsilon} = \mathrm{d}\varepsilon/\mathrm{d}t$, where ε = strain and t = time. Table 9.1 indicates a classification of dynamic or impact loading modes as a function of the strain rate.

Three major differences between static/quasi-static and dynamic/impact loading cases are usually evident. The first difference is about the stress field. In an impact loading situation, tensile stresses can occur even under compressive far-field loading, and stress concentrations can occur even without notches. The second difference is that the dynamic/impact structural behavior can vary as a function of the strain rate. The first and second aspects always interact. The third difference is about the failure pattern.

Table 9.1 Dynamic modes of loading versus the strain rate (Hayashi & Tanaka 1988).

Strain rate $\dot{\varepsilon}$(1/s)	$<10^{-5}$	10^{-5}–10^{-1}	10^{-1}–$10^{1.5}$	$10^{1.5}$–10^{4}	$>10^{4}$
Dynamic loading mode	Creep	Static or quasi-static	Dynamic	Impact	Hyper velocity impact
Examples	Constant loading machine	Dead or live loading on a ship hull girder	Impulse pressure effects on high-speed craft, wave breaking loads	Explosion, ship collision	Bombing

Under impact loading, brittle fracture is more of a possibility for structural steels which are predominantly ductile under static/quasi-static loading, since the energy absorption capacity by ductile yielding decreases at high strain rates subsequent to the increase of yield strength.

When externally applied dynamic (e.g., kinetic) energy is large, a dynamic plastic structural problem cannot be adequately solved using quasi-static analysis methods based on an 'equivalent' static loading and considering dynamic magnification factors. The general procedure for analysis of the dynamic plastic behavior of structures in such cases is similar to that used for the static behavior, except that a kinematically admissible velocity field which represents the motion of the structure should be considered in the dynamic problems instead of a statically admissible deformation field. The dynamic governing differential equations which involve an inertia term in addition to the static-equilibrium-related terms will then be solved to satisfy the initial and boundary conditions. The characteristics of the static collapse mode are in fact often helpful for establishing a kinematically admissible velocity field. Solutions are then found such that the yield condition associated with the presumed velocity field is satisfied.

It can be said with reasonable certainty that the elastic effects may be disregarded when the external dynamic energy (e.g., kinetic energy) is significantly larger than the maximum amount of strain energy which can be absorbed in a wholly elastic manner, provided that the duration of an impact loading pulse is sufficiently short compared to the natural elastic period of the structure. This implies that an approximation using rigid–perfectly plastic material (instead of elastic–perfectly plastic material or elastic–plastic material including strain hardening) may be used for the purposes of examining the dynamic plastic response (Johnson 1972, Jones 1997a, 1997b).

The limit state design of steel structures under impact loading can also be undertaken following Equation (1.1) in Chapter 1. The design procedure in this case is, however, better formulated in terms of energy-related parameters, unlike the design of structures for static or quasi-static loading which is based on the load effects and the corresponding load-carrying capacities. For instance, the demand in Equation (1.1) may be defined as the design loss of kinetic energy while the capacity may be the strain energy absorption capability in the limit state design of steel-plated structures under impact loads.

This chapter presents the fundamentals of structural impact mechanics. Applications of impact mechanics to accidental limit state design of steel-plated structures are also described.

9.2 Load Effects Due to Impact

The load effects (i.e., stresses) of steel structures under static or quasi-static loading are normally calculated by the classical theory of structural mechanics or linear elastic finite element analysis. Under impact loading, however, the methodologies for the analysis of load effects are entirely different from those for static loading.

This section describes some related considerations. Essentially, under dynamic loading, a structure not only deforms, but can also vibrate, implying that the load effects are time dependent and dynamic amplification of load effects is possible. Because in many cases the response is transient, many structures can tolerate dynamic loads far exceeding the same magnitude of static loads. Both simplified and more sophisticated methods exist for the calculation of structural response under dynamic loading. Finite element methods are useful for the calculation of dynamic structural response, taking account of material and geometric nonlinearities including plasticity and buckling. When using simplified methods, the local strength aspects themselves are often characterized using methods based on plastic theory.

Now consider the case of a rigid body with a mass, W, that falls freely as shown in Figure 9.1, resulting in axial impact loading to an elastic rod. The kinetic energy loss, E_k, for the falling body is given by

$$E_k = Wg(h + \delta) \tag{9.1a}$$

where g = acceleration of gravity, h = initial height of the falling object, δ = displacement.

The strain energy, E_s, absorbed by the elastic rod is calculated by

$$E_s = \frac{EA}{2L}\left(\frac{\delta}{L}\right)^2 \tag{9.1b}$$

where A = cross-sectional area, L = initial length of the elastic rod, E = Young's modulus.

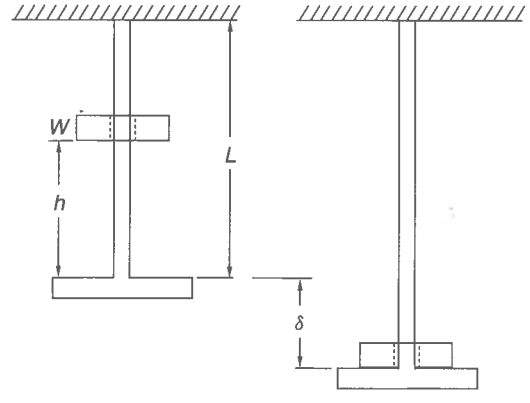

Figure 9.1 Impact by free fall

By the principle of energy conservation, $E_k = E_s$ and thus the displacement, δ, is determined. Therefore, the impact stress, σ, can be obtained as follows:

$$\sigma = \frac{E\delta}{L} = \frac{Wg}{A}\left(1 + \sqrt{1 + \frac{2EAh}{WgL}}\right) \tag{9.2}$$

The impact stress is time variant in nature. During contact of the falling object with the bottom plate, the falling object will be subjected to reaction forces from the rod as well as gravitational forces. The governing differential equation for the motion of the falling object is given by neglecting the effect of the rod mass as follows:

$$W\frac{d^2x}{dt^2} = Wg - A\sigma = Wg - \frac{EAx}{L} \tag{9.3}$$

where x represents the displacement of the rod. If the origin of the time, t, is taken as when the falling object comes into contact with the bottom plate, the initial conditions for the impact are given by

$$x = 0, \frac{dx}{dt} = V_0 \text{ at } t = 0 \tag{9.4}$$

where $V_0 = \sqrt{(2gh)}$ = velocity of free fall.

The solution of Equation (9.3) is then obtained by considering the initial conditions, Equation (9.4), as follows:

$$x = \frac{WgL}{EA}\left(1 - \cos\phi + \sqrt{\frac{2EAh}{WgL}}\sin\phi\right) \tag{9.5}$$

where $\phi = [EA/(WL)]^{1/2}t$.

Therefore, the time-variant impact stress, σ, is given using Equation (9.5) as follows:

$$\sigma = \frac{Ex}{L} = \frac{Wg}{A}\left\{1 + \sqrt{1 + \frac{2EAh}{WgL}}\sin\left[\sqrt{\frac{EA}{WL}}(t - T)\right]\right\} \tag{9.6}$$

where

$$T = \sqrt{\frac{WL}{EA}}\arctan\sqrt{\frac{WgL}{2EAh}}$$

It may be surmised from Equation (9.6) that the impact stress develops in a sinusoidal form with regard to the time and takes the maximum value equal to Equation (9.2) at the time, t_0, which is defined by

$$t_0 = \frac{\pi}{2}\sqrt{\frac{WL}{EA}} + T \tag{9.7}$$

It has been assumed here that the impact loads may be transferred to the fixed end of the rod immediately after striking between the falling object and the bottom plate occurs, and then the rod deforms uniformly along the length. Also, the effect of the stress wave propagation is neglected. For a higher speed impact loading, however, the latter assumption may not be appropriate since the propagation, reflection, refraction and interference of the stress wave may play an important role.

Related to the effect of the stress wave propagation, a simple example is now considered as studied by Hayashi & Tanaka (1988). When a rigid body with a velocity of V_0 strikes a column in the length direction, as shown in Figure 9.2, the resulting time-variant impact stress is estimated taking into account the effect of stress wave propagation.

Denote the propagation velocity of the stress wave and the velocity of a particle within the impacted body by V_p and V_m, respectively. The stress wave propagates from point B to point C, while point B deforms to point B′ at time $t = t^*$. In this case, the strain, ε, of the column at $t = t^*$ can be given, with the compressive strain taken as positive as follows:

$$\varepsilon = \frac{BB'}{BC} = \frac{V_m}{V_p} \tag{9.8}$$

During striking, the momentum imparted to the struck body is given by $\rho_0 A V_p t^* V_m$ since the part B'C of the column with cross-sectional area A moves with velocity V_m for the period of t^*. Also the pulse acting on the column during the same period is calculated by $A\sigma t^*$. Because of equilibrium between the two quantities, i.e., $\rho_0 A V_p t^* V_m = A\sigma t^*$, the impact stress, σ, is obtained by

$$\sigma = \rho_0 V_m V_p \tag{9.9a}$$

where ρ_0 = density of the column before being struck.

Using the strain given by Equation (9.8), the impact stress is also given by

$$\sigma = E\varepsilon = E\frac{V_m}{V_p} \tag{9.9b}$$

The propagation velocity of the stress wave can then be obtained from Equations (9.9a) and (9.9b) as follows:

$$V_p = \left(\frac{E}{\rho_0}\right)^{1/2} \tag{9.10}$$

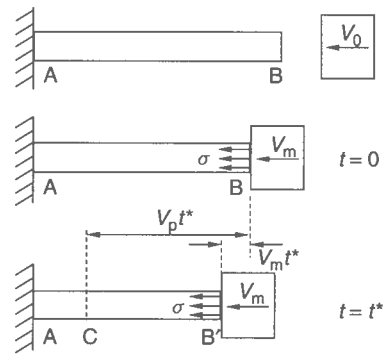

Figure 9.2 An example to illustrate the effects of impact stress wave propagation

Substitution of Equation (9.10) into Equation (9.9b) yields

$$\sigma = (E\rho_0)^{1/2} V_m \tag{9.11}$$

In the above, it is noted that the particle velocity, V_m, is not necessarily equal to the initial velocity, V_0, of the striking body. It is apparent that Equation (9.11) takes an entirely different expression from that of Equation (9.6). This is because Equation (9.11) represents the impact stress propagation immediately after striking, while Equation (9.6) indicates the stress after the stress wave ceases. For a more elaborate treatment of the stress wave effects in structural members under impact loading, Karagiozova & Jones (1998), Kolsky (1963) or Hayashi & Tanaka (1988), among others, may be referred to.

It is not always straightforward to calculate the load effects of steel structures under impact loading since propagation of the stress wave can play an important role. In the context of Equation (1.1), an easier alterative, therefore, is to use the loss of kinetic energy instead of the load effects as the measure of 'demand', while the energy absorption capability is employed as the measure of 'capacity'.

9.3 Material Constitutive Equation of Structural Steels under Impact Loading

The stresses in structural steels under a given magnitude of impact loading in the elastic–plastic regime increase as the strain rate increases. The mechanism of plastic deformation under impact loading in such a case may be classified into four regions, as shown in Figure 9.3 (Rosenfield & Hahn 1974, Perzyna 1974).

In region I, the yield (or flow) stress is not affected by strain rate and temperature. In region II, the yield (or flow) stress increases as the strain rate increases. In region III, i.e., at low temperatures, the effect of strain rate on the yield (or flow) stress becomes

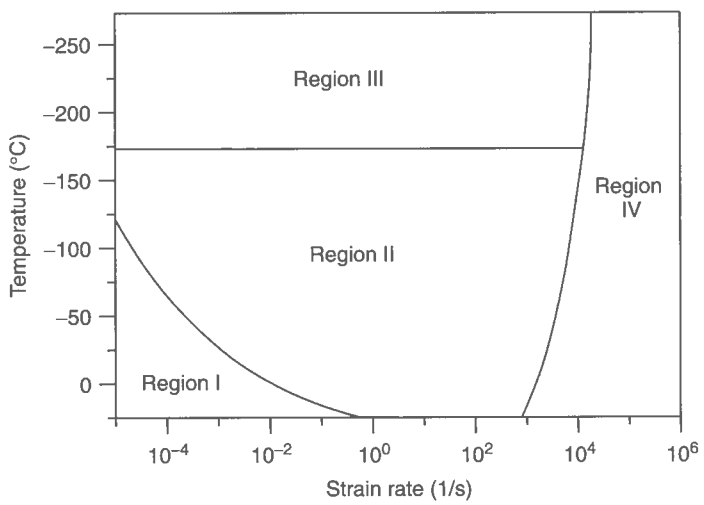

Figure 9.3 Classification of plastic deformation mechanisms as a function of strain rate and temperature

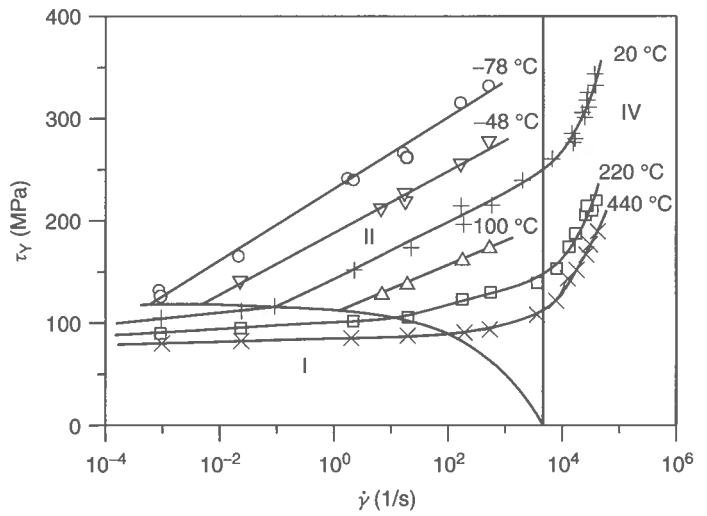

Figure 9.4 Variation of the dynamic shear yield stress of mild steel as a function of shear strain rate and temperature (symbols denote experimental results after Campbell & Ferguson 1970)

much moderate. Region III is distinguished from region II by a boundary which is termed the twinning mode of the plastic deformation mechanism due to low temperature. In region IV, the yield (or flow) stress is extremely sensitive to the strain rate.

Figure 9.4 shows a sample relationship between the dynamic shear yield stress and the shear strain rate for mild steels, varying the strain rate and temperature (Campbell & Ferguson 1970).

9.3.1 The Malvern Constitutive Equation

The stress–strain relationship for structural steels under impact loading in a one-dimensional form, which is typically applied in region II above, may be given by (Malvern 1969)

$$\sigma = f(\varepsilon) + c_1 \ln(1 + c_2 \dot{\varepsilon}^p) \tag{9.12}$$

where $\sigma = f(\varepsilon)$ = stress–strain relationship of material under static loading, $\dot{\varepsilon}^p$ = plastic strain rate, c_1, c_2 = material constants.

The plastic strain rate can then be obtained from Equation (9.12) as follows:

$$\dot{\varepsilon}^p = \frac{1}{c_2}\left\{\exp\left[\frac{\sigma - f(\varepsilon)}{c_1}\right] - 1\right\} \tag{9.13}$$

It may be surmised from Equation (9.13) that the plastic strain rate represents an effect of the excess of stress between the dynamic stress, σ, and the static stress, $f(\varepsilon)$. As the simplest expression, the excess stress may sometimes be expressed by a linear function as follows:

$$E\dot{\varepsilon}^p = c_3[\sigma - f(\varepsilon)] \tag{9.14}$$

where E = elastic modulus, c_3 = material constant.

Since the elastic component, $\dot{\varepsilon}^e$, of strain rate has a linear relationship with the corresponding stress $\dot{\sigma}$, i.e., $E\dot{\varepsilon}^e = \dot{\sigma}$, and the total strain is a sum of the elastic and plastic components, we get the following equation:

$$E\dot{\varepsilon} = E(\dot{\varepsilon}^e + \dot{\varepsilon}^p) = \dot{\sigma} + c_3[\sigma - f(\varepsilon)] \tag{9.15}$$

Equation (9.15) is sometimes called the Malvern constitutive equation and is widely used for the response analysis of steel structures under impact loading, primarily representing region II in Figure 9.3.

In analyzing the crashworthiness of steel structures under impact loading, the dynamic yield strength and fracture strain are thus the two primary influential parameters. The dynamic effect on the material properties is associated with the strain rate as previously noted.

9.3.2 Dynamic Yield Strength – the Cowper–Symonds Equation

The dynamic yield strength of the material may be expressed as follows (Karagiozova & Jones 1997):

$$\frac{\sigma_{Yd}}{\sigma_Y} = f(\dot{\varepsilon})g(\varepsilon) \tag{9.16}$$

where σ_Y, σ_{Yd} = static or dynamic yield stresses, $f(\dot{\varepsilon})$ = a function of strain rate sensitivity effect, $g(\varepsilon)$ = a material strain-hardening function, $\dot{\varepsilon}$ = strain rate.

If one neglects the effects of strain hardening, one can take that $g(\varepsilon) = 1$. The strain rate sensitivity parameter, $f(\dot{\varepsilon})$, is often given using the so-called Cowper–Symonds equation (Cowper & Symonds 1957) as follows:

$$\frac{\sigma_{Yd}}{\sigma_Y} = 1.0 + \left(\frac{\dot{\varepsilon}}{C}\right)^{1/q} \tag{9.17}$$

where C and q are coefficients to be determined based on test data, see Table 9.2.

Figure 9.5 plots the Cowper–Symonds equation together with the relevant coefficients for mild or high tensile steels when $g(\varepsilon) = 1$. Figure 9.6 shows the effects of both strain rate and temperature on the yield strength of a higher tensile steel. It is evident that the material yield strength increases with increase in the strain rate and decrease in temperature. Also, for higher tensile steel the percentage increase of σ_{Yd}/σ_Y is smaller than that for mild steel.

Table 9.2 Sample coefficients for the Cowper–Symonds constitutive equation.

Material	C (1/s)	q	Reference
Mild steel	40.4	5	Cowper & Symonds (1957)
High tensile steel	3200	5	Paik & Chung (1999)
Aluminum alloy	6500	4	Bodner & Symonds (1962)
α-titanium (Ti 50A)	120	9	Symonds & Chon (1974)
Stainless steel 304	100	10	Forrestal & Sagartz (1978)

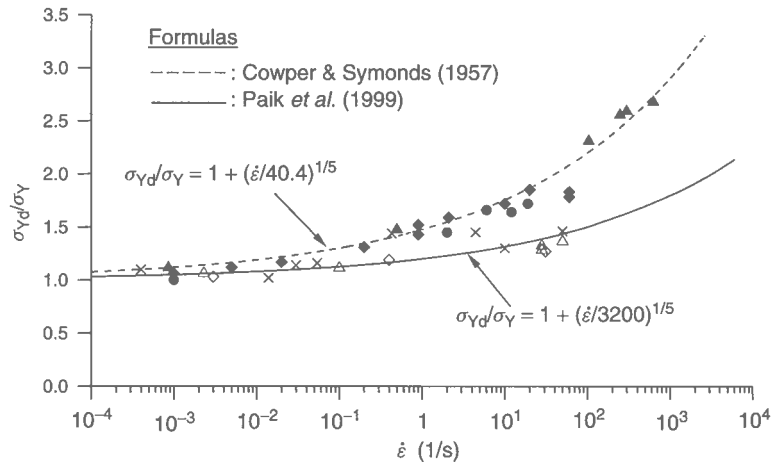

Figure 9.5 Dynamic yield strength (normalized by the static yield strength) plotted versus strain rate for mild and high tensile steels; references shown within the figure after Paik *et al.* (1999)

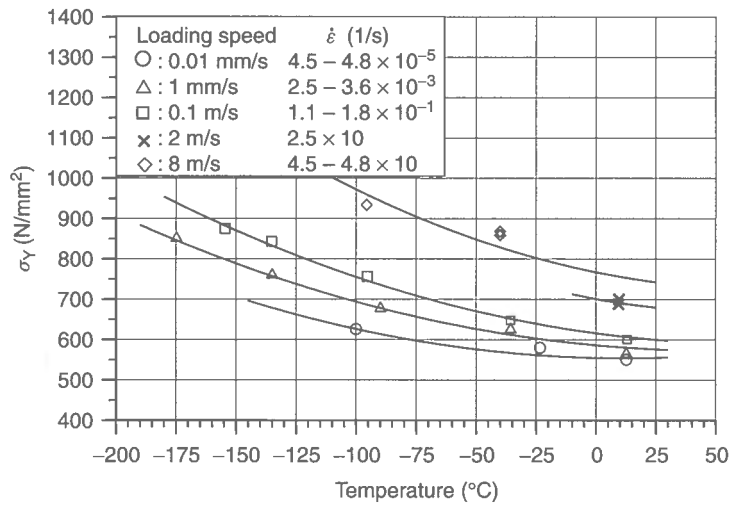

Figure 9.6 Effects of strain rate and temperature on the yield strength of a higher tensile steel (Toyosada *et al.* 1987)

9.3.3 Dynamic Fracture Strain

Both crushing effects and yield strength increase as the loading speed gets faster, while any fracture or tearing of steel (and the welded regions) of a structure tends to occur earlier. The following approximate formula, which is the inverse of the Cowper–Symonds constitutive equation for the dynamic yield stress, is then useful for estimating the dynamic fracture strain as a function of the strain rate (Jones 1989), namely

$$\frac{\varepsilon_{\mathrm{Fd}}}{\varepsilon_{\mathrm{F}}} = \xi \left[1.0 + \left(\frac{\dot{\varepsilon}}{C} \right)^{1/q} \right]^{-1} \tag{9.18}$$

where ε_{F}, $\varepsilon_{\mathrm{Fd}}$ = static or dynamic fracture strains, ξ = ratio of the total energies to rupture for dynamic and static uniaxial loadings.

If the energy to failure is assumed to be invariant, i.e., independent of $\dot{\varepsilon}$, then it may be taken that $\xi = 1$. Figure 9.7 plots Equation (9.18) with three sets of the coefficients together with experimental results for mild steels when $\xi = 1$. The expression in Equation (9.18) represents the decrease of the dynamic fracture strain with increase in the strain rate, but the coefficients for the dynamic fracture strain differ from those for the dynamic yield strength. It is again evident that the strain rate is a primary parameter affecting the impact mechanics.

9.3.4 Inertia Effects

The inertia effects may sometimes need to be considered for the impact response of thin-walled structures (Reid & Reddy 1983, Harrigan *et al.* 1999, Paik & Chung 1999, Karagiozova *et al.* 2000). Due to inertia effects and stress wave propagation phenomena

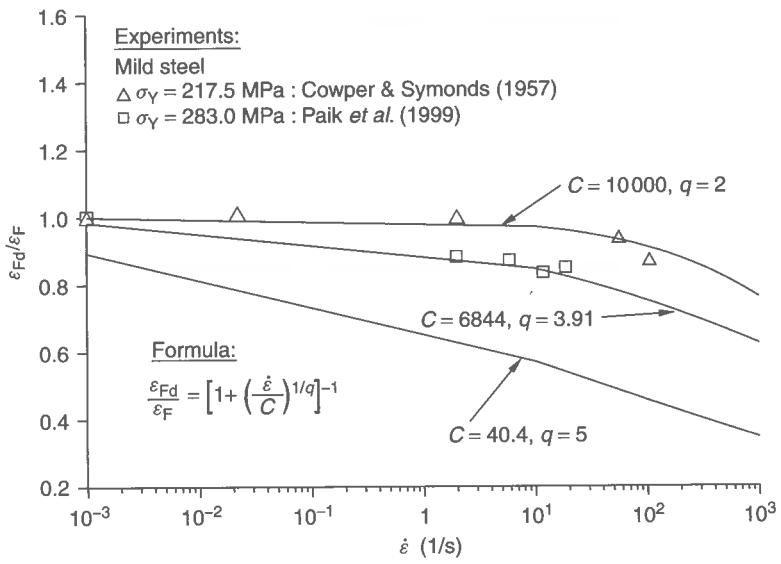

Figure 9.7 Dynamic fracture strain (normalized by the static fracture strain) versus strain rate for mild steels

within the structures during impact loading, the strain distribution (or deformation pattern) at any moment in time would be non-homogeneous. It is typically considered that the inertia effects become more important when the strain rate is greater than about $0.1\,\mathrm{s}^{-1}$.

To investigate the characteristics of inertia effects, Paik & Chung (1999) carried out a series of experiments on crushing square steel tubes. It was observed that as the maximum crushing indentation became larger and larger (indicating that the mass of the striking body and/or the impact speed became larger, thus increasing the initial kinetic energy involved), the inertia effects increased, but these effects could be ignored for strain rates less than about $50\,\mathrm{s}^{-1}$.

9.3.5 Friction Effects

During an impact loading process, the influence of friction would be normally large when there is a relative velocity between the struck body and the indentor (or striking body). This situation is often seen in ship grounding incidents when a ship with forward speed runs onto a rock pinnacle, for instance. For collisions of marine structures, the influence of friction may be ignored because the relative velocity between striking and struck bodies is normally comparatively small, but friction effects would normally need to be considered for the treatment of ship grounding mechanics.

9.4 Collapse Strength of Beams under Impact Lateral Loads

As previously studied in Chapter 2, it may be considered in the quasi-static case that a beam under lateral load, q, collapses if a plastic hinge mechanism is formed at $q = q_{\mathrm{c}}$. A beam which is made from a rigid–perfectly plastic material is supposed to remain rigid as long as the external lateral load is smaller than the static collapse lateral load, q_{c}. Hence static equilibrium cannot be achieved in the collapsed beam if the effects of strain hardening or large deformations are neglected.

On the other hand, when an external load larger than q_{c} is applied suddenly or impulsively, the beam deforms plastically and inertia forces are generated. If the external load pulse continues for a sufficiently long duration, the lateral deflection of the beam will become excessive. However, if the external load pulse is removed at a soon-enough point in time, or decays to a small-enough value after a certain time period, part of the kinetic energy will be absorbed by the beam, subsequent to permanent plastic deformations.

The governing differential equation of a plate–beam combination under dynamic lateral load, q, may be expressed by (Jones 1997b)

$$EI_{\mathrm{e}} \frac{\partial^4 w}{\partial x^4} = q - m \frac{\partial^2 w}{\partial t^2} \tag{9.19}$$

where $m = \rho A$ = mass per unit length of beam, ρ = density of material, t = time, EI_{e} = bending rigidity of the effective section beam, A = cross-sectional area of the beam.

The elastic strain energy in a beam can be given from Equation (2.68) in Chapter 2 as follows:

$$U = \int_{\mathrm{Vol}} \frac{\sigma_x^2}{2E} \mathrm{dVol} \tag{9.20a}$$

The maximum possible amount of the elastic strain energy which a beam can absorb is obtained when σ_x reaches the equivalent yield stress, σ_{Yeq}, in the entire volume of the beam, namely

$$U_{max} = \frac{\sigma_{Yeq}^2}{2E} LA \tag{9.20b}$$

where σ_{Yeq} takes account of the effect of different yield stresses of plating and stiffener, see Table 2.1 in Chapter 2; L = span of the beam.

Since local plastic deformations actually occur at smaller values of elastic strain energy, Equation (9.20b) represents the upper limit of the strain energy absorbed. The initial kinetic energy absorbed by the beam under a uniformly distributed impulsive velocity, V_0, may approximately be given by

$$E_k = \tfrac{1}{2}\rho LAV_0^2 \tag{9.21a}$$

For a beam struck by a total mass W traveling with an initial velocity V_0, the initial kinetic energy is given by

$$E_k = \tfrac{1}{2}WV_0^2 \tag{9.21b}$$

It appears that the rigid–perfectly plastic material approach may be relevant when the ratio of the initial kinetic energy to the maximum amount of the strain energy is larger than about 10, namely (Jones 1989a)

$$\frac{E_k}{U_{max}} > 10 \tag{9.22}$$

Figure 9.8 shows a schematic of a rectangular-type load pulse. The lateral pressure, p_0 ($p_0 = q_0/b$ for a plate–beam combination) is dynamically applied at the beginning and is maintained constant for a duration τ. After that, the load is removed. The rectangular pressure pulse is often termed an 'impulsive loading' when $p_0/p_c \gg 1$ ($p_c = q_c/b$ for a plate–beam combination) (i.e., $\eta = p_0/p_c \to \infty$) and $\tau \neq 0$. In this situation, the following condition must be satisfied from the conservation of linear momentum at $t \neq 0$:

$$I = \int_0^\tau p(t)\,\mathrm{d}t = p_0\tau = \mu V_0 \tag{9.23}$$

where I, μ = pulse, mass per unit area.

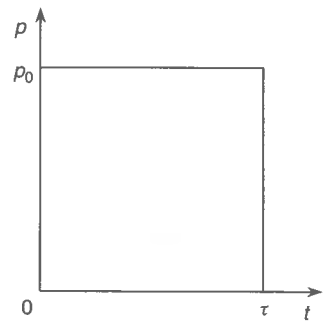

Figure 9.8 A schematic of a rectangular-shaped pressure pulse

It has been realized that the elastic effects are not important when the duration is sufficiently shorter than the corresponding elastic natural period, namely

$$\frac{\tau}{T} \ll 1 \tag{9.24a}$$

where T is the fundamental period of elastic vibration which may be taken as follows:

$$T = \frac{2L^2}{\pi}\left(\frac{m}{EI_e}\right)^{1/2} \quad \text{for a beam simply supported at both ends} \tag{9.24b}$$

$$T = \frac{2\pi L^2}{(4.73)^2}\left(\frac{m}{EI_e}\right)^{1/2} \quad \text{for a beam clamped at both ends} \tag{9.24c}$$

The maximum permanent lateral deflections, w_p, of clamped beams under dynamic lateral load with an initial impact velocity, V_0, may be calculated for rectangular cross-sections with breadth B and thickness H, taking into account the large-deflection effect, as follows (Jones 1997b):

$$\frac{w_p}{H} = \frac{1}{2}\left[\left(1 + \frac{\lambda}{2\alpha}\right)^{1/2} - 1\right] \quad \text{for impact loading } (\alpha \ll 1) \tag{9.25a}$$

$$\frac{w_p}{H} = \frac{1}{2}\left[\left(1 + \frac{3\lambda}{4}\right)^{1/2} - 1\right] \quad \text{for impulsive loading} \tag{9.25b}$$

where $\lambda = mV_0^2L^2/(4M_pH)$, $\alpha = mL/(2w)$, $M_p = \sigma_0 BH^2$, w = impact mass, σ_0 = flow stress, refer to Section 9.8.1.

For plate-stiffener combination cross-sections under dynamic loading, Schubak *et al.* (1989), Nurick *et al.* (1994) and Nurick & Jones (1995), among others, may be referred to.

9.5 Collapse Strength of Columns under Impact Axial Compressive Loads

The governing differential equation of small-deformation theory for a column with initial deflection under impact axial compressive load, P, may be expressed by (Jones 1997b)

$$EI\frac{\partial^4 w}{\partial x^4} + P\frac{\partial^2(w + w_0)}{\partial x^2} = -m\frac{\partial^2 w}{\partial t^2} \tag{9.26}$$

For a column simply supported at both ends, the lateral deflection functions may be assumed as follows:

$$w_0 = \delta_0 \sin\frac{\pi x}{L}, \quad w = \delta(t)\sin\frac{\pi x}{L} \tag{9.27}$$

where w_0 = initial deflection, w = added deflection due to applied loading, δ_0, δ = initial and added deflection amplitudes.

Substitution of Equation (9.27) into Equation (9.26) results in

$$\frac{d^2\delta(t)}{dt^2} + C_1\delta(t) = C_2 \tag{9.28}$$

where

$$C_1 = \left(\frac{\pi}{L}\right)^2 \left(\frac{P_E}{m}\right)\left(1 - \frac{P}{P_E}\right), \quad C_2 = \left(\frac{\pi}{L}\right)^2 \frac{P}{m}\delta_0$$

$P_E = \pi^2 E I_e / L^2 =$ Euler buckling load.

It is obvious that the second-order differential equation, Equation (9.28), has a different form of solution depending on the sign of the coefficient C_1: if $P < P_E$ then $C_1 > 0$, and if $P > P_E$ then $C_1 < 0$.

9.5.1 Oscillatory Response

When $P < P_E$, the coefficient C_1 is positive and thus Equation (9.28) has the solution as follows:

$$\delta(t) = \frac{C_2}{C_1}\left[1 - \cos(\sqrt{C_1}t)\right] \tag{9.29}$$

On substituting Equation (9.29) into Equation (9.27), the added deflection of the column is given, considering that the initial lateral velocity is zero (i.e., $d\delta/dt = 0$ at $t = 0$) and that the added deflection is zero (i.e., $\delta = 0$) at $t = 0$, as follows:

$$w = B_1(\tau)\delta_0 \sin\frac{\pi x}{L} \tag{9.30}$$

where

$$B_1(\tau) = \frac{P/P_E}{1 - P/P_E}\left\{1 - \cos\left[\left(1 - \frac{P}{P_E}\right)^{1/2}\tau\right]\right\}$$

$\tau = 2\pi t/T = \left[\pi^4 E I_e/(mL^4)\right]^{1/2} t =$ non-dimensional time, T is as defined in Equation (9.24).

Figure 9.9 plots Equation (9.30) at $x = L/2$, showing the variations of the maximum added deflections of the column versus non-dimensional time. It is seen from Figure 9.9 that the added deflection of a column under dynamic axial compressive load, P, smaller than P_E varies cyclically with time, but the dynamic buckling phenomenon does not take place. The added deflection increases significantly as P approaches P_E and the period of oscillation becomes infinite at $P = P_E$.

9.5.2 Dynamic Buckling Response

If $P > P_E$, then $C_1 < 0$. In this case, the second-order differential equation, Equation (9.28), involves hyperbolic functions. For convenience, Equation (9.28) may be rewritten as follows:

$$\frac{d^2\delta(t)}{dt^2} - C_1^*\delta(t) = C_2 \tag{9.31}$$

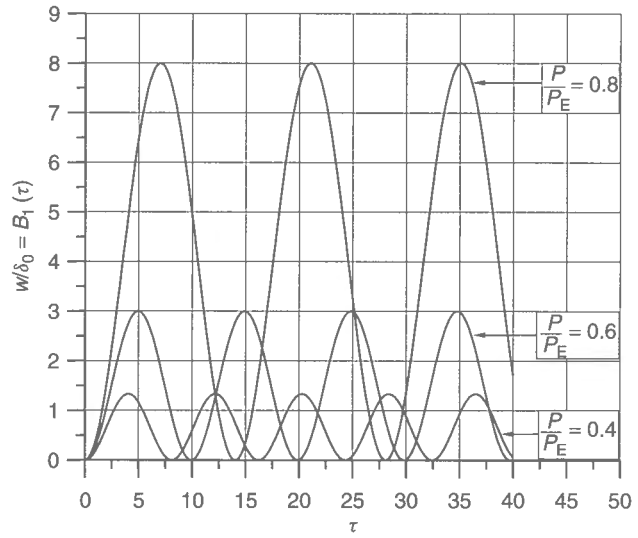

Figure 9.9 Oscillation of the added deflection of a column under dynamic axial compressive load, P, smaller than P_E versus time, as obtained from Equation (9.30) at $x = L/2$

where

$$C_1^* = \left(\frac{\pi}{L}\right)^2 \left(\frac{P_E}{m}\right)\left(\frac{P}{P_E} - 1\right)$$

The solution of the differential equation, Equation (9.31), is given by

$$\delta(t) = \frac{C_2}{C_1^*}\left[\cosh\left(\sqrt{C_1^*}t\right) - 1\right] \tag{9.32}$$

The added deflection of the column is then obtained by substituting Equation (9.32) into Equation (9.27b) as follows:

$$w = B_2(\tau)\delta_0 \sin\frac{\pi x}{L} \tag{9.33}$$

where

$$B_2(\tau) = \frac{P/P_E}{P/P_E - 1}\left\{\cosh\left[\left(\frac{P}{P_E} - 1\right)^{1/2}\tau\right] - 1\right\}$$

Figure 9.10 plots Equation (9.33) at $x = L/2$. It is evident from Figure 9.10 that the column-added deflection significantly increases with time and becomes very large at a certain point in time. This phenomenon is sometimes called dynamic buckling.

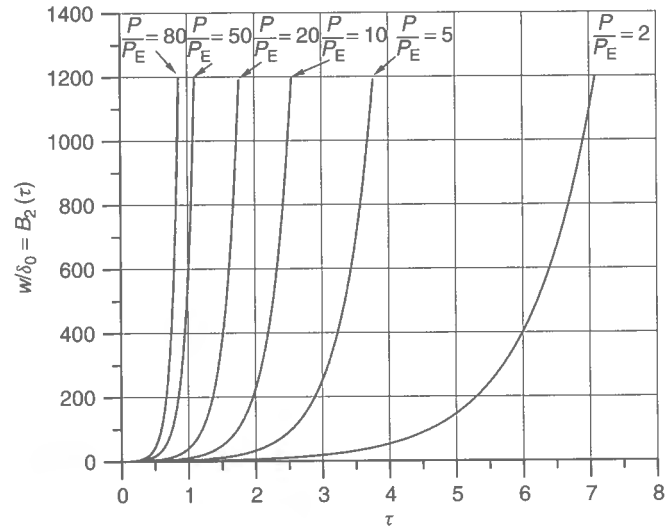

Figure 9.10 Dynamic buckling of a column under dynamic axial compressive load P larger than P_E, as obtained from Equation (9.33) at $x = L/2$

9.6 Collapse Strength of Plates under Impact Lateral Pressure Loads

9.6.1 Analytical Formulations – Small-deflection Theory

In a quasi-static loading condition, a plate under lateral pressure collapses if the applied pressure is greater than the collapse pressure load, p_c, as presented in Section 4.9.4 of Chapter 4. When the plate is subjected to impact pressure pulses which are applied for a short time period, however, it may withstand the loads even if the initial peak pressure is greater than p_c.

The plate under such a pressure pulse initially deforms, but the mass of the plate has a certain amount of kinetic energy when the pressure is removed. Thereafter this kinetic energy is absorbed by the structure, which deforms accordingly. The motion of the plate ceases when all kinetic energies are dissipated as strain energy. In this process, the plate response is time dependent and the inertia forces may play an important role in equilibrium equations.

The governing differential equations for the dynamic behavior of an element of a rectangular plate are given by taking into account the effect of inertia forces, as follows (for the symbols used, Figure 9.11 may be referred to unless otherwise specified below):

$$\frac{\partial Q_x}{\partial x} + \frac{\partial Q_y}{\partial y} + p = \mu \frac{\partial^2 w}{\partial t^2} \tag{9.34a}$$

$$\frac{\partial M_{yx}}{\partial y} + \frac{\partial M_x}{\partial x} - Q_x = 0 \tag{9.34b}$$

$$\frac{\partial M_{xy}}{\partial x} - \frac{\partial M_y}{\partial y} + Q_y = 0 \tag{9.34c}$$

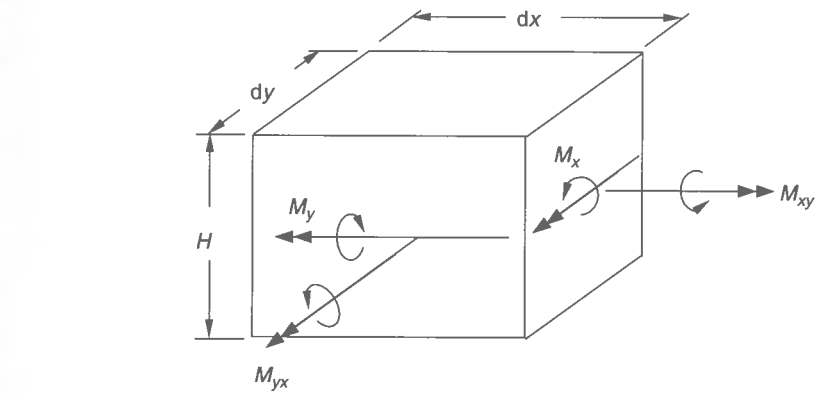

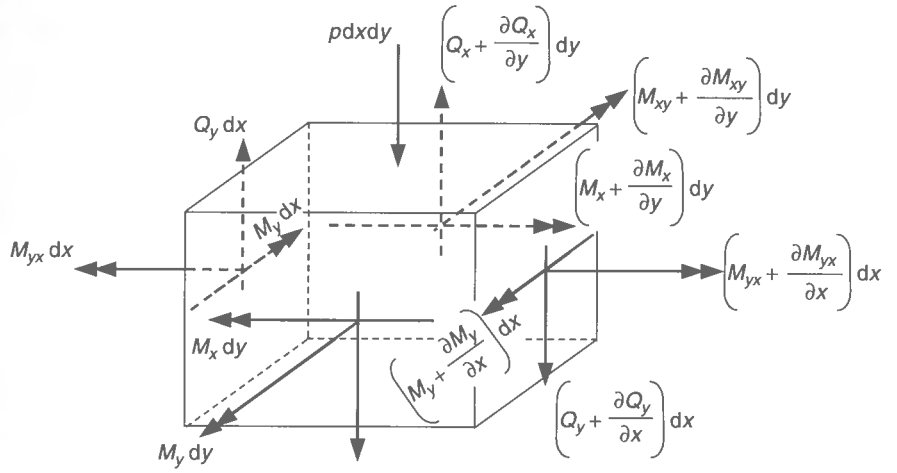

Figure 9.11 An infinitesimal element, dx dy, of a rectangular plate (H = plate thickness)

where p is the applied pressure which is a function of t (time), Q_x and Q_y are the transverse shear forces, $\mu = \rho H$ is the mass of the plate per unit area, H is the plate thickness, and ρ is the material density. Also, bending moments per unit length, M_x, M_y, and twisting moment per unit length, $M_{xy}(= -M_{yx})$, are given by

$$M_x = -D\left(\frac{\partial^2 w}{\partial x^2} + \nu \frac{\partial^2 w}{\partial y^2}\right) \tag{9.34d}$$

$$M_y = -D\left(\frac{\partial^2 w}{\partial y^2} + \nu \frac{\partial^2 w}{\partial x^2}\right) \tag{9.34e}$$

$$M_{xy} = -M_{yx} = D(1-\nu)\frac{\partial^2 w}{\partial x \partial y} \tag{9.34f}$$

where $D = EH^3/[12(1-\nu^2)]$ = plate bending rigidity, E = Young's modulus, ν = Poisson's ratio.

Eliminating Q_x and Q_y from Equations (9.34a) to (9.34c) and considering Equation (9.34f), we have

$$\frac{\partial^2 M_x}{\partial x^2} - 2\frac{\partial^2 M_{xy}}{\partial x \partial y} + \frac{\partial^2 M_y}{\partial y^2} = -p + \mu \frac{\partial^2 w}{\partial t^2} \tag{9.34g}$$

Substitution of Equations (9.34d) to (9.34f) into Equation (9.34g) yields

$$\frac{\partial^4 w}{\partial x^4} + 2\frac{\partial^4 w}{\partial x^2 \partial y^2} + \frac{\partial^4 w}{\partial y^4} = \frac{1}{D}\left(p - \mu \frac{\partial^2 w}{\partial t^2}\right) \tag{9.34h}$$

Jones (1997b) solved the governing differential equation, Equation (9.34g), for a simply supported square plate of $a/b = 1$ when a uniformly distributed pressure pulse with initial value of p_0 was applied for duration τ, following the pulse profile as shown in Figure 9.8. When p_0 is less than twice the static collapse pressure, which is equal to $24M_P/b^2$, the response has two phases: the first phase coincides with the period of application of the pressure and the second starts when the pressure is removed and ends when the kinetic energy of the plate becomes zero. The maximum permanent deflection, w_p, at the center of the plate is in this case given by

$$w_p = \frac{p_c \tau^2}{\mu}\eta(\eta - 1) \quad \text{for } p_c \le p_0 \le 2p_c \tag{9.35}$$

where $\eta = p_0/p_c$, $p_c = 24\,M_p/b^2$, $M_p = \sigma_0 H^2/4$, σ_0 = flow stress.

As noted above, Equation (9.35) has been derived considering the dynamic pressure profile shown in Figure 9.8. It has been shown that the resulting cross-sectional forces (i.e., bending moments M_x, M_y) are 'admissible', in the sense that the Tresca-type yield criterion is not violated, and also remain stationary. However, when the initial peak pressure, p_0, shown in Figure 9.8 is larger than twice the static collapse pressure, the two-phase response is not statically admissible, because the assumed velocity profile results in a violation of the assumed yield criterion. In this case, it is assumed that the response has three phases: the first phase coincides with the application of the pressure pulse, the second phase is characterized by moving hinge lines, and in the third phase the plastic hinges become stationary. At the end of the third phase the maximum lateral deflection of the square plate is given by

$$w_p = \frac{p_c \tau^2}{4\mu}\eta(3\eta - 2) \quad \text{for } p_0 > 2p_c \tag{9.36}$$

For both the two-phase response and the three-phase response noted above, the response time, T, is found to be equal to $\eta\tau$.

9.6.2 Analytical Formulations – Large-deflection Theory

Equation (9.35) or (9.36) was derived under the assumptions that the lateral deflections are not large enough to cause any change to the geometry of the plate, and the supports do not provide any resistance to the axial movement of the plate edges. However, when

the deflections are relatively large and the supports resist the axial movement of the plate edges, membrane stresses develop and the structure provides further resistance against the applied pressure. The resistance is experienced irrespective of whether the pressure is applied statically or dynamically.

Jones (1997b) proposes the rigid-plastic approach to compute the permanent deflection of beams and rectangular plates loaded by a pressure pulse, $p(t)$, taking into account the large-deflection effect. According to the Jones approach, if bending moments and membrane forces are developed within the plate, resulting from the axial restraint of the supports, the lateral deflection, w, obeys the following equation:

$$\int_A (p - \mu\,\ddot{w})\dot{w}\,\mathrm{d}A = \sum_{m=1}^{r} \int_{\ell_m} (M + Nw)\dot{\theta}_m\,\mathrm{d}\ell_m \tag{9.37}$$

where μ = mass of the plate per unit area, r = number of hinge lines, ℓ_m = length of the hinge line, θ_m = relative angular rotation across a hinge line; N and M are the membrane and bending forces, respectively, acting along the hinge lines. It has been assumed that the material is rigid–perfectly plastic and the loaded plate is divided into a number of rigid sections separated by straight-line hinges.

If it is further assumed that (1) the plate is clamped along its four edges, (2) the material obeys the Tresca-type yield criterion, and (3) shear forces do not affect yielding, then the maximum permanent deflection, w_p, of the plate is given by

$$w_p = H\frac{(3 - \xi_0)\left[\sqrt{1 + 2\eta(\eta - 1)(1 - \cos\gamma\tau)} - 1\right]}{2[1 + (\xi_0 - 2)(\xi_0 - 1)]} \tag{9.38}$$

where

$$\xi_0 = \alpha(\sqrt{3 + \alpha^2} - \alpha), \quad \gamma^2 = \frac{96M_P}{\mu b^2 H(3 - 2\xi_0)}\left(1 - \xi_0 + \frac{1}{2 - \xi_0}\right), \quad \alpha = \frac{b}{a}$$

a = plate length, b = plate breadth, $M_P = \sigma_0 H^2/4$, σ_0 = flow stress, H = plate thickness, η is as defined in Equation (9.35).

If the load is impulsive, i.e., $p \to \infty$ and $\tau \to 0$, Equation (9.38) can be rewritten as follows:

$$w_p = H\frac{(3 - \xi_0)\{\sqrt{1 + (\lambda\alpha^2/6)(3 - 2\xi_0)[1 - \xi_0 + 1/(2 - \xi_0)]} - 1\}}{2[1 + (\xi_0 - 2)(\xi_0 - 1)]} \tag{9.39}$$

where $\lambda = \rho V_0^2 a^2/(\sigma_0 H^2)$. The velocity, V_0, is calculated from the relationship $p_0\tau = \mu V_0 = I$, where I is the pulse, refer to Equation (9.23).

Using the same approach, similar equations can be derived for simply supported plates. In this case, the maximum permanent deflection is given by

$$w_p = H\frac{(3 - \xi_0)\left[\sqrt{1 + 2\eta(\eta - 1)(1 - \cos\gamma\tau)} - 1\right]}{4[1 + (\xi_0 - 2)(\xi_0 - 1)]} \tag{9.40}$$

To account for the effect of the strain rate on yield stress, Symonds & Jones (1972) suggested a correction factor, f, which will be multiplied by the flow stress, σ_0, in either Equation (9.39) or (9.40), namely

$$f = 1 + \left(\frac{H^2\lambda^{3/2}}{6Ca^3}\sqrt{\frac{\sigma_0}{\mu}}\right)^{1/q} \tag{9.41}$$

where C, q are as defined in Equation (9.17) or Table 9.2.

Yu & Chen (1992) showed that in case of intense impulse it is essential to consider the effect of traveling hinges, i.e., to update the mode of the assumed collapse mechanism during the response. A similar approach has been developed by Shen (1997) for the dynamic response of a thin rectangular plate struck transversely (laterally) by a wedge. Chen (1993) applied the rigid-plastic theory to derive closed-form expressions for predicting the permanent deflections of rectangular plates under impulsive loads, using two types of deflection patterns, namely roof-shaped and sinusoidal patterns. It was shown that the sinusoidal shape function gives larger permanent deflections than the roof-shaped deformation function.

The insights noted above are based on the assumption that the material is rigid-perfectly plastic, i.e., that neither elastic deformations nor strain-hardening effects occur. This may cause the overestimation of permanent deflections, while the influence of strain rate sensitivity, which tends to reduce the permanent deflections, may be accounted for using the Cowper–Symonds formula, Equation (9.17).

9.6.3 Empirical Formulations

Based on existing experimental data for plates under impact lateral pressure loading, numerous empirical formulations were derived by curve fitting for predicting the permanent lateral deflection of clamped rectangular plates as follows (see Nurick & Martin (1989)):

$$\frac{w_p}{H} = 0.471\phi_r + 0.001 \tag{9.42a}$$

and Saitoh *et al.* (1995):

$$\frac{w_p}{H} = 0.593\phi_r + 1.38 \tag{9.42b}$$

where $\phi_r = I/(2H^2\sqrt{ba\rho\sigma_0})$, ρ = density of material, I = pulse.

9.7 Collapse Strength of Stiffened Panels under Impact Lateral Loads

The literature on the collapse behavior of stiffened panels subject to impact lateral loads is very meager because of the complexity of the structural response phenomena involved. There are, however, a few closed-form formulas or analytical methods available which may be useful to predict stress levels or deflections of stiffened panels under impact lateral loads (Schubak *et al.* 1989, Nurick *et al.* 1994, 1995, Nurick & Jones 1995). The effects of impact loading on the elastic–plastic structural response of stiffened panels have been

investigated mainly experimentally (Jones *et al.* 1991, Saitoh *et al.* 1995) or numerically (Smith 1989, Rudrapatna *et al.* 2000).

A simple formula for predicting the damage of a stiffened panel under impact lateral loads was derived by Woisin (1979). He suggested that in the case of ship–ship collisions the energy absorbed by the impacted and damaged plating in MJ equals $0.5\sum_i h_i t_i^2$, where $h_i(m)$ is the height of broken or heavily deformed side shell plating or longitudinal bulkhead of constant thickness t_i(cm). The Woisin formula has been derived based on his own test results obtained using relatively large-scale collision test models. Woisin (1990) later modified his formula and suggested that the energy absorbed by a damaged plate under impact is better represented by $0.2\sum_i h_i t_i d_i$, where $d_i(m)$ is the distance between horizontal structural elements such as decks or stringers.

Jones *et al.* (1991) carried out a series of impact tests on steel and aluminum grillages (or cross-stiffened panels). The impactor had a mass of 3 kg and an impact speed ranging from 3 to 7 m/s. They also predicted deformations using a quasi-static analysis, which showed fair agreements with the test results. The conclusion drawn from the study of Jones *et al.* (1991) strengthens the opinion that relatively low-velocity impacts may be treated quasi-statically as long as the strain-hardening effect is taken into account.

9.8 Crushing Strength of Thin-walled Structures

9.8.1 Fundamentals of Crushing Behavior

Consider a thin-walled structure under predominantly compressive loads as shown in Figure 9.12. Figure 9.13 represents a typical history of the resulting load versus displacement curve. As the compressive load increases, the structure eventually reaches the ultimate strength, which is the first peak in Figure 9.13. If the displacement continues to increase, the internal load decreases rapidly. During the unloading process, some parts of the structure may be bent or stretched. A lobe emerges and folding of walls starts. As

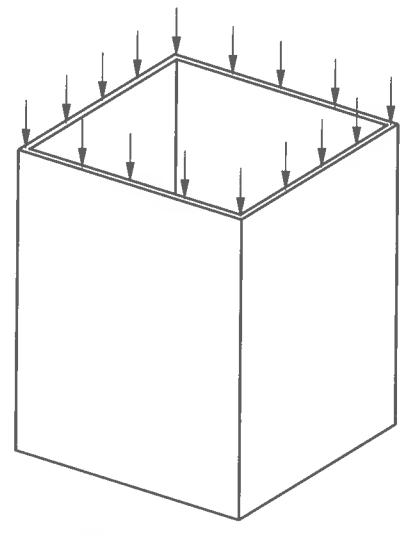

Figure 9.12 A thin-walled structure under predominantly axial compressive loads

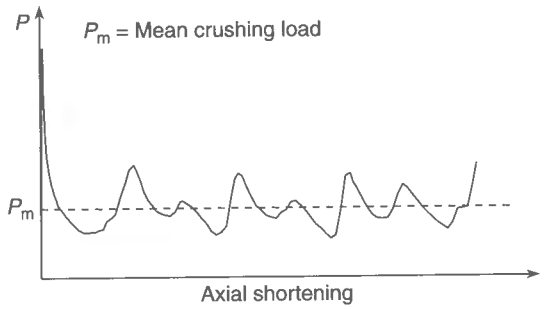

Figure 9.13 Crushing response of a thin-walled structure under predominantly compressive loads

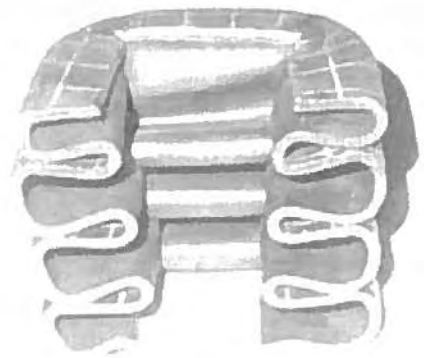

Figure 9.14 A thin-walled structure crushed under axial compressive loads and cut at its mid-section

the deformation continues, walls come into contact with each other, which ends the first fold and initiates a new fold. The internal load increases until the adjacent walls buckle. The structure starts to fold in a similar manner to the previous one. This process repeats itself until the entire structure is completely crushed. The completely folded structure then behaves as a rigid body until gross yielding occurs by compression. Each pair of peak and trough in Figure 9.13 is associated with the forming of one structural fold.

Figure 9.14 is a photograph of a crushed tube after cutting off half of the structure. It is apparent that many folds are formed during the crushing process. The forming of these folds results in large axial compressive displacements. Usually the folds develop sequentially from one end of the tube so that the phenomenon is known as progressive crushing. A ship's bow may possibly be designed to be crushable to achieve high-energy absorption capacity in a collision accident.

In a usual loading condition where the deformation is relatively small, the primary concern of a designer is the ultimate strength of the structure, or the initial peak load in Figure 9.13. In an accidental loading condition, however, the energy absorption capability is the more likely concern. The peak load of the structure is not always of primary interest, and the analysis of the detailed crushing behavior is not an easy task.

As long as the energy absorption capacity is of primary concern, a convenient alternative is to predict the 'mean crushing load' of the structure, which represents a mean value of fluctuating loads as shown in Figure 9.13. With this mean crushing load and the crushing displacement known, the absorbed energy can be calculated by multiplying these two values, which are approximately equal to the area below the corresponding load–displacement curve.

The insights gained from experiments on crushing thin-walled structures lead to an approximation widely applied in theoretical computations of the mean crushing strength: one structural fold forms at one time (Alexander 1960) so that one such fold can be analyzed independently. The influence of adjacent structures is therefore neglected. By means of the rigid–plastic theory, the mean crushing strength of structural elements can be estimated based on the kinematically admissible folding mechanisms. The response of complex plated structures is then calculated from the assemblage of such individual elements.

For the solution of crushing problems of thin-walled structures, where a plane stress state can be assumed and where the material is often modeled as a perfectly plastic material with a well-defined flow stress, σ_0, the classical theorem of upper bound plasticity is commonly used. Under this theorem, if the work rate of a structural system under the applied loads during any kinematically admissible collapse of the structure becomes equal to the corresponding internal energy dissipation rate, then this system under the applied loads will be at the point of collapse.

The analytical approach to calculate the crushing strength is typically based on introducing rigid–plastic collapse mechanisms into the basic structural unit. Two lines of thought currently exist regarding the modeling technique for a structure (Paik & Wierzbicki 1997). One technique, which is called the intersecting unit method (Amdahl 1983, Wierzbicki 1983, Pedersen *et al.* 1993), aims to model a structure as an assembly of typical intersecting units, such as L, T, Y and X (or cruciform) sections. The other technique, which is called the individual plate unit method (Murray 1983, Paik & Pedersen 1995), aims to model a structure as a collection of individual plate units. The intersecting unit method allows for a number of possible crushing mechanisms, and a crushing occurs in the mode which gives the lowest crushing strength.

For a complex plated structure under accidental crushing loads, the reaction force versus crushing displacement relationship is obtained by computing the mean crushing loads and the corresponding crushed distance as the striking body crushes into the struck body. The mean crushing strength may be obtained as a sum of the mean crushing strengths for individual elements. The energy absorption capability of the structure is then calculated by integrating the area below the reaction force versus crushing displacement curve.

In the following two sections, we present some useful analytical expressions for the mean crushing strength characteristics of individual plate units and intersecting elements.

While the derivation of all mean crushing strength formulations noted below is undertaken in a static loading condition, the effect of impact loading can be approximately accounted for by using the dynamic yield stress which accommodates the effect of strain rate sensitivity using Equation (9.16) in place of the static yield stress. Strain-hardening effects may also be approximately included, by using the so-called flow stress, σ_0, defined as the average of the yield stress, σ_Y, and the ultimate tensile stress, σ_T, given by $\sigma_0 = (\sigma_Y + \sigma_T)/2$.

9.8.2 Crushing Strength of Plates and Stiffened Panels

A plated structure may be regarded as an assembly of individual plate elements as shown in Figure 9.15. When thin-walled structures made up of such elements are subjected to axial compressive loads in one of the plate directions (see Figure 9.12), the other (unloaded) edges of the plate elements are usually connected with those of the surrounding structures. When at least two such plate edges meet, they can restrain each other and may even remain straight. Depending on the condition at the plate edges, there may be two different folding modes for the structure, as shown in Figures 9.16 and 9.17 (Murray 1983, Paik & Pedersen 1995): Mode I where one unloaded edge remains straight and the other unloaded edge is free to deform, and Mode II where both unloaded edges remain straight, or the bending deformation of the edges is small.

For the folding mechanisms shown in Figures 9.16 and 9.17, the plastic energy is mainly dissipated by in-plane deformations in triangular regions and the horizontal/vertical hinge lines. The contributions from plastic bending in the plastic hinges and membrane stretching in these triangular regions may be summed up, and then divided by the effective crushing

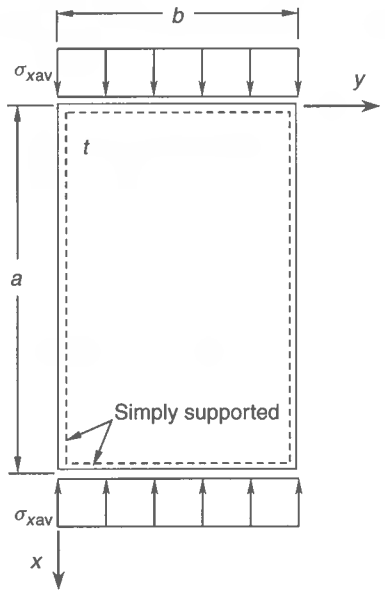

Figure 9.15 Geometry, boundary and loading of a rectangular plate element

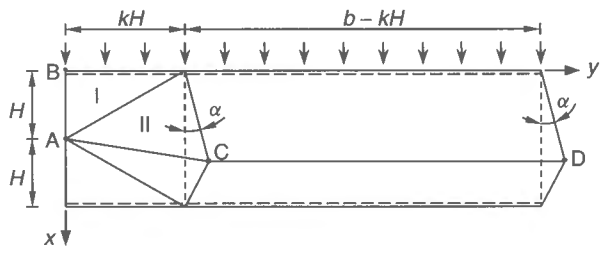

Figure 9.16 A schematic for the 'one edge straight/one edge free' folding mechanism (Mode I)

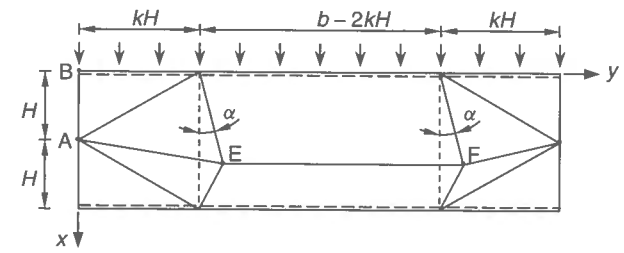

Figure 9.17 A schematic for the 'both edges straight' folding mechanism (Mode II)

length to yield the mean crushing strength. Using such a procedure based on rigid–plastic theory, Paik & Pedersen (1995) derived the following formulations for the mean crushing strength of unstiffened plate elements, namely

$$\frac{\sigma_{xm}}{\sigma_0} = \frac{1}{\eta_x}\left(1.0046\sqrt{\frac{t}{b}} + 0.1332\frac{t}{b}\right) \quad \text{for Mode I} \tag{9.43a}$$

$$\frac{\sigma_{xm}}{\sigma_0} = \frac{1}{\eta_x}\left(1.4206\sqrt{\frac{t}{b}} + 0.2665\frac{t}{b}\right) \quad \text{for Mode II} \tag{9.43b}$$

where σ_{xm} = mean crushing strength (stress) in the x direction, σ_0 = flow stress ($\sigma_0 = \sigma_Y$ is taken when the strain-hardening effect is ignored), t = plate thickness, b = plate width along the loaded edge, η_x = normalized effective crushing length, taken as 0.728.

For a continuous plated structure, the use of the mean crushing strength formula for Mode II, i.e., Equation (9.43b), may be more relevant since unloaded plate edges may in such cases remain straight.

Many engineering structures use stiffened panels. In terms of the energy absorption capacity, a stiffened panel with stiffeners in the longitudinal direction parallel to the compressive loading direction can be approximately replaced by an unstiffened plate with equivalent wall thickness (Paik & Wierzbicki 1997). The equivalent wall thickness is an increased thickness taking into account the cross-sectional area of both plate and stiffeners as follows:

$$t_{xeq} = t + \frac{A_{sx}}{b} \tag{9.44}$$

where t_{xeq} = equivalent wall thickness of a stiffened panel in the x direction, A_{sx} = cross-sectional area of stiffeners in the x direction, b = spacing of longitudinal stiffeners.

The contribution from transverse stiffeners in such cases can be neglected. The presence of longitudinal stiffeners in the direction of compressive loading does usually significantly affect (reduce) the effective crushing length since the stiffeners work against and thus disturb the folding process. Based on the crushing test data for thin-walled structures with stiffeners, Paik *et al.* (1996) derived an empirical formula by curve fitting for predicting the effective crushing length, as follows:

$$\eta_x = \begin{cases} 0.728 & \text{for } 0 < t_{xeq}/b \le 0.0336 \\ 704.49(t_{xeq}/b)^2 - 81.22t_{xeq}/b + 2.66 & \text{for } 0.0336 < t_{xeq}/b < 0.055 \\ 0.324 & \text{for } 0.055 \le t_{xeq}/b \end{cases} \tag{9.45}$$

Since Equation (9.45) is based on the crushing test data for stiffened square tubes, it may be available for the stiffened panel with the unloaded edges simply supported. The longitudinal mean crushing strength, σ_{xm}, of a stiffened panel with longitudinal stiffeners is then predicted from Equations (9.43) but using the applicable effective crushing length and the equivalent wall thickness for the stiffened panel as follows:

$$\frac{\sigma_{xm}}{\sigma_0} = \frac{1}{\eta_x}\left(1.0046\sqrt{\frac{t_{xeq}}{b}} + 0.1332\frac{t_{xeq}}{b}\right) \quad \text{for Mode I} \tag{9.46a}$$

$$\frac{\sigma_{xm}}{\sigma_0} = \frac{1}{\eta_x}\left(1.4206\sqrt{\frac{t_{xeq}}{b}} + 0.2665\frac{t_{xeq}}{b}\right) \quad \text{for Mode II} \tag{9.46b}$$

A similar expression may be relevant for predicting transverse mean crushing strength, σ_{ym}, of a stiffened panel as follows:

$$\frac{\sigma_{ym}}{\sigma_0} = \frac{1}{\eta_y}\left(1.0046\sqrt{\frac{t_{yeq}}{b}} + 0.1332\frac{t_{yeq}}{b}\right) \quad \text{for Mode I} \tag{9.47a}$$

$$\frac{\sigma_{ym}}{\sigma_0} = \frac{1}{\eta_y}\left(1.4206\sqrt{\frac{t_{yeq}}{b}} + 0.2665\frac{t_{yeq}}{b}\right) \quad \text{for Mode II} \tag{9.47b}$$

where

$$\eta_y = \begin{cases} 0.728 & \text{for } 0 < t_{yeq}/a \le 0.0336 \\ 704.49(t_{yeq}/a)^2 - 81.22t_{yeq}/a + 2.66 & \text{for } 0.0336 < t_{yeq}/a < 0.055 \\ 0.324 & \text{for } 0.055 \le t_{yeq}/a \end{cases}$$

$t_{yeq} = t + A_{sy}/a$ = equivalent wall thickness of a stiffened panel in the y direction, A_{sy} = cross-sectional area of stiffeners in the y direction, a = spacing of transverse stiffeners.

Under shearing force the plate element can crush. In this case, it is assumed that the mean crushing strength, τ_m, of an unstiffened or stiffened panel equals the shear flow stress as follows:

$$\tau_m = \tau_0 = \frac{\sigma_0}{\sqrt{3}} \tag{9.48}$$

In combined loads, the following interaction relationship for crushing is suggested as a function of the average stresses acting on the panel element (Paik & Pedersen 1996):

$$f_c = \left(\frac{\sigma_{xav}}{\sigma_{xm}}\right)^2 + \left(\frac{\sigma_{yav}}{\sigma_{ym}}\right)^2 + \left(\frac{\tau_{av}}{\tau_m}\right)^2 - 1 = 0 \tag{9.49}$$

where f_c = crushing function, σ_{xav}, σ_{yav}, τ_{av} = average stress components.

When the thin-walled structure with inclined sides is subjected to axial compressive loads as shown in Figure 9.18, the mean crushing strength may approximately be calculated from Equations (9.43) or (9.46) but considering the effect of inclination as follows:

$$\sigma^*_{xm} = \frac{1}{\cos\theta}\sigma_{xm} \tag{9.50}$$

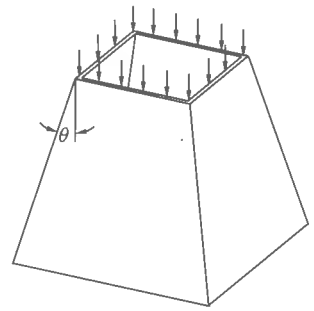

Figure 9.18 A thin-walled structure under axial compressive loads in the vertical direction, with sides inclined at an angle

where σ^*_{xm} = mean crushing strength for inclined loading, θ = angle between the structure and loading direction.

As previously noted, the dynamic loading effect may be approximately accounted for by replacing the flow or yield stress with the dynamic flow or yield stress which is determined from Equation (9.16) or (9.17).

9.8.3 Crushing Strength of L-, T- and X-Shaped Elements

In contrast to the modeling presented in Section 9.8.2, a thin-walled structure may also be modeled as an assembly of intersecting elements such as L-, T- or X-shaped elements (Paik & Wierzbicki 1997), as shown in Figure 9.19.

For L-shaped intersecting elements, two basic folding modes are relevant, namely the so-called quasi-inextensional and extensional modes, as shown in Figure 9.20 (Abramowicz & Wierzbicki 1989). The former mode consists of four trapezoidal elements undergoing rigid-body motions and separated by plastic hinges. The horizontal plastic hinges are stationary. The vertical plastic hinges travel in the plate elements. These hinges are formed where the material is bent and re-bent again.

While the structure may tend to follow an inextensional deformation mode, there may inevitably be extensions in some areas of the plate as shown in Figure 9.20(b). In this

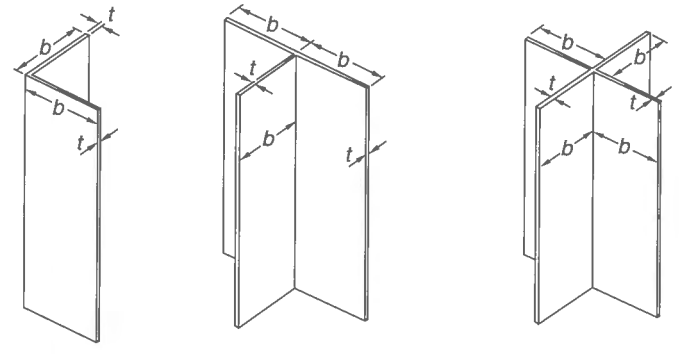

(a) L-shape (b) T-shape (c) X-shape

Figure 9.19 Intersecting plate element modeling of thin-walled structures

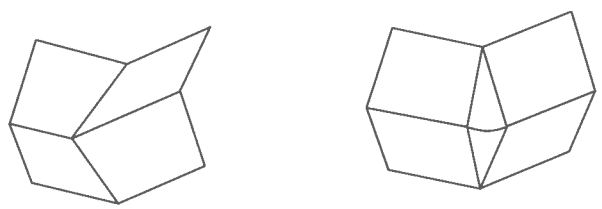

(a) Quasi-inextensional mode (b) Extensional mode

Figure 9.20 Schematic representation of the two basic folding modes for the L-shaped intersecting element

specific case, the extensional deformations in the circumferential directions are accommodated in a local zone of the vertical hinges. The extensional folding mode also consists of four trapezoidal elements. These four elements bend about the horizontal plastic hinges. As the vertical plastic hinges moves, the shape of the four elements distorts, and the material is stretched around the vertical connection.

While an L-shaped structure under crushing loads involves either a quasi-inextensional or extensional mode, complex intersecting elements with T- or X-shapes exhibit many more different folding patterns. These complicated symmetric and asymmetric and mixed folding patterns may be the results of different combinations of the above two basic folding modes. Any one such particular combination is generally triggered by the geometry of the structure, the shape of the initial buckling mode, and the initial imperfections.

Ohtsubo & Suzuki (1994), among others, derived the mean crushing strength formulations for L-, T- and X-shaped intersecting elements as follows:

$$\frac{\sigma_m}{\sigma_0} = \frac{1.5165}{\eta}\left(\frac{t}{b}\right)^{2/3} \quad \text{for L-shaped elements} \tag{9.51a}$$

$$\frac{\sigma_m}{\sigma_0} = \frac{1.1573}{\eta}\left(\frac{t}{b}\right)^{2/3} \quad \text{for T-shaped elements} \tag{9.51b}$$

$$\frac{\sigma_m}{\sigma_0} = \frac{1}{\eta}\left(1.2499\sqrt{\frac{t}{b}} + 0.2493\frac{t}{b}\right) \quad \text{for X-shaped elements} \tag{9.51c}$$

where σ_m = mean crushing strength, η = normalized effective crushing length, which may be taken as $\eta = 0.728$ for the unstiffened elements.

The effects of stiffeners, dynamic loading or inclined loading may approximately be accounted for as previously presented in Section 9.8.2.

9.9 Tearing Strength of Plates and Stiffened Panels

9.9.1 Fundamentals of Tearing Behavior

When a ship with a forward speed runs aground on a rock, its bottom may be torn resulting from the initial impact. If the kinetic energy is not entirely spent during the initial impact,

the ship will run on top of the rock for a distance. As a result, the grounding damage in the bottom can become a long gash extending tens or even hundreds of meters in length.

Similarly, when a ship collides with the side structure of another ship, the deck structure of the struck ship may be cut and penetrated by the striking bow. Steel is torn, separated and bent in a manner similar to a ship bottom in a grounding accident. The plate tearing also plays an important role in absorbing impact energy in a collision accident.

For purposes of investigating structural strength under such conditions, in the 1980s, many experiments were undertaken by dropping a heavy wedge into a vertical or near vertical steel plate in a drop-hammer rig (Vaughan 1980, Woisin 1982, Jones & Jouri 1987). Quasi-static tests were also carried out in the 1990s where wedges were pushed very slowly into plates (Lu & Calladine 1990, Wierzbicki & Thomas 1993, Paik 1994). A quasi-static test has the advantage of continuously recording various features.

Figure 9.21 shows a schematic of a cutting test setup where a sharp wedge is pushed into a steel plate. The wedge in such a case is generally made to be rigid so that the impact energy is entirely absorbed by the steel plate.

As the wedge is pushed into the plate, the plate buckles and bends out of plane. Load increases to a peak and then declines, but there is no separation of material. Eventually, as the wedge pushes further, cutting commences and load picks up again. The plate is torn apart in front of the wedge tip in the transverse direction. The separated material then bends over, forming two curls or flaps. The wedge keeps pushing the curved plate flaps, which roll up in the wake of the wedge. Near the wedge tip, the plate also develops a global deformation pattern, where the plate deforms out of the plane and separates. Under some circumstances, the plate may bend in the opposite direction and the curls reverse. Figure 9.22 shows plates cut by wedges, representing tearing and curling of the plate.

In such a process, there are several distinct mechanisms by which the energy is absorbed, namely tearing, bending and friction. In the vicinity of the wedge tip, the material is stretched transversely; the stress state there is mainly a result of membrane stretching. In the wake of the wedge, the plate bends out of the plane; the stress state there is primarily due to plastic bending. As the wedge moves, its side makes contacts with the plate, friction builds up and consumes a portion of energy.

The following sections present analytical and empirical formulations for the relationship between tearing force, F, and penetration, ℓ. All these formulations are derived in a quasi-static loading condition, but the dynamic effect may approximately be accounted for by including the effect of strain rate sensitivity on the material yield stress.

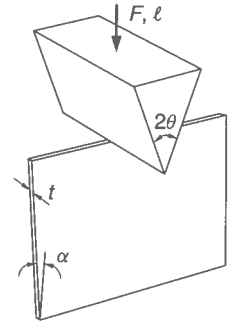

Figure 9.21 A schematic of a cutting test setup for a plate

(a)

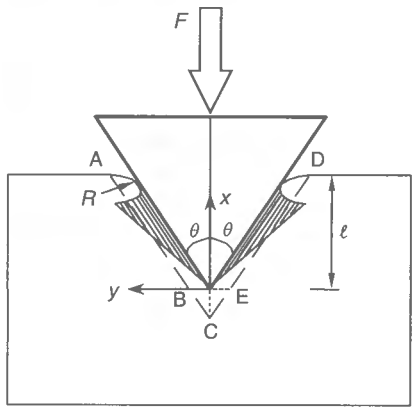

(b)

Figure 9.22 (a) A typical picture of tearing and curling of a plate upon being cut by a wedge (Thomas 1992); (b) A schematic of the analytical model on plate cutting by a rigid wedge (Zhang 2002)

9.9.2 Analytical Formulations

There are two distinct plastic deformation processes in play, namely the near-tip tearing and a global bending in the far field. Figure 9.23 shows a schematic of the plate damage including tearing and curling considered by Wierzbicki & Thomas (1993).

The work involved in the bending of the two curls or flaps in the far field includes contributions from both a continuous velocity field and a discontinuous velocity field.

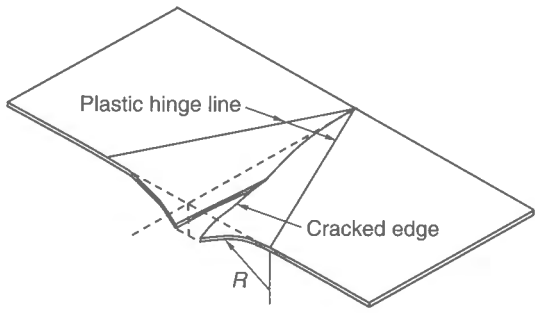

Figure 9.23 A schematic of the damage of a plate cut by a wedge

The integration of the continuous deformation field is performed over the plastically deforming zone, while the contribution from a discontinuous field is summed over a finite number of straight-line segments. These discontinuous velocity fields are related to local plastic hinges.

The calculation of plastic membrane work near the crack tip can be based on either a traditional rigid–plastic approach or a fracture mechanics approach. In the rigid–plastic approach such as that of Ohtsubo & Wang (1995), the membrane work to stretch the material is integrated over a continuous plastically deforming field. The extent of this membrane stretched plate may be determined using a criterion based on critical rupture strain (Zhang 2002). The fracture mechanics approach (e.g., Wierzbicki & Thomas 1993, Simonsen & Wierzbicki 1998) describes the local stress state using relevant parameters such as the crack tip opening displacement (CTOD), and calculates the work required to propagate the crack as a function of the CTOD parameter, refer to Chapter 10.

The membrane stretching and the curl bending are not independent, and are related through a single geometric parameter. This parameter is denoted by R, as depicted in Figure 9.23, which represents the instantaneous bending or rolling radius of the cylindrical flaps in the wake of the wedge. Specifically, the far-field bending work is inversely proportional to R, while the membrane work in the near-tip zone increases with the rolling radius.

The analytical expression for the plate tearing force versus the cutting length derived by Ohtsubo & Wang (1995), among others, using the rigid–plastic method is as follows:

$$F = 1.51\sigma_0 t^{1.5}\ell^{0.5}(\sin\theta)^{0.5}\left(1+\frac{\mu}{\tan\theta}\right) \tag{9.52}$$

where σ_0 = flow stress, t = plate thickness, ℓ = tearing length, 2θ = spreading angle of the wedge, μ = friction coefficient.

Using the fracture mechanics approach, Wierzbicki & Thomas (1993), among others, derived the following expression:

$$F = 1.67\sigma_0(\delta_t)^{0.2}\mathrm{t}^{1.6}\ell^{0.4}\frac{1}{(\cos\theta)^{0.8}}\left[(\tan\theta)^{0.4}+\frac{\mu}{(\tan\theta)^{0.6}}\right] \tag{9.53}$$

where δ_t = CTOD parameter, refer to Section 10.4.1 of Chapter 10.

Considering the critical rupture strain to membrane stretching, Zhang (2002) derived a semi-analytical expression as follows:

$$F = 1.942\sigma_0 t^{1.5}\ell^{0.5}\varepsilon_f^{0.25}(\tan\theta)^{0.5}\left(1+\frac{\mu}{\tan\theta}\right) \tag{9.54}$$

where ε_f = critical rupture strain.

Such analytical formulations noted above accommodate the coefficient of friction and the wedge's spreading angle as parameters of influence. In most laboratory experiments, there is no sign of a crack extending in front of the wedge tip, and local necking of the plate material is observed there before the material is separated. It is thus generally recognized that the material in front of the wedge may be torn apart rather than cut by the wedge, yet such a mechanism is very difficult to be precisely included in an analytical model. The material separation in front of the wedge is due to ductile failure. The rigid–plastic analysis approach describes a local deformation zone near the wedge

tip, while the fracture mechanics approach explains the mechanism driving the crack. Both approaches calculate the internal energy absorbed in the local area in the vicinity of the wedge tip, and the two estimates can be close to each other. In fact, the tearing force depends very weakly on the value of δ_t, the CTOD parameter, since the exponent involved is 0.2 as per Equation (9.53).

Once the relationship between tearing force, F, and cutting length, ℓ, is known as the wedge is pushed into the plate, the strain energy, W, absorbed until $\ell = \ell_m$ is reached can be calculated by integrating the area below the $F-\ell$ curve as follows:

$$W = \int_0^{\ell_m} F \, d\ell \tag{9.55}$$

9.9.3 Empirical Formulations

Based on mechanical test results, empirical formulations for the tearing force may also be derived by using dimensional analysis. The tearing force, F, depends on the geometrical parameters of the wedge, the thickness of the plate and the tearing length. It also depends on the material yield stress, as plastic deformation is evident in the process of penetration. The parameter of Young's modulus is not included since deep penetration is concerned while elastic deformation is limited to the stage up to the initial buckling.

If the dimensions of the problem are taken as tearing load and tearing length, there are two different dimensionless parameters involved. If two other parameters, i.e., the plate thickness and the yielding stress, are included, the problem involves four variables. The so-called Buckingham's Pi rule (Buckingham 1914, Jones 1997b) tells us that a four-variable problem has two independent dimensionless groups. One such expression satisfying the rule is

$$\frac{F}{\sigma_0 t^2} = C\left(\frac{\ell}{t}\right)^n \tag{9.56}$$

where F = tearing force, σ_0 = flow stress, t = plate thickness, ℓ = tearing length, C, n = constants. The value of C depends on many factors including the geometry of the wedge and parameters for friction. The value of n reflects the interdependence of major energy absorption mechanisms.

Based on curve fitting of their test results for unstiffened high tensile steel plates cut by a rigid wedge, Lu & Calladine (1990) found that the value of n is in the range of 0.2 to 0.4. The thickness of their test plates was in the range of 0.7–2 mm and $\alpha = 0$ degrees and $2\theta = 20$, 40 degrees. They further simplified the expression by using a single value of $n = 0.3$, and worked out the corresponding best-fitting values for C. Their resulting empirical relation is as follows:

$$F = C\sigma_0 t^{1.7}\ell^{0.3} \quad \text{for} \quad 5 \le \frac{\ell}{t} \le 150 \tag{9.57}$$

where C is a constant which is dependent on materials or test conditions.

Paik (1994) performed a series of cutting tests on high tensile steel panels with longitudinal stiffeners. The thickness of Paik's test panels was in the range of 3.4–7.8 mm and

$\alpha = 0$ degrees and $2\theta = 15$, 30, 45 and 60 degrees. This test series demonstrated a dependence of the value C in Equation (9.56) on the wedge's geometrical parameter in such a case. A least squares best fit to the experimental data provides the following expression:

$$F = 1.5C\sigma_0 t_{eq}^{1.5}\ell^{0.5} \tag{9.58a}$$

where t_{eq} = equivalent plate thickness as defined in Equation (9.44), C = a parameter accounting for the influences of a wedge's geometry, which is a function of the spreading angle of the wedge,

$$C = 1.112 - 1.156\theta + 3.760\theta^2 \tag{9.58b}$$

where θ is as defined in Figure 9.21 (in rad).

It is noted that while Equation (9.57) is employed for unstiffened steel plates, Equations (9.58) will be used for longitudinally stiffened steel panels. While Equations (9.57) and (9.58) are based on the test results for steel panels with relatively thin thickness, they may be approximately applied to thicker plates.

Figure 9.24 compares between the plate tearing force expressions for a given case. In this comparison, a mild steel plate with $t = 8$ mm and $\sigma_0 = 270$ MPa is considered to be cut by a rigid wedge. The coefficient of friction is assumed to be 0.25 and the critical rupture strain is taken as $\varepsilon_f = 0.25$. While the Paik formula is basically applicable to cutting of longitudinally stiffened panels, it is applied with $t_{eq} = t$ in this calculation.

It is seen from Figure 9.24 that a good agreement between all the methods is achieved when the wedge angle is relatively small, i.e., $2\theta = 40$ degrees, while some differences appear when the wedge angle becomes relatively large, i.e., $2\theta = 90$ degrees. For the case of a larger wedge angle which has a relatively large wedge width far behind the wedge tip in comparison to stiffener spacing, the Paik formula predicts larger tearing forces. This is because the Paik empirical formula is derived mainly based on longitudinally stiffened panels, while the rest of formulas are only based on unstiffened plates.

9.9.4 Concertina Tearing

When a stiffened panel is cut by a wedge, cracking of the plate may take place in the vicinity of stiffening members. Two or more cracking lines advance with the wedge; there is no crack directly in front of the wedge tip while the plate is folded like an 'accordion'. This type of tearing process is sometimes termed 'concertina tearing'. Figure 9.25 shows a photo of the concertina tearing on a stiffened panel cut by a wedge.

Concertina tearing is similar to the usual tearing process in the sense that the material is separated. It is also similar to the crushing of plating in the sense that the structure is folded. Applying rigid–plastic theory, Wierzbicki (1995) derived an analytical formula of the mean concertina tearing load for a steel plate. In this approach, the length of the folds is treated as a parameter in the relationship between the tearing load and the indentation, thus linking the membrane stretching and the bending at plastic hinges. The mean concertina tearing load formula is then derived by minimizing the load with regard to this parameter. The Wierzbicki formula of the mean concertina tearing load is given by

$$F_m = \frac{1}{\lambda}(3.25\sigma_0 b^{0.33} t^{1.67} + 2Rt) \tag{9.59}$$

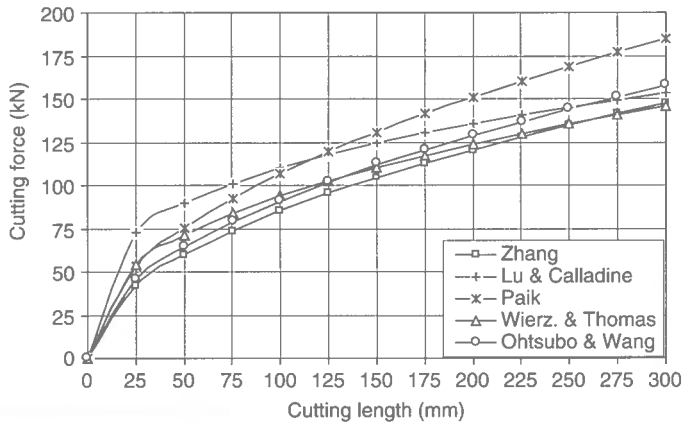

(a)

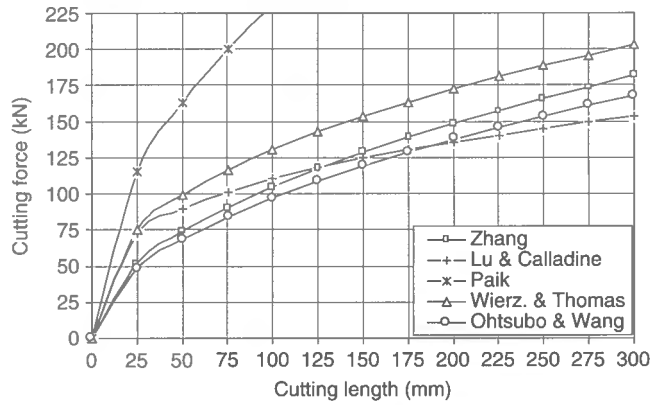

(b)

Figure 9.24 A comparison of cutting forces calculated by different methods for wedge angle of (a) $2\theta = 40$ degrees and (b) $2\theta = 90$ degrees, undertaken by Zhang (2002)

Figure 9.25 A concertina tearing

where F_m = mean concertina tearing load, σ_0 = flow stress, t = plate thickness, b = width of the folded plate, λ = factor for effective crushing length, R = fracture parameter.

9.10 Numerical Simulation for Structural Impact Mechanics

During the last few decades, the increased capacity of computers, as well as the increase of their speed, has allowed researchers to use broadly based numerical methods, and in particular the finite element method, for the prediction of the response of structures under dynamic loads.

The solution schemes that may be used for the solution of the equations of dynamic equilibrium may generally be classified in two major categories, which are embodied in the so-called implicit or explicit codes.

Following the explicit scheme for the time integration of the dynamic equations of motion, the equilibrium of the structure at time t is considered in order to calculate the displacements at time $t + \Delta t$. Neglecting the effect of a damping matrix, we have

$$[m]\{\ddot{w}\}^t = \{F\}^t - \{S\}^t \tag{9.60}$$

where $[m]$ = mass matrix of the structure, $\{w\}^t$ = vector of nodal displacements and rotations at time t, $[\ddot{w}]^t$ = corresponding acceleration vector, $\{F\}^t$ = vector of the external nodal forces, $\{S\}^t$ = vector of the internal forces–moments, equivalent to the internal stresses at time t. Vector $\{S\}^t$ depends on the current configuration of the structure, i.e., the displacements at time t, the stresses and the material constitutive models.

If a linear elastic response is assumed this vector may be given simply by $[K]\{w\}^t$, where $[K]$ is the constant in the time stiffness matrix. The solution for the nodal point displacements at the next time step, $t + \Delta t$, is obtained by substituting in the above equation an approximation for the acceleration vector. The most common approximation used is that obtained by using the central difference operator, given by

$$\{\ddot{w}\}^t = \frac{\{w\}^{t+\Delta t} - 2\{w\}^t + \{w\}^{t-\Delta t}}{\Delta t^2} \tag{9.61}$$

After this substitution, the equation can be solved for the displacements at time $t + \Delta t$. If, in addition, $[m]$ is a diagonal matrix (which is a common situation if a lumped mass matrix formulation is used in the analysis) then the equation is uncoupled and the response of the structure at time $t + \Delta t$ can be obtained without having to find the inverse of any coefficient matrix of the system. This is the main advantage of the use of the implicit time integration method. On the other hand, the major disadvantage is the necessity of the use of relatively very small solution time increments in order to obtain a stable and reliable solution.

According to the implicit time integration scheme, the displacements at time $t + \Delta t$ are obtained, considering the equilibrium of the structure as follows:

$$[m]\{\ddot{w}\}^{t+\Delta t} + [K]^t \Delta\{w\}^t = \{F\}^{t+\Delta t} - \{S\}^t \tag{9.62}$$

where $[K]^t$ is the tangent stiffness matrix of the structure at time t, and $\Delta\{w\}^t = \{w\}^{t+\Delta t} - \{w\}^t$. There are many implicit schemes for the approximation of the acceleration, $\{\ddot{w}\}^{t+\Delta t}$, in this equation. One of them is the trapezoidal rule, given by

$$\{\dot{w}\}^{t+\Delta t} = \{\dot{w}\}^t + \frac{\Delta t}{2}(\{\ddot{w}\}^t + \{\ddot{w}\}^{t+\Delta t}) \quad \text{and} \quad \{w\}^{t+\Delta t} = \{w\}^t + \frac{\Delta t}{2}(\{\dot{w}\}^t + \{\dot{w}\}^{t+\Delta t}) \tag{9.63}$$

After the above substitutions the equilibrium equation is transformed into

$$\left([K]^t + \frac{4}{\Delta t^2}[m]\right)\Delta\{w\}^t = \{F\}^{t+\Delta t} - \{S\}^t + [m]\left(\frac{4}{\Delta t}\{\dot{w}\}^t + \{\ddot{w}\}^t\right) \tag{9.64}$$

which can now be solved for the displacement increments, $\Delta\{w\}^t$. The solution requires the inversion of a matrix, and also a time step which is relatively larger than the one required for the explicit solution scheme.

One aspect of essential importance, which is under continuing refinement in order to improve the procedures used, is the material behavior including failure. One material model, which includes the effect of strain rate on yield stress, was developed in the early 1980s by Samuelides & Frieze (1989). The model relates the stress and strain increments by

$$\{\Delta\sigma\} = \left[E^*\right]\{\Delta\varepsilon\} + \{\Delta\sigma_c\} \tag{9.65}$$

where

$$\left[E^*\right] = [E_e] = \frac{E}{1-\nu^2}\begin{bmatrix} 1 & \nu \\ \nu & 1 \end{bmatrix}, \quad \{\Delta\sigma_c\} = 0$$

when the stress increment is in the elastic regime, and

$$\left[E^*\right] = \left[E_p\right] = [E_e]\left[[I] - \frac{\{\partial f/\partial\sigma\}\{\partial f/\partial\sigma\}^T[E]}{\{\partial f/\partial\sigma\}^T[E]\{\partial f/\partial\sigma\}}\right],$$
$$\{\Delta\sigma_c\} = -\frac{\sigma f}{\partial\sigma_Y}\Delta\sigma_Y\frac{[E]\{\partial f/\partial\sigma\}}{\{\partial f/\partial\sigma\}^T[E]\{\partial f/\partial\sigma\}}$$

when the stress increment is in the elastic–plastic regime, f = yield function, E = Young's modulus, ν = Poisson's ratio, $[I]$ = unit matrix, σ_Y = strain-rate-dependent yield stress; T denotes transpose.

For elastic-plastic large deflection analysis of ship plating under wave impact, Caridis & Stefanou (1997) applied the numerical approach noted above. Today there are a number of computer codes for the numerical simulation of elastic-plastic impacts with large deformations, which include the explicit ABAQUS/Explicit, DYTRAN, LS/DYNA3D, RADIOSS and the implicit ABAQUS/Standard, ANSYS, MARC and NASTRAN. Some applications to ship collisions and grounding using these codes are found in Kuroiwa (1996), Servis *et al.* (2001) and Kitamura (2002), among others.

9.11 Some Considerations for the Quasi-Static Approximation

The prediction of the response of structural members under dynamic or impact loading conditions is a complicated task, in particular in a case where the material is in the plastic range and consequently the behavior is nonlinear.

However, in some cases it is possible to relatively simplify the problem by using static load–displacement curves for the prediction of the dynamic behavior of a structure. This can be done if the mode of response of the structure under the dynamic load is similar to the mode corresponding to the static load–displacement curve and the inertia forces of the deformed structure are relatively low. This usually happens when the duration of the applied load is shorter than the natural period of the structure or the corresponding higher frequencies of the load pulse are lower than the natural frequencies of the structure. Thus inertia forces may be neglected when investigating the bending of the hull girder in waves, and the response of the side shell of a struck vessel involved in a collision.

In this regard, once the static load–displacement curve of the structure subjected to the dynamic load is known, it is possible to calculate the displacement of the structure when subjected to dynamic load, by equating the dissipated structural energy with the area under the load–displacement curve. Of course in this case the 'dynamic loading' must be expressed in terms of energy, which is absorbed by the structure. Suppose for example that the central deflection of a plate subjected to a static patch load is given by Figure 9.26, and that a mass, m, hits the plate with a velocity V. The energy of the mass when it hits the plate equals $mV^2/2$ and suppose that it is totally absorbed by the plate. If it is assumed that the mode of response of the plate under the impact is the same with the mode of deformation corresponding to the static load–displacement curve, it is straightforward to determine the central deflection of the plate under the impact, as shown in Figure 9.26. Such an approach is termed 'quasi-static' in the literature (Shen & Jones 1991, Jones 1995). For a relatively more accurate prediction of the response under the dynamic load the load–displacement curve should be modified to account for the effect of the strain rate on material properties (e.g., yield stress, fracture strain).

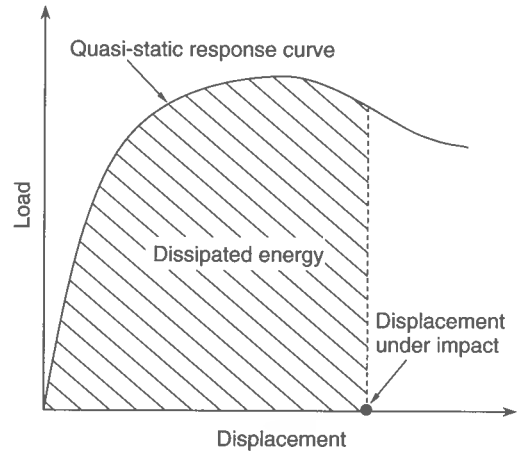

Figure 9.26 A schematic of the quasi-static approximation

9.12 Application to Ship Collision and Grounding Accidents

Ship collisions are normally classified into two groups, namely side collisions and head-on collisions. A side collision represents a situation in which the bow of a striking ship collides with the side structure of another ship. The initial kinetic energy is partly or entirely consumed by damage to both the side structure of the struck ship and the bow structure of the striking ship. A head-on collision typically represents a situation in which the bow of a vessel strikes fixed rigid walls such as piers and bridge abutments. In such a head-on collision, most of the kinetic energy is absorbed by damage to the bow structure of the striking vessel.

Ship grounding is defined as a phenomenon in which the ship bottom structure is damaged by accidental loading. Three possible scenarios, namely grounding, stranding and squatting, are normally considered. Grounding typically results in bottom raking damage when a vessel with forward speed runs onto a rock pinnacle or soft soil. Stranding takes place when the bottom structure of the vessel at standstill is pressed on a rock due to swells or tidal variations. The mechanics of stranding are quite similar to those of side collisions. Squatting can result in damage to the bottom shell due to fast water flow when the vessel operates in shallow water.

Oil pollution due to collision or grounding continues to attract worldwide attention. The governments of the world's maritime nations have now committed themselves individually and collectively to take all reasonable measures to minimize pollution from accidental side and bottom damage to oil tankers.

The functionality of a ship's structural system can also be viewed from the standpoint of casualty performance. In case of a casualty, the main objectives of salvage and rescue operations are to rescue crews and passengers, maintain the integrity of the ship, prevent or minimize cargo loss, and protect the environment from spilled cargo such as oil. From the standpoint of casualty avoidance or risk minimization, the primary considerations for structures are: resistance to accidental loads, sufficient residual strength, adequate stability, and containment of cargo from spilling. Structural crashworthiness, or the resistance of ship structures to accidental loads, thus plays a very important role, and is highlighted in many recent research and development efforts.

9.12.1 Fundamentals of Ship Accident Mechanics

Analysis of the accident mechanics can be split into two parts, namely the external and internal accident mechanics. The external accident mechanics involves simulation of the time-dependent rigid-body motion of the involved ships taking account of accident forces and the effects of the surrounding water. By analyzing the external accident mechanics, the total loss of the initial kinetic energy which should be dissipated in damaged ship structures can be computed. The internal accident mechanics includes evaluation of the structural failure response of the involved ships during the accident. Analysis of the internal accident mechanics can be used to obtain the reaction force versus damage extents. By integrating the area below the corresponding force versus structural damage amount curve, the absorbed strain energy for the ship structures involved can be estimated.

Considering the principle of energy conservation, the total loss in kinetic energy at the end of the accident should equal the total strain energy dissipated by the structural failure of the ship structures, namely

$$\Delta E = W \tag{9.66}$$

where ΔE = total loss in kinetic energy, W = total strain energy dissipated by structural damage of the involved ships.

Equation (9.66) is the basic equation representing the response of ship structures in a collision or grounding accident. By solving Equation (9.66) appropriately, structural damage of the ships during the accident can be computed. In reality, however, it is not so straightforward to solve Equation (9.66), and thus a reasonably approximate procedure is normally employed. In the following sections, the estimation of ΔE and W in Equation (9.66) is described for ship collisions or grounding.

9.12.2 Ship Collision

A ship collision involves at least one ship and a striking or struck object, or two ships. The nature of the collision is usually described as being right angle or oblique, referring to the relative position of the struck ship center line to the vector of velocity of the striking object or ship.

The analysis of ship collisions such as that illustrated in Figure 9.27 involves simulation of the time-dependent rigid-body ship motions and evaluation of the structural response as the collision proceeds. Figure 9.28 represents a procedure for the analysis of ship collision problems (Paik *et al.* 1999). Analysis of the external collision mechanics determines the total loss of the initial kinetic energy that must be absorbed by structures and dissipated in vessel motions. Analysis of the internal collision mechanics is necessary to obtain the force–indentation response for both the striking and struck ship structures. Integrating the area below the corresponding force–indentation curve gives an estimation of the absorbed strain energy components.

General procedures for computing the motion of striking ships may be found in Petersen (1982) and Samuelides & Frieze (1989), among others. For a nearly central right-angled collision situation, the total loss of kinetic energy during a collision of two ships in a free-floating condition can be given by the classical theory as follows (Paik *et al.* 1999):

$$\Delta E = \frac{1}{2}\frac{(1+C_{a1})(1+C_{a2})m_1 m_2}{(1+C_{a1})m_1 + (1+C_{a2})m_2}(V_r)^2 \tag{9.67a}$$

where m_1 and m_2 are the masses of the striking and struck ships, C_{a1} and C_{a2} are the added mass coefficients for the striking and struck ships, representing the effect of the

Figure 9.27 A ship–ship collision accident

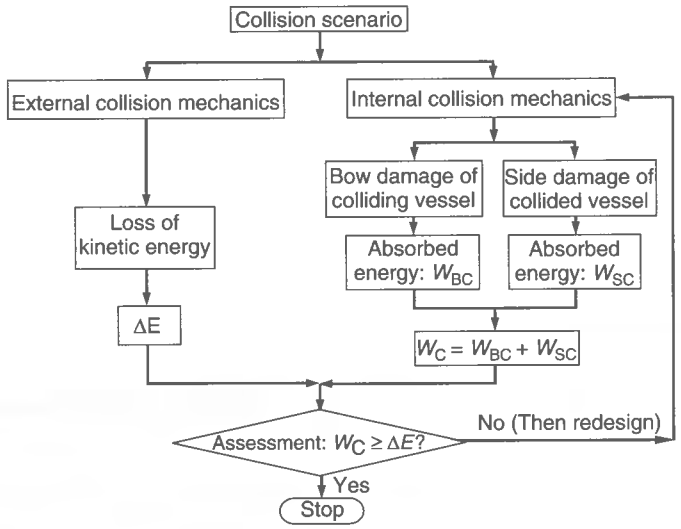

Figure 9.28 A procedure for analysis of a ship collision accident

surrounding water during the collision, often taken in the ranges of $C_{a1} = 0.03 - 0.1$ and $C_{a2} = 0.4 - 0.8$, and V_r is the relative velocity between the two ships.

In Equation (9.67a), it is assumed that the striking and struck ships move together after the collision with a common velocity in a direction perpendicular to the sailing direction of the struck ship. When the struck ship is at standstill, e.g., at a pier, the mass of the struck ship can be supposed to be infinite, i.e., $m_2 \to \infty$. In this case, the loss of kinetic energy without taking into account smaller effects such as the energy absorbed by the deformation of fenders can be computed by

$$\Delta E = \tfrac{1}{2}(1 + C_{a1})m_1 V^2 \tag{9.67b}$$

where V = impact speed of the striking ship.

To account for the effect of sway motion of the struck ship, Minorsky (1959) suggested the following expression for the kinetic energy loss when the struck ship is supposed to be at a standstill before the collision, namely

$$\Delta E = \frac{1}{2}\frac{m_1 m_2}{0.6m_1 + m_2}V^2 \tag{9.67c}$$

where the added mass coefficient for sway motion is assumed to be 0.6.

Finite element codes can be used for the simulation of ship–ship collisions (Servis *et al.* 2001, among others) in terms of the collision resistance assessment of ship structures. It is recognized that the energy absorption capacity obtained by such finite element simulations is significantly influenced by the assumed fracture strains of material (e.g., Lehmann *et al.* 2001). Minorsky (1959) studied the establishment of an empirical relationship between resistance to penetration and energy absorbed in collision that would be valid for a range of ship structures studied. Once such a relationship is established, the likely damage amount in collision can be estimated for any new vessel by equating the absorbed energy so predicted to the loss of kinetic energy. Based on the statistics of certain collision accidents (mainly between struck single hull ship side structures and the striking ship's

bow), Minorsky suggested an empirical linear correlation between the structural resistance parameter and absorbed energy as follows:

$$W_C = 414.5R_T + 121\,900 \tag{9.68a}$$

where W_C is the total energy absorbed by damage of both the striking and the struck ship structures, in tons-knots^2, and R_T is the 'resistance factor' for structural members of the two striking ships, in ft^2 · in.

Equation (9.68a) can be rewritten by changing the dimensional units for the parameters as follows:

$$W_C = 47.2R_T + 32.7 \tag{9.68b}$$

where W_C is in MJ and R_T is in m^3.

By assuming that the resistance factor, R_T, defined as a volume of the damaged structural members is proportional to the member thickness, Minorsky expressed R_T in terms of certain parameters relating to the amount of damage sustained and the member thickness involved, as follows:

$$R_T = \sum_{N=1} P_N L_N t_N + \sum_{n=1} P_n L_n t_n \tag{9.68c}$$

where P_N, P_n = depth of damage for the Nth member of the striking ship or for the nth member of the struck ship, respectively, L_N, L_n = length of damage for the Nth member of the striking ship or for the nth member of the struck ship, respectively, and t_N, t_n = thickness of the Nth member of the striking ship or of the nth member of the struck ship, respectively.

Substituting Equations (9.67) and (9.68) into Equation (9.66), the collision damage amount can be approximately calculated. The Minorsky method noted above has been widely used for the design of ship structures against collision. Many researchers have modified the original Minorsky formula using different constants and physical basis. Based on the collision tests for (single skin) structural models, for instance, Woisin (1979) derived a formula relating the energy absorbed by damage of both striking and struck ship structures to the resistance factor, which replaces the constant 32.7 in Equation (9.68b) with the expression $0.49\sum Ht^2$, where H is the height of rupture aperture in the side shell (m) and t is the side shell thickness (cm). Pedersen & Zhang (2000a) developed a new Minorsky expression reflecting differences in structural arrangement, material properties and damage patterns.

The original or modified Minorsky formulas thus far available consider damage of both the striking and the struck ship structures simultaneously. In a ship–ship collision accident, the damaged amount of ship structures is quite dependent on the interactions between the striking and the struck ships, which in individual cases can be difficult to assess.

Figure 9.29 represents the relationships between the reaction force and the penetration of both the striking bow structure and the struck side structure. During the collision, reaction force equilibrium between the striking and struck ships must be satisfied. Hence, $F_S = F_B$, where F_S and F_B are the reaction forces at the side structure of the struck ship and the bow structure of the striking ship, respectively. The amounts of damage (i.e., indentation) for the struck and striking ship structures are denoted by u_S and u_B, respectively, when $F_S = F_B$.

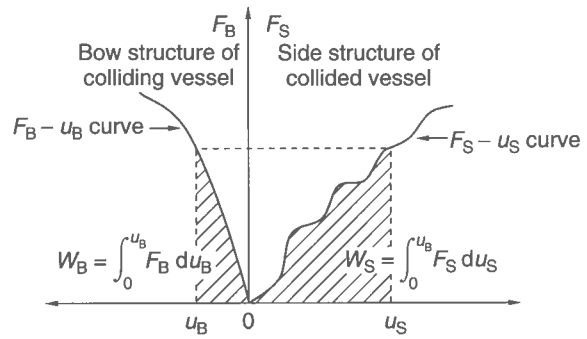

Figure 9.29 Energy components absorbed by the striking and struck ship structures

The strain energy component dissipated by damage of the side structure is usually computed by solving the internal collision mechanics problem for the struck ship side structure when the rigid bow crushes into the side structure. On the other hand, the strain energy component dissipated by damage of the bow structure is usually obtained by analyzing the internal collision mechanics problem for the striking ship bow structure when the bow crushes into a rigid vertical wall.

In this case, the strain energy component, W_S, dissipated by damage of the side structure, may be computed by solving the internal collision mechanics problem when the rigid bow crushes into the side structure, as shown in Figure 9.30(a). On the other hand, the strain energy component, W_B, dissipated by damage of the bow structure, can be obtained by analyzing the internal collision mechanics problem for the striking ship's bow structure when the bow crushes into a rigid vertical wall, as shown in Figure 9.30(b).

There have been remarkable advances of knowledge in the behavior of structures exposed to large impact loads. Some new patterns of plastic behavior of steel plates have been identified. Many involve mechanisms of membrane stretching, local plastic bending, complex object geometry, rupture, cracking and friction. These mechanisms interact in different ways, and can be effective in representing the different behaviors that may be exhibited by steel-plated structures subjected to large impact loads. The identified failure modes characterizing the behavior of ship plates in collision or grounding primarily include folding or crushing (Section 9.8) and cutting or tearing (Section 9.9).

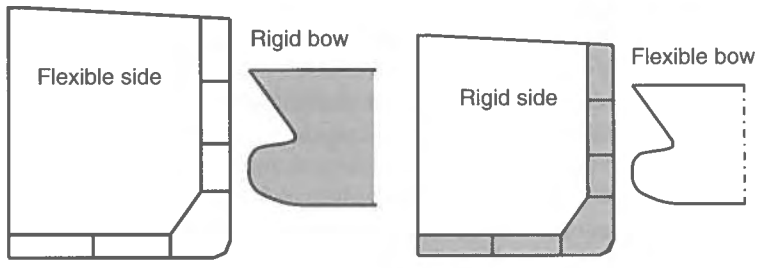

Figure 9.30 A schematic representation of the internal collision mechanics analysis of vessel structures in a ship–ship collision problem

As will be presented in Chapter 13 of this book, the structural response in such cases can be conveniently analyzed using a simplified FEM approach. That particular approach uses many special elements to model the damage behavior of plates, and gap/contact units for modeling the contact conditions between the struck side and striking bow. This group of approaches can be improved with the broadening of knowledge of the plastic behavior of plates in the future, by incorporating such knowledge into the special purpose finite element behavior.

The structural response under similar circumstances can also be analyzed using simplified analytical approaches as surveyed by Wang *et al.* (2001). These approaches are generally aimed at achieving a level of structural crashworthiness, and are well-established practice in some segments of the automobile industry. Developing such a method consists of: (1) identifying primary damage patterns of structural components according to observation of actual damage, (2) developing idealized theoretical models and deriving theoretical formulas to capture the main features of the damage patterns, (3) establishing global models for the entire damage process of the hull, and (4) combining the global damage models with formulas for individual structural components.

Under the penetration from a striking bow, shell plating develops into a membrane to resist the striking load. A plate subjected to lateral load (Section 9.6) is an appropriate analytical model for the side shell, provided the effects of the geometry of the striking bow are properly accounted for (Wang *et al.* 2000). The main supporting members and their intersections are subjected to a compression load. They develop lobes to accommodate very large deformations in a manner similar to crushing of thin-walled structures. A global damage model for the entire side structure can be established which captures the main features of the damage and neglects some secondary factors. With this global damage model, analytical models relevant to the behaviors of individual structural members can then be combined together to predict the load–penetration relationship.

Figure 9.31 shows statistical results for the probabilistic density distribution and the cumulative probabilities related to the longitudinal collision damage of merchant ships, which were collected by the International Maritime Organization (IMO) for ship collision accidents occurring during the period of 1945 to 1965 (Pedersen & Zhang 2000b). Two groups of ships in size are considered, namely the large-ship group with the ship length above 100 m and the small-ship group with the ship length below 100 m. The average ship length of the large- and small-ship groups is 135 m and 65 m, respectively. The collision database includes 139 cases for the large-ship group, while it includes 131 cases for the small-ship group. As may be seen from Figure 9.31, the small-ship group has a higher probability of larger relative collision damage to the ship length than that of the large-ship group. The probability that the relative collision damage extent to the ship length is above 10% is 25% for the small-ship group, while it is 17% for the large-ship group.

9.12.3 Ship Grounding

The grounding process may generally be characterized as one where an obstruction deflects the bottom inward and/or enters into and cuts through the structure as the vessel moves forward. The amount of deformation depends on the resistance of the bottom structure to the penetration as well as some other ship characteristics including hydrodynamic stability.

There are two loading situations pertinent to grounding of ship bottom structures: vertical loading and loading in the ship length direction, corresponding typically to a stranding and a typical raking accident, respectively. A stranding situation is similar to

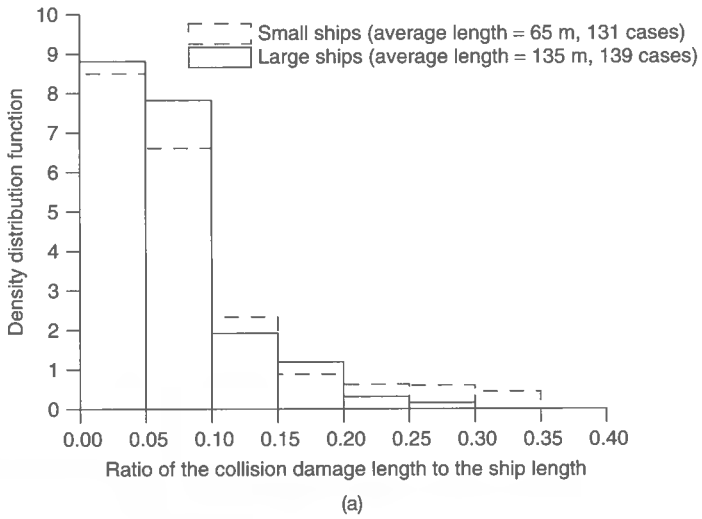

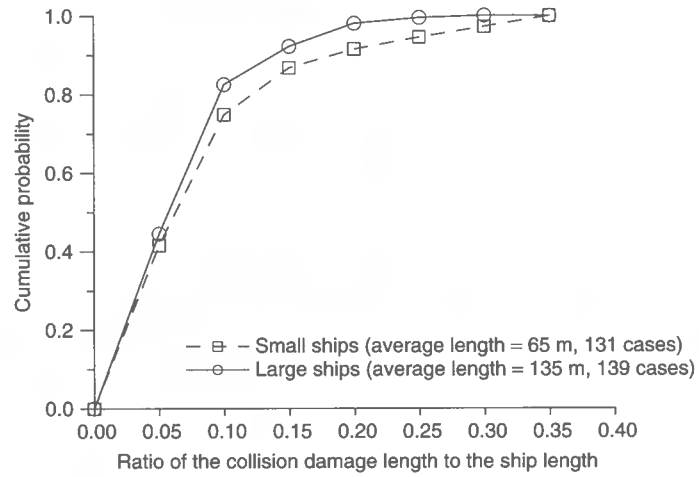

Figure 9.31 (a) Collision density versus longitudinal collision damage extent for merchant ships. Reprinted from *Ocean Engineering*, Vol. 27, Pedersen, P.T. & Zhang, S. Effect of ship structure and size on grounding and collision damage distributions, 1161-1179, 2000, with permission from Elsevier Science; (b) Cumulative probability of longitudinal collision damage extent for merchant ships. Reprinted from *Ocean Engineering*, Vol. 27, Pedersen, P.T. & Zhang, S. Effect of ship structure and size on grounding and collision damage distributions, 1161-1179, 2000, with permission from Elsevier Science

a collision where the struck side is subjected to mainly out-of-plane impact. A raking accident, when the impact load is applied mainly in the ship's longitudinal direction, often causes a very long gash in the bottom, as shown in Figure 9.32.

When a ship with a forward speed V runs onto a rock pinnacle, the initial kinetic energy may be approximately estimated by

$$\Delta E = \tfrac{1}{2}(1 + C_a) m V^2 \tag{9.69}$$

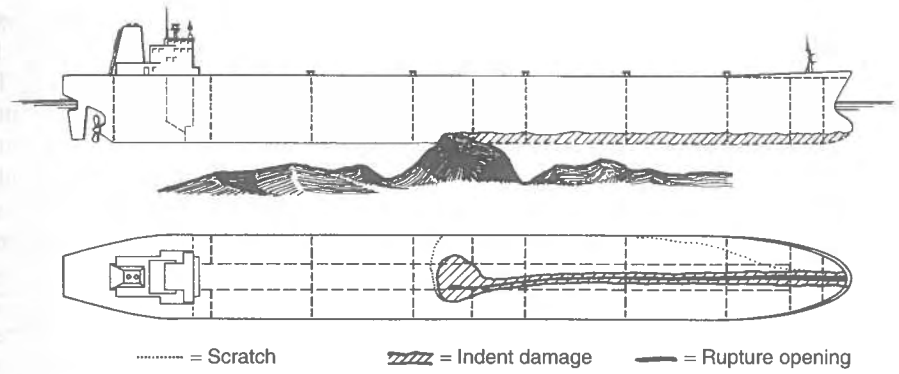

Figure 9.32 A schematic of a grounding accident and the resulting bottom raking damage distribution (Pedersen & Zhang 2000a, Kuroiwa 1996)

where m = mass of the grounded ship, C_a = added mass coefficient accounting for the surrounding water effect.

For the purposes of analytical treatment of ship raking response, a ship hull structure can be characterized as consisting of periodically arranged structural members. For example, going from the bow toward the stern in the longitudinal direction, frames and/or bulkheads occur at certain intervals. As a consequence of the periodicity of such structural elements, a ship's resistance during bottom raking can also be considered periodic under certain conditions. The load period in such a case starts from one transverse structure and ends at the next transverse structure. A raking scenario may hence be represented as shown in Figure 9.33 (Wang *et al.* 1997).

When a rock on the sea bed makes contact with a transverse structure such as floors, that structure and the bottom plating immediately behind it interact and can show a very complicated deformation pattern. The transverse frame in such a case fails mainly by in-plane stretching. The bottom plate behind the transverse structure bulges and folds in front of the intruding rock. Usually, many folds are found in that part of the bottom

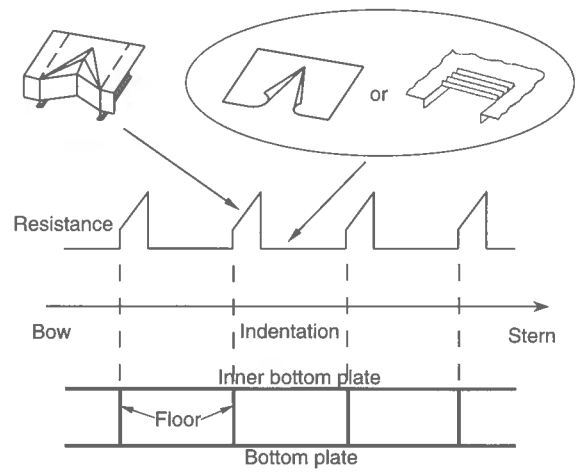

Figure 9.33 A raking bottom damage scenario in ship grounding (Wang *et al.* 1997)

plate. During this damage stage, the internal resistance force of the bottom increases as the rock's penetration increases. Eventually, as ductile rupture occurs in the overstretched plates, the resistance force reaches its ultimate value and then begins to decrease. This state of damage can then give way to a different damage process in which the contribution from the transverse structure becomes negligible. Only the bottom plate and inner bottom plate (in the case of a double bottom) may then provide resistance against the intruding rock. Usually the resistance force drops to a low level. The bottom plate (including inner bottom) may be torn open by the rock, and steel material within it separates at the part of the plate near the front of the rock. In the wake of the rock, the plate is subjected to load mainly in the lateral direction. It then deflects out of its original plane to avert compression, forming two flaps. A second possible type of damage is the wavy deformation pattern. The bottom plate in this case is peeled at its connection lines with the bottom longitudinal stiffeners or support members. The detached plate then folds in front of the rock. Now if the ship does not stop because it still has unspent kinetic energy, the next transverse structure will become involved in the raking process as well. This marks the end of one so-called structural resistance period and the beginning of a new period.

The grounded ship bottom structure is modeled as an assembly of individual structural elements. The grounding force versus damage relationship of the ship is then obtained by appropriately summing up the grounding force versus raking length relationships of individual elements as described in Section 9.9. In a ship grounding, the raking damage will continue until the initial kinetic energy is entirely consumed so that Equation (9.66) is satisfied.

Figure 9.33 is an idealized representation of a raking scenario. The damage to the bottom of a ship in a real ship grounding accident may be much more complex, which is very difficult to fully describe using a single theoretical model. An alternative to this analytical approach would be a semi-empirical formula, which retains one major parameter, the damage width, and embeds many other factors (e.g., rock shape, rock angle, friction) in an empirical manner (Zhang 2002). This simplification may be useful for estimating the average horizontal grounding force, which is given by

$$F_H = 3.58\sigma_0 t_{eq} t_{eqL}^{0.6} b^{0.4} \tag{9.70a}$$

where σ_0 = flow stress of the bottom material, t_{eqL} = equivalent thickness of the bottom plating including longitudinal members which may be taken as $t_{eqL} = t + A_L/s_L$ by smearing longitudinal stiffeners into the shell plating, t = plating thickness, A_L = cross-sectional area of longitudinal stiffeners and s_L = spacing of longitudinal stiffeners, t_{eq} = equivalent thickness of the bottom plating including both longitudinal and transverse members which may be taken as $t_{eq} = t_{eqL} + A_T/s_T$, A_T = cross-sectional area of the floor, s_T = spacing of floors, b = damage width of the bottom, which is taken as the rock width at the level of the bottom plating. For double bottom arrangement, Equation (9.70a) is applied to outer bottom and inner bottom separately.

A grounded ship may have motions of heave, pitch and roll. These motions have some effects on the vertical penetration (Simonsen 1999), but their effects on the raking damage length are known to be limited. The raking damage length, L_d, can then be approximately determined as follows:

$$L_d = \frac{\Delta E}{F_H} \tag{9.70b}$$

where ΔE is as defined in Equation (9.69), F_H is as defined in Equation (9.70a).

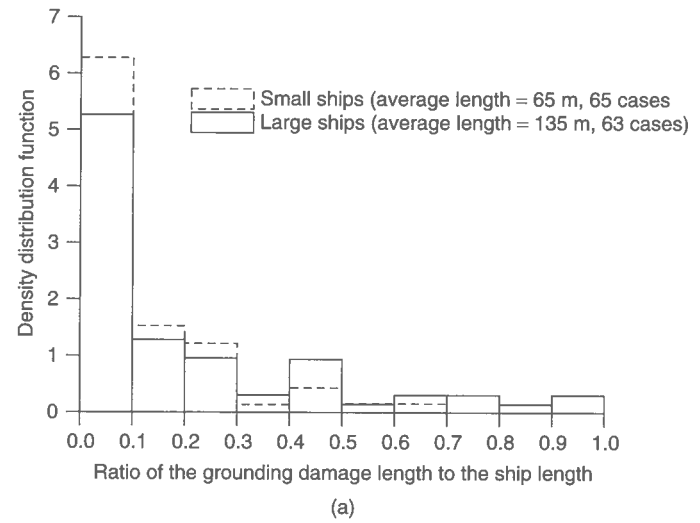

Figure 9.34 (a) Grounding density versus longitudinal grounding damage extent for merchant ships. Reprinted from *Ocean Engineering*, Vol. 27, Pedersen, P.T. & Zhang, S. Effect of ship structure and size on grounding and collision damage distributions, 1161–1179, 2000, with permission from Elsevier Science; (b) Cumulative probability versus longitudinal bottom raking damage extent for merchant ships. Reprinted from *Ocean Engineering*, Vol. 27, Pedersen, P.T. & Zhang, S. Effect of ship structure and size on grounding and collision damage distributions, 1161–1179, 2000, with permission from Elsevier Science

Figure 9.34 shows statistical results for the probability density function and the cumulative probability related to the bottom raking damage of merchant ships (Pedersen & Zhang 2000b). As previously presented in Figure 9.31, two groups of ships are considered, namely the small-ship group with the ship length below 100 mm and the large-ship group with the ship length above 100 m. A number of 128 grounding accidents in cargo ships

occurring during the period of 1945 to 1965 were analyzed. It is seen from Figure 9.34 that the large-ship group has a higher probability of larger bottom raking damage extent than that of the small-ship group. The probability that the longitudinal grounding damage extent is above 30% of the ship length is about 25% for the large-ship group, while it is about 9% for the small-ship group.

9.12.4 Design Standards for Ship Collision and Grounding

There has been a growing interest in reducing the risk of cargo spillage due to accidents involving oil tankers and other vessels which carry potentially polluting and/or hazardous cargo. As a result, regulations for tanker design have been strengthened. For instance, the *Exxon Valdez* grounding in 1989 resulted in the passage of the US Oil Pollution Act of 1990 (OPA 90) which requires that all tankers operating in US waters must have double hulls by the year 2015. The IMO has also established related requirements which are applied worldwide.

The means of protecting against such environmental disasters due to potential accidents is complex, but can generally be divided into two major groups, namely active and passive safety methods. The active method is aimed at preventing an accident itself. This group includes the auto-pilot system, crew training programs, e.g., with realistic simulators for ship operations, and traffic control systems. On the other hand, a passive safety method is brought into play after an accident has occurred. Such a method is designed to mitigate the risk of serious consequences, such as ingress of sea water and outflow of hazardous cargo. The passive method may involve improvements to structural crashworthiness, and rapid salvage and rescue operations.

The risk of cargo spillage in accidents can be mitigated by maximizing the energy absorption capability (or resistance) of the struck ship. That is, for minor or moderate accidents, the kinetic energy loss should be entirely absorbed before tearing of the inner skin plating in contact with hazardous cargo.

The double hull design concept is one of the effective ways for oil pollution prevention during collision and grounding accidents of oil tankers. However, not all of the design requirements for structural scantlings and arrangements of double hulls are necessarily sufficiently well advanced. For instance, the IMO requirements for determining the side ballast tank width and double bottom height are based on the accident damage statistics mainly for single skin tanker structures in collision or grounding. They are formulated mainly as a function of the vessel size, and do not directly address the structure involved.

In accidental situations involving vessels, such as collision or grounding, the deformation of the struck vessel structure can normally be quite large and as a result the strength members can experience failure modes such as yielding, crushing and rupture. In a double-skinned structure, the inner plating will possibly deflect from the very beginning of the collision or stranding process. Since oil outflow presumably occurs after the inner hull plating ruptures, tearing of the inner skin plating would be a more rational design criterion for double hull tanker side structures against collision or double hull tanker bottom structures against grounding than tearing of the outer skin plating which has previously been used.

Tearing of the inner hull of a struck ship is very much dependent on the dimensions and arrangements of the side structure. In some cases, the inner hull may not rupture even after the bow of the striking ship penetrates the original position of the inner hull. In other cases, the inner hull may rupture even before the bow of the striking ship advances to the original position of the inner hull, depending on the particulars of the structure.

It is hence essential to better understand the structural crashworthiness of ships involved in collision or grounding so that the resistance of vessel structures against such accidents can be improved in a quantitative and reliable manner.

Damage from an accident may be to the vessel, the environment or the personnel involved. The potentially costly consequences to crew, property, material, environment, related industries, and in public perceptions have been the driving forces for the development of standards for design against accidents.

A standard for design against accidents must include the following three items (Wang *et al.* 2001): (1) definition of accident scenarios, (2) procedures for evaluating consequences, and (3) criteria for approval or acceptance of a design. Whether a design is acceptable or not is judged by examining if the consequences of the design for a set of accident scenarios fall within a specified acceptance range using the specified (or recommended) evaluation procedures.

Accident scenarios define the situations which have unfavorable influences on the safety of ships, personnel and/or the environment. These scenarios represent situations that are as close as possible to those encountered by real ships. The collision scenarios must characterize ship speed, striking location/angle, loading condition, draft/trim, bow shape, relative orientation between striking and struck ships, and sea condition (e.g., wave, wind, current). The grounding scenarios must include ship speed, load condition, draft/trim, sea-bed condition, grounding location, water depth, and sea condition. The probability of occurrence for each scenario should be taken into account. In addition to the worst cases with small likelihood, cases that are likely to happen but have moderate or small influences should also be considered.

Evaluation approaches related to the structural performance consequences of any given accident may use simple calculation formulas, or simplified analytical methods. The associated risk may be mitigated in many ways, including by design changes or by operational procedure implementation. In some cases, established engineering practice may be used or recommended for risk mitigation instead, where a code or other standard specifies the basic requirements and procedures for consistency in evaluation. Evaluation procedures should be based on the physics or mechanics of the phenomenon involved. Ship hull structures must be properly modeled. The damage process needs to be realistically simulated. The selected methods should be applicable to different designs and cover the various different accident scenarios of interest.

Figure 9.35 shows the mid-ship section for a typical double hull oil tanker. To reduce the risk of oil outflow from such tankers in a collision or grounding accident, the OPA 90 and IMO require that the minimum width 'w' of each wing ballast tank or void space is not to be less than $0.5 + \text{dwt}/20\,000$ (m) or $w = 2.0$ (m), whichever is the lesser, where dwt is the deadweight of the vessel in tonnes. In no case is w to be less than 1.0 (m). The OPA 90 and IMO also require that the minimum vertical height 'h' of each double bottom ballast tank or void space is not to be less than 2.0 m or $B/15$ (B = the vessel's beam), whichever is the lesser, but in no case is the height to be less than 1.0 m.

Figure 9.36 shows the variation of the side ballast tank (or wing tank) width plotted versus vessel displacement and the double bottom height versus vessel beam for existing double hull oil tankers. The minimum values required by the OPA 90 and IMO are also shown. It is seen from Figure 9.36 that the side ballast tank width and double bottom

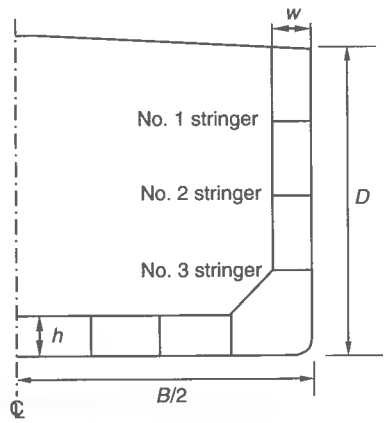

Figure 9.35 A schematic mid-ship section for a typical double hull oil tanker

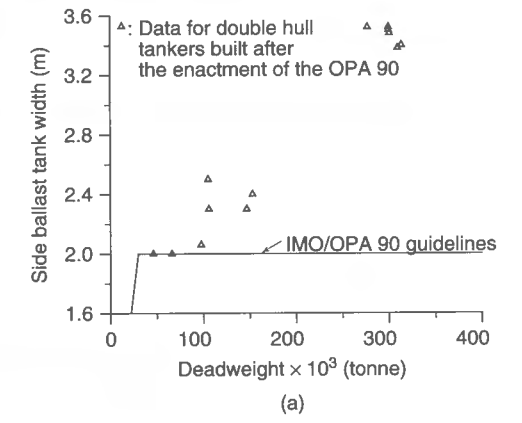

Figure 9.36 (a) Side ballast tank width plotted against vessel deadweight; (b) double bottom height plotted versus vessel beam

height of larger oil tankers are determined by the ballast capacity than by the OPA 90 requirements.

The accidental limit state design criterion can also be expressed by Equation (1.1) in Chapter 1. In this case, the 'demand' represents the loss of initial kinetic energy, while the 'capacity' indicates the energy absorption capability of the structure. The criteria for considering a design acceptable also provide a means to balance numerous variables in order to achieve an optimal solution by defining limits to damage extent, oil outflow, residual strength of the damaged ship, reserve stability and cost (Egge & Böckenhauer 1991). Environmental risk should be properly considered (Rawson *et al.* 1998), and variations in ship structural design should be accounted for. The format of the criteria may be deterministic, probabilistic or semi-probabilistic.

References

Abramowicz, W. & Wierzbicki, T. (1989). Axial crushing of multi-corner sheet metal columns. *Journal of Applied Mechanics*, 156: 113–119.

Alexander, J.M. (1960). An approximate analysis of the collapse of thin cylindrical shells under axial loading. *Quarterly Journal of Mechanics and Applied Mathematics*, 13(1): 10–15.

Amdahl, J. (1983). Energy absorption in ship-platform impacts. Division of Marine Structures, University of Trondheim, Report No. UR-83-34, September.

Bodner, S.R. & Symonds, P.S. (1962). Experimental and theoretical investigation of the plastic deformation of cantilever beams subjected to impulsive loading. *Journal of Applied Mechanics*, 29: 719–728.

Bucklingham, E. (1914). On physically similar systems: illustrations of the use of dimensional equations. *Physics Review*, 4: 347–350.

Campbell, J.D. & Ferguson, W.G. (1970). The temperature and strain-rate dependence of the shear strength of mild steel. *Philosophical Magazine*, 21: 63.

Caridis, P.A. & Stefanou, M. (1997). Dynamic elastic/viscoplastic response of hull plating subjected to hydrodynamic wave impact. *Journal of Ship Research*, 41(2): 130–146.

Chen, W. (1993). A new bound solution for quadrangular plates subjected to impulsive loads. Proceedings of the 3rd International Offshore and Polar Engineering Conference, Singapore, June 6–11, IV: 702–708.

Cowper, G.R. & Symonds, P.S. (1957). Strain-hardening and strain-rate effects in the impact loading of cantilever beams. Technical Report No. 28, Division of Applied Mathematics, Brown University, September.

Egge, E.D. & Böckenhauer, M. (1991). Calculation of the collision resistance of ships and its assessment for classification purpose. *Marine Structures*, 4: 35–56.

Forrestal, M.J. & Sagartz, M.J. (1978). Elastic–plastic response of 304 stainless steel beams to impulse loads. *Journal of Applied Mechanics*, 45: 685–687.

Harrigan, J.J., Reid, S.R. & Peng, C. (1999). Inertia effects in impact energy absorbing materials and structures. *International Journal of Impact Engineering*, 22(9): 955–979.

Hayashi, T. & Tanaka, Y. (1988). *Impact engineering*. Nikkan Kogyo Simbunsha (Daily Engineering Newspaper Company), Tokyo (in Japanese).

Hayduk, R.J. & Wierzbicki, T. (1984). Extensional collapse modes of structural members. *Computers & Structures*, 18(3): 447–458.

Johnson, W. (1972). *Impact strength of materials*. Edward Arnold, London and Crane Rissak, New York.

Jones, N. (1989). On the dynamic inelastic failure of beams. Chapter 5 in *Structural Failure*, John Wiley & Sons, New York, 133–159.

Jones, N. (1995). Quasi-static analysis of structural impact damage. *Journal of Constructional Steel Research*, 33: 151–177.

Jones, N. (1997a). Dynamic plastic behaviour of ship and ocean structures. *RINA Transactions*, 139: 65–97.

Jones, N. (1997b). *Structural impact*, Paperback Edition. Cambridge University Press, Cambridge.
Jones, N. & Jouri, W.S. (1987). A study of plate tearing for ship collision and grounding damage. *Journal of Ship Research*, 31: 253–268.
Jones, N., Liu, T., Zheng, J.J. & Shen, W.Q. (1991). Clamped beam grillages struck transversely by a mass at the center. *International Journal of Impact Engineering*, 11: 379–399.
Karagiozova, D. & Jones, N. (1997). Strain-rate effects in the dynamic buckling of a simple elastic–plastic model. *Journal of Applied Mechanics*, 64: 193–200.
Karagiozova, D., Alves, M. & Jones, N. (2000). Inertia effects in axisymmetrically deformed cylindrical shells under axial impact. *International Journal of Impact Engineering*, 24: 1083–1115.
Karagiozova, D. & Jones, N. (1998). *Stress wave effects on the dynamic axial buckling of cylindrical shells under impact. Structures under Shock and Impact V*. Computational Mechanics Publications, Southampton, 201–210.
Kitamura, O. (2002). FEM approach to the simulation of collision and grounding damage. *Marine Structures*, 15(4/5): 403–428.
Kolsky, H. (1963). *Stress waves in solids*. Dover, New York.
Kuroiwa, T. (1996). Numerical simulation of actual collision & grounding accidents. *Proceedings of International Conference on Design and Methodologies for Collision and Grounding Protection of Ships, San Francisco, August 22–23*, Paper No. 7, 1–12.
Lehmann, E., Egge, E.D., Scharrer, M. & Zhang, L. (2001). Calculation of collisions with the aid of coarse FE models. *Proceedings of the 8th International Symposium on Practical Design of Ships and Other Floating Structures (PRADS'2001), Shanghai, China, September 16–21*, II: 1293–1298.
Lu, G. & Calladine, C.R. (1990). On the cutting of a plate by a wedge. *International Journal of Mechanical Science*, 32: 293–313.
Malvern, L.E. (1969). *Introduction to the mechanics of continuous media*. Prentice Hall, Englewood Cliffs, NJ.
Minorsky, V.U. (1959). An analysis of ship collision with reference to protection of nuclear power ships. *Journal of Ship Research*, 3(2): 1–4.
Murray, N.W. (1983). The static approach to plastic collapse and energy dissipation in some thin-walled steel structures. Chapter 2 in *Structural Crashworthiness*. Butterworths, London, 44–65.
Nurick, G.N. & Martin, J.B. (1989). Deformation of thin plates subjected to impulsive loading – a review. Part II experimental studies. *International Journal of Impact Engineering*, 8: 171–186.
Nurick, G.N. & Jones, N. (1995). Prediction of large inelastic deformations of T-beams subjected to uniform impulsive loads. in *High Strain Rate Effects on Polymer Metal and Ceramic Matrix Composites and Other Advanced Materials*, The American Society of Mechanical Engineers, New York, 48: 127–153.
Nurick, G.N., Jones, N. & von Alten-Reuss, G.V. (1994). Large inelastic deformations of T-beams subjected to impulsive loads. *Proceedings of the 3rd International Conference on Structures under Shock and Impact*. Computational Mechanics Publications, Southhampton and Boston, 191–206.
Nurick, G.N., Olson, M.D., Fagnan, J.R. & Levin, A. (1995). Deformation and tearing of blast loaded stiffened square plates. *International Journal of Impact Engineering*, 16: 273–291.
Ohtsubo, H. & Suzuki, K. (1994). The crushing mechanics of bow structures in head-on Collision (1st report). *Journal of the Society of Naval Architects of Japan*, 176: 301–308 (in Japanese).
Ohtsubo, H. & Wang, G. (1995). An upper-bound solution to the problem of plate tearing. *Journal of Marine Science and Technology*, 1: 46–51.
Paik, J.K. (1994). Cutting of a longitudinally stiffened plate by a wedge. *Journal of Ship Research*, 38(4): 340–348.
Paik, J.K. & Chung, J.Y. (1999). A basic study on static and dynamic crushing behavior of a stiffened tube. *KSAE Transactions*, 7(1): 219–238 (in Korean).
Paik, J.K. & Pederson, P.T. (1995). Ultimate and crushing strength of plated structures. *Journal of Ship Research*, 39(3): 259–261.
Paik, J.K. & Pedersen, P.T. (1996). Modeling of the internal mechanics in ship collisions. *Ocean Engineering*, 23(2): 107–142.
Paik, J.K. & Wierzbicki, T. (1997). A benchmark study on crushing and cutting of plated structures. *Journal of Ship Research*, 41(2): 147–160.
Paik, J.K., Chung, J.Y. & Chun, M.S. (1996). On quasi-static crushing of a stiffened square tube. *Journal of Ship Research*, 40(3): 258–267.

Paik, J.K., Chung, J.Y., Choe, I.H., Thayamballi, A.K., Pedersen, P.T. & Wang, G. (1999). On the rational design of double hull tanker structures against collision. *SNAME Transactions*, 107: 323–363.
Pedersen, P.T. & Zhang, S. (2000a). Absorbed energy in ship collisions and grounding – revising Minorsky's empirical method. *Journal of Ship Research*, 44(2): 140–154.
Pedersen, P.T. & Zhang, S. (2000b). Effect of ship structure and size on grounding and collision damage distributions. *Ocean Engineering*, 27: 1161–1179.
Pedersen, P.T., Valsgaard, S., Olsen, D. & Spangenberg, S. (1993). Ship impacts – bow collisions. *International Journal of Impact Engineering*, 13: 163–187.
Perzyna, P. (1974). The constitutive equations describing thermo-mechanical behavior of materials at high rates of strain. *Mechanical properties at high rates of strain*, Conference Series. American Institute of Physics, New York, 21: 138–153.
Petersen, M.J. (1982). Dynamics of ship collisions. *Ocean Engineering*, 9(4): 295–329.
Rawson, C., Crake, K. & Brown, A. (1998). Assessing the environmental performance of tankers in accidental grounding and collision. *SNAME Transactions*, 106: 41–58.
Reid, S.R. & Reddy, T.Y. (1983). Experimental investigation of inertia effects in one-dimensional metal ring systems subjected to end impact – part I fixed-ended systems. *International Journal of Impact Engineering*, 1(1): 85–106.
Rosenfield, A.R. & Hahn, G.T. (1974). Numerical descriptions of the ambient low-temperature and high strain rate flow and fracture behavior of plain carbon steel. *ASM Transactions*, 59: 138.
Rudrapatna, N.S., Vaziri, R. & Olson, M.D. (2000). Deformation and failure of blast loaded stiffened plates. *International Journal of Impact Engineering*, 24: 457–474.
Saitoh, T., Yosikawa, T. & Yao, H. (1995). Estimation of deflection of steel panel under impulsive loading. JSME *Transactions, The Society of Mechanical Engineers of Japan*, 61(590): 2241–2246 (in Japanese).
Samuelides, M. & Frieze, P.A. (1989). Fluid-structure interaction in ship collisions. *Marine Structures*, 2: 65–88.
Schubak, R.B., Anderson, D.L. & Olson, M.D. (1989). Simplified dynamic analysis of rigid-plastic beams. *International Journal of Impact Engineering*, 8(1): 27–42.
Servis, D., Samuelides, M., Louka, T. & Voudouris, G. (2001). The implementation of finite element codes for the simulation of ship-ship collisions. *Proceedings of the 2nd International Conference on Collision and Grounding of Ships, Copenhagen, July 1–3*, 115–124.
Shen, W.Q. (1997). Dynamic response of rectangular plates under drop mass impact. *International Journal of Impact Engineering*, 19(3): 207–229.
Shen, W.Q. & Jones, N. (1991). A comment on the low speed impact of clamped beam by a heavy striker. *Mechanics of Structures and Machines*, 19(4): 527–549.
Simonsen, B.C. (1999). Ship grounding on rock: I & II. *Marine Structures*, 10: 519–584.
Simonsen, B.C. & Wierzbicki, T. (1998). Plasticity, fracture, friction in steady-state plate cutting. *International Journal of Impact Engineering*, 21(5): 387–411.
Smith, C.S. (1989). Chapter 13 *Behavior of composite and metallic superstructures under blast loading. Structural Failure*. John Wiley & Sons, New York, 435–462.
Symonds, P.S. & Chon, C.T. (1974). Approximation techniques for impulsive loading of structures of time-dependent plastic behaviour with finite-deflections. *Mechanical properties of materials at high rates of strain*, Conference Series, American Institute of Physics, New York, No. 21, 299–316.
Symonds, P.S. & Jones, N. (1972). Impulsive loading of fully clamped beams with finite plastic deflections. *International Journal of Mechanical Sciences*, 14: 49–69.
Thomas, P.F. (1992). Application of plate cutting mechanics to damage prediction in ship grounding. MIT–Industry Joint Program on Tanker Safety, Report No. 8, Department of Ocean Engineering, Massachusetts Institute of Technology, Cambridge, MA.
Toyosada, M., Fujii, E., Nohara, K., Kawaguchi, Y., Arimochi, K. & Isaka, K. (1987). The effect of strain rate on critical CTOD and J-integral. *Journal of the Society of Naval Architects of Japan*, 161: 343–356 (in Japanese).
Vaughan, H. (1980). The tearing of mild steel plate. *Journal of Ship Research*, 24(2): 96–100.
Wang, G., Ohtsubo, H. & Liu, D. (1997). A simple method for predicting ships' grounding strength. *Journal of Ship Research*, 41: 241–247.

Wang, G., Arita, H. & Liu, D. (2000). Behavior of a double hull in a variety of stranding or collision scenarios. *Marine Structures*, 13: 147–187.
Wang, G., Spencer, J. & Chen, Y.J. (2001). Assessment of ship's performance in accidents. *Proceedings of the 2nd International Conference on Collision and Grounding of Ships, Copenhagen, July 1–3*, 241–251.
Wierzbicki, T. (1983). Crushing behavior of plate intersections. *Proceedings of the 1st International Symposium on Structural Crashworthiness, University of Liverpool, September*, 66–95.
Wierzbicki, T. (1995). Concertina tearing of metal plates. *International Journal of Solid Structures*, 19: 2923–2943.
Wierzbicki, T. & Thomas, P. (1993). Closed-form solution for wedge cutting force through thin metal sheets. *International Journal of Mechanical Science*, 35: 209–229.
Woisin, G. (1979). Design against collision. *Proceedings of International Symposium on Advances in Marine Technology, Trondheim.*
Woisin, G. (1982). Comments on Vaughan: the tearing strength of mild steel plate. *Journal of Ship Research*, 26: 50–52.
Woisin, G. (1990). Analysis of the collisions between rigid bulb and side shell panel. *Proceedings of the 7th International Symposium on Practical Design of Ships and Mobile Units (PRADS'90), The Hague*, 165–172.
Yu, T.X. & Chen, F.L. (1992). The large deflection dynamic plastic response of rectangular plates. *International Journal of Impact Engineering*, 12(4): 603–616.
Zhang, S. (2002). Plate tearing and bottom damage in ship grounding. *Marine Structures*, 15: 101–117.

10 Fracture Mechanics and Ultimate Strength of Cracked Structures

10.1 Fundamentals of Fracture Mechanics

Under the action of repeated loading, fatigue cracks may be initiated in the stress concentration areas of the structure. Initial defects may be formed in the structure by the fabrication procedure and may conceivably remain undetected over time. Cracks may initiate from such defects, and propagate. In addition to propagation under repeated cyclic loading, cracks may also grow in an unstable way under monotonically increasing extreme loads, a circumstance which can conceivably lead to catastrophic failure of the structure. This possibility is of course tempered by the ductility of the material involved, and the presence of reduced stress intensity regions in a complex structure that may serve as crack arresters even in an otherwise monolithic structure.

For residual strength assessment of aging steel structures under extreme loads, it is thus often necessary to take into account a known (existing or premised) crack as a parameter of influence. This chapter is primarily concerned with the limit state assessment of steel-plated structures with existing crack damage and under monotonic extreme loading. The propagation of a crack under cyclic loading is also briefly treated, since such technology may be necessary to predict the size of a crack subject to cyclic loading, at any given point in time, starting with a known initial crack size.

Structural fracture modes associated with cracks may be classified into three groups, namely brittle fracture, ductile fracture and rupture (Machida 1984). When the strain at fracture of material is very small, it is called brittle fracture. In steel structures made of ductile material with adequately high fracture toughness, however, the fracture strain can be comparatively large. When the material is broken by necking associated with large plastic flow, it is called rupture. As a failure mode, ductile fracture is an intermediate phenomenon between brittle fracture and rupture.

The progress of ductile fracture from an existing sharp-tipped crack may be separated into four regimes, namely blunting of the initially sharp crack tip, initial crack growth,

stable crack growth and unstable crack propagation (Shih *et al.* 1977). The ductile fracture characteristics generally depend on the material toughness, but can also be affected by the loading rate and environmental factors such as corrosion and temperature. For high-toughness materials, the crack tip may be significantly blunted and the stable crack growth regime can be substantial prior to fracture. For low-toughness materials, however, there is likely to be relatively little crack tip blunting and unstable crack extension can occur even without a stable crack growth regime.

In the rare situation when the structure has been weakened by large cracks or large-scale plasticity associated with cracks, resulting in a decrease of structural stiffness, large deformations are likely to develop. Figure 10.1 shows a schematic representation of the nonlinear behavior of cracked steel structures under monotonic loading. It is noted that, for similar structures, the stiffness and ultimate strength of cracked structures is, as expected, smaller than those of uncracked structures.

Fracture behavior for ductile materials is quite different from that of brittle materials. Ductile materials generally exhibit slow stable crack growth accompanied by considerable plastic deformation. In other words, there is crack growth resistance during crack extension. The study of the fracture behavior of materials, components and structures is now known as fracture mechanics. Fracture mechanics is hence the engineering discipline that can be used to quantify the conditions under which a load-bearing structure can fail due to the enlargement of a crack.

It is commonly agreed that the modern era of fracture mechanics originated with the work of A.A. Griffith (1920) who resolved the infinite crack tip stress dilemma inherent in the use of the theory of elasticity for cracked structures. However, the study of fracture remained for some time of scientific interest only. One reason for this was the apparent non-applicability of the Griffith theory to engineering materials (i.e., metals) whose fracture resistance values are typically orders of magnitude greater than that of brittle materials such as glass.

The next major contributions to the subject were made independently by Irwin (1948) and Orowan (1948) who extended Griffith's approach to metals by including the energy

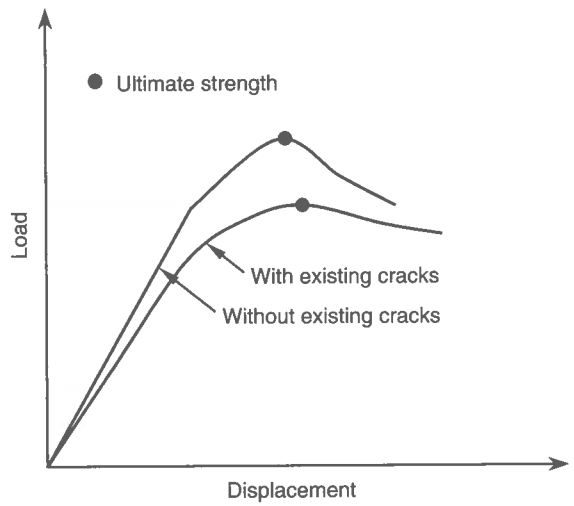

Figure 10.1 A schematic representation of the cracking damage effect on the ultimate strength behavior of steel structures

dissipated by local plastic flow. During this same period, Mott (1948) extended Griffith's theory to a rapidly propagating crack.

Irwin (1956) developed the energy release rate concept and related it to Griffith's theory. Using the approach of Westergaard (1939) who developed a method to analyze stresses and displacements ahead of a sharp crack, Irwin (1957) showed that the stresses and displacements near the crack tip could be described by a single parameter which was related to the energy release rate. This crack tip characterizing parameter is the stress intensity factor. During the same period, Williams (1957) also calculated the stress distribution at the crack tip but using a somewhat different technique from the Irwin approach. Both results were essentially identical.

Linear elastic fracture mechanics (LEFM) is generally found to be accurate for brittle materials. Direct application of LEFM to ductile materials is found to yield overly conservative predictions. In the 1960s it was realized that LEFM is not applicable when large-scale yielding at the crack tip precedes failure. To accommodate the effect of yielding at the crack tip several researchers proposed approximate methods, mostly by correcting and expanding on LEFM (Dugdale 1960, Wells 1961, 1963, Barenblatt 1962). While Dugdale (1960) proposed an idealized model based on a narrow strip of yielded material at the crack tip, Wells (1961, 1963) suggested the displacement of the crack faces as an alternative fracture criterion when large-scale plasticity occurs at the crack tip. The Wells parameter is now known as the crack tip opening displacement (CTOD).

Rice (1968) introduced another parameter to characterize nonlinear material behavior ahead of a crack tip. He generalized the energy release rate to nonlinear materials by idealizing plastic deformation as nonlinear elastic. The resulting parameter is the J-integral. During this same period, Hutchinson (1968) and Rice & Rosengren (1968) showed that the J-integral could be used to represent the characteristics of crack tip stress fields in the nonlinear elastic range of material behavior.

To apply fracture mechanics to structural design, a mathematical relationship between material toughness, stress and flaw size must be established. While these relationships for linear elastic problems had been available for a time, Shih & Hutchinson (1976) were perhaps the first to provide the theoretical framework to establish such a relationship for nonlinear problems. Shih (1981) also established a relationship between the J-integral and CTOD.

For an elaborate summary of early fracture mechanics research undertaken during 1913 to 1965, Barsom (1987) is referred to. A comprehensive historical overview on fracture mechanics from 1960 to 1980 is provided by Anderson (1995). The details of fracture mechanics can be found in the textbooks by Machida (1984), Kanninen & Popelar (1985), Broek (1986) and Anderson (1995), among others. For practical application, many handbooks are also available (e.g., Sih 1973, Tada *et al.* 1973, Rooke & Cartwright 1976, Murakami 1987).

This chapter describes the fundamentals of fracture mechanics, with the eventual aim of application to ductile steel structures. A simplified procedure for analyzing the limit state capacity of cracked steel-plated structures under monotonic extreme loads is presented. The ultimate limit state (ULS) criterion is still expressed by Equation (1.1) in Chapter 1. However, in this case, the 'capacity' represents the ultimate strength of the cracked structure under monotonic extreme loads, while the 'demand' indicates the extreme working stress or load. Any mathematical details omitted in this chapter may be found in the reference material noted above.

10.2 Basic Concepts for Fracture Mechanics Analysis

Figure 10.2 represents a schematic of appropriate approaches for fracture analysis of a cracked structure as a function of material fracture toughness. It is seen from Figure 10.2 that for low-toughness materials, brittle fracture is predominant and LEFM is valid. For very high-toughness materials, however, rupture is dominant because of large-scale plasticity until the structure collapses. In this case, limit-load analysis (LLA) is more relevant. There is a transition between brittle fracture and rupture when the fracture toughness is intermediate. This is termed the ductile fracture regime, and in this case nonlinear fracture mechanics concepts, now generally termed elastic–plastic fracture mechanics (EPFM), will be more relevant to assess failure characteristics of the structure.

In this section, these various basic concepts of fracture mechanics are described.

10.2.1 Energy-based Concept

In the Griffith energy concept, it is considered that the fracture takes place if crack-growth-related energy exceeds the material's resistance to fracture. Mathematically, the following criterion must be satisfied for fracture to occur:

$$G \geq G_C \tag{10.1}$$

where G is called the strain energy release rate or, alternatively, the crack driving force, and G_C represents the material's resistance to crack growth.

For a cracked infinite plate under tensile stress σ, as shown in Figure 10.3, it can be shown that G and G_C are given by

$$G = \frac{\pi\sigma^2 a}{E} \tag{10.2a}$$

$$G_C = \frac{\pi\sigma_f^2 a}{E} \tag{10.2b}$$

where E = Young's modulus, a = half crack length, σ_f = failure stress.

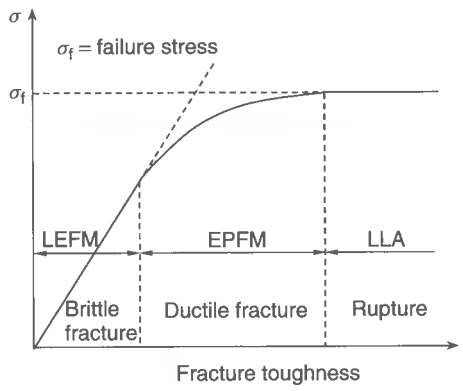

Figure 10.2 A schematic of appropriate approaches for fracture analysis as a function of material fracture toughness (LEFM = linear elastic fracture mechanics, EPFM = elastic-plastic fracture mechanics, LLA = limit-load analysis)

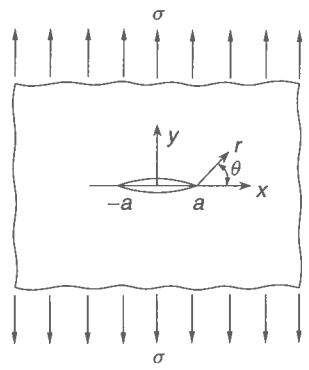

Figure 10.3 A cracked infinite plate under tensile loading

It is surmised from Equations (10.2) that the failure stress, σ_f, is proportional to $1/\sqrt{a}$ for a constant value of G_C, implying that the failure stress decreases in that manner with increase in the flaw size.

10.2.2 Stress Intensity Factor Concept

For a cracked body with a linear elastic material as shown in Figure 10.4, stress components near the crack tip in the xy plane may be shown to be given by

$$\sigma_x = \frac{K_I}{\sqrt{2\pi r}} \cos\left(\frac{\theta}{2}\right)\left[1 - \sin\left(\frac{\theta}{2}\right)\sin\left(\frac{3\theta}{2}\right)\right] \tag{10.3a}$$

$$\sigma_y = \frac{K_I}{\sqrt{2\pi r}} \cos\left(\frac{\theta}{2}\right)\left[1 + \sin\left(\frac{\theta}{2}\right)\sin\left(\frac{3\theta}{2}\right)\right] \tag{10.3b}$$

$$\tau_{xy} = \frac{K_I}{\sqrt{2\pi r}} \cos\left(\frac{\theta}{2}\right)\sin\left(\frac{\theta}{2}\right)\cos\left(\frac{3\theta}{2}\right) \tag{10.3c}$$

where K_I is called the Mode I stress intensity factor. Mode I is the direct opening mode for a crack; more will be said about crack modes later.

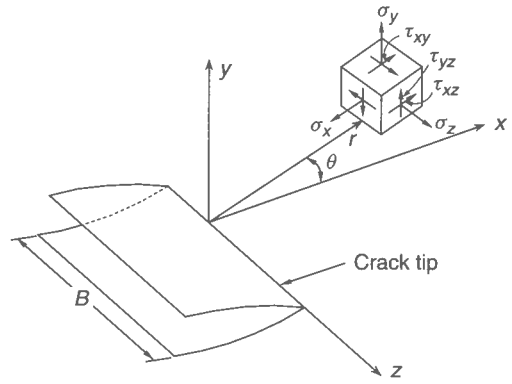

Figure 10.4 Local coordinate system and the resulting stress components for a cracked body (B = plate thickness)

The dimensions of the stress intensity factor are given by [stress] × [length]$^{1/2}$ = [force] × [length]$^{-3/2}$ (e.g., kgf/mm$^{3/2}$, MN/m$^{3/2}$).

It is evident from Equations (10.3) that each stress component is proportional to the stress intensity factor.

For the cracked plate shown in Figure 10.3, the Mode I stress intensity factor is given by

$$K_I = \sigma\sqrt{\pi a} \tag{10.4}$$

From Equations (10.2a) and (10.4), one can get a relationship between K_I and G if necessary. In today's LEFM, it is considered that the fracture takes place when the following criterion is satisfied:

$$K \geq K_C \tag{10.5}$$

where K = stress intensity factor, K_C = critical stress intensity factor which represents a measure of the material's resistance. It can be shown that the critical value of the stress intensity factor is related to the critical value of the crack driving force by the following equations:

$$K_C = \sqrt{EG_C} \text{ for plane stress} \tag{10.6a}$$

$$K_C = \sqrt{(1-\nu^2)EG_C} \text{ for plane strain} \tag{10.6b}$$

Standard test procedures exist for obtaining the Mode I plane strain fracture toughness. Table 10.1 indicates a limited collection of such fracture toughness data for maraging steels according to Broek (1986). It is seen from Table 10.1 that for high-yield-strength materials, the K_{IC} values are in the range of 50 to 350 kg/mm$^{3/2}$, while low-yield-strength materials have fracture toughness of the order of 500 kg/mm$^{3/2}$ or more. Depending on the yield stress of the materials, the required specimen thickness may be in the order of 2 to 20 mm, but test specimens with a thickness less than about 10 mm may not normally be useable because of buckling. In any event, since the combination of a high toughness and a low yield stress leads to extremely high values of $(K_{IC}/\sigma_Y)^2$, where σ_Y = material yield stress, the required specimen thickness for a standard test may reach the order of 1 meter as indicated in Table 10.1.

Table 10.1 Illustrative collection of fracture toughness data for maraging steels (Broek 1986).

Material	Condition	σ_Y (kg/mm^2)	K_{IC} (kg/mm$^{3/2}$)	B_{min} (mm)
300	900 °F 3 h	200	182	2.1
300	850 °F 3 h	170	300	7.8
250	900 °F 3 h	181	238	4.3
D6AC steel	Heat treated	152	210	4.8
	Heat treated	150	311	10.7
	Forging	150	178–280	–
4340 steel	Hardened	185	150	1.7
A533B	Reactor steel	35	≅ 630	810
Carbon steel	Low strength	24	>700	2150

Notes: B_{min} = minimum thickness required for the K_{IC} test specimen.

In today's practice, it is normally required that the following equation be satisfied for a through-thickness crack in a plate of thickness B, if plane strain conditions are to be assured at the crack tip in a static test:

$$B \geq 2.5\left(\frac{K_{IC}}{\sigma_Y}\right)^2 \tag{10.7}$$

Apart from the fact that it is not practical to perform a valid K_{IC} test on most ductile materials, it is also not useful because the materials with a thickness in the order of 1 meter will never be used. This shows one of the limitations of LEFM, which is that it is applicable readily only to materials with a ratio of modulus to yield stress which is roughly smaller than 200 to 250 at room temperature. Of course LEFM may apply to low-strength steels at lower temperatures and/or higher loading rates, conditions under which the same material may behave in an appreciably more brittle manner. Such cases may or may not be of interest in specific applications involving through thickness cracks. In cases where it can be used, once the crack situation (e.g., through-thickness crack in an infinite plate), fracture toughness and applied loading details are known, the critical crack size at failure can be calculated using LEFM.

10.3 More on LEFM and the Modes of Crack Extension

In previous sections, we have based the discussion on a Mode I (direct tensile opening mode) through-thickness crack in an infinite plate. In this section, the concept and applications of the stress intensity factor as a representative parameter in LEFM are further described, considering modes of crack extension other than Mode I as well.

The stress intensity factor, K, is determined as a function of crack size, geometric properties and loading conditions. An investigation of crack tip stress and displacement fields and their relationship to K is important because these fields are typically the ones that govern the fracture process occurring at the crack tip.

A cracked body as shown in Figure 10.4 is now considered. The crack plane lies in the xz plane and the crack front is parallel to the y axis. In this case, three basic fracture modes are relevant as depicted by Figure 10.5. Mode I is the opening or tensile mode where the crack faces separate symmetrically with respect to the xy and xz planes. In Mode II, the sliding or in-plane shearing mode, the crack faces slide relative to each other symmetrically about the xy plane, but antisymmetrically with respect to the xz plane. In the tearing or anti-plane or out-of-plane shearing mode, Mode III, the crack faces also slide relative to each other but antisymmetrically with respect to the xy and xz planes.

For plane problems with homogeneous, isotropic, linear elastic materials, the stress intensity factors corresponding to the three modes are given as follows (see Kanninen & Popelar 1985, among others)

$$K_I = \lim_{r\to 0} \sigma_y|_{\theta=0}\sqrt{2\pi r} \tag{10.8a}$$

$$K_{II} = \lim_{r\to 0} \tau_{xy}|_{\theta=0}\sqrt{2\pi r} \tag{10.8b}$$

$$K_{III} = \lim_{r\to 0} \tau_{yz}|_{\theta=0}\sqrt{2\pi r} \tag{10.8c}$$

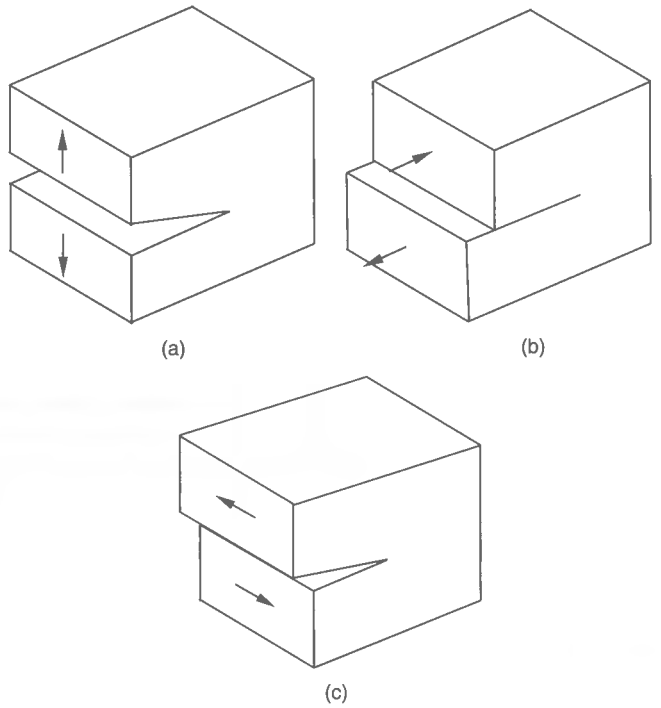

Figure 10.5 Three basic loading modes for a cracked body: (a) Mode I, opening mode; (b) Mode II, sliding mode (or in-plane shear mode); (c) Mode III, tearing mode (or out-of-plane shear mode)

where r, θ and the coordinates are defined in Figure 10.4. σ_y, τ_{xy} and τ_{yz} are stress components as defined in Figure 10.4.

An elastic body with a crack length of $2a$ and under uniform tensile stress, σ, is considered, although much of the treatment in Equations (10.9) to (10.12) are in fact more general and are applicable to arbitrary types of loading and crack geometry. The local coordinate system of the body is defined as shown in Figure 10.4. The stresses and displacements at the crack tip may be given as follows (Machida 1984):

$$\begin{Bmatrix} \sigma_x \\ \sigma_y \\ \tau_{xy} \end{Bmatrix} = \frac{K_{\mathrm{I}}}{\sqrt{2\pi r}} \cos\frac{\theta}{2} \begin{Bmatrix} 1 - \sin(\theta/2)\sin(3\theta/2) \\ 1 + \sin(\theta/2)\sin(3\theta/2) \\ \sin(\theta/2)\cos(3\theta/2) \end{Bmatrix} \tag{10.9a}$$

$$\tau_{xz} = \tau_{yz} = 0 \tag{10.9b}$$

$$\sigma_z = \begin{cases} \nu(\sigma_x + \sigma_y) & \text{for plane strain state} \\ 0 & \text{for plane stress state} \end{cases} \tag{10.9c}$$

$$\begin{Bmatrix} u \\ v \\ w \end{Bmatrix} = \frac{K_{\mathrm{I}}}{2\mu}\sqrt{\frac{r}{2\pi}} \begin{Bmatrix} \cos(\theta/2)[\kappa - 1 + 2\sin^2(\theta/2)] \\ \sin(\theta/2)[\kappa + 1 - 2\cos^2(\theta/2)] \\ 0 \end{Bmatrix} \tag{10.9d}$$

where $\kappa = 3 - 4\nu$ for the plane strain state and $\kappa = (3 - \nu)/(1 + \nu)$ for the plane stress state, $K_{\mathrm{I}} = \sigma\sqrt{(\pi a)}$, a = crack length, $\mu = E/[2(1 + \nu)]$, E = elastic modulus, ν = Poisson's ratio, u, v, w = translational displacements in the x, y and z directions.

It is evident from Equations (10.9) that the stress or displacement components at the crack tip include a common parameter, K_{I}. The relative displacements used represent a distance between the two crack surfaces. This type of displacement is called Mode I or opening mode, as shown in Figure 10.5(a).

A cracked body under shear stress τ is now considered. In this case, the stress and displacement components are given as follows:

$$\begin{Bmatrix} \sigma_x \\ \sigma_y \\ \tau_{xy} \end{Bmatrix} = \frac{K_{\mathrm{II}}}{\sqrt{2\pi r}} \begin{Bmatrix} -\sin(\theta/2)\left[2 + \cos(\theta/2)\cos(3\theta/2)\right] \\ \sin(\theta/2)\cos(\theta/2)\cos(3\theta/2) \\ \cos(\theta/2)\left[1 - \sin(\theta/2)\sin(3\theta/2)\right] \end{Bmatrix} \tag{10.10a}$$

$$\tau_{xz} = \tau_{yz} = 0 \tag{10.10b}$$

$$\sigma_z = \begin{cases} \nu(\sigma_x + \sigma_y) & \text{for plane strain state} \\ 0 & \text{for plane stress state} \end{cases} \tag{10.10c}$$

$$\begin{Bmatrix} u \\ v \\ w \end{Bmatrix} = \frac{K_{\mathrm{II}}}{2\mu}\sqrt{\frac{r}{2\pi}} \begin{Bmatrix} \sin(\theta/2)\left[(3 - \nu)/(1 + \nu) + 1 + 2\cos^2(\theta/2)\right] \\ -\cos(\theta/2)\left[(3 - \nu)/(1 + \nu) - 1 - 2\sin^2(\theta/2)\right] \\ 0 \end{Bmatrix} \tag{10.10d}$$

where $K_{\mathrm{II}} = \tau\sqrt{(\pi a)}$.

In this case, the displacements follow Mode II or the in-plane shear mode as shown in Figure 10.5(b).

When the body is subjected to uniform shear stress, s, in the direction normal to the xy plane, the stress and displacement components are given by

$$\begin{Bmatrix} \tau_{xz} \\ \tau_{yz} \end{Bmatrix} = \frac{K_{\mathrm{III}}}{\sqrt{2\pi r}} \begin{Bmatrix} -\sin(\theta/2) \\ \cos(\theta/2) \end{Bmatrix} \tag{10.11a}$$

$$\sigma_x = \sigma_y = \sigma_z = \tau_{xy} = 0 \tag{10.11b}$$

$$w = \frac{2K_{\mathrm{III}}}{\mu}\sqrt{\frac{r}{2\pi}}\sin\frac{\theta}{2} \tag{10.11c}$$

$$u = v = 0 \tag{10.11d}$$

where $K_{\mathrm{III}} = s\sqrt{\pi a}$. In this case, the displacements follow Mode III or anti-plane (or out-of-plane) shear mode as shown in Figure 10.5(c).

For an angled crack, similar expressions of stresses and displacements can be relevant (Anderson 1995). When the three modes noted above are combined, the stress or displacement components may be given as a sum of those for each mode as follows (Machida 1984):

$$\sigma_{ij}(r, \theta) = \frac{1}{\sqrt{2\pi r}}\left\{K_{\mathrm{I}} f_{ij}^{\mathrm{I}} + K_{\mathrm{II}} f_{ij}^{\mathrm{II}} + K_{\mathrm{III}} f_{ij}^{\mathrm{III}}\right\} \tag{10.12a}$$

$$u_i(r, \theta) = \frac{1}{2\mu}\sqrt{\frac{r}{2\pi}}\left\{K_{\mathrm{I}} g_i^{\mathrm{I}} + K_{\mathrm{II}} g_i^{\mathrm{II}} + 4K_{\mathrm{III}} g_i^{\mathrm{III}}\right\} \tag{10.12b}$$

where f_{ij}^{I}, f_{ij}^{II}, f_{ij}^{III} = stress functions of θ for Modes I, II and III as defined in Equations (10.9) to (10.11), g_i^{I}, g_i^{II}, g_i^{III} = displacement functions of θ for Modes I, II and III as defined in Equations (10.9) to (10.11).

It is apparent that the K parameters are independent of the coordinate system while they are affected by geometric properties and loading conditions (e.g., crack size, dimensions of the structure), and can hence be employed as the measure of crack extension resistance at the crack tip as long as the structure remains in the linear elastic regime.

10.3.1 Useful K Solutions

In relation to LEFM, calculations of the stress intensity factor involve the most part of the work. Generally speaking, analytical approaches and numerical approaches can be used to determine the stress intensity factors, many essentially exploiting the relationships between K and the crack tip stress field previously described. Some useful K solutions are now described below.

For steel plates with typical types of cracks under tensile stress as shown in Figure 10.6, the K value for Mode I is approximately given as follows (Broek 1986):

(1) Center crack, see Figure 10.6(a)

$$K_{\mathrm{I}} = F\sigma\sqrt{\pi a} \tag{10.13a}$$

where

$$F = \left(\sec\frac{\pi a}{b}\right)^{1/2}$$

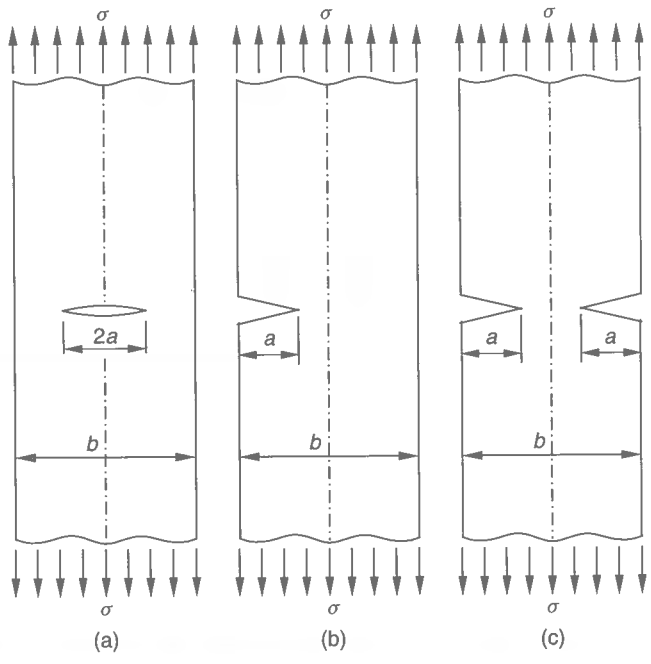

Figure 10.6 Typical crack locations in a plate under tensile stress: (a) center crack; (b) crack on one side; (c) crack on both sides

(2) Crack on one side, see Figure 10.6(b)

$$K_{\mathrm{I}} = F\sigma\sqrt{\pi a} \tag{10.13b}$$

where

$$F = 30.38\left(\frac{a}{b}\right)^4 - 21.71\left(\frac{a}{b}\right)^3 + 10.55\left(\frac{a}{b}\right)^2 - 0.23\left(\frac{a}{b}\right) + 1.12$$

(3) Crack on both sides, see Figure 10.6(c)

$$K_{\mathrm{I}} = F\sigma\sqrt{\pi a} \tag{10.13c}$$

where

$$F = 15.44\left(\frac{a}{b}\right)^3 - 4.78\left(\frac{a}{b}\right)^2 + 0.43\left(\frac{a}{b}\right) + 1.12$$

If the plate width were infinite, the solution in the first of the above three cases would revert to the classical exact solution, namely $K_{\mathrm{I}} = \sigma\sqrt{(\pi a)}$ since $F = 1$ in this case.

10.3.2 Fracture Toughness Testing

Recall that fracture takes place if the K value of the structure reaches the critical K value, K_{C}, namely

$$K \geq K_{\mathrm{C}}$$

where K_{C} is sometimes called fracture toughness, which is typically determined experimentally for a given material, crack and loading situation. Under plane strain conditions, the notation K_{IC} is used. The fracture toughness parameter, K_{C} or K_{IC}, must be obtained by testing. Widely accepted test methods exist for K_{IC} as noted in Section 10.2.2.

In such testing, K_{C} is determined once the ultimate fracture loads (or failure loads) and the crack sizes are obtained for a mechanical test specimen with the stress intensity factor known. In general, the fracture toughness, K_{C}, is affected by strain rate, temperature and plate thickness. As the plate thickness decreases, the K_{C} value tends to significantly increase. This is because with decrease in the plate thickness the crack tip stress state approaches the plane stress case, and essentially Mode II or III based on shear fracture and mixtures of these with Mode I are more likely to take place than pure Mode I.

For thicker plates, Mode I fracture associated with the plane strain state is more likely to occur. In this case, the fracture toughness, K_{C}, is no longer a function of plate thickness. Figure 10.7 shows a schematic representation of the critical K value at the crack tip versus the plate thickness. For a given plate thickness, in contrast to through-thickness cracks, surface cracks may sometimes exhibit plane strain behavior because of the related conditions at the crack tip.

It is noted that the critical stress intensity value given in this section, which is used as a material parameter to define the fracture toughness, should strictly speaking be called the static fracture toughness as it relates to fracture under static loading. There are also other fracture toughness measures useful in other situations, such as the dynamic fracture toughness and the crack arrest toughness, descriptions of which are beyond the scope of the present book; the interested reader is referred, for example, to Broek (1986).

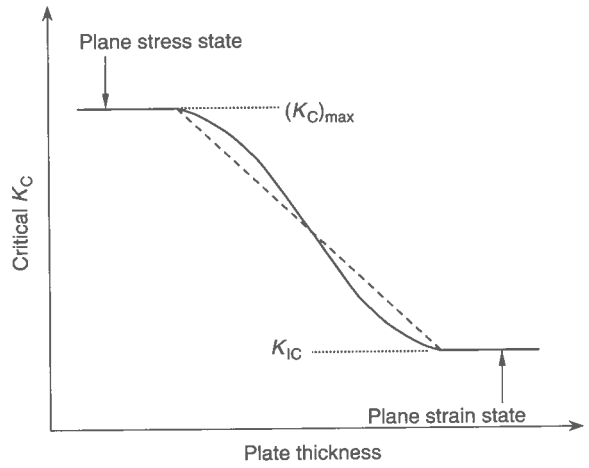

Figure 10.7 A schematic representation of the critical K_I value versus the plate thickness, B

10.4 Elastic–Plastic Fracture Mechanics

As is apparent from Equations (10.13) in LEFM, the failure stress, $\sigma_f = K_{IC}/F\sqrt{(\pi a)}$, at the crack tip becomes infinite when the crack size, a, approaches zero. This is unrealistic because in real structures behaving in a ductile manner, the crack tip is likely to yield and strictly speaking LEFM may not be valid. For a body with relatively large flaws, LEFM may of course approximately be dealt with using the K values to an extent, as long as the plastic zone at the crack tip is small in size. The better alternative in this regard is to use the concepts of EPFM. As will now be presented, the concepts of CTOD or the J-integral accommodate the effect of yielding at the crack tip in a more rigorous way. These types of procedures are also variously called nonlinear fracture mechanics or post-yield fracture mechanics, in addition to EPFM.

10.4.1 Crack Tip Opening Displacement

Beyond general yield condition, plastic deformation is likely to occur at the crack tip. The crack may propagate if the plastic strain at the crack tip exceeds a critical value. The change of stress at the yielded crack tip may be small when the effect of strain hardening is neglected, and the fracture will take place after a large plastic deformation occurs at the crack tip.

In an effort to account for limited amounts of crack tip yielding as an extension of LEFM, Dugdale (1960), Wells (1961, 1963) and Barenblatt (1962) independently introduced cohesive yield strip zones extending from the crack tip to take account of the inelastic response of real materials in this region.

The CTOD concept as now used emanated from these early treatments. The plastic deformation at the crack tip can be measured in terms of the CTOD. Wells (1961, 1963) considered that fracture takes place if the CTOD exceeds a critical value.

In LEFM, the crack opening displacement (COD) is given by (see Figure 10.8)

$$\text{COD} = 2v = \frac{4\sigma}{E}\sqrt{a^2 - x^2} \tag{10.14a}$$

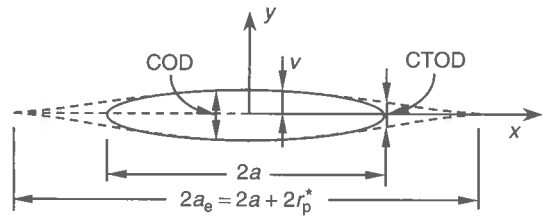

Figure 10.8 Crack opening displacement and CTOD

The maximum COD occurs at the center of the crack, i.e., at $x = 0$, as follows:

$$\text{COD}_{max} = \frac{4\sigma a}{E} \tag{10.14b}$$

The Irwin Approach

Equations (10.14) are the elastic solutions of crack problems while most engineering materials deform plastically. Strictly speaking, Equations (10.14) cannot be applied to the crack problems involving the plastic deformations at the crack tip. The size (distance) of the crack tip plastic zone can be approximately calculated by

$$\frac{K_I}{\sqrt{2\pi r_p^*}} = \sigma_Y \quad \text{or} \quad r_p^* = \frac{K_I^2}{2\pi\sigma_Y^2} = \frac{\sigma^2 a}{2\sigma_Y^2} \tag{10.15a}$$

where σ_Y = material yield stress, r_p^* = size of the crack tip plastic zone, see Figure 10.8.

Irwin (1956) assumed that due to the occurrence of plasticity, the equivalent crack tip size becomes longer than the physical size. In this regard, the COD is given by applying the plastic zone correction as follows:

$$\text{COD} = \frac{4\sigma}{E}\sqrt{(a + r_p^*)^2 - x^2} \tag{10.15b}$$

The CTOD is then found for $x = a$ as follows:

$$\text{CTOD} \equiv \delta = \frac{4\sigma}{E}\sqrt{(a + r_p^*)^2 - a^2} \approx \frac{4\sigma}{E}\sqrt{2ar_p^*} = \frac{4}{\pi}\frac{K_I^2}{E\sigma_Y} \tag{10.15c}$$

It is not straightforward to measure CTOD, but using the K value CTOD can be obtained from Equation (10.15c). By substituting Equation (10.15c) into Equation (10.15b), the following relation between COD and CTOD is approximately obtained by regarding $(r_p^*)^2$ as infinitesimal, namely

$$\text{COD} = \frac{4\sigma}{E}\sqrt{a^2 - x^2 + \left(\frac{E}{4\sigma}\right)^2 \delta^2} \tag{10.15d}$$

In testing, the COD can be measured easily so that the CTOD is determined from Equation (10.15d) in terms of the maximum COD, i.e., at $x = 0$.

The Dugdale Approach

Dugdale (1960) treated yielding at the crack tip by replacing the yielded region with the equivalent elastic (unyielded) crack model.

As shown in Figure 10.9(a), the crack tip is likely to yield and the yielding may expand around the crack tip. In the Dugdale approach, however, yielding is assumed to be limited inside a region along the straight line of the crack, as shown in Figure 10.9(b). This situation is considered equivalent to a virtual elastic structure which has the crack length of $2b = 2a + 2d$, including the yielded region, and the yielded region is subjected to a 'negative' internal pressure ('tensile' stress) equal to the yield stress, σ_Y, on the crack surfaces, which tends to 'close' the virtual crack strip yielding zone opening caused by the external stress as shown in Figure 10.9(c). In this case, the K value at the tip of the virtual elastic crack must be zero, and hence the following applies:

$$K_\sigma + K_Y = 0 \tag{10.16a}$$

where $K_\sigma = K$ value due to applied stress σ, $K_Y = K$ value due to the closure yield stress which is taken as $K_Y = -\sigma_Y$.

The extent of the plastic region, d, can be calculated using Equation (10.16a) as follows:

$$d = b - a = a\left[\sec\left(\frac{\pi\sigma}{2\sigma_Y}\right) - 1\right] \tag{10.16b}$$

where σ_Y = material yield stress.

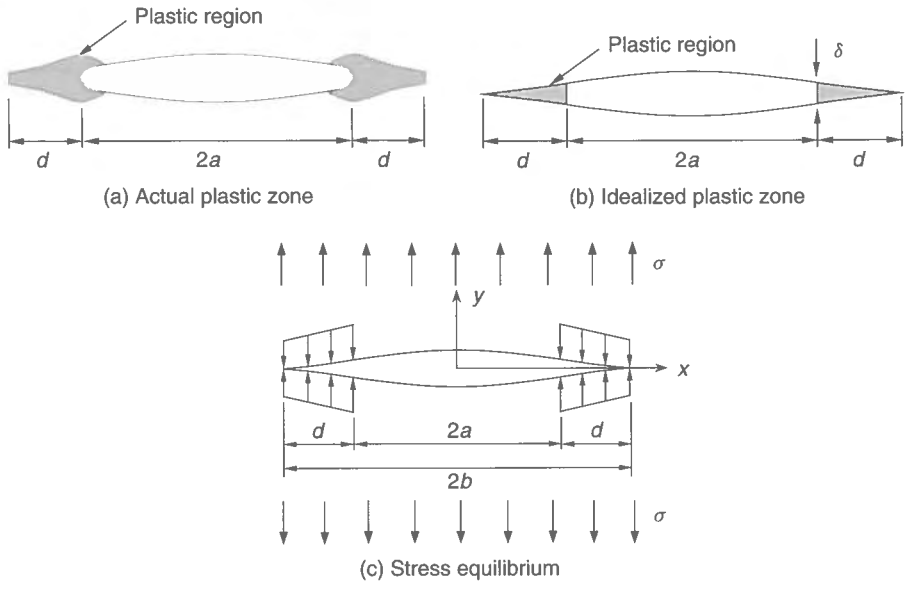

Figure 10.9 A schematic representation of the Dugdale approach (the shaded areas represent the plastic zones)

The CTOD value, δ, at $x = a$ may approximately be considered as the CTOD of the real structure, namely

$$\delta = \frac{8a\sigma_Y}{\pi E}\ln\left[\sec\left(\frac{\pi\sigma}{2\sigma_Y}\right)\right] \tag{10.16c}$$

When $\sigma \ll \sigma_Y$, i.e., representing small-scale yielding, Equation (10.16c) may be simplified to

$$\delta = \frac{\pi\sigma^2 a}{E\sigma_Y} = \frac{G_I}{\sigma_Y} = \frac{K_I^2}{E\sigma_Y} = \frac{J}{\sigma_Y} \tag{10.16d}$$

where G is as defined in Equation (10.2a) and J is the J-integral value as defined in Section 10.4.2.

When the FEM is applied for EPFM analysis to obtain the CTOD for a structure, the COD value at the crack tip is often approximately taken as the extrapolated value as shown in Figure 10.10 (Machida 1984).

The CTOD Design Curve

The CTOD concept is now increasingly applied to fracture control of structural steels. It is also used as a quality control measure in the offshore industry. In applying the CTOD concept, it is considered that ductile fracture under limited amounts of crack tip plasticity takes place if the CTOD, δ, reaches the critical COD value, δ_C. The critical value involved may be determined as a function of material properties, plate thickness, crack type and so on by established test procedures. But consistent application of the procedure to a real structure necessitates EPFM analysis to model crack tip behavior, for which special purpose finite elements may be used. Because of this consideration, the CTOD has been of greater attraction as a quality control aid; the larger the CTOD for a material, the higher its toughness, so to speak. Necessarily CTOD values for some applications in this regard have been recommended based on successful past experience.

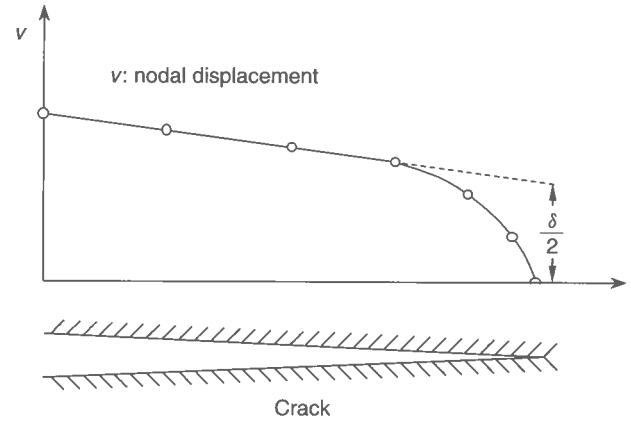

Figure 10.10 Extrapolation of the COD value at the crack tip in finite element analysis

The non-dimensionalized critical CTOD value, Φ, is normally defined by

$$\Phi = \frac{\delta_C}{2\pi\varepsilon_Y a} \tag{10.17}$$

where δ_C = critical CTOD value, ε_Y = elastic yield strain, a = half crack length.

To facilitate the applicability of the CTOD to real steel structural design, Burdekin & Dawes (1971) and Dawes (1974) proposed the semi-empirical expression of the normalized critical CTOD value as a function of the failure strain, ε_f, as follows:

$$\Phi = \begin{cases} (\varepsilon_f/\varepsilon_Y)^2 & \text{for } \varepsilon_f/\varepsilon_Y \le 0.5 \\ (\varepsilon_f/\varepsilon_Y) - 0.25 & \text{for } \varepsilon_f/\varepsilon_Y > 0.5 \end{cases} \tag{10.18}$$

While Equation (10.18) is primarily based on correlation test data for steel plates loaded in tension, it is generally called the CTOD design curve, and was in fact fitted to the data so as to obtain 'lower bound' or pessimistic predictions of fracture behavior. Figure 10.11 plots Equation (10.18). In the CTOD design curve approach, a relevant point associated with the applied strain and crack size in a structure along with the critical CTOD value for the material can be plotted in the figure. If the point lies above the design curve, it is considered that the structure is safe and otherwise the fracture is supposed to occur.

To apply the CTOD design curve approach to a complex structure, the British Standards document (BS 1980) suggests that the CTOD measure be based on the maximum total strain in the structural cross-section, ε_{max}, which is estimated by

$$\varepsilon_{max} = \frac{1}{E}[K_t(S_m + S_b) + S_s] \tag{10.19}$$

where K_t = elastic stress concentration factor, S_m = primary membrane stress, S_b = primary bending stress, S_s = secondary stress including thermal or residual stresses, E = Young's modulus.

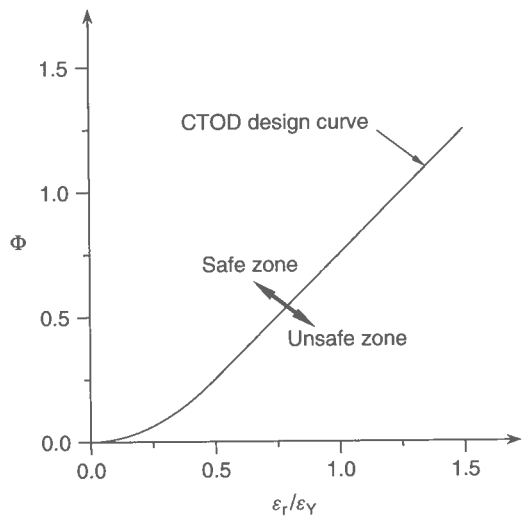

Figure 10.11 The CTOD design curve

10.4.2 Other EPFM Measures: J-integral and Crack Growth Resistance Curve

The J-Integral

The concept of the J-integral is useful to analyze ductile fracture mechanics involving small-scale plasticity at the crack tip in a somewhat rigorous way. The basic work on the J-integral was contributed from a theoretically point of view, primarily by Rice (1968), and by Hutchinson (1968). They envisaged a path-independent integral, called the J-integral, calculated along a contour around the tip of the crack, as a parameter that characterized the fracture behavior at the crack tip. The path independence of the integral followed from the principles of energy conservation, and the integral is in theory a nonlinear but elastic concept. Rice showed that the J-integral, when taken around a crack tip, was also equivalent to the change in potential energy for a virtual crack extension.

Without going into details, within the context of LEFM, the following relationship between stress intensity factor and J-integral can be shown to exist, namely

$$J = G \tag{10.20}$$

Hence, within the range of validity of LEFM, the four fracture parameters thus far introduced are all interrelated. For instance, for plane strain conditions in the 'opening' mode (i.e., Mode I), it can be shown that

$$G = J = \frac{1-\nu^2}{E}K_I^2 = \delta\sigma_Y \tag{10.21}$$

In view of Equation (10.21), which of the four basic parameters involved in LEFM is the 'most basic' is not a question of much consequence. However, it turns out that it is considerably more important that J is potentially a better parameter to use when it becomes necessary to select the basis of nonlinear fracture mechanics for elastic–plastic conditions.

In seeking a fracture criterion that could predict fracture for both small- and large-scale plasticity, Begley & Landes (1972) recognized that the J-integral provides three distinct attractive features so as to be useful for its intended purpose. These were: (1) for linear elastic behavior it is identical to G; (2) for elastic–plastic behavior it characterizes the crack tip region and, hence, would be expected to be equally valid under nonlinear conditions; and (3) it can be evaluated experimentally in a convenient manner. The third of these follows from the path-independent property of the J-integral and its energy release rate interpretation.

The successful application of the J-integral to a case involving crack tip plasticity depends on two factors: (1) the ability to calculate the integral for a specific crack situation in a structure, which is evident in part from its path-independent property, although a specific detailed analysis may be needed; and (2) the ability to measure the critical value of the J-integral using appropriate testing which will involve crack tip plasticity. Regarding (2), recall that we no longer have a convenient relationship between, say, J and K, as we did in LEFM. Without going into details, the latter aspect is facilitated by the fact that J can be determined from the load versus displacement diagram for crack extension in a specific case, subject to the limitations of the deformation theory of plasticity. For a complete explanation, one may consult Broek (1986).

As an illustration, consider the calculation of the J-integral in an example case where crack tip plasticity is involved, and the needed experimental results are available for a

plate with cracks under tensile loading as shown in Figure 10.12(a). The J-integral value in the elastic–plastic case may be shown to be approximated by

$$J = G + \frac{2}{bB}\left(\int_0^u P\,\mathrm{d}u - \frac{1}{2}Pu\right) \tag{10.22}$$

where G = strain energy release rate, B = plate thickness. $\int_0^u P\,\mathrm{d}u - \frac{1}{2}Pu$ is represented by the shaded area of the force–displacement curve shown in Figure 10.12(b).

In Equation (10.22), G is normally given as a function of the K parameter. For Mode I fracture, the strain energy release rate, G_I, is given by

$$G_\mathrm{I} = \frac{\kappa + 1}{8\mu}K_\mathrm{I}^2 \tag{10.23}$$

where κ, μ are as defined in Equations (10.9).

For combined fracture modes, G is given by

$$G = \frac{\kappa + 1}{8\mu}(K_\mathrm{I}^2 + K_\mathrm{II}^2) + \frac{1}{2\mu}K_\mathrm{III}^2 = \frac{1}{E^*}(K_\mathrm{I}^2 + K_\mathrm{II}^2) + \frac{1}{2\mu}K_\mathrm{III}^2 \tag{10.24}$$

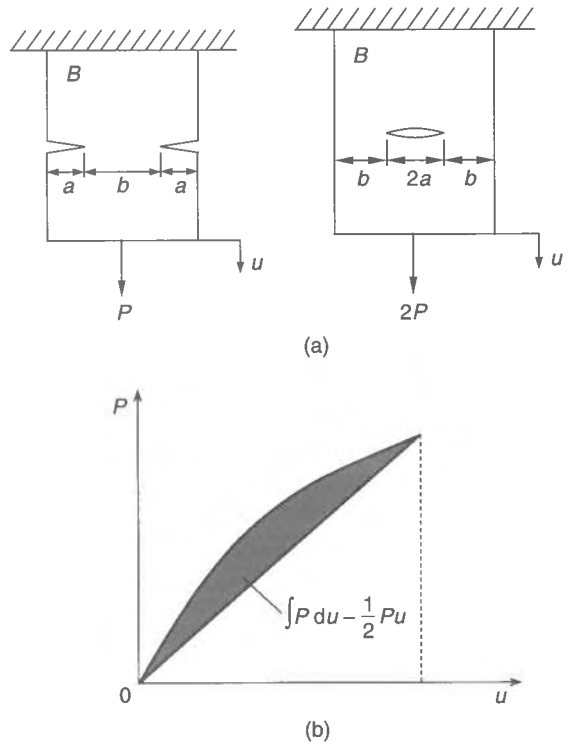

Figure 10.12 (a) Cracked plates under axial tensile loading; (b) The force–displacement curve of the plate with cracks under tensile loading

where $E^* = E/(1-\nu^2)$ for plane strain state, $E^* = E$ for plane stress state, μ is as defined in Equations (10.9).

In applying the J-integral criterion to EPFM, it is then considered that fracture takes place if the J-integral value of the structure reaches a critical J-integral value, J_C, namely

$$J \geq J_C \tag{10.25}$$

The Crack Growth Resistance Curve

The concepts described in the previous sections lead to fracture indices applicable at the tip of a crack which is not propagating. For high-toughness materials, however, the structure may not reach the ULS immediately after the fracture criteria noted in the previous sections are satisfied. This is to imply that even after initial crack extension, there can be further substantial stable crack growth until the ULS is reached by unstable crack propagation. This might be true even under plane strain conditions at the crack tip. The concept of the crack growth resistance, termed R (resistance), associated with the potential energy which is required for crack extension is then useful to assess the characteristics of stable crack growth and predict the circumstances of failure. The curve representing the variation of R as a function of incremental crack extension is called the crack growth resistance curve (or R curve).

The use of the J-integral as the crack driving force parameter in a resistance curve approach was broached soon after the establishment of the J-integral as an elastic–plastic fracture parameter by Begley & Landes (1972), but it was the subsequent work of Paris and his co-workers (Paris *et al.* 1979) that led to the acceptance of this concept. In essence, the crack growth resistance curve concept was simply reformulated as $J_R = J_R(\Delta a)$, where Δa denotes the extent of stable crack growth. Fracture instability then occurs when $\mathrm{d}J/\mathrm{d}a$ exceeds $\mathrm{d}J_R/\mathrm{d}a$. Paris *et al.* formalized this concept by defining the parameters

$$T \equiv \frac{E}{\sigma_0^2}\frac{\mathrm{d}J}{\mathrm{d}a} \tag{10.26a}$$

$$T_R \equiv \frac{E}{\sigma_0^2}\frac{\mathrm{d}J_R}{\mathrm{d}a} \tag{10.26b}$$

where σ_0 = flow stress of the material. The dimensionless parameter, T, is known as the tearing modulus, with its critical value $T_R = T_R(\Delta a)$ taken to be a property of the material.

The Paris *et al.* concept is illustrated in Figure 10.13 where Figure 10.13(a) shows a typical J–resistance curve. It is important to recognize that all such relations have a finite range of applicability. The limit is denoted by the value $(\Delta a)_\mathrm{lim}$, which can be estimated from the ω parameter introduced in the work of Hutchinson & Paris (1979). This is defined by

$$\omega = \frac{b}{J}\frac{\mathrm{d}J}{\mathrm{d}a} \tag{10.27}$$

where b denotes the smallest relevant dimension from the crack tip to the boundary of the cracked component. The work of Hutchinson & Paris shows that $\omega \gg 1$ for the theory to be valid, whereupon there will be some value of $(\Delta a)_\mathrm{lim}$ that designates the largest

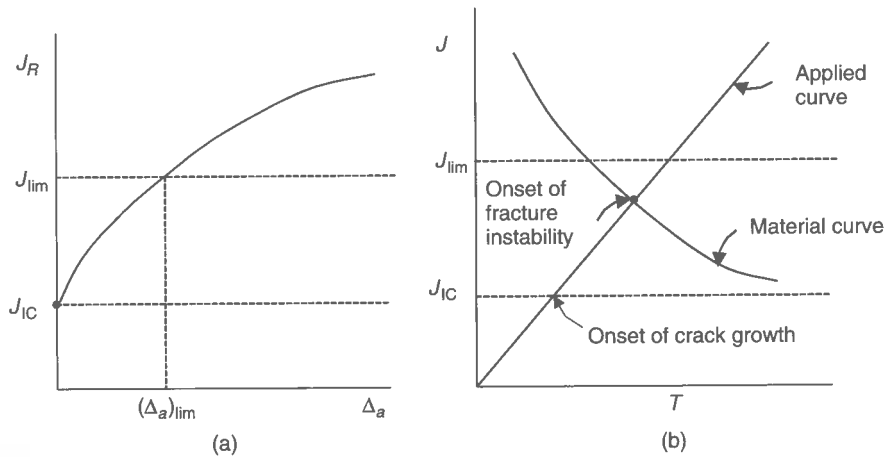

Figure 10.13 A schematic representation of the tearing modulus prediction of fracture instability

amount of crack growth (and J-integral value) for which the theory is valid. Assuming that the fracture instability point would occur before $(\Delta a)_{lim}$ is reached, its determination can be readily found via the $J-T$ diagram shown as Figure 10.13(b). Clearly, to use this approach, one needs the J–resistance curve (and some means for accurately determining its slope) together with estimates of J and T for the crack/structure/load conditions of interest.

The J-resistance curve will be unique only for limited amounts of stable crack growth; otherwise, the curves would exhibit geometry dependence. To overcome this deficiency, the J–resistance curve that properly reflects the degree of plastic constraint at the crack tip must be used. The triaxiality that is known to determine the degree of plastic constraint varies significantly as the primary loading on the remaining ligament changes from tension to bending. Thus, for extended amounts of crack extension, at least two fracture parameters would in principle be required to characterize the intensity of the deformation as well as the triaxiality.

For more elaborate descriptions, the interested reader may refer to Machida (1984), Broek (1986) and Anderson (1995), among others.

10.5 Fatigue Crack Growth Rate and its Relationship to the Stress Intensity Factor

Distinct from the stable crack extension or growth thus far described, the rate of cyclic growth of a fatigue crack in Mode I (direct tensile opening mode) has also been correlated to the fracture mechanics parameters such as the stress intensity factor or the energy release rate. This is useful for predicting the growth of a known initial crack when subject to cyclic loading.

Figure 10.14 illustrates the schematic variation of the crack size versus time in a cyclic loading (fatigue) situation, as obtained by the integration of Equation (10.28) below. The initial crack size, a_0, is one that may be detected by non-destructive examination or close-up surveys with any certainty. The critical crack size, a_c, at failure, usually under

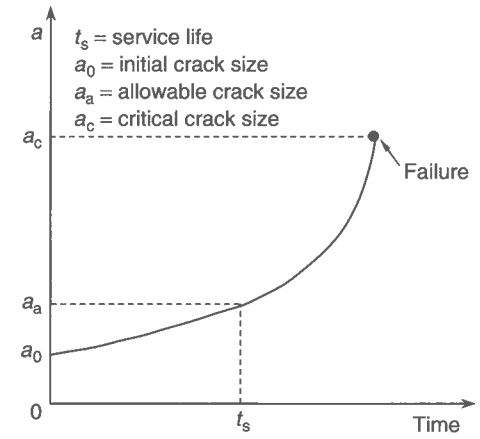

Figure 10.14 A schematic of the crack size variation versus time

the tensile maximum stress, can be computed from LEFM concepts where applicable, or estimated by other means including the need to avoid severing important structural member ligaments. The maximum 'allowable' crack size, a_a, may then be defined by dividing the critical crack size by a safety factor. In this regard, the service life of a structure can be consistently defined as the time when the crack size grows from the initial size to the maximum allowable size.

In the LEFM approach it has been recognized that the fatigue crack growth rate can be related to the cyclic elastic stress field at the tip of a long crack subjected to low to intermediate values of cyclic stress (Paris *et al.* 1961). Later, investigators found that the crack growth rate curve is not necessarily linear for all the ranges of ΔK on a log–log scale. The general crack growth rate behavior for Mode I cracks in metals is usually as shown in Figure 10.15.

The sigmoidal shape of the crack growth curve in Figure 10.15 suggests a subdivision into three regions. In region I, the crack growth rate goes asymptotically to zero as ΔK approaches a threshold value ΔK_{th}. This means that for stress intensities below ΔK_{th}, there is no crack growth, i.e., there is a fatigue limit.

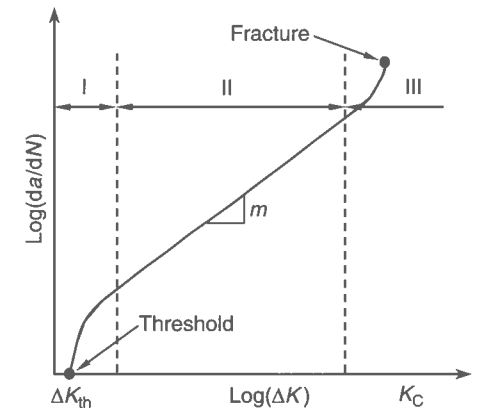

Figure 10.15 Crack growth rate curve showing the three regions

A crack growth relationship for the threshold region has been proposed by Donahue *et al.* (1972) as follows:

$$\frac{da}{dN} = C(\Delta K - \Delta K_{th})^m \tag{10.28}$$

The linear region of the log–log plot (i.e., region II) in Figure 10.15 follows a power law (Paris & Erdogan 1960) as given by

$$\frac{da}{dN} = C(\Delta K)^m \tag{10.29}$$

where da/dN represents the crack growth per cycle, ΔK is the stress intensity range at the crack tip being considered, and C and m are material constants, obtained on the basis of test data. According to Equation (10.29), the fatigue crack growth rate, da/dN, depends only on ΔK and is not sensitive to the R ratio (as defined in Equation (10.30)) in region II. Equation (10.29) is often called the Paris–Erdogan law (or the Paris law).

Region III crack growth exhibits a rapidly increasing growth rate toward 'infinity' as the crack size increases, representing either ductile tearing and/or brittle fracture. This behavior led to the relationship proposed by Forman *et al.* (1967), namely

$$\frac{da}{dN} = \frac{C(\Delta K)^m}{(1-R)K_C - \Delta K} \tag{10.30}$$

where K_C is the fracture toughness of the material and R is the K ratio defined by $R = K_{min}/K_{max}$.

Crack growth rate relations attempting to combine the behavior at high, intermediate and low ΔK values also exist. Table 10.2 contains a sample collection of these relationships.

Given an initial crack size, when the crack growth rate is known, the crack length at any instant of a structure's life can be calculated through integration if the fatigue loading history is also known. For further details, the reader is referred to Broek (1986), among others. Then, given the crack size and other related details, one can study the effect of a fatigue crack on ultimate strength as described in the following section.

Table 10.2 Crack growth relationships covering all regions.

Crack growth relation	Proposer
$\frac{da}{dN} = C\left(\frac{\Delta K - \Delta K_{th}}{K_C - K_{max}}\right)^m, \quad \Delta K_{th} = A(1-R)^\gamma, \quad 0.5 < \gamma < 1.0$	Priddle (1976), Schijve (1979)
$\frac{da}{dN} = C\left(\frac{\Delta K}{(1-R)^n}\right)^m, \quad m = 4, n = 0.5$	Walker (1970)
$\frac{da}{dN} = \frac{A}{E\sigma_Y}(\Delta K - \Delta K_{th})^2\left(1 + \frac{\Delta K}{K_{IC} - K_{max}}\right)$ $\Delta K_{th} = \left(\frac{1-R}{1+R}\right)^2 (\Delta K)_0$	McEvily & Groeger (1977)
$\frac{da}{dN} = \frac{C(1+\beta)^m(\Delta K - \Delta K_{th})^n}{K_C - (1+\beta)\Delta K}, \quad \beta = \frac{K_{max} + K_{min}}{K_{max} - K_{min}}$	Erdogan (1963)

10.6 Ultimate Strength of Cracked Structures under Monotonic Extreme Loading

10.6.1 Crack Damage Model

In this section, aspects of calculating and assessing the residual strength of steel structures under monotonic extreme loads are described particularly with regard to the effect of a fatigue crack on the ultimate strength. It is of primary interest to obtain insights into the ultimate strength behavior of ductile structures given one or more cracks, and to be able to use such knowledge within the current framework of ultimate strength calculation for a complex structural system.

To predict the ultimate strength of steel-plated structures with existing fatigue cracks, it is sometimes considered that the structures reach their ULS if any fracture criterion described in the previous sections is satisfied.

In contrast to the above noted methods, if one presupposes a very ductile material, one may postulate a simpler and intuitive model to predict the ultimate strength of structures. For instance, for a center- or edge-cracked plate under controlled displacement conditions and constructed of ductile material one may predict the ultimate strength on the basis of the reduced cross-sectional area, taking into account the loss of load-carrying material due to the crack damage. In this case, the ultimate strength of a steel-plated structural component with existing cracks and under monotonic extreme loading may be approximately obtained by

$$\sigma_u = \frac{A_c}{A_0}\sigma_{uo} \tag{10.31}$$

where σ_u, σ_{uo} = ultimate strengths of cracked or original (uncracked) structure, A_c, A_0 = cross-sectional areas of cracked or original (uncracked) structural component.

A crack in a panel under axial compressive loading may close, and buckling may then occur. It is also possible that some lateral deflection may take place, because of either initial deformations or additional local out-of-plane loading. After buckling, lateral deformation is a near certainty. In cases with lateral deformation, the crack can affect (reduce) the panel collapse strength as out-of-plane deformation increases. It may therefore be pessimistically assumed that the effect of the cracking damage on the panel ultimate compressive strength is similar to that on the panel ultimate tensile strength, pending further study.

10.6.2 Ultimate Strength of Plates with Existing Crack

As a typical example, Figure 10.16 shows a steel plate component with existing crack damage and subject to monotonic axial tensile loads. Using the simplified model noted in Equation (10.31), the ultimate strength of a cracked plate can then be predicted as follows:

$$\sigma_u = \frac{b - c_p}{b}\sigma_{uo} \tag{10.32}$$

where σ_{uo} = ultimate strength of the uncracked plate.

The applicability of Equation (10.32) may be verified by comparison to experiments on steel plates with an existing crack. In the structural testing related to residual strength, a small hole is mechanically made first either at the center or edge of the plate, and axial fatigue loading is then applied in the plane of the plate until a desired size of crack

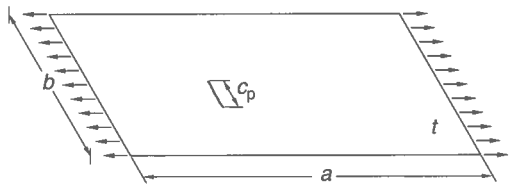

Figure 10.16 A schematic of a simply supported steel plate with existing crack

is achieved. The aim of this process is to embody the fatigue crack-like damage in the plate. Finally, increasing controlled displacements corresponding to different levels of monotonic uniaxial tensile loads are applied and are progressively increased in a quasi-static condition until the cracked plate is split into two pieces, as shown in Figure 10.17. It will be appreciated that, because of the thin plates and quasi-static loading rates involved, the overall test plate behavior in these room temperature tests carried out under controlled displacement conditions essentially remains ductile.

Figure 10.18 shows the variation of the ultimate tensile strength of steel plates as a function of the crack length as obtained by the experiments and by the simplified model noted above, i.e., reducing the cross-sectional area to account for the crack damage. It is evident that the simplified model provides adequate results at some pessimistic side. However, as is evident from Figure 10.18, there is an apparent tendency for the experimental data points to lie above the simplified model prediction, the degree of deviation seeming to increase with plate thickness. This perhaps is a manifestation of tearing and/or strain hardening.

In some of the above tests, carried out under monotonically increasing tensile loads, the size/location of the artificial cracks and also the plate thickness were varied. Some additional insights so obtained are as follows:

(1) As the crack length increases, the ultimate tensile strength and the elongation to failure decrease significantly. This is due to the fact that the cross-sectional area is reduced by the crack and also the initial crack grows as the tensile load increases, i.e., a certain amount of tearing occurs.
(2) As the plate thickness increases, the elongation slightly increases. While more data may be necessary to generalize results for thin plates to relatively thicker plates, the

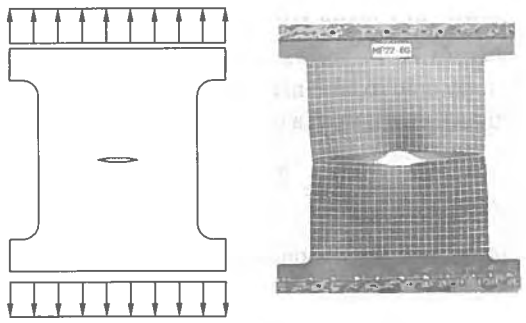

Figure 10.17 A typical pattern of the crack extension immediately before the plate is split into two pieces

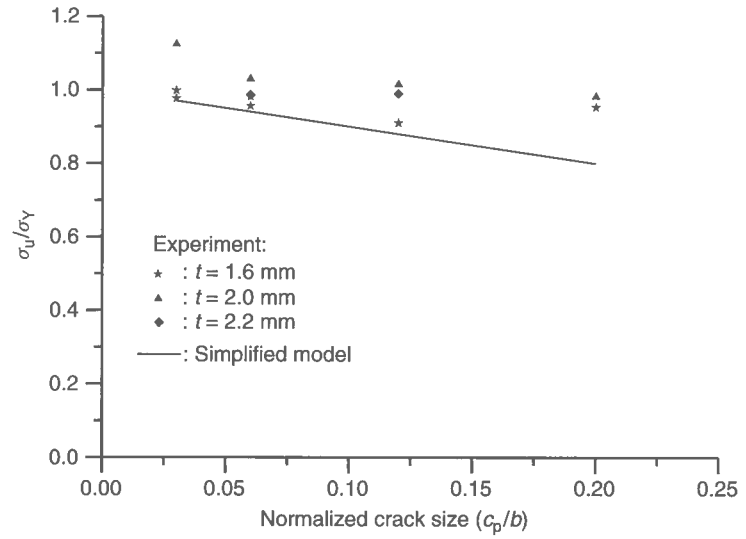

Figure 10.18 Variation of the ultimate tensile strength as a function of the crack length, as obtained by experiment and by the simplified model, σ_Y being the measured yield stress

effect of plate thickness on strength is approximately supposed to be proportional to thickness.
(3) The effect of the crack location on the ultimate tensile strength of the overall test plates is not significant under the controlled displacement conditions employed.

10.6.3 Ultimate Strength of Stiffened Panels with Existing Crack

Figure 10.19 shows a steel stiffened panel with existing crack damage and under monotonic axial tensile loading. While a more refined procedure for the collapse analysis of cracked stiffened panels is presented by Broek (1986), the ultimate (tensile) strength for this case can be predicted using the simplified model noted in Equation (10.31) as follows:

$$\sigma_u = \frac{(b - c_p)t\sigma_{Yp} + (h_w - c_s)t_w\sigma_{Ys}}{bt + h_w t_w} \tag{10.33}$$

where c_p = crack length for the plating, c_s = crack length for the stiffener, $\sigma_{Yp} = \sigma_Y$ = yield strength of plating, σ_{Ys} = yield strength of stiffener.

For this illustrative example, results from nonlinear finite element analyses (FEAs) using LS-DYNA3D (2001) are compared to the predictions of the simplified model. The panel dimensions are $b = 400$ mm, $a = 1600$ mm, $t = 15$ mm, $h_w = 150$ mm, $t_w = 12$ mm, and the material properties are $\sigma_{Yp} = \sigma_{Ys} = 249.7$ MPa, $E = 202.2$ GPa and $\nu = 0.3$. Two sets of the crack length are considered, namely $2c_p = 50$ mm or 150 mm at the plating (i.e., $c_p = 25$ mm or 75 mm on each side of the stiffener) and $c_s = 25$ mm or 75 mm at the stiffener.

In the present LS-DYNA3D analyses under displacement control, two types of panel material models are employed: (1) the stress–strain relationship of the panel material obtained by the tensile coupon test is used, meaning that the effects of strain hardening,

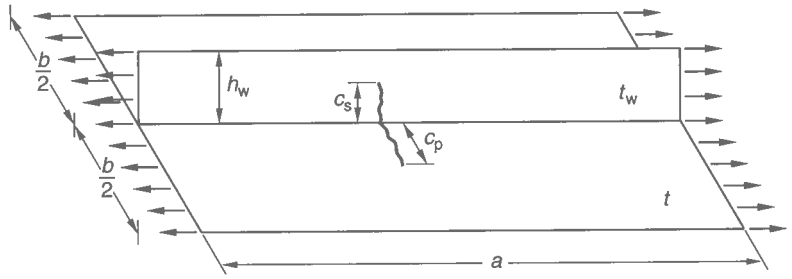

Figure 10.19 A stiffened steel panel component with existing crack

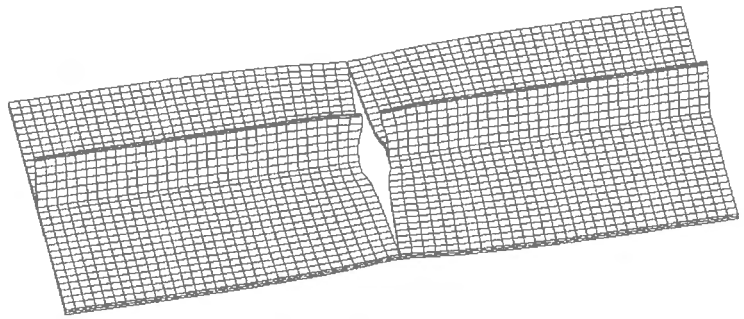

Figure 10.20 Deformed shape immediately before the entire fracture of the stiffened panel under monotonic tensile loads, as obtained by LS-DYNA3D

necking and ductile fracture are accounted for to the extent possible; and (2) the elastic–perfectly plastic material model is used by neglecting the effect of strain hardening, but taking into account ductile fracture. For all analyses, the effect of crack extension by tearing is taken into consideration as the external tensile loads monotonically increase.

Figure 10.20 shows a typical deformed shape immediately before the panel is entirely fractured. Figure 10.21 shows the LS-DYNA3D results for the average stress–strain relation for the stiffened panel under monotonically applied axial tensile loads until the panel is broken into two pieces.

Applying the simplified model indicated in Equation (10.33), the ultimate tensile strength of the stiffened panel can be predicted by $P_u = (b - 2c_p)t\sigma_{Yp} + (h_w - c_s)t_w\sigma_{Ys} = 3183.7\,\text{kN}$ or $\sigma_u = 230.7\,\text{MPa}$ for $c_p = c_s = 25\,\text{mm}$, and $P_u = 2659.3\,\text{kN}$ or $\sigma_u = 192.7\,\text{MPa}$ for $c_p = c_s = 75\,\text{mm}$. Table 10.3 compares the solutions by the simplified model to the LS-DYNA3D. While the ultimate strengths predicted by the simplified model are in the range 74–78% of the LS-DYNA3D solutions for the material model (1) noted above, they are in the range 91–94% of the LS-DYNA3D solutions for the material model (2). The pessimism of the simplified model of Equation (10.33) is partly also due to the fact that the effect of strain hardening is neglected, and perhaps partly also due to stable crack extension. It is evident that, in these illustrative cases at least, the simplified crack model can be useful for prediction of the ultimate tensile strength of the stiffened panels with existing crack damage, but on the pessimistic side.

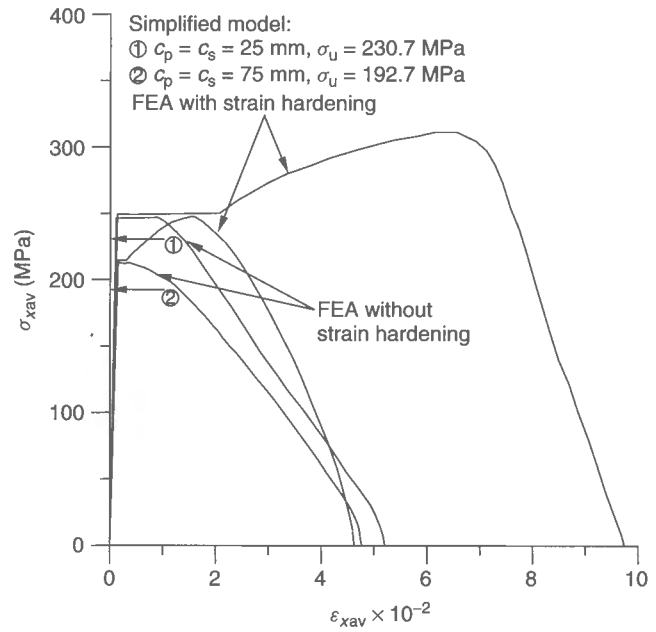

Figure 10.21 The elastic–plastic behavior of a stiffened panel with premised cracks and under monotonic tensile loads

Table 10.3 Comparison of the simplified model solutions with FEA.

c_p (mm)	c_s (mm)	σ_u (MPa) (A)	σ_u (MPa) (B)	$\frac{(A)}{(B)}$	Effect of strain hardening
25	25	230.7	311.4	0.741	Included
			246.8	0.935	Not included
75	75	192.7	247.8	0.778	Included
			212.9	0.905	Not included

Notes: (A) = simplified model, (B) = LS-DYNA3D. The simplified model does not account for the effect of strain hardening.

References

Anderson, T.L. (1995). *Fracture mechanics: fundamentals and applications*, Second Edition, CRC Press, London.

Barenblatt, G.I. (1962). The mathematical theory of equilibrium cracks in brittle fracture. *Advances in Applied Mechanics*, 7:55–129.

Barsom, J.M. (ed.) (1987). *Fracture mechanics retrospective: early classic papers (1913–1965)*. The American Society of Testing and Materials (RPS 1), Philadelphia, PA.

Begley, J.A. & Landes, J.D. (1972). *The J-integral as a fracture criterion*, ASTM STP 514. The American Society for Testing and Materials, Philadelphia, PA, 1–20.

Broek, D. (1986). *Elementary engineering fracture mechanics*. Martinus Nijhoff, Dordrecht/Boston/Lancaster.

BS (1980). *Guidance on some methods for the derivation of acceptance levels for defects in fusion welded joints*, PD 6493. British Standards Institution, London.

Burdekin, F.M. & Dawes, M.G. (1971). Practical use of linear elastic and yielding fracture mechanics with particular reference to pressure vessels. *Proceedings of the Institute of Mechanical Engineers Conference, London, May*, 28–37.
Dawes, M.G. (1974). Fracture control in high yield strength weldments. *Welding Journal*, 53: 369–380.
Donahue, R.J., Clark, H.M., Atanmo, P., Kumble, R. & McEvily, A.J. (1972). Crack opening displacement and the rate of fatigue crack growth. *International Journal of Fracture Mechanics*, 8:209–219.
Dugdale, D.S. (1960). Yielding of steel sheets containing slits. *Journal of the Mechanics and Physics of Solids*, 8:100–108.
Erdogan, F. (1963). Stress intensity factors. *Journal of Applied Mechanics*, 50:992–1002.
Forman, R.G., Kearney, V.E. & Engle, R.M. (1967). Numerical analysis of crack propagation in cyclic-loaded structures. *Journal of Basic Engineering*, 89:459–464.
Griffith, A.A. (1920). The phenomena of rupture and flow in solids. *Philosophical Transactions, Series A*, 221:163–198.
Hutchinson, J.W. (1968). Singular behavior at the end of a tensile crack in a hardening material. *Journal of the Mechanics and Physics of Solids*, 16:13–31.
Hutchinson, J.W. & Paris, P.C. (1979). *Stability analysis of J-controlled crack growth*, ASTM STP 668. The American Society for Testing and Materials, Philadelphia, PA, 37–64.
Irwin, G.R. (1948). Fracture dynamics. In *Fracturing of Metals*. The American Society for Metals, Cleveland, OH, 147–166.
Irwin, G.R. (1956). Onset of fast crack propagation in high strength steel and aluminum alloys. *Singapore Research Conference Proceedings*, 2:289–305.
Irwin, G.R. (1957). Analysis of stresses and strains near the end of a crack traversing a plate. *Journal of Applied Mechanics*, 24:361–364.
Kanninen, M.F. & Popelar, C.H. (1985). *Advanced fracture mechanics*. Oxford University Press, New York.
LS-DYNA3D (2001). *User's manual (version 960)*. Livermore Software Technology Corp., Livermore, CA.
Machida, S. (1984). *Ductile Fracture Mechanics*. Nikkan Kogyo Shimbunsha (Daily Engineering Newspaper Company), Tokyo (in Japanese).
McEvily, A.J. & Groeger, J. (1977). On the threshold for fatigue-crack growth. *The Fourth International Conference on Fracture*. University of Waterloo Press, Waterloo, Ontario, 2:1293–1298.
Mott, N.F. (1948). Fracture of metals: theoretical considerations. *Journal of Engineering*, 165: 16–18.
Murakami, Y. (ed.) (1987). *Stress intensity factors handbook*. Pergamon Press, New York.
Orowan, E. (1948). Fracture and strength of solids. *Reports on Progress in Physics*, XII:185–232.
Paris, P.C. & Erdogan, F. (1960). A critical analysis of crack propagation law. *Journal of Basic Engineering*, 85(4):528–534.
Paris, P.C., Gomez, M.P. & Anderson, W.P. (1961). A rational analytical theory of fatigue, *The Trend in Engineering*, 13:9–14.
Paris, P.C., Tada, H., Zahoor, A. & Ernst, H.A. (1979). *Instability of the tearing mode of elastic–plastic crack growth*, ASTM STP 668. The American Society for Testing and Materials, Philadelphia, PA, 5–36 and 251–265.
Priddle, E.K. (1976). High cycle fatigue crack propagation under random and constant amplitude loadings. *International Journal of Pressure Vessels and Piping*, 4:89–117.
Rice, J.R. (1968). A path independent integral and the approximate analysis of strain concentrations by notches and cracks. *Journal of Applied Mechanics*, 35:379–386.
Rice, J.R. & Rosengren, G.F. (1968). Plane strain deformation near a crack tip in a power-law hardening material. *Journal of the Mechanics and Physics of Solids*, 16:1–12.
Rooke, D.R. & Cartwright, D.J. (1976). *Compendium of stress intensity factors*. Hillington, Uxbridge.
Schijve, J. (1979). Four lectures on fatigue crack growth. *Engineering Fracture Mechanics*, 11: 167–221.
Shih, C.F. (1981). Relationship between the J-integral and the crack opening displacement for stationary and extending cracks. *Journal of the Mechanics and Physics of Solids*, 29:305–326.

Shih, C.F. & Hutchinson, J.W. (1976). Fully plastic solutions and large scale yielding estimates for plane stress crack problems. *Journal of Engineering Materials and Technology*, 98:289–295.
Shih, C.F., deLorenzi, H.G. & Andrews, W.R. (1977). Studies on crack initiation and stable crack growth. *Proceedings of the International Symposium on Elastic–plastic Fracture, The American Society for Testing and Materials, Atlanta, GA, November*, 64–120.
Sih, G.C. (1973). *Handbook of stress intensity factors*. Lehigh University, Bethlehem, PA.
Tada, H., Paris, P.C. & Irwin, G.R. (1973). *Stress analysis of cracks handbook*. Del Research Corp., Hellertown, PA.
Walker, K. (1970). *The effect of stress ratio during crack propagation and fatigue for 2024-T3 and 7075-T6 aluminum*, ASTM STP 462. The American Society for Testing and Materials, Philadelphia, PA, 1–14.
Wells, A.A. (1961). Unstable crack propagation in metals: cleavage and fast fracture. *Proceedings of the Crack Propagation Symposium, Cranfield, UK*, Paper No. 84, 210–230.
Wells, A.A. (1963). Application of fracture mechanics at and beyond general yield. British Welding Research Association, Report No. M13/63.
Westergaard, H.M. (1939). Bearing pressures and cracks. *Journal of Applied Mechanics*, 6:49–53.
Williams, M.L. (1957). On the stress distribution at the base of a stationary crack. *Journal of Applied Mechanics*, 24:109–114.

11 A Semi-analytical Method for the Elastic–Plastic Large-deflection Analysis of Plates under Combined Loading[1]

11.1 Features of the Method

This chapter presents a semi-analytical method (called the incremental Galerkin method) for analysis of the elastic–plastic large-deflection behavior of steel or aluminum plates up to their ultimate limit state (ULS). The basic idea of this particular semi-analytical method is that it is designed to accommodate the geometric nonlinearity associated with buckling by an analytical procedure, while the material nonlinearity associated with plasticity is taken account of by a numerical procedure (Paik *et al.* 2001).

A unique feature of the method presented is to analytically formulate the incremental forms of nonlinear governing differential equations for the elastic large-deflection plate theory. Upon solving these incremental governing differential equations using the Galerkin approach (Fletcher 1984), a set of linear first-order simultaneous equations for the unknowns will be obtained, which can be easily solved. This facilitates a reduction in the computational effort that would be otherwise required.

It is normally difficult to formulate the nonlinear governing differential equations representing both geometric and material nonlinearities for plates, although not impossible.

[1] Reprinted from *Thin Walled Structures*, Vol. 39, Paik, J.K., Thayamballi, A.K., Lee, S.K. & Kang, S.J. A semi-analytical method for the elastic–plastic large deflection analysis of welded steel or aluminum plating under combined in-plane and lateral pressure loads, 125–152, 2001, with permission from Elsevier Science.

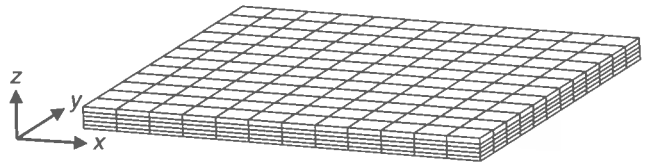

Figure 11.1 Example subdivision of plate mesh regions used for treatment of plasticity (note that geometric nonlinearity is handled analytically). Reprinted from *Thin Walled Structures*, Vol. 39, Paik, J.K., Thayamballi, A.K., Lee, S.K. & Kang, S.J. A semi-analytical method for the elastic–plastic large deflection analysis of welded steel or aluminum plating under combined in-plane and lateral pressure loads, 125–152, 2001, with permission from Elsevier Science

A major source of difficulty is that an analytical treatment of plasticity with increase in the applied loads is quite cumbersome. An easier alternative is to deal with progress of the plasticity numerically.

In the method presented in this chapter, it is assumed that a plate element bounded by support members along its four edges is composed of a number of membrane strings (or fibers) in the plate length and breadth directions. Each fiber has a number of layers in the thickness direction. The membrane stresses for each region can be analytically calculated at every step of the load increments and yielding at local regions of plating can also be checked analytically. If any local region in the fiber yields, the fiber (i.e., string) will be cut such that the related membrane action is not available further, resulting in a larger deflection.

This idea is not something new but rather classical, now facilitated because of modern computational facilities. In the following, the important basic hypotheses used for formulating the present method to compute the elastic–plastic large-deflection behavior of plates are now described:

(1) The plate is rectangular. The material of the plate is isotropic homogeneous steel or aluminum, and the boundaries of the plate are simply supported, clamped or some combination of those two. In-plane movements of a boundary are freely allowed, while keeping the boundary edges straight.
(2) The plate may be subjected to any combination of longitudinal axial compression/tension, transverse axial compression/tension, longitudinal in-plane bending, transverse in-plane bending, edge shear and lateral pressure, as shown in Figure 3.1 of Chapter 3.
(3) The fabrication-related distortions and residual stresses may be idealized as presented in Section 1.7 of Chapter 1.
(4) For the approximate evaluation of plasticity, it is assumed that the plate is composed of a number of membrane fibers in the x and y directions. Each membrane fiber is considered to have a number of layers in the z direction, as shown in Figure 11.1.

11.2 Analysis of Elastic Large-deflection Behavior

In the present method, the differential equations governing the elastic large-deflection behavior of steel plates are analytically solved. Two approaches, namely the traditional and incremental approaches, can be used for that purpose, as now described. For our purposes, the incremental approach will eventually be used.

11.2.1 The Traditional Approach

As previously noted in Equations (4.3) of Chapter 4, the elastic large-deflection behavior of steel plates with initial deflections is governed by two differential equations, one representing the equilibrium condition and the other representing the compatibility condition (Marguerre 1938). These equations are as follows (for the symbols used below, Equations (4.3) in Chapter 4 may be referred to unless otherwise specified):

$$\Phi = D\left(\frac{\partial^4 w}{\partial x^4} + 2\frac{\partial^4 w}{\partial x^2 \partial y^2} + \frac{\partial^4 w}{\partial y^4}\right) - t\left[\frac{\partial^2 F}{\partial y^2}\frac{\partial^2 (w+w_0)}{\partial x^2} + \frac{\partial^2 F}{\partial x^2}\frac{\partial^2 (w+w_0)}{\partial y^2} - 2\frac{\partial^2 F}{\partial x \partial y}\frac{\partial^2 (w+w_0)}{\partial x \partial y} + \frac{p}{t}\right] = 0 \quad (11.1a)$$

$$\frac{\partial^4 F}{\partial x^4} + 2\frac{\partial^4 F}{\partial x^2 \partial y^2} + \frac{\partial^4 F}{\partial y^4} - E\left[\left(\frac{\partial^2 w}{\partial y \partial x}\right)^2 - \frac{\partial^2 w}{\partial x^2}\frac{\partial^2 w}{\partial y^2} + 2\frac{\partial^2 w_0}{\partial x \partial y}\frac{\partial^2 w}{\partial x \partial y} - \frac{\partial^2 w_0}{\partial x^2}\frac{\partial^2 w}{\partial y^2} - \frac{\partial^2 w}{\partial x^2}\frac{\partial^2 w_0}{\partial y^2}\right] = 0 \quad (11.1b)$$

where $D = Et^3/[12(1-\nu^2)]$.

By using Airy's stress function, F, the stress components at a certain location inside the plate may be calculated as follows:

$$\sigma_x = \frac{\partial^2 F}{\partial y^2} - \frac{Ez}{1-\nu^2}\left(\frac{\partial^2 w}{\partial x^2} + \nu\frac{\partial^2 w}{\partial y^2}\right) \quad (11.2a)$$

$$\sigma_y = \frac{\partial^2 F}{\partial x^2} - \frac{Ez}{1-\nu^2}\left(\frac{\partial^2 w}{\partial y^2} + \nu\frac{\partial^2 w}{\partial x^2}\right) \quad (11.2b)$$

$$\tau = \tau_{xy} = -\frac{\partial^2 F}{\partial x \partial y} - \frac{Ez}{2(1+\nu)}\frac{\partial^2 w}{\partial x \partial y} \quad (11.2c)$$

Also, the corresponding strain components at a certain location inside the plate are given by

$$\varepsilon_x = \frac{\partial u}{\partial x} + \frac{1}{2}\left(\frac{\partial w}{\partial x}\right)^2 + \frac{\partial w}{\partial x}\frac{\partial w_0}{\partial x} - z\frac{\partial^2 w}{\partial x^2} \quad (11.2d)$$

$$\varepsilon_y = \frac{\partial v}{\partial y} + \frac{1}{2}\left(\frac{\partial w}{\partial y}\right)^2 + \frac{\partial w}{\partial y}\frac{\partial w_0}{\partial y} - z\frac{\partial^2 w}{\partial y^2} \quad (11.2e)$$

$$\gamma_{xy} = \frac{\partial u}{\partial y} + \frac{\partial v}{\partial x} + \frac{\partial w}{\partial x}\frac{\partial w}{\partial y} + \frac{\partial w_0}{\partial x}\frac{\partial w}{\partial y} + \frac{\partial w}{\partial x}\frac{\partial w_0}{\partial y} - 2z\frac{\partial^2 w}{\partial x \partial y} \quad (11.2f)$$

where u, v = axial displacements in the x and y directions.

Each strain component noted above is expressed as a function of stress components as follows:

$$\varepsilon_x = \frac{1}{E}(\sigma_x - \nu\sigma_y) \quad (11.2g)$$

$$\varepsilon_y = \frac{1}{E}(\sigma_y - \nu\sigma_x) \tag{11.2h}$$

$$\gamma_{xy} = \frac{2(1+\nu)}{E}\tau_{xy} \tag{11.2i}$$

In solving the nonlinear governing differential equations, Equations (11.1a) and (11.1b), by the Galerkin method, the added deflection, w, and initial deflection, w_0, can be assumed as follows:

$$w = \sum_{m=1}\sum_{n=1} A_{mn} f_m(x) g_n(y) \tag{11.3a}$$

$$w_0 = \sum_{m=1}\sum_{n=1} A_{0mn} f_m(x) g_n(y) \tag{11.3b}$$

where $f_m(x)$ and $g_n(y)$ are functions which satisfy the boundary conditions for the plate. A_{mn} and A_{0mn} are unknown and known deflection coefficients, respectively.

Upon substituting Equations (11.3) into Equation (11.1b), and solving for the stress function, F, the particular solution, F_P, may be expressed as follows:

$$F_P = \sum_{r=1}\sum_{s=1} K_{rs} p_r(x) q_s(y) \tag{11.4}$$

where the coefficients K_{rs} will be second-order functions with regard to the unknown deflection coefficients A_{mn}.

Including the applied loading, the complete stress function, F, may be given by

$$F = F_H + \sum_{r=1}\sum_{s=1} K_{rs} p_r(x) q_s(y) \tag{11.5}$$

where F_H is the homogeneous solution of the stress function which satisfies the applied loading condition.

To compute the unknown coefficients A_{mn}, one may use the Galerkin method for the equilibrium equation, Equation (11.1a), resulting in the following equation:

$$\iiint \Phi f_r(x) g_s(y)\, \mathrm{dVol} = 0, r = 1, 2, 3\cdots, s = 1, 2, 3\cdots \tag{11.6}$$

Substituting Equations (11.3) and (11.5) into Equation (11.6), and performing the integration over the whole volume of the plate, a set of third-order simultaneous equations with regard to the unknown coefficients, A_{mn}, will be obtained.

Solving the simultaneous equations to get the coefficients A_{mn} normally requires an iteration process. Since the solution of each coefficient should be unique, one will have to correctly select one among the three solutions obtained for each coefficient. Unfortunately, it is not always an easy task to solve a set of such third-order simultaneous equations, especially when the number of unknown coefficients, A_{mn}, becomes large.

11.2.2 The Incremental Approach

To more efficiently solve the nonlinear governing differential equations for plates subjected to the combined loads, an incremental approach is possible (Ueda *et al.* 1987). The basic idea of the method is to first formulate the incremental forms of the governing differential equations for plates. Upon analytically solving these incremental governing differential equations using the Galerkin method, a set of linear (i.e., first-order) simultaneous equations for the unknowns (which can be easily solved for) will be obtained. Such a method will normally drastically reduce the computational effort from what would otherwise be required. Another benefit of the procedure is that the solution is uniquely determined, unlike the traditional approach noted above.

In the following, the incremental forms of governing differential equations for steel plates are derived. First, it is assumed that the load is applied incrementally. At the end of the $(i-1)$th load increment step, the deflection and stress functions can be denoted by w_{i-1} and F_{i-1}, respectively. In the same manner, the deflection and stress functions at the end of the ith load increment step are denoted by w_i and F_i, respectively.

Therefore, the equilibrium equation, Equation (11.1a), and the compatibility equation, Equation (11.1b), at the end of the $(i-1)$th load increment step are written as follows:

$$\Phi_{i-1} = D\left(\frac{\partial^4 w_{i-1}}{\partial x^4} + 2\frac{\partial^4 w_{i-1}}{\partial x^2 \partial y^2} + \frac{\partial^4 w_{i-1}}{\partial y^4}\right) - t\left[\frac{\partial^2 F_{i-1}}{\partial y^2}\frac{\partial^2 (w_{i-1}+w_0)}{\partial x^2} + \frac{\partial^2 F_{i-1}}{\partial x^2}\frac{\partial^2 (w_{i-1}+w_0)}{\partial y^2} - 2\frac{\partial^2 F_{i-1}}{\partial x \partial y}\frac{\partial^2 (w_{i-1}+w_0)}{\partial x \partial y} + \frac{p_{i-1}}{t}\right] = 0 \tag{11.7a}$$

$$\frac{\partial^4 F_{i-1}}{\partial x^4} + 2\frac{\partial^4 F_{i-1}}{\partial x^2 \partial y^2} + \frac{\partial^4 F_{i-1}}{\partial y^4} - E\left[\left(\frac{\partial^2 w_{i-1}}{\partial y \partial x}\right)^2 - \frac{\partial^2 w_{i-1}}{\partial x^2}\frac{\partial^2 w_{i-1}}{\partial y^2} + 2\frac{\partial^2 w_0}{\partial x \partial y}\frac{\partial^2 w_{i-1}}{\partial x \partial y} - \frac{\partial^2 w_0}{\partial x^2}\frac{\partial^2 w_{i-1}}{\partial y^2} - \frac{\partial^2 w_{i-1}}{\partial x^2}\frac{\partial^2 w_0}{\partial y^2}\right] = 0 \tag{11.7b}$$

In the same manner, Equations (11.1a) and (11.1b) at the ith load increment step are given by

$$\Phi_i = D\left(\frac{\partial^4 w_i}{\partial x^4} + 2\frac{\partial^4 w_i}{\partial x^2 \partial y^2} + \frac{\partial^4 w_i}{\partial y^4}\right) - t\left[\frac{\partial^2 F_i}{\partial y^2}\frac{\partial^2 (w_i+w_0)}{\partial x^2} + \frac{\partial^2 F_i}{\partial x^2}\frac{\partial^2 (w_i+w_0)}{\partial y^2} - 2\frac{\partial^2 F_i}{\partial x \partial y}\frac{\partial^2 (w_i+w_0)}{\partial x \partial y} + \frac{p_i}{t}\right] = 0 \tag{11.8a}$$

$$\frac{\partial^4 F_i}{\partial x^4} + 2\frac{\partial^4 F_i}{\partial x^2 \partial y^2} + \frac{\partial^4 F_i}{\partial y^4} - E\left[\left(\frac{\partial^2 w_i}{\partial y \partial x}\right)^2 - \frac{\partial^2 w_i}{\partial x^2}\frac{\partial^2 w_i}{\partial y^2} + 2\frac{\partial^2 w_0}{\partial x \partial y}\frac{\partial^2 w_i}{\partial x \partial y} - \frac{\partial^2 w_0}{\partial x^2}\frac{\partial^2 w_i}{\partial y^2} - \frac{\partial^2 w_i}{\partial x^2}\frac{\partial^2 w_0}{\partial y^2}\right] = 0 \tag{11.8b}$$

It is assumed that the added deflection, w_i, and stress function, F_i, at the end of the ith load increment step are calculated by

$$w_i = w_{i-1} + \Delta w \tag{11.9a}$$

$$F_i = F_{i-1} + \Delta F \tag{11.9b}$$

where Δw and ΔF are the increments of the deflection and stress functions, respectively, where the prefix Δ indicates the increment for the variable.

Substituting Equations (11.9) into Equations (11.8), and subtracting Equation (11.7a) from Equation (11.8a) or Equation (11.7b) from Equation (11.8b), respectively, the necessary incremental forms of governing differential equations emerge as follows:

$$\Delta\Phi = D\left(\frac{\partial^4 \Delta w}{\partial x^4} + 2\frac{\partial^4 \Delta w}{\partial x^2 \partial y^2} + \frac{\partial^4 \Delta w}{\partial y^4}\right) - t\left[\frac{\partial^2 F_{i-1}}{\partial y^2}\frac{\partial^2 \Delta w}{\partial x^2} + \frac{\partial^2 \Delta F}{\partial y^2}\frac{\partial^2 (w_{i-1} + w_0)}{\partial x^2}\right.$$
$$+ \frac{\partial^2 F_{i-1}}{\partial x^2}\frac{\partial^2 \Delta w}{\partial y^2} + \frac{\partial^2 \Delta F}{\partial x^2}\frac{\partial^2 (w_{i-1} + w_0)}{\partial y^2} - 2\frac{\partial^2 F_{i-1}}{\partial x \partial y}\frac{\partial^2 \Delta w}{\partial x \partial y}$$
$$\left. - 2\frac{\partial^2 \Delta F}{\partial x \partial y}\frac{\partial^2 (w_{i-1} + w_0)}{\partial x \partial y} + \frac{\Delta p}{t}\right] = 0 \tag{11.10a}$$

$$\frac{\partial^4 \Delta F}{\partial x^4} + 2\frac{\partial^4 \Delta F}{\partial x^2 \partial y^2} + \frac{\partial^4 \Delta F}{\partial y^4} - E\left[2\frac{\partial^2 (w_{i-1} + w_0)}{\partial x \partial y}\frac{\partial^2 \Delta w}{\partial x \partial y}\right.$$
$$\left. - \frac{\partial^2 (w_{i-1} + w_0)}{\partial x^2}\frac{\partial^2 \Delta w}{\partial y^2} - \frac{\partial^2 \Delta w}{\partial x^2}\frac{\partial^2 (w_{i-1} + w_0)}{\partial y^2}\right] = 0 \tag{11.10b}$$

where the terms of very small quantities with order higher than second order of the increments Δw and ΔF have been neglected.

At the end of the $(i-1)$th load increment step, the deflection, w_{i-1}, and the stress function, F_{i-1}, will have been obtained as follows:

$$w_{i-1} = \sum_{m=1}\sum_{n=1} A_{mn}^{i-1} f_m(x) g_n(y) \tag{11.11a}$$

$$F_{i-1} = F_H^{i-1} + \sum_{i=1}\sum_{j=1} K_{ij}^{i-1} p_i(x) q_j(y) \tag{11.11b}$$

where A_{mn}^{i-1} and K_{ij}^{i-1} are the known coefficients, and F_{H}^{i-1} is a homogeneous solution for the stress function satisfying the applied loading condition. The welding-induced residual stresses can be included in the stress function, F_{H}^{i-1}, as initial stress terms.

The deflection increment, Δw, associated with the load increment at the ith step can be assumed to be as follows:

$$\Delta w = \sum_{k=1}\sum_{l=1} \Delta A_{kl} f_k(x) g_l(y) \tag{11.12}$$

where ΔA_{kl} is the unknown added deflection increment.

Substituting Equations (11.3b), (11.9a) and (11.12) into Equation (11.10b), the stress function increment, ΔF, can be obtained by

$$\Delta F = \Delta F_{\mathrm{H}} + \sum_{i=1}\sum_{j=1} \Delta K_{ij} p_i(x) q_j(y) \tag{11.13}$$

where ΔK_{ij} are linear (i.e., first-order) functions in the unknown coefficients, ΔA_{kl}.ΔF_{H} is a homogeneous solution for the stress function increment which satisfies the applied loading condition.

To compute the unknown coefficients, ΔA_{kl}, the Galerkin method can then be applied to Equation (11.10a), namely

$$\iiint \Delta\Phi f_r(x) g_s(y) \mathrm{dVol} = 0, r = 1, 2, 3\cdots, s = 1, 2, 3\cdots \tag{11.14}$$

Substituting Equations (11.3b), (11.11)–(11.13) into Equation (11.14), and performing the integration over the entire volume of the plate, a set of linear simultaneous equations for the unknown coefficients, ΔA_{kl}, will be obtained. Solving these linear simultaneous equations is normally easy. Having obtained ΔA_{kl}, one can then calculate Δw, i.e., from Equation (11.12), ΔF, i.e., from Equation (11.13), $w_i (= w_{i-1} + \Delta w)$, i.e., from Equation (11.9a), and $F_i (= F_{i-1} + \Delta F)$, i.e., from Equation (11.9b), at the end of the ith load increment step.

By repeating the above procedure with increase in the applied loads, the elastic large-deflection behavior of the plate can be obtained. In this process, it is evident that the load increments must be small in order to get more accurate solutions by avoiding non-equilibrating forces. Since the computational effort required for this procedure is normally small, using smaller load increments would not usually lead to any severe penalties, unlike the case of usual nonlinear numerical methods.

11.3 Application to the Elastic Large-deflection Analysis of Simply Supported Plates

The incremental Galerkin method can be applied to the nonlinear analysis of plates subject to various edge conditions, namely clamped, simply supported or some combination of them as was previously noted. In the following, the formulations of the incremental Galerkin method for simply supported plates alone are described in detail.

The simply supported edge conditions for the plate should satisfy

$$w = 0, \quad \frac{\partial^2 w}{\partial y^2} + \nu\frac{\partial^2 w}{\partial x^2} = 0 \text{ at } y = 0, b \tag{11.15a}$$

$$\frac{\partial^2 w}{\partial y^2} = 0 \text{ at } y = 0, b \tag{11.15b}$$

$$w = 0, \frac{\partial^2 w}{\partial x^2} + \nu\frac{\partial^2 w}{\partial y^2} = 0 \text{ at } x = 0, a \tag{11.15c}$$

$$\frac{\partial^2 w}{\partial x^2} = 0 \text{ at } x = 0, a \tag{11.15d}$$

The Fourier series deflection functions that need to satisfy the boundary conditions can be assumed to be as follows:

$$w_0 = \sum_{m=1}\sum_{n=1} A_{0mn} \sin\frac{m\pi x}{a} \sin\frac{n\pi y}{b} \tag{11.16a}$$

$$w_{i-1} = \sum_{m=1}\sum_{n=1} A_{mn}^{i-1} \sin\frac{m\pi x}{a} \sin\frac{n\pi y}{b} \tag{11.16b}$$

$$\Delta w = \sum_{k=1}\sum_{l=1} \Delta A_{kl} \sin\frac{k\pi x}{a} \sin\frac{l\pi y}{b} \tag{11.16c}$$

where $A_{0mn}(= A^0_{mn})$ and A^{i-1}_{mn} are the known coefficients and ΔA_{kl} are the unknown coefficients to be calculated for the external load increments.

The condition of combined load application, namely biaxial loads, biaxial in-plane bending, edge shear and lateral pressure loads, gives

$$\int_0^b \frac{\partial^2 F}{\partial y^2} t\,\mathrm{d}y = P_x \text{ at } x = 0, a \tag{11.17a}$$

$$\int_0^b \frac{\partial^2 F}{\partial y^2} t\left(y - \frac{b}{2}\right)\mathrm{d}y = M_x \text{ at } x = 0, a \tag{11.17b}$$

$$\int_0^a \frac{\partial^2 F}{\partial x^2} t\,\mathrm{d}x = P_y \text{ at } x = 0, b \tag{11.17c}$$

$$\int_0^a \frac{\partial^2 F}{\partial x^2} t\left(x - \frac{a}{2}\right)\mathrm{d}x = M_y \text{ at } x = 0, b \tag{11.17d}$$

$$\frac{\partial^2 F}{\partial x \partial y} = -\tau \text{ at all boundaries} \tag{11.17e}$$

where P_x, P_y = axial loads in the x and y directions, M_x, M_y = in-plane bending moments in the x and y directions.

For simplicity in expressing the various functions, the following abbreviations are used from now on:

$$\mathrm{sx}(m) = \sin\frac{m\pi x}{a}, \quad \mathrm{sy}(n) = \sin\frac{n\pi y}{b}, \quad \mathrm{cx}(m) = \cos\frac{m\pi x}{a}, \quad \mathrm{cy}(n) = \cos\frac{n\pi y}{b}$$

To get the stress function increment, ΔF, substitution of Equations (11.16) into Equation (11.10b) yields

$$\frac{\partial^4 \Delta F}{\partial x^4} + 2\frac{\partial^4 \Delta F}{\partial x^2 \partial y^2} + \frac{\partial^4 \Delta F}{\partial y^4} = \frac{E\pi^4}{4a^2b^2} \sum_m \sum_n \sum_k \sum_l \Delta A_{kl} A^{i-1}_{mn}$$
$$\times [-(kn - ml)^2 \mathrm{cx}(m - \mathrm{k})\mathrm{cy}(n - l) + (kn + ml)^2 \mathrm{cx}(m - k)\mathrm{cy}(n + l)$$
$$+ (kn + ml)^2 \mathrm{cx}(m + k)\mathrm{cy}(n - l) - (kn - ml)^2 \mathrm{cx}(m + k)\mathrm{cy}(n + l)] \tag{11.18}$$

A particular solution, ΔF_{P}, for the stress function increment is then obtained as follows:

$$\Delta F_P = \sum_m \sum_n \sum_k \sum_l [B_1(m, n, k, l)\mathrm{cx}(m - k)\mathrm{cy}(n - l)$$
$$+ B_2(m, n, k, l)\mathrm{cx}(m - k)\mathrm{cy}(n + l) + B_3(m, n, k, l)\mathrm{cx}(m + k)\mathrm{cy}(n - l)$$
$$+ B_4(m, n, k, l)\mathrm{cx}(m + k)\mathrm{cy}(n + l)] \tag{11.19}$$

Substitution of Equation (11.19) into Equation (11.18) by using $\Delta F = \Delta F_{\mathrm{P}}$ yields the coefficients $B_1 - B_4$, as follows

$$B_1(m, n, k, l) = \frac{E\alpha^2\pi^4}{4} \Delta A_{kl} A^{i-1}_{mn} \frac{-(kn - ml)^2}{[(m - k)^2 + \alpha^2(n - l)^2]^2} \tag{11.20a}$$

$$B_2(m, n, k, l) = \frac{E\alpha^2\pi^4}{4} \Delta A_{kl} A^{i-1}_{mn} \frac{(kn + ml)^2}{[(m - k)^2 + \alpha^2(n + l)^2]^2} \tag{11.20b}$$

$$B_3(m, n, k, l) = \frac{E\alpha^2}{4} \Delta A_{kl} A^{i-1}_{mn} \frac{(kn - ml)^2}{(m + k)^2 + \alpha^2(n - l)^2} \tag{11.20c}$$

$$B_4(m, n, k, l) = \frac{E\alpha^2}{4} \Delta A_{kl} A^{i-1}_{mn} \frac{-(kn - ml)^2}{(m + k)^2 + \alpha^2(n + l)^2} \tag{11.20d}$$

where $\alpha = a/b$.

Substituting Equations (11.20) into Equation (11.19), ΔF_{P} can be written in a more simplified form as follows:

$$\Delta F_{\mathrm{P}} = \frac{E\alpha^2\pi^4}{4} \sum_m \sum_n \sum_k \sum_l \Delta A_{kl} A^{i-1}_{mn}$$
$$\times \sum_{r=1}^{2} \sum_{s=1}^{2} (-1)^{r+s+1} h_1[(-1)^r k, (-1)^r l]\mathrm{cx}[m + (-1)^r k][n + (-1)^s l] \tag{11.21}$$

where

$$h_1[\omega_1, \omega_2] = \frac{(-n\omega_1 + m\omega_2)^2}{[(m + \omega_1)^2 + \alpha^2(n + \omega_2)^2]^2}$$

$h_1 = 0$ if $m + \omega_1 = 0$ and $n + \omega_2 = 0$.

By considering the condition of load application, the homogeneous solution, ΔF_{H}, for the stress function increment is given by

$$\Delta F_{\mathrm{H}} = \Delta P_x \frac{y^2}{2bt} + \Delta P_y \frac{x^2}{2at} - \Delta M_x \frac{y^2(2y - 3b)}{b^3 t} - \Delta M_y \frac{x^2(2x - 3a)}{a^3 t} - \Delta\tau_{xy} xy \tag{11.22}$$

The overall stress function increment may then be expressed by the sum of the particular and homogeneous solutions as follows:

$$\Delta F = \Delta F_{\mathrm{P}} + \Delta F_{\mathrm{H}} \tag{11.23}$$

In the same manner, to get the stress function, F^{i-1}_{P}, at the end of the $(i - 1)$th load increment step, Equations (11.16) is substituted into Equation (11.10b) at the end of the $(i - 1)$th load increment step, resulting in the following equation:

$$\frac{\partial^4 F_{i-1}}{\partial x^4} + 2\frac{\partial^4 F_{i-1}}{\partial x^2 \partial y^2} + \frac{\partial^4 F_{i-1}}{\partial y^4} = \frac{E\pi^4}{4a^2b^2} \sum_m \sum_n \sum_k \sum_l (A^{i-1}_{mn} A^{i-1}_{kl} - A^0_{mn} A^0_{kl})$$
$$\times [ml(kn - ml)\mathrm{cx}(m - k)\mathrm{cy}(n - l) + ml(kn + ml)\mathrm{cx}(m - k)\mathrm{cy}(n + l)$$
$$+ ml(kn + ml)\mathrm{cx}(m + k)\mathrm{cy}(n - l) + ml(kn - ml)\mathrm{cx}(m + k)\mathrm{cy}(n + l)] \tag{11.24}$$

A particular solution, F_P^{i-1}, for the stress function, $F_{i-1}(\equiv F^{i-1})$, can then be given by

$$F_{\mathrm{P}}^{i-1} = \sum_m \sum_n \sum_k \sum_l [C_1(m,n,k,l)\mathrm{cx}(m-k)\mathrm{cy}(n-l) + C_2(m,n,k,l)\mathrm{cx}(m-k)\mathrm{cy}(n+l) + C_3(m,n,k,l)\mathrm{cx}(m+k)\mathrm{cy}(n-l) + C_4(m,n,k,l)\mathrm{cx}(m+k)\mathrm{cy}(n+l)] \tag{11.25}$$

The coefficients C_1–C_4 of Equation (11.25) can be determined by substituting Equation (11.25) into Equation (11.24) since $F_{i-1} = F_{\mathrm{P}}^{i-1}$, as follows:

$$C_1(m,n,k,l) = \frac{E\pi^4}{4\alpha^2}(A_{mn}^{i-1}A_{kl}^{i-1} - A_{mn}^0 A_{kl}^0)\frac{ml(kn-ml)}{[(m-k)^2+(n-l)^2/\alpha^2]^2} \tag{11.26a}$$

$$C_2(m,n,k,l) = \frac{E\pi^4}{4\alpha^2}(A_{mn}^{i-1}A_{kl}^{i-1} - A_{mn}^0 A_{kl}^0)\frac{ml(kn+ml)}{[(m-k)^2+(n+l)^2/\alpha^2]^2} \tag{11.26b}$$

$$C_3(m,n,k,l) = \frac{E\pi^4}{4\alpha^2}(A_{mn}^{i-1}A_{kl}^{i-1} - A_{mn}^0 A_{kl}^0)\frac{ml(kn+ml)}{[(m+k)^2+(n-l)^2/\alpha^2]^2} \tag{11.26c}$$

$$C_4(m,n,k,l) = \frac{E\pi^4}{4\alpha^2}(A_{mn}^{i-1}A_{kl}^{i-1} - A_{mn}^0 A_{kl}^0)\frac{ml(kn-ml)}{[(m+k)^2+(n+l)^2/\alpha^2]^2} \tag{11.26d}$$

By substituting Equations (11.26) into Equation (11.25), F_{P}^{i-1} can be rewritten as follows:

$$F_{\mathrm{p}}^{i-1} = \frac{E\pi^4}{4\alpha^2}\sum_m\sum_n\sum_k\sum_l(A_{mn}^{i-1}A_{kl}^{i-1} - A_{mn}^0A_{kl}^0) \times \sum_{r=1}^{2}\sum_{s=1}^{2}(-1)^{r+s}h_2[(-1)^r k,(-1)^r l]\mathrm{cx}[m+(-1)^r k]\mathrm{cy}[n+(-1)^s l] \tag{11.27}$$

where

$$h_2[\omega_1,\omega_2] = \frac{m\omega_2(n\omega_1 - m\omega_2)}{[(m+\omega_1)^2+(n+\omega_2)^2/\alpha^2]^2}$$

$h_2 = 0$ if $m+\omega_1 = 0$ and $n+\omega_2 = 0$.

The homogeneous solution, F_{H}^{i-1}, can be expressed by considering the condition of load application as follows:

$$F_{\mathrm{H}}^{i-1} = P_x^{i-1}\frac{y^2}{2bt} + \sigma_{\mathrm{rx}}\frac{y^2}{2} + P_y^{i-1} + \sigma_{\mathrm{ry}}\frac{x^2}{2} - M_x^{i-1}\frac{y^2(2y-3b)}{b^3t} - M_y^{i-1}\frac{x^2(2x-3a)}{a^3t} - \tau_{xy}^{i-1}xy \tag{11.28}$$

where σ_{rx} and σ_{ry} are the welding-induced residual stresses as indicated in Equation (1.13) of Chapter 1 which are included as initial stress terms.

Therefore, the stress function, F^{i-1}, at the end of the $(i-1)$th load increment step can be obtained by the sum of Equations (11.27) and (11.28) as follows:

$$F^{i-1} = F_{\mathrm{P}}^{i-1} + F_{\mathrm{H}}^{i-1} \tag{11.29}$$

To efficiently calculate Equation (11.14), a numerical technique can be used. With the panel subdivided (meshed) into a number of regions in the x, y and z directions, Equation (11.14) may then be expressed by

$$\sum_u\sum_v\sum_w\int_{a_u}^{a_{u+1}}\int_{b_v}^{b_{v+1}}\int_{t_w}^{t_{w+1}}\Delta\Phi(x,y,z)\mathrm{sx}(r)\mathrm{sy}(s)\,\mathrm{d}x\,\mathrm{d}y\,\mathrm{d}z = 0, \quad r = 1,2,3\ldots, s = 1,2,3\ldots \tag{11.30}$$

where $\sum_u$, $\sum_v$ and $\sum_w$ indicate the summation for mesh regions in the x, y and z directions, respectively.

Substitution of Equation (11.10a) into Equation (11.30) yields the following expression, given in detail:

$$\sum_u\sum_v\sum_w\int_{a_u}^{a_{u+1}}\int_{b_v}^{b_{v+1}}\int_{t_w}^{t_{w+1}}\left[\frac{E}{1-\nu^2}\left(\frac{\partial^4\Delta w}{\partial x^4} + 2\frac{\partial^4\Delta w}{\partial x^2\partial y^2} + \frac{\partial^4\Delta w}{\partial y^4}\right)z^2 - \left(\frac{\partial^2F_{i-1}}{\partial y^2}\frac{\partial^2\Delta w}{\partial x^2} + \frac{\partial^2\Delta F}{\partial y^2}\frac{\partial^2 w_{i-1}}{\partial x^2} - 2\frac{\partial^2F_{i-1}}{\partial x\partial y}\frac{\partial^2\Delta w}{\partial x\partial y} - 2\frac{\partial^2\Delta F}{\partial x\partial y}\frac{\partial^2 w_{i-1}}{\partial x^2} + \frac{\partial^2F_{i-1}}{\partial x^2}\frac{\partial^2\Delta w}{\partial y^2} + \frac{\partial^2\Delta F}{\partial x^2}\frac{\partial^2 w_{i-1}}{\partial y^2}\right)\right]\mathrm{sx}(r)\mathrm{sy}(s)\,\mathrm{d}x\,\mathrm{d}y\,\mathrm{d}z - \sum_u\sum_v\int_{a_u}^{a_{u+1}}\int_{b_v}^{b_{v+1}}\Delta p\,\mathrm{sx}(r)\mathrm{sy}(s)\,\mathrm{d}x\,\mathrm{d}y = 0 \tag{11.31}$$

where $D = \sum_w\int_{-t/2}^{t/2}Ez\,\mathrm{d}z/(1-\nu^2)$ and $t = \sum_w\int_{-t/2}^{t/2}\mathrm{d}z$ have been used. Also, the lateral pressure loads are considered as distributed on the surface of the plate, and the related integration is performed in the two directions in the xy plane, i.e., no integration associated with the lateral pressure loads is undertaken for the z direction.

The integration of Equation (11.31) eventually results in a set of linear (i.e., first-order) simultaneous equations for the unknown coefficients, ΔA_{kl}. The equations can be written in matrix form as follows:

$$\{\Delta P\} = ([P_{\mathrm{O}}] + [K_{\mathrm{B}}] + [K_{\mathrm{M}}])\{\Delta A\} \tag{11.32}$$

where $\{\Delta P\}$ = external load increments, $[P_{\mathrm{O}}]$ = stiffness matrix associated with initial stress (including welding-induced residual stresses), $[K_{\mathrm{B}}]$ = bending stiffness matrix, $[K_{\mathrm{M}}]$ = stiffness matrix due to membrane action, $\{\Delta A\}$ = unknown coefficients of deflection amplitudes.

11.4 Treatment of Plasticity

Thus far, the differential equations governing the elastic large-deflection behavior of plates have been formulated and are solved analytically, but the effects of plasticity have not been included. As previously noted, it is normally not straightforward to formulate governing differential equations representing both geometric and material nonlinearities simultaneously, although not impossible for plates.

A major source of difficulty is that an analytical treatment of plasticity with increase in the applied loads is very difficult. An easier alternative is to deal with the progress of the plasticity numerically.

In the present method, therefore, the progress of plasticity with increase in the applied loads is treated by a numerical approach. For this purpose, the plate is subdivided into a number of mesh regions in the three directions similar to the conventional finite element method, as depicted by Figure 11.1. The average membrane stress components for each mesh region can be calculated at every load increment step. Yielding for each mesh region is checked by using the relevant yield criteria, e.g., the Mises–Hencky yield condition, Equation (1.7c) in Chapter 1, neglecting the strain-hardening effect.

As the applied loads increase, the stiffness matrices for the plate are redefined by considering the progress of plasticity. In Equation (11.32), the stiffness matrix associated with external loads should be calculated for the whole volume of the plate regardless of the plasticity. However, the bending stiffness will be reduced by the plasticity if any mesh region yields. In the calculation (i.e., integration) of the bending stiffness matrix, therefore, the contribution to the yielded regions is removed.

It is assumed that the plate is composed of a number of membrane strings (or fibers) in the two (i.e., x, y) directions. Each fiber has a number of layers in the z direction. The end condition for each fiber would satisfy the plate edge condition as well.

In fact, due to the membrane action of the fibers, the occurrence of the additional plate deflection may to some extent be disturbed with further increase in the applied loads. However, if any local region in the fiber yields, the fiber (i.e., string) will be cut such that the membrane action is not available further.

In calculating (and integrating) the stiffness matrix due to membrane action, therefore, the entire fiber associated with yielded regions is not included. It should be noted that a mesh region inside the plate may be common to two fibers, i.e., in the x (i.e., length) and y (i.e., breadth) directions. In this case, the contribution from the two fibers (i.e., strings) should be removed in the calculation of the stiffness matrix associated with the membrane effects. The stiffness for the plate will be progressively reduced by the large deflection and local yielding. The plate can be considered to have reached the ULS when the plate stiffness eventually becomes zero (or negative).

11.5 Computer Software ALPS/SPINE

11.5.1 Outline of the Computer Software

The theory presented in this chapter is automated within the computer program ALPS/SPINE, which stands for nonlinear analysis of large plated structures/steel (or aluminum) panels using the incremental energy method. ALPS/SPINE computes the applied load–displacement behavior of steel or aluminum plates. The program automatically stops if the

ULS is reached, i.e., when the determinant of the total stiffness matrix for the whole plate reaches zero (or is negative). From Equations (11.2), strain components or axial displacements as well as stress components can also be computed at a certain location inside the plate.

In contrast to the usual nonlinear finite element analyses (FEAs), a benefit of the ALPS/SPINE method is that preparation of the input data required is quite easy. Also, it is now well recognized that the strength of welded aluminum structures is significantly affected by post-weld initial imperfections in the form of initial deflection and residual stress. The ALPS/SPINE method will be quite useful for the elastic–plastic large-deflection analysis of aluminum plates under combined in-plane and lateral pressure loading.

The ALPS/SPINE program, together with the user's manual can be downloaded from the web site given in the appendices to this book.

11.5.2 Application Examples

In this section, some application examples of the SPINE method are demonstrated and the ultimate strength characteristics of steel plates are investigated, varying plate dimensions, load application and post-weld initial imperfections. For the boundary condition, plate is assumed to be simply supported at all (four) edges in all cases. Young's modulus and Poisson's ratio are assumed as $E = 205.8\,\text{GPa}$ and $\nu = 0.3$, respectively, for all calculations. Test examples with known solutions are used in order to confirm that the present theory works reasonably well. Also, cases of interest, for which other solutions do not currently exist, are analyzed by ALPS/SPINE alone.

Longitudinal Axial Compression

Elastic–plastic large-deflection analyses for plates subject to uniaxial compression are carried out until the ultimate strength is reached, varying the plate aspect ratio. Figure 11.2 shows the mean stress versus deflection curves for a rectangular plate with $a/b = 3$ where the initial and added deflection functions of Equations (11.16) are assumed to consist of two terms, with $m = 1$ and 3, while $n = 1$, as follows:

$$w_0 = \left(A_{011}\sin\frac{\pi x}{a} + A_{031}\sin\frac{3\pi x}{a}\right)\sin\frac{\pi y}{b},\ w = \left(A_{11}\sin\frac{\pi x}{a} + A_{31}\sin\frac{3\pi x}{a}\right)\sin\frac{\pi y}{b}$$

It is seen from Figure 11.2 that at the beginning of loading, one half-wave mode is predominant, but with increases in the applied loads the plating collapses with a half-wave number of three which correctly corresponds to the buckling mode of the plate with aspect ratio $a/b = 3$.

Figure 11.3 shows the variation of the ultimate strength for the plates plotted versus the aspect ratio. A comparison of the ALPS/SPINE solutions for this case is made against an empirical formula developed by curve fitting based on the nonlinear FEA (Ohtsubo & Yoshida 1985).

Transverse Axial Compression

A long steel plate (of aspect ratio $a/b = 3$) subject to uniaxial transverse compression is considered. The initial and added deflection functions are again assumed as per the

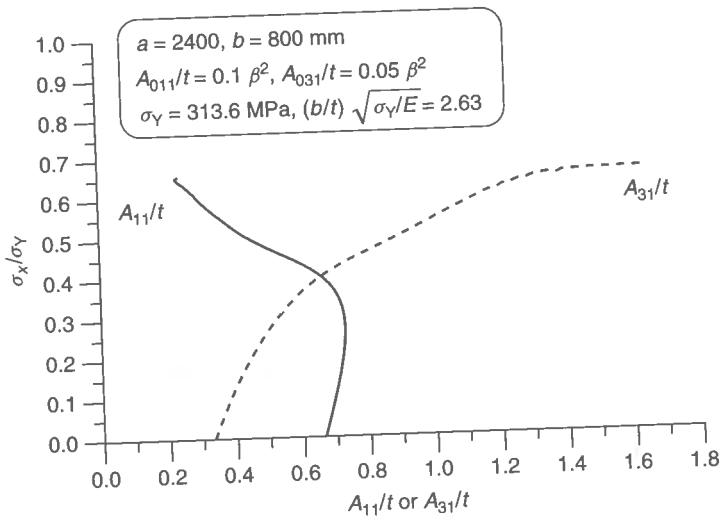

Figure 11.2 Mean stress versus deflection curves of a simply supported rectangular plate subject to longitudinal axial compression. Reprinted from *Thin Walled Structures*, Vol. 39, Paik, J.K., Thayamballi, A.K., Lee, S.K. & Kang, S.J. A semi-analytical method for the elastic–plastic large deflection analysis of welded steel or aluminum plating under combined in-plane and lateral pressure loads, 125–152, 2001, with permission from Elsevier Science

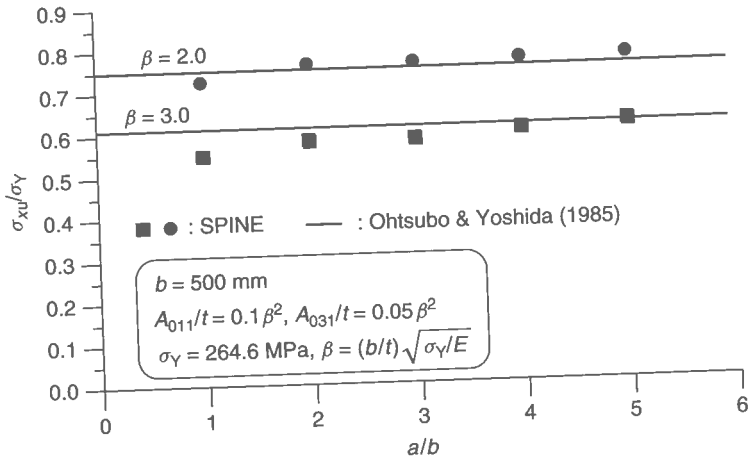

Figure 11.3 Comparison of ultimate strength results for steel plates subject to uniaxial longitudinal compression ($i = 2, 3, 4, 5$ for $a/b = 2, 3, 4, 5$, respectively). Reprinted from *Thin Walled Structures*, Vol. 39, Paik, J.K., Thayamballi, A.K., Lee, S.K. & Kang, S.J. A semi-analytical method for the elastic–plastic large deflection analysis of welded steel or aluminum plating under combined in-plane and lateral pressure loads, 125–152, 2001, with permission from Elsevier Science

first subsection in Section 11.5.2. Figure 11.4 shows the load versus deflection curves of the plate. From the beginning of the load application, the two deflection terms increase together, but it is clear that one half-wave mode is always predominant.

Figure 11.5 shows the deformed shape of the plate at the ULS. It is seen from Figure 11.5 that the plate deflection pattern is not sinusoidal but has a 'bath tub' (or bulb)

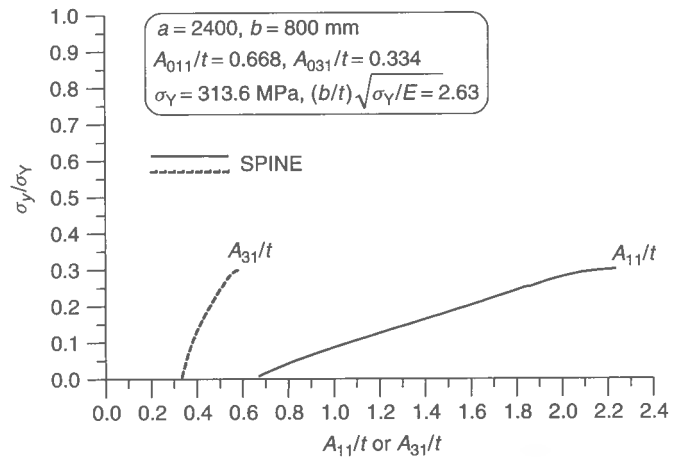

Figure 11.4 Mean stress versus deflection curves for a simply supported rectangular plate subject to transverse axial compression. Reprinted from *Thin Walled Structures*, Vol. 39, Paik, J.K., Thayamballi, A.K., Lee, S.K. & Kang, S.J. A semi-analytical method for the elastic–plastic large deflection analysis of welded steel or aluminum plating under combined in-plane and lateral pressure loads, 125–152, 2001, with permission from Elsevier Science

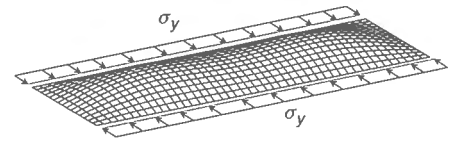

Figure 11.5 A so-called 'bath tub'-shaped deflection of the simply supported rectangular plate under transverse axial compression at the ULS, as obtained by ALPS/SPINE, $a/b = 3$. Reprinted from *Thin Walled Structures*, Vol. 39, Paik, J.K., Thayamballi, A.K., Lee, S.K. & Kang, S.J. A semi-analytical method for the elastic–plastic large deflection analysis of welded steel or aluminum plating under combined in-plane and lateral pressure loads, 125–152, 2001, with permission from Elsevier Science

shape around the edges. Figure 11.6 shows the progressive expansion of the plastic zone at the top layer of the plate. Figure 11.7 shows the variation of the ultimate transverse compressive strength for the plates plotted against the plate aspect ratio. The nonlinear FEA results by Ohtsubo & Yoshida (1985) are also compared in the figure. The figure indicates that a good agreement between the SPINE and finite element solutions is achieved.

Edge Shear

The elastic–plastic large-deflection response of a square plating under edge shear up to the ultimate strength is now analyzed using the ALPS/SPINE method. The initial and added deflection functions in this case are assumed as follows:

$$w_0 = \sum_{m=1}^{3}\sum_{n=1}^{3} A_{0mn} \sin\frac{m\pi x}{a}\sin\frac{n\pi y}{b},\ w = \sum_{m=1}^{3}\sum_{n=1}^{3} A_{mn} \sin\frac{m\pi x}{a}\sin\frac{n\pi y}{b}$$

where $A_{0mn} = 0$ is taken except for $A_{011} = 0.1\beta^2 t$ and $A_{033} = 0.05\beta^2 t$.

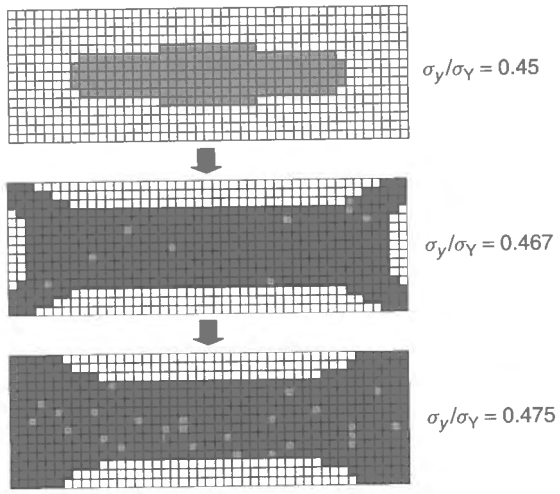

Figure 11.6 Progressive expansion of the plastic zone at the top layer of a simply supported rectangular plate ($a/b = 3$) under transverse axial compression, as obtained by ALPS/SPINE. Reprinted from *Thin Walled Structures*, Vol. 39, Paik, J.K., Thayamballi, A.K., Lee, S.K. & Kang, S.J. A semi-analytical method for the elastic–plastic large deflection analysis of welded steel or aluminum plating under combined in-plane and lateral pressure loads, 125–152, 2001, with permission from Elsevier Science

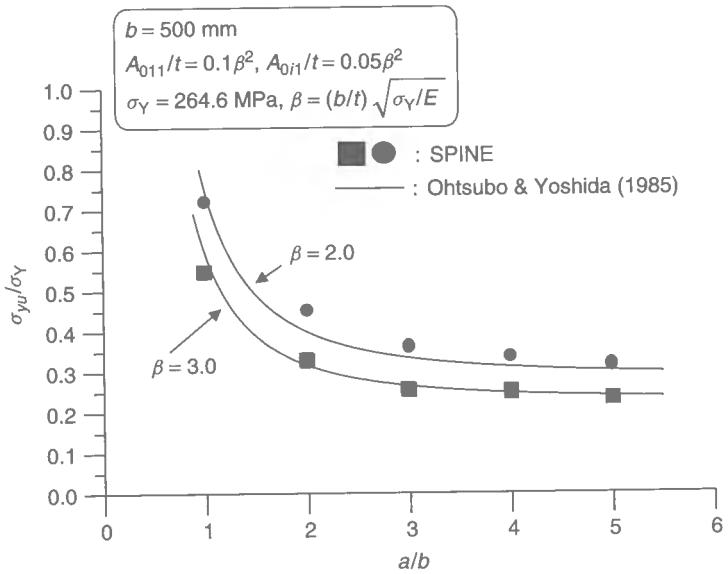

Figure 11.7 Variation of the ultimate strength of a simply supported rectangular plate subject to uniaxial transverse compression ($i = 2, 3, 4, 5$, for $a/b = 2, 3, 4, 5$). Reprinted from *Thin Walled Structures*, Vol. 39, Paik, J.K., Thayamballi, A.K., Lee, S.K. & Kang, S.J. A semi-analytical method for the elastic–plastic large deflection analysis of welded steel or aluminum plating under combined in-plane and lateral pressure loads, 125–152, 2001, with permission from Elsevier Science

Figure 11.8 shows the load versus deflection curves for a square plate subject to edge shear. Figure 11.9 shows the deformed shape of the plate under edge shear at the ULS. Figure 11.10 shows the progressive expansion of the plastic zone at the top layer of the plate under edge shear.

In-plane Bending

The elastic–plastic large-deflection response of a square plate under in-plane bending moment is now analyzed by the ALPS/SPINE method. The initial and added deflection

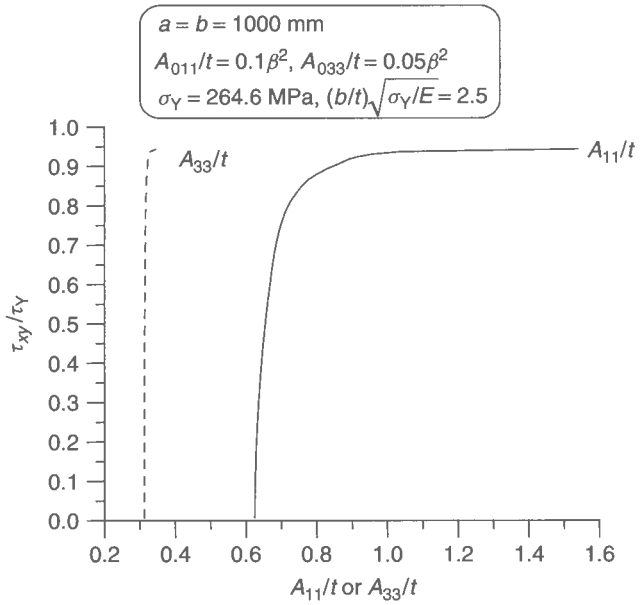

Figure 11.8 Mean stress versus deflection curves for a simply supported square plate subject to edge shear. Reprinted from *Thin Walled Structures*, Vol. 39, Paik, J.K., Thayamballi, A.K., Lee, S.K. & Kang, S.J. A semi-analytical method for the elastic–plastic large deflection analysis of welded steel or aluminum plating under combined in-plane and lateral pressure loads, 125–152, 2001, with permission from Elsevier Science

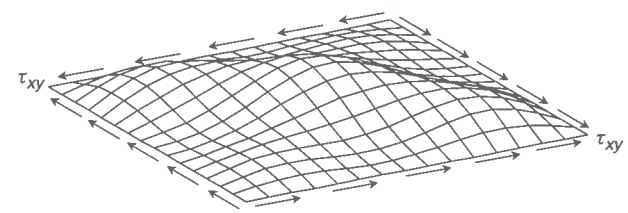

Figure 11.9 Deformed shape of a simply supported square plate under edge shear, at the ULS. Reprinted from *Thin Walled Structures*, Vol. 39, Paik, J.K., Thayamballi, A.K., Lee, S.K. & Kang, S.J. A semi-analytical method for the elastic–plastic large deflection analysis of welded steel or aluminum plating under combined in-plane and lateral pressure loads, 125–152, 2001, with permission from Elsevier Science

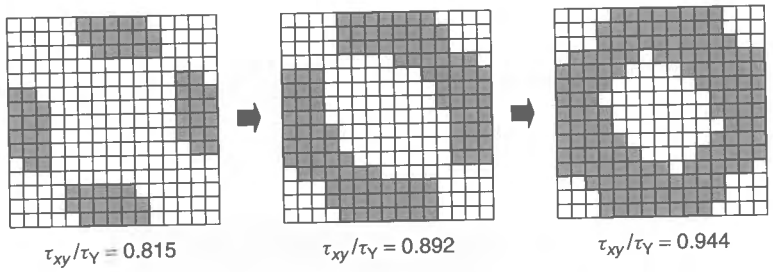

Figure 11.10 Progressive expansion of the plastic zone at the top layer of a simply supported square plate under edge shear. Reprinted from *Thin Walled Structures*, Vol. 39, Paik, J.K., Thayamballi, A.K., Lee, S.K. & Kang, S.J. A semi-analytical method for the elastic–plastic large deflection analysis of welded steel or aluminum plating under combined in-plane and lateral pressure loads, 125–152, 2001, with permission from Elsevier Science

functions for this case are assumed as follows:

$$w_0 = \sum_{m=1}^{5}\sum_{n=1}^{5} A_{0mn} \sin\frac{m\pi x}{a} \sin\frac{n\pi y}{b},\ w = \sum_{m=1}^{5}\sum_{n=1}^{5} A_{mn} \sin\frac{m\pi x}{a} \sin\frac{n\pi y}{b}$$

where $A_{0mn} = 0$ is taken except for $A_{011} = A_{055} = 0.1\beta^2 t$.

Figure 11.11 shows the load versus deflection curve for a square plate under in-plane bending in one direction.

Lateral Pressure

The elastic–plastic large-deflection response of a square plate under uniformly distributed lateral pressure loads up to the ultimate strength is now analyzed using the ALPS/SPINE

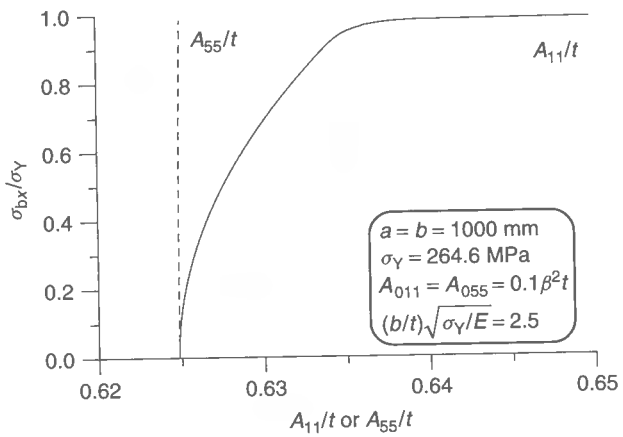

Figure 11.11 Mean stress versus deflection curve for a simply supported square plate subject to in-plane bending. Reprinted from *Thin Walled Structures*, Vol. 39, Paik, J.K., Thayamballi, A.K., Lee, S.K. & Kang, S.J. A semi-analytical method for the elastic–plastic large deflection analysis of welded steel or aluminum plating under combined in-plane and lateral pressure loads, 125–152, 2001, with permission from Elsevier Science

method. The plate deflection function is assumed with only one half wave, i.e., $m = n = 1$. Figure 11.12 shows the load versus deflection curves of a simply supported square plate under lateral pressure load. It is seen from Figure 11.12 that the plate deflection is to some extent resisted by membrane action in the beginning, but progressively increases due to plasticity. Figure 11.13 shows the progressive expansion of the plastic zone at the top layer of a square plate under lateral pressure load at the ULS.

Combined Transverse Axial Compression and Edge Shear

The elastic–plastic large-deflection response of rectangular plates (with aspect ratio $a/b = 2$) subject to combined transverse axial compression and edge shear is now analyzed, varying the slenderness ratio. The initial deflection for the plate is taken to be given by

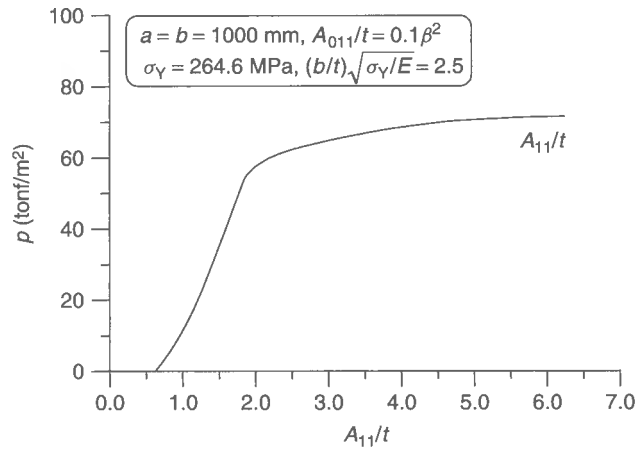

Figure 11.12 Mean stress versus deflection curve for a simply supported square plate subject to lateral pressure load. Reprinted from *Thin Walled Structures*, Vol. 39, Paik, J.K., Thayamballi, A.K., Lee, S.K. & Kang, S.J. A semi-analytical method for the elastic–plastic large deflection analysis of welded steel or aluminum plating under combined in-plane and lateral pressure loads, 125–152, 2001, with permission from Elsevier Science

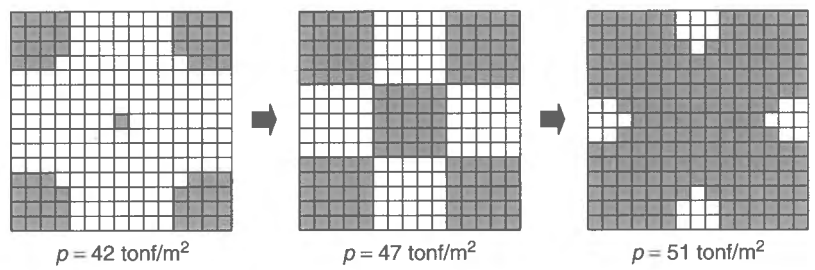

Figure 11.13 Progressive expansion of the plastic zone at the top layer of a simply supported square plate under lateral pressure load. Reprinted from *Thin Walled Structures*, Vol. 39, Paik, J.K., Thayamballi, A.K., Lee, S.K. & Kang, S.J. A semi-analytical method for the elastic–plastic large deflection analysis of welded steel or aluminum plating under combined in-plane and lateral pressure loads, 125–152, 2001, with permission from Elsevier Science

the following:

$$w_0 = A_{011} \sin\frac{\pi x}{a} \sin\frac{\pi y}{b} + A_{021} \sin\frac{2\pi x}{a} \sin\frac{\pi y}{b}$$

where $A_{011} = 0.1\beta^2 t$, $A_{021} = 0.05\beta^2 t$.

The added deflection function for this case needs some special consideration. Since the deflection pattern may possibly be complex when the edge shear is a predominant load component, more deflection terms should be used. The added deflection function for the present calculations may thus be assumed to consist of five half-wave terms in the x direction and three half-wave terms in the y direction as follows

$$w = \sum_{m=1}^{5}\sum_{n=1}^{3} A_{mn} \sin\frac{m\pi x}{a} \sin\frac{n\pi y}{b}$$

In the analysis, the loading ratio defining the proportion of axial compressive stresses to edge shear stresses is kept constant for each calculation point until the ultimate strength is reached. Figure 11.14 shows the resulting ultimate strength interaction relationships for the plates of $a/b = 2$ in the case of combined transverse compression and edge shear. In the same figure, the corresponding nonlinear FEA solutions obtained by Ohtsubo & Yoshida (1985) are compared to the present results. A good agreement is apparent.

Other Types of Combined Load Applications

The ALPS/SPINE method can be applied for steel or aluminum plates under any combination of the six load components, namely longitudinal axial compression/tension, transverse axial compression/tension, longitudinal in-plane bending, transverse in-plane bending,

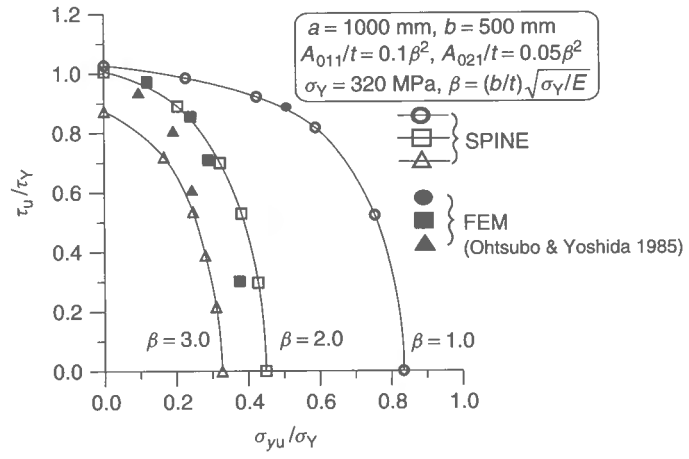

Figure 11.14 Ultimate strength interaction relationship for a simply supported rectangular plate subject to combined transverse compression and edge shear. Reprinted from *Thin Walled Structures*, Vol. 39, Paik, J.K., Thayamballi, A.K., Lee, S.K. & Kang, S.J. A semi-analytical method for the elastic–plastic large deflection analysis of welded steel or aluminum plating under combined in-plane and lateral pressure loads, 125–152, 2001, with permission from Elsevier Science

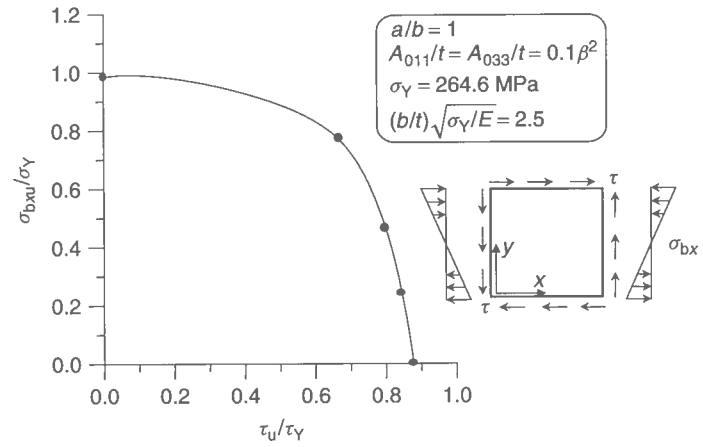

Figure 11.15 Ultimate strength interaction relationship for a simply supported square plate subject to combined in-plane longitudinal bending and edge shear. Reprinted from *Thin Walled Structures*, Vol. 39, Paik, J.K., Thayamballi, A.K., Lee, S.K. & Kang, S.J. A semi-analytical method for the elastic–plastic large deflection analysis of welded steel or aluminum plating under combined in-plane and lateral pressure loads, 125–152, 2001, with permission from Elsevier Science

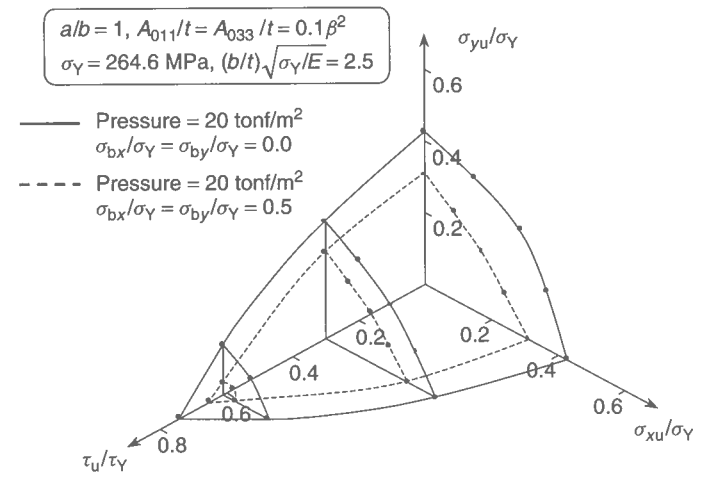

Figure 11.16 Ultimate strength interaction relationship for a simply supported square plate subject to combined biaxial compression, edge shear, biaxial in-plane bending and lateral pressure load. Reprinted from *Thin Walled Structures*, Vol. 39, Paik, J.K., Thayamballi, A.K., Lee, S.K. & Kang, S.J. A semi-analytical method for the elastic–plastic large deflection analysis of welded steel or aluminum plating under combined in-plane and lateral pressure loads, 125–152, 2001, with permission from Elsevier Science

edge shear and lateral pressure. Figures 11.15 and 11.16 show the ultimate strength interaction relationship of steel plates under combined in-plane bending and edge shear, and under all of the six load components, respectively.

While it is normally not straightforward to analyze the elastic–plastic large-deflection behavior of plates under these types of complex load combinations, the ALPS/SPINE method will be a powerful tool for that purpose.

References

Fletcher, C.A.J. (1984). *Computational Galerkin method*. Springer-Verlag, New York.
Marguerre, K. (1938). Zur Theorie der gekreummter Platte grosser Formaenderung. *Proceedings of the 5th International Congress for Applied Mechanics*, Cambridge.
Ohtsubo, H. & Yoshida, J. (1985). Ultimate strength of rectangular plates under combination of loads (Part 2): interaction of compressive and shear stresses. *Journal of the Society of Naval Architects of Japan*, 158: 368–375 (in Japanese).
Paik, J.K., Thayamballi, A.K., Lee, S.K. & Kang, S.J. (2001). A semi-analytical method for the elastic–plastic large deflection analysis of welded steel or aluminum plating under combined in-plane and lateral pressure loads. *Thin-Walled Structures*, 39: 125–152.
Ueda, Y., Rashed, S.M.H. & Paik, J.K. (1987). An incremental Galerkin method for plates and stiffened plates. *Computers & Structures*, 27(1): 147–156.

12 The Nonlinear Finite Element Method

12.1 Introduction

The finite element method is one of the most powerful approaches available to analyze the nonlinear behavior of structures. In a general case, the method requires a large amount of computational effort due mainly to the large number of unknowns to be addressed in the solution procedure and also because of the fairly complicated numerical integration procedures employed, especially for obtaining the nonlinear stiffness matrices for the finite elements as they deform.

A comprehensive discussion of nonlinear finite element analysis would require at least one complete volume, but this chapter is a start. In addition to the basics of the nonlinear solution procedure, this chapter presents a useful selected set of nonlinear finite element methods (called the plastic node method) which use special purpose elements for more efficiently analyzing the time-independent elastic–plastic large-deflection behavior of steel-plated structures for the ultimate limit state behavior. The present finite element formulations will also be employed for developments of the idealized structural unit method which will be the subject of Chapter 13 of this book.

12.2 Solution Procedures for Nonlinear Problems

In structural mechanics, a problem is linear when the stiffness matrix is determined solely by geometric and material properties of the undeformed structure, i.e., independent of the displacements. However, it is nonlinear if the stiffness matrix varies as the applied loads increase and where the load vector depends on the displacements. For finite element analysis of a time-independent problem expressed by $\{R\} = [K]\{U\}$, where $\{R\}$ = load vector, $\{U\}$ = displacement vector and $[K]$ = (secant) stiffness matrix, both $[K]$ and $\{R\}$ are regarded as independent of $\{U\}$ in linear analysis, while $[K]$ and/or $\{R\}$ are nonlinear functions of $\{U\}$ in nonlinear analysis.

Nonlinearity in structural mechanics can normally be split into two classes, namely geometric nonlinearity and material nonlinearity, both of which normally interact as the structure deforms. Geometric nonlinearity is associated with changes in geometric configuration (e.g., large deflection or buckling) and material nonlinearity is associated with

changes in material properties (e.g., plasticity). In heat transfer, nonlinearity may arise from temperature-dependent conductivity and/or radiation, where the stiffness matrix is a nonlinear function of temperature. Many useful procedures for solving the nonlinear finite element stiffness equations are presented in other textbooks (e.g., Owen & Hinton 1980, Bathe 1982, White 1985, Cook *et al.* 1989, among others).

In the following, some of the basic procedures for solving the nonlinear equations are first summarized for the convenience of the reader. As discussed above, the finite element stiffness equation for a time-independent nonlinear problem can be expressed as $\{R\} = [K]\{U\}$, where $[K]$ is a function of $\{U\}$. We are now going to compute $\{U\}$ for a given $\{R\}$. As an illustrative example, a one-dimensional problem is selected, i.e., for a nonlinear spring under load P, as shown in Figure 12.1. The secant stiffness of the nonlinear spring is denoted by k which is composed of k_0 and k_N, the former being a constant term and the latter being a function of displacements. Therefore, the nonlinear stiffness equation can in this case be given by

$$P = (k_0 + k_N)u \tag{12.1}$$

where $k_N = f(u)$.

When load P is applied, we are required to compute displacement u. However, it is evident from Equation (12.1) that it is not straightforward to determine u in terms of P. Iterative procedures described in the following are then needed to compute displacement u for a given load P.

12.2.1 The Direct Method

When $P = P_A$, we are going to determine $u = u_A$ by applying the direct method. For the first iteration, the stiffness term associated with nonlinearity is set to be zero, i.e., $k_N = 0$. Therefore, we get $u = P_A/k_0 \equiv u_1$ as the first iterative approximation. Using displacement u_1, obtained by the first iteration, the spring stiffness is approximated to $k = k_0 + f(u_1)$. In the second step of iteration, we get $u = [k_0 + (k_N)_1]^{-1} P_A \equiv u_2$, where $(k_N)_1 = f(u_1)$. By generating the sequence of such iteration steps in the process, we get displacement approximation u_{i+1} after the $(i + 1)$th step of iteration is completed, as follows:

$$u = [k_0 + (k_N)_i]^{-1} P_A \equiv u_{i+1} \tag{12.2}$$

where $(k_N)_i = f(u_i)$ and u_i is the displacement obtained as the ith iterative approximation.

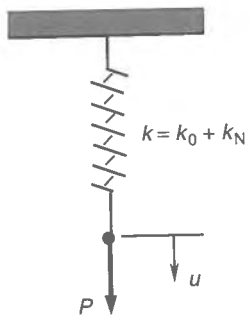

Figure 12.1 A nonlinear spring, k_0 = constant, $k_N = f(u)$

A number of iterations are normally required until convergence is attained so that $P_A/u_A \approx k_0 + k_N$ is achieved with a prescribed accuracy, and the solution of the equation may thus be approximated to $u = u_A$. To get the entire relationship between P and u, a series of points on the curve of P versus u are needed, which are obtained by applying the iterative process repeatedly. For a structure with multi-degrees of freedom, k becomes $[K] = [K_0 + K_N]$, P becomes $\{R\}$, and u becomes $\{U\}$.

12.2.2 The Incremental Method

When the load is incrementally increased, the solution procedure is called incremental rather than iterative. From Equation (12.1), the variation of loads with regard to displacements can be given by

$$\frac{dP}{du} = \frac{d}{du}(k_0 + k_N)u = k_0 + \frac{d}{du}(k_N u) \equiv k_t \tag{12.3}$$

where k_t is typically called the tangent stiffness.

For load increments ΔP, displacement increments Δu can then be approximately computed from Equation (12.3) as follows:

$$\Delta u = (k_t)^{-1} \Delta P \tag{12.4}$$

Starting from $P = 0$ at $k_t = k_0 \equiv (k_t)_0$ since $u = 0$, the displacement u_1, at the first step of load increments ΔP_1, will be $u_1 = (k_t)_0^{-1} \Delta P_1$. Using $u = u_1$ we compute the new tangent stiffness, $k_t = (k_t)_1$, and thus the displacement u_2, at the second step of load increments ΔP_2, can be determined as $u_2 = u_1 + (k_t)_1^{-1} \Delta P_2$. By generating the sequence of incremental loading steps, we get the displacement u_i at the ith step of load increments as follows:

$$u_i = u_{i-1} + (k_t)_{i-1}^{-1} \Delta P_i \tag{12.5}$$

where $(k_t)_{i-1}$ represents the tangent stiffness which is evaluated at $u = u_{i-1}$.

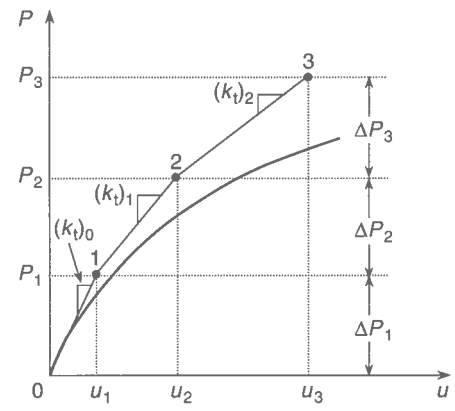

Figure 12.2 The incremental method (Cook *et al.* 1989)

In the incremental method, the approximate solution normally drifts further from the exact one as the step of load increments continues, as depicted in Figure 12.2. The drift is caused by the difference between the applied loads, $\sum \Delta P_i$, and the internal forces, $\sum (k_t)_{i-1}(u_i - u_{i-1})$. To eliminate the unbalanced forces, the Newton–Raphson method or the modified Newton–Raphson method is widely used.

12.2.3 The Newton–Raphson Method

It is considered that the displacement, u_A, has been somehow obtained for the load, P_A. In this case, the stiffness equation can be given from Equation (12.1) as follows:

$$P_A = \{k_0 + (k_N)_A\}u_A \tag{12.6}$$

where $(k_N)_A$ represents that k_N is evaluated at $u = u_A$.

After the load is increased to a value P_{n+1}, we are going to compute the corresponding displacement, u_B. A truncated Taylor series expansion of $P = f(u)$ about u_A, given by

$$f(u_A + \Delta u_1) = f(u_A) + \left(\frac{dP}{du}\right)_A \Delta u_1 \tag{12.7}$$

is used, where $(dP/du)_A \equiv k_t$ represents the tangent stiffness with k_t being evaluated from Equation (12.3) at $u = u_A$.

At the first iteration, the displacement increment, Δu_1, is computed from Equation (12.7) as follows:

$$\Delta u_1 = (k_t)_0^{-1}(P_B - P_A) \tag{12.8}$$

since $P_B = f(u_A + \Delta u_1)$ and $P_A = f(u_A) \cdot (k_t)_0$ represents that k_t is evaluated from Equation (12.3) at $u = u_A \equiv u_0$.

As the first displacement approximation, we can determine it as $u = u_A + \Delta u_1 \equiv u_1$. As indicated in Figure 12.3(a), however, there can be some unbalanced forces. For the

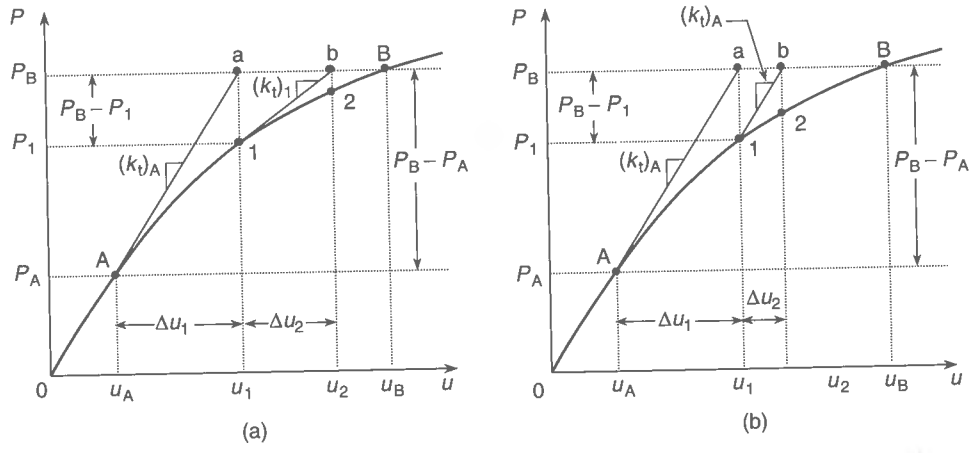

Figure 12.3 The (a) original and (b) modified Newton–Raphson methods (Cook *et al.* 1989)

next iteration, therefore, we obtain a new tangent stiffness, $(k_t)_1$, from Equation (12.3) at $u = u_1$ and the unbalanced force, $P_B - P_1$. The displacement increment, Δu_2, at the second iteration is determined from Equation (12.7) as follows:

$$\Delta u_2 = (k_t)_1^{-1}(P_B - P_1) \tag{12.9}$$

The second displacement approximation is now determined as $u = u_1 + \Delta u_2 \equiv u_2$. The iteration process is continued until the unbalanced force is fully reduced to an acceptable tolerance so that the displacement increment becomes almost zero. At the ith iteration, the displacement increment is obtained as $\Delta u_i = (k_t)_{i-1}^{-1}(P_B - P_{i-1})$ and thus the resulting displacement for load, P_B, is computed as $u = u_B = u_{i-1} + \Delta u_i$.

12.2.4 The Modified Newton–Raphson Method

A major feature of the modified Newton–Raphson method which is different from the original Newton–Raphson method is that the tangent stiffness either is not updated or is updated infrequently, while in the original Newton–Raphson method the tangent stiffness is recalculated with updated displacements after each step of iteration is completed. Figure 12.3(b) shows a schematic representation of the modified Newton–Raphson method for a one-dimensional problem.

For a nonlinear analysis with multi-degrees of freedom, the modified Newton–Raphson method can avoid the extensive repetitions of forming and updating the tangent stiffness matrix. However, more iterative cycles are normally necessary to get an acceptable accuracy in comparison to the original Newton–Raphson method.

12.2.5 The Arc Length Method

The methods noted above in Sections 12.2.1 to 12.2.4 may not be appropriate to apply if the structure displays unstable post-collapse behavior because they cannot converge to a solution in the post-collapse regime. To solve unstable post-collapse behavior, the so-called arc length method (Crisfield 1981) is typically useful.

In the arc length method, the load increment, ΔP, is no longer considered constant, but is varied during the iterative process, which may be given by

$$\Delta P = \lambda_i \times \Delta P_0 \tag{12.10}$$

where ΔP_0 = initial load increment, λ_i = load magnification factor as shown in Figure 12.4(a).

To get the coefficient λ_i at the ith iteration process, the arc length, ΔL, as shown in Figure 12.4(a), can be defined as follows:

$$\Delta L = \sqrt{\{\Delta u\}_i^T \{\Delta u\}_i} \tag{12.11}$$

where $\{\Delta u\}_i$ = incremental nodal displacement vector at the ith iteration process.

This procedure is carried our iteratively until the unbalanced force vector converges to zero within some specified tolerance limit. Figure 12.4(b) shows an application example of the arc length method to the so-called 'snap-through' problem.

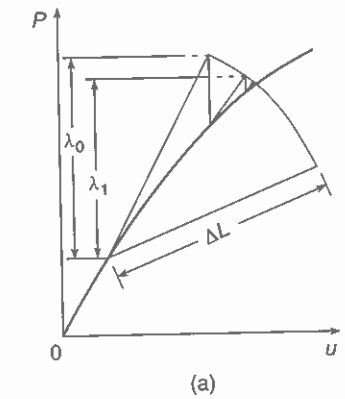

(a)

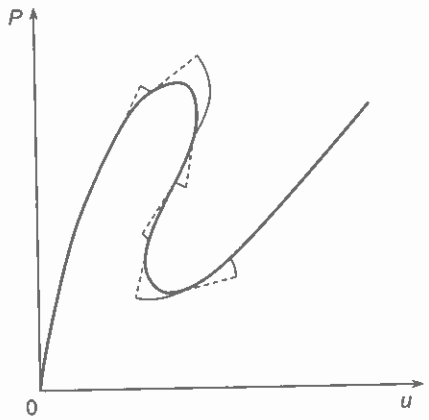

(b)

Figure 12.4 (a) The arc length method; (b) Application example of the arc length method to the so-called 'snap-through' problem

12.3 Features of the Plastic Node Method

A useful special purpose nonlinear finite element method is the so-called plastic node method. A brief history of the plastic node method is now reviewed. Matrix methods became a powerful tool for structural analysis with the rapid development of digital computers. Methods for the elastic analysis of framed structures became well established. Meanwhile, the plastic analysis of structures continued to be performed using plastic mechanisms together with the moment distribution method or the linear programming method. However, with such methods it continued to be difficult to analyze the elastic–plastic behavior of framed structures over an entire process of loading.

Hodge (1959) made an extensive study of the elastic–plastic strength of plane frames subject to bending, and demonstrated a method to analyze the frame behavior by inserting hinges at yielded sections. Ueda *et al.* (1968) developed a new plastic hinge mechanism concept based on the flow theory and established a new method for the elastic–plastic analysis of framed structures in two or three dimensions. The new plastic hinge mechanism

is characterized by continuity being maintained at the yielded section throughout the entire process of elastic–plastic behavior, with rigidity reduced automatically by plastification of the section. The structural deformation is obtained at each step of loading and the corresponding plastic collapse load is evaluated.

The original method of Ueda *et al.*, however, assumes that the loading on a structure is applied proportionally and that there is no yielded section where unloading occurs under proportional loading. In actual cases, it is important to investigate the behavior of structures under more general conditions. In 1969, Ueda *et al.* thus proposed examining unloading at yielded sections for each loading step for a framed structure. In 1979, they extended the plastic node method for the analysis of the strength of plates based on the finite element procedure (Ueda *et al.* 1979). By applying such a generalized plastic hinge method, several examples including elastic–plastic large-deflection problems were analyzed, and the effectiveness of the method was demonstrated (Ueda & Yao 1982). The theory was further developed in 1983 for the analysis of thermal elastic–plastic problems and dynamic behavior of structures (Ueda *et al.* 1983).

In the following, the nonlinear finite element method using the Ueda plastic node approach is described in detail for a rectangular plate-shell element formulated by Paik & Kim (1989). Note that a similar procedure can be applied for other types of elements such as a triangular plate-shell element. The method presented in this chapter has the following characteristics which make possible considerable savings of computational effort while still providing reasonably accurate solutions:

(1) The method uses a plate-shell element which has only corner nodal points with six degrees of freedom at each nodal point.
(2) The method includes geometric nonlinearity effects due to both in-plane and out-of-plane large deflections of the element, because for the thin plates widely used in many classes of structures, the influence of the former may not be insignificant and thus cannot always be ignored.
(3) The expanded yield zone in the plate thickness direction of the element is condensed into a plastic node inserted at the nodal point, based upon the concept of the Ueda plastic node method, so that the elastic–plastic stiffness matrix of the element can be calculated by simple matrix operations without having to perform complicated numerical integration once the elastic stiffness matrix has been established.
(4) The incremental procedure with the modified Newton–Raphson method is used for solving the nonlinear finite element stiffness equations.

12.4 Formulation of Nonlinear Rectangular Plate-Shell Element

12.4.1 Nodal Forces and Nodal Displacements

The combined in-plane and out-of-plane deformation behavior for a rectangular plate element can be expressed by the nodal force vector, $\{R\}$, and the displacement vector, $\{U\}$, with six degrees of freedom at each corner nodal point which is taken to be located in the mid-thickness of the element as shown in Figure 12.5, namely

$$\{R\} = \{R_{x1}\, R_{y1}\, R_{z1}\, M_{x1}\, M_{y1}\, M_{z1} \cdots R_{x4}\, R_{y4}\, R_{z4}\, M_{x4}\, M_{y4}\, M_{z4}\}^{\mathrm{T}} \tag{12.12a}$$

$$\{U\} = \{u_1\, v_1\, w_1\, \theta_{x1}\, \theta_{y1}\, \theta_{z1} \cdots u_4\, v_4\, w_4\, \theta_{x4}\, \theta_{y4}\, \theta_{z4}\}^{T} \tag{12.12b}$$

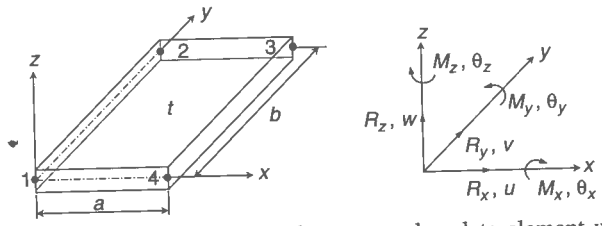

Figure 12.5 The local coordinate system for the rectangular plate element with its nodal forces and displacements

where R_x, R_y and R_z are the translational nodal forces in the x, y and z directions, respectively. M_x and M_y are the out-of-plane bending moments with regard to the x and y directions, respectively; M_z is the torsional moment with regard to the z direction. u, v and w are the translational displacements in the x, y and z directions, respectively. θ_x $(= -\partial w/\partial y)$, θ_y $(= \partial w/\partial x)$ and θ_z are the rotations with respect to the x, y and z directions, respectively. $\{\}^{\mathrm{T}}$ represents the transpose of the vector. A digit in the subscript indicates the node number of the rectangular element. For a triangular plate element, the number of nodal points will be three and similar expressions for nodal force and displacement vectors can be defined.

12.4.2 Strain–Displacement Relationship

The strain versus displacement relationship taking into account out-of-plane as well as in-plane large-deformation effects for the element is given in the Cartesian coordinate system by the following:

$$\varepsilon_x = \frac{\partial u}{\partial x} - z\frac{\partial^2 w}{\partial x^2} + \frac{1}{2}\left[\left(\frac{\partial u}{\partial x}\right)^2 + \left(\frac{\partial v}{\partial x}\right)^2\right] + \frac{1}{2}\left(\frac{\partial w}{\partial x}\right)^2 \tag{12.13a}$$

$$\varepsilon_y = \frac{\partial v}{\partial y} - z\frac{\partial^2 w}{\partial y^2} + \frac{1}{2}\left[\left(\frac{\partial u}{\partial y}\right)^2 + \left(\frac{\partial v}{\partial y}\right)^2\right] + \frac{1}{2}\left(\frac{\partial w}{\partial y}\right)^2 \tag{12.13b}$$

$$\gamma_{xy} = \left(\frac{\partial u}{\partial y} + \frac{\partial v}{\partial x}\right) - 2z\frac{\partial^2 w}{\partial x \partial y} + \left[\left(\frac{\partial u}{\partial x}\right)\left(\frac{\partial u}{\partial y}\right) + \left(\frac{\partial v}{\partial x}\right)\left(\frac{\partial v}{\partial y}\right)\right] + \left(\frac{\partial w}{\partial x}\right)\left(\frac{\partial w}{\partial y}\right) \tag{12.13c}$$

where ε_x, ε_y and γ_{xy} are the generalized strain components for a plane stress state.

The first term on the right hand side of the above equations represents the small-deformation in-plane strain. The second term denotes the small-deformation out-of-plane strain. The third and fourth terms are nonlinear strain components due to large deflections in plane and out of plane, respectively. It is evident from Equations (12.13) that the component for the rotation with respect to the z axis which is normal to the plane of the element does not affect the strains of the element.

The incremental expressions corresponding to Equations (12.13) are written as

$$\Delta\varepsilon_x = \frac{\partial \Delta u}{\partial x} - z\frac{\partial^2 \Delta w}{\partial x^2} + \left(\frac{\partial u}{\partial x}\right)\left(\frac{\partial \Delta u}{\partial x}\right) + \left(\frac{\partial v}{\partial x}\right)\left(\frac{\partial \Delta v}{\partial x}\right) + \left(\frac{\partial w}{\partial x}\right)\left(\frac{\partial \Delta w}{\partial x}\right) + \frac{1}{2}\left[\left(\frac{\partial \Delta u}{\partial x}\right)^2 + \left(\frac{\partial \Delta v}{\partial x}\right)^2\right] + \frac{1}{2}\left(\frac{\partial \Delta w}{\partial x}\right)^2 \tag{12.14a}$$

$$\Delta\varepsilon_y = \frac{\partial \Delta v}{\partial y} - z\frac{\partial^2 \Delta w}{\partial y^2} + \left(\frac{\partial u}{\partial y}\right)\left(\frac{\partial \Delta u}{\partial y}\right) + \left(\frac{\partial v}{\partial y}\right)\left(\frac{\partial \Delta v}{\partial y}\right) + \left(\frac{\partial w}{\partial y}\right)\left(\frac{\partial \Delta w}{\partial y}\right) + \frac{1}{2}\left[\left(\frac{\partial \Delta u}{\partial y}\right)^2 + \left(\frac{\partial \Delta v}{\partial y}\right)^2\right] + \frac{1}{2}\left(\frac{\partial \Delta w}{\partial y}\right)^2 \tag{12.14b}$$

$$\Delta\gamma_{xy} = \left(\frac{\partial \Delta u}{\partial y} + \frac{\partial \Delta v}{\partial x}\right) - 2z\frac{\partial^2 \Delta w}{\partial x \partial y} + \left(\frac{\partial u}{\partial x}\right)\left(\frac{\partial \Delta u}{\partial y}\right) + \left(\frac{\partial u}{\partial y}\right)\left(\frac{\partial \Delta u}{\partial x}\right) + \left(\frac{\partial v}{\partial x}\right)\left(\frac{\partial \Delta v}{\partial y}\right) + \left(\frac{\partial v}{\partial y}\right)\left(\frac{\partial \Delta v}{\partial x}\right) + \left(\frac{\partial w}{\partial x}\right)\left(\frac{\partial \Delta w}{\partial y}\right) + \left(\frac{\partial w}{\partial y}\right)\left(\frac{\partial \Delta w}{\partial x}\right) + \left(\frac{\partial \Delta u}{\partial x}\right)\left(\frac{\partial \Delta u}{\partial y}\right) + \left(\frac{\partial \Delta v}{\partial x}\right)\left(\frac{\partial \Delta v}{\partial y}\right) + \left(\frac{\partial \Delta w}{\partial x}\right)\left(\frac{\partial \Delta w}{\partial y}\right) \tag{12.14c}$$

where the prefix Δ denotes an infinitesimal increment of the variable.

For convenience in the formulations of the element, the nodal displacement vector, $\{U\}$, is split into three components, namely the in-plane component, $\{S\}$, the out-of-plane component, $\{W\}$, and the component for the rotations about the z axis. Thus Equations (12.14) can be rewritten in matrix form using the vectors $\{S\}$ and $\{W\}$, as follows:

$$\begin{aligned}\{\Delta\varepsilon\} &= [B_{\mathrm{p}}]\{\Delta S\} - z[B_{\mathrm{b}}]\{\Delta W\} + [C_{\mathrm{p}}][G_{\mathrm{p}}]\{\Delta S\} + [C_{\mathrm{b}}][G_{\mathrm{b}}]\{\Delta W\} \\ &\quad + \frac{1}{2}[\Delta C_{\mathrm{p}}][G_{\mathrm{p}}]\{\Delta S\} + \frac{1}{2}[\Delta C_{\mathrm{b}}][G_{\mathrm{b}}]\{\Delta W\} \\ &= [B]\{\Delta U\}\end{aligned} \tag{12.15}$$

where $\{\Delta\varepsilon\} = \{\Delta\varepsilon_x \Delta\varepsilon_y \Delta\gamma_{xy}\}^{\mathrm{T}}$ = increment of strain vector, $\{U\} = \{SW\}^{\mathrm{T}}$ = nodal displacement vector, $\{S\} = \{u_1 v_1 u_2 v_2 u_3 v_3 u_4 v_4\}^{\mathrm{T}}$ = in-plane displacement vector, $\{W\} = \{w_1 \theta_{x1} \theta_{y1} w_2 \theta_{x2} \theta_{y2} w_3 \theta_{x3} \theta_{y3} w_4 \theta_{x4} \theta_{y4}\}^{\mathrm{T}}$ = out-of-plane displacement vector, $[B]$ = strain versus displacement matrix, and

$$\left\{\frac{\partial u}{\partial x}\frac{\partial v}{\partial y}\frac{\partial u}{\partial y} + \frac{\partial v}{\partial x}\right\}^{\mathrm{T}} = [B_{\mathrm{p}}]\{S\}, \left\{\frac{\partial^2 w}{\partial x^2}\frac{\partial^2 w}{\partial y^2}2\frac{\partial^2 w}{\partial x \partial y}\right\}^{\mathrm{T}} = [B_{\mathrm{b}}]\{W\},$$

$$\left\{\frac{\partial u}{\partial x}\frac{\partial v}{\partial x}\frac{\partial u}{\partial y}\frac{\partial v}{\partial y}\right\}^{\mathrm{T}} = [G_{\mathrm{p}}]\{S\}, \left\{\frac{\partial w}{\partial x}\frac{\partial w}{\partial y}\right\}^{T} = [G_b]\{W\}$$

$$[C_{\mathrm{p}}] = \begin{bmatrix} \partial u/\partial x & \partial v/\partial x & 0 & 0 \\ 0 & 0 & \partial u/\partial y & \partial v/\partial y \\ \partial u/\partial y & \partial v/\partial y & \partial u/\partial x & \partial v/\partial x \end{bmatrix},$$

$$[C_{\mathrm{b}}] = \begin{bmatrix} \partial w/\partial x & 0 \\ 0 & \partial w/\partial y \\ \partial w/\partial y & \partial w/\partial x \end{bmatrix}$$

12.4.3 Stress–Strain Relationship

The membrane stress increments, $\{\Delta\sigma\}$, due to the strain increments, $\{\Delta\varepsilon\}$, can be calculated for a plane stress state as follows:

$$\{\Delta\sigma\} = [D]^{\mathrm{E}}\{\Delta\varepsilon\}^{\mathrm{E}} \tag{12.16}$$

where the superscript E represents the elastic component of the variable. $\{\Delta\sigma\} = \{\Delta\sigma_x \; \Delta\sigma_y \Delta\tau_{xy}\}^{\mathrm{T}}$ is the increment of average membrane stress components for a plane stress state, and

$$[D]^{\mathrm{E}} = \frac{E}{1-\nu^2}\begin{bmatrix} 1 & \nu & 0 \\ \nu & 1 & 0 \\ 0 & 0 & (1-\nu)/2 \end{bmatrix} \tag{12.17}$$

is the elastic stress versus strain matrix, E Young's modulus and ν Poisson's ratio.

12.4.4 Elastic Tangent Stiffness Matrix

Two approaches, namely the total Lagrangian formulation and the updated Lagrangian formulation, are widely used for calculating the nonlinear finite element stiffness matrix. The latter will be used in the present finite element method. In the following, it is convenient to deal separately with the matrix components related to the rotations with regard to the z axis which is normal to the plane of the element.

The Total Lagrangian Approach

Consider that an elastic structure under the nodal forces $\{R\}$, resulting in the internal stresses $\{\sigma\}$, is in an equilibrium condition. Assume that the structure remains in equilibrium even after the increase of the virtual displacement increments, $\delta\{\Delta U\}$, corresponding to the virtual strain increments, $\delta\{\Delta\varepsilon\}$, which will develop the nodal forces $\{\Delta R\}$ and the resultant stresses $\{\Delta\sigma\}$.

By applying the principle of virtual work, the following equation should be satisfied:

$$\delta\{\Delta U\}^{\mathrm{T}}\{R + \Delta R\} = \int_{\mathrm{V}} \delta\{\Delta\varepsilon\}^{\mathrm{T}}\{\sigma + \Delta\sigma\}\,\mathrm{dVol} \tag{12.18}$$

where the term on the left hand side represents the external work undertaken by the virtual displacement increments and that on the right hand side denotes the strain energy dissipated by the deformation during the applied loading. $\int_{\mathrm{V}} ()\,\mathrm{dVol}$ indicates integration over the entire volume of the element and δ indicates a virtual value.

The virtual value of strain components, $\delta\{\Delta\varepsilon\}$, can be obtained by the differentiation of Equation (12.15) with respect to the increment of displacements as follows:

$$\begin{aligned}\delta\{\Delta\varepsilon\} = {} & [B_{\mathrm{p}}]\delta\{\Delta S\} - z[B_{\mathrm{b}}]\delta\{\Delta W\} + [C_{\mathrm{p}} + \Delta C_{\mathrm{p}}][G_{\mathrm{p}}]\delta\{\Delta S\} \\ & + [C_{\mathrm{b}} + \Delta C_{\mathrm{b}}][G_{\mathrm{b}}]\delta\{\Delta W\}\end{aligned} \tag{12.19}$$

Substituting Equations (12.16) and (12.19) into Equation (12.18) and neglecting the infinitesimal terms having higher than second-order increments, the elastic stiffness equation for the element can be shown to be given by

$$\{L\} + \{\Delta R\} = [K]^{\mathrm{E}}\{\Delta U\} \tag{12.20}$$

where $[K]^{\mathrm{E}}$ is the elastic tangent stiffness matrix for the element, $\{L\} = \{R\} - \{r\}$ is the unbalanced forces caused by the differences between the total external forces, $\{R\}$, and the total internal forces, $\{r\}$, which in turn is calculated by

$$\{r\} = \int_{\mathrm{V}} [B_{\mathrm{p}}]^{\mathrm{T}}\{\sigma\}\,\mathrm{dVol} + \int_{\mathrm{V}} [G_{\mathrm{p}}]^{\mathrm{T}}[C_{\mathrm{p}}]^{\mathrm{T}}\{\sigma\}\,\mathrm{dVol} + \int_{\mathrm{V}} [G_{\mathrm{b}}]^{\mathrm{T}}[C_{\mathrm{b}}]^{\mathrm{T}}\{\sigma\}\,\mathrm{dVol} \tag{12.21}$$

where $\{\sigma\} = \{\sigma_x \sigma_y \tau_{xy}\}^{\mathrm{T}}$ is the total average membrane stress components. The unbalanced forces should be eliminated at every step of load increments. For that purpose, the Newton–Raphson method or the modified Newton–Raphson method is used.

The elastic tangent stiffness matrix, $[K]^{\mathrm{E}}$, in Equation (12.20) can generally be subdivided into four terms, namely

$$[K]^{\mathrm{E}} = [K_{\mathrm{p}}] + [K_{\mathrm{b}}] + [K_{\mathrm{g}}] + [K_{\sigma}] \tag{12.22}$$

On the right hand side of the above equation, the first and second terms represent the stiffness matrices related to the in-plane and the out-of-plane small deformations, respectively. The third term is the so-called initial deformation stiffness matrix, which in turn consists of three terms representing the geometric nonlinear effects associated with the in-plane and out-of-plane deformations and their interactions. The fourth term is the so-called initial stress stiffness matrix, which is produced by the initial stresses for the element, in which a term related to their interactions does not appear.

Each term mentioned above can be developed in more detail as follows:

$$\begin{aligned}[K_{\mathrm{p}}] &= \begin{bmatrix} [K_1] & 0 \\ 0 & 0 \end{bmatrix}, [K_{\mathrm{b}}] = \begin{bmatrix} 0 & 0 \\ 0 & [K_2] \end{bmatrix}, [K_{\mathrm{g}}] = \begin{bmatrix} [K_3] & [K_4] \\ [K_4]^{\mathrm{T}} & [K_5] \end{bmatrix} \\ [K_{\sigma}] &= \begin{bmatrix} [K_6] & 0 \\ 0 & [K_7] \end{bmatrix}\end{aligned} \tag{12.23}$$

where

$$[K_1] = \int_{\mathrm{V}} [B_{\mathrm{p}}]^{\mathrm{T}}[D]^{\mathrm{E}}[B_{\mathrm{p}}]\,\mathrm{dVol}, [K_2] = \int_{\mathrm{V}} [B_{\mathrm{b}}]^{\mathrm{T}}[D]^{\mathrm{e}}[B_{\mathrm{b}}]z^2\,\mathrm{dVol}$$

$$\begin{aligned}[K_3] = {} & \int_{\mathrm{V}} [G_{\mathrm{p}}]^{\mathrm{T}}[C_{\mathrm{p}}]^{\mathrm{T}}[D]^{\mathrm{E}}[B_{\mathrm{p}}]\,\mathrm{dVol} + \int_{\mathrm{V}} [B_{\mathrm{p}}]^{\mathrm{T}}[D]^{\mathrm{E}}[C_{\mathrm{p}}][G_{\mathrm{p}}]\,\mathrm{dVol} \\ & + \int_{\mathrm{V}} [G_{\mathrm{p}}]^{\mathrm{T}}[C_{\mathrm{p}}]^{\mathrm{T}}[D]^{\mathrm{e}}[C_{\mathrm{p}}][G_{\mathrm{p}}]\,\mathrm{dVol}\end{aligned}$$

$$[K_4] = \int_{\mathrm{V}} [B_{\mathrm{p}}]^{\mathrm{T}}[D]^{\mathrm{E}}[C_{\mathrm{b}}][G_{\mathrm{b}}]\,\mathrm{dVol} + \int_{\mathrm{V}} [G_{\mathrm{p}}]^{\mathrm{T}}[C_{\mathrm{p}}]^{\mathrm{T}}[D]^{\mathrm{E}}[C_{\mathrm{b}}][G_{\mathrm{b}}]\,\mathrm{dVol}$$

$$[K_5] = \int_{\mathrm{V}} [G_{\mathrm{b}}]^{\mathrm{T}}[C_{\mathrm{b}}]^{\mathrm{T}}[D]^{\mathrm{E}}[C_{\mathrm{b}}][G_{\mathrm{b}}]\,\mathrm{dVol}, [K_6] = \int_{\mathrm{V}} [G_{\mathrm{p}}]^{\mathrm{T}}[\sigma_{\mathrm{p}}][G_{\mathrm{p}}]\,\mathrm{dVol}$$

$$[K_7] = \int_{\mathrm{V}} [G_{\mathrm{b}}]^{\mathrm{T}}[\sigma_{\mathrm{b}}][G_{\mathrm{b}}]\,\mathrm{dVol}$$

$$[\sigma_{\mathrm{p}}] = \begin{bmatrix} \sigma_x & 0 & \tau_{xy} & 0 \\ 0 & \sigma_x & 0 & \tau_{xy} \\ \tau_{xy} & 0 & \sigma_y & 0 \\ 0 & \tau_{xy} & 0 & \sigma_y \end{bmatrix}, [\sigma_{\mathrm{b}}] = \begin{bmatrix} \sigma_x & \tau_{xy} \\ \tau_{xy} & \sigma_y \end{bmatrix}$$

In calculating Equation (12.23), the terms involving the first order of the variable z would become zero after completing the integration for the entire volume of the element in the elastic regime. Even in the elastic–plastic regime, the plasticity is condensed into

the plastic nodes and the inside of the element, except for the plastic nodes, is assumed to be elastic in the present method. Thus these terms can be eliminated from the expressions.

The Updated Lagrangian Approach

The tangent stiffness matrix, $[K]^{\mathrm{E}}$, in Equation (12.22) was derived by the total Lagrangian approach considering that the local coordinate system for the element is fixed with regard to the global coordinate system, which makes possible the use of an identical transformation matrix throughout the whole incremental loading process.

On the other hand, in the so-called updated Lagrangian approach one needs to update the local coordinate system at every incremental loading process such that the transformation matrix from the local coordinate to the global system is newly set up each time. The benefit of the updated Lagrangian approach is that the initial deformation matrix, $[K_{\mathrm{g}}]$, can be eliminated from Equation (12.22) since the initial deformation at the beginning of every incremental loading process can be set to zero. Therefore, the tangent elastic stiffness matrix, $[K]^{\mathrm{E}}$, can simplify to

$$[K]^{\mathrm{E}} = [K_{\mathrm{p}}] + [K_{\mathrm{b}}] + [K_{\sigma}] \tag{12.24}$$

Stiffness Matrix for the Displacement Component, θ_z

The stiffness matrix components for the rotations with respect to the z axis may normally be set to zero, but this can in some cases produce numerical instability in the computation of the structural stiffness equation. To get a stabilizing effect in the numerical computation, the stiffness matrix components for the displacement component, θ_z, can be added to the stiffness matrix, Equation (12.24). The stiffness equation for the displacement component, θ_z, may be given by (Zienkiewicz 1977)

$$\begin{Bmatrix} M_{z1} \\ M_{z2} \\ M_{z3} \\ M_{z4} \end{Bmatrix} = \alpha EAt \begin{bmatrix} 1 & -\frac{1}{2} & -\frac{1}{2} & -\frac{1}{2} \\ -\frac{1}{2} & 1 & -\frac{1}{2} & -\frac{1}{2} \\ -\frac{1}{2} & -\frac{1}{2} & 1 & -\frac{1}{2} \\ -\frac{1}{2} & -\frac{1}{2} & -\frac{1}{2} & 1 \end{bmatrix} \begin{Bmatrix} \theta_{z1} \\ \theta_{z2} \\ \theta_{z3} \\ \theta_{z4} \end{Bmatrix} \tag{12.25}$$

where t is the plate thickness, and A the surface area of the element. The constant α may normally be taken to be a very small value, e.g., 5.0×10^{-5}.

12.4.5 Displacement (Shape) Function

To attain a uniform state of shear stresses inside the element, a nonlinear function is in the present finite element method assumed for the in-plane displacements, u and v, while a polynomial function is assumed for the out-of-plane displacement, w, which is expressed in terms of 12 parameters. We thus have

$$u = a_1 + a_2x + a_3y + a_4xy + \frac{b_4}{2}(b^2 - y^2) \tag{12.26a}$$

$$v = b_1 + b_2x + b_3y + b_4xy + \frac{a_4}{2}(a^2 - x^2) \tag{12.26b}$$

$$w = c_1 + c_2x + c_3y + c_4x^2 + c_5xy + c_6y^2 + c_7x^3 + c_8x^2y + c_9xy^2 + c_{10}y^3 + c_{11}x^3y + c_{12}xy^3 \tag{12.26c}$$

where $a_1, a_2, \ldots, c_{12}$ are unknown coefficients which are expressed in terms of nodal displacements $\{U\}$.

For the rectangular plate element with a length of a and a breadth of b, the coefficients of the displacement functions can be obtained by substituting local coordinates and displacements at nodes into Equations (12.26).

12.4.6 Yield Condition

Plasticity in the element is checked at the element corner nodal points located in the middle plane of the element thickness by applying the Ueda plastic node concept. A fully plastic condition under combined in-plane and out-of-plane loads through the thickness of the element is used as the yield condition.

By applying the Mises–Hencky yield condition, the yield function, f_i, for the ith nodal point can be expressed in terms of the resultant membrane stress and generalized bending stress components as follows:

$$f_i = n_i^2 + |m_i| - 1 = 0 \tag{12.27}$$

where

$$n_i^2 = n_{xi}^2 - n_{xi}n_{yi} + n_{yi}^2 + 3n_{xyi}^2, m_i = (m_{xi}^2 - m_{xi}m_{yi} + m_{yi}^2 + 3m_{xyi}^2)^{1/2}$$

$$n_{xi} = \frac{\sigma_{xi}}{\sigma_{\mathrm{Y}}}, n_{yi} = \frac{\sigma_{yi}}{\sigma_{\mathrm{Y}}}, n_{xyi} = \frac{\tau_{xyi}}{\sigma_{\mathrm{Y}}}, m_{xi} = \frac{2\sigma_{xbi}}{3\sigma_{\mathrm{Y}}}, m_{yi} = \frac{2\sigma_{ybi}}{3\sigma_{\mathrm{Y}}}, m_{xyi} = \frac{2\tau_{xybi}}{3\sigma_{\mathrm{Y}}}$$

$\{\sigma_i\} = \{\sigma_{xi} \ \ \sigma_{yi} \ \ \tau_{xyi}\}^{\mathrm{T}}$ = nodal membrane stress components, $\{\sigma_{\mathrm{b}i}\} = \{\sigma_{xbi} \ \ \sigma_{ybi} \ \ \tau_{xybi}\}^{T}$ = nodal maximum generalized bending stress components in the outer fiber of the cross-section, σ_{Y} = yield stress of the element material.

The resultant membrane and bending stress components used in Equation (12.27) can be calculated by accumulating the increments of the corresponding stress components through each incremental loading step. The increments of the stress components in the ith nodal point are calculated by

$$\{\Delta\sigma_i\} = [D]^{\mathrm{E}}\{\Delta\varepsilon\}^{\mathrm{E}} = [D]^{\mathrm{E}}[B_i]\{\Delta U\}^{\mathrm{E}} \tag{12.28a}$$

$$\{\Delta\sigma_{\mathrm{b}i}\} = -\frac{t^2}{6}[D]^{\mathrm{E}}\{\Delta\varepsilon\}^{\mathrm{E}} = -\frac{t^2}{6}[D]^{\mathrm{E}}[B_{\mathrm{b}i}]\{\Delta W\}^{\mathrm{E}} \tag{12.28b}$$

where $[B_i]$ and $[B_{\mathrm{b}i}]$ can be defined by substituting the local coordinates for the ith nodal point into the matrices $[B]$ and $[B_{\mathrm{b}}]$, respectively, in Equation (12.15).

The yield function, f_i, may be represented as shown in Figure 12.6 where the curve represents the yield surface. If the value of the yield function at any nodal point is less than zero, indicating that the value is located inside the yield surface, e.g., the point A of Figure 12.6, the nodal point is still in elastic. As the applied loads increase incrementally, the value of the yield function will reach zero so that its value is just on the yield surface,

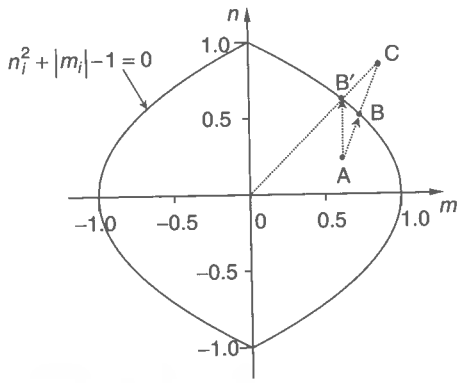

Figure 12.6 A diagram of the yield surface

i.e., the points B or B′ of Figure 12.6. In this case, it is assumed that the node becomes plastic, and the plastic node is inserted at the nodal point even if the inside of the element except for the plastic nodes is considered to be elastic. The value of the yield function should in any case not be greater than zero.

Since the structural response is nonlinear, it is normally not an easy task to ensure that the value of the yield function is just on the yield surface as the applied loads increase incrementally. One of the methods used to facilitate this is to apply the smallest load increment so that the most highly stressed elastic node is just yielded. In this method, the elastic nodes are yielded one by one through the incremental loading step so that the value of the yield function will always be just on the yield surface.

The smallest load increment necessary to yield the most highly stressed elastic node can be defined by a load magnification factor with regard to the initial standard load increments. For an elastic node, it is assumed that the node just yields by applying a load increment of $\beta\{\Delta R\}$, where $\{\Delta R\}$ is the prescribed initial standard load increment and β is a positive multiplier. Therefore, at the node one must satisfy the yield condition as follows:

$$\begin{aligned}(n_x + \beta\Delta n_x)^2 - (n_x + \beta\Delta n_x)(n_y + \beta\Delta n_y) + (n_y + \beta\Delta n_y)^2 + 3(n_{xy} + \beta\Delta n_{xy})^2 \\ + [(m_x + \beta\Delta m_x)^2 - (m_x + \beta\Delta m_x)(m_y + \beta\Delta m_y)(m_y + \beta\Delta m_y)^2 \\ + 3(m_{xy} + \beta\Delta m_{xy})^2]^{1/2} - 1 = 0\end{aligned} \tag{12.29}$$

where the prefix Δ denotes the increment.

By neglecting the infinitesimal terms, i.e., those with higher than the second-order of the increments, this equation becomes a quadratic equation with regard to the multiplier as follows:

$$\left(C_1 + \frac{C_4}{2\sqrt{C_6}}\right)\beta^2 + \left(C_2 + \frac{C_5}{2\sqrt{C_6}}\right)\beta + C_3 + \sqrt{C_6} - 1 = 0 \tag{12.30}$$

where

$$C_1 = \Delta n_x^2 - \Delta n_x \Delta n_y + \Delta n_y^2 + 3\Delta n_{xy}^2$$

$$C_2 = (2n_x - n_y)\Delta n_x + (2n_y - n_x)\Delta n_y + 6n_{xy}\Delta n_{xy}$$

$$C_3 = n_x^2 - n_x n_y + n_y^2 + 3n_{xy}^2,\ C_4 = \Delta m_x^2 - \Delta m_x \Delta m_y + \Delta m_y^2 + 3\Delta m_{xy}^2$$

$$C_5 = (2m_x - m_y)\Delta m_x + (2m_y - m_x)\Delta m_y + 6m_{xy}\Delta m_{xy}$$

$$C_6 = m_x^2 - m_x m_y + m_y^2 + 3m_{xy}^2$$

The positive solution of this equation will then give the minimum load multiplier, β, as follows:

$$\beta = \frac{-\alpha_2 + \sqrt{\alpha_2^2 - 4\alpha_1\alpha_3}}{2\alpha_1} \tag{12.31}$$

where

$$\alpha_1 = C_1 + \frac{C_4}{2\sqrt{C_6}},\ \alpha_2 = C_2 + \frac{C_5}{2\sqrt{C_6}},\ \alpha_3 = C_3 + \sqrt{C_6} - 1$$

In the actual numerical process for the structural response analysis, the smallest value of β for all elastic nodes can be determined. The next step of the load increment will then continue by applying the load increment of $\beta\{\Delta R\}$ so that the most highly stressed elastic node just yields.

In some cases, the value of the yield function may be found to be apparently located outside the yield surface, e.g., the point C of Figure 12.6, implying that the prescribed load increment is too large. In these cases, an iterative procedure is needed until the desired accuracy is obtained so that the value of the yield function is just on or very near the yield surface.

12.4.7 Elastic–Plastic Tangent Stiffness Matrix

As previously mentioned, the elastic–plastic tangent stiffness matrix for the element in the local coordinate system is derived by applying the plastic node method. While the strain-hardening effect can be taken into account without difficulty, the elastic-perfectly plastic model for the stress–strain relation is adopted in the present formulation, as shown in Figure 12.7. Upon attaining convergence of the unbalanced forces, $\{L\}$, required to secure the equilibrium of the structure, the elastic tangent stiffness equation for the element will become

$$\{\Delta R\} = [K]^{\mathrm{E}}\{\Delta U\}^{\mathrm{E}} \tag{12.32}$$

where $[K]^{\mathrm{E}}$ = elastic tangent stiffness matrix for the element, $\{\Delta U\}^{\mathrm{E}}$ = elastic component of displacement increments which are equal to the total displacement increments, $\{\Delta U\}$, if the element behavior is still in the elastic regime.

Since the nodal force vectors are related to only the elastic components of the displacements, this equation should be available even for the elastic–plastic regime. If the resultant stress components at any nodal point of the element satisfy the yield condition, plastic nodes are inserted and plastic deformation will be produced. Therefore, the total displacement increments, $\{\Delta U\}$, in the elastic–plastic regime can be calculated by the sum of the elastic and plastic components of the displacement increments as follows:

$$\{\Delta U\} = \{\Delta U\}^{\mathrm{E}} + \{\Delta U\}^{\mathrm{P}} \tag{12.33}$$

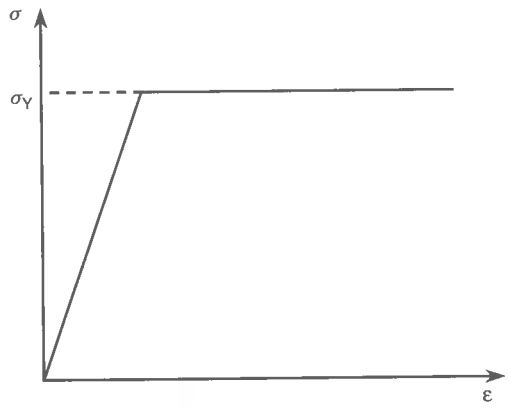

Figure 12.7 The elastic–perfectly plastic model for the stress–strain relationship

where $\{\Delta U\}^{\mathrm{E}}$ and $\{\Delta U\}^{\mathrm{P}}$ are the elastic and plastic components of the displacement increments, respectively.

By applying plastic flow theory, the plastic component of the displacement increments after the ith node has yielded can be calculated by

$$\{\Delta U\}^{\mathrm{P}} = \Delta\lambda_i\{\phi_i\} \tag{12.34}$$

where $\{\phi_i\} = \{\partial f_i/\partial R\}$ and $\Delta\lambda_i$ is a positive scalar characterizing the magnitude of the plastic displacement. $\{\phi_i\}$ in this equation represents the outward vector normal to the yield surface which can be expressed in terms of nodal forces as follows:

$$\{\phi_i\} = \sigma_{\mathrm{Y}}^2\left(\left\{\frac{\partial f_i}{\partial \sigma_i}\right\}^{\mathrm{T}}\left\{\frac{\partial \sigma_i}{\partial R}\right\} + \left\{\frac{\partial f_i}{\partial \sigma_{\mathrm{b}i}}\right\}^{\mathrm{T}}\left\{\frac{\partial \sigma_{\mathrm{b}i}}{\partial R_{\mathrm{w}}}\right\}\right) \tag{12.35}$$

where σ_{Y}^2 appears because the yield function, f_i, of Equation (12.27) was expressed in a non-dimensional form with regard to the yield stress, σ_{Y}.

In this equation, $\{R_{\mathrm{w}}\}$ indicates the out-of-plane component of nodal forces, with the increments of $\{R_{\mathrm{w}}\}$ being calculated by

$$\{\Delta R_{\mathrm{w}}\} = [K_{\mathrm{w}}]^{\mathrm{E}}\{\Delta W\}^{\mathrm{E}} \tag{12.36}$$

where the subscript w denotes the vector or matrix for the out-of-plane component.

By reducing the degrees of freedom with regard to the rigid-body motion of the element, the relationships between the nodal forces and displacements or between the stresses and displacements can be expressed by

$$\{\Delta R\} = [K^*]^{\mathrm{E}}\{\Delta U^*\}^{\mathrm{E}} \tag{12.37a}$$

$$\{\Delta R_{\mathrm{w}}\} = [K_{\mathrm{w}}^*]^{\mathrm{E}}\{\Delta W^*\}^{\mathrm{E}} \tag{12.37b}$$

$$\{\Delta\sigma_i\} = [D]^{\mathrm{E}}[B_i^*]\{\Delta U^*\}^{\mathrm{E}} \tag{12.37c}$$

$$\{\Delta\sigma_{\mathrm{b}i}\} = -\frac{t^2}{6}[D]^{\mathrm{E}}[B_{\mathrm{b}i}^*]\{\Delta W^*\}^{\mathrm{E}} \tag{12.37d}$$

where the asterisk indicates the reduced degree of freedom after removing the rigid-body motion of the element.

Calculating the nodal displacements, $\{\Delta U^*\}^{\mathrm{E}}$ and $\{\Delta W^*\}^{\mathrm{E}}$ from Equations (12.37a) and (12.37b), respectively, and substituting them into Equations (12.37c) and (12.37d), the resultant stresses can be expressed as functions of the nodal forces as follows:

$$\{\Delta\sigma_i\} = \frac{[D]^{\mathrm{E}}[B_i^*]([K^*]^{\mathrm{E}})^{\mathrm{T}}}{([K^*]^{\mathrm{E}})^{\mathrm{T}}[K^*]^{\mathrm{E}}}\{\Delta R\} \tag{12.38a}$$

$$\{\Delta\sigma_{\mathrm{b}i}\} = -\frac{t^2}{6}\frac{[D]^{\mathrm{E}}[B_{\mathrm{b}i}^*]([K_{\mathrm{w}}^*]^{\mathrm{E}})^{\mathrm{T}}}{([K_{\mathrm{w}}^*]^{\mathrm{E}})^{\mathrm{T}}[K_{\mathrm{w}}^*]^{\mathrm{E}}}\{\Delta R_{\mathrm{w}}\} \tag{12.38b}$$

To calculate the outward normal vector, $\{\phi_i\}$, of Equation (12.35), $\{\partial f_i/\partial\sigma_i\}$ and $\{\partial f_i/\partial\sigma_{\mathrm{b}i}\}$ are first computed by differentiating the yield function, f_i, Equation (12.27), with regard to the stress components as follows:

$$\left\{\frac{\partial f_i}{\partial \sigma_i}\right\} = \frac{1}{\sigma_{\mathrm{Y}}^2}\{(2\sigma_{xi} - \sigma_{yi})(2\sigma_{yi} - \sigma_{xi})(6\tau_{xyi})\}^{\mathrm{T}} \tag{12.39a}$$

$$\left\{\frac{\partial f_i}{\partial \sigma_{\mathrm{b}i}}\right\} = \frac{1}{3\sigma_{\mathrm{Y}}\sqrt{S}}\{(2\sigma_{x\mathrm{b}i} - \sigma_{y\mathrm{b}i})(2\sigma_{y\mathrm{b}i} - \sigma_{x\mathrm{b}i})(6\tau_{xyi})\}^{\mathrm{T}} \tag{12.39b}$$

where $S = \sigma_{x\mathrm{b}i}^2 - \sigma_{x\mathrm{b}i}\sigma_{y\mathrm{b}i} + \sigma_{y\mathrm{b}i}^2 + 3\tau_{xyi}^2$.

Also, $\{\partial\sigma_i/\partial R\}$ and $\{\partial\sigma_{\mathrm{b}i}/\partial R_{\mathrm{w}}\}$ are computed by differentiating Equations (12.38a) and (12.38b) with regard to the nodal forces as follows:

$$\left\{\frac{\partial \sigma_i}{\partial R}\right\} = \frac{[D]^{\mathrm{E}}[B_i^*]([K^*]^{\mathrm{E}})^{\mathrm{T}}}{([K^*]^{\mathrm{E}})^{\mathrm{T}}[K^*]^{\mathrm{E}}} \tag{12.40a}$$

$$\left\{\frac{\partial \sigma_{\mathrm{b}i}}{\partial R_{\mathrm{w}}}\right\} = -\frac{t^2}{6}\frac{[D]^{\mathrm{E}}[B_{\mathrm{b}i}^*]([K_{\mathrm{w}}^*]^{\mathrm{E}})^{\mathrm{T}}}{([K_{\mathrm{w}}^*]^{\mathrm{E}})^{\mathrm{T}}[K_{\mathrm{w}}^*]^{\mathrm{E}}} \tag{12.40b}$$

Then the outward normal vector, $\{\phi_i\}$, can be computed by substituting Equations (12.39) and (12.40) into Equation (12.35). In the numerical computation process, a drift in the value of the yield function from the yield surface can occur and this should be prevented to get the desired accuracy of solution.

When the resultant stress components of the ith nodal point satisfy the yield condition, the value of the yield function must be located just on the yield surface, e.g., the point O of Figure 12.8(a), in which the outward normal vector denoted $\{\phi_i\}_0$ will be developed. As the external loads increase, the nodal force vector at the plastic node should move along the yield surface in the tangent direction and thus the point O may move to a point outside the yield surface, e.g., the point A of Figure 12.8(a) where the outward normal vector, $\{\phi_i\}_{\mathrm{A}}$, will be produced. Likewise, in the next step of load increments, the point A may move to a point which is more distant from the yield surface, e.g., the point B of Figure 12.8(a) with the outer normal vector $\{\phi_i\}_{\mathrm{B}}$.

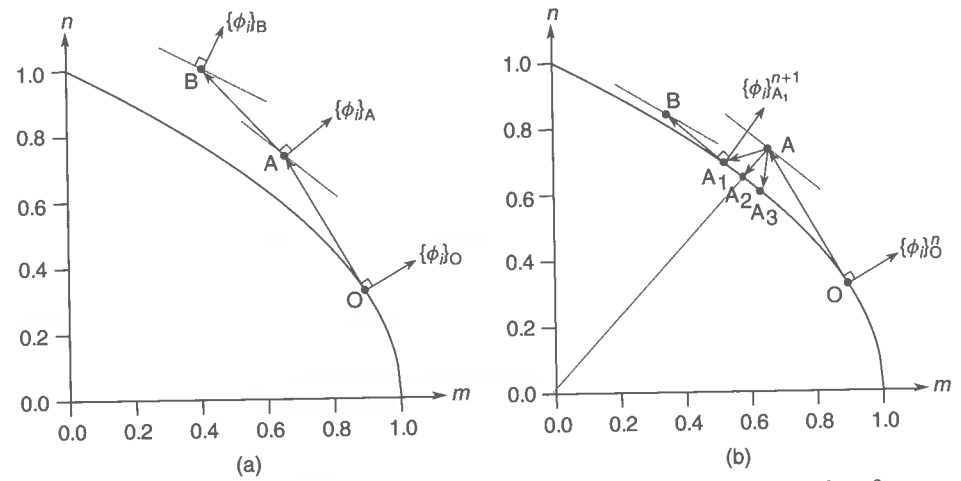

Figure 12.8 (a) The drift in the value of the yield function; (b) A two-step procedure for convergence to the yield condition

In fact, as long as the value of the yield function is located outside the yield surface, the outward normal vector is not real and if its drift from the yield surface is too big the resulting response obtained in the subsequent loading step may no longer be reliable. It is hence of importance to control and remove the drift of the value of the yield function during the incremental loading process.

Several useful approaches, namely the iterative method (Wen & Farhoomand 1970), five-step correction method (Orbison *et al.* 1982) and two-step correction procedure (Paik & Kim 1989), among others, have been proposed to reduce the drift of the value of the yield function. In the illustrative examples of this chapter, the two-step correction method is applied. The method is described in the following.

As previously noted, the elastic nodes of the structure are yielded one by one through the incremental loading step so that the value of the yield function will be located just on or very near the yield surface. It is considered that at the nth step of load increment the value of the yield function for the ith plastic node is just on the yield surface, e.g., the point O of Figure 12.8(b) with the outward normal vector, $\{\phi_i\}_O^n$. Assume that the value of the yield function moves to the point A along the tangent vector OA in the next (i.e., $(n+1)$th) step of load increments. If the drift of the point A from the yield surface exceeds an acceptable tolerance, the location of the point A is corrected by multiplying by the linearly determined correction factor to the point on the yield surface, e.g., A_1, A_2 or A_3 of Figure 12.8(b). The correction factor can be estimated in a similar manner to the computation of the load magnification factor indicated in Equation (12.31). If the point A returns to the yield surface, e.g., at the point A_1, the nodal forces will produce the outward normal vector, $\{\phi_i\}_{A_1}^{n+1}$, and the tangent vector, A_1B, for the $(n+1)$th step of load increments. This approach is quite simple to handle and gives sufficient accuracy for practical use.

If m numbers of the nodal points for an element are in the plastic condition, the plastic component of displacement increments can then be computed by the superposition of Equation (12.34) as follows:

$$\{\Delta U\}^{\mathrm{P}} = \sum_{i=1}^{m} \Delta\lambda_i \{\phi_i\} \tag{12.41}$$

where the maximum number of m will be four for the rectangular plate element since the number of nodal points is four.

Substituting Equations (12.33) and (12.41) into Equation (12.32), the tangent stiffness equation for the element becomes

$$\{\Delta R\} = [K]^{\mathrm{E}} \left(\{\Delta U\} - \sum_{i=1}^{m} \Delta\lambda_i \{\phi_i\} \right) \tag{12.42}$$

Neglecting the strain-hardening effect, i.e., considering an elastic–fully plastic material, the following equation should be satisfied at every plastic node as long as the loading process continues:

$$\Delta f_i = \{\phi_i\}^{\mathrm{T}} \{\Delta R\} = 0 \tag{12.43}$$

Substitution of Equation (12.42) into Equation (12.43) leads to

$$\{\Delta\lambda\} = \frac{[\phi]^{\mathrm{T}}[K]^{\mathrm{E}}}{[\phi]^{\mathrm{T}}[K]^{\mathrm{E}}[\phi]} \{\Delta U\} \tag{12.44}$$

where $[\phi] = [\{\phi_1\}\{\phi_2\}\cdots\{\phi_m\}]^{\mathrm{T}}$, $\{\Delta\lambda\} = \{\Delta\lambda_1 \Delta\lambda_2 \cdots \Delta\lambda_m\}^{\mathrm{T}}$.

By substituting Equation (12.44) into Equation (12.42), the tangent stiffness matrix for the element in the elastic–plastic regime can be written as follows:

$$\{\Delta R\} = \left([K]^{\mathrm{E}} - \frac{[K]^{\mathrm{E}}[\phi][\phi]^{\mathrm{T}}[K]^{\mathrm{E}}}{[\phi]^{\mathrm{T}}[K]^{\mathrm{E}}[\phi]} \right) \{\Delta U\} = [K]^{P} \{\Delta U\} \tag{12.45}$$

where

$$[K]^{\mathrm{P}} = [K]^{\mathrm{E}} - \frac{[K]^{\mathrm{E}}[\phi][\phi]^{\mathrm{T}}[K]^{\mathrm{E}}}{[\phi]^{\mathrm{T}}[K]^{\mathrm{E}}[\phi]}$$

is the elastic–plastic tangent stiffness matrix of the element.

It is evident from Equation (12.45) that the elastic–plastic tangent stiffness matrix, $[K]^{\mathrm{P}}$, can be calculated by a matrix operation without having to perform the numerical integration over the volume of the element once the elastic tangent stiffness matrix, $[K]^{\mathrm{E}}$, is obtained. In the calculation of Equation (12.45), the loading state for every plastic node should be checked, and when unloading is detected, i.e., if $\Delta\lambda_i < 0$ for the ith plastic node, the node should be treated as an elastic one.

12.4.8 Treatment of the Bauschinger Effect

The Bauschinger effect may play an important role in the nonlinear response of steel structures which are likely to be subjected to cyclic extreme loading. In this case, the so-called sublayer model (also called the overlay or fraction model) may be relevant for the elastic–perfectly plastic material.

When the strain-hardening effect is of primary concern, the kinematic hardening model or combined isotropic and kinematic hardening model is typically used where the origin of the yield function can be moved as stress components vary, as shown in Figure 12.9. The kinematic hardening model keeps the shape and size of the yield function, while the

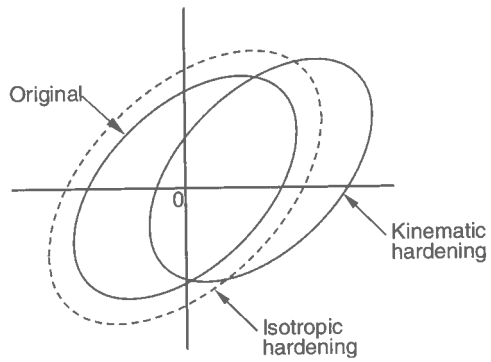

Figure 12.9 The isotropic hardening versus the kinematic hardening

combined model may allow for expansion of the yield function. In contrast, the isotropic hardening model, which neglects the Bauschinger effect, has a fixed origin of the yield function which can expand due to the strain-hardening effect.

12.4.9 Local to Global Transformation Matrix

An exact formulation of the transformation matrix for a rectangular plate element is difficult to define. In the approximate formulation, it is normally considered that the element is in a plane containing at least three nodal points of the element. The transformation matrix, $[T]$, from the local coordinate system to the global coordinate system can then be obtained in Cartesian terms (i.e., as functions of global coordinates at nodal points). Therefore, the element stiffness matrix in the local coordinate system can be transformed to the global system coordinate as follows:

$$[K]_g = [T]^T [K]_l [T] \tag{12.46}$$

where $[K]_l$ and $[K]_g$ are the element stiffness matrices in the local and global coordinates, respectively, and $[T]$ is the transformation matrix from the local coordinate system to the global coordinate system.

All element stiffness matrices in the global coordinate system are then assembled in the usual manner for the finite element procedure to obtain the stiffness matrix for the entire structure. By solving the resulting stiffness equations for the prescribed load increments and boundary conditions, the structural response is obtained.

12.5 Computer Software NATS

12.5.1 Outline of the Computer Software

The theory presented in this chapter is automated within the computer program NATS, which stands for nonlinear analysis of thin-walled structures. The NATS program, together with the user's manual, can be downloaded from the web site following the instructions given in the appendices to this book. The visualization of output is currently not supported by the software, and is hence a user's responsibility.

12.5.2 Application Examples

As application examples of the NATS method, the elastic–plastic large-deflection behavior of a rectangular steel plate and a stiffened steel panel subjected to uniaxial compressive loads is now analyzed until the ultimate strength is reached.

A Steel Plate under Axial Compression

The ultimate strengths for two rectangular plates in axial compression, which are relatively thick and thin respectively, are analyzed by the present method and the conventional nonlinear finite element program ANSYS (1999). For the boundary condition the plates are considered to be simply supported, with edges kept straight. Each plate has a slight level of initial deflections (i.e., $w_{0pl}/t = 0.01$, w_{0pl} = maximum initial deflection at plate center, t = plate thickness). Because of the geometric symmetry, a quarter of the plate is taken as the extent of analysis.

Figures 12.10 and 12.11 show the load versus plate center deflections of the plates as obtained by the present method. The nonlinear solutions obtained by ANSYS are also shown. The figures show the spread of plasticity with increase in the applied load magnitude as obtained by the present method. It is seen from the comparisons that the NATS method using the plastic node method provides reasonably accurate solutions of nonlinear behavior for rectangular steel plates. The computing time required for the NATS calculations was one-sixth of the time of the conventional FEA for this specific case.

A Steel Stiffened Panel under Axial Compression

The ultimate strength for a simply supported stiffened panel in axial compression as shown in Figure 12.12 is analyzed by the NATS method and the ANSYS program. The panel has

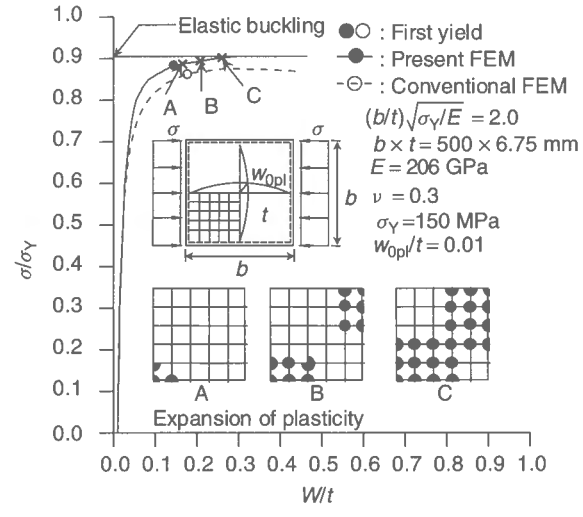

Figure 12.10 The load versus central deflection curves for a simply supported rectangular plate subject to uniaxial compressive loads (relatively thick plate)

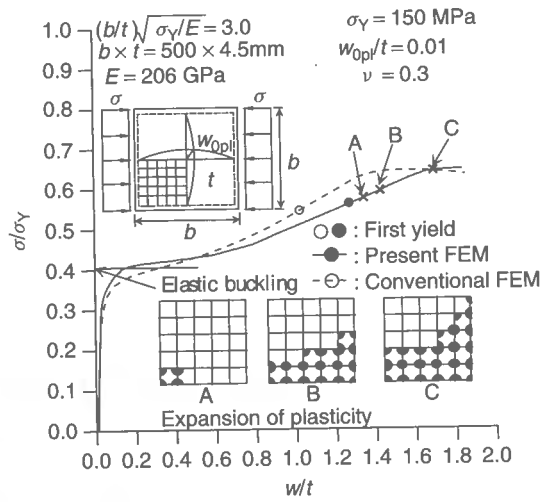

Figure 12.11 The load versus central deflection curves for a simply supported rectangular plate subject to uniaxial compressive loads (relatively thin plate)

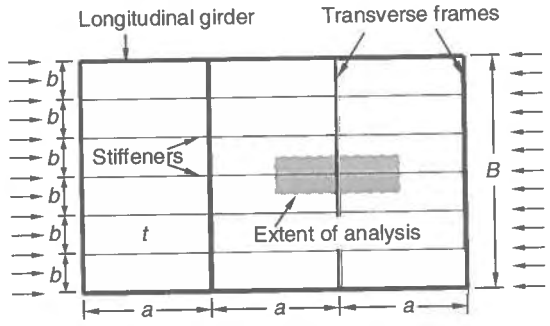

Figure 12.12 Extent for analysis of a stiffened structure subject to uniaxial compression

a number of flat-bar stiffeners. As the extent of analysis, a plate–stiffener combination with a two-span extent is selected as the representative of the stiffened panel.

As indicated in Figure 12.13, the plate–stiffener combination is taken to be supported by a heavy transverse frame at the mid-span. Plating and stiffener are modeled by rectangular plate-shell finite elements. The transverse support frame is not modeled by finite elements, but lateral deflections are restrained along the support member. The initial deflection of plating between stiffeners is assumed to be 1% of the plate thickness. The global initial deflection for the stiffener, i.e., a column-type distortion in the plane of the stiffener, is assumed to be 0.15% of the column length in this example. Welding-induced residual stresses are not considered in the analysis. A uniform edge displacement is applied and incrementally increased.

Figure 12.14 shows the resulting load versus end-shortening curves for the panel with flat-bar stiffeners subject to axial compression. With increase in the applied loads, the plating buckles and collapses locally, but the panel sustains further loading as long

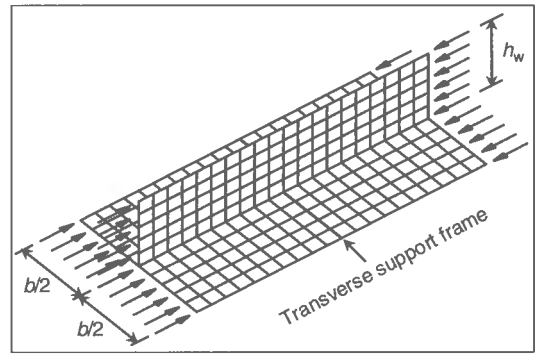

Figure 12.13 Finite element modeling of a plate–stiffener combination with a two-span extent for nonlinear analysis

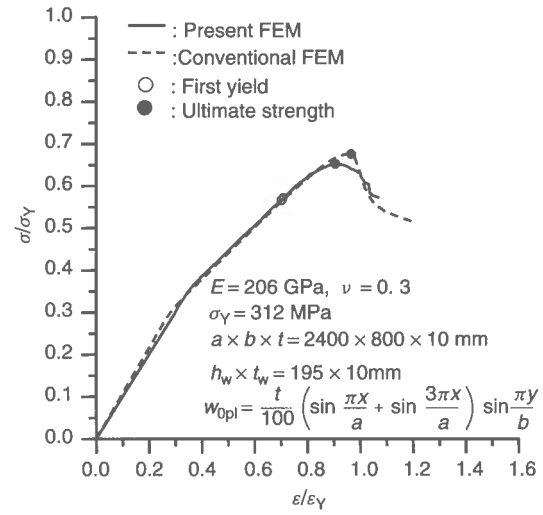

Figure 12.14 The load versus end-shortening (strain) curves for the plate–stiffener combination model under a uniform end thrust

as the stiffener keeps straight. However, the panel eventually reaches the ULS by lateral–torsional buckling of the stiffener since the stiffener web height is relatively large. It is noted that the collapse mode described here is of course for a specific case of the present example panel. As previously noted in Chapter 6, the collapse mode of a stiffened panel will significantly depend on the properties of the plating and stiffeners, among others. The ANSYS nonlinear solutions are also shown in Figure 12.14. It is again seen that the NATS method gives reasonably accurate solutions in comparison to the conventional nonlinear finite element method.

References

ANSYS (1999). *ANSYS user's manual (Version 5.5.3)*. Swanson Analysis Systems Inc., Houston, TX.

Bathe, K.J. (1982). *Finite element procedures in engineering analysis*. Prentice Hall, Englewood Cliffs, NJ.

Cook, R.D., Malkus, D.S. & Plesha, M.E. (1989). *Concepts and applications of finite element analysis*. John Wiley & Sons, New York.
Crisfield, M.A. (1981). A fast incremental/iterative solution procedure that handles 'snap-through'. *Computers & Structures*, 13: 55–62.
Hodge, P.G. (1959). *Plastic Analysis of Structures*. McGraw-Hill, New York.
Orbison, J.G., McGuire, W & Abel, J.F. (1982). Yield surface applications in nonlinear steel frame analysis. *Journal of Computer Methods in Applied Mechanics and Engineering*, 33(1–3): 557–573.
Owen, D.R.J & Hinton, E. (1980). *Finite elements in plasticity*. Pineridge Press, Swansea.
Paik, J.K. & Kim, C.Y. (1989). A simplified finite element method for the ultimate strength analysis of plates with initial imperfections. *Journal of the Society of Naval Architects of Korea*, 26(1): 24–38.
Ueda, Y., Akamatsu, T. & Ohmi, Y. (1969). Elastic–plastic analysis of framed structures using the matrix method (2nd Report). *Journal of the Society of Naval Architects of Japan*, 126: 253–260 (in Japanese).
Ueda, Y., Matsuishi, M., Yamakawa, T. & Akamatsu, T. (1968). Elastic–plastic analysis of framed structures using the matrix method. *Journal of the Society of Naval Architects of Japan*, 124: 183–191 (in Japanese).
Ueda, Y., Nakacho, K., Fujikubo, M. & Ishikawa, Y. (1983). Application of the plastic node method to thermal elastic–plastic and dynamic problems. *Journal of the Society of Naval Architects of Japan*, 153: 200–209 (in Japanese).
Ueda, Y. & Yao, T. (1982). The plastic node method: a new method of plastic analysis. *Journal of Computational Method, Applied Mechanics and Engineering*, 34(1–3): 1089–1104.
Ueda, Y., Yao, T. & Fujikubo, M. (1979). Generalization of the plastic node method. *Journal of the Society of Naval Architects of Japan*, 146: 307–313 (in Japanese).
Wen, R.K. & Farhoomand, F. (1970). Dynamic analysis of inelastic space frames. *Journal of Engineering Mechanics Division*, ASCE, 96(5): 667–687.
White, R.E. (1985). *An introduction to the finite element method with applications to nonlinear problems*. John Wiley & Sons, London.
Zienkiewicz, O.C. (1977). *The finite element method*, Third Edition. McGraw-Hill, London & New York.

13 The Idealized Structural Unit Method

13.1 Features of the Method

Under extreme or accidental loading, steel structures can be involved in a highly nonlinear response associated with yielding, buckling, crushing and sometimes rupture of individual structural components. As previously noted in Chapter 12, quite accurate solutions of the elastic–plastic structural response can be obtained by application of the conventional nonlinear finite element method (FEM). However, a weak feature of the conventional FEM is that it requires enormous modeling effort and computing time for nonlinear analysis of large-sized structures. In this regard, much effort has been devoted to the reduction of modeling and computing time for the nonlinear analyses of structures.

The most obvious way to reduce modeling effort and computing time is to reduce the number of degrees of freedom so that the number of unknowns in the finite element stiffness matrix decreases. Modeling the object structure with very large-sized structural units is perhaps the best way to do that. In order to avoid loss of accuracy, this requires the use of special purpose finite elements. Properly formulated structural units in such an approach can then be used to efficiently model the actual nonlinear behavior of the corresponding large parts of structures.

Ueda & Rashed (1974, 1984), who suggested this idea, called it the idealized structural unit method (ISUM). Their first effort in this regard was to analyze the ultimate strength of a transverse framed structure of a ship as an assembly of the so-called deep girder units.

In an almost parallel development to ISUM, Smith (1977) suggested a similar approach to predict the ultimate bending moment of a ship hull. He modeled the ship hull as an assembly of plate–stiffener combinations, i.e., stiffeners with attached plating (or the beam–column units), such as those shown in Figure 2.2(a) of Chapter 2. The load versus end-shortening relationships for these beam–column units were obtained using nonlinear finite element analysis (FEA) taking account of initial imperfections. The behavior of the larger structure was then constructed. While this method is sometimes called the Smith method, it may also be classified as a type of ISUM.

ISUM is a simplified nonlinear FEM. Unlike the conventional nonlinear FEM, ISUM idealizes a structural component making up the structure as one ISUM unit with a few

nodal points. As a typical example, Figure 13.1 compares structural modeling for the elastic–plastic large-deflection analysis of a rectangular plate under a complex load application (e.g., edge shear), as made by the conventional FEM and ISUM for comparable accuracy in results. In the conventional finite element modeling, finer meshes should normally be used, while on the other hand the plate is modeled using a single ISUM plate unit for ISUM analysis. It is noted that in this example the entire plate is taken as the extent of FEA because of unsymmetric characteristics related to deformations.

It is interest to note that the computational efforts required for the nonlinear analysis of a structure may be estimated, with definitions as follows:

- Ratio of number of unknowns: m = FEM/ISUM;
- Ratio of number of iterative loading steps: n = FEM/ISUM; and
- Ratio of computing time: CPU = FEM/ISUM = $n \times m^c$, with $c = 1$–3.

For the plate shown in Figure 13.1, it was found that $m \approx 300$, $n = 5$–10 and CPU ratio $\approx 5 \times 10^3$–10^4. For larger sized structures with more complex geometries, the discrepancy due to the number of elements between the two methods will become much more significant as well. By applying ISUM, therefore, the size of numerical computations is much reduced leading to dramatic savings of modeling and computing times, compared to those of the conventional FEM. One trade-off is of course the possible loss of generality of the method, in that ISUM uses specially formulated finite elements.

This chapter presents the most up-to-date theory of the ISUM units which are available for the nonlinear analyses of steel-plated structures subjected to extreme or accidental loading.

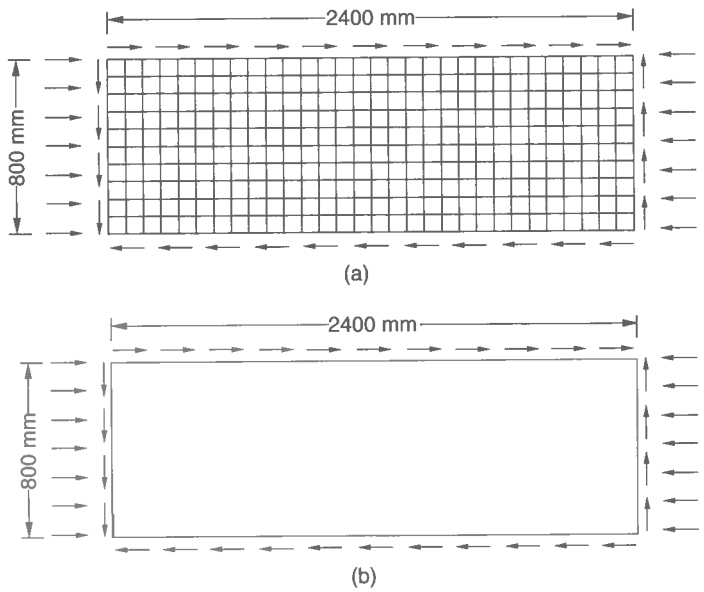

Figure 13.1 Sample comparison of (a) FEM and (b) ISUM models for elastic–plastic large-deflection analysis of a rectangular plate of $a/b = 3$ under a complex load application

13.2 ISUM Modeling Strategies for Steel-plated Structures

As previously described in Section 2.1 of Chapter 2, a steel-plated structure may be modeled as an assembly of many simpler structural elements, each type of which behaves in a known manner under given load application, and the assembly of which behaves in nearly the same way as the actual structure.

Steel-plated structures are typically composed of several different types of structural members such as support members (or beam–columns), rectangular plates and stiffened panels. In ISUM modeling, such members are regarded as ISUM units. It is important to realize that an identical structure may be modeled in somewhat different ways by different analysts, but it is of course always the aim to model so that the idealized structure behaves in (nearly) the same way as the actual structure.

Figure 13.2 shows some typical examples of ISUM modeling for steel-plated structures. One of the common approaches is to model the structure as an assembly of plate–stiffener combinations as shown in Figure 13.2(b). This type of modeling may not be very appropriate when the stiffeners are relatively weak or unusually strong. In such cases, the plate–stiffener separation models as shown in Figure 13.2(c) may be used, where plating between stiffeners is modeled as one ISUM plate element, while the stiffener without attached plating is modeled as an ISUM beam–column element.

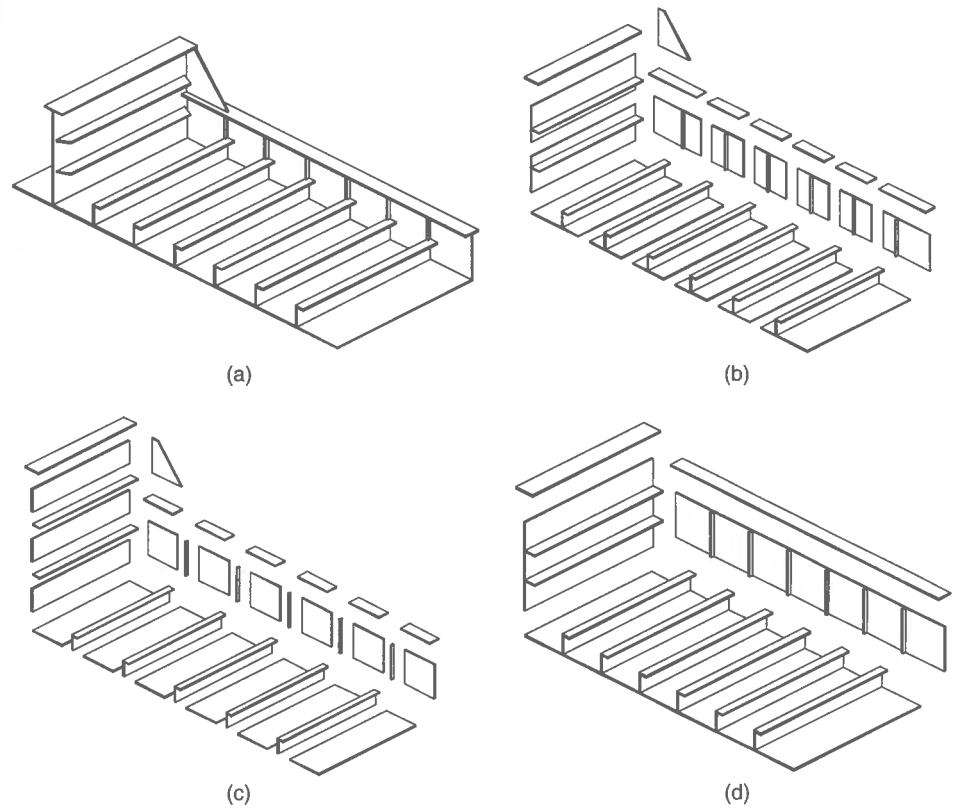

Figure 13.2 (a) A steel-plated structure; (b)–(d) various types of idealizations

An entire panel together with stiffeners in either one or both directions can also be modeled by one ISUM stiffened panel unit as shown in Figure 13.2(d). While a small stiffener with or without attached plating may be modeled as a beam–column unit, the girder or support member with a deep web may need to be modeled as an assembly of the plate unit and the beam–column unit, the former being for the web and the latter being for the flange.

In ISUM analyses, the load and boundary conditions are applied in a similar way to the conventional FEM. The initial imperfections and structural degradation as well as geometric and material properties of the ISUM units can be prescribed as parameters of influence as well.

13.3 Procedure for Development of the ISUM Units

For the nonlinear analysis of steel-plated structures, it is apparent that various types of the ISUM units are necessary to make a complete structural model, and these units should then be developed in advance. Figure 13.3 represents the procedure to develop the ISUM units. The nonlinear behavior of each type of structural member is idealized and expressed in the form of a set of failure functions defining the necessary conditions for different failures which may take place in the corresponding ISUM unit. A set of stiffness matrices representing the nonlinear relationship between the nodal force vector and the nodal displacement vector is then formulated until or after the limit state is reached. The ISUM units (elements) so developed are then used within the framework of the nonlinear matrix displacement procedure, by applying the incremental method, much like in the case of conventional FEM.

Many types of the ISUM units have so far been developed. For the purposes of ultimate strength analyses, the deep girder unit (Ueda & Rashed 1974, 1984), the tubular beam–column unit (Ueda *et al.* 1983), the I-section beam–column unit (Paik 1995), the rectangular plate unit (Ueda *et al.* 1984, 1986a, 1986b, Bai *et al.* 1993, Masaoka *et al.* 1998, Fujikubo *et al.* 2000) and the stiffened panel unit (Ueda *et al.* 1984, 1986a,

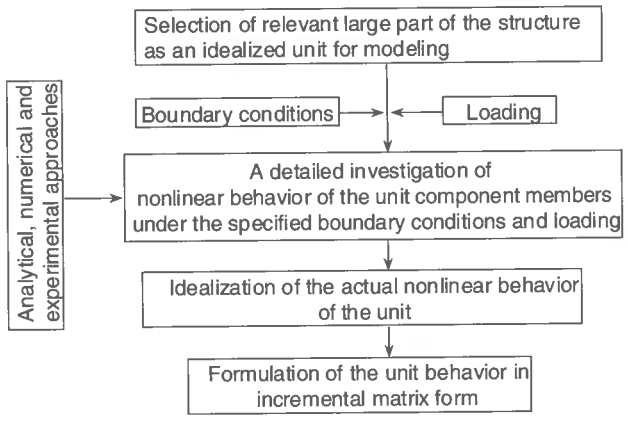

Figure 13.3 Procedure for the development of an idealized structural unit (Paik 1987)

1986b, Bai *et al.* 1993, Paik 1995) are available. For analysis of the internal mechanics in collisions and grounding, the rectangular plate unit, the stiffened panel unit and the gap/contact unit have been developed (Paik & Pedersen 1996).

It is important to realize that individual developers of the ISUM units may employ somewhat different approaches from each other to idealize and to formulate the actual nonlinear behavior of the structural members. Also, the features of existing ISUM units may be advanced continually to accommodate more factors of influence or to improve their computational accuracy. Even though the geometric features of the ISUM units are identical, their characteristics in terms of structural behavior will differ based on the purpose of the analyses, e.g., for ultimate strength or accidental mechanics.

ISUM has been successfully applied to the nonlinear analysis of ship structures in overload situations (e.g., Paik *et al.* 1996, 2001, among others), in collision or grounding accidents (e.g., Paik *et al.* 1999, 2002, Brown *et al.* 2000, Wang *et al.* 2000, among others), and also for other marine structures (Ueda & Rashed 1991, Moan *et al.* 1985). It is also noted that ISUM can readily be applied to the nonlinear analysis of land-based structures such as box girder bridges or cranes, bins and bunkers.

In the following sections, the most recent ISUM formulations for the nonlinear analyses of steel-plated structures are described.

13.4 The ISUM Beam–Column Unit

Figure 13.4 shows the ISUM beam–column unit with or without attached plating, the former being typically called the plate–stiffener combination model, i.e., a stiffener with attached plating. This unit has two nodal points, i.e., the node number 1 at the left end and the node number 2 at the right end.

A deflected (or buckled) beam–column member can be replaced by an equivalent straight (undeflected) member, but with the reduced axial stiffness due to the existence of the lateral deflection. This idealization leads to a decrease in the degrees of freedoms to be considered at each node. As a result, rotational degrees of freedom at each node are not always needed to represent the nonlinear behavior of the unit and only three translational degrees of freedom (i.e., in the x, y and z directions) at each node are included in the formulation of the ISUM unit.

Since the incremental method is used in ISUM analyses, the nodal force and displacement vectors of the beam–column unit are given in incremental form as follows:

$$\{\Delta R\} = \{\Delta R_{x1}\Delta R_{y1}\Delta R_{z1}\Delta R_{x2}\Delta R_{y2}\Delta R_{z2}\}^T \tag{13.1a}$$

$$\{\Delta U\} = \{\Delta u_1\Delta v_1\Delta w_1\Delta u_2\Delta v_2\Delta w_2\}^T \tag{13.1b}$$

where $\{\Delta R\}$ = nodal force increment vector, $\{\Delta U\}$ = nodal displacement increment vector.

The relationship between the nodal force increment and the nodal displacement increment can be expressed by

$$\{\Delta R\} = [K]\{\Delta U\} \tag{13.2}$$

where $[K]$ = tangent stiffness matrix, which is a nonlinear function of the nodal displacements.

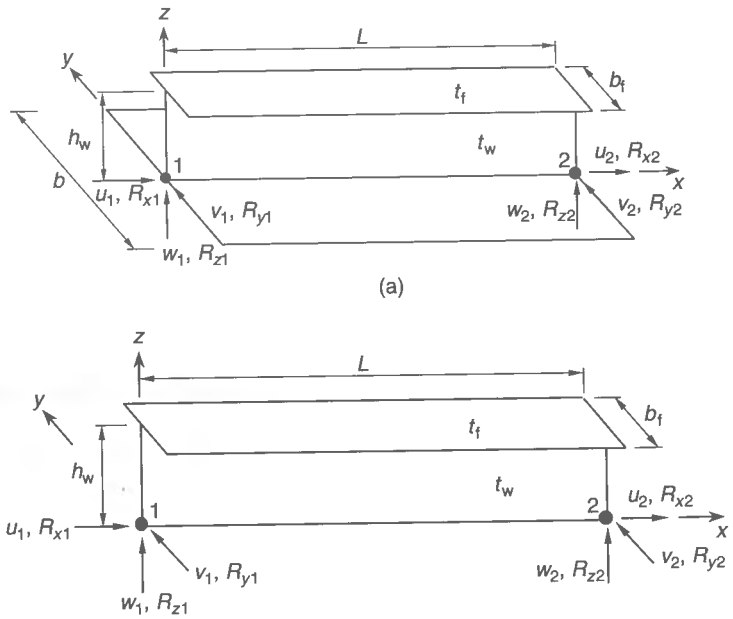

Figure 13.4 The ISUM beam–column unit (a) with and (b) without attached plating (●, nodal points)

As the applied loads increase, the beam–column unit can buckle or yield until the ultimate limit state (ULS) is reached. The tangent stiffness matrix, $[K]$, can then vary depending on the condition of such failures together with load application.

Figure 13.5 represents the idealized behavior of the beam–column unit for the purpose of ultimate strength analysis. In contrast to plates, this beam–column unit would not have reserve strength once buckling occurs, and thus the unit reaches the ULS immediately after buckling. The effect of strain hardening is usually neglected in the formulations of the unit, while it can of course be accounted for as necessary.

In the numerical computations, the end conditions of the unit can be applied in the same way as the conventional FEM. For instance, all of the three translational degrees of freedom may need to be restrained for a nodal point fixed in space.

However, it is important to realize that an ISUM unit will behave in accordance with the insights and knowledge built in by its developer. While one may of course try to idealize the nonlinear behavior of the unit under more relevant end conditions, the formulations presented in this section are for a beam–column unit that is simply supported at both ends.

The tangent stiffness matrix, $[K]$, of Equation (13.2) or the condition of failures of the beam–column unit under combined axial and lateral loads can be evaluated from the theory presented in Chapter 2. The tangent stiffness matrix of the failure-free unit, $[K]^{\mathrm{E}}$, is given by Equation (2.112). The ultimate load, P_{u}, or the gross yield capacity, P_{P}, can be obtained as described in Section 2.11.2. The tangent stiffness matrix of the beam–column unit in the post-ultimate regime, $[K]^{\mathrm{U}}$, is given by Equation (2.118). Table 13.1 summarizes these various idealizations of the ISUM beam–column unit. The validity of the ISUM beam–column unit is verified by comparison to the more refined nonlinear FEA in Section 2.11.4 of Chapter 2.

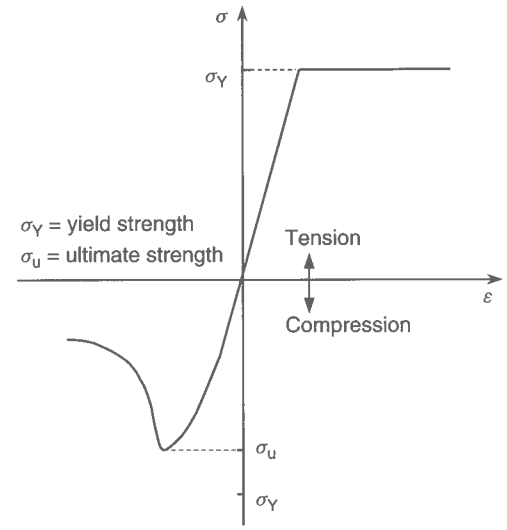

Figure 13.5 Idealized structural behavior of the ISUM beam–column unit for analysis of ultimate strength

Table 13.1 Summary of the idealizations for the ISUM beam–column unit.

Status	$[K]$ or failure condition
Failure-free regime	$[K] = [K]^{\mathrm{E}}$, Equation (2.112)
Ultimate strength	Section 2.11.2
Post-ultimate strength regime	$[K] = [K]^{\mathrm{U}}$, Equation (2.118)

13.5 The ISUM Rectangular Plate Unit for Analysis of Ultimate Strength

Figure 13.6 shows the ISUM rectangular plate unit which has four nodal points, i.e., one at each corner. A buckled (deflected) plate may be replaced by an imaginary flat (undeflected) plate, but with the corresponding reduced effective in-plane stiffness. In this case, rotational degrees of freedom at each nodal point are not always necessary to represent the nonlinear behavior of the ISUM rectangular plate. As a result, only three translational degrees of freedom at each corner nodal point are used to formulate the nonlinear response similar to the beam–column unit.

The nodal force increment vector, $\{\Delta R\}$, and the nodal displacement increment vector, $\{\Delta U\}$, of the ISUM rectangular plate unit are then given by

$$\{\Delta R\} = \{\Delta R_{x1}\Delta R_{y1}\Delta R_{z1}\ldots\Delta R_{x4}\Delta R_{y4}\Delta R_{z4}\}^T \tag{13.3a}$$

$$\{\Delta U\} = \{\Delta u_1\Delta v_1\Delta w_1\ldots\Delta u_4\Delta v_4\Delta w_4\}^T \tag{13.3b}$$

The relationship between the nodal force increments and the nodal displacement increments can also be given by Equation (13.2). Figure 13.7 represents the idealized behavior

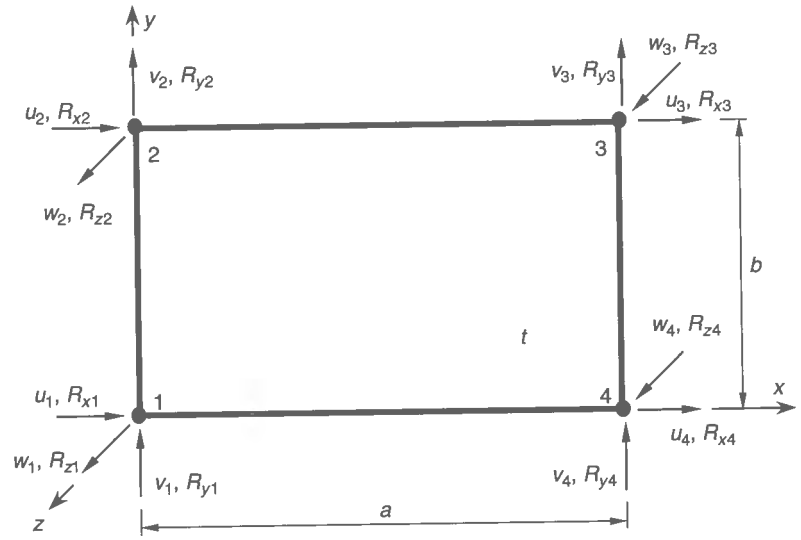

Figure 13.6 The ISUM rectangular plate unit (●, nodal points)

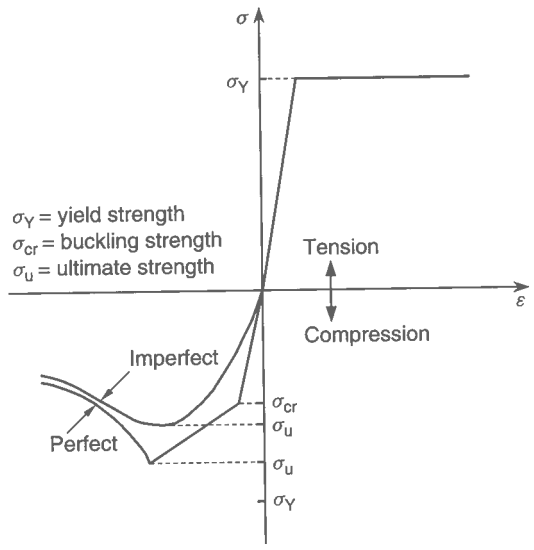

Figure 13.7 Idealized structural behavior of the ISUM rectangular plate unit for analysis of ultimate strength

of the ISUM rectangular plate unit until and after the ultimate strength is reached. In this case, the tangent stiffness matrices and the condition of the ULS behavior can be evaluated using the theory of plates under combined loads taking into account the effects of initial imperfections and other types of structural degradation, as presented in Chapters 4 and 12.

The tangent stiffness matrix of the failure-free unit, $[K]^E$, is calculated by taking into account the effects of both in-plane and out-of-plane large deformations and is given

Table 13.2 Summary of the idealizations of the ISUM rectangular plate unit for analysis of the ultimate strength.

Status	$[K]$, $[D]$ or failure condition
Failure-free regime	$[K] = [K]^E$, Equation (12.24), with $[D] = [D_p]^B$, Equation (4.48)
Yielding at node	Equation (1.7c)
Elastic–plastic regime before the ultimate strength	$[K] = [K]^P$, Equation (12.45), with $[D] = [D_p]^B$, Equation (4.48)
Ultimate strength	Equation (4.58)
Post-ultimate strength regime	$[K] = [K]^U = [K]^E$, Equation (12.24), with $[D] = [D_p]^U$, Equation (4.65)

Notes: $[K]$ = stiffness matrix, $[D]$ = stress–strain matrix.

by Equation (12.24) in Chapter 12 applying the updated Lagrangian approach. In this case, the stress–strain matrix, $[D]^E$, in Equation (12.24) is given by $[D]^E = [D_p]^B$ with Equation (4.48) in Chapter 4.

Before the unit reaches the ULS, the internal stresses at some nodal points may satisfy the Mises–Hencky yield condition, Equation (1.7c), and if so, plastic nodes are then inserted into the corresponding nodal points. In this case, the elastic–plastic stiffness matrix, $[K]^P$, of Equation (12.45) is applied.

The ISUM rectangular plate unit reaches the ultimate strength if Equation (4.58) of Chapter 4 is satisfied upon substituting the internal stress components. In the post-ultimate regime of the unit, the stress–strain matrix, $[D]^E$, in Equation (12.24) should be replaced by $[D_p]^U$, Equation (4.65), while the stiffness matrix of the collapsed unit, $[K]^U$, is still given by $[K]^E$ of Equation (12.24). Table 13.2 summarizes these various idealizations of the ISUM rectangular plate unit for analysis of the ultimate strength. The validity of the ISUM rectangular plate unit for analysis of the ultimate strength is verified in Section 4.10.2 of Chapter 4.

13.6 The ISUM Rectangular Plate Unit for Analysis of Collision and Grounding Mechanics

While the collision and grounding mechanics of a plate are also nominally represented by the ISUM rectangular plate unit with four nodal points, as shown in Figure 13.6, the characteristics of the unit for analysis of collision and grounding mechanics are different from those for analysis of ultimate strength. The relationship between the nodal force increment vector, $\{\Delta R\}$, and the nodal displacement increment vector, $\{\Delta U\}$, is also given by Equation (13.2) where $\{\Delta R\}$ and $\{\Delta U\}$ are defined by Equations (13.3).

Figure 13.8 shows the idealized behavior of the ISUM rectangular plate unit used for analysis of collision and grounding mechanics. As the predominantly compressive load increases, the unit crushes if a crushing condition is fulfilled. It is assumed that the internal stresses of the crushed unit are unchanged even if the compressive displacement increases. However, the folding process ends if the compressive strain of the unit exceeds a critical value. The unit behaves as a rigid body after the folding process ends. The crushed unit eventually reaches the gross yield condition as the crushing loads increase further.

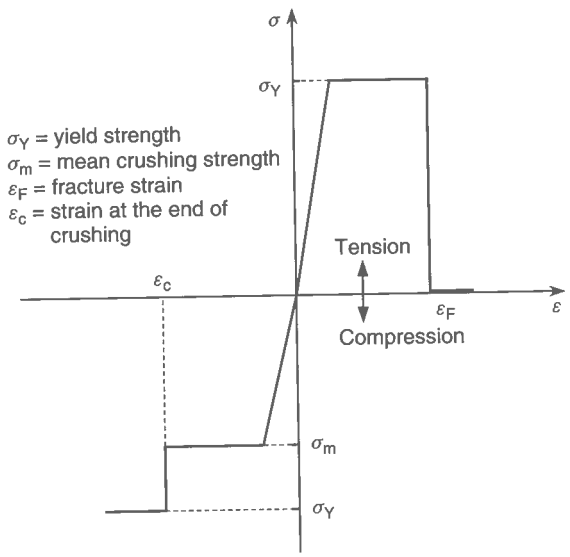

Figure 13.8 Idealized structural behavior of the ISUM rectangular plate unit for analysis of collision and grounding accident mechanics

On the other hand, with an increase in the predominantly tensile loads, some nodes of the unit will yield if the yield condition is satisfied and then plastic nodes are inserted into the corresponding nodal points. As long as all of the four nodes do not yield, the unit may not reach the gross yield condition, but it will show an elastic–plastic behavior. If the equivalent tensile strain exceeds the fracture strain, then ductile fracture takes place. The internal stresses of any fractured unit must be released, with the unit losing its resistive load capacity.

The tangent stiffness matrix of the failure-free unit, $[K]^E$, is given by Equation (12.24) in Chapter 12 applying the updated Lagrangian approach. As far as energy absorption capacity is concerned, the effect of initial deflections may be neglected. The stress–strain matrix, $[D]^E$, of Equation (12.24) is thus given by $[D]^E = [D_p]^E$ with Equation (3.1) in Chapter 3 until either crushing or yielding occurs. As the applied loads increase, the unit begins to be folded if the condition of crushing, Equation (9.49) in Chapter 9, is satisfied. The stress–strain matrix, $[D]^E$, of the crushed unit is assumed to become zero, while the tangent stiffness matrix is still calculated from Equation (12.24) of Chapter 12.

The folding process of the plate elements under crushing loads may stop if the folding length reaches a 'critical' value which is a function of the geometric and material properties of the plate. After the folding process ends, the unit behaves as a rigid body and thus the stress–strain matrix, $[D]^E$, may become infinite, e.g., with a very large magnitude of Young's modulus. However, if the internal stress components satisfy the yield condition (e.g., Equation (1.7c) in Chapter 1) at any node then a plastic node is inserted into the yielded node of the crushed unit and the elastic–plastic stiffness matrix of Equation (12.45) is applied. Under predominantly tensile loading, some nodes may yield if the yield condition, Equation (1.7c), is satisfied and the elastic–plastic stiffness matrix of Equation (12.45) is applied. The yielded unit may eventually rupture if the equivalent strain reaches the rupture strain. The ruptured unit releases its internal stresses and takes

Table 13.3 Summary of the idealizations of the ISUM rectangular plate unit for analysis of the collision and grounding mechanics.

Status	$[K]$, $[D]$ or failure condition
Failure-free regime	$[K] = [K]^E$, Equation (12.24), with $[D] = [D_p]^E$, Equation (3.1)
Crushing	Equation (9.49)
Post-crushing regime before the end of crushing	$[K] = [K]^E$, Equation (12.24), with $[D] = [0]$
End of crushing	$\varepsilon \geq \varepsilon_c$, where ε = applied compressive strain, ε_c = maximum crushing strain
Post-crushing regime after the end of crushing	$[K] = [K]^E$, Equation (12.24), with $[D] = [D]^E$, Equation (3.1), but with an infinite value of the elastic modulus
Ductile fracture	$\varepsilon_{eq} = \varepsilon_F$, where ε_{eq} = equivalent strain, ε_F = fracture strain
Post-ductile fracture before the end of stress release	$[K] = [K]^E$, Equation (12.24), with $[D] = [D_p]^E$, Equation (3.1), but with a negative value of the elastic modulus
End of stress release after ductile fracture	Internal stresses of the fractured unit must be zero
Post-ductile fracture regime after end of stress release	$[K] = [K]^E$, Equation (12.24), with $[D] = [0]$
Yielding at node	Mises–Hencky yield condition, Equation (1.7c)
Elastic–plastic regime after yield of nodes	$[K] = [K]^P$, Equation (12.45), with $[D] = [D_p]^E$, Equation (3.1)

Notes: $[K]$ = stiffness matrix, $[D]$ = stress–strain matrix, $[0]$ = zero matrix.

a zero value in the stress–strain matrix, $[D]^E$. Table 13.3 summarizes the idealizations of the ISUM rectangular plate unit for analysis of the collision and grounding mechanics.

13.7 The ISUM Stiffened Panel Unit for Analysis of Ultimate Strength

Figure 13.9 shows an ISUM stiffened panel unit. The panel with stiffeners in either one or both directions, bounded by support members, is modeled as a unit by means of the ISUM stiffened panel unit. When the stiffeners are relatively strong so that they would not fail prior to plating between stiffeners, the same panel may also be modeled as an assembly of rectangular plate units and beam–column units, the latter being without attached plating.

For a panel with relatively weak stiffeners so that the overall panel buckling mode may be predominant, or in other cases where the level of resolution likely to be obtained can be accommodated, however, the ISUM stiffened panel unit may be more appropriate.

Like the rectangular plate unit, the stiffened panel unit has four nodal points, i.e., one at every corner. The relationship between the nodal force increment vector, $\{\Delta R\}$, and the nodal displacement increment vector, $\{\Delta U\}$, is given by Equation (13.2) where $\{\Delta R\}$ and $\{\Delta U\}$ are defined by Equations (13.3).

While the collapse patterns of the stiffened panel unit are much more complex than those of the rectangular plate unit, the idealizations of both units are similar, as described

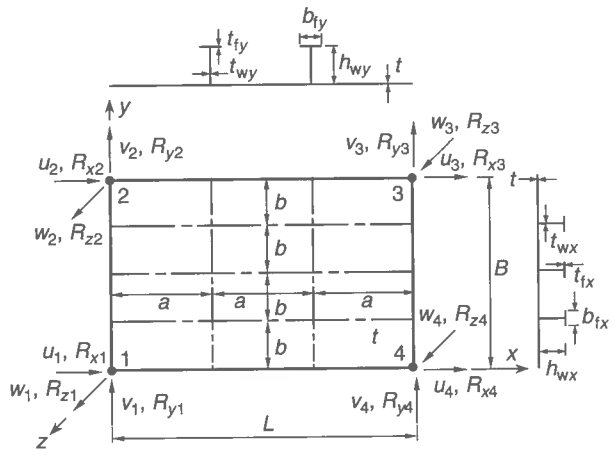

Figure 13.9 The ISUM stiffened panel unit (●, nodal points)

Table 13.4 Summary of the idealizations of the ISUM stiffened panel unit for analysis of the ultimate strength.

Status	$[K]$, $[D]$ or failure condition
Failure-free regime	$[K] = [K]^{E}$, Equation (12.24), with $[D] = [D_{sp}]^{B}_{O}$, Equation (6.31), for overall panel buckling mode, or $[D] = [D_{sp}]^{B}_{L}$, Equation (6.34), for local plate buckling mode
Yielding at node	Mises–Hencky yield condition, Equation (1.7c)
Elastic–plastic regime before the ultimate strength	$[K] = [K]^{P}$, Equation (12.45), with $[D]$ as defined in the failure-free regime above
Ultimate strength	Section 6.7
Post-ultimate strength regime	$[K] = [K]^{U} = [K]^{E}$, Equation (12.24), with $[D] = [D_{sp}]^{U}_{O}$, Equation (6.54), for overall panel collapse mode, or $[D] = [D_{sp}]^{U}_{L}$, Equation (6.55), for local plate collapse mode

Notes: $[K]$ = stiffness matrix, $[D]$ = stress–strain matrix.

in Section 13.5 or Figure 13.7. Table 13.4 summarizes the idealizations of the ISUM stiffened panel unit for analysis of the ultimate strength. The validity of the ISUM stiffened panel unit for analysis of the ultimate strength is verified in Section 6.8.2 of Chapter 6.

13.8 The ISUM Stiffened Panel Unit for Analysis of Collision and Grounding Mechanics

The geometry and dimensions of the ISUM stiffened panel unit for analysis of the collision and grounding mechanics are also represented similar to that of Figure 13.9. The unit has four nodal points, i.e., one at every corner nodal point. Each node has the three translational degrees of freedom. The force and displacement vectors of the unit can thus be given by Equations (13.3). The idealizations of the ISUM stiffened panel unit for

Table 13.5 Summary of the idealizations of the ISUM stiffened panel unit for analysis of the collision and grounding mechanics.

Status	$[K]$, $[D]$ or failure condition
Failure-free regime	$[K] = [K]^{E}$, Equation (12.24), with $[D] = [D_{sp}]^{E}$, Equation (5.4)
Crushing	Equation (9.49)
Post-crushing regime before the end of crushing	$[K] = [K]^{E}$, Equation (12.24), with $[D] = [0]$
End of crushing	$\varepsilon \geq \varepsilon_c$, where ε = compressive strain, ε_c = maximum crushing strain
Post-crushing regime after the end of crushing	$[K] = [K]^{E}$, Equation (12.24), with $[D] = [D_{sp}]^{E}$, Equation (5.4), but with an infinite value of the elastic modulus
Ductile fracture	$\varepsilon_{eq} = \varepsilon_F$, where ε_{eq} = equivalent strain, ε_F = fracture strain
Post-ductile fracture before the end of stress release	$[K] = [K]^{E}$, Equation (12.24), with $[D] = [D_{sp}]^{E}$, Equation (5.4), but with a negative value of the elastic modulus
End of stress release after ductile fracture	Internal stresses of the fractured unit must be zero
Post-ductile fracture regime after the end of stress release	$[K] = [K]^{E}$, Equation (12.24), with $[D] = [0]$
Yielding at node	Mises–Hencky yield condition, Equation (1.7c)
Elastic–plastic regime after yield of nodes	$[K] = [K]^{P}$, Equation (12.45), with $[D] = [D_{sp}]^{E}$, Equation (5.4)

Notes: $[K]$ = stiffness matrix, $[D]$ = stress–strain matrix, $[0]$ = zero matrix.

analysis of the collision and grounding mechanics can be made in a manner similar to that of the rectangular plate unit as described in Section 13.6 or Figure 13.8. Table 13.5 summarizes the various idealizations of the ISUM stiffened panel unit for analysis of the collision and grounding mechanics.

13.9 The ISUM Gap/Contact Unit

In collision or grounding accidents, the interface between the striking and the struck bodies will change. In this case, the gap and contact conditions between the two bodies are modeled by means of the gap/contact unit.

The gap/contact unit is a reduced type of the ISUM beam–column unit described in Section 13.4. The gap unit has two nodal points and each node has three translational degrees of freedom. In the structural modeling using the gap/contact unit, one node may be positioned at the striking body and the other at the struck body. The gap/contact unit may also be used for connecting two nodes which are both in the struck body as well.

Two such nodes are then connected by a gap/contact unit with nonlinear characteristics. As the striking body is pushed into the struck body, the length of the unit in the gap condition will be reduced without resistance, and eventually both nodes will come into contact. Coordinates of both nodes are updated at every incremental loading step. It is

considered that the unit is in the contact condition if the length of the unit becomes smaller than a prescribed tolerance.

The gap/contact units have only axial stiffness. In the gap condition, the unit does not carry any external forces, but under contact it behaves as a rigid body. Therefore, nearly zero stiffness is assumed for the gap condition, while a very large stiffness is assumed for the contact condition. The stiffness equation of the gap/contact unit may then be given, as follows:

$$\begin{Bmatrix} \Delta R_{x1} \\ \Delta R_{x2} \end{Bmatrix} = \frac{E_{gc}A}{L} \begin{bmatrix} 1 & -1 \\ -1 & 1 \end{bmatrix} \begin{Bmatrix} \Delta u_1 \\ \Delta u_2 \end{Bmatrix} \tag{13.4}$$

where A = cross-sectional area. It may be assumed that $E_{gc} = E \times 10^{-7}$ for the gap condition or $E_{gc} = E \times 10^{7}$ for the contact condition, where E = elastic modulus.

In practice, some axial stresses may develop in the gap/contact unit because the assumed stiffness is neither zero nor infinite, but this effect is generally quite small and negligible. Also, the node positioned at the striking body and the other node at the struck body may 'overlap' if the increment of axial deformation is too large, but this problem can be overcome by using small load increments.

13.10 Treatment of Dynamic/Impact Load Effects

Ship collision or grounding accidents are dynamic in nature, and this fact will affect the crushing and rupture response of structures as previously described in Chapter 9. Three aspects of a dynamic loading situation are possibly relevant, namely material strain rate sensitivity, inertia effects and dynamic frictional effects. With an increase in the strain rate for steel, the yield strength of the material increases and the rupture strain may decrease. Due to inertia effects, deformation patterns may be varied. Also, it is known that as the speed of dynamic loading increases, the coefficient of friction becomes lower.

When dynamic loads are applied, the crushing response is mainly affected by the material strain rate sensitivity. During the crushing response, the material strain rate generally varies with displacements. For simplicity, however, the average value of the strain rate during the dynamic loading phase may be used. The average strain rate for rectangular plates or stiffened plates can be approximately estimated by considering that the loading speed is linearly reduced to zero until the accidental loading is finished. Therefore, the strain rate, $\dot{\varepsilon}$, of the ISUM units under accidental loads may be approximated to

$$\dot{\varepsilon} \approx \frac{1}{\delta}\frac{V_0 + 0}{2} = \frac{V_0}{2\delta} \tag{13.5}$$

where δ = average displacement, V_0 = initial speed of impact load.

To estimate the dynamic yield strength of the material, the Cowper–Symonds equation, Equation (9.17), has been widely used. The crushing effects and yield strength increase as the collision speed gets faster, while any rupture or tearing of steel occurs earlier. Equation (9.18) may be employed to estimate the dynamic rupture strain, which is the inverse of the Cowper–Symonds equation for the dynamic yield stress.

As previously noted in Section 9.3.4 of Chapter 9, the inertia effects may be ignored when the strain rates are less than about 50/s. On the other hand, the friction effects may play an important role during the grounding process as noted in Section 9.3.5, while they

can be ignored for crushing of structures since the relative velocity between striking and struck bodies is then normally comparatively small.

In the ISUM calculations of crushing and rupture behavior taking account of dynamic effects, the theoretical developments derived for a quasi-static condition are employed, but with the use of the dynamic yield stress or the dynamic fracture strain in place of their static counterparts.

13.11 Computer Software ALPS/ISUM

13.11.1 Outline of the Computer Software

The ISUM theory described in this chapter is automated within the computer program ALPS/ISUM, which stands for the nonlinear analysis of large plated structures using the idealized structural unit method. ALPS/ISUM can quickly and accurately simulate the progressive collapse behavior of steel-plated structures under either extreme or accidental loading. ALPS/ISUM has three main modules for different purposes:

- ALPS/GENERAL;
- ALPS/HULL; and
- ALPS/SCOL.

ALPS/GENERAL simulates the progressive collapse behavior of general steel-plated structures, e.g., box girder bridges, box girder cranes, ship structures (e.g., double bottoms, decks, side shells or entire ships), offshore platform decks, individual structural elements (e.g., stiffened panels, plates, beam–columns) under extreme loading. ALPS/HULL is a special purpose module for the automated calculation of the progressive collapse analysis of ship hulls under extreme hull girder loads which can include any combination of vertical bending, horizontal bending, sectional shear and torsion. ALPS/SCOL simulates the structural crashworthiness of steel-plated structures (e.g., ships) under crushing loads arising from accidents such as ship collisions or stranding.

In ALPS/ISUM computations, the applied loads are incrementally increased. While ALPS/GENERAL and ALPS/HULL computations may typically continue either until or after the ultimate strength of the whole structure is reached, ALPS/SCOL may continue until the initial kinetic energy in the accident is entirely absorbed or dissipated.

Any execution of ALPS/ISUM generates a variety of important information at each incremental loading step, which will be recorded in the output data files. The output data of ALPS/ISUM at each incremental loading step include:

- Nodal forces and nodal displacements (all modules);
- Stresses and strains of every ISUM unit (all modules);
- Structural failure status and modes of every ISUM unit (all modules);
- Ship hull cross-section data, e.g., moment of inertia, section moduli, neutral axis (ALPS/HULL module only);
- Data to draw the relationship between hull girder loads and displacements, e.g., the vertical bending moment versus curvature curve (ALPS/HULL module only); and
- Data to draw the variation of neutral axis position of ship hull cross-section (ALPS/HULL module only).

The ALPS/ISUM program together with the user's manual can be downloaded from the web site given in the appendices to this book.

13.11.2 Application Examples

Progressive Collapse Analysis of a Cantilever Box Girder

The ultimate strength of a cantilever box girder is analyzed by ISUM and conventional nonlinear FEM (ANSYS 1999). The box girder is fixed at one end and free at the other end, and it is subjected to a uniformly distributed load at the free end, as shown in Figure 13.10. The cross-section of the structure is square, while three transverse diaphragms are arranged within. The dimensions, material properties and initial imperfections of individual plate elements are as follows:

- Plate units: $a \times b \times t = 1000 \times 1000 \times 15\,\text{mm}$
- Young's modulus: $E = 205.8\,\text{GPa}$
- Yield stress: $\sigma_Y = 352.8\,\text{MPa}$
- Poisson's ratio: $\nu = 0.3$
- Initial deflection: $w_{0pl}/t = 0.15$
- Welding residual stresses: $\sigma_{rcx} = \sigma_{rcy} = 0.0$.

Figures 13.11 and 13.12 show typical examples of structural modeling for use by ANSYS and ALPS/GENERAL, respectively. In ISUM modeling, each plate element is modeled as one ISUM rectangular plate unit, while a number of fine meshes are used in conventional finite element modeling where a half of the box girder with respect to the center line is taken as the extent of conventional nonlinear FEA, considering the symmetric behavior. Figure 13.13 shows the applied load versus deflection curves at the free end of the structure, as obtained by ANSYS and ALPS/GENERAL computations.

For reference, the plastic collapse load of a cantilever beam can be predicted from Equation (2.35) in Chapter 2 when local buckling is not accounted for. The result is as follows:

$$P_c = \frac{M_p}{L} = \frac{1}{4000}\frac{36}{4}(1000^3 - 970^3) \times 9.8 = 1925.56\,\text{kN}.$$

Figure 13.13 also notes selected structural failure events, as obtained by ALPS/GENERAL. As the applied loads increase, the compressed flange near the fixed end collapses and the box girder reaches the ultimate strength it the transverse floors near the fixed end fail. It is of benefit to structural designers to have detailed information about the progressive collapse behavior until the ultimate strength is reached. It is seen from Figure 13.13 that the ISUM results correlate well with the more refined nonlinear FEA.

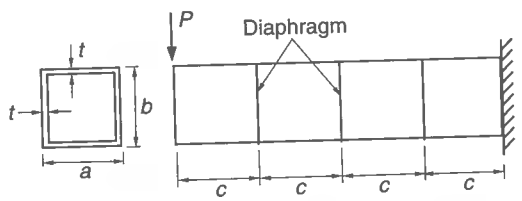

Figure 13.10 An internally stiffened cantilever box girder

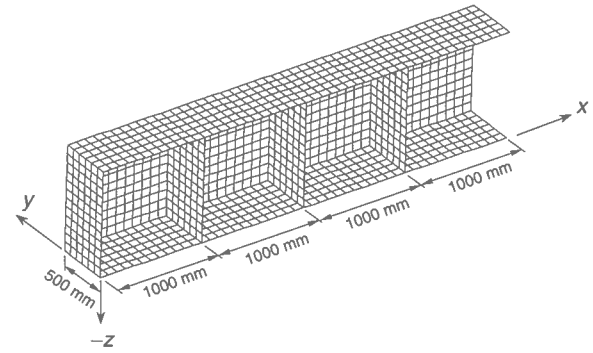

(a)

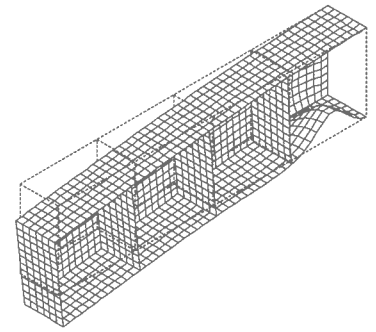

(b)

Figure 13.11 (a) Undeformed and (b) deformed shape for the conventional nonlinear finite element model for the cantilever box girder at the ULS

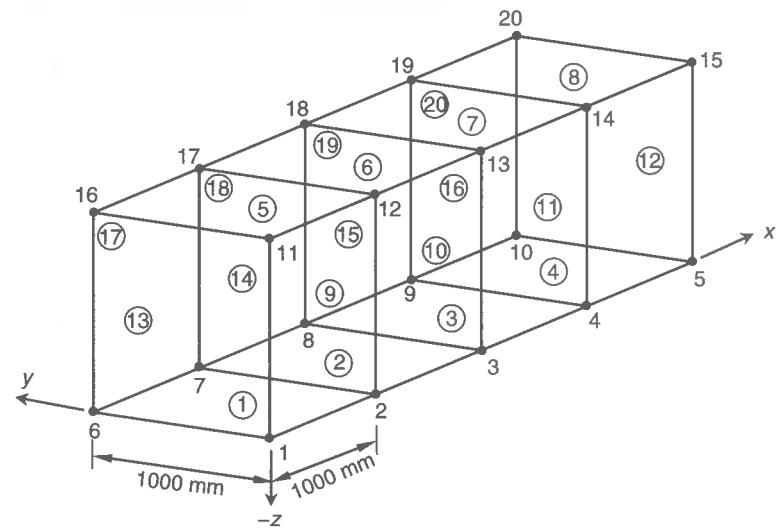

Figure 13.12 ALPS/GENERAL model for the cantilever box girder

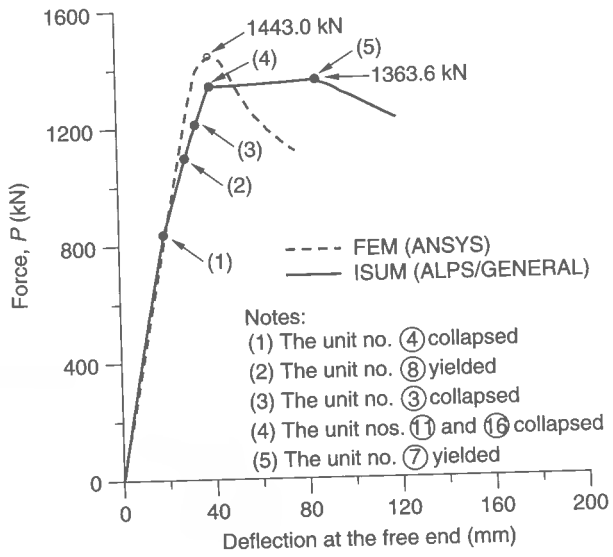

Figure 13.13 The force versus deflection curves at the free end of the cantilever box girder, as obtained by ISUM and conventional nonlinear FEM

Interestingly, the computing time used was 2 minutes for the ISUM analysis and 4.5 hours for the FEA using a Pentium III personal computer. The structural modeling effort for the ISUM analysis is also much smaller than that for FEA.

Progressive Collapse Analysis of a Box Column

The ultimate strength of a box column is analyzed in this example by ISUM and conventional nonlinear FEM (ANSYS 1999). The structure is simply supported at both ends, as shown in Figure 13.14. It has a number of transverse diaphragms (floors). The dimensions, material properties and initial imperfections of the structure are as follows:

- Plate elements: $a \times b \times t = 500 \times 500 \times 7.5\,\text{mm}$
- Young's modulus: $E = 205.8\,\text{GPa}$
- Yield stress: $\sigma_Y = 352.8\,\text{MPa}$
- Poisson's ratio: $\nu = 0.3$
- Initial deflection function of plate elements: $A_0/t = 0.05$
- Column-type initial deflection function for the whole structure: $w_0 = \delta_0 \sin(\pi x/L)$ where $\delta_0/L = 0.0015$
- Welding residual stresses: $\sigma_{rcx} = \sigma_{rcy} = 0.05$ for ISUM analysis and $\sigma_{rcx} = \sigma_{rcy} = 0.0$ for ANSYS analysis.

Figures 13.15 and 13.16 show typical examples of structural modeling for this case, by conventional FEM (ANSYS 1999) and ALPS/GENERAL, respectively. In ISUM modeling, each plate element is modeled as one ISUM rectangular plate unit and, due to the symmetry, a half length of the box column is taken as the extent of analysis. For conventional nonlinear FEA, a quarter of the box column is subdivided into a number

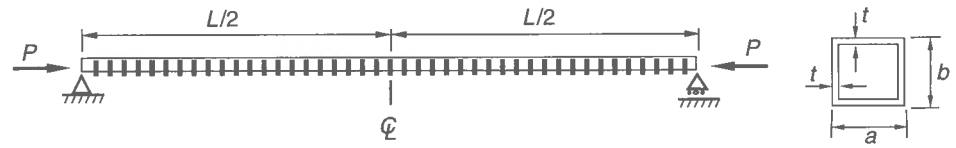

Figure 13.14 A box column with both ends simply supported

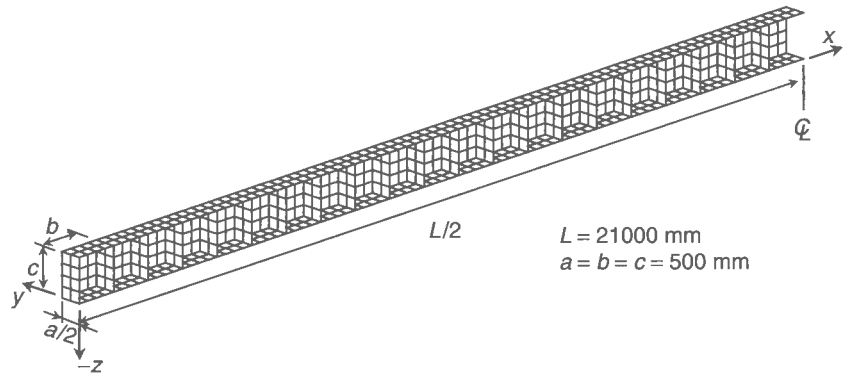

Figure 13.15 Conventional finite element model for a quarter region of the box column

of fine meshes. For convenience related to computational effort, some coarse meshing was adopted for the conventional nonlinear FEA such that the local plate buckling effect (i.e., local geometric nonlinearity) is not taken into consideration in the ANSYS analysis, although the influence of plasticity (material nonlinearity) and column-type buckling (global geometric nonlinearity) is accounted for.

Figure 13.17 shows the axial compressive load versus mid-span deflection curves for the box column. The Euler elastic column buckling load, which neglects the influence of local plate buckling, is also plotted in the figure. With the structure involving both local and global buckling, the ultimate buckling strength of the box column is about 67% of the Euler column buckling load. It is evident that the effect of local geometric nonlinearity as well as global geometric nonlinearity is of crucial importance for nonlinear analysis of slender structures (e.g., box column). Interestingly, the computing time used was 3 minutes for the ISUM analysis and 6 hours for the FEA using a Pentium III personal computer.

Progressive Collapse Analysis of a Ship Hull under Vertical Moment

A physical test for investigating the progressive collapse characteristics under vertical sagging moment was undertaken on a welded steel frigate ship structure model of 1/3 scale to the original ship dimensions (Dow 1991, Yao *et al.* 2000). ALPS/HULL is now used to analyze the progressive collapse behavior of the Dow test model and the results are then compared to the experimental results. In the ALPS/HULL computations, both sagging and hogging cases are considered.

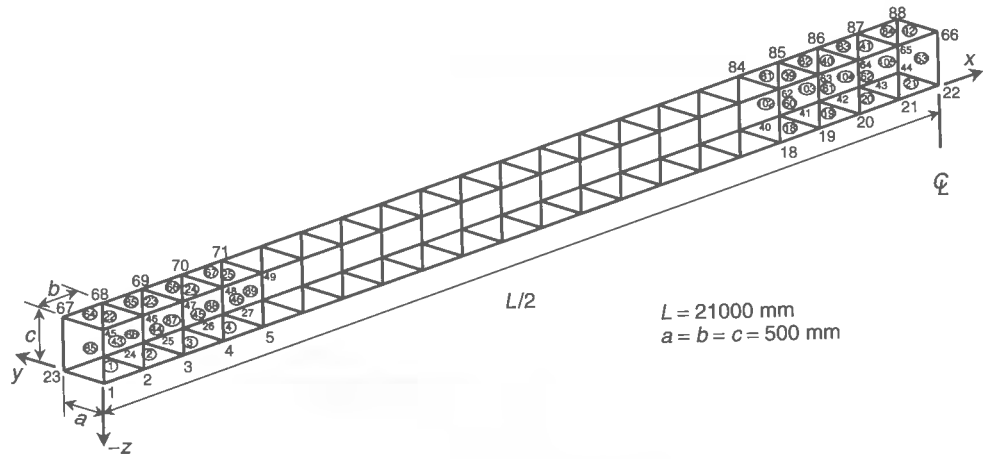

Figure 13.16 ALPS/GENERAL model for a half length of the box column

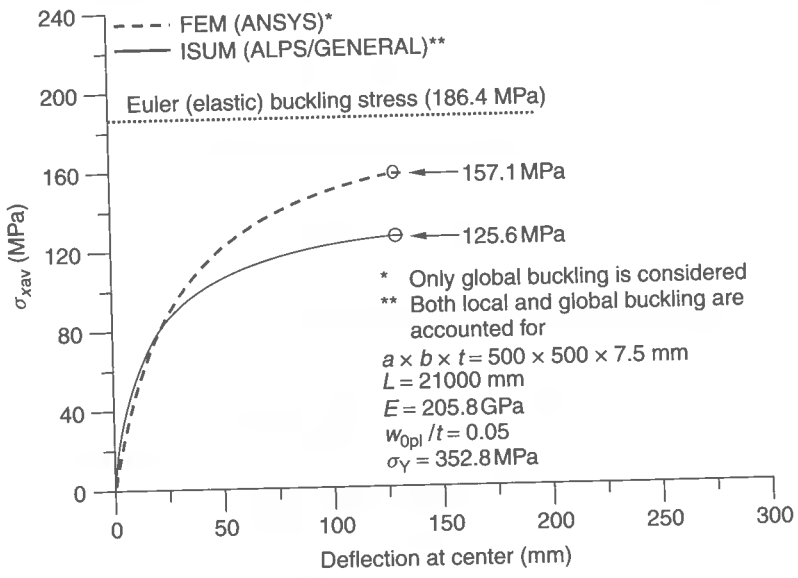

Figure 13.17 The axial compressive load versus deflection curves of the box column, as obtained by ISUM and conventional nonlinear FEM

Figure 13.18 shows the ALPS/HULL model for the test structure. For simplicity, the hull module between two transverse frames is taken as the extent of the present analysis, while it is not difficult to take the entire structure as the extent of the ISUM analysis if needed. Plating between stiffeners is modeled using the ISUM rectangular plate unit and stiffeners without attached plating are modeled using the ISUM beam–column unit. The webs of deep girders in bottom structures are also modeled using the ISUM rectangular plate units, while their flanges are modeled using the ISUM beam–column units.

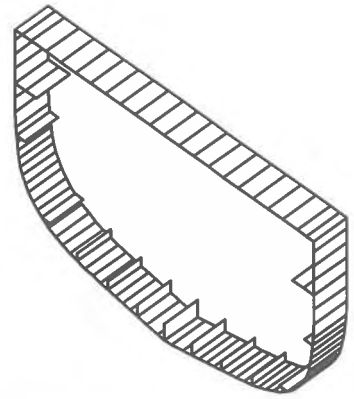

Figure 13.18 ALPS/HULL model for the progressive collapse analysis of the Dow frigate test structure

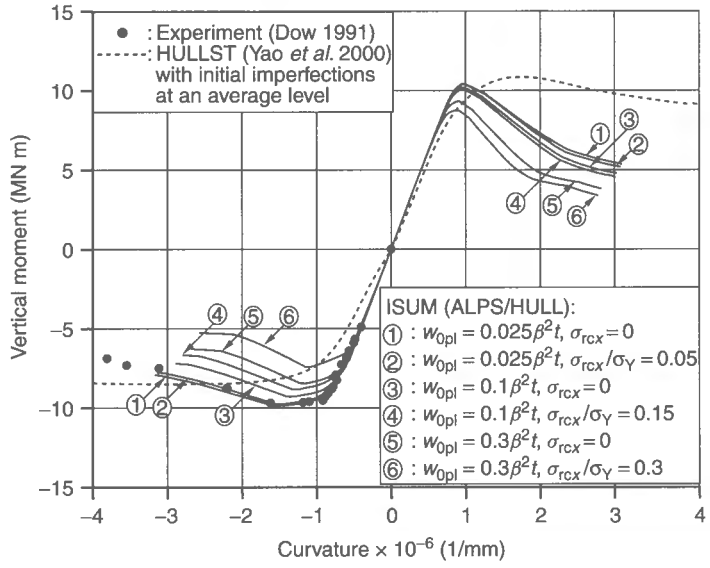

Figure 13.19 Progressive collapse behavior of the Dow test structure under vertical moment

Figure 13.19 shows the progressive collapse behavior of the Dow test structure under sagging or hogging moment, as obtained by ALPS/HULL. The Dow test result for sagging is also plotted. In the ALPS/HULL computations, the magnitude of initial imperfections is varied. Figure 13.19 also plots the results of Yao *et al.* (2000) as obtained using the Smith method which models the structure as an assembly of only plate–stiffener combinations. It is seen from Figure 13.19 that ALPS/HULL provides quite accurate results when compared to the experiment. Interestingly, the computing time used was 2 minutes for the ISUM analysis using a Pentium III personal computer.

As another example, the 105 000 dwt double hull tanker hull with one center–longitudinal bulkhead as shown in Figure 8.4(b) of Chapter 8 is now analyzed with a view

to illustrate the influence of structural idealization techniques on the progressive collapse behavior under vertical bending. Based on the structural idealization techniques previously noted in Section 13.2, six types of ALPS/HULL modeling methods are considered as shown in Figure 13.20. As the extent of the analysis, the first five models (i.e., models I to V) take a single hull segment between two adjacent transverse frames or floors, while model VI takes one cargo hold between two transverse bulkheads.

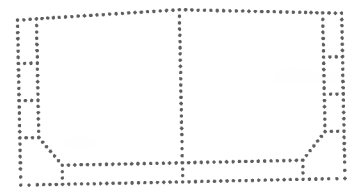

(a) Number of plate units = 0, number of beam–column units = 282, number of stiffened panel units = 0

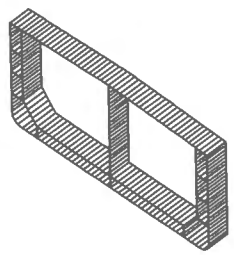

(b) Number of plate units = 293, number of beam–column units = 255, number of stiffened panel units = 0

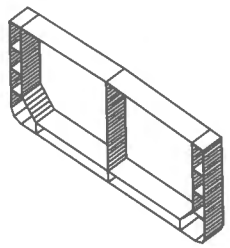

(c) Number of plate units = 145, number of beam–column units = 111, number of stiffened panel units = 19

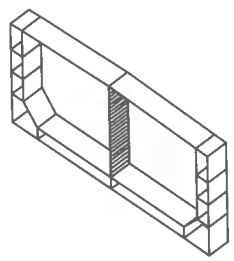

(d) Number of plate units = 59, number of beam–column units = 23, number of stiffened panel units = 35

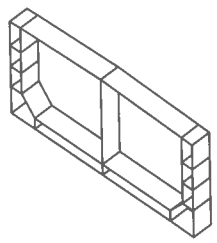

(e) Number of plate units = 36, number of beam–column units = 0, number of stiffened panel units = 36

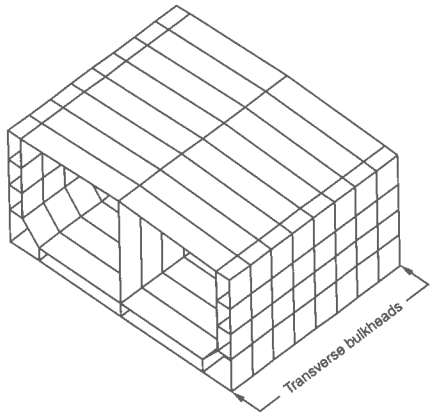

(f) Number of plate units = 372, number of beam–column units = 0, number of stiffened panel units = 288

Figure 13.20 (a)–(f) ALPS/HULL models I–VI, respectively, for the double hull tanker with one center–longitudinal bulkhead

Model I idealizes the structure as an assembly of plate–stiffener combination models. In model II, the entire structure is idealized by the plate–stiffener separation elements. While deck and bottom stiffened panels in models III and IV are modeled by the stiffened panel units, model III idealizes all vertical members using the plate–stiffener separation elements, and model IV models the center-longitudinal bulkhead using the plate–stiffener separation elements. In model V, all members are modeled by the stiffened panel units. It is supposed that individual ISUM units have a slight level of initial imperfections in the form of initial deflection and residual stresses; buckling mode initial deflection of plating = 5% of the plate thickness, residual stress = 5% of the yield stress, column-type initial deflection of stiffeners (plate–stiffener combinations) = 0.15% of the member length.

Figure 13.21 shows the progressive collapse behavior of the ship hull under vertical bending moment. It is observed that the results obtained from the six types of ALPS/HULL modeling considered are similar, except for model I in sagging which tends to underestimate the ultimate bending capacity. A similar tendency for model I using only the plate–stiffener combination elements is also found from the HULLST results of Yao *et al.* (2000) as shown in Figure 13.19. This implies that the plate–stiffener combination models for relatively light structures (e.g., deck panels) under predominantly compressive loads may not be relevant as previously described in Section 2.1 of Chapter 2.

In this regard, the simpler models extending between two adjacent transverse web frames may usually be relevant for the progressive collapse analysis of ship hulls, at least in this case where lateral pressure effects are not present. However, the modeling method of model I using only the plate–stiffener combination elements may not be appropriate for the progressive collapse analysis of ship hulls under sagging moment.

Internal Collision Mechanics Analysis of an LNG Carrier Side Structure

As a hypothetical collision scenario, it is now considered that the bow of an LNG (liquefied natural gas) carrier with the same size as the object LNG carrier strikes the mid-side

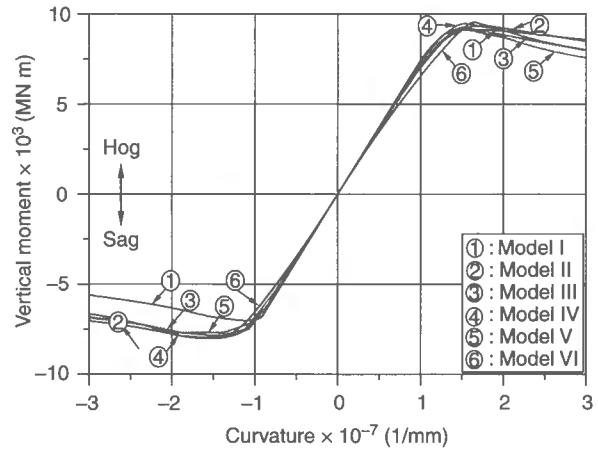

Figure 13.21 A comparison of the progressive collapse behavior of the double hull tanker hull with one center–longitudinal bulkhead under vertical bending moment as obtained by the various modeling methods

structure of the object LNG carrier (Paik *et al.* 2002). At the initiation of the collision event, the striking ship operates at 50% of the full design speed, while the struck LNG carrier is considered to be at standstill at a pier.

The penetrating depth of the striking ship from the initial contact to the boundary of the LNG cargo tanks or to the bow position which may cause the fracture of LNG cargo tanks varies in accordance with the fore-end shape of the striking ship and the initial contact positions and related details for the two ships. The bulbous bow shape under the sea water level and/or the fore-end shape of the striking ship determine the initial contact position for the two ships and may also affect the absorbed energy in the side structure of the struck ship.

Both the striking and struck LNG carriers are assumed to be in the full-load condition. Two computer programs, namely MSC/DYTRAN (1998) and ALPS/SCOL, are used to obtain the collision force–penetration curves as the collision proceeds. Figures 13.22 and 13.23 represent the structural models used for MSC/DYTRAN and ALPS/SCOL, respectively.

In the MSC/DYTRAN model, the entire ship structure is included using fine meshes around the impact location, while coarse meshes are used at the other parts away from the collision location. In the ALPS/SCOL model, a quarter of the mid-ship cargo hold of the struck ship including the LNG tank together with the striking ship bow are taken as the extent of the analysis, using ISUM plate and stiffened panel units to model the struck structures and gap/contact units to represent the gap and contact conditions between the struck ship side and the striking ship bow.

In the MSC/DYTRAN computations, the motion of both the striking and struck ships with the surrounding water is taken into consideration, while the ALPS/SCOL computations assume that the struck ship is fixed when the striking ship penetrates with a constant speed. In both models, it is assumed that the striking ship bow is a rigid body which does not dissipate any strain energy.

The fracture strain of the structural members in both ship hull and cargo tank structures is supposed to be 10% in the ALPS/SCOL models which use large-sized elements, while it is assumed to be 20% in the MSC/DYTRAN models which use fine meshes. This is because the MSC/DYTRAN method using a fine mesh can automatically handle the localized tearing behavior inside the plate members, while the ALPS/SCOL method using

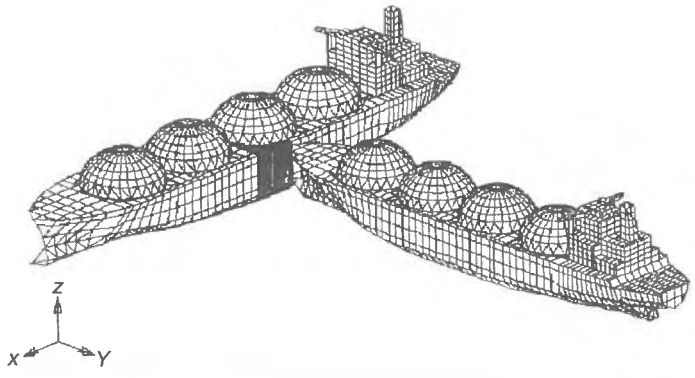

Figure 13.22 MSC/DYTRAN model for the LNG carrier collision

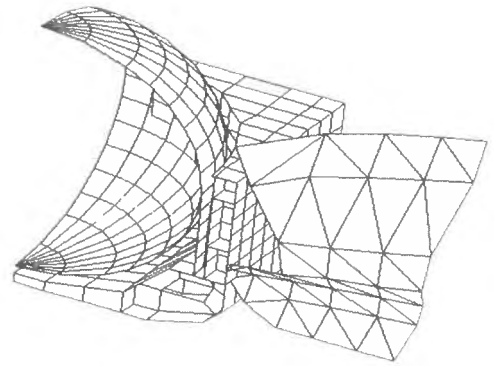

Figure 13.23 ALPS/SCOL model for the LNG carrier collision

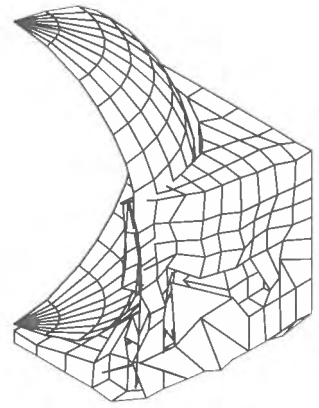

Figure 13.24 Deformed shape of the ALPS/SCOL model immediately after the struck LNG cargo tank starts to fracture

large-sized elements must necessarily account for such behavior at a macroscopic level. In the failure state of finite elements, the strain is typically concentrated at the tip of the crack or around the fractured area. The representative fracture strain should then become smaller in large-sized elements to properly account for the effect of localized fracture inside the plate unit. Hence in the ALPS/SCOL model, a fracture strain that is likely to be more characteristic of weld metal fracture is used. With the larger value of fracture strain, the energy absorption capability of the structure will of course increase.

The computations were continued until the struck LNG carrier reaches the accidental limit states in the following two conditions: (1) the striking ship bow penetrates the boundary of the struck ship cargo tank, and (2) the LNG cargo tanks start to rupture. In reality, the energy dissipation capability of the struck LNG carrier must be evaluated at the earlier of these two limiting conditions.

Figure 13.24 shows the deformed shape of the ALPS/SCOL model. Figures 13.25 and 13.26 show the collision force–penetration curves and the absorbed energy–penetration curves, respectively, the two curves in each figure being obtained by MSC/DYTRAN and ALPS/SCOL. Oscillations in the force–penetration curves obtained by MSC/DYTRAN

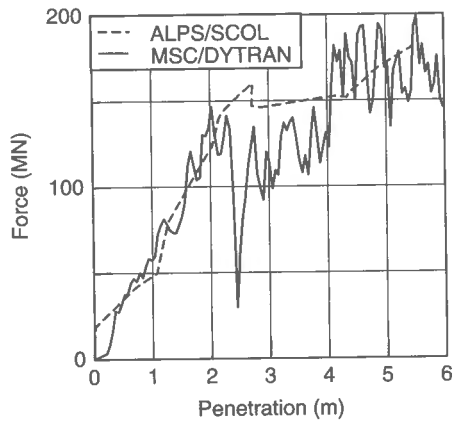

Figure 13.25 The collision force–penetration curves

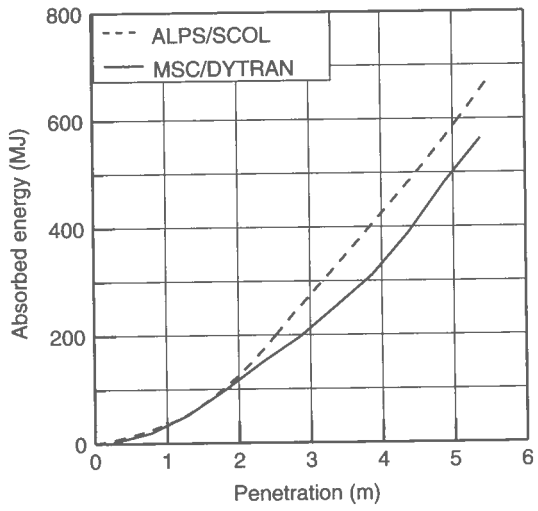

Figure 13.26 The absorbed energy–penetration curves

are primarily due to simulation based on the time-variant impact theory. Also, the behavior of localized failure including tearing and folding is more accurately described by the MSC/DYTRAN method using very fine meshes, while the ALPS/SCOL method is more concerned with an 'average' nature of the failure response.

As is evident, both MSC/DYTRAN and ALPS/SCOL predictions correlate relatively well. The energy dissipation capability of the struck LNG carrier so quantified may be used for purposes of design stage damage tolerance and safety assessment.

Interestingly, the computing time used for the ALPS/SCOL analysis in this case was about 2 hours using a Pentium III personal computer, while it was more than 14.4 hours for the MSC/DYTRAN analysis using the SGI Power Challenge XL Series computer. As is evident, the computational efficiency of ISUM will be of benefit when quick estimates are important, such as for carrying out a series of collision analyses with a variety of accident scenarios, or for the routine damage tolerance and safety assessment of designs.

References

ANSYS (1999). *User's manual (Version 5.6)*. ANSYS Inc., Canonsburg, PA.

Bai, Y., Bendiksen, E. & Pedersen, P.T. (1993). Collapse analysis of ship hulls. *Marine Structures*, 6:485–507.

Brown, A., Tikka, K., Daidola, J.C., Lutzen, M. & Choe, I.H. (2000). Structural design and response in collision and grounding. *SNAME Transactions*, 108:447–473.

Dow, R.S. (1991). Testing and analysis of 1/3-scale welded steel frigate model. *Proceedings of the International Conference on Advances in Marine Structures, Dunfermline, Scotland*, 749–773.

Fujikubo, M., Kaeding, P. & Yao, T. (2000). ISUM rectangular plate element with new lateral shape function – longitudinal and transverse thrust. *Journal of the Society of Naval Architects of Japan*, 187:209–219.

Masaoka, K., Okada, H. & Ueda, Y. (1998). A rectangular plate element for ultimate strength analysis. Proceedings of the 2nd International Conference on Thin-Walled Structures, Singapore, 1–8.

Moan, T., Amdahl, J., Engseth, A.G. & Granli, T. (1985). Collapse behavior of truss work steel platforms. *Proceedings of the 4th International Conference on Behavior of Offshore Structures (BOSS'85), Delft, The Netherlands, July*. Elsevier, Amsterdam, 255–268.

MSC/DYTRAN (1998). *User's manual (Version 4.5)*. The MacNeal Schwendler Corp., Los Angeles, CA.

Paik, J.K. (1987). Ultimate strength analysis of ship structures using the idealized structural unit method. Dr. Eng. Dissertation, Osaka University (in Japanese).

Paik, J.K. (1995). Advanced idealized structural units considering the excessive tension deformation effects. *Journal of Hydrospace Technology*, 1(1):125–145.

Paik, J.K. & Pedersen, P.T. (1996). Modeling of the internal mechanics in ship collisions. *Ocean Engineering*, 23(2):107–142.

Paik, J.K., Thayamballi, A.K. & Che, J.S. (1996). Ultimate strength of ship hulls under combined vertical bending, horizontal bending, and shearing forces. *SNAME Transactions*, 104:31–59.

Paik, J.K., Chung, J.Y., Choe, I.H., Thayamballi, A.K., Pedersen, P.T. & Wang, G. (1999). On rational design of double hull tanker structures against collision. *SNAME Transactions*, 107: 323–363.

Paik, J.K., Choe, I.H. & Thayamballi, A.K. (2002). Predicting resistance of spherical-type LNG carrier structures to ship collisions. *Marine Technology*, 39(2): 86–94.

Paik, J.K., Thayamballi, A.K., Pedersen, P.T. & Park, Y.I. (2001). Ultimate strength of ship hulls under torsion. *Ocean Engineering*, 28:1097–1133.

Smith, C.S. (1977). Influence of local compressive failure on ultimate longitudinal strength of ship's hull. *Proceedings of the International Symposium on Practical Design in Shipbuilding, Tokyo*, 73–79.

Ueda, Y. & Rashed, S.M.H. (1974). An ultimate transverse strength analysis of ship structures. *Journal of the Society of Naval Architects of Japan*, 136:309–324 (in Japanese).

Ueda, Y. & Rashed, S.M.H. (1984). The idealized structural unit method and its application to deep girder structures. *Computers & Structures*, 18(2):277–293.

Ueda, Y. & Rashed, S.M.H. (1991). Advances in the application of ISUM to marine structures. *Proceedings of the 2nd International Conference on Advances in Marine Structures, Dunfermline, Scotland, May*, 628–649.

Ueda, Y., Rashed, S.M.H., Nakacho, K. & Sasaki, H. (1983). Ultimate strength analysis of offshore structures – application of idealized structural unit method. *Journal of the Kansai Society of Naval Architects of Japan*, 190:131–142 (in Japanese).

Ueda, Y., Rashed, S.M.H. & Paik, J.K. (1984). Plate and stiffened plate units of the idealized structural unit method (1st report) – under in-plane loading. *Journal of the Society of Naval Architects of Japan*, 156:389–400 (in Japanese).

Ueda, Y., Rashed, S.M.H. & Paik, J.K. (1986a). Plate and stiffened plate units of the idealized structural unit method (2nd report) – under in-plane and lateral loading considering initial deflection and residual stress. *Journal of the Society of Naval Architects of Japan*, 160:321–339 (in Japanese).

Ueda, Y., Rashed, S.M.H., Paik, J.K. & Masaoka, K. (1986b). The idealized structural unit method including global nonlinearities – idealized rectangular plate and stiffened plate elements. *Journal of the Society of Naval Architects of Japan*, 159:283–293 (in Japanese).

Wang, G., Arita, H. & Liu, D. (2000). Behavior of a double hull in a variety of stranding or collision scenarios. *Marine Structures*, 13:147–187.

Yao, T., Astrup, O.C., Caridis, P., Chen, Y.N., Cho, S.R., Dow, R.S., Niho, O. & Rigo, P. (2000). Ultimate hull girder strength. *Report of the ISSC Special Task Committee VI.2, International Ship and Offshore Structures Congress*. Elsevier, Amsterdam, 2:321–391.

Appendices

A.1 How to Download the Computer Programs Presented in This Book

The computer programs introduced in this book can be downloaded together with the related user manuals and selected application examples from an Internet web site. To do this, visit the web site of the Ship Structural Mechanics Laboratory of the Pusan National University, Busan, Korea, at http://ssml.naoe.pusan.ac.kr. The computer programs may be occasionally updated so that the users are recommended to visit the web site to download the most up-to-date version. Those who have any questions on the computer programs and illustrative problems may contact Prof. J.K. Paik using his e-mail address jeompaik@pusan.ac.kr.

A.2 Source Listing of the FORTRAN Computer Program CARDANO

Consider a third-order equation with regard to an unknown variable, W, given by

$$C_1 W^3 + C_2 W^2 + C_3 W + C_4 = 0$$

This equation can be solved by the so-called Cardano method. The following is the source listing of FORTRAN subroutine CARDANO to solve the above equation.

```
      SUBROUTINE CARDANO(C1,C2,C3,C4,W)
      IMPLICIT REAL*8(A-H,O-Z)
      C
      C*** C1*W**3+C2*W**2+C3*W+C4=0
      C*** INPUT: C1,C2,C3,C4
      C*** OUTPUT: W
      C     PROGRAMMED BY PROF. J.K. PAIK
      C     (C) J.K. PAIK. ALL RIGHTS RESERVED.
      C
            S1=C2/C1
            S2=C3/C1
            S3=C4/C1
            P=S2/3.0-S1**2/9.0
```

```
Q=S3-S1*S2/3.0+2.0*S1**3/27.0
Z=Q**2+4.0*P**3
IF(Z.GE.0.0) THEN
AZ=(-Q+SQRT(Z))*0.5
BZ=(-Q-SQRT(Z))*0.5
AM=ABS(AZ)
BM=ABS(BZ)
IF(AM.LT.1.0E-10) THEN
CA=0.0
ELSE
CA=AZ/AM
END IF
IF(BM.LT.1.0E-10) THEN
CB=0.0
ELSE
CB=BZ/BM
END IF
W=CA*AM**(1.0/3.0)+CB*BM**(1.0/3.0)-S1/3.0
ELSE
TH=ATAN(SQRT(-Z)/(-Q))
W=2.0*(-P)**0.5*COS(TH/3.0)-S1/3.0
END IF
RETURN
END
```

A.3 SI Units

A.3.1 Conversion Factors

Quantity	SI unit	Other unit	Inverse factor
Length	1 m = 1000 mm 1 cm = 10 mm 1 km = 1000 m	3.28084 feet (ft) 0.393701 inch (in) 0.539957 nautical mile (nm) 0.621371 mile	1 ft = 0.3048 m 1 inch = 2.54 cm 1 nm = 1.852 km 1 mile = 1.609344 km
Area	$1\ m^2$ $1\ mm^2$	$10.7639\ ft^2$ $0.00155\ in^2$	$1\ ft^2 = 0.09290304\ m^2$ $1\ in^2 = 645.16\ mm^2$
Volume	$1\ m^3$ $1000\ cm^3 = 1$ liter	$35.3147\ ft^3$ 0.219969 gal (UK) 0.264172 gal (US) 1 bushel (UK) = 8 gal (UK) 1 barrel (US) = 42 gal (US)	$1\ ft^3 = 0.0283168\ m^3$ 1 gal (UK) = 4.54609 liters 1 gal (US) = 3.78541 liters 1 gal (UK) = 0.125 bushel (UK) 1 gal (US) = 0.02381 barrel (US)
Mass	1 kg 1 mg 1 g	2.20462 pound (lb) 0.0154323 grain (gr) 0.035274 ounce (oz)	1 lb = 0.45359237 kg 1 gr = 64.79891 mg 1 oz = 28.3495 g

Quantity	SI unit	Other unit	Inverse factor
	1 tonne	0.984204 long tonne (LT) (UK) 1.10231 short tonne (ST) (US)	1 LT = 1.01605 tonne 1 ST = 0.907185 tonne
Velocity, speed	1 m/s = 3.6 km/h	3.28084 ft/s 2.23694 mile/h 1.94384 knot (kt) (meter system) 1.94260 knot (kt) (yard–pound system)	1 ft/s = 0.3048 m/s 1 mile/h = 0.44704 m/s 1 kt (meter system) = 0.514444 m/s 1 kt (Yard-Pound system) = 0.514773 m/s
Speed–length ratio	$1\ \frac{m/s}{\sqrt{m}}$	0.31933 Froude no. ($V/\sqrt{Lg}$) $1.94384\ \frac{kt}{\sqrt{m}}$ $1.07249\ \frac{kt}{\sqrt{ft}}$	1 Froude no. = $3.13156\ \frac{m/s}{\sqrt{m}}$ $1\ \frac{kt}{\sqrt{m}} = 0.51444\ \frac{m/s}{\sqrt{m}}$ $1\ \frac{kt}{\sqrt{ft}} = 0.93241\ \frac{m/s}{\sqrt{m}}$
Acceleration	$1\ m/s^2$	$100\ cm/s^2$(Gal) 0.101972 G	1 Gal = $0.01\ m/s^2$ 1 G = $9.80665\ m/s^2$
Density	$1\ kg/m^3$	3.61273×10^{-5} lb/in^3 1.00224×10^{-2} lb/gal (UK) 8.3454×10^{-3} lb/gal (US)	1 lb/in^3 = 2.76799×10^4 kg/m^3 1 lb/gal (UK) = 99.7764 kg/m^3 1 lb/gal (US) = 119.826 kg/m^3
Kinematic viscosity	$1\ m^2/s$	$10.7639\ ft^2/s$	$1\ ft^2/s = 9.2903 \times 10^{-2} m^2/s$
Force	1 N	0.101972 kgf 0.1 Mdyn 0.224809 lbf	1 kgf = 9.80665 N 1 Mdyn = 10 N 1 lbf = 4.44822 N
Pressure	1 Pa = $1\ N/m^2$ = 1.01972×10^{-5} kgf/cm^2	1.45038×10^{-4} lbf/in^2 (psi) 1.0×10^{-5} bar 9.86923×10^{-6} atm	1 psi = 6894.76 Pa 1 bar = 1.0×10^5 Pa 1 atm = 1.01325×10^5 Pa
Stress	1 N/mm^2 = 1 MPa = 0.101972 kgf/mm^2, 1 kgf/mm^2 = 9.80665 MPa		
	1 N/mm^2	145.038 lbf/in^2	1 lbf/in^2 = 6.89476×10^{-3} MPa
Impact value	1 J/cm^2 = 0.101972 kgf·m/cm^2	4.75845 lbf·ft/in^2	1 lbf·ft/in^2 = 0.210152 J/cm^2
Energy	1 J = 1 N·m, 1 kJ = 101.972 kgf·m, 1 kgf·m = 9.80665 J		
	1 kJ	737.563 lbf·ft 0.238889 kcal	1 lbf·ft = 1.35582×10^{-3} kJ 1 kcal = 4.18605 kJ
Power	1 kW = 101.972 kgf·m/s, 1 kgf·m/s = 9.80665×10^{-3}kW		
	1 kW	1.35962 PS (meter system) 1.34102 HP (yard–pound system) 737.562 lbf·ft/s 0.238889 kcal/s	1 PS (meter system) = 0.7355 kW 1 HP (yard–pound system) = 7.457×10^{-3} kW 1 lbf·ft/s = 1.35582×10^{-3} kW 1 kcal/s = 4.18605 kW
Temperature	$°C = (°F - 32) \times \frac{5}{9}$, $°F = °C \times \frac{9}{5} + 32$, $K = °C + 273.15$		

A.3.2 SI Unit Prefixes

Exa	(E) $= 10^{18}$	Deci	(d) $= 10^{-1}$
Peta	(P) $= 10^{15}$	Centi	(c) $= 10^{-2}$
Tera	(T) $= 10^{12}$	Milli	(m) $= 10^{-3}$
Giga	(G) $= 10^{9}$	Micro	(μ) $= 10^{-6}$
Mega	(M) $= 10^{6}$	Nano	(n) $= 10^{-9}$
Kilo	(k) $= 10^{3}$	Pico	(p) $= 10^{-12}$
Hecto	(h) $= 10^{2}$	Femto	(f) $= 10^{-15}$
Deca	(da) $= 10$	Atto	(a) $= 10^{-18}$

A.4 Density and Viscosity of Water and Air

Temperature (°C)	Density (kg/m^3)			Kinematic viscosity (m^2/s)		
	Fresh water	Salt water	Dry air	Fresh water	Salt water	Dry air
0	999.8	1028.0	1.293	1.79×10^{-6}	1.83×10^{-6}	1.32×10^{-5}
10	999.7	1026.9	1.247	1.31×10^{-6}	1.35×10^{-6}	1.41×10^{-5}
20	998.2	1024.7	1.205	1.00×10^{-6}	1.05×10^{-6}	1.50×10^{-5}
30	995.6	1021.7	1.165	0.80×10^{-6}	0.85×10^{-6}	1.60×10^{-5}

Index

Page numbers in italics, e.g. *10*, refer to figures. Page numbers in bold, e.g. **13**, indicate entries in tables.